Ultrathin and nanowire-based GaAs solar cells

Hung-Ling Chen

université PARIS-SACLAY

NNT: 2018SACLS355

Thèse de doctorat

UNIVERSITÉ PARIS SUD

Comprendre le monde, construire l'avenir®

Ultrathin and nanowire-based GaAs solar cells

Thèse de doctorat de l'Université Paris-Saclay
préparée à l'Université Paris-Sud

École doctorale n° 575: electrical, optical, bio-physics and engineering (EOBE)
Spécialité de doctorat: électronique et optoélectronique, nano- et microtechnologies

Thèse présentée et soutenue à Palaiseau, le 16 octobre 2018, par

M. Hung-Ling Chen

Composition du jury:

M. Jean-Jacques Greffet Professeur, IOGS, France	Président du jury
M. Marko Topič Professeur, University of Ljubljana, Slovénie	Rapporteur
M. Nicolas Chauvin Chargé de Recherche, INL, France	Rapporteur
M. Henri Mariette Directeur de recherche, Institut Néel, France	Examinateur
M. Oliver Höhn Chercheur, Fraunhofer ISE, Allemagne	Examinateur
M. Stéphane Collin Chargé de Recherche, C2N-CNRS, France	Directeur de thèse
M. Andrea Cattoni Chargé de Recherche, C2N-CNRS, France	Co-encadrant de thèse

夸父與日逐走，入日，渴欲得飲，飲於河、渭。河、渭不足，北飲大澤。未至，道渴而死。棄其杖，化為鄧林。

《山海經》

In antiquity, a God named Kua Fu determined to chase the Sun. Afterward, he almost caught the Sun while he was too thirsty to continue, draining the Yellow River and the Wei River. As he marched to search for the Great Lake, he died of dehydration at halfway. Finally, his wooden cane grew into a vast forest of peach trees.

"Classic of Mountains and Seas"

Acknowledgements

After several years of studying and fastidious exams on maths and physics at the *classe préparatoire* and École polytechnique, I had the chance to get to know *Laboratoire de Photonique et de Nanostructures* (LPN, previous name of C2N)—far from RER train stations, where *Marcoussian* people make beautiful devices and do science in a realistic way. I have been fascinated by the intriguing properties of light and the great potential of sunlight to power the worldwide electricity needs, so this PhD thesis fits very well my curiosity and my scientific background. Therefore, I would like to give my first thanks to my supervisor: Stéphane Collin, who accepted me firstly as an internship student in Spring 2014, and then proposed a thesis subject for Autumn 2015. Thank you for the freedom you gave me and for the scientific supports, especially during the revision of my thesis manuscript and the preparation before the final presentation. I apologize to have made you read pieces of the manuscript during your summer holidays when you were on the mountain! I have learned a lot from numerous interactions and discussions with you: either "constructive" light trapping for new limits with multi-resonant absorption, or "destructive" photonic bandgap narrowing of voltage penalty!

I would also like to express my special thanks to Andrea Cattoni—an expert on nanoimprint and nanofabrication, who helped me a lot in the clean room to improve the fabrication process. Thank you for the insightful suggestions when I struggled with the disordered slides of presentation and for being the impartial "judge" between me and Stéphane! A particular thanks goes to Laurent Lombez, with whom I did the M2 internship at IRDEP in Spring 2015, just before my PhD started. I learned from the *médecin des cellules solaires* ("medical doctor" of solar cells in French) the practical diagnostics of solar cells (i.e. IV curves and EQE) and the useful method in luminescence characterization. I also appreciate the discussions with Jean-François Guillemoles, who always offered constructive and decisive points of view. I remember very well Erik Johnson, Martin Foldyna and Pere Roca i Cabarrocas for their clear and inspiring photovoltaic courses at École polytechnique. I would like to express my gratitude to the referees of my thesis: Prof. Marko Topič and Dr. Nicolas Chauvin for their great attention on reviewing the thesis, and to all the other jury members: Prof. Jean-Jacques Greffet, Dr. Henri Mariette and Dr. Oliver Höhn for the kind acceptance and fruitful discussions we had. Thank you all for taking your precious time and bring up valuable questions in the PhD defense, which certainly opened interesting and new challenges for the future.

The research work in laboratories is an occasion for me to work closely with many brilliant people. First, I would like to thank Nicolas Vandamme, who taught me the methods of characterization in our home-made VISIR dark room and guided me in the big clean room of Marcoussis. At the beginning, I knew nothing about experiments or clean room process, so it was really nice of him to teach me step by step. Alexandre Gaucher also helped me a lot to use the equipment for characterization and provided useful and practical suggestions. Later on, Julie Goffard helped me to get familiar with the new VISIR setup: improved photocurrent measurement by Fourier transformation and the one sun measurement. Benoît Behaghel always gave straightforward remarks. We collaborated closely while he was away in Japan and he even sent samples of solar cells back to France. I also appreciate the time spent working with Pierre Rale when we aligned

laser at IRDEP, as well as dealt with the new cathodoluminescence setup at C2N.

I also recall a lot of people in our team, in particular PhD students who will certainly make further the scientific contributions: Romaric De Lépinau for fabricating even more efficient nanowire solar cells, Louis Gouillart for ultrathin CIGS solar cells and Thomas Bidaud for cathodoluminescence characterization. There are people I met (nearly) every Monday morning in the group meeting: Daniel Pelati, Amadeo Michaud, Ahmed Ben Slimane, Jérôme Michallon, and so on. I would like to thank Andrea Scaccabarozzi for his good humor and for offering plenty of interesting nanowire samples. The collaborations with the material department of C2N: Fabrice Oehler, Aristide Lemaître and Jean-Christophe Harmand were full of surprising results. I would like to thank Chalermchai Himwas and Maria Tchernycheva for collaborating and sharing their techniques with me in order to understand nanowire properties. I would like to acknowledge all the people whom I had the chance to work with: Alexandre Jaffre and Charles Renard for GaAs microcrystals; Amaury Delamarre, Maxime Giteau, Kentaroh Watanabe and Masakazu Sugiyama from NextPV Japan/France joint lab for fabrication of ultrathin GaAs solar cells; Oliver Höhn and Frank Dimroth from Frauhnofer ISE for providing high-quality III-V epitaxial layers.

I would like to give my special thanks to Christophe Dupuis for my training on the electronic microscope and for the valuable instructions on nearly every fabrication steps in the clean room! He has been very generous with his time giving me encouraging and inspiring words. Assistance provided by Nathalie Bardou on chemistry, etching and lithography was very helpful. I would like to thank all the staffs who work in the clean room: Abdelmounaim Harouri for photolithography; Laurent Courant, Laetitia Leroy, Alan Durnez and Xavier Lafosse for metal and dielectric deposition. I want to thank people from the IT service, particularly Alain Péan for his kind and prompt assistance, and also people in the administration who have been taking care of my visa application, the PhD contract, the missions, and so on.

Besides my research work, I am immensely grateful to my family for unconditionally supporting me to study abroad and follow what I love to do. I would also like to show my warm gratitude to my high school teachers for their excellent mentorship. It has had an enormous influence on my personal and scientific development. I recall my friends from my high school in Taiwan and the classmates I met in Taiwan or in France. They are now all around the world working in different fields, so that we have the chance to share very different experiences with each other and talk about the cultural shock we have encountered. Finally, I would like to express my deepest appreciation to my wife: 黃莉雯 (Huang Li-Wen), with whom I shared frustrating moments after failed experiments, as well as joyful moments of day-to-day life. I really valued those wonderful time. I hope we can go further and grow stronger together in life and in work.

陳紘翎 (Chen Hung-Ling), October 2018

Contents

General introduction

Solar energy is one of the most abundant nature resources, and its conversion into electrical power source can meet the ever-increasing demand of electricity and the need for a renewable energy system. The worldwide installation of solar panels increases rapidly, and commercial photovoltaic modules of efficiency over 20% are already available. For large-area use, the photovoltaic industry is looking for new solutions to further increase the efficiency and decrease the cost of solar cells. One of the main trends is to use thinner and thinner Si wafers in solar photovoltaic panels. The thickness of thin-film photovoltaics (CIGS, CdTe, III-V, etc.) is also decreased steadily to save scarce materials such as indium and tellurium. Using thinner semiconductor layers also favors the fabrication of light-weight or flexible devices suited for numerous niche applications, and lead to higher radiation tolerance for space power applications. In other words, decreasing the absorber thickness in photovoltaics is a way to consume less material and to support new applications. It may also provide new routes toward high efficiency photovoltaics.

Solar cells convert sunlight into electricity based on the photovoltaic effect, involving various disciplines like optics, material science and solid states physics. Recent developments take advantage of research advances in other optoelectronic devices, in materials, and in nanophotonics. For instance, decreasing the solar cell thickness requires nanophotonic light-trapping structures to compensate for the lower absorber volume and to maintain a high photocurrent generation. Such nanostructures can be implemented in the fabrication process of solar cells thanks to the recent technological progress of the semiconductor industry and research laboratories. The emergence of large-area and low-cost nanofabrication processes, like nanoparticle self-assembly and nanoimprint lithography, are of particular interest for the photovoltaic industry. Light confinement in nanostructures results in higher photogenerated carrier densities, and may also provide new opportunities to explore novel concepts for high-efficiency, like intermediate-band or hot-carrier solar cells.

Recent advances in material science are another source of innovation for the improvement of photovoltaic devices. Low-dimensional semiconductors like 2D materials, quantum structures, and nanowires, for instance, bring new solutions to create semiconductor heterostructures and to assemble various semiconductor compounds into a single photovoltaic devices. In this context, the ability to growth perfect low-dimensional crystals on lattice-mismatched substrates is of particular interest. Single semiconductor nanostructures like nanowires are also an attractive platform to investigate the fundamental mechanisms related to high carrier densities, or to the passivation and collection of carriers at the nanoscale. The understanding of these mechanisms may serve many photovoltaic technologies, for instance polycristalline thin films made of submicrometer grains (with major challenges in grain boundary passivation), and hot-carrier solar cells that are made of ultrathin absorbers and selective contacts.

In the following, we focus on III-V semiconductors, and more particularly on GaAs-based solar cells and nanostructures. GaAs is chosen as a model material to explore high-efficiency photovoltaic devices with a reduced volume of active material. Thanks to their high quality and the well-controlled fabrication processes, GaAs thin films are the core of the record single-junction

solar cells which reached 28.8% efficiency. III-V materials have also allowed the development of high-efficiency multi-junction solar cells (three- and four-junction solar cells with efficiencies up to 46%), and have been used for the most recent advances of high-efficiency concepts. For these reasons, III-V are materials of choice to explore new concepts for light-trapping, for the direct growth of semiconductor nanostructures on lattice-mismatched substrates (Si in particular), or for the investigation of material properties and electronic transport in semiconductor nanostructures.

In this thesis, I have studied two approaches separately. The first one uses 200 nm-thick ultrathin GaAs absorber, corresponding to a tenfold thickness reduction as compared to state-of-the-art thin-film GaAs solar cells. To achieve record efficiency, we propose a periodic nanostructured back mirror for efficient light harvesting in the ultrathin GaAs layer. The second approach aims to use nanowires as the active solar cell absorber. Semiconductor nanowires constitute a completely different domain of nanotechnology. The unique shape of nanowires exhibits light-trapping properties for next-generation photovoltaics. Moreover, III-V nanowires can be grown on lattice-mismatched Si substrates instead of the more expensive GaAs or InP substrates. I mainly focus on modeling and characterization in order to understand nanowire properties and growth mechanisms. The organization of this manuscript is as follows:

In Chapter 1, I give an introduction on solar cell operation and an overview of photovoltaic research areas, and I present our motivations toward low-cost and high-efficiency solar cells. Chapter 2 describes essential theoretical background to understand the operation principle of a solar cell. This includes electromagnetic wave optics in one part, and physics of semiconductors in the second part. These theories provide a solid basis to design and analyze solar cell devices. Chapter 3 summarizes the theory of luminescence and describes the cathodoluminescence (CL) setup at C2N. Throughout this thesis work, I use extensively the CL tool to characterize the properties of semiconductor nanowires. The concept of light emission is also governing many aspects of this thesis. For instance, the detailed balance principle of light absorption and emission leads to the fundamental limit of photovoltaic conversion efficiency, which provides a guideline for researchers to improve the efficiency of solar cells.

In Chapter 4, I present my work on of ultrathin GaAs solar cells. Theoretically, we show optical simulations of ultrathin solar cell structures with a metallic back grating reflector and we investigate the mechanisms of multi-resonances. We also use 1D electrical transport simulations as well as a simple analytical model of resistive losses to identify the optimal design of ultrathin GaAs solar cells. Concerning experimental works, detailed fabrication steps and characterization are shown. We present the analysis of current-voltage characteristics and spectral responses, and we compare the results with theoretical calculations in order to further improve the efficiency.

In the second part of the thesis work, we focus on the use of GaAs nanowires as a potential photovoltaic absorber. Toward efficient III-V nanowire solar cells, several challenges arise in the research of semiconductor nanowires. One of the issues is to characterize the doping at the nanoscale. In Chapter 5, I propose an advanced contactless and quantitative doping assessment method based on the luminescence analysis using the generalized Planck's law. Hall effect measurements and CL measurements are compared on a series of GaAs thin-film samples at different doping levels in order to validate the doping assessment method by cathodoluminescence. In Chapter 6, we present CL measurements on GaAs nanowires grown in C2N. We demonstrate both p-type and n-type doping assessments in single GaAs nanowires by CL. By accident, we also discover systematically an usual wurtzite GaAs segment in single GaAs nanowires. The optical properties of undoped, Be-doped and Si-doped wurtzite GaAs are studied by CL polarimetry.

Finally, Chapter 7 is dedicated to the description of nanowire-array solar cells. We study the

optical absorption in ordered GaAs nanowire arrays, and we calculate the electrostatic built-in potential in core-shell p-n junctions as a function of the nanowire doping levels. These results provide a reasonable design guideline for high-efficiency nanowire solar cells. At the end, we show the recent progress of nanowire solar cell performances at C2N.

I would like to detail here my contribution to the work presented in this manuscript. The optical simulations of Chapter 4 (ultrathin solar cells) and Chapter 7 (nanowire array solar cells) have been performed by myself with the Reticolo code supplied by Philippe Lalanne from LP2N (Laboratoire Photonique, Numérique et Nanosciences) and Christophe Sauvan from IOGS (Institut d'Optique Graduate School). I adapted part of the Reticolo code to compute the rate of photogeneration in solar cells by integrating the absorbed radiation power over the solar spectrum. I also conducted electrical simulation for ultrathin solar cells using the integrated photogeneration rates as inputs to SCAPS-1D solar cell device simulator (Burgelman and coworkers, University of Gent, Belgium). For nanowire solar cells, I implemented a numerical solver with Matlab code to compute the built-in potential in nanowire core-shell junction.

In Chapter 5 and 6, all the CL measurements and analysis presented are carried out by myself, with the help of Pierre Rale and Stéphane Collin at the beginning of my thesis work to get used to the new CL system in C2N. I developed hyperspectral data analysis and systematic CL mapping visualization with Matlab code, and I adapted the generalized Planck's law to fit the whole CL spectra for quantitative doping assessment. I also proposed polarization-resolved CL experiments to investigate the optical properties of wurtzite GaAs. Epitaxial thin-film GaAs samples were provided by Aristide Lemaître and Hall measurements on thin-film GaAs were conducted by Romaric De Lépinau and Andrea Scaccabarozzi (C2N). III-V semiconductor nanowires were grown by several people in the Material Department at C2N: Fabrice Oehler, Chalermchai Himwas, Andrea Scaccabarozzi and Romaric De Lépinau. This part of the work aims to understand the fundamental material properties, and was performed in interaction with nanowire-related projects supervised by Maria Tchernycheva and Jean-Christophe Harmand.

Regarding the fabrication of ultrathin GaAs solar cells presented in Chapter 4, the epitaxy of the GaAs layers as well as double-layer MgF_2/Ta_2O_5 anti-reflection coating have been done at the Fraunhofer Institute for Solar Energy Systems (ISE). I did nearly every other steps of the solar cell processes: photolithography, wet etching, metal deposition and lift-off, bonding and substrate removal. I also realized the nanoimprint lithography with the help of Andrea Cattoni. Solar cell current-voltage measurements, spectral responses (EQE) as well as data analysis were performed by myself.

For nanowire-based solar cells presented in Chapter 7, I contributed mainly to the early-stage material qualities and doping characterizations. I carried out optical and electrical modeling to target the geometry and doping levels required in a core-shell junction nanowire solar cells. Continuous experimental work had been done at C2N by Andrea Cattoni for patterned Si substrates using electron-beam lithography, Andrea Scaccabarozzi for epitaxial growth of III-V nanowire arrays, and Romaric De Lépinau for improved device fabrication. This work has been done within the ARN project NANOCELL for efficient GaAs nanowire solar cells and IPVF project E for III-V nanowire solar cells on Si.

Chapter

1 Introduction

Chapter content

According to the International Energy Agency (IEA)[1], in 2015, the world total primary energy supply (TPES) is 13 647 Mtoe (million tonnes of oil equivalent, 1 toe = 11 630 kWh). The energy supply still relies on fossil fuels such as oil (31.7%), coal (28.1%) and natural gas (21.6%). Part of these primary sources are used to generate electricity. The total electricity production was 24 255 TWh in 2015, including renewable generations such as hydroelectricity production 3 978 TWh (16.4%), wind energy production 838 TWh (3.5%) and solar photovoltaic electricity production 247 TWh (1.0%). In 2017, the worldwide photovoltaic electricity production increases up to 443 TWh and the cumulative installation rises to 415 GW according to recent photovoltaics report[2]. Nowadays, transition toward renewable energy is urgent to lower the dependence on limited fossil resources and to reduce emission of CO_2 which is responsible for greenhouse effect.

Solar energy is an abundant natural resource. If we take the power density of 1000 W/m^2 that the Sun illuminates the Earth, with projected cross-section of 1.275×10^{14} m^2 (Earth radius is 6371 km), the Earth will capture the energy of 2015 world total primary energy supply in less than 2 hours! Of course, transforming efficiently the sunlight into useful forms of energies such as electricity is not so easy, and we cannot cover the whole surface of the Earth by solar panels. But still, with 20% solar panel efficiency to convert sunlight into electricity and 1% of the projected Earth surface, 4 days are enough to collect the total electricity production of a whole year. Solar cell researches have led to important technical progress and allowed world-wide photovoltaic electricity generations toward future sustainable energy system.

1.1 Solar spectrum

Figure 1.1(a) sketches the situations of sunlight arriving at the ground surface of the Earth. We observe the solar disc with an angular diameter of about 0.53° (half-angle $\theta = 0.266°$). For a solar panel oriented toward the sun, nearly all direct sunlight comes perpendicularly. Beside

[1] International Energy Agency (IEA): http://www.iea.org/

[2] Simon Philipps, Fraunhofer ISE and Werner Warmuth, PSE Conferences & Consulting GmbH (Last updated: June 19, 2018): https://www.ise.fraunhofer.de/en/publications/studies/photovoltaics-report.html

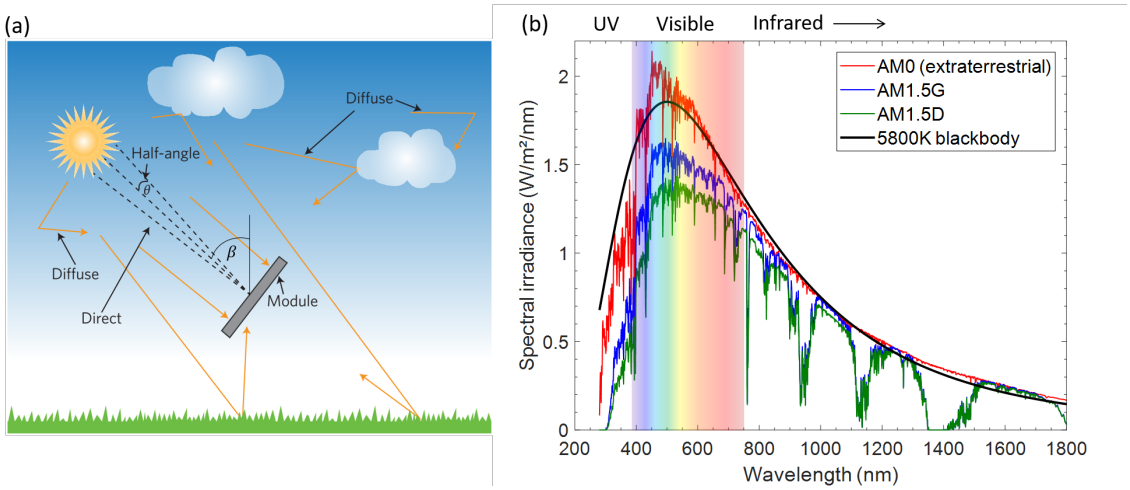

Figure 1.1 – *(a) Solar angles and atmospheric effects in the received sunlight on Earth, showing direct and diffuse components, ground reflection, minimum acceptance angle θ and solar zenith angle β (Figure adapted from Ref. [1]). (b) Reference solar spectral irradiance from American Society for Testing and Materials (ASTM G173)[3]. Red curve shows the extraterrestrial solar radiation (AM0) and black curve is the blakebody radiation spectrum calculated at 5800 K (normalized to an integrated power of 1366 W/m^2). Blue curve is the global spectral radiation from the solar disk plus diffused component (AM1.5G, integrated power 1000 W/m^2). Green curve is the direct normal irradiance from the solar disc (AM1.5D, integrated power 900 W/m^2). Colored background marks the spectral positions of visible light around 380 nm to 750 nm.*

direct sunlight, diffuse light can also strike on a solar panel. In sunny days, we see clear blue sky because small molecules in atmosphere scatter light at short wavelengths efficiently. This is also why the sun looks yellow and becomes reddish at sunrise or sunset. When direct sunlight travels a thicker atmosphere, most blue-green part of the solar spectrum is scattered off. The cloud looks white because bigger molecules (e.g. ice/water particles and aerosols) scatter light equally in wavelengths, and may strongly attenuate sunlight in cloudy days. The light we receive at the ground will depend on time, location, weather or season and so on.

Reference sunlight radiations are defined in order to standardize performance measurement of solar cells. They are shown in Figure 1.1(b). The *Air Mass* (AM) defines the direct light path length through the atmosphere, expressed as a ratio to the light path length at the zenith. We denote β the zenith angle of the sun, then AM $= 1/\cos(\beta)$. Air Mass 1.5 is chosen as standard test condition for terrestrial solar cells. AM1.5D is for direct component of sunlight (integrated power 900 W/m^2), and AM1.5G includes for direct and diffuse components (integrated power 1000 W/m^2). AM0 is referred to the solar radiation on top of the atmosphere for space solar cell evaluation. The solar radiation can also be approximated by a blackbody radiation of 5800 K, which is approximately the surface temperature of the sun (black curve in Figure 1.1(b)).

1.2 Solar cell operations

Figure 1.2(a) shows a typical solar cell structure. The active region that absorbs light is usually made of a crystalline semiconductor p-n junction. Here, the front or top side of the solar cell is opened to receive the sunlight, and the structure consists of n-type emitter and p-type base. Thereafter, the front contact grid is a cathode and the rear contact is an anode. The top surface is usually covered with anti-reflection coating (ARC) to reduce reflection of light thus maximize

[3] ASTM G173-03 spectra: https://rredc.nrel.gov/solar/spectra/am1.5/ASTMG173/ASTMG173.html
[4] PVEducation: https://pveducation.org/

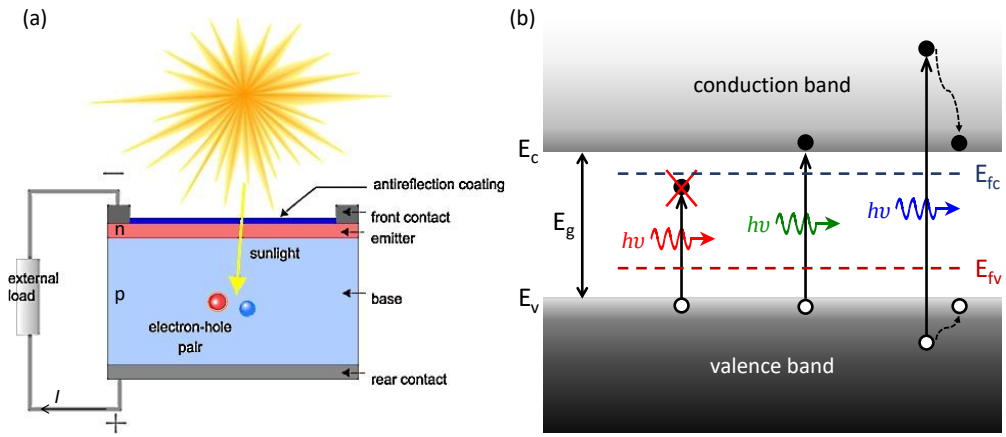

Figure 1.2 – *(a) Typical solar cell structure using a semiconductor p-n junction (p-base and n-emitter) with front contact electrode (cathode) and rear contact electrode (anode). Under sunlight illumination, the solar cell generates electricity and power the external load (Figure adapted from PVEducation[4]). (b) Schematic energy diagram of a semiconductor (bandgap E_g). A photon with energy $h\nu < E_g$ is not absorbed by the semiconductor. The absorption of a photon with energy $h\nu \geq E_g$ will generate an electron-hole pair, but the excess photon energy $E_g - h\nu$ is lost due to thermalization of electrons and holes to the band edges E_c and E_v, respectively. The quasi-Fermi levels E_{fc} and E_{fv} characterize the electrochemical potential of electrons and holes, respectively.*

the number of photons entering the solar cell. Under illumination, the solar cell can power the external load connected to it.

Figure 1.2(b) depicts the situations when a photon arrives in the active region of a semiconductor. The photons with energies $h\nu$ smaller than the bandgap E_g of the semiconductor cannot be absorbed. The photons with energies $h\nu$ equal or higher than the bandgap E_g can be absorbed to generate an electron-hole pair in the semiconductor. If the photon energy $h\nu$ is higher than the bandgap E_g, the initially created electron (resp. hole) is above the conduction band (resp. below the valence band), but is rapidly thermalized to the band edges. The thermalization process is mainly due to energy lost to vibrations of the crystal lattice (phonons) and happens in a time scale of 10^{-12} s [2]. Under steady-state illumination, an excess population of electrons and holes is maintained in the semiconductor and two different *quasi-Fermi levels* F_{fc} and F_{fv} are used to described the electrochemical potential of electrons and holes, respectively.

The solar cell operation is characterized by its current-voltage curve. Figure 1.3(a) gives an equivalent electrical circuit of a solar cell and Figure 1.3(b) shows the current-voltage (JV) curve (black solid line). The total electrical current I delivered by the solar cell is normalized to its surface area so we use systematically current density J with the unit of mA/cm^2. Here we adapt the convention for a generator so that $V > 0$ and $J > 0$ correspond to positive power generated by the solar cell. The solar cell is modeled by several components:

- an ideal (photo-)current generator J_{ph},
- a rectifying diode (with diode ideality n) to ensure the photogenerated current is flowing in one direction and not the opposite,
- a parallel resistance R_p taking into account the non-ideal rectifying effect or equivalently the existence of an ohmic shunt,
- a series resistance R_s for resistive losses in the solar cell.

It is assumed that the current under illumination $J_{\text{light}}(V)$ is the sum of a constant net photogenerated current J_{ph} and the current $J_{\text{dark}}(V)$ measured in dark with the same bias voltage. This is the so-called *principle of superposition*, which is a good approximation for p-n

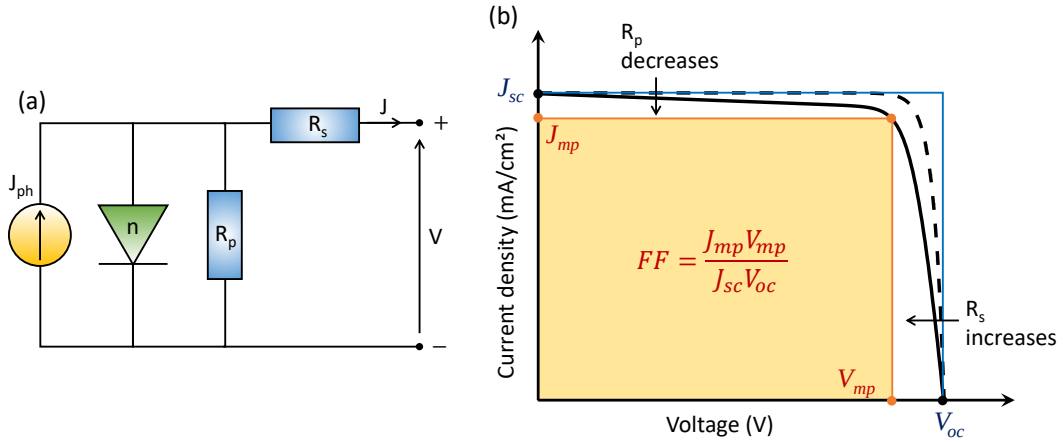

Figure 1.3 – *(a) Equivalent electrical circuit of a solar cell, including a current generator (photocurrent J_{ph}), a rectifying diode (ideality factor n), parallel resistance R_p and series resistance R_s. (b) Current-voltage (J-V) characteristic of a typical solar cell (black solid line). J_{sc} is the short-circuit current density and V_{oc} the open-circuit voltage of the solar cell. The maximum power (mp) point is where the output power JV is maximal (orange zone). Fill factor (FF) of the solar cell is the ratio of $J_{mp}V_{mp}$ divided by $J_{sc}V_{oc}$. The black dashed line shows the J-V characteristic of the ideal solar cell. Increasing R_s and decreasing R_p will lower the FF and result in apparently different slopes near V_{oc} and J_{sc}, respectively.*

homojunction solar cells. This is written as

$$J_{\text{light}}(V) = J_{ph} + J_{\text{dark}}(V) \tag{1.1}$$

Note that $J_{\text{dark}}(V)$ is negative with the convention of generator, because the solar cell in dark absorbs power from the measurement instrument. The dark current is connected to the diode characteristics n and parasitic resistances R_p and R_s through

$$J_{\text{dark}} = -J_0 \left[\exp\left(\frac{q(V + R_s J_{\text{dark}})}{nk_BT}\right) - 1\right] - \frac{V + R_s J_{\text{dark}}}{R_p} \tag{1.2}$$

where k_B is the Boltzmann constant and T the absolute temperature. For an ideal solar cell, we have an diode ideality $n = 1$, infinite parallel resistance and zero series resistance. The current-voltage characteristic of the ideal solar cell under illumination is simply given by

$$J(V) = J_{ph} - J_0 \left[\exp\left(\frac{qV}{k_BT}\right) - 1\right]. \tag{1.3}$$

In Figure 1.3(b), the black dashed line is an ideal JV curve and the black solid line is a perturbed JV curve by a finite parallel resistance and non-zero series resistance. The short-circuit current density (J_{sc}) and the open-circuit voltage (V_{oc}) are indicated. We denote (J_{mp},V_{mp}) the current and voltage of the solar cell operating at the maximum power point. The fill factor (FF) of the solar cell is defined by the maximum output power divided by the product $J_{sc}V_{oc}$.

$$FF = \frac{J_{mp}V_{mp}}{J_{sc}V_{oc}}. \tag{1.4}$$

The efficiency η of the solar cell is the power density generated at the maximum power point divided by the power density of the incident light P_{in} (100 mW/cm^2 for 1 sun AM1.5G reference spectrum).

$$\eta = \frac{J_{mp}V_{mp}}{P_{in}} = \frac{J_{sc}V_{oc}FF}{P_{in}} \tag{1.5}$$

In Figure 1.3(b), we can see the effect of resistances on the JV characteristics of the solar cell. J_{sc} and V_{oc} are not influenced by a small change in non-ideal resistances. A finite R_p (ohmic shunt) gives rise to an apparent slope near J_{sc}, and a non-zero R_s results in a less steep slope near V_{oc}. Finite R_p and parasitic R_s thus affect the FF and lower the efficiency of solar cells.

1.3 Overview of photovoltaic technologies

Figure 1.4 shows the up-to-date efficiencies of solar cells as a function of the bandgap of the material used. The lines plot the Shockley-Queisser (SQ) limit (see Chapter 3.3), which predicts the upper limit of the photovoltaic conversion efficiency using a single bandgap semiconductor (solid line: 1 sun illumination, dashed line: 46 200 full concentration). The J_{sc} of a single junction solar cell depends on its ability to absorb photons from the solar spectrum. If absorption of one photon generates only one electron-hole pair in the semiconductor, then the maximum J_{sc} is limited by the bandgap of the semiconductor.

On the other hand, the V_{oc} of a solar cell is given by the difference in the electrochemical potential of electrons and holes

$$qV_{oc} = E_{fc} - E_{fc}. \tag{1.6}$$

With increased bandgap of the material, the upper limit of V_{oc} is increased, but the total photon absorption and thus J_{sc} decreases. As a consequence, there is a trade-off between current and voltage that governs the fundamental limit of photovoltaic conversion efficiency. With increasing sunlight intensities, a larger separation of quasi-Fermi levels leads to higher voltage, thus higher efficiency.

Figure 1.5 is the 2017 efficiency chart of research solar cells classified by materials and types from *National Renewable Energy Laboratory* (NREL). The efficiency progress with years is impressive, owning to technical efforts and understanding in material science. We summarize shortly each photovoltaic domain in the following.

1.3.1 Wafer-based silicon solar cells

Crystalline silicon (c-Si) is the most matured semiconductor technology used for the production of solar cells. Contrary to amorphous silicon (a-Si), c-Si is the crystalline forms of silicon and can be further distinguished between mono-crystalline silicon (mono-Si or single-crystal Si, continuous crystal) and multi-crystalline silicon (multi-Si or poly-Si, small crystals separated by grain boundaries). The state-of-art c-Si solar cell efficiency is 26.7% (Kaneka) using interdigitated back contacts and high-quality a-Si:H/c-Si heterojunction passivation (J_{sc} = 42.65 mA/cm^2, V_{oc} = 0.738 V, FF = 0.849) [3, 4]. Commercial mono-Si solar panels with efficiency between 19% to 22% are already available in the market, for example, Panasonic HIT (heterojunction with intrinsic thin-layer)[6], LG NeON n-type mono-crystalline[7] and SunPower back contact modules[8]. For commercial multi-Si panels, typical efficiency is found between 16% to 19%. Fabrication of multi-Si solar cells is cheaper than mono-Si solar cells because mono-Si wafers require a re-crystallization step (Czochralski process) which is very energy-consuming.

1.3.2 Thin-film and emerging technologies

Unlike c-Si using thick wafer (160–190 μm) to absorb sunlight, thin-film technologies use direct bandgap semiconductors so that a few μm are enough to absorb sunlight. These materials include

[5] NREL, photovoltaic research: https://www.nrel.gov/pv/
[6] Panasonic solar: https://panasonic.net/ecosolutions/solar/
[7] LG solar: http://www.lg-solar.com/
[8] SunPower: https://us.sunpower.com/

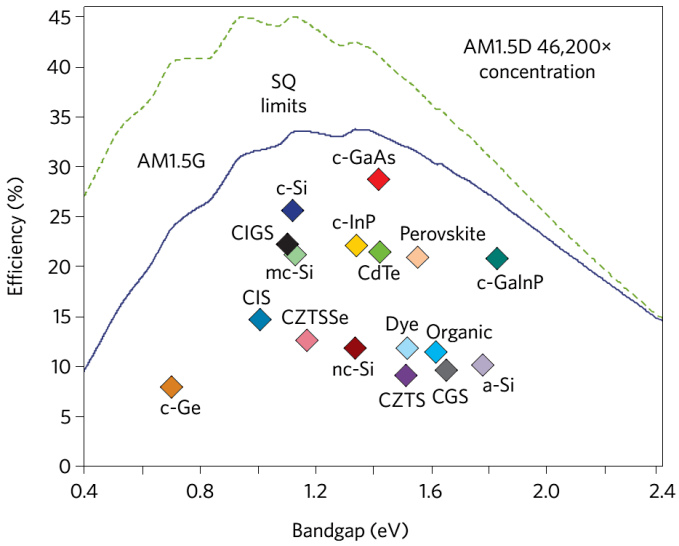

Figure 1.4 – *Shockley-Queisser limit of the conversion efficiency for single-junction solar cells as function of the bandgap. Solid line: efficiency limit with AM1.5G 1 sun illumination. Dashed line: efficiency limit with 46 200× AM1.5D full concentration. State-of-art solar cell efficiencies at 1 sun are marked by points for different materials (Figure extracted from Ref. [1]).*

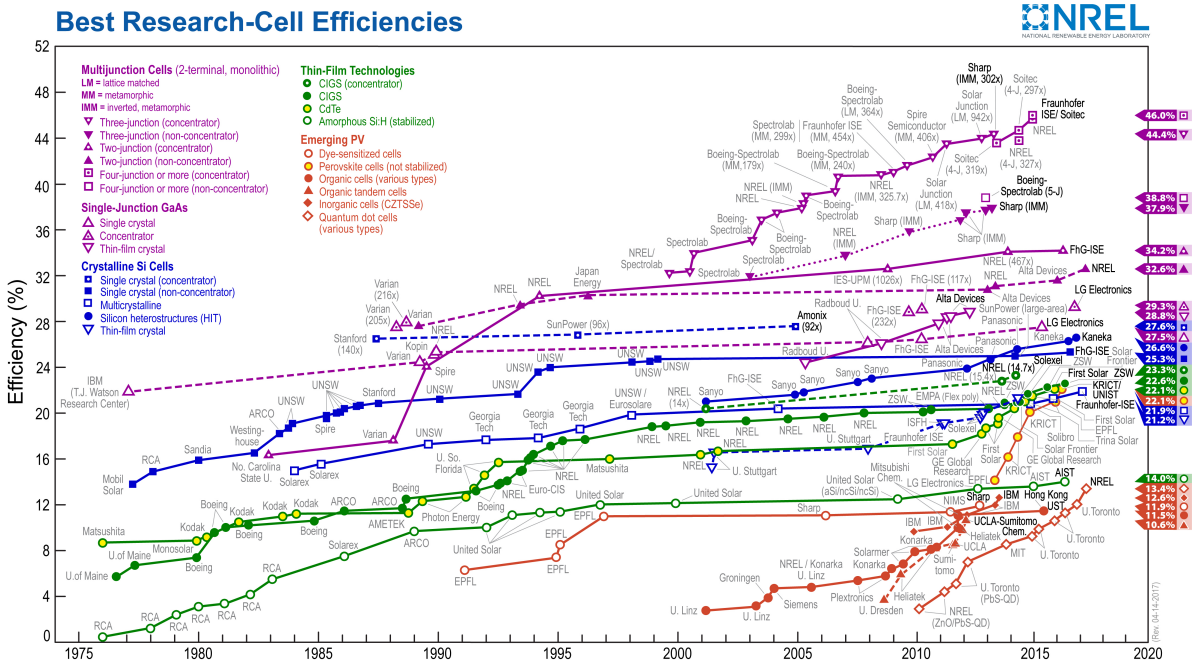

Figure 1.5 – *Efficiency evolution of best research photovoltaic cells*[5]*. They are classified by materials: single- and multi-junction III-V semiconductors for high-efficiency cells, crystalline silicon based solar cells, thin-film technologies (chalcogenides, amorphous silicon) and other emerging photovoltaic cells (organic solar cells, perovskite, etc.)*

copper indium gallium diselenide (CIGS), cadmium telluride (CdTe), amorphous silicon (a-Si) thin-film III-V compounds and so on.

CIGS and CdTe

CIGS solar cells are usually fabricated using ZnO/CdS/CIGS heterojunction. Up-to-date record efficiency of laboratory cell is 22.6% at 1 sun from ZSW (Germany) using heavy alkali elements post treatment for CIGS absorber [5], and later 22.9% demonstrated by Solar Frontier (Japan)[9]. Because of the toxicity of cadmium element, Solar Frontier also develops CIGS solar cells with Cd-free buffer layers and shows 22.0% cell efficiency and near 20% efficiency for mini modules at 1 sun [6]. Commercial Solar Frontier module efficiency is about 16% to 19% at 1 sun. Due to scarcity of indium element, large-area CIGS solar panel may still not be competitive with c-Si modules. Indium-free chalcogenide thin-film like CZTS (copper zinc tin sulfide/selenide) is also investigated in laboratories. State-of-art CdTe thin-film solar cells have 22.1% efficiency at 1 sun demonstrated by First Solar (USA)[10], who provides commercial modules of efficiency in the 15% to 18% ranges and may be more tolerant than c-Si under high temperature operation.

III-V semiconductors and multijunction solar cells

III-V compound semiconductors are grown by epitaxy to make high-efficiency thin-film solar cells. For example, GaAs is up-to-now the most efficient material to make a single junction solar cell, with efficiency up to 28.8% at 1 sun ($J_{sc} = 29.68\,\mathrm{mA/cm^2}$, $V_{oc} = 1.122\,\mathrm{V}$, $FF = 0.865$) [7]. Without being exhaustive, there are also InP solar cells with efficiency of 24.2% at 1 sun ($J_{sc} = 31.15\,\mathrm{mA/cm^2}$, $V_{oc} = 0.939\,\mathrm{V}$, $FF = 0.826$) [4], and GaInP with efficiency of 20.8% ($J_{sc} = 16.0\,\mathrm{mA/cm^2}$, $V_{oc} = 1.455\,\mathrm{V}$, $FF = 0.893$) [8].

Because of a wide variety of III-V compounds and alloys, it is possible to grow several junctions with different bandgaps in a well controlled manner. Since high-energy photons tend to be absorbed near the top surface of semiconductors, stacking high-bandgap material at the top allows to absorb high-energy photons and to prevent their thermalization losses. Low-energy photons pass through the top junction and are absorbed deeper in the low-bandgap materials. These III-V multijunction solar cells provide higher efficiencies beyond the SQ limit. The simplest way to contact multijunction solar cells is through a two-terminal configuration, i.e. each junction is connected in series using a tunnel junction. In this case, the operation current will be limited by the lowest current delivered by one of the junctions. The condition for current matching in all the individual junctions is critical for optimal power generation and requires careful design for the choice of material types and thicknesses. State-of-art two-junction GaInP/GaAs shows 32.8% efficiency at 1 sun (LG), and three-junction InGaP/GaAs/InGaAs has 37.9% efficiency at 1 sun (Sharp) [9].

Combining III-V semiconductors onto c-Si industry is a promising future technology breakthrough. Since III-V compounds provide better optical characteristics and also high electron mobility and high-frequency response, it is appearing not only for photovoltaics but also in other semiconductor-on-insulator (SOI) platform. Essig et al. demonstrated 1-sun efficiency of III-V on Si solar cells to 32.8% (GaInP/Si) and 35.9% (GaInP/GaAs/Si), using mechanical stacking to transfer III-V cells grown on GaAs substrate onto Si bottom cells in a 4-terminal configuration [10]. Cariou et al. demonstrated III-V-on-silicon (GaInP/GaAs/Si) solar cells reaching 33.3% 1-sun efficiency in a 2-terminal configuration by direct wafer bonding [11].

The bottleneck for III-V cells is their high cost due to slow crystal growth, expensive III-V crystalline substrates, and raw material scarcity. They are mainly used in satellites and partly in

[9] Solar Frontier: http://www.solar-frontier.com
[10] First Solar: http://www.firstsolar.com/

terrestrial solar concentrating system. Using large-area Fresnel lens or parabolic mirror, small-area III-V multijunction cells are sufficient to convert sunlight into electricity with unprecedented high efficiency. Fraunhofer ISE/Soitec/CEA have shown 46% efficiency of a 4-junction bonded solar cells (GaInP/GaAs;GaInAsP/GaInAs) under concentrated sunlight of 508 times the solar AM1.5D (ASTM E927-10) spectrum[11].

Perovskite solar cells

Perovskite is another new photovoltaic material with fast-rising efficiencies since 2010. The crystal structure of Perovskite has a general chemical formula ABX_3 where A and B are two cations of very different size and X is an anion that bonds to both A and B. The most common perovskite solar cells use hybrid organic-inorganic lead or tin halide-based materials, such as methylammonium lead halides ($CH_3NH_3PbX_3$ or $MAPbX_3$ where X=I, Br or Cl). The advantage of perovskite solar cells is the possibility of low-temperature and atmospheric process, leads to lower fabrication costs. Perovskite solar cells with high efficiency up to 22.7% at 1 sun is demonstrated by KRICT (Korea) ($J_{sc} = 24.92\,\mathrm{mA/cm^2}$, $V_{oc} = 1.144\,\mathrm{V}$, $FF = 0.796$) [12]. High-bandgap perovskite is also compatible as top cell on c-Si. Monolithic perovskite/Si tandem solar cells with stabilized efficiency of 23.6% is demonstrated [13]. Stability issues, light degradation and hysteresis are still problematic for hybrid perovskite materials.

Summary

Wafer-based c-Si is generally referred to as 1st generation solar cells and 2nd generation is used for thin-film solar cells. Figure 1.6 shows the graph of efficiency-cost of photovoltaic technologies. The dashed lines represent the constant module price per watt peak (Wp). c-Si modules have reduced the market price below 1 USD/Wp since 2013[12]. This is due to improved efficiency and thinner c-Si wafers (nowadays about 160–190 μm, in contrast to 300 μm in the early 2000s).

In 2017, the worldwide photovoltaic module production is estimated around 97.5 GWp. 95% of the total production is from wafer-based Si technology (62% multi-Si and 33% mono-Si) and 5% of the total production is from thin-film technologies (CdTe, CIGS and a-Si)[13]. III-V multijunction and concentrating photovoltaic (CPV) systems still account for very few percentage in the terrestrial photovoltaic application. Toward 3rd generation photovoltaics, which is defined as low-cost and high-efficiency thin-film solar cells, advanced concepts are investigated in research laboratories.

1.3.3 Motivation toward ultrathin and nanowire solar cells

In this thesis, we focus on ultrathin and nanowire-based GaAs solar cells. Reducing the active region of semiconductor absorber contributes to cheaper photovoltaic application by diminishing the material consumption, which can be achieved using ultrathin layers or nanowires. GaAs is the material of choice to demonstrate the possibility of high efficiency. Of course, these structures can also be applied to other photovoltaic technologies. Through experimental works and theoretical investigations, we study both optical light-trapping and electronic design of GaAs solar cells for next generation high-efficiency and low-cost photovoltaics.

For ultrathin GaAs solar cells, the main results are presented in Chapter 4 and more details of state-of-art GaAs solar cells can be found in the beginning of this chapter (Section 4.1). We study

[11] Press release, Fraunhofer ISE, 1 December 2014: https://www.ise.fraunhofer.de/en/press-media/press-releases/2014/new-world-record-for-solar-cell-efficiency-at-46-percent.html

[12] IEA technology roadmap (2014): https://www.iea.org/publications/freepublications/publication/TechnologyRoadmapSolarPhotovoltaicEnergy_2014edition.pdf

[13] Photovoltaics report (Last updated: June 19, 2018): https://www.ise.fraunhofer.de/en/publications/studies/photovoltaics-report.html

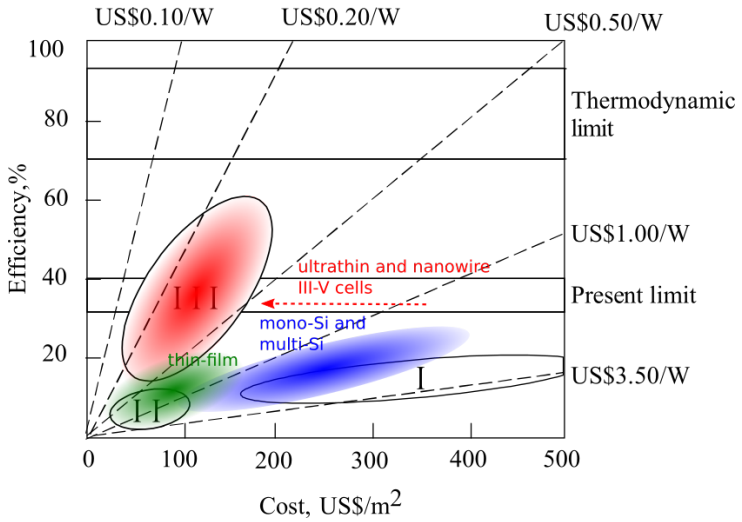

Figure 1.6 – *Efficiency-cost for the three generations of solar cell technology: (I) wafer, (II) thin-films and (III) advanced concepts. The dashed lines show constant module price per watt peak (figure adapted from Ref. [14], 2006). The price of mono- and multi-crystalline silicon modules have been dropped considerably in recent years, and thin-film technologies (CIGS and CdTe) continue to progress in efficiency. High-efficiency and low-cost 3rd generation solar cells may use ultrathin films or nanowires for light harvesting.*

advanced light management in ultrathin layers (200 nm-thick, ten-fold thinner than conventional thin-film GaAs solar cells) and discuss its potential to achieve high efficiency. Nanowires constitute another interesting research domain. They offer promising light concentrating property and provide the possibility of direct growth of III-V compounds on lattice-mismatched Si substrates, leading to potential high efficiency and at the same time overcome the high cost of III-V substrates. The small sizes of nanowires make the growth and characterization of the materials difficult, hence, we develop an alternative characterization method by cathodoluminescence in Chapter 5. This method is used to characterize GaAs nanowires (Chapter 6) and can be applied to other materials and nanostructures. The study of GaAs nanowire solar cells is presented in Chapter 7 and more details of the state-of-art III-V nanowire solar cells can be found in the beginning of this chapter (Section 7.1).

Chapter

2 Physics of Solar Cells

Chapter content

This chapter is dedicated to the description of theoretical background and some notions that are useful to understand the working principle of solar cells. Wave optics is essential for our studies which focus on the light management in a reduced volume of active semiconductor absorber (Section 2.1). Interference by multiple reflection in multi-layer structure is calculated using the scattering matrix method, while analysis of diffraction structures in solar cells requires numerical tools. We use simulations based on the Rigorous coupled-wave analysis (RCWA) whose basic features are described.

Beside optical absorption, electronic designs of solar cells are also important for high-efficiency photovoltaics. Electronic characteristics of solar cells are essentially related to the properties of semiconductors. Hence, we describe important bases of the physics of semiconductors in the second part (Section 2.2). Semiconductor p-n junction is the mostly used solar cell structure. We introduce carrier concentrations (doping), transport properties, generation and recombination in semiconductors. To characterize photovoltaic materials and understand the dynamics of photogenerated carriers, important parameters such as diffusion length and carrier lifetime should be considered.

2.1 Optics

Photovoltaic solar cells convert the energy of sunlight into electricity. The first task is to absorb light as much as possible in the solar cell, therefore, we need to understand the fundamental properties of light. Ray optics is well intuitive to describe the propagation of light through space, the reflection and transmission at the interface between two mediums. Light can be considered as particles moving with the velocity c_0 in vacuum ($c_0 \approx 2.998 \times 10^8$ m/s). Einstein interpreted

light in quanta of discrete energy $E = h\nu$, where h is the Planck constant ($h \approx 6.626 \times 10^{-34}$ J·s) and ν is the frequency. Nowadays, these quanta are called *photons*.

On the other hand, light also shows wave character when we look at the experience of double slit interference or the diffraction effect occurred when light encounters an obstacle or a small aperture. Solar cells are usually made of thin-film semiconductors. Hence, the wave nature of light emerges, especially when we deal with light-trapping in small volume of semiconductor in presence of nanostructures. The classical theory of electromagnetism is used to describe optical phenomena in these cases. We will adapt both wave-particle descriptions depending on the practical situation. To summarize, the photon energy E and momentum p are related by $E = pc_0$. The energy and momentum of a photon depend only on its frequency ν or inversely, on its wavelength λ:

$$\begin{aligned} E &= \hbar\omega = \frac{hc_0}{\lambda} \\ \mathbf{p} &= \hbar\mathbf{k} \end{aligned} \tag{2.1}$$

where $\omega = 2\pi\nu$ is the angular frequency and $\hbar = h/2\pi$ is the reduced Planck constant. $\mathbf{k}$ is the wavevector, where the wavenumber is $k = |\mathbf{k}| = 2\pi/\lambda$, and the direction of $\mathbf{k}$ indicates the propagation direction of light. In addition, the photon also carries a quantity called spin angular momentum of $\pm\hbar$. In the following, we give the essential notions of electromagnetism relevant in studying light management in solar cells.

2.1.1 Maxwell equations

We consider electromagnetic radiation in matter, in the framework of linear optics. Some reasoning and remarks follow the reference book *Semiconductor Optics* [15]. The four Maxwell equations couple the electric and magnetic fields to their sources, i.e. electric charges and current densities. They are given by

$$\begin{aligned} \nabla \cdot \mathbf{D}(\mathbf{r}, t) &= \rho(\mathbf{r}, t) \\ \nabla \times \mathbf{E}(\mathbf{r}, t) &= -\frac{\partial \mathbf{B}(\mathbf{r}, \mathbf{t})}{\partial t} \\ \nabla \cdot \mathbf{B}(\mathbf{r}, t) &= 0 \\ \nabla \times \mathbf{H}(\mathbf{r}, t) &= \frac{\partial \mathbf{D}(\mathbf{r}, \mathbf{t})}{\partial t} + \mathbf{j}(\mathbf{r}, t) \end{aligned} \tag{2.2}$$

where $\mathbf{r}$ and t denote location and time, respectively. $\mathbf{D}$ is the electric displacement, $\mathbf{E}$ the electric field, $\mathbf{B}$ the magnetic induction and $\mathbf{H}$ the magnetic field. ρ is the free charge density and $\mathbf{j}$ is the free current density.

The electric displacement is related to the electric field via the constitutive relation

$$\mathbf{D} = \varepsilon_r \varepsilon_0 \mathbf{E} \tag{2.3}$$

where ε_r is the relative permittivity of the medium in which the electric fields are observed and $\varepsilon_0 \approx 8.854 \times 10^{-12}$ F/m is the vacuum permittivity. The relative permittivity arises from the polarizability of the medium that expresses the linear dependence of the density of induced electric dipole moments with the electric field. In vacuum, we have $\varepsilon_r = 1$. In general $\varepsilon_r > 1$ for semiconductors and dielectric materials, and is frequency-dependent. A scalar value of ε_r is sufficient to describe an isotropic medium, in which the induced dipole moment is independent of the direction. In general, ε_r is a tensor in an anisotropic material (e.g. hexagonal wurtzite structure of several semiconductors). This is called birefringence or dichroism because the optical properties depend on the polarization and propagation direction of light. Similarly, the magnetic induction is related to the magnetic field via the constitutive relation

$$\mathbf{B} = \mu_r \mu_0 \mathbf{H} \tag{2.4}$$

where μ_r is the relative permeability of the medium and $\mu_0 = 4\pi \times 10^{-7}\,\mathrm{H/m}$ is the permeability of vacuum. We may assume all the important materials for solar cells to be non-magnetic, i.e. $\mu_r \equiv 1$, in the usual range of the electromagnetic spectrum, so that the magnetization of the medium has negligible influence on the optical properties.

Electromagnetic wave equation

To derive the wave equation that governs the propagation of light, we consider a homogeneous and isotropic medium and assume that there is no macroscopic free space charges: $\rho(\mathbf{r}, t) \equiv 0$ in Maxwell equations. The current $\mathbf{j}$ is driven by the electric field

$$\mathbf{j} = \sigma \mathbf{E} \tag{2.5}$$

where σ is the conductivity of the material. For intrinsic and weakly doped semiconductors, the carrier density is small and consequently σ is small as well. Then the inequality holds: $|\mathbf{j}| = |\sigma \mathbf{E}| \ll |\omega \mathbf{D}|$. In the following, we consider only this case and neglect $\mathbf{j}$ in Maxwell equations. For heavily doped semiconductors this is no longer valid and σ will have some influence on the optical properties at least in the infrared (IR) region of the electromagnetic spectrum [15]. The wave equation for electric field (and similar for magnetic field) is written

$$\Delta \mathbf{E} = \frac{\varepsilon_r}{c_0^2} \frac{\partial^2 \mathbf{E}}{\partial t^2} \tag{2.6}$$

where $\Delta \mathbf{E} \equiv \nabla^2 \mathbf{E} \equiv \nabla(\nabla \cdot \mathbf{E}) - \nabla \times (\nabla \times \mathbf{E})$ is the vector Laplacian of a vector field $\mathbf{E}$. $c_0 = 1/(\mu_0 \varepsilon_0)$ is the propagation speed of the wave in free space (vacuum).

Properties of plane harmonic waves

The simplest solution to the wave equation is the plane harmonic wave, where light of constant angular frequency ω propagates in the direction of $\mathbf{k}$. We express the field using complex values, but keeping in mind that the physical magnitude is the real part of the complex field.

$$\mathbf{E}(\mathbf{r}, t) = \mathbf{E}_0 \exp\left(i(\mathbf{k} \cdot \mathbf{r} - \omega t)\right) \tag{2.7}$$

The time-harmonic dependence of the fields is taken as $\exp(-i\omega t)$ and complex values are used throughout the whole mathematical manipulations. In this way, the time derivative becomes multiplication by $-\mathrm{i}\omega$ on the complex amplitude of fields, and the nabla operator ∇ is transformed by applying $i\mathbf{k}$. We can derive that the electromagnetic wave is transverse: $\mathbf{E}$ and $\mathbf{H}$ are perpendicular to $\mathbf{k}$ and are perpendicular to each other. Moreover, the plane wave should fulfill the following dispersion relation:

$$k^2 = \frac{\omega^2}{c_0^2} \varepsilon_r(\omega). \tag{2.8}$$

In general, the relative permittivity $\varepsilon_r(\omega)$, also called dielectric function, is complex. For the square root of ε_r we introduce a new quantity $\tilde{n}(\omega)$, called the complex index of refraction.

$$\tilde{n}(\omega) = n(\omega) + i\kappa(\omega) = \sqrt{\varepsilon_r(\omega)} \tag{2.9}$$

The real part of $\tilde{n}$ is usually called *refractive index* in connection with Snell's law of refraction and the imaginary part is called *extinction coefficient*. Here the wavevector is also complex

$$\mathbf{k} = (n + i\kappa)\mathbf{k}_0 = \mathbf{k}' + i\mathbf{k}'' \tag{2.10}$$

with $k_0 = 2\pi/\lambda_0$ and λ_0 is the wavelength in vacuum. In this way $\exp(i\mathbf{k} \cdot \mathbf{r}) = \exp(i\mathbf{k}' \cdot \mathbf{r}) \exp(-\mathbf{k}'' \cdot \mathbf{r})$. We can see that planes of constant phase (wavefronts) are planes perpendicular to $\mathbf{k}'$ and $n(\omega)$

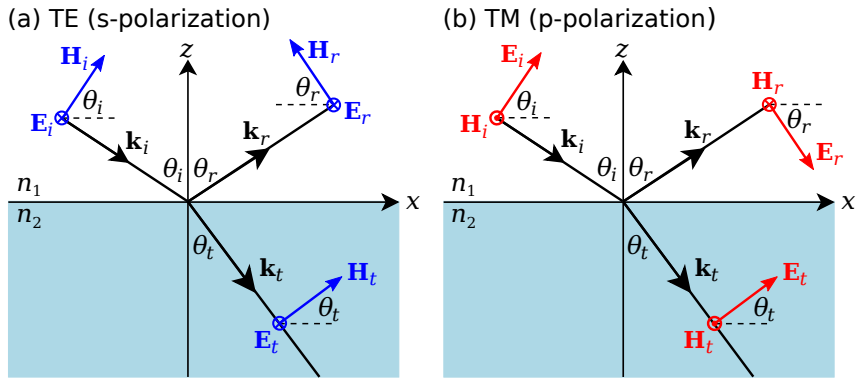

Figure 2.1 – *Scheme of light, reflected and transmitted (refracted) at an interface between two isotropic media for two orthogonal, linear polarization: (a) transverse electric (TE or s-polarization) and (b) transverse magnetic (TM or p-polarization).*

describes the spatial oscillation of light in matter. The amplitude of fields decreases in direction of $\mathbf{k}''$ so $\kappa(\omega)$ describes the damping of the wave in the direction of propagation (for example z). The light intensity $I(z)$ is proportional to the square of the field amplitude. In connection with the Beer-Lambert law $I(z) = I(0)\exp(-\alpha z)$, the absorption coefficient α is related to the imaginary part of the complex index of refraction

$$\alpha(\omega) = \frac{2\omega}{c_0}\kappa(\omega) = \frac{4\pi}{\lambda_0}\kappa(\omega). \tag{2.11}$$

A quantity that is often used to judge the absorptivity of a material at a certain wavelength is the penetration depth $\delta = 1/\alpha$. At this depth, the intensity has decayed to a fraction $1/\mathrm{e}$ of the initial value. For example, the penetration depth of GaAs is about 100 nm at $\lambda_0 = 500\,\mathrm{nm}$, and increases rapidly for longer wavelength of light. We arrive at a penetration depth of 740 nm at $\lambda_0 = 800\,\mathrm{nm}$.

2.1.2 Reflection and transmission at interface

In this section, we consider the reflection and transmission (refraction) of light at the plane interface between two media. We assume homogeneous and isotropic media described by the complex index of refraction $\tilde{n}_1$ and $\tilde{n}_2$. We first recall the boundary conditions imposed by the Maxwell equations between two media, then we derive the Fresnel equations for reflection and transmission of light.

Boundary conditions

Maxwell equations are applied in each medium 1 and 2. At the interface, boundary conditions are obtained by two general laws of vector analysis, that is the law of Gauss and law of Stokes. We note $\mathbf{n}_{12}$ normal unit vector from medium 1 to medium 2. These conditions are

$$\begin{aligned}(\mathbf{D}_2 - \mathbf{D}_1)\cdot\mathbf{n}_{12} &= \sigma_s \\ \mathbf{n}_{12}\times(\mathbf{E}_2 - \mathbf{E}_1) &= 0 \\ (\mathbf{B}_2 - \mathbf{B}_1)\cdot\mathbf{n}_{12} &= 0 \\ \mathbf{n}_{12}\times(\mathbf{H}_2 - \mathbf{H}_1) &= \mathbf{j}_s\end{aligned} \tag{2.12}$$

where σ_s is the surface charge and $\mathbf{j}_s$ is the surface current density between the media. We will drop these two terms for the general solar cell application. Therefore, the normal component of the field $\mathbf{D}$ and $\mathbf{B}$ is continuous across the interface, and so is the tangential component of the field $\mathbf{E}$ and $\mathbf{H}$.

Law of reflection and refraction

As illustrated in Figure 2.1, the plane of incidence is the plane defined by the interface normal and the wavevector of the incident wave. A part of the incident light is reflected, with the angle of the reflected light θ_r is equal to the incident angle θ_i. The other part of light enters medium 2, where the angle of the refracted light θ_t is related to θ_i via Snell's law of refraction

$$n_1 \sin(\theta_i) = n_2 \sin(\theta_t) \tag{2.13}$$

An important consequence of Snell's law is *total internal reflection*. If $n_1 > n_2$, there is a critical angle θ_c at which light can no longer be transmitted to medium 2:

$$\sin(\theta_c) = \frac{n_2}{n_1}. \tag{2.14}$$

For $\theta_i > \theta_c$, there is a totally reflected beam but no longer a transmitted one. The reflected wave has the same intensity as the incident one. However, the boundary conditions require finite field amplitudes in medium 2. An evanescent wave exists which propagates parallel to the surface and its amplitudes decay exponentially in the direction normal to the interface over a distance of a few wavelengths [15]. For a GaAs-air interface ($n_{\mathrm{GaAs}} \approx 3.68$ at $\lambda_0 = 800\,\mathrm{nm}$), we find $\theta_c \approx 15.8°$.

Fresnel equations

For weak absorption media (i.e. $|\kappa| \ll |n|$), relations between the magnitudes of the incident, reflected and transmitted fields are given by Fresnel equations. These equations can be obtained by expressing the field in each medium with plane waves, then using the boundary conditions. For strong absorption material like metal or semiconductors in certain frequency ranges, Fresnel equations are still valid but the angles and index of refraction are complex values and do not have obvious geometrical interpretation.

We have to distinguish between perpendicular and parallel polarized light. In the first case, the electric field is perpendicular to the plane of incidence and is called transverse electric (TE) polarization or s-polarization (*senkrecht* is German for perpendicular). The Fresnel equations are

$$\begin{aligned} r_{12,\,\mathrm{TE}} &\equiv \left(\frac{E_r}{E_i}\right)_{\mathrm{TE}} = \frac{n_1 \cos(\theta_i) - n_2 \cos(\theta_t)}{n_1 \cos(\theta_i) + n_2 \cos(\theta_t)} \\ t_{12,\,\mathrm{TE}} &\equiv \left(\frac{E_t}{E_i}\right)_{\mathrm{TE}} = 1 + r_{12,\,\mathrm{TE}} \end{aligned} \tag{2.15}$$

In the case of electric field parallel to the plane of incidence, we call this transverse magnetic (TM) polarization or p-polarization. The Fresnel equations are different from the case for TE polarization

$$\begin{aligned} r_{12,\,\mathrm{TM}} &\equiv \left(\frac{E_r}{E_i}\right)_{\mathrm{TM}} = \frac{n_1 \cos(\theta_t) - n_2 \cos(\theta_i)}{n_1 \cos(\theta_t) + n_2 \cos(\theta_i)} \\ t_{12,\,\mathrm{TM}} &\equiv \left(\frac{E_t}{E_i}\right)_{\mathrm{TM}} = \frac{n_1}{n_2}\left(1 - r_{12,\,\mathrm{TM}}\right) \end{aligned} \tag{2.16}$$

The measurable quantities are the reflectivity R and the transmittance T, which are given by the ratio of the square of the electric field. In the weak absorption regime, we can see that $|r_{12,\,\mathrm{TM}}|$ can go to zero at a certain incident angle θ_B, known as *Brewster angle*. The condition for $|r_{12,\,\mathrm{TM}}| = 0$ is $n_1 \cos(\theta_t) = n_2 \cos(\theta_i)$. Apart from $n_1 = n_2$, we have $\theta_i + \theta_t = 90°$, i.e. at the incident angle where the reflected and refracted beams would propagate perpendicularly to each other. For $\theta_i = \theta_B$, only the component polarized perpendicularly to the plane of incidence is reflected.

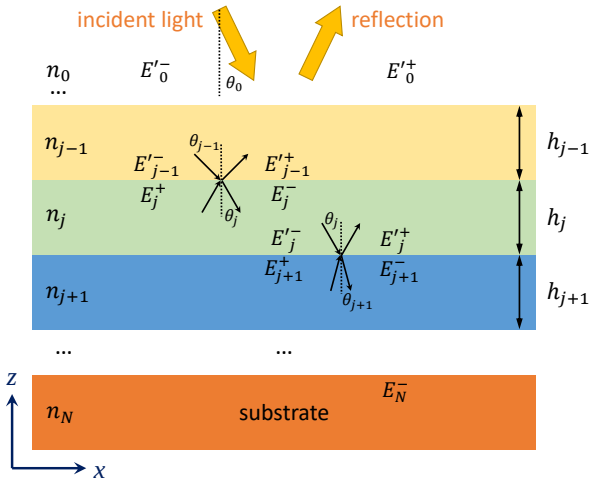

Figure 2.2 – *General multi-layer system composed of (N-1) layers with N parallel interfaces between a semi-infinite medium (optical index n_0) and a semi-infinite substrate (optical index n_N). Each layer j ($j = 1, 2, .., N-1$) has a thickness h_j and is characterized by its complex optical index n_j. The electric field at the vicinity of the interface is denoted by the subscript j for the layer j and by the superscript $+$ (resp. $-$) for the upward (resp. downward) propagating field. A prime is used for the field at the bottom of the layer (above an interface).*

If we send light on the interface polarized differently than TE or TM to the plane of incidence, we can always decompose it into two components with the above orientations, then calculate their reflected or transmitted amplitudes and superpose them again. For unpolarized light, we can simply take the mean values of the two polarizations. For the reflectivity that is $R = (|r_{12,\,\mathrm{TE}}|^2 + |r_{12,\,\mathrm{TM}}|^2)/2$. At normal incidence $\theta_i = 0$ we have R independently for the two polarizations:

$$R = \left|\frac{n_1 - n_2}{n_1 + n_2}\right|^2 . \tag{2.17}$$

Due to high refractive index of typical semiconductors (3–4 in general), the reflectivity in flat air-semiconductor interface is high. For example, the reflectivity at air-GaAs interface is 33% at $\lambda_0 = 800$ nm. This results in approximately one third of the solar energy not being absorbed by the solar cell. To reduce reflection loss, anti-reflection coating or surface texturing can be applied.

2.1.3 Scattering-matrix method

In real solar cell structures, there are usually several layers of different thicknesses, for example top single-layer or double-layer anti-reflection coatings. In these cases, we can use the so-called scattering-matrix method to calculate recursively the total reflectivity and to deduce the optical absorption in each layer. As illustrated in Figure 2.2, we consider $N-1$ flat layers of different materials (linear, homogeneous and isotropic). Each layer j ($j = 1, 2, ..., N-1$) has a thickness h_j and is described by their complex refractive indices n_j. An incident plane wave comes from the ambient medium (refractive index $n_0 = 1$) with an angle θ_0 to the surface normal. The refracted angle in each layer j is denoted by θ_j. The substrate is assumed to be a semi-infinite medium of complex refractive index n_N. The electric field is denoted by E_j (resp. E'_j) at top (resp. bottom) of the layer j, and is represented by the superposition of two components: one propagating in the positive and one in the negative z direction, E_j^+ and E_j^-, respectively.

The formalism of the scattering matrix method is to write the output field as a function of the input field, in the direction of propagation of the incident light (here top-down). The tangential component of the electric field is continuous, leading to the Fresnel equations shown

previously. From the linearity of the equations governing the propagation of the electric field, matrix notations are introduced to conveniently express the relation that should be satisfied for the two components of the electric field. Beginning with the most simple case with two semi-infinite media separated by an interface ($N = 1$):

$$\begin{aligned}\begin{bmatrix} E_0'^{+} \\ E_1^{-} \end{bmatrix} &= S^{(1)} \begin{bmatrix} E_0'^{-} \\ E_1^{+} \end{bmatrix} \\ &= \begin{bmatrix} r_{01} & t_{10} \\ t_{01} & r_{10} \end{bmatrix} \begin{bmatrix} E_0'^{-} \\ E_1^{+} \end{bmatrix}\end{aligned} \tag{2.18}$$

where r_{01} and t_{01} are the Fresnel complex reflection and transmission coefficients at the interface between the medium 0 and the medium 1. These coefficients depend on the complex refractive indices of the media, the angle of incidence and TE or TM polarization (see Equations 2.15 and 2.16). $S^{(1)}$ is the scattering matrix in the simple case of two-medium system ($N = 1$).

Now we consider the case of j layers ($j = 1, ..., N-1$) and assume that the problem to be solved up to the top of the layer j. Inside the layer j, the propagation of field induces a phase change:

$$\begin{aligned} E_j' &= E_j^{-} \exp(i\delta_j) \\ E_j^{+} &= E_j'^{+} \exp(i\delta_j) \end{aligned} \tag{2.19}$$

where $\delta_j = 2\pi n_j h_j \cos(\theta_j)/\lambda_0$ is related to the phase change and the attenuation (n_j complex) as the wave propagates through the layer j. Finally, the outgoing fields can be related to the incident fields by the scattering matrix $S^{(N)}$ through a recursive algorithm [16]:

$$\begin{bmatrix} E_0'^{+} \\ E_N^{-} \end{bmatrix} = S^{(N)} \begin{bmatrix} E_0'^{-} \\ E_N^{+} \end{bmatrix} \tag{2.20}$$

Since no input field is comping from the semi-infinite substrate, we have $E_N^{+} = 0$. Hence, we can calculate explicitly the reflection and transmission of light using the coefficients of the matrix $S^{(N)}$:

$$\begin{bmatrix} E_r \\ E_t \end{bmatrix} = \begin{bmatrix} s_{11} & s_{12} \\ s_{21} & s_{22} \end{bmatrix} \begin{bmatrix} E_i \\ 0 \end{bmatrix} \tag{2.21}$$

As a consequence, the complex coefficient for the reflection of light is $r = s_{11}$ and the reflectivity is given by the square of the absolute value of r.

Considering the case of a single-layer anti-reflection coating on a semiconductor wafer ($N = 2$), we can write the reflectivity at normal incidence after manipulation of the scattering matrix $S^{(2)}$.

$$R = \left| \frac{r_{01} + r_{12} \exp(i2\delta_1)}{1 + r_{01} r_{12} \exp(i2\delta_1)} \right|^2 . \tag{2.22}$$

We can thus suppress the reflection of light by choosing $r_{01} = r_{12}$ and $\exp(i2\delta_1) = -1$. The former leads to the choice of the refractive index n_1 of the dielectric layer to be the square root of that of the semiconductor: $n_1 = \sqrt{n_2}$ ($n_1 = 1.8$–2.0 is relevant for general application), and the latter results in the optimal thickness of the dielectric coating:

$$h_1 = \frac{\lambda_0}{4 n_1}. \tag{2.23}$$

These conditions can be understood as a destruction interference of reflected waves, and are strictly achieved at one wavelength. Further optimization of broadband anti-reflection can be done using double-layer coating and graded optical indices.

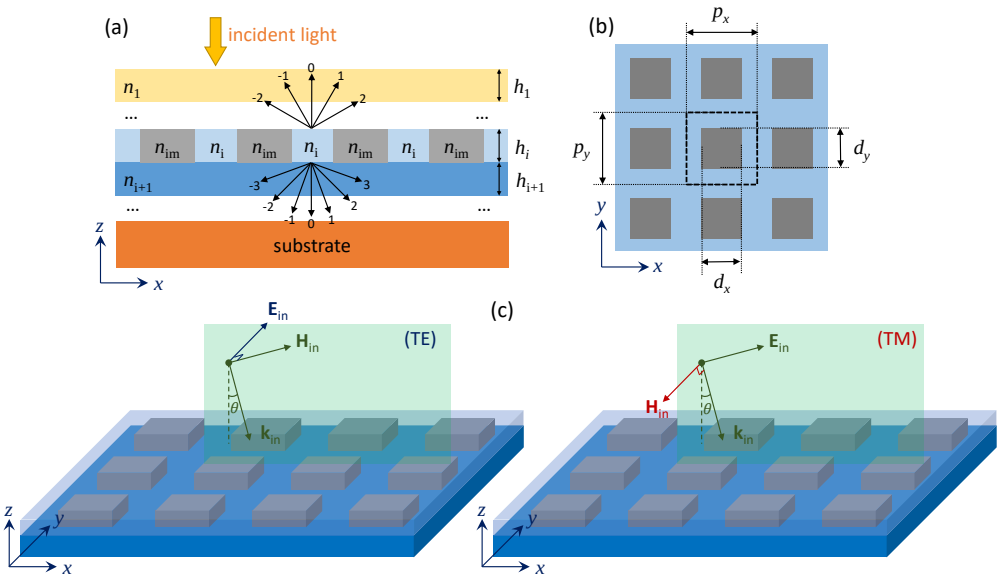

Figure 2.3 – *General description of a layer stack containing 2-dimensional periodic nanostructures used with Reticolo to calculate the electromagnetic field inside the device. (a) Side-view (cross-section) of the device structure. Arrows with numbers 0, ±1, ±2... represent the orders of diffraction. (b) Top-view of the nanostructured layer. The dashed frame delimits an unit cell of size p_x and p_y and the widths of the nanostructures are noted d_x and d_y. (c) Perspective views of a device with the axis orientation for an incident plane wave polarized in TE mode (left) and in TM mode (right). The incidence plane is shown in green.*

2.1.4 RCWA for optical absorption

For optical absorption with more complex nanostructures like periodic diffraction grating, we will employ numerical tools. In this thesis, we used the program Reticolo to perform 3-dimensional electromagnetic calculations for the diffraction problem. It has been developed by Philippe Lalanne and Jean-Paul Hugonin, and Christophe Sauvan (IOGS, Institute d'Optique Graduate School) contributed to the customized software that was provided to our group. Reticolo is written in the Matlab language, and implements a frequency-domain modal method, known as the Rigorous Coupled-Wave Analysis (RCWA) [17–19]. A free version of the software is available online.[1]

A general structure solved by Reticolo is shown in Figure 2.3. It is basically a multi-layer system (here: stacked vertically along the z-direction). One or several layers contains periodic 1-dimensional or 2-dimensional sub-wavelength patterns which have all identical periods in the x- and y-directions. Definition of 2-dimensional shapes other than rectangles (lozenges, polygons, circles, etc.) is also possible (parameter *Ntre*) using the convex envelop of several Cartesian patterns. We mainly focus on 2-dimensional gratings with the same period p_x and p_y and the same nanostructure size d_x and d_y so that the solar cell is not polarization-dependent at normal incidence.

In general, incoming light strikes on the top of the structure with an oblique incidence angle θ as shown in Figure 2.3(c) for the incident plane wave polarized in the TE mode (left: electric field perpendicular to the incidence plane) and for the incident plane wave polarized in the TM mode (right: magnetic field perpendicular to the incidence plane). Calculation for the incident plane wave forming a non-zero azimuthal angle (conical diffraction) is also possible, but the calculation time and computer memory increase considerably as the symmetry of the system decreases.

[1] Reticolo RCWA software (available online): https://www.lp2n.institutoptique.fr/Membres-Services/Responsables-d-equipe/LALANNE-Philippe

Reticolo software relies on the exact determination of monochromatic electromagnetic fields from Maxwell equations. The periodic relative permittivity $\varepsilon_r(x,y)$ of the grating layer can be expanded in a Fourier series of the form

$$\varepsilon_r(x,y) = \sum_{m,n} \hat{\varepsilon}_r(m,n) \exp\left(i2\pi\left(m\frac{x}{p_x} + n\frac{y}{p_y}\right)\right), \tag{2.24}$$

where $\hat{\varepsilon}_r(m,n)$ is the Fourier component of the relative permittivity in the grating region (m,n are integers). The electromagnetic fields in the grating region are then calculated using the same space-harmonic expansion. We call (M_x, M_y) the orders of Fourier decomposition of the fields (typically $M_x = M_y = 20$ in Reticolo calculation for 2-dimensional diffraction problem). Using Maxwell equations, the Fourier components of the electric and magnetic fields are coupled in a linear differential equation [20], which can be solved similarly to the resolution of the eigenmode problem of a matrix. Note that the size of this matrix scales to $2 \times (2M_x + 1) \times (2M_y + 1)$.

Once the eigenmodes in all the layers of the grating structure are known, a Rayleigh expansion (propagating and evanescent plane waves) is used in every homogeneous layer above and below the grating layers. The mode amplitudes in the different layers are calculated recursively based on a scattering matrix approach in order to match the boundary conditions at different layer interfaces. Finally, the electromagnetic power absorbed in each layer of the structure is obtained by integration of the field over the whole volume or using the Poynting vector. The RCWA optical simulation is used in Chapter 4.3 for ultrathin solar cells with a nanostructured back mirror, and in Chapter 7.2 for nanowire array solar cells.

2.2 Semiconductors

Modern semiconductor technology is the main building block of the photovoltaic industry. The first successful solar cell was made of crystalline silicon (c-Si), which is still the most widely used photovoltaic material. High-efficiency multi-junction solar cells are made of thin-films direct-gap III-V semiconductors. A semiconductor is by definition a material which can have a wide range of electrical conductivity between that of a conductor and an insulator. The conducting properties are controlled by introduction of impurities into the crystal lattice, where n-type or p-type semiconductors can be formed depending on the polarity of charge carriers. The invention of p-n junction constitutes the basis of diodes, transistors and all modern electronics. To understand the electrical characteristics of semiconductors and the impact on solar cell operation, we describe in this section the fundamental physics of semiconductors. The reasoning is adapted from part of the book *Solar Energy* [21] and *Physics of Semiconductor Devices* [22].

2.2.1 Carrier concentrations

The concentration (or density) of charge carriers in semiconductors is manipulated by *doping*, which can be of two different types: *donor atoms* which donate free electrons, or *acceptor atoms* which accept electrons thus leave behind *free holes*. The concentrations of donor and acceptor atoms are denoted by N_D and N_A, respectively. Depending on the impurity type in the crystal lattice structure and the temperature, donor atoms (resp. acceptor atoms) may not be totally *ionized*. We denote by N_D^+ and N_A^- the density of the ionized donor and acceptor atoms, respectively. The superscript $+$ for ionized donor atoms indicates that they create a fixed positive charge after donating a free electron and vice-versa for ionized acceptor atoms with $-$ superscript. Free electron and hole concentration is noted n and p, respectively. Inside a semiconductor, the local charge density ρ is thus given by

$$\rho = q\left(p + N_D^+ - n - N_A^-\right) \tag{2.25}$$

where $q \approx 1.602 \times 10^{-19}$ C is the elementary charge. At low temperature, free carriers tend to fix to their parent atoms thus the concentration of free carrier decreases. At room temperature, the thermal energy is sufficient to ionize almost all the dopant atoms. We may assume $N_D^+ \simeq N_D$ and $N_A^- \simeq N_A$.

A crystalline semiconductor is characterized by its band structure: valence electrons contained in the covalent bonds have their allowed energies in the *valence band* (VB) and the allowed energies of electrons liberated from the covalent bonds form the *conduction band* (CB). The maximum of VB energy is denoted E_v and the minimum of CB energy is denoted E_c. The energy difference between the edges of CB and VB is called the bandgap: $E_g = E_c - E_v$. The density of energy states in the CB close to E_c and in the VB close to E_v are calculated using the concept of effective mass in solid state physics (see details in Section 3.1 basics of semiconductors). The occupation probability of free electron in the CB and holes in the VB is described by the Fermi-Dirac distribution function

$$f(E) = \frac{1}{\exp(\frac{E-E_f}{k_B T}) + 1} \tag{2.26}$$

where k_B is the Boltzmann constant ($k_B \approx 1.38 \times 10^{-23}$ J/K) and T the absolute temperature. E_f is the so-called *Fermi energy* or *Fermi level*. The total concentration of electrons in the conduction band and holes in the valence band is obtained via integration over all energy ranges of the density of energy states multiplied by the occupation probability. In a general simple case, free carrier concentrations are related to the Fermi level through

$$\begin{aligned} n &= N_c \exp\left(\frac{E_f - E_c}{k_B T}\right) \qquad \text{for} \quad E_c - E_f \geq 3k_B T \\ p &= N_v \exp\left(\frac{E_v - E_f}{k_B T}\right) \qquad \text{for} \quad E_f - E_v \geq 3k_B T \end{aligned} \tag{2.27}$$

where N_c and N_v are the effective densities of the conduction band states and the valence band states, respectively. At 300 K we have for c-Si $N_c = 3.2 \times 10^{19}\,\text{cm}^{-3}$, $N_v = 1.8 \times 10^{19}\,\text{cm}^{-3}$, and for GaAs $N_c = 4.2 \times 10^{17}\,\text{cm}^{-3}$, $N_v = 9.5 \times 10^{19}\,\text{cm}^{-3}$. We note that the very different values for GaAs are due to specific band structures of III-V compounds. At degenerate concentrations ($n > N_c$ or $p > N_v$), the Fermi integral should be used instead of a simple exponential. A more rigorous treatment including high concentration effect, non-parabolicity of the conduction band, heavy- and light-hole valence band for GaAs is shown in Chapter 5.4.1.

For the moment, we drop the deviation due to high concentration. If an intrinsic semiconductor is in equilibrium, we have $n = p = n_i$. By multiplying the corresponding expression of n and p in Equation 2.27 we obtain

$$np = n_i^2 = N_c N_v \exp\left(-\frac{E_g}{k_B T}\right) \tag{2.28}$$

which is independent from the position of the Fermi level and thus valid for doped semiconductors as well. This relation is also called the *law of mass action*. n_i is the *intrinsic carrier concentration*. At 300 K, we found for c-Si $n_i = 9.65 \times 10^9\,\text{cm}^{-3}$ and for GaAs $n_i = 2.1 \times 10^6\,\text{cm}^{-3}$. Considering a n-type semiconductor in equilibrium with $N_D \gg N_A$ and assuming all donor atoms are ionized, the local charge of the uniformly doped semiconductor is zero, leading to $n \simeq N_D$ and from the law of mass action, $p \simeq n_i^2/N_D$. This shows the existence of majority carriers (electrons) and minority carriers (holes) in n-type material, and vice-versa for p-type material.

2.2.2 Transport properties

Under operation conditions, a net electrical current may flow through a semiconductor device. The electrical currents in a semiconductor come from the transport of charge by electrons and holes. The two basic transport mechanisms are *drift* and *diffusion*.

Drift

Drift is the motion of charged particles in response to an electric field. In a semiconductor, electrons and holes are accelerated by the electric field $\mathbf{E}$. Due to collisions with thermally vibrating lattice and scattering by ionized impurity atoms, the carrier acceleration is frequently disturbed. The resulting motion of electrons and holes is described by average drift velocities $\mathbf{v}_{n,\text{drift}}$ and $\mathbf{v}_{p,\text{drift}}$. In the case of low electric fields, the drift velocities are proportional to the electric field

$$\begin{aligned} \mathbf{v}_{n,\text{drift}} &= -\mu_n \, \mathbf{E} \\ \mathbf{v}_{p,\text{drift}} &= +\mu_p \, \mathbf{E} \end{aligned} \tag{2.29}$$

The proportionality factors μ_n and μ_p are called *mobility* of electrons and holes, respectively. Although the electrons move in the opposite direction to the electric field due to their negative charges, the resulting electrical currents still flow in the same direction as the electric field. The electron and hole drift current densities are given by

$$\begin{aligned} \mathbf{J}_{n,\text{drift}} &= q \, n \, \mu_n \, \mathbf{E} \\ \mathbf{J}_{p,\text{drift}} &= q \, p \, \mu_p \, \mathbf{E} \end{aligned} \tag{2.30}$$

Mobility is a measure of how easily the charge carriers can move through a semiconductor. At lower temperature, the probability of collision with the vibrating lattice decreases, thus the mobility increases. On the other hand, the probability to encounter ionized impurity atoms or charged carriers increases at high doping concentrations, leading to decreased mobility. In practice, the mobility in thin-film semiconductors is measured by Hall effect (see Chapter 5.2).

Diffusion

Diffusion is a process whereby particles tend to spread out from regions of high particle concentration into regions of low particle concentration as a result of random thermal motion. The driving force of diffusion is a gradient of the particle concentration, and the particles flow from high concentration region to low concentration region (opposite sign to the gradient). They are written as

$$\begin{aligned} \mathbf{J}_{n,\text{diff}} &= +q \, D_n \nabla n \\ \mathbf{J}_{p,\text{diff}} &= -q \, D_p \nabla p \end{aligned} \tag{2.31}$$

The proportionality constants D_n and D_p are called the electron and hole *diffusion coefficient*, respectively. The diffusion coefficient is linked with the mobility by the Einstein relationship

$$\frac{D_n}{\mu_n} = \frac{D_p}{\mu_p} = \frac{k_B T}{q}. \tag{2.32}$$

Continuity equation

Combining drift and diffusion, the total electron and hole current density is the sum in terms of electric field and gradient of concentration. In general, the carrier concentrations in non-equilibrium condition are described by two quasi-Fermi levels E_{fc} for electrons and E_{fv} for holes, which represent the electrochemical potentials of electrons and holes. We can write the current density in a more compact form using E_{fc} and E_{fv} [2, 23].

$$\begin{aligned} \mathbf{J}_n = q \, (n \, \mu_n \, \mathbf{E} + \, D_n \nabla n) \quad &= n \, \mu_n \nabla E_{fc} \\ \mathbf{J}_p = q \, (p \, \mu_p \, \mathbf{E} - \, D_p \nabla p) \quad &= p \, \mu_p \nabla E_{fv} \end{aligned} \tag{2.33}$$

Applying the conservation law to electrons and holes, we formulate the continuity equation, which translates that the time variation of the particle concentration is caused either by the transport of the particles (divergence of the current density) or by particle creation and annihilation.

$$\begin{aligned}\frac{\partial n}{\partial t} &= \frac{1}{q}\nabla\cdot\mathbf{J}_n + G_n - R_n \\ \frac{\partial p}{\partial t} &= -\frac{1}{q}\nabla\cdot\mathbf{J}_p + G_p - R_p\end{aligned} \tag{2.34}$$

Here G_n (resp. G_p) is the generation rate of electrons (resp. holes) due to other processes, such as photogeneration. R_n (resp. R_p) is the net recombination rate of electrons (resp. holes). They are discussed in the following.

2.2.3 Generation and recombination

Generation of electrons and holes in a piece of semiconductor can be achieved in several manners: for example illumination by sunlight, injection of carriers by electrical excitation or irradiation by an electron-beam. We note n_0 and p_0 the electron and hole concentration at equilibrium. Under excitation, we have clearly an excess carriers: $n = n_0 + \Delta n$ and $p = p_0 + \Delta p$. The generation in a semiconductor may not be homogeneous in the whole volume. Upon illumination by a monochromatic light, the photogeneration from the absorption of light decreases exponentially from the top surface, following the Beer-Lambert law. In presence of nanostructures, distribution in volume of the photogeneration would be more complex due to near field effect. Under sunlight illumination, we calculate the generation in ultrathin GaAs solar cells (Chapter 4.3 photogeneration rate) and in nanowire-array solar cells (Chapter 7.2 photogeneration in cylindrical symmetry). The generation of excess carriers by an electron-beam excitation is also presented in Chapter 3.4 using Monte-Carlo simulation for the electon-beam matter interaction (CASINO software) in a cathodoluminescence system.

Considering that the external excitation is suddenly switched off at time $t = 0$, the excess electrons will recombine with holes until the equilibrium state is reached again. Depending on the properties of the semiconductor, different types of recombination will occur. The time required for the excess carriers to decay to 1/e of the initial concentration is the *lifetime* of excess carriers. Lifetime is an important material parameter linked to the total recombination rate, which is strongly correlated to the performance of solar cells. In practice, measuring the lifetime can be done, for example, using time-resolved techniques in photoluminescence or cathodoluminescence system. We summarize the different types of recombination mechanisms in the following.

Radiative recombination

Radiative recombination is the process in which an electron recombines directly with a hole and creates a photon. This is also called band-to-band recombination and it mainly occurs in direct-bandgap semiconductors. Direct recombination is very limited for indirect semiconductors because both transfer in energy and momentum must take place. The recombination rate is proportional to the product np of concentration of electrons and holes. The proportionality is denoted by B with the unit of $\mathrm{cm^3 s^{-1}}$. The net radiative recombination rate R_{rad} $[\mathrm{cm^{-3} s^{-1}}]$ is written as

$$R_{\mathrm{rad}} = B(np - n_i^2). \tag{2.35}$$

Here $Bn_i^2 = Bn_0p_0$ represents the thermal generation and recombination of electron-hole pair at equilibrium. Considering a n-type semiconductor ($n_0 \simeq N_D \gg p_0$) at low injection level (i.e. $\Delta n \ll n_0$), the net radiative recombination rate becomes

$$R_{\mathrm{rad}} \simeq Bn_0(p - p_0) = \frac{p - p_0}{\tau_{\mathrm{rad}}}, \tag{2.36}$$

where $\tau_{\mathrm{rad}} = 1/(Bn_0) \simeq 1/(BN_D)$ is the lifetime of the minority holes in a n-type semiconductor. Assuming that a constant generation rate G is present throughout the volume of a semiconductor,

the excess carrier concentration is given by: $p - p_0 = G\,\tau_{\text{rad}}$. Similarly, $\tau_{\text{rad}} = 1/(BN_A)$ is the lifetime of the minority electrons in a p-type semiconductor. The radiative lifetime decreases with increasing doping concentrations. For example, the measurement of GaAs radiative lifetime as a function of doping can be found in Ref. [24, 25].

Auger recombination

In Auger recombination, energy and momentum of the recombining hole and electron is conserved by transferring energy and momentum to another electron or hole. The third particle is excited into higher energy levels and relaxes again, transferring its energy and momentum to lattice vibrations (phonons), and finally heat. In comparison to direct recombination which involves two particles, Auger recombination is a three-particle process. The Auger recombination rate R_{Aug} thus strongly depends on the carrier densities. The net recombination rate is written as

$$R_{\text{Aug}} = (C_n\, n + C_p\, p)\left(np - n_i^2\right) \tag{2.37}$$

where C_n and C_p are proportionality constants that are strongly dependent on the temperature. Auger recombination is more significant in indirect semiconductors, and is the major efficiency limiting factor for c-Si solar cells [26, 27]. For GaAs, we have typically $C_n \approx C_p \approx 10^{-30}\,\text{cm}^6 s^{-1}$ so is generally negligible at 1 sun illumination, but might become important at high injection levels.

Shockley-Read-Hall recombination

In Shockley-Read-Hall (SRH) recombination process, the recombination of electrons and holes is assisted by an impurity atom or a lattice defect. These recombination centers introduce allowed energy levels E_T within the forbidden gap, so-called trap states. The process is generally non-radiative and the excess energy is dissipated into the lattice in the form of heat. Though the concentration of traps N_T is usually small compared to the doping concentration N_D or N_A, it may be the dominant recombination process in semiconductors at most operation conditions.

The SRH statistics are based on four processes that are involved in recombination with a single trap level [28]: capture/emission of an electron from/to the conduction band, and capture/emission of a hole from/to the valence band. For example, we think about acceptor-like traps in a n-type semiconductor. The rate of electron (resp. hole) capture is proportional to the concentration of free electron n in the conduction band (resp. hole concentration p in the valence band), the concentration of unoccupied (resp. occupied) trap states, the corresponding thermal velocity $v_{n,h}$ of free carriers and a constant called capture cross-section σ_n (resp. σ_p). The thermal velocity is the average velocity of the electrons and holes due to thermal movement. Since electrons and holes have three degrees of freedom, we have

$$\frac{1}{2}m_e^* v_n^2 = \frac{3}{2}k_B T \qquad \frac{1}{2}m_h^* v_p^2 = \frac{3}{2}k_B T \tag{2.38}$$

where m_e^* and m_h^* are the effective masses of the electrons and holes, respectively. For electrons in c-Si and GaAs, the thermal velocity is about 10^7 cm/s. The electron capture cross-section σ_n describes the effectiveness of the trap state to capture an electron. It has the unit of area. Similarly σ_p describes the effectiveness of the trap state to capture a hole. On the other hand, the electron (resp. hole) emission rate is proportional to the concentration of occupied (resp. unoccupied) trap states. The proportionality factor is the emission coefficient, which is related to other semiconductor parameters by considering the equilibrium condition. Finally, the SRH recombination rate is written in general for a steady-state illumination condition

$$R_{\text{SRH}} = \frac{np - n_i^2}{\tau_p(n + n_1) + \tau_n(p + p_1)} \tag{2.39}$$

with

$$\tau_n = \frac{1}{\sigma_n v_n N_T} \quad \text{and} \quad \tau_p = \frac{1}{\sigma_p v_p N_T}$$
$$n_1 = n_i \exp\left(\frac{E_T - E_i}{k_B T}\right) \quad \text{and} \quad p_1 = n_i \exp\left(\frac{E_i - E_T}{k_B T}\right) \tag{2.40}$$

$$E_i = \frac{1}{2}(E_c + E_v) + \frac{1}{2} k_B T \ln\left(\frac{N_v}{N_c}\right) \quad \text{the intrinsic Fermi energy.} \tag{2.41}$$

Here τ_n and τ_p represents the SRH lifetime of electron and hole, respectively. They depend on the doping concentration, temperature and presence of an electric field. Empirical Scharfetter relation can be used to model these effects in the device simulations [29, 30]. We can see that SRH recombination rate is maximum approximately when the trap level is equal to the intrinsic Fermi level of the semiconductor: $E_T = E_i$, which is often invoked as trap states at the mid-gap, hence $p_1 = n_1 = n_i$.

The lifetime of the minority carriers due to SRH recombination becomes clear when we consider for example a n-type semiconductor at low injection level. Equation 2.39 is reduced to

$$R_{\text{SRH}} \simeq \frac{p - p_0}{\tau_p}. \tag{2.42}$$

Similar situation is applied for the lifetime of minority electrons τ_n due to SRH recombination in a p-type semiconductor. The SRH lifetime is inversely proportional to the trap density N_T, Hence, for a good semiconductor device it is critical to keep N_T low. In reality, the total recombination rate is the sum of several recombination mechanisms. The overall lifetime τ is thus related to the lifetimes of each process. For example

$$\frac{1}{\tau} = \frac{1}{\tau_{\text{rad}}} + \frac{1}{\tau_{\text{SRH}}} + ... \tag{2.43}$$

Typical minority carrier lifetime in GaAs is about 1 ns, and the short carrier lifetime due to SRH recombination is often the main limiting factor.

Surface recombination

The surface of a semiconductor is the place where crystalline covalent bonds interrupt, resulting in so-called dangling bonds. Dangling bonds create a high energetic surface, which may form covalent bonds with chemicals present in the atmosphere such as oxygen to lower the surface energy. The surface crystal defects and the presence of foreign chemical species may lead to creation of trap states in the forbidden gap of the semiconductor, resulting in efficient SRH recombination. In very pure semiconductors, recombination might be dominated by surface recombination. The surface recombination rate R_s [$\text{cm}^{-2}\text{s}^{-1}$] for an n-type semiconductor can be approximated with

$$R_s \simeq v_{th} \sigma_p N_s (p_s - p_0) \tag{2.44}$$

where v_{th} is the thermal velocity in cm/s (see Equation 2.38), σ_p is the capture cross-section for holes in cm^2, N_s is the surface trap density in cm^{-2}. p_s is the hole concentration in the proximity of the surface and p_0 is the equilibrium hole concentration in the n-type semiconductor. For a p-type semiconductor, we just need to replace the corresponding parameters. The product $v_{th}\sigma_p N_s$ has the unit of a velocity, which is generally called the *surface recombination velocity*

$$S = v_{th} \sigma N_s. \tag{2.45}$$

We should note that the surface recombination will impose a surface boundary condition on the current density in the continuity equation.

$$D_p \left.\frac{\partial p}{\partial x}\right|_{\text{surface}} = S(p_s - p_0). \tag{2.46}$$

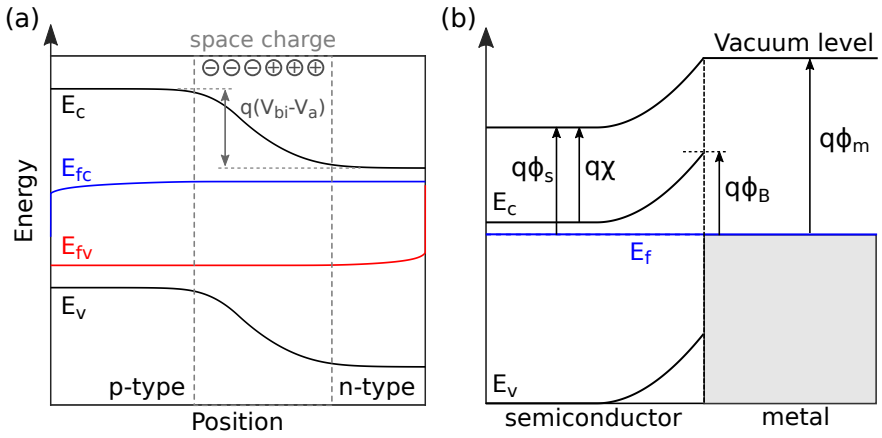

Figure 2.4 – *Schematic band diagram for (a) semiconductor p-n junction and (b) semiconductor-metal junction. The semiconductor p-n junction is under steady-state excitation so excess carriers are generated and described by two quasi-Fermi levels E_{fc} and E_{fv} for electrons and holes, respectively. The semiconductor-metal junction is shown for a n-type semiconductor in equilibrium.*

where D_p is the diffusion coefficient. Even with a uniform generation of excess carriers, the steady-state distribution of minority carrier concentration will decrease toward the surface if non-zero surface recombination velocity S exists. This situation is similar to a local generation of excess carriers. In this case diffusion of excess carriers takes place in the semiconductor until they recombine with majority carriers. The distance over which the minority carriers diffuse is given by

$$L_p = \sqrt{D_p \tau_p} \tag{2.47}$$

Here the lifetime of minority holes τ_p is the resulting sum of all recombination mechanisms. L_p is called the *minority carrier diffusion length*. It follows from the solution of the steady-state continuity equations 2.34 and indicates the distance over which the minority carrier densities drop by a factor of $1/e$. For high quality GaAs, typical diffusion length is several μm, and decreases with increasing doping concentrations [31]. Experimental determination of the diffusion length is also very valuable to examine the quality of photovoltaic materials. This can be achieved, for example, using photocurrent measurement, photoluminescence imaging technique and cathodoluminescence mapping.

2.2.4 Semiconductor junctions

Almost all solar cells contain junctions between materials of different doping types to facilitate selective extraction of electrons at one side and holes at the other side. A p-n homojunction is fabricated with the same semiconductor material. A p-n heterojunction is formed by two chemically different semiconductors. In a p-i-n junction the region of the internal electric field is extended by inserting an intrinsic layer. A Schottky barrier formed at the metal-semiconductor interface is another type of junction. We discuss some important examples in the following: p-n homojuction and metal-semiconductor contact.

When an n-type and a p-type semiconductor are brought together, the large difference in electron concentration between n- and p-type regions causes a diffusion of electrons from the n-type material to the p-type material. Due to diffusion, the region close to the junction becomes almost completely depleted of mobile charge carriers, and gives rise to the *space charge region* or *depletion region* due to ionized impurity atoms. Regions outside the depletion region in which the charge neutrality is conserved are called *quasi-neutral regions*. The space charge around the junction results in the formation of an internal electric field which opposes the electron diffusion until equilibrium is formed. The presence of electric field means that there is an electrostatic

potential difference V_{bi} across the space charge region, called *built-in potential* which is given by

$$V_{\text{bi}} = \frac{k_B T}{q} \ln\left(\frac{N_A N_D}{n_i^2}\right) \tag{2.48}$$

where N_A and N_D is the doping concentration in the p-type and n-type semiconductor, respectively. n_i is the intrinsic carrier concentration of the semiconductor. The total space-charge width w is

$$w = \sqrt{\frac{2\varepsilon V_{\text{bi}}}{q}\left(\frac{N_A N_D}{N_A + N_D}\right)} \tag{2.49}$$

where $\varepsilon = \varepsilon_0 \varepsilon_r$ is the dielectric permittivity of the semiconductor. The calculation of built-in potential and depletion zone are extended to the study of core-shell junction in nanowire-based solar cells in Section 7.3.

When an external voltage V_a is applied to a p-n junction, the potential difference between the n- and p-type regions across the space-charge region become $(V_{\text{bi}} - V_a)$. Under reverse-bias voltage, the potential barrier across the junction is increased, resulting in a wider space charge region. Under forward-bias voltage, the potential across the junction decreases, the space charge region becomes narrower, and a significantly net current density J is flowing through the p-n junction due to higher concentration of minority carriers at the edges of the space charge region compared to the situation in equilibrium. This process is referred to minority carrier injection, which causes the so-called recombination current density J_{rec} since the diffusing minority carriers recombine with the majority carriers in the bulk [21]. J_{rec} is compensated by the so-called thermal generation current J_{gen}, caused by the drift of minority carriers. For $V_a = 0$, we have $J = J_{\text{rec}} - J_{\text{gen}} = 0$. Under moderate forward-bias voltage V_a, it is assumed that the recombination current increases with the Boltzmann factor $\exp(qV_a/k_B T)$, while the generation current is almost independent of the potential barrier. The external net current density can be expressed as

$$J = J_{\text{rec}}(V_a) - J_{\text{gen}}(V_a) = J_0 \left[\exp\left(\frac{qV_a}{k_B T}\right) - 1\right] \tag{2.50}$$

where $J_0 = J_{\text{rec}}(0) = J_{\text{gen}}(0)$ is the *saturation current density* or *dark current density*. This equation is known as the Shockley diode equation that describes the current-voltage behavior of an ideal p-n diode. The saturation current density represents the flux of thermally generated minority carriers across the junction and is given by (Ref. [22] page 95)

$$J_0 = q n_i^2 \left(\frac{D_n}{L_n N_A} + \frac{D_p}{L_p N_D}\right). \tag{2.51}$$

For real devices, several factors may influence the current-voltage characteristics of a p-n junction and thus of the solar cell. We have shown in Chapter 1 the influence of a series resistance and a parallel resistance (shunt) on the fill factor (FF) of solar cells. The Shockley diode has an diode ideality $n = 1$, as can be seen from Equation 2.50, and the saturation current density J_0 (Equation 2.51) is given by the direct (radiative) recombination of minority carriers in the quasi-neutral region. In thin-film p-n junction, the recombination of minority carriers near the surface may dominate over bulk radiative recombination and strongly increases J_0 depending on the quality of surface passivation. At moderate forward bias, SRH may be the dominant recombination process, and the dark current density will increase in $\exp(qV_a/(2k_B T))$ with the applied voltage V_a. This is interpreted as SRH recombination in the space-charge region, since the SRH recombination rate is maximum at the region where $n \simeq p$ [32]. The diode ideality factor and associated saturation current density will strongly affect the V_{oc} of the solar cells, and will change the shape of JV curve thus change the FF.

Schottky barrier and ohmic contact

As metal-semiconductor interfaces are formed to connect the solar cells to external electric circuit, it is important to understand possible junction configurations between metal and semiconductor. Depending on the material properties, metal-semiconductor junctions can be of rectifying type or ohmic type. An important parameter for the metal is the work function ϕ_B, which is the energy that is required to remove an electron from the Fermi level to the vacuum level. Considering an n-type semiconductor, the energy barrier $q\phi_B$ between a metal and a semiconductor is predicted by the Schottky-Mott rule to be the difference of the metal work function ϕ_B and the semiconductor electron affinity χ. A metal-semiconductor junction is rectifying if the barrier height is large, i.e. $q\phi_B \gg k_BT$. In contrast to p-n junction where current transport is mainly due to transport of minority carriers, for Schottky barriers, the dominant transport mechanism is *thermionic emission* of the majority carriers over the barrier into the metal. The general current-voltage characteristics is given by (Ref. [22] page 156)

$$J(V) = J_s \left[\exp\left(\frac{qV}{k_BT}\right) - 1\right] \tag{2.52}$$

where the saturation current density J_s is expressed as

$$J_s = A^*T^2\exp\left(-\frac{q\phi_B}{k_BT}\right). \tag{2.53}$$

The constant A^* is the effective *Richardson constant* for thermionic emission, which is

$$A^* = \frac{4\pi q m_e^* k_B}{h^3} \tag{2.54}$$

with the effective mass of electron m_e^*, h the Planck constant.

In solar cells, the contact resistance at a metal-semiconductor junction should be as small as possible. Reducing the barrier height is often not possible due to limited choice of materials. The situation is different if a junction is formed between a metal and a highly-doped semiconductor. The width of the depletion region in proximity of the semiconductor surface decreases if doping is increased. As a result, tunneling of electrons through the barrier becomes the major current transport mechanism. The tunneling current has the expression (Ref. [22] page 166)

$$J_{\text{tunnel}} \propto \exp\left(-\frac{\sqrt{m_e^*\varepsilon}\phi_B}{\sqrt{N_D}\hbar}\right). \tag{2.55}$$

For a given semiconductor-metal barrier height, the tunneling current will increase exponentially with $\sqrt{N_D}$. A highly doped GaAs layer above 10^{18} cm^{-3} is usually preferred to facilitate ohmic contacts.

2.3 Summary

In this chapter, we give the essential notions in the understanding of the underlying physics in a solar cell device. In terms of optics, the Maxwell equations in matter are introduced with the given boundary conditions between two media. We emphasized the use of complex notation of fields and complex refraction indices so that the imaginary part of the wavevector is linked to the absorption of radiation in matter. Fresnel equations for reflection and refraction at the interface are given and some features between TE and TM waves are discussed. For absorption in multi-layer solar cell structures, Fresnel coefficients are applied to a general scattering matrix formalism. To calculate optical absorption with periodic nanostructures, we use numerical simulations based on the Rigorous coupled-wave analysis (RCWA) for solving diffraction problem.

The second part is dedicated to the description of semiconductor physics. Semiconductors have fundamentally two different doping types and present a wide variety of conductivity controlled by doping concentrations. The carrier concentrations and transport properties are described using material parameters (mobility and diffusion coefficient) and the quasi-Fermi levels for electrons and holes. Photogeneration of excess carriers in the semiconductor and the recombination mechanisms are discussed. We describe the carrier lifetime and diffusion length of minority carrier, which are important quantities for photovoltaic materials. Semiconductor p-n junction is described in connection with the ideal Shockley diode equation. Non-ideal current-voltage characteristics are discussed in terms of recombination mechanisms. These provide a basic understanding for designing solar cell structures and improving the device performance.

Chapter

3 Luminescence for Photovoltaic Materials

Chapter content

Luminescence is emission of light from a substance caused by spontaneous emission. In biology, light-emitting substances help scientists to observe the cellular processes in real time. In material science, luminescence provides wealthy information on the properties of the light-emitting specimen. Photovoltaic materials need to absorb light efficiently, and we will show that the emission of light is ultimately related to the absorption characteristics of the materials (Section 3.2). The balance between absorption and emission also leads to fundamental limits of photovoltaic conversion efficiency (Section 3.3). Therefore, luminescence constitutes one of the most useful characterization techniques in photovoltaic researches.

Depending on how the material is excited, we can distinguish photoluminescence (PL, luminescence as a result of absorption of photons), electroluminescence (EL, luminescence produced from injection of electric currents) and cathodoluminescence (CL, luminescence caused by irradiation of electron-beam). For all the above mentioned techniques, luminescence spectra resolved in photon energies give insights in the involved electronic transitions in the material. Excitation power and temperature dependent measurements may provide more detailed information about the recombination mechanisms. Spatially resolved and time-resolved techniques are very useful to probe the carrier dynamics (diffusion length and carrier lifetime) in luminescent materials.

This chapter deals with the semiconductor luminescence theory and its application for photovoltaic materials. In Section 3.1, basic notions of semiconductors are summarized and some

luminescence features commonly observed in semiconductors are described. In Section 3.2, the generalized Planck's law is derived step-by-step, which provides a powerful theoretical background relating emission of light to important photovoltaic characteristics, such as absorption of the material and the separation of quasi-Fermi levels. The generalized Plank's law is also shown to be useful in the characterization of semiconductor doping (see also Chapter 5.4). In Section 3.3, the Shockley-Queisser efficiency limit of solar cells is revisited, and a more general formulation is given to capture the non-ideal absorption characteristics of the materials and light-trapping designs of the devices. Section 3.4 is dedicated to the experimental setup description of cathodoluminescence equipment in our laboratory. Monte Carlo simulation (CASINO) for the electron beam-material interaction is shown briefly.

3.1 Semiconductor luminescence

We focus on inorganic crystalline semiconductors, which present long-range periodic structure of atoms. To describe such systems, basic knowledge of solid-state physics is essential. The reference books *Fundamentals of Semiconductors* [33] and *The Physics of Semiconductors* [34] are used. *Semiconductor Optics* [15] also provides comprehensive explanations for optical phenomena in semiconductors. We recall some physical basis of semiconductors which are useful in the understanding of light spectrum emitted by semiconductors, including electronic band structures in a perfect crystal, effective mass approximation, density of states and occupation probability of electrons and holes. The interaction of light with semiconductor is then described in a semi-classical way to derive a general formulation of the absorption coefficient. To understand some common features of semiconductor luminescence, influences of excitons, shallow defect states and doping effect are also addressed. The theory allows to understand direct-gap semiconductors (e.g. CdTe, GaAs, InP, GaSb, and III-V alloys) which are good candidates for photovoltaic applications owning to their high optical absorption properties.

3.1.1 Basics of semiconductors

Electronic band structures and the effective mass concept

In a perfect solid crystal (infinite periodic arrangement of atoms and invariant by translation of a lattice vector $\mathbf{R}$), electronic states constitute the so-called band structures, describing the range of energies that an electron within the solid may have. Starting from free electrons and assuming that the periodically arranged atoms and all interaction potentials between electrons together form an average static potential $V(\mathbf{r})$ where $\mathbf{r}$ is the position vector. It is assumed that the potential is also invariant by translation of the lattice vector: $V(\mathbf{r}+\mathbf{R}) = V(\mathbf{r})$. The single-electron Schrödinger equation is solved, giving Bloch waves as solutions:

$$\psi_{n,\mathbf{k}}(\mathbf{r}) = \exp(i\mathbf{k}\cdot\mathbf{r})\, u_{n,\mathbf{k}}(\mathbf{r}). \tag{3.1}$$

$\mathbf{k}$ is the wavevector of electron in the crystal. The Bloch function is a product of a plane wave and a term $u_{n,k}(\mathbf{r})$ having the same periodicity as the crystal lattice. For each value of $\mathbf{k}$, there are multiple solutions to the Schrödinger equation, labeled by a band number n. The collection of all eigenenergies $E_n(\mathbf{k})$ forms the band structures (or dispersion relations) of the semiconductor.

With the band structures, all electrons can be put into bands using Fermi-Dirac statistics. Beginning with zero temperature, some of the energetically lower-lying bands are completely filled. They are called valence bands. All partly filled or empty bands are conduction bands. The important region for transport and optical properties is that around the upper valence bands and the lower conduction bands. The energy separation between the highest valence bands and the lowest conduction bands is the bandgap E_g of a semiconductor. If the maximum of the

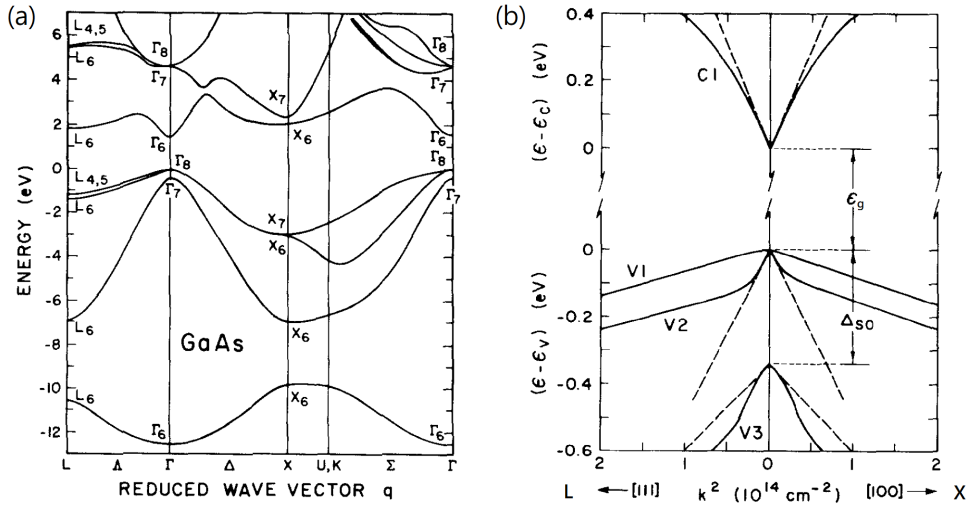

Figure 3.1 – *Electronic band structures for zincblende GaAs (a) Electron energy vs reduced wavevector for the four GaAs valence bands and the first several conduction bands, calculated from a nonlocal empirical pseudo-potential model. (b) An approximation for energy vs k^2 near the zone center for the lowest conduction band (C1) and the three highest valence bands (V1,V2,V3). (Figure adapted from Blakemore [35])*

valence bands and minimum of the conduction bands occur at the same k, the semiconductor is called direct gap. Otherwise, the semiconductor has an indirect gap (e.g. Si, Ge, GaP, AlAs, AlP...). Materials with E_g lower than approximately 0.5 eV (e.g. InAs, InSb...) are referred as narrow-gap semiconductors. On the other hand, materials with E_g between approximately 2 and 4 eV are wide-gap semiconductors (e.g. CdS, ZnSe, GaN or ZnO...).

Now, considering a semiconductor with a completely filled valence band containing N electrons per cm^3 ($N \sim 10^{23}$) and a completely empty conduction band, if we add one more electron, this electron will be placed into the conduction band states. If we remove one of the N electrons, this electron will come from the valence band states. For an almost filled valence band, it is easier to consider the few empty states and their properties instead of the many occupied ones. This idea leads to the concept of *holes*. The properties of the hole are connected with the properties of the electron that has been removed from the valence band. Because a semiconductor with a completely filled valence band is electrically neutral and has total momentum and spin equal to zero, these properties of the hole are exactly the opposite values of those of the removed electron. For instance, a hole carries a positive elementary charge $e \approx 1.602 \times 10^{-19}$ C.

To describe the transport properties in a semiconductor, one finds that the crystal electron and hole move under the influence of external fields like a particle, with an effective mass given by:

$$\frac{1}{m_{\text{eff}}} = \frac{1}{\hbar^2}\frac{\partial^2 E}{\partial k^2} = \frac{1}{\hbar^2}\frac{\partial^2 E}{\partial k_i \partial k_j} \quad i,j = x,y,z. \tag{3.2}$$

The electrons and holes in a semiconductor crystal are called quasi-particles (Fermions). The quantity $\hbar\mathbf{k}_{e,h}$ of crystal electron and hole is a quasi-momentum (only conserved to within a reciprocal lattice vector). The effective mass is actually a tensor and depends on the direction in which the electron or hole moves. In general, the bands of semiconductors tend to be parabolic in the vicinity of the band extrema. These extrema are the most important for the optical and transport properties. The effective masses are constant in these regions, leading to the so-called effective-mass approximation. It should be noted that the band curvature may change if moving away from the extrema. The adequate choice of effective mass value depends on the band structures of semiconductors.

The calculation of band structure is essential to correctly predict the semiconductor prop-

erties. It takes basically two approaches. In one case, free electrons (i.e. plane waves) are considered and a weak periodic potential as perturbation is introduced. These techniques include the nearly-free-electron model and the pseudo-potential approximation. The other method begins with the atomic orbitals of the semiconductor atoms, summing up the atomic orbitals at every lattice site. These techniques include the tight-binding approximation and the linear combination of atomic orbitals.

Figure 3.1 gives the calculated band structure of zinc-blende GaAs. The upper valence bands arise from the highest occupied atomic p-levels of the anions (Ga). The lowest conduction bands come from the lowest empty s-levels of the cations (As). The valence band has its maximum at the Γ point (i.e. $k = 0$). It is six-fold degenerate (including spin), inherited from the parent p-orbitals. It splits from the spin-orbit coupling into an upper four-fold degenerate band of Γ_8 symmetry and a lower two-fold degenerate band of Γ_7 symmetry. The Γ_8 valence band splits for $k \neq 0$ into two bands which have different curvature and are known as heavy- and light-hole bands. In GaAs, the light-hole band is practically spherical, while the heavy-hole band is strongly warped. In addition, mainly the light-hole band is non-parabolic. The split-off valence band has its maximum about 0.34 eV below that of the upper valence band. It is isotropic, but not parabolic. The ability of the split-off band to attract holes in thermal equilibrium is extremely small, thus its contribution can practically be neglected for temperature up to the melting point [35]. On the other hand, the conduction band minimum at the Γ point has a cubic Γ_6 symmetry, it is practically isotropic and slightly non-parabolic. Conduction band minima higher than Γ_6 can also be found near the L and X points, with an energy separation of about $\Delta_{\Gamma L} = 0.29\,\text{eV}$ and $\Delta_{\Gamma X} = 0.48\,\text{eV}$ at room temperature. The thermal occupation of electrons in the higher L- or X-valley can be neglected at least at room temperature [35].

Density of states and occupation probability

Now, we consider the density of states $D(E)$ for crystal electrons and holes, starting with simple parabolic bands within the effective mass approximation:

$$E(\mathbf{k}_e) = E_c + \frac{\hbar^2 k_e^2}{2m_e}. \tag{3.3}$$

E_c is the energy of the conduction band minimum. The density of states $D(E)$ is such that $D(E)dE$ is the number of states with energy comprised between E and $E + dE$ per unit volume. With the help of a quantum mechanical model describing a particle in the box, one can deduce the density of states according to the dimensionality of the system. For electron in the conduction band, the $E - k$ dispersion relation is given by the effective mass approximation, and the density of states including spin in a 3-dimensional semiconductor is given by:

$$D_c(E) = \frac{1}{2\pi^2}\left(\frac{2m_e}{\hbar^2}\right)^{3/2}\sqrt{E - E_c} \quad (\text{for } E > E_c). \tag{3.4}$$

The density of states is zero for energy E lower than E_c, and proportional to the square root of the energy above E_c. The statistics with which we describe the occupation probability of electrons and holes are the Fermi-Dirac statistics. It reads for electrons:

$$f_c(E) = \frac{1}{\exp\left(\frac{E - E_{fc}}{k_B T}\right) + 1} \tag{3.5}$$

E_{fc} is the Fermi energy (or electrochemical potential) for electrons in the conduction band. The Fermi energy depends on the concentration of electrons, on the temperature of the electron gas, and on other material parameters such as the electron effective mass. The total amount of electron concentration in the conduction band is then given by the integral over the whole

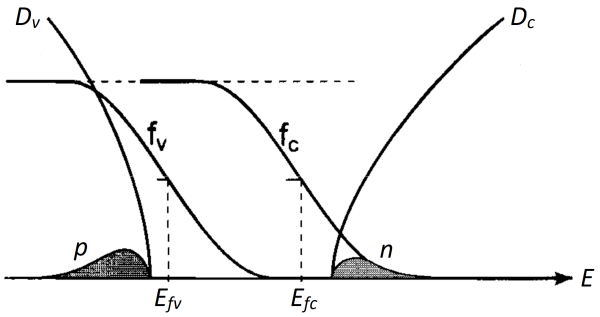

Figure 3.2 – *Schematics of semiconductor density of states: D_c for the conduction band and D_v for the valence band. The concentrations of electron and hole are described by two different Fermi distributions f_c and f_v (Figure adapted from Ref. [2]).*

energy range of the density of states multiplied by the occupation probability (see Figure 3.2 for illustration). For parabolic bands, we find for the total density of electrons in the conduction band n:

$$n = \int_{E_c}^{\infty} D_c(E) f_c(E) dE = N_c \times \mathcal{F}_{1/2}(\eta), \tag{3.6}$$

with $\eta = (E_{fc} - E_c)/(k_B T)$ a dimensionless parameter describing the electron Fermi energy E_{fc} relative to the conduction band edge E_c and

$$\mathcal{F}_{1/2}(\eta) = \frac{2}{\sqrt{\pi}} \int_0^{\infty} \frac{\sqrt{x}}{\exp(x - \eta) + 1} dx \tag{3.7}$$

is the Fermi integral of order 1/2.

$$N_c = 2 \left(\frac{2\pi m_e k_B T}{h^2} \right)^{3/2} \tag{3.8}$$

is the so-called effective density of conduction band states, which depends on the temperature T and on the electron effective mass. The expression of electron density cannot be solved analytically, but the values of Fermi integral are either tabulated or computed numerically. For non-degenerate electron gas ($E_c - E_{fc} \gg k_B T$), the Fermi function which overlaps with a finite density of states can be approximated quite well by the Boltzmann function. With this assumption, the Fermi-Dirac statistics can be replaced by classical Boltzmann statistics and the integral can be solved analytically:

$$n = N_c \times \exp\left(-\frac{E_c - E_{fc}}{k_B T} \right). \tag{3.9}$$

If the electron gas is degenerate, i.e., if E_{fc} is situated in the conduction band, for example with n-type doping concentration above approximately 4×10^{17} cm^{-3} in GaAs, the full expression using the Fermi function is needed. Moreover, the non-parabolic feature of the Γ_6 conduction band minimum need to be considered in order to calculate correctly the electron concentration as a function of the Fermi energy. The proper treatment for the non-parabolicity of the GaAs conduction band is carried out in Chapter 5.4.1.

In analogy, the density of states for holes in the valence bands and occupation probability can be written, always within the effective mass approximation. Although the hole energy increases when going deeper into the valence bands, we still share the energy scale E for hole by convenience. The density of states in the valence bands in a 3-dimensional system is given by:

$$D_v(E) = \frac{1}{2\pi^2} \left(\frac{2m_h}{\hbar^2} \right)^{3/2} \sqrt{E_v - E} \quad (\text{for } E < E_v), \tag{3.10}$$

where E_v presents the energy of the valence bands maximum. The density of states is assumed to be zero for energy E higher than the valence bands edge E_v. If two or more valence bands are present at E_v, like in most of the zincblende III-V compounds, contributions from heavy-hole and light-hole band is added to the total density of states, or simply employing a combined effective hole mass m_h, for which

$$m_h = (m_{hh}^{3/2} + m_{lh}^{3/2})^{2/3}, \tag{3.11}$$

where m_{hh} (resp. m_{lh}) denotes the effective mass for the heavy-hole bands (resp. light-hole bands). The occupation probability of a hole $f_v(E)$ can be thought as the probability of not being occupied by an electron in the valence bands. It reads:

$$f_v(E) = 1 - \frac{1}{\exp\left(\frac{E-E_{fv}}{k_BT}\right)+1} = \frac{1}{\exp\left(\frac{E_{fv}-E}{k_BT}\right)+1}. \tag{3.12}$$

Similarly, the total concentration of holes p in the valence bands is obtained with an effective density of valence band states N_v multiplied by the Fermi function:

$$p = N_v \times \mathcal{F}_{1/2}(\xi), \tag{3.13}$$

where $\xi = (E_v - E_{fv})/(k_BT)$ is a dimensionless parameter of the hole Fermi energy E_{fv} relative to the valence bands edge E_v, and the effective density of valence band states

$$N_v = 2\left(\frac{2\pi m_h k_B T}{h^2}\right)^{3/2}. \tag{3.14}$$

Although complicated features are present in the $E-k$ dispersion relation of the heavy- and light-hole bands extrema, a scalar (or spherical equivalent) effective mass is generally used and many observable hole properties can be interpreted fairly well. Using the combined hole effective mass, the effective density of valence band states in GaAs is found to be $N_v \approx 10^{19}\,\mathrm{cm}^{-3}$, about 25 times larger than that of conduction band. Therefore, degenerate hole concentration is less common for p-type GaAs and the above description is sufficient in most cases.

3.1.2 Optical process in semiconductors

After given essential notions of semiconductor physics, what happens now when light is shined onto semiconductors? A photon of energy lower than the semiconductor bandgap is not absorbed, while a photon of higher energy can be absorbed and creates an electron-hole pair in the semiconductor. We want to answer how the optical absorption depends on the incident photon energy, so we need to review the electronic transitions underlying optical processes in semiconductors. The spectral dependence of absorption and emission is mainly determined from the joint density of states of the semiconductor, and an excitonic enhancement near bandgap is discussed.

Microscopic description of optical transitions

A semi-classical approach of the light-matter interaction is presented according to Ref. [33] to gain more insight on the absorption and emission processes in semiconductors. In this approach, the electromagnetic field is treated classically while the electrons are described by quantum mechanical Bloch wave functions. Starting with an unperturbed one-electron Hamiltonian in the mean-field approximation (assuming every electron experiences the same average potential $V(\mathbf{r})$):

$$H_0 = \frac{\mathbf{p}^2}{2m_0} + V(\mathbf{r}), \tag{3.15}$$

where m_0 is the free-electron mass. $\mathbf{p} = \frac{\hbar}{i}\nabla$ is the momentum operator. $V(\mathbf{r})$ is a crystal periodic potential. The presence of a radiative field is considered as a small perturbation, i.e. it does not change much the eigenstates and eigenenergies of the electron. To describe this electromagnetic field, a vector potential $\mathbf{A}(\mathbf{r}, t)$ is introduced. The Coulomb gauge is chosen, in which $\nabla \cdot \mathbf{A} = 0$. In this gauge, the electric field and magnetic field are given by:

$$\mathbf{E} = -\frac{\partial \mathbf{A}}{\partial t} \quad \text{and} \quad \mathbf{B} = \nabla \times \mathbf{A}. \tag{3.16}$$

The quantum mechanical Hamiltonian describing the motion of an electron in an external electromagnetic field is obtained by replacing the electron momentum operator $\mathbf{p}$ by $\mathbf{p} + e\mathbf{A}$ [33]:

$$H = \frac{1}{2m_0}(\mathbf{p} + e\mathbf{A})^2 + V(\mathbf{r}). \tag{3.17}$$

The operators can be developed and simplified using the Coulomb gauge. Compared with the unperturbed Hamiltonian H_0, an extra term H_1 linear with $\mathbf{A}$ describes the interaction between the radiation and a Bloch electron. This term is referred as the electron-radiation interaction Hamiltonian.

$$H_1 = \frac{e}{m_0}\mathbf{A}\cdot\mathbf{p} \tag{3.18}$$

The term $H_2 = e^2/(2m_0)\mathbf{A}^2$ is a second order perturbation, neglected here as we only deal with linear optical phenomenon. We assume that $\mathbf{A}$ is weak enough so we can apply time-dependent perturbation theory in the form of the Fermi's golden rule to calculate the optical absorption rate r_a per unit volume for an electron in the valence band state $|v\rangle$ (initial state with energy $\mathcal{E}_h$ and wavevector $\mathbf{k}_h$) to the conduction band state $|c\rangle$ (final state with energy $\mathcal{E}_e$ and wavevector $\mathbf{k}_e$). To calculate the transition rate r_a, the matrix element needs to be evaluated:

$$\langle c|H_1|v\rangle = \frac{e}{m_0}\langle c|\mathbf{A}\cdot\mathbf{p}|v\rangle\,. \tag{3.19}$$

Now we write explicitly an expression for the radiation field:

$$\mathbf{A} = \frac{A_0}{2}\left[\exp\left(i(\mathbf{q}\cdot\mathbf{r} - \omega t)\right) + \exp\left(-i(\mathbf{q}\cdot\mathbf{r} - \omega t)\right)\right]\mathbf{e}_A, \tag{3.20}$$

where A_0 and $\mathbf{e}_A$ are the amplitude and the unit vector in the direction of the vector potential, $\mathbf{q}$ is the wavevector of the radiation field. The stationary wavefunctions of electrons in the valence band and in the conduction band are given by the Bloch functions:

$$|v\rangle = u_{v,\mathbf{k}_h}(\mathbf{r})\exp(i\mathbf{k}_h\cdot\mathbf{r}) \quad \text{and} \quad |c\rangle = u_{c,\mathbf{k}_e}(\mathbf{r})\exp(i\mathbf{k}_e\cdot\mathbf{r}). \tag{3.21}$$

We consider the first term of the vector potential in Equation 3.20 which yields the absorption process. At $t < 0$, we imagine that all electrons are in the valence band states $|v\rangle$, then we switch on the small perturbation at $t = 0$. The time-dependent Schrödinger equation describes the evolution of the two-level electronic system. A significant transition rate of electrons from the valence band states to the conduction band states occurs only if the time dependent exponential $\exp(i(\mathcal{E}_e - \mathcal{E}_h)t/\hbar - i\omega t)$ vanishes. The integration over time of the term $\exp(-i\omega t)$ and the corresponding eigenenergy of electron Bloch functions leads to formally the delta function $\delta\left(\mathcal{E}_e(\mathbf{k}_e) - \mathcal{E}_h(\mathbf{k}_h) - \hbar\omega\right)$. This is also the energy conservation law. If we consider the second term of the vector potential in Equation 3.20, the delta function becomes $\delta\left(\mathcal{E}_e(\mathbf{k}_e) - \mathcal{E}_h(\mathbf{k}_h) + \hbar\omega\right)$, which describes the stimulated emission process in presence of radiation field.

The calculation of the matrix element involves integration over space. In periodic lattice structure, the integration can be restricted to an unit cell because every position vector can be

brought into an unit cell: $\mathbf{r} = \mathbf{R}_j + \mathbf{r}'$ where $\mathbf{r}'$ is within the unit cell and $\mathbf{R}_j$ is a lattice vector.

$$\begin{aligned}&\int u^*_{c,\mathbf{k}_e} \exp\left(i(-\mathbf{k}_e + \mathbf{q} + \mathbf{k}_h)\cdot \mathbf{r}\right)(\mathbf{e}_A \cdot \mathbf{p}) u_{v,\mathbf{k}_h} \mathbf{dr} = \\ &\sum_j \exp\left(i(-\mathbf{k}_e + \mathbf{q} + \mathbf{k}_h)\cdot \mathbf{R}_j\right) \int_{\text{unit cell}} u^*_{c,\mathbf{k}_e} \exp\left(i(-\mathbf{k}_e + \mathbf{q} + \mathbf{k}_h)\cdot \mathbf{r}'\right)(\mathbf{e}_A \cdot \mathbf{p}) u_{v,\mathbf{k}_h} \mathbf{dr}'\end{aligned} \tag{3.22}$$

The summation over all lattice vectors leads to formally the delta function $\delta(\mathbf{k}_e - \mathbf{k}_h - \mathbf{q})$. This term ensures that the wavevector is conserved in the absorption process. Since the wavelength of most visible light is much larger than the size of the crystal unit cell, the wavevector of the radiation $\mathbf{q}$ is much smaller than the size of the Brillouin zone. The wavevector for electron in the valence band and that in the conduction band is nearly the same upon absorption and thus simply noted $\mathbf{k}$. This constitutes the electric dipole approximation. In the following, the matrix element is simply noted P_{cv} (unit of a momentum):

$$P_{\text{cv}} = \langle c|\mathbf{e}_A \cdot \mathbf{p}|v\rangle\,, \tag{3.23}$$

which is not strongly dependent on $\mathbf{k}$. Using the Fermi's golden rule, the electric dipole transition rate r_a for photon absorption is given by $[\text{s}^{-1}\text{m}^{-3}]$:

$$r_a = \frac{2\pi}{\hbar}\left(\frac{eA_0}{2m_0}\right)^2 |P_{\text{cv}}|^2 \sum_{\mathbf{k}} \delta\left(\mathcal{E}_e(\mathbf{k}) - \mathcal{E}_h(\mathbf{k}) - \hbar\omega\right). \tag{3.24}$$

The summation should be restricted to those $\mathbf{k}$ allowed per unit volume of crystal. The amplitude of the vector potential can be written with a more familiar form using the electric field: $A_0 = E_0/\omega$. The power lost by the electromagnetic field due to absorption in unit volume of the medium is thus the transition rate multiplying the photon energy: $r_a\hbar\omega$ $[\text{Js}^{-1}\text{m}^{-3}]$. This power loss can be expressed in term of the complex dielectric function ε_r in the classical electromagnetic framework: $\frac{1}{2}\omega\varepsilon_0 \text{Im}(\varepsilon_r)E_0^2$. The imaginary part of the relative dielectric function is then written as

$$\text{Im}(\varepsilon_r) = \frac{\pi e^2 |P_{\text{cv}}|^2}{m_0^2 \varepsilon_0 \omega^2} \sum_{\mathbf{k}} \delta\left(\mathcal{E}_e(\mathbf{k}) - \mathcal{E}_h(\mathbf{k}) - \hbar\omega\right). \tag{3.25}$$

The real part of the dielectric function can also be expressed using the Kramers-Kronig relations and is given in Ref. [33] (page 261). We give the expression of the absorption coefficient: $\alpha = \omega \text{Im}(\varepsilon_r)/(nc_0)$, where n is the refractive index of the material.

$$\alpha(\omega) = \frac{\pi e^2 |P_{\text{cv}}|^2}{m_0^2 \varepsilon_0 c_0 n \omega} \sum_{\mathbf{k}} \delta\left(\mathcal{E}_e(\mathbf{k}) - \mathcal{E}_h(\mathbf{k}) - \hbar\omega\right). \tag{3.26}$$

A dimensionless quantity is defined as [33]

$$f_{\text{cv}} = \frac{2|P_{\text{cv}}|^2}{m_0 \hbar \omega}, \tag{3.27}$$

which represents the number of oscillators with frequency ω. The quantity f_{cv} is known as the *oscillator strength* of the optical transition. The absorption coefficient in Equation 3.26 expresses essentially the oscillator strength in one part, and the summation over allowed transition states in the other part. The latter describes the density of initial and final states accounted for the momentum conservation. In semiconductors where energy bands form a continuum, it is equivalent to the evaluation of the joint density of states, discussed in the following.

Joint density of states

The joint density of states for a transition energy $E_{cv} = \mathcal{E}_e - \mathcal{E}_h$ between the valence band and the conduction band in semiconductors is defined as (Ref. [33] page 361):

$$D_j(E_{cv}) = 2 \int \frac{dS_{\mathbf{k}}}{8\pi^3} \frac{1}{|\nabla_{\mathbf{k}} E_{cv}|}, \tag{3.28}$$

where $S_{\mathbf{k}}$ is the constant energy surface defined by $E_{cv}(\mathbf{k})$ equal to a constant. The spin causes doubly degenerate bands and accounts for the prefactor 2. It is firstly noted that singularities appear where $\nabla_{\mathbf{k}} E_{cv}$ vanishes. This occurs when the gradient for both bands is zero or parallel in $\mathbf{k}$-space. Singularities of joint density of states are called van-Hove singularities, or more commonly, critical points. Assuming that $k = 0$ is a critical point, the energy dispersion relation can be expanded as a function of k in 3-dimensional space:

$$E(\mathbf{k}) = E(0) + \frac{\hbar^2 k_x^2}{2m_x} + \frac{\hbar^2 k_y^2}{2m_y} + \frac{\hbar^2 k_z^2}{2m_z}. \tag{3.29}$$

The critical points are classified as M_0, M_1, M_2 and M_3 with the index being the number of effective masses that are negative. M_0 (resp. M_3) describes a minimum (resp. maximum) of the band separation. M_1 and M_2 are saddle points [34].

Let us look at the absorption edge of direct-gap semiconductors where luminescence occurs. The bandgap E_g is also called E_0 gap in connection with critical points because the joint density of states has a minimum at E_g. For a given transition energy $E_{cv} = \mathcal{E}_e - \mathcal{E}_h$, the excess energy of electron near the conduction band edge and that of hole near the valence band edge is weighted according to the effective mass of electron and hole.

$$\begin{aligned} \mathcal{E}_e &= E_c + \frac{\hbar k^2}{2m_e} = E_c + \frac{\mu}{m_e}(E_{cv} - E_g) \\ \mathcal{E}_h &= E_v - \frac{\hbar k^2}{2m_h} = E_v + \frac{\mu}{m_h}(E_{cv} - E_g), \end{aligned} \tag{3.30}$$

where k is the wavevector of electron and hole. μ is the reduced mass given by:

$$\frac{1}{\mu} = \frac{1}{m_e} + \frac{1}{m_h}. \tag{3.31}$$

The joint density of states D_j is calculated near the parabolic band edges such that $D_j dE_{cv} = D_c d\mathcal{E}_e = D_v d\mathcal{E}_h$, using Equation 3.30 and the explicit expressions for the density of states of the conduction band (Equation 3.4) or of the valence band (Equation 3.10).

$$D_j(E) = \frac{1}{2\pi^2} \left(\frac{2\mu}{\hbar^2}\right)^{3/2} \sqrt{E - E_g} \quad (\text{for } E > E_g). \tag{3.32}$$

We can rewrite the absorption coefficient (Equation 3.26) using the oscillator strength and the joint density of states.

$$\alpha(\hbar\omega) = \frac{\pi \hbar e^2 f_{\text{cv}}}{2m_0 \varepsilon_0 c_0 n} D_j(\hbar\omega) \tag{3.33}$$

At a first approximation, assuming constant matrix element, the absorption coefficient rises as square root of energies above the fundamental bandgap E_g. This absorption is based on the joint density of states and does not account for carrier occupation probabilities. It will be discussed in Section 3.2 for the generalized Planck's law, the general relation between absorption, stimulated and spontaneous emission accounting for the band filling effect. Luminescence spectra can then be fully determined through the absorption characteristics near the fundamental bandgap.

Exciton

The absorption coefficient in direct-gap semiconductors is described near bandgap, to a first approximation, by a parabolic dependence in photon energy. In reality, the absorption raises faster than a parabolic band near and above the bandgap. Figure 3.3 show the absorption coefficient of GaAs measured at various temperatures [36]. A sharp absorption peak near the bandgap edge is attributed to exciton absorption, arise from the Coulomb interaction of the electron-hole pairs. This effect is even more pronounced at low temperature.

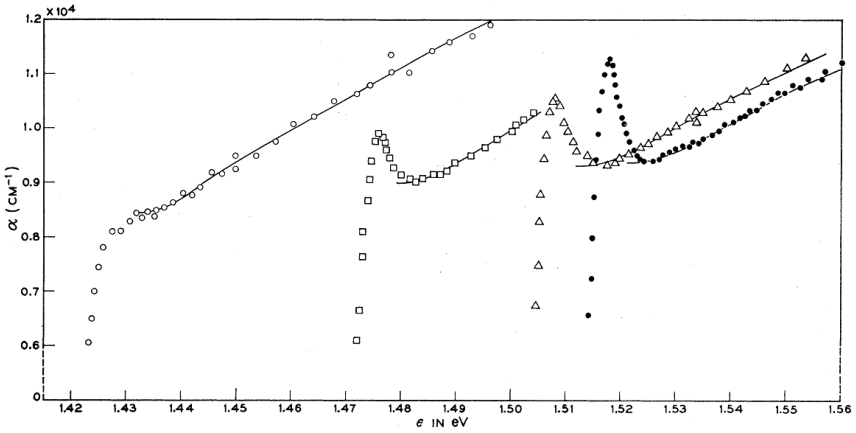

Figure 3.3 – *Absorption measurement in high-purity GaAs near bandgap, showing excitonic absorption characteristics; ○ 294 K, □ 186 K, △ 90 K, • 21 K. (figure extracted from Sturge [36])*

To describe the exciton absorption, the one-electron picture is not sufficient. Using the effective mass approximation, the Coulomb interaction between electron and hole leads to a hydrogen-like problem with an additional Coulomb potential term in the total Hamiltonian for a two-particle system:

$$H' = \frac{-e^2}{4\pi\varepsilon\,|\mathbf{r}_e - \mathbf{r}_h|}, \tag{3.34}$$

with the permittivity of the medium $\varepsilon = \varepsilon_0\varepsilon_r$, ε_0 is the permittivity of free space and ε_r is the dielectric constant. $\mathbf{r}_e$ (resp. $\mathbf{r}_h$) is the position of electron (resp. hole). For simple parabolic bands and a direct-gap semiconductor, one can separate the relative motion of electron and hole, and the motion of the center of mass. This leads to the dispersion relation of excitons [15]:

$$E_X(n, \mathbf{K}) = E_g - R_X \frac{1}{n^2} + \frac{\hbar^2 \mathbf{K}^2}{2M} \tag{3.35}$$

with $n = 1, 2, 3...$ principal quantum number, $M = m_e + m_h$ the translational mass and $\mathbf{K} = \mathbf{k}_e + \mathbf{k}_h$ wavevector of the exciton. The exciton Rydberg energy R_X is related to the hydrogen Rydberg energy R_H through the reduced mass of the exciton, and the dielectric constant of the medium in which the exciton moves:

$$R_X = \frac{1}{\varepsilon_r^2}\frac{\mu}{m_0} R_H \quad \text{exciton Rydberg energy,} \tag{3.36}$$

with

$$\mu = \frac{m_e m_h}{m_e + m_h} m_0 \quad \text{exciton reduced mass,} \tag{3.37}$$

and

$$R_H = \frac{m_0 e^4}{8\varepsilon_0^2 h^2} = 13.6\,\text{eV} \quad \text{hydrogen Rydberg energy.} \tag{3.38}$$

Depending on the material parameters for typical semiconductors, we have $1\,\text{meV} \leq R_X \leq 200\,\text{meV} \ll E_g$. For the exciton ground state in GaAs, we find typically $\varepsilon_r = 12.9$ and an exciton reduced mass about $\mu = 0.059\,m_0$, leading to $E_X \approx 4.8\,\text{meV}$. Photoluminescence [37] and absorption measurement [38] at liquid helium temperature gave similar values of about 4.2 to 4.4 meV. The radius of the exciton can also be related to the Bohr radius a_0 of the hydrogen atom, modified by the dielectric constant ε_r and the exciton reduced mass μ:

$$a_X = a_0 \varepsilon_r \frac{m_0}{\mu} \quad \text{exciton Bohr radius,} \tag{3.39}$$

with

$$a_0 = \frac{4\pi\varepsilon_0\hbar^2}{m_0 e^2} = 0.53\,\mathring{A}. \tag{3.40}$$

For GaAs again, the exciton Bohr radius is evaluated to be $a_X \approx 12.6\,\text{nm}$. For typical inorganic semiconductors, the exciton Bohr radius is larger than the lattice constant. This implies that the "orbit" of electron and hole around their common center of mass average over many unit cells and this in turn justifies the effective mass approximation in a self-consistent way. These excitons are called Wannier excitons. On the other hand, excitons with electron-hole pair wavefunctions confined in one unit cell are called Frenkel excitons, which cannot be described in the effective mass approximation. A quantum mechanical treatment of the exciton absorption in the effective mass approximation was given by Elliott [39]. In the ideal case, exciton is an electron-hole pair that is able to move freely in the lattice space (free exciton). The presence of impurities or defects in semiconductors may trap excitons and lower the excitonic transition energies. For instance, low-temperature photoluminescence generally reveal exciton lines corresponding to the presence of certain chemical species even in very low concentration. We will give an overview of defect luminescence in the following.

3.1.3 Defect luminescence

Lattice defects exist in every real semiconductors. Defects may be unintentional (imperfect crystal growth, contamination, etc.) or intentional (i.e. doping). Defects can cause severe non-radiative recombination that lower the overall radiative efficiency of the light-emitting material and are detrimental for the device operation. Defects can also change the optical processes and yield luminescence peaks due to specific chemical specious even at low concentrations. In particular, low-temperature luminescence is very sensitive to the defect-related electronic states. Here, we give a description of luminescence related to the semiconductor defects.

Defects in semiconductors

Defects in semiconductors can be classified according to the dimension: point defects, one-dimensional defects like dislocations, two-dimensional defects like stacking faults and grain boundaries, or three-dimensional ones like precipitates. Point defects include vacancies, anti-sites, interstitial and substitutional atoms. Here we consider the electronic states connected with localized point defects. Figure 3.4 sketches various electronic energy levels of point defects. A donor is a shallow center which has an energy level just below the conduction band and can easily give an electron (e.g. by thermal ionization) to this band. Donors are often formed by substitutional atoms in the periodic table one column to the right of the atom which they replace, like P in Si or Ge, Si on Ga site in GaAs, etc. In analogy, acceptors can easily accommodate an electron from the valence band, i.e., they emit a hole into it. Acceptors may be formed by substitutional atoms which have one electron less than the one been replaced. Thus the impurities are often found in the periodic table to the left of the atom which they replace, for example, B in Si or Ge, Si on As site in GaAs, etc. Some vacancies or interstitials can also act as donors or acceptors.

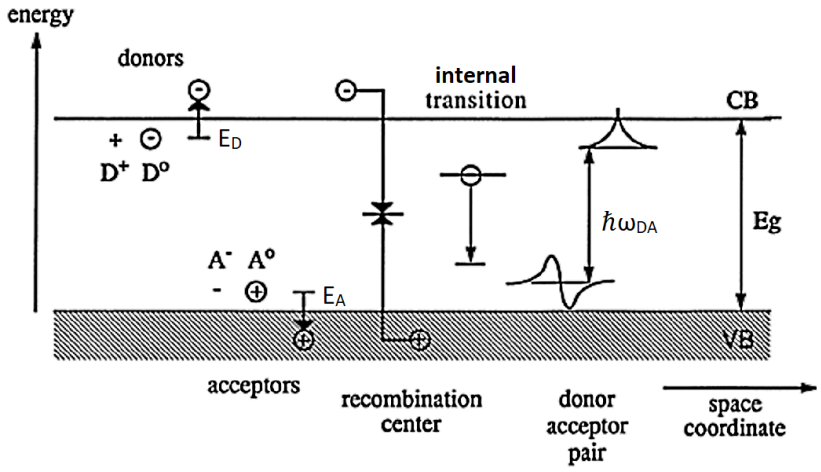

Figure 3.4 – *Schematic drawing of various impurity levels in semiconductors (Figure adapted from Ref. [15]).*

A semiconductor which has a higher concentration of donors (resp. acceptors) is called n-type (resp. p-type). Controlling either n-type or p-type conductivity constitutes the foundation of modern semiconductor devices.

A shallow donor (resp. acceptor) can be considered as a positively (resp. negatively) charged center to which an electron (resp. hole) is bound by Coulomb interaction. So we face a problem similar to that of a hydrogen atom or excitons as discussed shortly in the previous paragraph. In the simplest approximation a shallow donor or acceptor leads to a series of states with binding energy

$$E_{D,A} = \frac{1}{\varepsilon_r^2}\frac{m_{e,h}}{m_0} R_H \frac{1}{n^2} \tag{3.41}$$

where R_H is the Rydberg energy of the H atom ($R_H = 13.6\text{eV}$), n the main quantum number and ε_r the dielectric constant. Since the donor or acceptor is in a semiconductor and not in vacuum, the electric field binding force is somewhat weakened due to polarization of the neighboring atoms. Therefore, we must replace the dielectric permittivity of free space in the binding energy by the permittivity of the semiconductor and use the effective mass. In Figure 3.4, only the ground states for $n = 1$ are shown. As for excitons, the excited states of shallow donors or acceptors converge for $n \to \infty$ to the ionization continuum. Depending on the materials properties, we usually find the values for the donor and acceptor binding energies of: $5\,\text{meV} \leq E_D \leq 50\,\text{meV}$, and $20\text{meV} \leq E_A \leq 200\text{meV}$. Taking an example for GaAs and its usual parameters of dielectric constant and effective masses, we get $E_D \approx 5.5\,\text{meV}$ and $E_A \approx 42\,\text{meV}$. The radius of the $n = 1$ state is given by:

$$a_{D,A} = a_0 \varepsilon_r \frac{m_0}{m_{e,h}} \tag{3.42}$$

where $a_0 = 0.53\,\mathring{A}$ is the Bohr radius for H atom. For GaAs, theoretical values give $a_D \approx 10\,\text{nm}$ and $a_A \approx 1.3\,\text{nm}$. Note that $a_{D,A} > a_{\text{lattice}}$ justifies the use of the effective mass approximation. For different impurities, there is some small influence of the chemical nature of the atom forming the donor or acceptor.

Pairs of donors and acceptors which are so close in space that their wavefunctions overlap are known as donor-acceptor pairs (DA). An electron on a donor and a hole on an acceptor can then recombine. The energy of the photon resulting from radiative DA recombination is given by [15]

$$\hbar\omega_{DA} = E_g - E_{D^0} - E_{A^0} + \frac{e^2}{4\pi\varepsilon_0\,\varepsilon_r r_{DA}} \tag{3.43}$$

E_{D^0,A^0} are the binding energies of electron and hole to their respective centers, and the last term depending on the distance r_{DA} of the donor-acceptor pair reflects the Coulomb energy of the ionized centers after the recombination. With increasing excitation power density, the number of occupied donor and acceptor centers increases and their average distance r_{DA} decreases. As a consequence, the emission maximum of the DA band shifts to the blue with increasing pump power due to the Coulomb term in Equation 3.43. Another recombination process connected with neutral donors or acceptors is the so-called free-to-bound (FB) transition. In this case, a free electron or hole recombines with a neutral acceptor or donor, respectively. The corresponding emission peak is

$$\hbar\omega_{FB} = E_g - E_{D^0,A^0} \tag{3.44}$$

Free-to-bound transition and donor-acceptor pair recombination together with their phonon replica often overlap in one complex or broadened luminescence spectrum.

Similar to the way that free carriers can be bound to point defects, it is found that excitons can also be bound to defects. An exciton (X) can be localized on a neutral or ionized donor or acceptor, giving rise to exciton-impurity complex. The binding energy of an exciton is lowest for an ionized donor (D^+X), slightly higher for a neutral donor (D^0X), and highest for a neutral acceptor (A^0X). An ionized acceptor does not usually bind an exciton since a neutral acceptor and a free electron are energetically more favorable. The energy of the emitted photon from the recombination of bound-excitons (BX) is:

$$\hbar\omega_{BX} = E_g - R_X - E_{BX}, \tag{3.45}$$

where E_{BX} is called the exciton localization energy, that is the energy required to remove the exciton from the impurity. It has been shown empirically that the localization energy for exciton bound to neutral donors or acceptors is much smaller than the impurity binding energy, and depends linearly on it: i.e. $E_{BX} = a + bE_{D,A}$. This is known as the Haynes rule [40].

For deep centers, the approach similar to the hydrogen atom is not adequate. The wavefunction is better described by the parent atomic orbitals, modified by the influence of the surrounding atoms. Cu, Ni, Fe, Cr and other elements can give rise to such deep levels. Some deep centers can exchange carriers with both the conduction and the valence band. In this case they are called recombination centers. The recombination can be radiative or non-radiative and some centers provide fast channels for de-excitation of electron-hole pairs.

Heavy doping effect

Heavy doping changes the physics of shallow impurities and the main features of luminescence spectra compared to pure or lightly-doped semiconductors. Heavy doping means a doping density such that the rough criterion $N_{D,A} \geq a_{D,A}^{-3}$ is satisfied, where $N_{D,A}$ is the donor or acceptor concentration and $a_{D,A}$ is the effective Bohr radius (Equation 3.42). For example, we have calculated the effective Bohr radius of a shallow donor in GaAs to be roughly 10 nm, corresponding to a threshold for heavy doping density of $N_D \approx 10^{18}$ cm^{-3}. At near zero temperature, the wavefunctions of shallow impurities are rather isolated at low doping concentration and overlap for heavy doping. The large amount of dopants induces a high free carrier density in the bands and a high density of ionized dopant ions. These facts in turn cause a modification of the density of states near band edges with respect to the undoped case, including the formation of impurity bands, band tails and bandgap narrowing.

In pure semiconductors, theory shows that the density of state is zero for energies in the bandgap, corresponding to a sharp absorption edge at the long-wavelength side. In real materials containing more or less degree of disorders, an exponential decrease of absorption below the bandgap is usually observed, which is called the Urbach tail [41]. As shown in Figure 3.5(a), the density of state is modeled as a usual parabolic band, decreasing exponentially for energies below

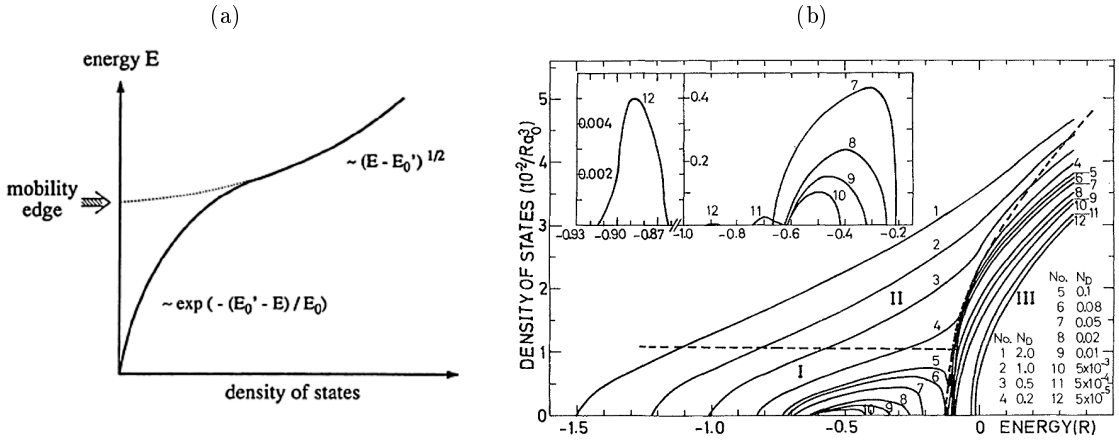

Figure 3.5 – *(a) The exponential decrease of density of states near the parabolic band edge (Figure extracted from Ref. [15]). (b) Density of states as functions of energy for different donor concentrations N_D. The insets show the impurity band (enlarged scales) for several (low) concentrations. Regions I, II and III delimited by dashed lines are domains of existence of localized, hybrid and extended states (Figure extracted from Ref. [43]).*

the bandgap. In doped semiconductors, the band tail appears for several reasons. For example, an ionized donor exerts an attractive force on the conduction electrons and a repulsive force on the valence band holes (acceptors act conversely). In view of the non-homogeneous distribution of impurities on a microscopic level, the local interactions will be more or less strong, making the density of states a summation of parabolas beginning at various energies, and thus smear both band edges. Moreover, the accommodation of impurities in the lattice results in localized strains. The resulting deformation potential increases locally the energy gap (compression) and elsewhere decreases it (dilation). The overall perturbation also smears both band edges [42]. This effect is also applied for alloy semiconductors, where composition fluctuation in atomic scales may contribute to significant broadening of band-edge luminescence spectra.

A direct modification of the density of states near band edges is the formation of impurity bands. The spatial overlap of impurity levels broadens the latter into a band. At high concentrations, the impurity band merges with the nearest intrinsic band. Figure 3.5(b) shows a numerical simulation of density of states for different donor concentrations over 5 order of magnitudes [43]. At given concentration, calculations are made for different energies around the bottom of the conduction band. The energies are given in units of effective Rydberg energy R (Equation 3.41) and lengths are given in units of effective Bohr radius a_0 (Equation 3.42). The doping concentrations N_D are expressed in $(\pi/3)/(4a_0)^3$. As can be seen, at high concentrations, the conduction band shows a tail extended toward low energies. As N_D decreases, an impurity band is formed and separated from the conduction band. This appears at $N_D \approx 0.1$ (i.e. $N_D^{1/3} a_0 \approx 0.12$ in usual units). The gap between the impurity band and the bottom of the conduction band widens out as N_D decreases and tends toward the hydrogenic limit ($1R$).

When we look closer to the electronic states in the band tails, they can be distinguished from the conduction band continuum by their localization nature. In fact, the wavefunctions for tail states or impurity band present a broad maximum around $k = 0$ and extend widely in the k-space. The behavior is typical for a localized state in view of the uncertainty relation. At higher energies, the wavefunctions resemble Bloch waves and extend in real space. This behavior, like free electrons, is characteristic for an extended state. The energy which separates extended from localized states is called the mobility edge [44]. At near zero temperature, the Fermi level can be situated above or below the mobility edge. In the first case, the system is called a metal, since it has finite conductivity at $T \to 0$, in the second it is an insulator. The transition from an

insulator to a metal with increasing doping is known as the Mott transition [45]. This transition density in semiconductors is roughly given for $N_D^{1/3} a_D \approx 0.2$.

An important consequence of disorder system is that it is no longer invariant with respect to translations of lattice vectors. The wavevector is no longer a good quantum number, and the k-selection rule in optical transitions can be relaxed. A disordered system is in principle characterized only by its density of states. In the following, we will introduce the generalized Planck's law to describe luminescence spectra (Section 3.2), and reproduce the luminescence features of doped semiconductors (Section 3.2.4).

3.2 The generalized Planck's law

In this section, the generalized Planck's law is reviewed based on the work of Würfel for the general consideration of chemical potentials in semiconductors [46]. The reasoning follows partly the reference book *Physics of Solar Cells* [2]. Beginning with the photon density in the thermal radiation of a black body, semiconductor luminescence in quasi-equilibrium is obtained similarly in connection with the chemical potential of electrons and holes. Detailed balance consideration is presented and the relation between absorption, stimulated and spontaneous emission is deduced. The light spectra emitted by a semiconductor can then be fully modeled, and depending on applications, important material properties (e.g. absorptivity, carrier temperature, Fermi energies or carrier concentrations) can be extracted from the measurement of luminescence spectra.

3.2.1 Black body radiation

We start with the back body radiation, known as Planck's law, describing the spectral density of electromagnetic radiation emitted by a black body in thermal equilibrium at a given temperature T. The law is named after Max Planck, who proposed it in 1900.

Photon density in a cavity

A black body is an ideal object that completely absorbs radiation of all photons with arbitrary energy $\hbar\omega$. Its absorptance or absorptivity (probability that a photon is absorbed) is $A(\hbar\omega) = 1$. A conceptual model for the black body is a tiny hole in a cavity with opaque walls. The hole absorbs all incoming photons. When the temperature of the cavity increases, the hole begins to emit photons. This emitted radiation at thermodynamic equilibrium is only characteristic of the temperature, thus is called thermal radiation. The photon density $n_\gamma(\hbar\omega)$ is the number of photons per volume and per energy interval. It is the product of the photon density of states $D_\gamma(\hbar\omega)$ with the photon distribution function $f_\gamma(E)$. The density of states $D_\gamma(\hbar\omega)$ can be deduced from quantum mechanical consideration, similarly to the electron density of states shown previously. Imaging a volume delimited by infinite potential, we count the total amount of states in k-space. In particularly, a volume element in k-space comprises two photon states with opposite spins. The density of states for photons including spin degeneracy in 3-dimensions is given by:

$$D_\gamma(\hbar\omega) = \frac{(\hbar\omega)^2}{\pi^2 \hbar^3 c^3}. \tag{3.46}$$

Here $\hbar = h/(2\pi)$ is the reduced Planck's constant, c is the velocity of photons in the cavity. If the cavity is empty, $c = c_0$ is the velocity of light in vacuum. With increasing index of refraction n in the medium, the velocity of photons decreases as $c = c_0/n$, resulting in an increasing density of states for the photons. Furthermore, assuming an isotropic distribution of states in k-space, we might normalize the density of states per solid angle by dividing D_γ by 4π, the factor including whole directions in 3-dimensional space. When we calculate photon currents which

are directional, it is important to take into account the angular distribution. The distribution function defines the probability for the occupation of states with the energy $\hbar\omega$. Because photons have spin ± 1, the Bose-Einstein distribution applies for the photons:

$$f_\gamma(\hbar\omega) = \frac{1}{\exp(\frac{\hbar\omega - \mu_\gamma}{k_B T}) - 1}. \tag{3.47}$$

In the combination $k_B T$, k_B denotes the Boltzmann constant and T the temperature. μ_γ is the chemical potential of photons. In general, like for thermal radiation, $\mu_\gamma = 0$ because the number of photons is not conserved. A more general consideration of this term for semiconductors is discussed later. Together with the density of states for photons, we obtain the photon density in a 3-dimensional medium:

$$n_\gamma(\hbar\omega) = \frac{(\hbar\omega)^2}{\pi^2 \hbar^3 (c_0/n)^3} \frac{1}{\exp(\frac{\hbar\omega}{k_B T}) - 1}. \tag{3.48}$$

If we multiply the above expression by the photon energy $\hbar\omega$, then we obtain the energy density, also called the spectrum (per photon energy). It has its maximum value at a photon energy of $\hbar\omega_{\max} = 2.82\, k_B T$, the maximum energy of the spectrum shifts linearly toward higher energy with the increased temperature. For example, the solar spectrum can be approximated by a black body radiation at a temperature of about 5800 K, with the maximum value at the photon energy around 1.41 eV (close near infra-red). Another spectrum is also used, called wavelength spectrum. It is the energy distribution per photon wavelength, which may present different characteristics. The 5800 K black body and the solar spectrum per wavelength (e.g. AM0 radiation) is somewhat peaked at 500 nm, in the blue-green visible region.

Photon current emission

Now we want to find the photon current emission of a black body. Considering a small hole in the black body cavity with surface area $\mathrm{d}A$, a direction into a small solid angle element $\mathrm{d}\Omega$, forming an angle θ with the normal of the surface element, the volume in the cavity that can transport photons to the hole within a short time $\mathrm{d}t$ is: $\mathrm{d}V = c\,\mathrm{d}t\,\mathrm{d}A\cos\theta$. This volume contains the number of photons $n_\gamma(\hbar\omega)\,\mathrm{d}V\,\mathrm{d}\Omega/(4\pi)$ that are moving toward the hole thus will fly through the hole after time $\mathrm{d}t$ (assuming isotropic distribution of photons). So we can write the photon current per unit surface $\mathrm{d}j_\gamma(\hbar\omega)$ into the solid angle $\mathrm{d}\Omega$:

$$\mathrm{d}j_\gamma(\hbar\omega) = n_\gamma(\hbar\omega)\, c \cos(\theta)\, \frac{\mathrm{d}\Omega}{4\pi}. \tag{3.49}$$

The factor $\cos(\theta)$ describes the angular dependence of the emission (Lambert's cosine law). If we integrate $\mathrm{d}j_\gamma(\hbar\omega)$ over the hemisphere of emission, a factor $1/4$ is found to describe the photon current flowing in one direction: $j_\gamma(\hbar\omega) = (1/4)\, c\, n_\gamma(\hbar\omega)$. We obtain the spectral irradiance of a black body, noted ϕ_{bb} with the unit of photons/(s.m^2).

$$\phi_{\mathrm{bb}}(\hbar\omega) = \frac{(\hbar\omega)^2}{4\pi^2 \hbar^3 (c_0/n)^2} \frac{1}{\exp(\frac{\hbar\omega}{k_B T}) - 1} \tag{3.50}$$

This is known as the Planck's law of black body radiation.

Kirchhoff's law of radiation for non-black bodies

By regarding the equilibrium between a black and a non-black body of equal temperature, Kirchhoff deduced in 1859: *For a body of arbitrary material, emitting and absorbing thermal radiation*

at every wavelength in thermodynamic equilibrium, the ratio of its emissive power to its dimensionless absorptivity equal to a universal function only of radiative wavelength and temperature. That universal function describes the perfect black-body emissive power. This universal function is exactly the formula found by Planck latter in 1900. In other words, for a non-black body, its emissivity (ratio of emitting radiation to black-body one) is equal to its absorptivity. Thus, the mathematical description of the thermal radiation can be applied to a non-black body. It is the simple product of the absorptivity $A(\hbar\omega)$ and the emission of a black body $\phi_{\mathrm{bb}}(\hbar\omega)$ given in Equation 3.50. In the following, we will deduce a generalization of Kirchhoff's law applied to semiconductors (non-black body) emitting light at quasi-thermal equilibrium.

3.2.2 Semiconductor in quasi-thermal equilibrium

In 1954, van Roosbroeck and Shockley (vRS) derived the famous relationship between the volumic rate of *internal* spontaneous radiative emission and the spectral absorption coefficient at thermal equilibrium [47]. Later, Lasher and Stern generalized the vRS result of the spontaneous emission rate in terms of the quasi-Fermi level splitting under quasi-thermal equilibrium [48]. Würfel further expressed the *external* flux of spontaneous radiative emission using the spectral absorptivity of the material [46]. Here, the importance of the quasi-Fermi levels is addressed.

Fermi energy and electrochemical potential

In the following, we discuss the term μ_γ called chemical potential of radiation. According to Gibbs, the exchange of an amount of energy $\mathrm{d}E$ in a system is related to other quantities, which are exchanged as well.

$$\mathrm{d}E(S,V,N_i,Q...) = T\mathrm{d}S - p\mathrm{d}V + \sum_i \mu_i \mathrm{d}N_i + \varphi \mathrm{d}Q + ... \tag{3.51}$$

If only entropy S is exchanged with the energy, the energy exchanged is called heat. $-p\mathrm{d}V$ is the compressional energy, $\mu_i \mathrm{d}N_i$ is the chemical energy of the particle species i, and $\varphi \mathrm{d}Q$ is the electrical energy. These energy forms are in all cases products of "intensive variables"(T, p, μ_i and φ) and of "extensive" quantity-like variables (S, V, N_i and Q). The intensive variables define the amount of energy exchanged per unit quantity of the respective energy carriers. The gradient of the intensive variables drive currents of the respective energy carriers to lower the overall energy of the system. When the current is vanished or the corresponding intensive variable is constant everywhere, the system is in equilibrium with respect to this intensive variable, while it is not necessary in equilibrium with respect to other variables.

For an electron-hole system, an exchange of electrons or holes is accompanied by an exchange of electrical charges. If we add $\mathrm{d}N_e$ electrons to the system, the energy of the system changes by $\mu_i \mathrm{d}N_i + \varphi \mathrm{d}Q = (\mu_e - e\varphi)\mathrm{d}N_e$. Similarly for adding $\mathrm{d}N_h$ holes, the energy of the system changes by $(\mu_h + e\varphi)\mathrm{d}N_h$. The combined chemical and electrical potential is simply called electrochemical potential. In semiconductor terminology, the electrochemical potential is identified as the quasi-Fermi level for electrons and holes, respectively. It is indeed the thermodynamic work required to add one electron (resp. one hole) to the system. Considering a semiconductor with light illumination (or more generally with excitation, e.g. injection current or electron-beam irradiation), absorption of one photon creates one electron-hole pair and vice-versa. In steady-state, the reaction $e^- + h^+ \leftrightarrow \gamma$ is balanced, and is characterized by a constant (electro)chemical potential. The chemical potential of radiation is related to the separation of the quasi-Fermi levels:

$$\mu_\gamma = \mu_e + \mu_h = E_{fc} - E_{fv} \tag{3.52}$$

Absorption, stimulated and spontaneous emission

Before deriving a general form of light spectrum emitted by a semiconductor, we examine in detail the photon absorption and emission rates per volume in a direct-gap semiconductor. Within the effective mass concept, a simple band diagram with allowed optical transitions is illustrated in Figure 3.6. We consider radiative transitions between states at energies near $\mathcal{E}_h$ in the valence band and near $\mathcal{E}_e$ in the conduction band, resulting in photons in the energy range from $\hbar\omega$ to $\hbar\omega$+d$\hbar\omega$. At a given photon energy $\hbar\omega$ and, for example, a known energy level in the valence band, the energy level in the conduction band is in fact fixed due to the electronic band structure and the conservation of energy and momentum. The combined conduction and valence band density of states for a given transition energy $\hbar\omega$ is the joint density of states $D_j(\hbar\omega)$ (see Equation 3.32). Moreover, the states are occupied according to two *different* Fermi functions $f_c(\mathcal{E}_e)$ and $f_v(\mathcal{E}_h)$ under quasi-thermal equilibrium.

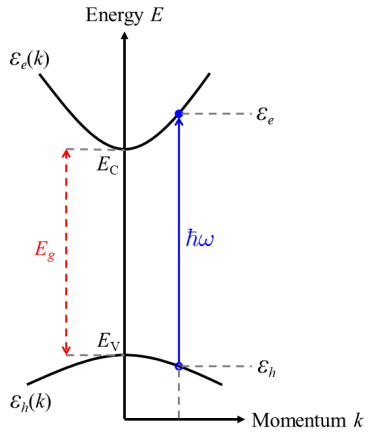

Figure 3.6 – *Simplified band diagram of a direct-gap semiconductor with allowed optical transitions which conserve energy and momentum.*

Photons of energy $\hbar\omega$ impinging on a material can trigger both upwards transition (rate of absorption $r_a(\hbar\omega)$) and downwards transition (rate of stimulated emission $r_{st}(\hbar\omega)$). These transition rates are proportional to the photon density $n_\gamma(\hbar\omega)$, the transition probability and the joint density of states $D_j(\hbar\omega)$ between the valence and the conduction band, as well as the occupation probabilities in the respective bands. For upwards transitions from states at $\mathcal{E}_h$ to states at $\mathcal{E}_e$, the occupation factors are the probability that the valence band is occupied (by electron) and the probability that the conduction band is empty.

$$r_a(\hbar\omega) = n_\gamma(\hbar\omega)\ |M|^2\, D_j(\hbar\omega)\, f_v(\mathcal{E}_h)\,(1 - f_c(\mathcal{E}_e)), \tag{3.53}$$

where M contains matrix element for the transition probability, which can be calculated from the Fermi's golden rule (see Equation 3.24). The rate of stimulated emission is likewise, with the probability that the valence band is empty and the probability that the conduction band is occupied:

$$r_{st}(\hbar\omega) = n_\gamma(\hbar\omega)\ |M|^2\, D_j(\hbar\omega)\,(1 - f_v(\mathcal{E}_h))\, f_c(\mathcal{E}_e). \tag{3.54}$$

Note that the absorption and stimulated emission are two reciprocal processes, thus the matrix element has the same absolute value, or because the Hamiltonian operator is always self-adjoint. It may slightly depend on the energy $\hbar\omega$, but in many cases it is assumed constant. Stimulated emission is a process by which a photon is duplicated, produced one additional photon in exactly the same state as the incident photon initiating the transition. These photons cannot be distinguished from non-absorbed photons. Therefore, the net absorption rate $r_{a,net}$ ($\mathrm{cm^{-3}\,s^{-1}}$) at which photons disappear is given by the difference between the absorption $r_a(\hbar\omega)$ and the

stimulated emission $r_{st}(\hbar\omega)$ rates:

$$r_{a,net}(\hbar\omega) = n_\gamma(\hbar\omega)\ |M|^2\, D_j(\hbar\omega)\, (f_v(\mathcal{E}_h) - f_c(\mathcal{E}_e)). \tag{3.55}$$

On the other hand, the photon current density $\mathbf{j}_\gamma(\hbar\omega)$ is related to the photon density $n_\gamma(\hbar\omega)$ through the group velocity $\mathbf{c}$: $\mathbf{j}_\gamma(\hbar\omega) = n_\gamma(\hbar\omega)\mathbf{c}$ where $c = c_0/n$ and n is the refractive index of the medium. The net photon absorption rate can also be written as the divergence of the photon current density:

$$r_{a,net}(\hbar\omega) = -\nabla\cdot\mathbf{j}_\gamma \approx \alpha(\hbar\omega)\, j_\gamma(\hbar\omega), \tag{3.56}$$

in a homogeneous and isotropic medium, the first order development gives rise to the Beer-Lambert law which involves the absorption coefficient $\alpha(\hbar\omega)$. A relation for the absorption coefficient which includes the effect of carrier occupancy is found to be:

$$\alpha(\hbar\omega) = \frac{|M|^2\, D_j(\hbar\omega)}{(c_0/n)}\, (f(\mathcal{E}_h) - f(\mathcal{E}_e))\,. \tag{3.57}$$

This expression indicates that the interband transition rate can be in one of the three regimes [49]:

- $f_v(\mathcal{E}_h) - f_c(\mathcal{E}_e) \approx 1$: interband absorption rate is strong. This is the usual property for semiconductors in which the valence band is nearly full and the conduction band is nearly empty.
- $f_v(\mathcal{E}_h) - f_c(\mathcal{E}_e) \approx 0$: interband absorption rate is zero. The transition has been bleached due to high occupancy in both levels.
- $f_v(\mathcal{E}_h) - f_c(\mathcal{E}_e) \approx -1$: interband absorption rate is negative. The semiconductor is behaving as an optical gain medium (laser action).

All conventional solar cells operate in the first regime, where the occupancy factor is normally close to one since the ground state can be assumed to be filled and empty excited states are always available. The situation is different for a system presenting more than three energy levels (e.g. intermediate-band solar cells) or for the heavy doping effect.

Unlike absorption and stimulated emission where the probability of transition is proportional to the strength of the radiative field, the *spontaneous emission* is a process where an electron in the excited state (conduction band) returns to the ground state (valence band) and emits a photon. The spontaneous emission occurs without an external radiation field [33]. The spontaneous emission cannot be described in the semi-classical framework of Schrödinger equation for the electronic states and of classical electromagnetic wave, because the wavefunction of an electron in the excited state does not overlap with that in the ground state. Quantification of the electromagnetic field is required and the quantum states of electrons are coupled to that of photons, leading to the theory of quantum electrodynamics. The origin of the spontaneous emission is due to the quantum fluctuation process or so-called *vacuum fluctuation*. It is out of the scope in this thesis to deduce a rigorous description, but simply give the expression similar to that of Equation 3.53 and 3.54. The spontaneous emission rate is still proportional to the joint density of states, the matrix element and the occupancy of the conduction and valence bands, but is not related to the number of incident photons. Instead, it is connected with the density of states for photons [2]:

$$r_{sp}(\hbar\omega) = D_\gamma(\hbar\omega)\ |M|^2\, D_j(\hbar\omega)\, (1 - f_v(\mathcal{E}_h))\, f_c(\mathcal{E}_e). \tag{3.58}$$

It is thus related to the absorption coefficient through:

$$\begin{aligned} r_{sp}(\hbar\omega) &= \alpha(\hbar\omega)\frac{c_0}{n} D_\gamma(\hbar\omega)\frac{(1 - f_v(\mathcal{E}_h))\, f_c(\mathcal{E}_e)}{f_v(\mathcal{E}_h) - f_c(\mathcal{E}_e)} \\ &= \alpha(\hbar\omega)\frac{c_0}{n} D_\gamma(\hbar\omega)\frac{1}{\exp\left(\frac{\hbar\omega - (E_{fc} - E_{fv})}{k_B T}\right) - 1} \end{aligned} \tag{3.59}$$

We have used the Fermi function with respective Fermi levels for electrons and holes. With the explicit expression of the density of states for photons in a 3-dimensional medium (Equation 3.46), the spontaneous emission rate is written:

$$r_{sp}(\hbar\omega) = \frac{(\hbar\omega)^2}{\pi^2\hbar^3(c_0/n)^2} \frac{\alpha(\hbar\omega)}{\exp\left(\frac{\hbar\omega-(E_{fc}-E_{fv})}{k_BT}\right)-1} \tag{3.60}$$

The final expressions for the spontaneous emission rate do not depend on the energy $\mathcal{E}_e$ and $\mathcal{E}_h$ explicitly, but only on their difference $\hbar\omega$. Each pair of states with an energy difference $\hbar\omega$ contributes to Equation 3.59 through the joint density of states, and is lumped into the absorption coefficient. The term for chemical potential of radiation $\mu_\gamma = E_{fc} - E_{fv}$ is reduced to zero at thermal equilibrium, then the expression of Equation 3.60 is reduced to the known van-Roosbroeck-Shockley relation [47]. Here the expression is more general and applied for semiconductors under quasi-thermal equilibrium (e.g. steady-state illumination of light).

3.2.3 Light emitted by semiconductors

Previously, the transition rates in the *volume* of semiconductors were described, but the internal emission rate of photons cannot be observed. What can be observed and measured is the photon current emitted through a surface. We consider a homogeneous and isotropic semiconductor layer of thickness d and we assume that the only variation is along the direction x perpendicular to the layer surface (see Figure 3.7).

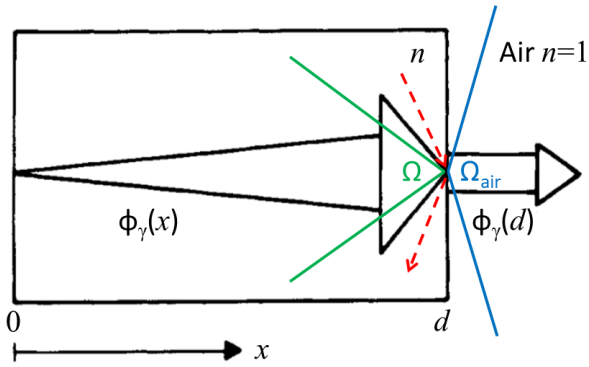

Figure 3.7 – *Schematic illustration for the spontaneous emission, re-absorption and light emitted outside a semiconductor (Figure adapted from Ref. [2]).*

To find the emitted photon current, we have to integrate the difference between photon emission and absorption rates.

$$\frac{d\phi_\gamma}{dx} = \frac{1}{4} r_{sp} - \alpha\, \phi_\gamma. \tag{3.61}$$

Only 1/4 of all photons generated spontaneously contribute to the current in one direction, because of the isotropic distribution of solid angles (see for example Equation 3.49). The net absorption rate, difference between the absorption and the stimulated emission, is expressed in term of absorption coefficient α. Here, r_{sp} is considered to be independent of the coordinate x. Since no photon current enters from the left ($x = 0$), integration of the continuity equation over a semiconductor of thickness d yields the expression for photon current *inside* the semiconductor:

$$\phi_\gamma(x) = \frac{r_{sp}}{4\alpha}\left[1 - \exp(-\alpha x)\right]. \tag{3.62}$$

At the interface between the semiconductor and the air, the photon current is partly reflected to the interior of the semiconductor, with the reflectivity R'. Because of a refractive index $n > 1$

in the material, a part of the photon current in the semiconductor follows total reflection. As shown in Figure 3.7, photons with the maximum solid angle π from outside can penetrate into the semiconductor, while only the photons within a solid angle of π/n^2 can be emitted to the air. Since we look at the variation along the direction perpendicular to the surface, the reflectivity R of an incident light from outside of the semiconductor is related to R' at normal incidence through: $1 - R' = (1 - R)/n^2$. Finally, the photon current emitted to exterior is:

$$\begin{aligned} \phi_{lum} &= (1 - R')\, \phi_\gamma(d) \\ &= \frac{1 - R}{n^2}\, \frac{r_{sp}}{4\alpha}\, [1 - \exp(-\alpha \mathrm{d})] \\ &= A(\hbar\omega)\, \frac{cD_\gamma}{4n^2}\, \frac{1}{\exp(\frac{\hbar\omega - (E_{fc} - E_{fv})}{k_B T}) - 1}. \end{aligned} \tag{3.63}$$

Here $A(\hbar\omega)$ is the absorptivity of the semiconductor layer.

$$A(\hbar\omega) = (1 - R(\hbar\omega))\, [1 - \exp(-\alpha(\hbar\omega)d)]\,. \tag{3.64}$$

Inserting the bulk photon density of states (Equation 3.46) in Equation 3.63, we arrive at the general expression of light emitted by a semiconductor (generalized Planck's law):

$$\phi_{lum}(\hbar\omega) = A(\hbar\omega)\, \frac{(\hbar\omega)^2}{4\pi^2 \hbar^3 c_0^2}\, \frac{1}{\exp\left(\frac{\hbar\omega - (E_{fc} - E_{fv})}{k_B T}\right) - 1}. \tag{3.65}$$

In most of the cases, the difference between the emitted photon energy and the splitting of quasi-Fermi levels is large compared to the thermal energy: $\hbar\omega - (E_{fc} - E_{fv}) \gg k_B T$, the Bose-Einstein distribution can be approximated by the Maxwell-Boltzmann distribution (neglecting the term -1 in the denominator of Equation 3.65). This expression is simplified to

$$\phi_{lum}(\hbar\omega) = A(\hbar\omega)\, \phi_{bb}(T, \hbar\omega) \exp\left(\frac{E_{fc} - E_{fv}}{k_B T}\right), \tag{3.66}$$

where ϕ_{bb} stands for the spectrum of black body radiation. Note that the splitting of quasi-Fermi levels affects only the global intensity, whereas the absorption and temperature determine the shape of the spectrum. The multiplicative term of absorptivity indicates that a good absorber is also a good emitter. The generalized Planck's law was verified experimentally on direct band gap GaAs light emitting diode (LED) [50]. Uncertainty was mainly attributed to the sub-band gap absorption coefficient of the diode material. It was even verified on Si solar cells under forward bias at room temperature despite the participation of phonons for indirect transition [51].

To summarize, from Kirchhoff's law the mathematical expression of black body radiation is extended to a non-black body by simply multiplying the material's absorptivity. From thermal radiation to general semiconductor luminescence, a non-zero chemical potential for photons is introduced. The difference in the Fermi energies $E_{fc} - E_{fv}$ is the *free energy* per electron-hole pair. It is free of entropy and we may therefore hope to transfer it into electrical energy without loss [2]. Radiative recombination of electron-hole pairs generates photons, which are emitted. These photons carry the free energy of electron-hole pairs $\mu_\gamma = E_{fc} - E_{fv}$, recognized as the chemical potential of the photons. From internal spontaneous emission rate to external emitted photon current, an integration of the continuity equation was used. In general, the equilibrium exists because photons are repeatedly emitted and re-absorbed before they reach the surface. Even if the excitation is not homogeneous, the generalized Planck's law is valid as long as the Fermi energies are well defined. We note that the above treatment is applied even if $E_{fc} - E_{fv} > \hbar\omega$, where the denominator in Equation 3.60 is negative. Under the same condition, the absorption coefficient becomes negative too, and the spontaneous emission remains positive. $E_{fc} - E_{fv} > \hbar\omega$ is also known as the condition for laser action.

3.2.4 Doping influence of luminescence spectra

Here, we apply the generalized Planck's law for doped semiconductors. The upmost importance is the absorption behaviors near the bandgap. Therefore, we need to model the impact of doping on the absorption coefficient. Urbach first noticed the exponential decay of the absorption coefficient below the bandgap [41]. These Urbach tails can be described by

$$\alpha(E) \sim \exp\left(-\frac{E_1 - E}{E_0}\right), \tag{3.67}$$

where E_1 corresponds to a translation in energy and E_0 is an energy parameter that characterizes the width of the tail (called Urbach energy). Behaviors comprising a sharper decay of tail states have also been analyzed for doped semiconductors. A general treatment consists in a semi-classical approach to determine the density of states and the absorption coefficient. Kane showed that the functional form of the tail states is given by a Gaussian function [52]:

$$\alpha(E) \sim \exp\left(-\left(\frac{E_1 - E}{\sqrt{2}\sigma}\right)^2\right), \tag{3.68}$$

Here σ is the root-mean-square depth of the potential well created by the charge impurities: $\sigma = e^2/(4\pi\varepsilon_r\varepsilon_0)(Nr_0)^{1/2}$, where N is the average impurity density and r_0 is the screening length. Other models also exist, together with the Urbach tail and Kane's model, the sub-bandgap absorption is described by an exponential of energy to a power factor between 1 and 2. A simple method allowed to unify the absorption band tail used by Katahara and Hillhouse consists in convoluting the ideal absorption with a decay function [53]. As we only observed simple exponential decays in the lower-energy part of CL spectra, an Urbach tail with an adjustable energy parameter γ is mainly used. The absorption coefficient is expressed as:

$$\alpha_0(\hbar\omega) = \frac{1}{2\gamma}\int_{-\infty}^{\hbar\omega - E_g} \alpha_{\text{ideal}}(\hbar\omega - \mathcal{E}) \exp\left(-\left|\frac{\mathcal{E}}{\gamma}\right|\right) d\mathcal{E} \tag{3.69}$$

To account for the bandgap narrowing in heavy-doped semiconductors, the bandgap E_g can be entered in the fitted parameters. For energies well above the bandgap $\hbar\omega > E_g$, either a simple parabolic band or experimental curves can be used. For GaAs, we use a parabolic model for the absorption of undoped GaAs (α_{ideal}) with the value $\alpha = 14800\,\text{cm}^{-1}$ fixed at $\hbar\omega = 1.6\,\text{eV}$ for all doping levels, since absorption of doped GaAs at energies above 1.6 eV is rather independent from the doping levels [54]. Experimental measurement from Sturge of high-purity GaAs can also be used [36].

In the next step, the band filling effect needs to be taken into account, especially for degenerate n-type doping. The occupation probability is described by two Fermi functions characterized by the respective Fermi energy for electrons in the conduction band f_c and holes in the valence band f_v. The correct absorption term is written, according to Equation 3.57

$$\begin{aligned} \alpha(\hbar\omega) &= \alpha_0(\hbar\omega) \times (f_v - f_c) \\ f_v - f_c &= \frac{1}{\exp\left(\frac{\mathcal{E}_h - E_{fv}}{k_B T}\right) + 1} - \frac{1}{\exp\left(\frac{\mathcal{E}_e - E_{fc}}{k_B T}\right) + 1} \end{aligned} \tag{3.70}$$

In practice, the valence band filling only appears at very high p-doping concentrations, which is not very common. Therefore, Fermi level for holes is considered much higher than the valence band edge so that $f_v \approx 1$ and the position of E_{fv} will not influence the shape of the luminescence spectra (but change only the total intensity). The occupation factor is mainly determined by the position of electron Fermi level E_{fc}. To express explicitly the occupation term, the excess

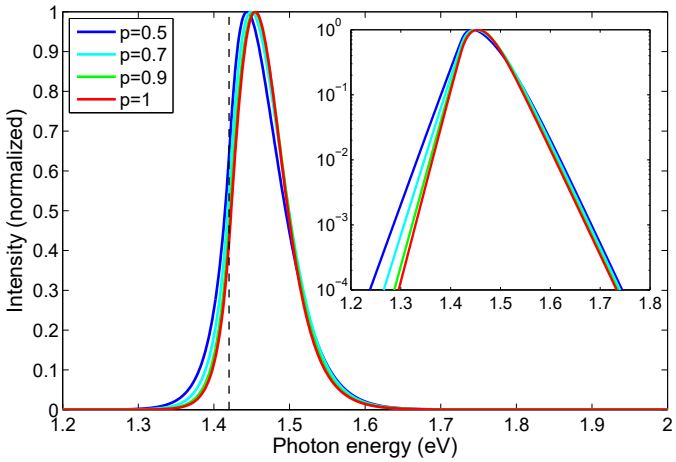

Figure 3.8 – *Calculated luminescence spectra (Equation 3.65) with various values for the parameter p used in Equation 3.71 for the weight between electron and hole effective masses. The model for α_{ideal} in Equation 3.69 is parabolic with fixed bandgap $E_g = 1.42$ eV and Urbach tail $\gamma = 15$ meV. The occupation parameter is fixed for $E_{fc} = 60$ meV above the conduction band minimum in Equation 3.70. The parameter d is fixed to 2 μm in Equation 3.64. The temperature is $T = 300$ K.*

energy $\hbar\omega - E_g$ is weighted between electrons and holes according to their respective effective masses. By convenience, we write the relations using a parameter p between 0 and 1:

$$\begin{aligned} \mathcal{E}_e - E_c &= p(\hbar\omega - E_g) \quad \text{and} \\ E_v - \mathcal{E}_h &= (1-p)(\hbar\omega - E_g). \end{aligned} \tag{3.71}$$

$p = 1/2$ corresponds the case where electron and hole effective masses are equal. This is not the case for usual zinc-blende III-V semiconductors, and p close to 1 is more realistic where the excess energy is taken by electrons rather than holes. For GaAs, with the electron effective mass of $0.063m_0$ and heavy hole effective mass of $0.050m_0$, the ratio gives rise to $p = 0.89$. In Figure 3.8 , we give an example of the influence of the parameter p on the calculated luminescence spectra. Slight modification in the slope at low energy is observed depending on the choice of the parameter p.

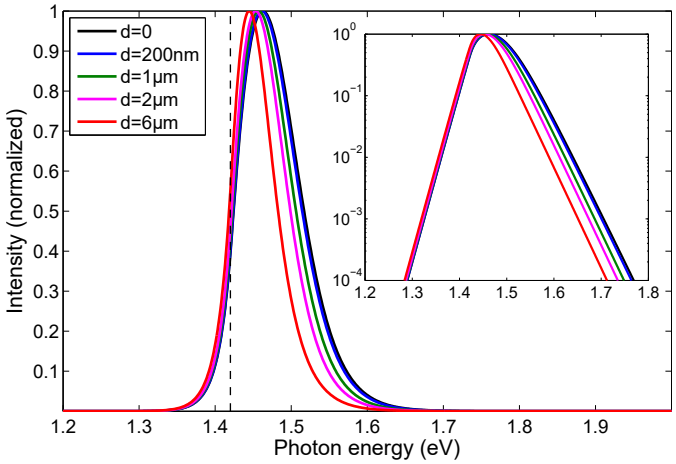

Figure 3.9 – *Calculated luminescence spectra (Equation 3.65) with various values of the parameter d used in Equation 3.64. The model for α_{ideal} in Equation 3.69 is parabolic with fixed bandgap $E_g = 1.42$ eV and Urbach tail $\gamma = 15$ meV. The occupation parameter is fixed for $E_{fc} = 60$ meV above the conduction band minimum in Equation 3.70. The parameter p is fixed to 0.9, and the temperature is $T = 300$ K.*

Finally, the absorption coefficient changes by several orders of magnitude in the small spectral range near the bandgap, low-energy photons have a much larger probability than high-energy

photons to escape through the front surface before they are re-absorbed. Therefore, the external luminescence spectrum may be distorted and redshifted as compared to the internal emission rate given by the *volumic* spontaneous emission of Equation 3.60. For a homogeneously excited slab of thickness d, the light spectrum emitted is described in term of the absorptivity of the material (Equation 3.65). In general, local excitation is used in CL or PL and the injection profile decreases in depth. As minority carriers diffuse, the final carrier concentrations depend on the density of non-radiative recombination centers and eventual electric field. d can be described as a characteristic length scale over which carriers are generated, travel and recombine radiatively [53]. In presence of nanostructures or optical resonances, this macroscopic approach might fail and appropriate absorptivity model need to be used depending on the object under study.

In most cases, d can be considered as a fitted parameter. In Figure 3.9, we give an example of the influence of the parameter d on the calculated luminescence spectra using $A = (1-R)(1-\exp(-\alpha d))$ in Equation 3.65. d changes essentially the spectral shape at the high-energy tail. d close to zero means that the luminescence is produced close to the surface and the re-absorption is negligible. For larger d values, the luminescence is produced deep in the layer so that significant re-absorption alters the spectral shape of externally emitted light.

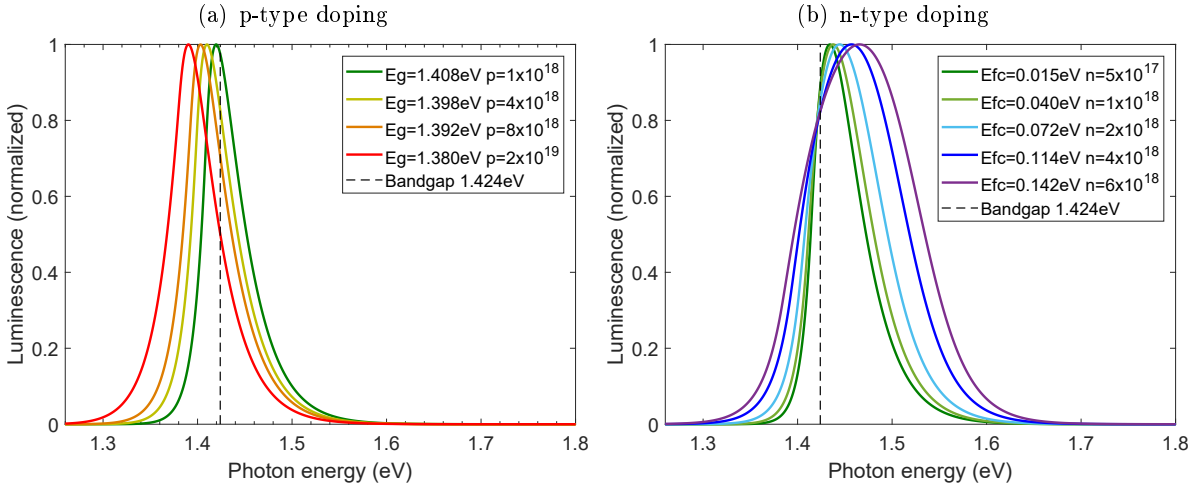

Figure 3.10 – *Calculated luminescence spectra (Equation 3.65) for (a) p-type GaAs (bandgap narrowing effect) and (b) n-type GaAs (bandgap narrowing and degenerate electron filling in the conduction band). For p-type doping, the bandgap E_g and Urbach tail γ are varying. For n-type doping, the bandgap E_g, Urbach tail γ and electron Fermi level E_{fc} are varying. Doping concentrations are indicative and given in the unit of cm^{-3}. All other parameters are fixed.*

Figure 3.10 shows the calculated evolution of luminescence spectra with p-type and n-type doped GaAs (undoped bandgap 1.424 eV). We can see that luminescence spectra contain rich information about the material under study. For p-type GaAs, bandgap narrowing and band tail effects are dominant. For n-type GaAs, bandgap narrowing, band tail and conduction band filling are relevant. CL measurements of doped GaAs thin-films are presented in Chapter 5.3, and rigorous analysis of CL spectra to extract carrier concentrations is given in Chapter 5.4. The same method is applied to GaAs nanowires, as presented in Chapter 6.3 and 6.4.

3.3 Efficiency limit of solar cells

The famous detailed balance limit derived by Shockley and Queisser (SQ) in 1961 predicts the maximum power conversion efficiency that can be obtained with a solar cell using a single bandgap absorber material [55]. The calculation only relies on the balance of absorption and emission of photon currents. Surprisingly, the basic thermodynamic principle of detailed balance properly

describes the fundamental physics of solar cells and derives the current-voltage (JV) of such an ideal device.

3.3.1 Detailed balance limit

The assumptions and reasoning leading to the SQ-limit are summarized [56]:

(A1) The solar cell absorbs every photon of energy higher than the bandgap

(A2) When one photon is absorbed, it produces one electron-hole pair and when one electron-hole pair recombines it produces one photon.

(A3) Radiative generation-recombination mechanism is the only one existing (radiative limit).

(A4) The quasi-Fermi levels of electrons and holes are uniformly split in all the volume of the device and the split equals the external voltage applied. This can be assumed if we admit that the mobility tends to infinity since the electron and hole current is proportional through the mobility to the slope of the corresponding quasi-Fermi level

Considering a solar cell in thermal equilibrium with the ambient at the temperature T, any incoming and absorbed electromagnetic radiation flux ϕ_{in}^0 is counterbalanced by the same amount ϕ_{em}^0 of emitted radiation. When the device is illuminated with the solar radiation ϕ_{sun}, the steady-state physics of solar cell is described by the quasi-Fermi levels. We assume that each photo-generated minority carrier is collected by the junction and the flow of majority carriers to the ohmic contact does not induce ohmic losses. The short-circuit current density J_{sc} of the solar cell can readily be calculated:

$$J_{sc} = q \int_{E_g}^{\infty} \phi_{sun}(E) dE, \tag{3.72}$$

where q denotes the elementary charge and E the photon energy. The perfect connection of the junction to the entire volume in the solar cell must be reflected in the fact that the quasi-Fermi levels splitting $\Delta\mu = E_{fc} - E_{fv}$ is controlled by the junction voltage V via $\Delta\mu = qV$. The emitted photon flux under the applied bias voltage V is therefore given by:

$$\phi_{em}(E, V) = \frac{2\pi}{h^3 c_0^2} \frac{E^2}{\exp\left(\frac{E-qV}{k_B T}\right) - 1}, \tag{3.73}$$

where h is the Planck constant, c_0 the velocity of light in vacuum, and $k_B T$ is the thermal energy. Here, the dimension of the emitted flux ϕ_{em} is the number of photons per unit time, per unit area and per unit of energy. For voltages that are small compared with the emitted photon energies, that is, $E - qV \gg k_B T$, the Bose-Einstein term can be approximated by a Boltzmann distribution and simplified to:

$$\phi_{em}(E, V) = \phi_{bb}(E) \exp\left(\frac{qV}{k_B T}\right), \tag{3.74}$$

where ϕ_{bb} is the blackbody radiation expressed in number of photons emitted per second, per unit area and per energy interval.

$$\phi_{bb}(E, T) = \frac{2\pi}{h^3 c_0^2} \frac{E^2}{\exp\left(\frac{E}{k_B T}\right) - 1}. \tag{3.75}$$

Note that the factor π comes from the emission integrated over the whole hemisphere. This is true for a Lambertian emitter where the emitted flux scales with the factor $\cos(\theta)$ (θ for the

angle between the direction of emission and the surface normal), and is a good approximation for planar layers. For advanced nanophotonic structures containing an angular selective filter or nanowire emissions, the factor π should be revised depending on the specific case.

From the detailed balance point of view, the current density J drawn from the solar cell must be equal to the difference between generation and recombination of charged carriers. In the radiative limit, there are no other possibilities to recombine than radiative recombination. Assuming that photons can only escape from the front surface of the solar cell (perfect back mirror), the emission is caused by the radiative recombination current of the charge carriers injected by the junction. The balance equation is written:

$$\begin{aligned} J &= q\int_{E_g}^{\infty}\phi_{sun}(E)dE + q\int_{E_g}^{\infty}\phi_{bb}(E)dE - q\int_{E_g}^{\infty}\phi_{bb}(E)\exp\left(\frac{qV}{k_BT}\right)dE \\ &= J_{sc} - J_0\left(\exp\left(\frac{qV}{k_BT}\right) - 1\right). \end{aligned} \tag{3.76}$$

In Equation 3.76, J is the current density from the solar cell and V is the applied voltage. The first term is the photo-generated current. The second term corresponds to the absorption due to emission from the ambient surroundings at temperature T, which is much smaller than the flux from the sun. The third term is the emission current raised from the radiative recombination of charged carriers. Using Equation 3.76, the current-voltage characteristics can be calculated numerically. The solar light source is taken from the standard AM1.5G spectrum, and the resulting limit efficiencies (1 sun) are plotted in Figure 3.11.

3.3.2 Generalization of the Shockley-Queisser limit

In this part, we generalize the above SQ-limit taken into account the real material absorption coefficient instead of a step-function absorption, and considering the absorber thickness within different light-trapping schemes. Non-radiative loss and angular dependence of the absorption and emission is also discussed. Sandhu et al. calculated the efficiency limits for solar cells containing nanophotonic structures and showed that a V_{oc} enhancement over bulk cells is possible through the absorption *suppression* in the immediate spectral region above the bandgap [57]. Xu et al. illustrated high-efficiency nanostructured solar cells through a built-in optical concentrator (e.g. for nanowire solar cells) [58]. We show in detail the steps leading to generalized 1 sun limit efficiencies for GaAs absorber at various thicknesses for three simple configurations. The same method can be applied to other materials and light-trapping systems.

Absorption of real materials

For most semiconductors, the absorption below bandgap does not decrease to zero abruptly. Instead, a so-called Urbach tail with exponential decay is usually observed as discussed in Section 3.2.4. Figure 3.12 shows the absorption coefficient of GaAs from the measurement of Sturge (black circle) and modeling with an Urbach tail to different extend of the exponential decay. An Urbach tail of 10 meV is suitable for slightly-doped GaAs (blue curve). For heavily-doped n-type GaAs, the absorption edge shifts to higher energy due to electron filling in the conduction band (Burstein-Moss shift). An Urbach tail of 20 meV is reasonable to describe heavily-doped p-type GaAs. For higher p-type doping, bandgap narrowing effect may become non-negligible and further shifts the absorption edge to lower energy. These effects will be further discussed in Chapter 5. Without explicit mention, the blue curve (Urbach tail 10 meV) is used to calculate absorption in GaAs.

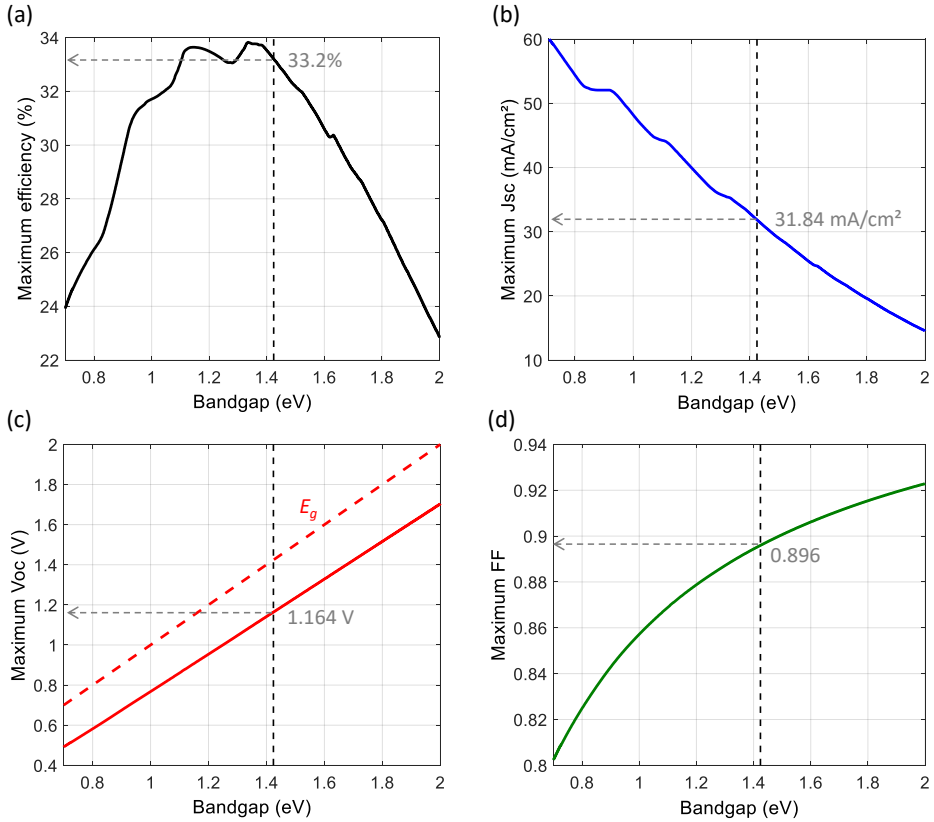

Figure 3.11 – *Limit efficiencies of solar cells as a function of the material bandgap (SQ-limit) assuming a step-function absorption and the standard AM1.5G solar spectrum. (a) Maximum efficiency versus bandgap. (b) Maximum J_{sc} versus bandgap. (c) Maximum V_{oc} versus bandgap (solid line), the dashed line shows the bandgap values. (d) FF versus bandgap. The vertical dashed lines mark the bandgap of GaAs (1.424 eV) and the corresponding maximal photovoltaic parameters are indicated.*

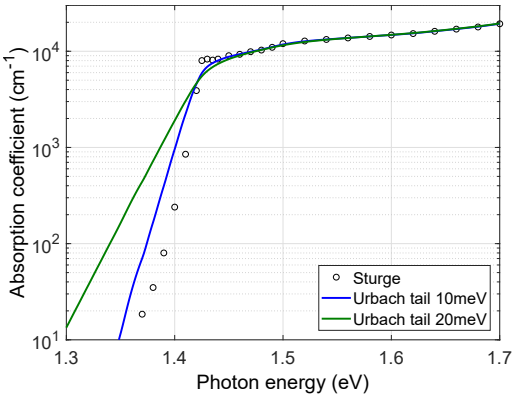

Figure 3.12 – *Absorption coefficient of GaAs near bandgap. Black dots are Sturge absorption measurement for high-purity GaAs [36]. Blue and green line is an extension below bandgap with an Urbach tail of energy width 10 meV and 20 meV, respectively.*

Light trapping in a semiconductor slab

The absorption coefficient $\alpha(E)$ is a material-related parameter, while the absorptivity or absorptance $A(E)$ of the solar cell depends on the device geometry (absorber thickness) and on the solar cell structure (back mirror or light-trapping design). Knowing the spectral absorptivity of the solar cell, the short-circuit current J_{sc} is derived directly:

$$J_{sc} = q \int_0^{\infty} A(E)\phi_{sun}(E)dE. \tag{3.77}$$

The emission characteristics are also related to the absorptivity of the solar cell according to the generalized Kirchoff's law. An extension of the Equation 3.74 becomes:

$$\phi_{em}(E,V) = A(E)\,\phi_{bb}(E)\exp\left(\frac{qV}{k_BT}\right). \tag{3.78}$$

Note that this Equation is valid for low-injection regime where the Boltzmann approximation holds. At this step, we can see that determining the absorptivity of the solar cell is essential. For a complex light-tapping structure, numerical computation employing either light tracing or full wave solver is needed. We consider here an absorber layer of thickness L and three simple structures are investigated:

- On substrate: the absorber layer is on an inactive substrate of the same refractive index. This is the general case for an epitaxially grown semiconductor on a wafer. The front surface is supposed to have a perfect anti-reflection coating. The absorption in the active layer corresponds to a single-pass absorption.

$$A(E) = 1 - \exp\left(-\alpha(E)L\right). \tag{3.79}$$

- Back mirror: the absorber is supposed to be placed on a perfect flat mirror. The front surface has always a perfect anti-reflection coating. The absorption in the semiconductor slab corresponds to a double-pass absorption (photons enter in the semiconductor slab, encounter a reflection by the mirror, travel back and leave the front surface)

$$A(E) = 1 - \exp\left(-2\alpha(E)L\right). \tag{3.80}$$

- Lambertian light-trapping: light trapping by randomly texturing the surface, combined with a perfect back reflector. The maximum absorption is expressed in term of the optical enhancement factor $4n^2$, where n denotes the refractive index of the semiconductor [59, 60].

$$A(E) = \frac{\alpha(E)L}{\alpha(E)L - 1/(4n^2)}. \tag{3.81}$$

Non-radiative recombination and external luminescence efficiency

For realistic devices, non-radiative recombination and parasitic optical loss are always present. In particular, ideal SQ-limit results in an unity photoluminescence quantum yield, i.e. every absorbed photon is radiatively re-emitted and escapes the solar cell at open-circuit. Ross noted that a sub-unity photoluminescence quantum yield would degrade the maximum potential in photochemical systems [61]. Two aspects can be distinguished in this regard: one is due to non-radiative recombination which is related to material qualities, the other concerns imperfect photon extraction from the front surface due to the optical design of the solar cell. For the former, *internal radiative efficiency* (IRE or η_{int}) can be defined as a phenomenological parameter that describes the probability of a recombination event to be radiative. It is written as the ratio of

the radiative recombination rate to the total recombination rate, or equivalently by the ratio of the corresponding lifetimes:

$$\eta_{int} = \frac{R_{rad}}{R_{rad} + R_{nr}} = \frac{\tau_{nr}}{\tau_{rad} + \tau_{nr}}. \tag{3.82}$$

IRE is mainly a material-related property. Non-radiative recombination includes bulk Shockley-Read-Hall recombination, surface and interface recombination and Auger recombination. High-quality GaAs with double heterostructures is shown to reach over 99% internal radiative efficiency [62] owning to excellent control of the crystal growth and the surface passivation. The optical design then becomes important for a material of high internal radiative efficiency. It has been recognized that the recycling (or re-absorption) of radiatively emitted photons is a key element for high conversion efficiency toward the SQ-limit [56]. *External luminescence efficiency* (η_{ext}) or *external radiative efficiency* (ERE) quantifies the ratio of the emitted photon current J_{em} to the total recombination current (including non-radiative recombination J_{nr} and parasitic optical losses J_{opt}).

$$\eta_{ext} = \frac{J_{em}}{J_{em} + J_{nr} + J_{opt}}. \tag{3.83}$$

$\eta_{ext} = 100\%$ corresponds to the original assumption of Shockley and Queisser. Lowered η_{ext} indicates the presence of additional loss channels. Green collected ERE of state-of-the-art photovoltaic cells have shown ERE=22.5% for the record GaAs solar cell [63]. This term is closely related to external LED quantum efficiency in Rau's reciprocity relation [64]. The balance equation of 3.76 can then be modified to explicitly account for the absorptivity of the solar cell and for the non-radiative and parasitic optical losses through the definition of η_{ext} [65].

$$J = q\int_0^\infty A(E)\phi_{sun}(E)dE - \frac{q}{\eta_{ext}}\left(\exp\left(\frac{qV}{k_BT}\right) - 1\right)\int_0^\infty A(E)\phi_{bb}(E)dE. \tag{3.84}$$

In Figure 3.13, we give the calculated photovoltaic performances of GaAs solar cells as a function of the absorber thickness using Equation 3.84. The absorption characteristics in the three configurations illustrated here are given in Equation 3.79, 3.80 and 3.81. With a back mirror, we assume that η_{ext} can reach 100% in the radiative limit. Meanwhile, for the solar cell on a GaAs substrate, η_{ext} is limited to only 2% and a V_{oc} penalty of about 0.1 eV for 200 nm-thick GaAs due to parasitic absorption loss in a substrate (J_{opt} term in η_{ext}). The procedure to evaluate the optical loss into a substrate is given by Miller et al. through the calculation of absorption from back side of the solar cell via the reciprocity of light [66]. This V_{oc} loss is even more prominent if the absorber is thinner [67]. In Figure 3.13, we recognize several features such as increased V_{oc} with decreased absorber thickness, and lowered V_{oc} with lambertian light-trapping. Overall, the gain in J_{sc} for an ideal light-trapping system is still more valuable than a slightly loss in V_{oc} due to enhanced radiative emission.

Angular dependence of absorption and emission

When a solar cell is designed using nanophotonic structures, strong optical resonances may lead to significant angular dependent absorption and emission. Using a solar tracker, the absorption of the direct sun light is close to the normal incidence because of small solar disk seen on the Earth. Meanwhile, the emission back to the whole hemisphere dependents on the incident polar angle θ and eventually on the azimuthal angle φ. Absorption spectra with varying incident angle in both TE and TM polarization can be computed by RCWA simulation. The total emission to the whole hemisphere can then be calculated using known angular distribution of the absorptivity. If strong angular dependence exists, the absorptivity used in Equation 3.84 should be replaced by an angle-weighted and polarization-averaged absorptivity $\bar{A}(E)$.

$$\bar{A}(E) = \frac{1}{\pi}\int_0^{2\pi}\int_0^{\pi/2} A(E,\theta)\cos(\theta)\sin(\theta)\,d\theta\,d\varphi. \tag{3.85}$$

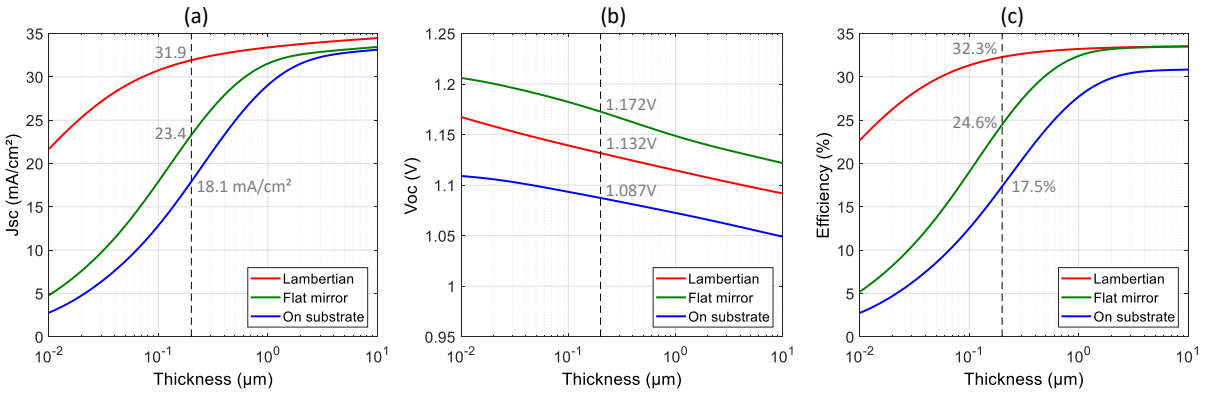

Figure 3.13 – *Calculated GaAs solar cell efficiency as a function of the absorber thickness in three configurations: (blue) on GaAs substrate, (green) flat back mirror, (red) lambertian light trapping. (a) Maximum J_{sc}, (b) maximum V_{oc} and (c) maximum 1 sun efficiency as a function of thickness. The photovoltaic performances for 200 nm-thick GaAs are indicated along the vertical dashed lines.*

To summarize this section, we see that the luminescence concept is closely related to the ideal SQ-limit of a single-junction solar cell through the detailed balance of absorption and emission. It also provides a guideline on how to improve the efficiency of solar cells in terms of external radiative efficiency. Light-trapping and advanced photonic structures may constitute one of the important design considerations for future photovoltaic devices.

3.4 Cathodoluminescence

In this thesis work, cathodoluminescence is extensively used to characterize photovoltaic materials with the capability of resolution down to the nanoscale. Experimental results are given in Chapter 5 and 6, showing the usefulness of cathodoluminescence technique in studying the crystal phase and uniformity, effectiveness of surface passivation and doping level determination. The cathodoluminescence setup and electron beam-material interaction is described here.

3.4.1 Cathodoluminescence setup

CL measurements were performed with the Attolight Allalin 4027 Chronos quantitative cathodoluminescence microscope[1]. Figure 3.14(a) gives an overview the CL setup. The whole system is composed of two parts, namely electronics and optics, which are described separately. Samples should be pasted on a special holder, which contains specific contact scheme with the stage for EBIC measurements. The stage has a 6-axis control with a good stability and nano-positioning ability, compatible with the helium cryostat.

A more detailed picture of the electronic part of the CL equipment is given in Figure 3.14(b). The electron source is a Schottky thermal field emission gun using a ZrO coated tungsten tip. It can be operated in continuous or pulsed mode. Continuous electron emission is obtained from direct heating of the electron gun. Pulsed electron source is achieved by photoemission with a high-energetic laser (355 nm) focused on the tip. The laser has a repetition rate of 81.8 Mhz (every 12 ns) and pulse width of about 5 ps [68, 69]. A negatively charged suppressor directs the electron emission to a positively charged extractor. The divergence of the electron beam is then controlled by an electromagnetic lens called *gun lens*, which determines the spread of the electron beam onto an aperture. Apertures of diameter 100, 50, 30 and 25 μm can be switched manually. The electron beam is then focused through another electromagnetic lens called *objective lens*,

[1] Attolight: https://attolight.com/

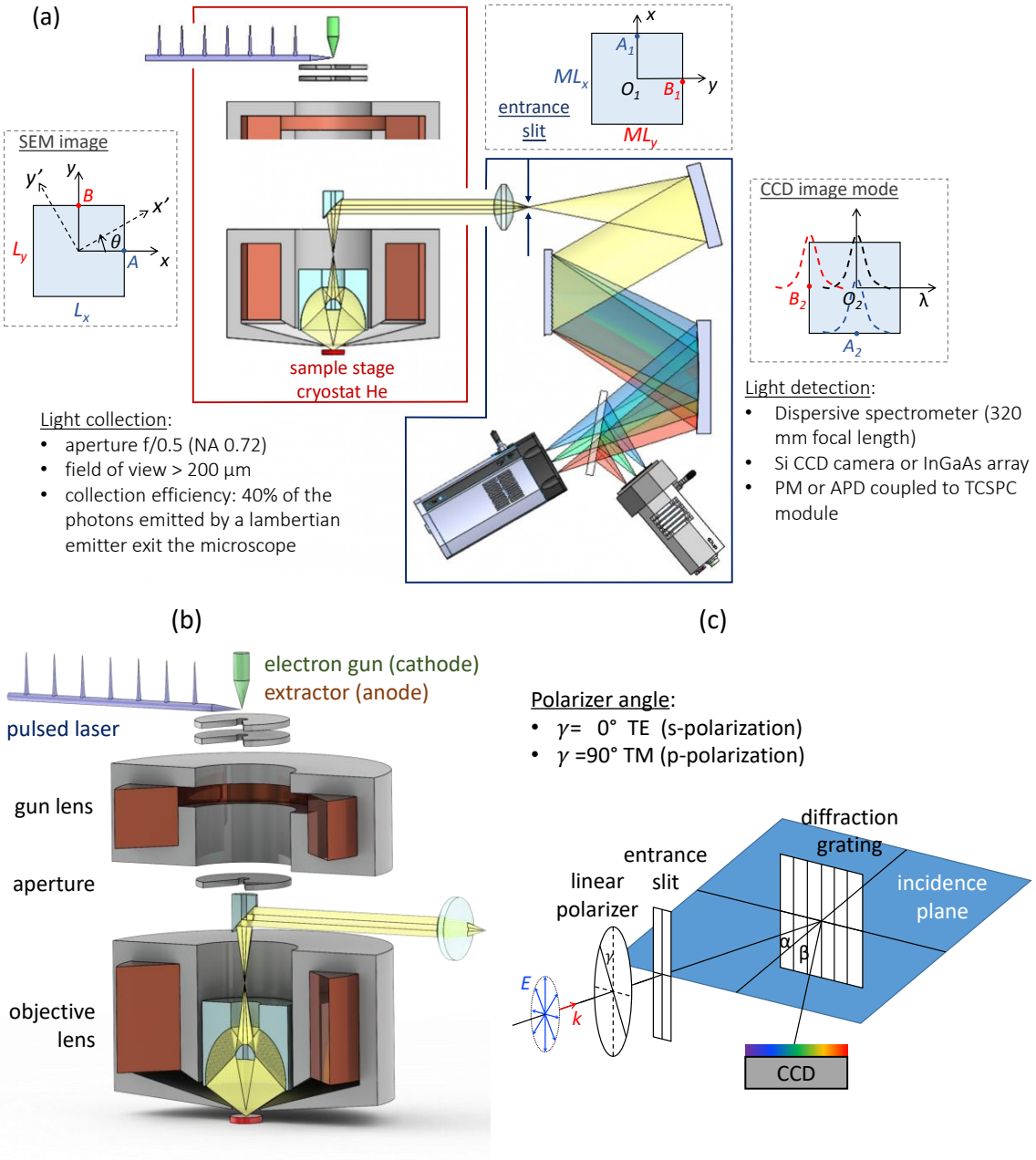

Figure 3.14 – *Schematics of the CL setup. (a) Overview of the Attolight cathodoluminescence system including an electron microscope (red frame) and a spectrometer (blue frame). Gray dashed frames show the respective orientation of the sample image, the secondary image at the entrance slit, and the final image on the focal plane of the spectrometer. (b) Detail picture of the CL chamber showing the electron gun, apertures, electromagnetic lenses and collection optics (Figure adapted from Attolight[1]). (c) Illustration for the use of a linear polarizer to measure the degree of polarization of luminescence.*

and is eventually corrected with stigmatic aberration. The final spot size of the focused electron beam is about 10 nm of less.

Light emission from the sample is collected through an achromatic reflective objective with a numerical aperture of 0.72. The dedicated objective uses a similar concept as a Cassegrain reflector. This particular design allows to obtain a large field-of-view up to 200 μm, and a high collection efficiency (40% of the photons from a lambertian emitter exit the microscope, and are constant over the field of view). The collected light is then directed to the Horiba iHR320 spectrometer. Light is focused on the entrance slit of the spectrometer, and dispersed with a reflective diffraction grating. Several gratings with different groove densities and blazed wavelengths are available depending on the sensing spectral ranges. CL spectra are recorded on an Andor Newton silicon CCD camera for visible to near infra-red light or on an InGaAs array. In the pulsed operation mode, a photomulpilier tube (PMT) or an avalanche photodiode (APD) can be used with the time correlation single photon counting system (TCSPC).

Spatial resolution

In the hyperspectral acquisition mode, the electron beam scans over the selected region of the sample surface (raster scan), and a luminescence spectrum is recorded at each position of the electron-beam excitation, corresponding to one pixel in the CL map. Since the light is collected from the whole surface, eventual luminescence produced by the diffusion of carriers and radiatively recombined elsewhere is lumped into the pixel position of excitation. The interaction volume of electrons with materials depends on the electron beam acceleration voltage and the average volumic mass density of the material (see CASINO simulation), typically in the 20-30 nm in lateral size and depth up to several hundreds of nm. The spatial variations of CL maps depend essentially on the diffusion length of carriers, which can extended up to several μm for high-quality passivated III-V semiconductors. In presence of defects or sharp internal fields (e.g. heterojunction), local features down to several tens of nm or less can be observed in CL maps, in particularly at low temperature where exciton is very sensitive to local crystal defects.

Spectral resolution and hyperspectral correction

The spectral resolution depends essentially on the groove density of the grating[2]. Combined with the CCD camera (1024×256 pixel array with pixel size of 26 μm) in our CL setup, the grating of 150 grooves/mm disperses light for 0.53 nm/pixel and the grating of 600 grooves/mm (blazed at 750 nm) disperses light for 0.12 to 0.13 nm/pixel. The spectral resolution is sometimes defined by three times the dispersion per pixel (need three pixels to construct a peak), hence 1.6 nm for 150 grooves/mm and 0.4 nm for 600 grooves/mm. For the spectral correction of recorded CL spectra, the diffraction grating and the CCD camera are essentially the two elements which are wavelength-sensitive in our CL detection system. The correct CL spectra emitted by a specimen can be obtained from the recorded spectra divided by the spectral response of the grating and that of the CCD camera used.

For a large-area hyperspectral map, a light source far from the center of the optical axis may also induce a spectral shift of the recorded spectrum and need to be corrected. A schematic illustration is given in Figure 3.14(a). The sample area undergoes the electron-beam scan that is represented as a square (or rectangle) of size L_x and L_y. Points A and B are indicated as frontier points in x- and y-directions. The corresponding secondary image formed on the entrance slit is represented with a rectangle of size ML_x and ML_y, where $M = 13$ is the optical magnification of the optical system between the sample and the entrance slit of the spectrometer. We note that the orientation of the secondary image (entrance slit) is a mirror of the first SEM image with

[2]Horiba: http://www.horiba.com/scientific/products/diffraction-gratings/grating-tools/

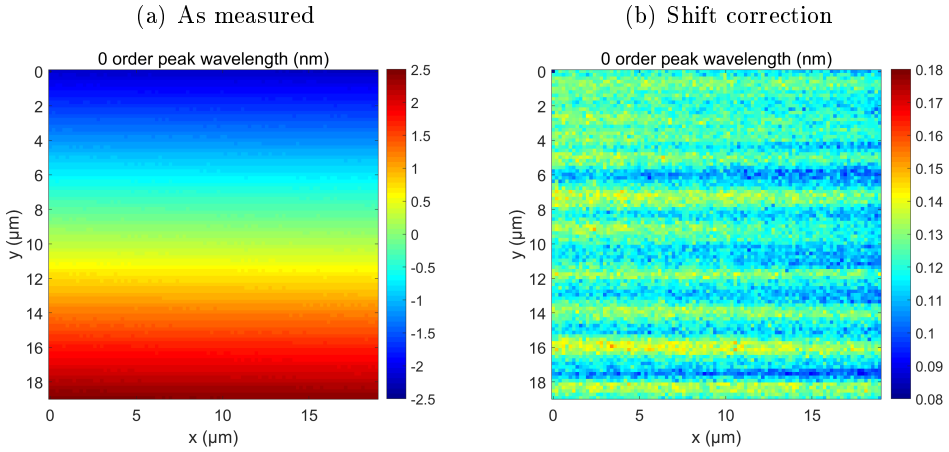

Figure 3.15 – *Cartography the central wavelength of the 0-order peak measured on a planar p+GaAs sample over image size of about 19 µm (a) as-measured without shift correction, we can see the spectra shift linearly along the vertical direction. (b) with linear spectral shift correction of 0.245 nm per µm vertical distance.*

respect to the axis of the bisector of the x- and y-axis due to specific geometry of the reflective Cassegrain objective. Light is then dispersed horizontally and forms a third image on the plane of the CCD sensors, the spectrum is obtained by summing vertically over the 256 pixels. The optical magnification of the spectrometer is approximately one so that the total magnification is about 13.

We can see that for a light source located at B which is separated vertically from the center O seen from the SEM image, the spectrum recorded is shifted in wavelength. Figure 3.15(a) shows the recorded zero-order peak wavelength measured on a planar GaAs sample scanned over an area of about 19μm×19μm. We can observe clearly the spectral shift along the vertical direction, and the shifted value is about 0.245 nm per μm. We then subtract this spectral shift linearly along the vertical direction and the zero-order peak wavelength becomes Figure 3.15(b). Note that small oscillation is still persistent, but the amplitude of oscillation is well smaller than the dispersion per pixel of the grating (150 groove/mm). Therefore, we should correct systematically this spectral shift for a hyperspectral CL map of larger than 2 μm.

Polarization-resolved CL

In certain cases (e.g. hexagonal wurtzite crystals), the emitted light possesses a privileged polarization direction. It is possible to probe the polarization state of the luminescence using a linear polarizer placed before the entrance of the spectrometer, as sketched in Figure 3.14(c). We denote the zero reference polarizer angle aligned vertically with the entrance slit, and can be easily turned forming an angle θ. The polarization of light emitted by a horizontally lying nanowire, for example, can then be probed by adjusting the polarizer angle with respected to the orientation of the nanowire image at the entrance slit of the spectrometer. Note that the nanowire image is a mirror at 45° of the SEM image, so a vertical nanowire seen from SEM is in fact horizontal seen at the entrance slit of the spectrometer.

The grating it self may be also sensitive to the polarization of incoming light. We call TE incident light for zero degree of the polarizer angle, and TM incident light for 90° of the polarizer angle, as seen from the ruled grating. We measured the signal recorded with varying polarizer angle θ on a reference undoped GaAs layer. The first order spectra are shown in Figure 3.16(a) for the 150 grooves/mm (blue curve) and for the 600 grooves/mm (red curve). Their maximum intensities are normalized and plotted together. The integrated intensities of the first order

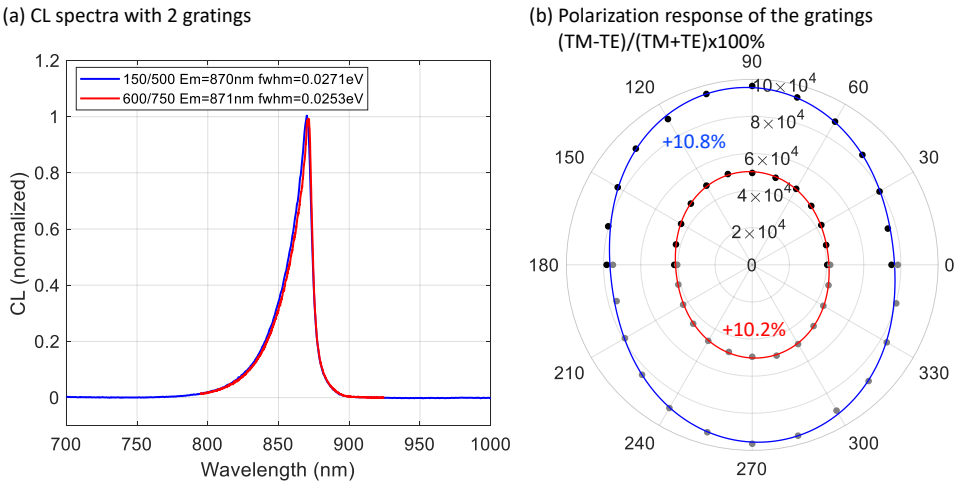

Figure 3.16 – *(a) Comparison of the CL spectra using two diffraction gratings (room temperature, undoped GaAs layer). (b) Polar plot of the integrated CL intensity. The blue curve (resp. red curve) is the polarization response of the 150/500 grating (resp. 600/750).*

diffraction at different polarizer angles are given in the polar plot of Figure 3.16(b). We define the polarization response of the grating as the ratio of intensities: $(\mathrm{TM}-\mathrm{TE})/(\mathrm{TM}+\mathrm{TE})$, and the TM light is slightly enhanced by the grating at the spectral range of GaAs emission. We confirmed that this polarization response is rather constant in the spectral range of about 800 to 900 nm, thus the ratio can be used to correct for the GaAs emission.

3.4.2 Monte-Carlo simulation of electron-matter interactions (CASINO)

The electron beam-material interactions are simulated using CASINO v2.42 program (Monte Carlo simulation of electron trajectory in solids)[3]. A detail explanation of the program functionalities is found in Ref. [70]. The main part of the program is the simulation of a complete electron trajectory on the basis of a single-scattering algorithm. An initial electron-beam energy is chosen (typically 2-10 keV for SEM-CL applications) and the electron-beam diameter is set by user (here 10 nm). CASINO program assumes a Gaussian-shaped electron-beam with 99.9% of the total distribution of impinging electrons land in a circle of diameter 10 nm. The incident penetration is set to the surface normal, and no scattering angle is initially calculated. The distance between two successive collisions is evaluated based on the density of the region, atomic weight fraction of the elements and the cross-section for each chemical element of the region. The program neglects the effect of inelastic scattering on electron deviation. The energy losses in keV between collisions are calculated depending on the atomic number and mean ionization potential of elements. The elastic collision angle is determined using pre-calculated values of partial elastic cross-section and a random number. These steps are repeated until the electron energy is less than 50 eV or the electron escapes the surface of the sample, recorded as a back-scattered electron [70]. An example of simulated electron trajectories is given in Figure 3.17(a)

Once the electron trajectories are simulated in the material, the absorbed or dissipated energies in the sample are represented (Figure 3.17(b)). The contour with percentage shows that this percentage of the total dissipated energy is located within this contour plot. Figure 3.17(b) presents the absorbed energy summed over the y-direction, and the inset shows the absorbed energy summed over the z-direction (top-view). We can see that near 90% of the total energy is spread within a 30 nm diameter centered at the excitation position.

[3]CASINO software: http://www.gel.usherbrooke.ca/casino/index.html

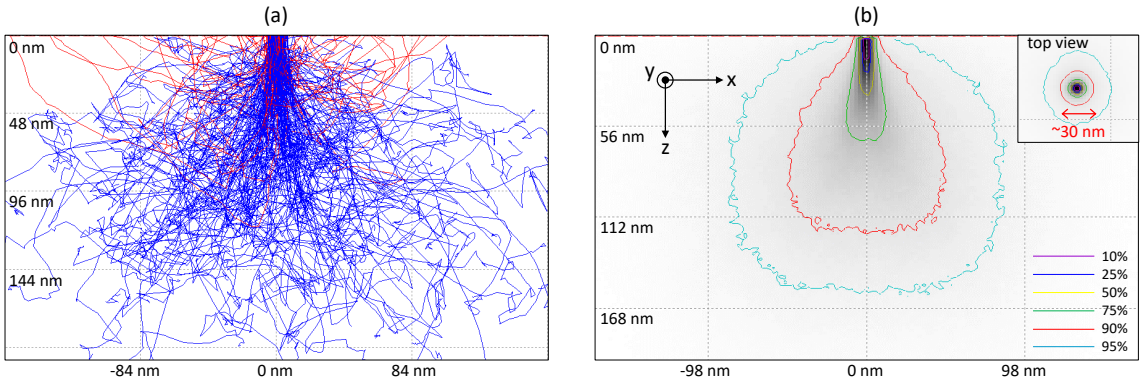

Figure 3.17 – *CASINO simulation of electron scattering in GaAs with incident electron-beam energy of 6 keV and probe diameter of 10 nm. (a) Simulated electron trajectory in GaAs. Red lines show the trajectories of back-scattered electrons. (b) Distribution of dissipated energy summed over the y-direction. The contour plot indicates the percentage of total dissipated energy within the corresponding contour. Inset shows the top-view distribution of dissipated energy summed over the z-direction.*

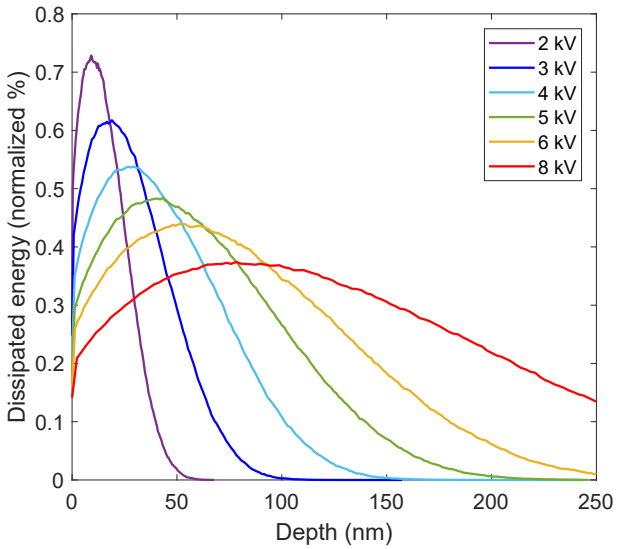

Figure 3.18 – *CASINO simulation for the distribution in depth of the dissipated energy in bulk GaAs. The electron beam size is set to 10 nm, and the beam energy is varied from 2 kV to 8 kV. The dissipated energy is normalized such that the integrated energy over the depth corresponds to the total excitation energy.*

In Figure 3.18, the dissipated energy is summed over the x- and y-directions to show the distribution in depth (z-direction). Several curves of different acceleration voltages are plotted together, showing increased penetration depth at higher electron-beam energies. The back-scattering coefficients do not varying much in these acceleration voltage, we thus assume the total absorbed energy is proportional to the electron-beam energy. The different curves are normalized such that the integral over z corresponds to the total absorbed energy. We can observe that, for lower acceleration voltage, higher energy density is deposited near the surface of the sample.

Table 3.1 gives the volumic mass density of Si and several III-V compounds for comparison, together with simulated back-scattering coefficients and penetration depths with electron-beam acceleration voltage of 6 kV. The values of penetration depth depend on the definition it self: we show the depth corresponding to the maximum dissipated energy, and the depth for the cut-off energy of 60% and 80% of the total dissipated energy. Between different semiconductors, we can see the trend that electrons penetrate less deeper in a denser material. Cathodoluminescence measurements are presented in Chapter 5 for GaAs thin-films and in Chapter 6 for GaAs nanowires.

Table 3.1 – *Material densities and CASINO simulation for the backscattering coefficient and electron penetration depth in the materials, with electron beam energy of 6 kV.*

Material	Density [g/cm^3]	Backscattering [%]	Max depth [nm]	Depth 60% [nm]	Depth 80% [nm]
Si	2.329	14.9	150	203	276
GaP	4.14	25.1	71	115	162
InP	4.81	32.4	58	102	145
GaAs	5.32	29.1	54	90	128
$Al_{0.4}Ga_{0.6}As$	4.70	27.7	61	104	147
InAs	5.68	33.9	50	87	125

3.5 Summary

In this chapter, we present in detail the theory of luminescence and discuss the usefulness of luminescence in the characterization of photovoltaic materials. Firstly, a microscopic description of light-matter interaction is shown. The absorption coefficient of a direct-gap semiconductor is related the oscillator strength and to the joint density of states. The latter determines essentially the spectral shape of absorption near bandgap, which rises parabolically with photon energies in a first approximation. The influences of excitons, shallow donor and acceptor states and heavy doping effects are discussed. These excitonic and defect-related features can be well distinguished with low-temperature luminescence measurement.

Secondly, the generalized Planck's law is derived to relate the luminescence light spectrum to the absorption characteristics of the semiconductor. The quasi-Fermi levels for electrons and holes are important parameters that describe the concentration of electrons and holes. They are also known as the electrochemical potentials. The separation of quasi-Fermi levels is thus linked to the voltage, which is a good figure-of-merit for photovoltaic materials. The generalized Plank's law is also adapted to take into account the effects of material doping: bandgap narrowing, band tail and conduction band filling in n-type III-V semiconductors. The concept of light emission also leads to the fundamental limit of photovoltaic conversion efficiency. Therefore, luminescence constitutes one of the most useful characterization methods in photovoltaic research.

In the last part, we describe the cathodoluminescence (CL) setup in C2N laboratory. It provides hyperspectral mapping with high spatial resolution down to the nanoscale and capability of time-resolved CL measurement. Electron-matter interactions are simulated using Monte-Carlo algorithm to have a clear image for the distribution of dissipated energy in the CL system.

Chapter

4 Ultrathin GaAs Solar Cells

Chapter content

GaAs is one of the most prominent materials for photovoltaic solar cells owning to its optimum bandgap around 1.42 eV to achieve the maximum Shockley-Queisser limit. GaAs is also a direct-gap semiconductor, therefore, efficient optical absorption makes 2–3 μm-thick thin-film GaAs sufficient to fully absorb the solar spectrum up to its bandgap. Meanwhile, the growth of high-quality GaAs relies on the epitaxy on a single-crystal substrate. In a typical GaAs single junction solar cell, the structure consists of a thin (50–150 nm) highly-doped n-type emitter and a thick (1–2 μm) lightly-doped p-type base, cladded by higher bandgap materials that operate as window and back surface field (BSF).

Reducing further the active layer thickness by one order of magnitude leads to ultrathin GaAs solar cells of thickness in the 200 nm range. Ultrathin absorber allows fast crystal growth and scarce material saving, leading to high throughput on fabrication lines and overall cost-reduction. Ultrathin GaAs solar cells are also studied under high-energetic proton irradiation and show better radiation tolerance than conventional thick cells, suitable for space power applications [71]. Moreover, the bulk non-radiative recombination current may be reduced using a thinner active

layer, leading to a potentially higher V_{oc}. However, ultrathin absorber is detrimental for full absorption of the solar spectrum, resulting in lowered J_{sc}. Efficient light trapping structures are needed to maintain a high photocurrent in ultrathin solar cells.

In this chapter, we study ultrathin GaAs solar cells with nanostructured back mirror as an effective light trapping structure. In Section 4.1, we give a detailed review of the state-of-the-art single-junction GaAs solar cells, and we summarize light trapping strategies used for photovoltaic solar cells. In Section 4.2, we give shortly the basics of epitaxy growth and describe the stack of III-V semiconductor layers used to fabricate ultrathin GaAs solar cells. In Section 4.3, we calculate the optical absorption with periodic nanostructured back mirror to identify the optimal geometry of the nanostructures and discuss multi-resonant light trapping mechanisms. In Section 4.4, we present 1D device simulations for ultrathin GaAs solar cells, and we estimate the losses due to the resistive effect in order to define the spacing of front contact grids. Section 4.5 shows the detailed fabrication processes, and Section 4.6 presents the characterizations of fabricated ultrathin GaAs solar cells. We discuss the losses of photovoltaic performances and provide a pathway toward high-efficiency ultrathin GaAs solar cells.

4.1 State-of-the-art

4.1.1 GaAs solar cells

Since 2004, researchers at Radboud University Nijmegen fabricated thin-film GaAs solar cells using the weight-induced epitaxial lift-off (ELO) technique to detach active layers from the substrate [72, 73]. This allows to process the rear side of the devices and to fabricate light-weight, flexible or bifacial solar cells, and the GaAs substrate can be reused for another epitaxial growth, leading to further cost-reduction. With a mirror back contact, the GaAs thickness can typically be reduced to 2 μm or thinner, which improves the radiation resistance for use in space applications and enhances the open-circuit voltage. In 2006, Bauhuis et al. demonstrated 26.1% thin-film GaAs solar cells with a gold mirror back contact ($J_{sc} = 29.5$ mA/cm^2, $V_{oc} = 1.045$ V, $FF = 0.846$) [74]. These cells were grown by metal-organic vapor-phase epitaxy (MOVPE) at 700°C with a standard n-on-p structure: 100 nm-thick n-GaAs emitter (disilane) and 2 μm-thick p-GaAs base (dimethyl-zinc). The Au mirror was deposited over the full area of p+GaAs layer to have sufficiently low contact resistance. Front contact grids (∼2% shading) were fabricated using low-temperature annealed (175°C) Pd/Ge/Au contact on n+GaAs instead of regularly used Ni/Ge/Au n-type contact which requires high-temperature annealing (450°C) to achieve low-resistivity contacts on the solar cell. After low-temperature annealing treatment, the back mirror conserved a high reflectance of about 90% over the 650-880 nm wavelength range.

At 2011, Alta Devices Inc. announced a breakthrough of the GaAs solar cell efficiency of 27.6% ($J_{sc} = 29.6$ mA/cm^2, $V_{oc} = 1.107$ V, $FF = 0.841$) at the 37th IEEE Photovoltaic Specialists Conference [75]. Later on, Alta Devices improved the efficiency up to 28.8% ($J_{sc} = 29.68$ mA/cm^2, $V_{oc} = 1.122$ V, $FF = 0.865$) [7], which is still the record efficiency for single-junction solar cells up to date. High V_{oc} and FF are reflected by the low value of dark current at high ($V > 1$ V) and moderate ($V < V_{mp}$) forward bias conditions. From the two-diode fit of the dark current-voltage characteristics, it was extracted the saturation current densities: $J_{01} \approx 6 \times 10^{-18}$ mA/cm^2 and $J_{02} \approx 1 \times 10^{-9}$ mA/cm^2. The remarkable high value of V_{oc} is related to the so-called photon recycling effect. Photon recycling is the process by which photons absorbed in the main absorber region of the device are radiatively re-emitted, and then re-absorbed in the same absorber. Efficient photon recycling allows a higher carrier density to build up within the device, which in turn leads to larger quasi-Fermi level splitting. This needs a sufficient quality of the material to ensure that the lifetime associated with any non-radiative recombination is much larger than the radiative lifetime, and the back contact to be highly

reflective. Researchers realize that the highest efficiencies cannot be achieved unless the solar cell is also designed to be a good light emitting diode (LED). The physics of light extraction at open-circuit becomes an important design consideration for high-efficient cells [66, 76]. Indeed, Ross proposed that the open-circuit voltage is penalized by poor *external luminescence efficiency* η_{ext} as [61]:

$$qV_{oc} = qV_{oc}^{rad} - kT\left|\log \eta_{ext}\right|, \tag{4.1}$$

where q is the electronic charge and kT denotes the thermal energy. V_{oc} is the actual open-circuit voltage of the device, and η_{ext} is the probability of an internally emitted photon to escape through the front surface of the cell. qV_{oc}^{rad} is the ideal open-circuit voltage calculated in the detailed balance limit:

$$qV_{oc}^{rad} = kT \log\left(\frac{J_{sc}}{J_0^{rad}}\right), \tag{4.2}$$

where J_{sc} is the short-circuit current density delivered by the solar cell under illumination, and J_0^{rad} corresponds to the dark recombination current density in the radiative limit (in absence of any non-radiative loss), represents also the equilibrium emission current per unit area escaping the front surface of the solar cell. Detailed calculation of the radiative limit efficiencies can be found in Chapter 3 section 3.3. To give a number, J_0^{rad} is about 6.8×10^{-19} mA/cm^2 calculated with a step-rise absorptivity at 1.424 eV (25°C), results in $V_{oc}^{rad} = 1.164$ V at 1 sun illumination using AM1.5G solar spectrum.

The detailed structure of the Alta Devices GaAs solar cells is unknown, but it is believed to have 1-2μm-thick GaAs absorber. The III-V layers were grown by MOVPE and solar cells with a gold back mirror contact were fabricated using the ELO technique. This solar cell was also tested under external photon recycling using a metallic dome and demonstrated a slightly V_{oc} enhancement of 4 mV through a restriction of radiative emission [77]. Steiner and coworkers in NREL studied the photon recycling effect in GaAs solar cells [78]. An optical model was used to calculate the external radiative efficiency of the solar cell as a function of the internal radiative efficiency of the material and wavelength-dependent reflectances at the front and back side of the solar cell structure. Solar cells with an electroplated gold back contact were fabricated to compare with the model. The epilayers were grown by MOVPE using triethyl-zinc, carbon tetrachloride (p-type dopant) and hydrogen selenide (n-type dopant). The structure was n-on-p with the junction located near the back side, so that the emitter ($\sim$2 μm, n-type doped to $\sim 10^{17}$ cm^{-3}) constituted the majority of the active region and the thin base layer was p-type doped to $\sim 10^{18}$ cm^{-3}. The highest efficiency was 27.81% ($J_{sc} = 29.46$ mA/cm^2, $V_{oc} = 1.101$ V, $FF = 0.858$). The evolution of measured V_{oc} values at various back contact reflectances and several cell thicknesses were in fair agreement with the model prediction.

It should be noted that the so-called deep junction design (junction located near the back side), instead of shallow junction (junction located near the top surface), has a potential for higher V_{oc} and fill factor. Deep junction III-V solar cells were investigated to operate mainly in the radiative recombination regime at the maximum power point, while in the shallow junction cells non-radiative recombination dominated [79]. This is probably due to the fact that most of the photogenerated carriers are close to the top surface, and that the non-radiative Sah-Noyce-Shockley junction recombination [80] occurs mainly in the space charge region (e.g. junction and perimeter) through trap levels in the mid-gap. On the other hand, the diffusion length of minority carriers in the thick emitter of a deep junction design is critical to achieve efficient collection thus has impact on J_{sc}. Deep junction design was also used in a 20.8%-efficient GaInP single-junction solar cells with a mirror back contact [8]. Non-radiative junction recombination current was reduced by placing the junction at the back of the cell in a higher band gap AlGaInP layer, thus favored the optical enhancement of the voltage by photon recycling effect. Recently, similar deep junction design with n-GaAs/bandgap graded n-AlGaAs/p-AlGaAs heterostructures were fabricated and achieved high-efficiency of 28.7% under 1 sun illumination ($J_{sc} = 30.0$ mA/cm^2,

$V_{oc} = 1.108$ V, $FF = 0.865$) [81].

4.1.2 Overview of light trapping strategies

In Figure 4.1, we place several experimental J_{sc} values of GaAs solar cells from the literature (black dots), and we plot three J_{sc} limits calculated using different absorption models as a function of the GaAs thickness t. The blue line is obtained by the single-pass absorption assuming a perfect anti-reflection coating (no backside reflection):

$$A(\lambda) = 1 - \exp\left(-\alpha(\lambda)t\right), \tag{4.3}$$

where $\alpha(\lambda)$ is the absorption coefficient of GaAs and λ the wavelength of light.

With a perfect flat mirror at the back side, the light path length is doubled, assuming again a perfect-anti-reflection. The absorption is written as (double-pass absorption):

$$A(\lambda) = 1 - \exp\left(-2\alpha(\lambda)t\right). \tag{4.4}$$

The resulting J_{sc} is plotted as the green line in Figure 4.1. For example, Vandamme et al. used high-reflectivity Ag mirror combined with localized back contacts to avoid parasitic absorption losses in the GaAs back contacts, leading to a high J_{sc} of 16.3 mA/cm^2 for $t = 120$ nm and of 20.7 mA/cm^2 for $t = 220$ nm [82]. We can notice that even with a flat mirror, the J_{sc} drops considerably for the GaAs absorber thinner than 600 nm. Hence, other light trapping structures are essential.

Lambertian light trapping

The basic ideal of light trapping is to redirect incident sunlight in the plane of the absorber layers. Lambertian light trapping consists of a randomly textured surface enabling light to be scattered into a direction other than the surface normal with an isotropic $\cos(\theta)$ angular distribution, thus increases the light path length in the active layer of the solar cells. Combining with a perfect back mirror, light reflected back to the front surface of the solar cell is trapped in the high-index semiconductor layers due to the internal total reflection. Yablonovitch used statistical ray optics approach in a semiconductor slab and showed the maximal optical path enhancement factor to be $4n^2$ in the low absorption regime, where n is the refractive index of the solar cell [83]. In this case, the absorption is given by:

$$A(\lambda) = \frac{\alpha(\lambda)t}{\alpha(\lambda)t - 1/(4n^2)}. \tag{4.5}$$

The resulting J_{sc} is plotted as the red line in Figure 4.1, which is served as a reference to compare with experimental J_{sc} values. In practice, realization of such a scattering surface or interface without electronic degradation is difficult, and experimental demonstration of high J_{sc} from broadband lambertian light trapping is still challenging.

For example, Yang et al. demonstrated ultrathin (300 nm) GaAs solar cells with a scattering back mirror and achieved an efficiency of 19.1% under 1 sun illumination ($J_{sc} = 24.5$ mA/cm^2, $V_{oc} = 1.00$ V, $FF = 0.778$) [86]. The solar cell structure is p-on-n, with 30 nm-thick p-GaAs emitter ($p = 1.25 \times 10^{17}$ cm^{-3}) and 270 nm-thick n-GaAs base ($n = 7 \times 10^{16}$ cm^{-3}), embedded with 30 nm-thick GaInP window and BSF layer. An additional layer of AlInP is grown to form a rough surface for gold mirror deposition, combined with n-type point contact at the back side of the solar cell. High EQE in the 400 nm region indicates an efficient extraction of photo-generated carriers in the window layer due to shallow junction and the extension of depletion region into the window layer. Lower EQE than expected in the long-wavelength range suggests a lower scattering efficiency of the back mirror compared to an ideal lambertian back scattering [89].

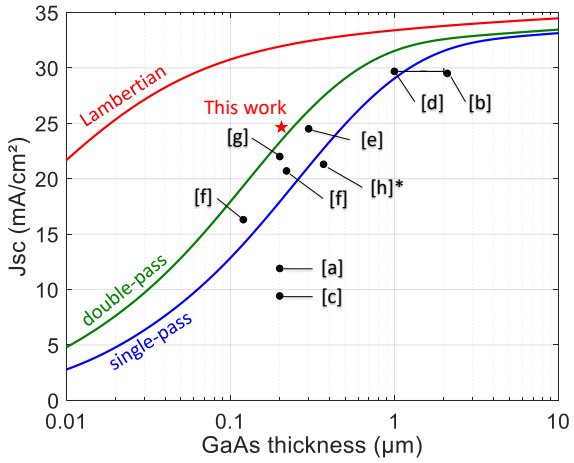

Figure 4.1 – *Maximum J_{sc} as a function of GaAs absorber thickness with three simple models assuming perfect anti-reflection: (blue) single pass-absorption, (green) double-pass absorption and (red) lambertian light trapping. Black dots are experimental results: [a] Nakayama et al. [84], [b] Bauhuis et al. [74], [c] Liu et al. [85], [d] Kayes et al. (thickness 1-2 µm) [75], [e] Yang et al. [86], [f] Vandamme et al. [82], [g] Lee et al. [87] and [h] Aberg et al. (equivalent planar thickness for the nanowire array) [88]. We have realized a high $J_{sc} = 24.64$ with 205 nm-thick GaAs absorber.*

Low FF value of 77.8% is mainly attributed to the series resistance (0.5 $\Omega\,\mathrm{cm}^2$ from the fit of JV curve in dark). Low junction doping, poor current spreading at the front side and point contacts at the back side of the solar cell may be responsible for the improvable fill factor.

Beside randomly scattering of light, advanced light trapping strategies have been developed thanks the progresses in micro- and nano-technologies. For instance, plasmonic effects and high-index periodic nanostructures have been explored for light trapping in thin solar cells, as we discuss in the following.

Plasmonics for photovoltaics

Plasmonics is the study of interactions between photons and plasmons (collection oscillations of free electron gas in metals). Plasmonics provides a promising way for light trapping in thin solar cells because of its ability to confine light at the nanoscale well below the wavelength of light. It can be achieved using metallic nanoparticles as subwavelength scattering elements or corrugated metallic film to couple sunlight into surface plasmon polariton (SPP) modes supported at the metal/semiconductor interface [90]. However, there are few experimental demonstrations showing the beneficial effects of plasmonics on the photovoltaic conversion efficiencies [91, 92].

For instance, metal nanoparticles placed at the front side of the solar cell can preferentially scatter light into the semiconductor thin-film, and thus light is trapped through high-angle scattering and multiple internal reflection. Metal nanoparticles were used in 200 nm-thick GaAs solar cell and showed a slightly increase in the generated photocurrent [84, 85]. However, the photovoltaic performance remained very low (<6% efficiency at 1 sun) due to lack of back mirror and probably, to the electronic degradation of the solar cell. The scattering from metal nanoparticles shows EQE enhancement in the long-wavelength range, but is penalized by the loss in the short-wavelength range. Introducing metal in the semiconductor active layers may also deteriorate the electronic properties of the semiconductor and increase parasitic absorption losses in the metal. Another approach consists in fabricating metal/semiconductor/metal plasmonic cavities. A subwavelength metal nanogrid was used and resulted in a high optical absorption in a 25 nm-thick GaAs absorber [93].

Nanophotonic structures

Periodic nanostructures of dielectrics or semiconductors have been investigated to enhance absorption of light and to avoid parasitic absorption in metals. The concept of nanophotonic light trapping is to couple incident light efficiently into the resonant modes supported by the solar cell structures. Depending on the sizes and arrangements of the nanostructures, a variety of resonant modes can be exited. These optical resonances may overlap, leading to a broadband multi-resonant absorption. In some cases, the theoretical limits of multi-resonanct light trapping can even exceed the classical ray-optic limit of Yablonovitch [94, 95].

A comprehensive classification of optical resonant modes can be found in Ref. [96] and they are usually studied using the dispersion of resonant wavelengths as a function of the angle of incident light. In general, we can distinguish Fabry-Perot resonances resulted from the interference of waves between the reflecting top surface of a semiconductor layer and the metallic back reflector. Guided-mode resonances arise because the periodic nanostructures act as a grating that ensures phase-matched coupling of a normally incident plane wave to a waveguide mode of the semiconductor layer. Mie resonances are referred to as localized excitations that enable efficient scattering of light in the semiconductor layer.

Lossless dielectric nanostructures are usually used on the front surface of a solar cell, enabling an improved anti-reflection and thus an enhanced photocurrent generation. For examples, ITO nanocolumns were used in the front surface of GaAs solar cells that acted as an efficient anti-reflection coating and at the same time as a conductive front electrode [97]. CdS quantum dots embedded in a PDMS film were tested for anti-reflection with additional photon down-conversion capability [98]. Periodic arrangement of SiO_2 dielectric nanospheres above the GaAs solar cells allows light coupling into confined resonant modes of the nanospheres and enhances absorption in the underlying active layer [99]. TiO_2 sub-wavelength structures were fabricated on top of GaAs solar cells for wide-angle and broadband anti-reflection properties [100]. Nanostructured front surface were also fabricated by etching the AlGaAs window of GaAs solar cells [101].

On the other hand, nanopatterning the rear side of a solar cell is also possible. It is generally demonstrated by direct conformal deposition of amorphous or polycrystalline semiconductors on a patterned substrate. For instance, CIGS was fabricated on SiO_2 patterned Mo back contacts and showed enhanced light trapping from the dielectric scattering patterns and increased photovoltaic conversion efficiency compared to flat solar cells [102]. A p-i-n micro-crystalline Si was deposited on a nanopatterned ZnO:Al/Ag back contact reflector and exhibited an enhanced spectral response in the long-wavelength range compared to flat reference cells [103]. Using a periodic nanostructured back reflector, enhanced optical absorption may be explained by the excitation of guided-mode resonances via the grating coupler. Indeed, the electric field patterns of waveguide modes were observed using the scanning near-field optical microscopy [104]. Rear side patterns of III-V solar cells requires an additional step to detach the active layers from their growth substrates, leading to the possible substrate reuse and contributing to cost-reduction.

In Ref. [87], Lee et al. combine front surface periodic TiO_2 nanostructures and a flat or diffused back reflector in 200 nm-thick GaAs solar cells and obtain 16.2% efficiency (J_{sc} = 21.96 mA/cm^2, V_{oc} = 0.942 V, FF = 0.78). The solar cell structure is n-on-p, with 50 nm-thick n-GaAs emitter ($n = 2 \times 10^{18}$ cm^{-3}) and 150 nm-thick p-GaAs base ($p = 3 \times 10^{17}$ cm^{-3}), embedded with 40 nm-thick n-AlGaAs window layer and 100 nm-thick BSF. Extensive optical simulation is performed to find the optimum configuration of TiO_2 nanostructures, but the electronic performance of the cells has not been discussed. The similar fabrication method is also applied for multilayer-grown III-V semiconductor stacks which enables even faster solar cells assemblies in a continuous transfer printing processes [105].

From the above examples, we can see that ultrathin GaAs solar cells usually show lower electrical properties than state-of-the-art GaAs solar cells, and there is still room for improvements for efficient light trapping. Electrical properties of solar cells can in principal be preserved

for ultrathin absorber, but proper junction design and careful processing are needed. Surface degradation may have more impact on ultrathin solar cell performance because of higher surface-to-volume ratio. Photon recycling effect can also be explored in ultrathin GaAs solar cells given a high-quality material and a high reflective back mirror. In the following, our works on ultrathin GaAs solar cells are presented.

4.2 Epitaxial growth

III-V semiconductors for device applications are usually prepared from epitaxial growth, which involves the growth of active semiconductor films on a suitable substrate. The substrate provides a template of the similar crystal structure and lattice constant for high-quality crystal growth. Elemental constituents of the film are brought into contact with the substrate surface at elevated temperatures. Impurity dopants may be introduced with the elemental constituents to dope particular layers. In general, the quality of the epitaxial layers is much higher than that of the underlying substrate. Active layers of a device are normally grown after growth of a suitable thickness of a buffer layer to filter out defects in the substrate. Modern epitaxial growth techniques include *molecular beam epitaxy* (MBE) and *metal-organic chemical vapor deposition* (MOCVD), which are described shortly in the following.

Molecular beam epitaxy (MBE) takes place in ultra-high-vacuum environment (10^{-8} – 10^{-12} Torr). Flux of atoms or molecules are directed to a heated substrate where epitaxial growth occurs. The atom fluxes typically come from heated crucibles (effusion cells) that evaporate solid sources in the vacuum. The rate of material impinging on the substrate surface is controlled through the heating temperature of the crucible and can be switched on and off by a shutter. The term *beam* means that evaporated atoms do not interact with others until they reach the substrate, due to the long *mean free paths* of the atoms in low-pressure environment. When the atoms reach the heated substrate, most of them stick on the surface where they diffuse around until they find a lattice site to incorporate. Heating sufficiently the substrate allows for a good atomic mobility on the surface without excessive desorption of the atoms. The growth rate is generally defined by the flux of one or two of the atoms and the others are kept under excess. For GaAs growth, gallium and arsenic atoms are asymmetric in the sense that As is much more easily desorbed than Ga and one must maintain a high V/III ratio during growth. In general, the As flux must be maintained during growth interruptions or during initial surface treatments so that the lattice does not begin to decompose. The advantage of MBE is the very precise control of the structure and uniformity. Purity and control of dopants are also very high due to high vacuum and the available high-purity source materials. The main disadvantages of MBE is the relatively low growth rate compared with MOCVD.

Metal-organic vapor phase epitaxy (MOVPE), also known as **Metal-organic chemical vapor deposition (MOCVD)**, is a chemical deposition method occurring at pressures close to atmospheric pressure. In contrast to MBE, the growth of crystals is by chemical reaction and not physical deposition. Ultra pure gases are injected into a reactor where they are mixed so that they flow uniformly. Since MOCVD machines do not require a directed flux but rather mix large volumes of source gases, they can scale-up more easily. Modern source gases employ metal-organic compounds, such as trimethyl-gallium ($Ga(CH_3)_3$) and arsine (AsH_3) for GaAs growth. The heated organic precursor molecules decompose in absence of oxygen. This is so-called pyrolysis, which leaves atoms on the substrate surface and creates conditions for crystal growth. The growth and control for high-quality semiconductors is thus a complicated process requiring optimizations of temperature, pressure and V/III ratio.

Semiconductor layer stacks for ultrathin solar cells.

The III-V semiconductor layers of our ultrathin GaAs solar cells were grown by MOVPE at the Fraunhofer Institute for Solar Energy Systems (ISE). The layers with target thickness and doping level are described in Table 4.1. Note that the final solar cell structure is reversed compared to the growth order. The growth was conducted on a n-type GaAs(100) substrate, consisting of buffer GaAs, AlGaAs etch stop for substrate removal purpose, n+GaAs/GaInAs contact layers, n-AlInP window, 205 nm-thick GaAs homojunction as the main absorber, p-AlGaAs back surface field (BSF) and p+GaAs contact. Wide-gap AlGaAs and AlInP alloys are used to passivate the GaAs surface and act as minority carrier blocking layers to reduce surface recombination losses. High Al composition in AlInP alloy aims to reduce parasitic absorption in the window layer.

Table 4.1 – *Stack of the III-V semiconductor layers (C2853) grown by MOVPE at the Fraunhofer Institute for Solar Energy Systems (ISE). The growth sequence begins from the bottom to the top of the table. Target thickness and doping level of each layer are indicated.*

material	function	thickness [nm]	doping [cm^{-3}]
p-GaAs	contact	300	9×10^{18}
p-$Al_{0.4}Ga_{0.6}As$	BSF	100	2×10^{18}
p-GaAs	base	100	1×10^{18}
i-GaAs		5	
n-GaAs	emitter	100	-1×10^{18}
n-$Al_{0.61}In_{0.39}P$	strained window	25	-2×10^{18}
n-$Ga_{0.87}In_{0.13}As$	cap (Si) layer	100	-5×10^{18}
n-GaAs	cap (Si) layer	250	-9×10^{18}
n-$Al_{0.85}Ga_{0.15}As$	etch stop	300	-1×10^{18}
n-GaAs	buffer	250	-5×10^{18}

4.3 Light trapping in ultrathin GaAs absorber

4.3.1 Design of multi-resonant absorption

Ultrathin GaAs solar cells require light trapping structures to compensate for the decreased absorber volume. A reflective back mirror is needed for efficient light harvesting and for exploring the photon recycling effect. We choose silver because it has the highest reflectivity among metals in the visible–NIR spectral range. III-V active layers are preferentially kept flat to avoid electronic degradation induced by increased surfaces. A periodical pattern is desired to enhance absorption through multiple guided-mode resonances. The number of resonances increases with the period p, but diffraction losses at shorter wavelengths ($\lambda < p$ at normal incidence) may induce optical losses. For this reason, the periodic structure is designed at the backside in the form of a nanostructured metallic mirror so that diffraction in free space can only occur after double-pass absorption. The light trapping structure is shown in Figure 4.2, with front side anti-reflection coating (ARC) made of MgF_2/Ta_2O_5 and back side nanostructured TiO_2/Ag mirror. A two-dimensional grating with the same periodicity p in both x- and y-direction is used to have a polarization-independent response at normal incidence.

To calculate the absorption with a grating structure, we use numerical computations based on the rigorous coupled-wave analysis (RCWA) method (see Chapter 2.1.4 for description). We denote the plane of incidence by the x-z plane and consider impinging plane waves linearly polarized. We call transverse electric (TE) incident polarization for electric field along the y-axis, and transverse magnetic (TM) incident polarization for magnetic field along the y-axis. We

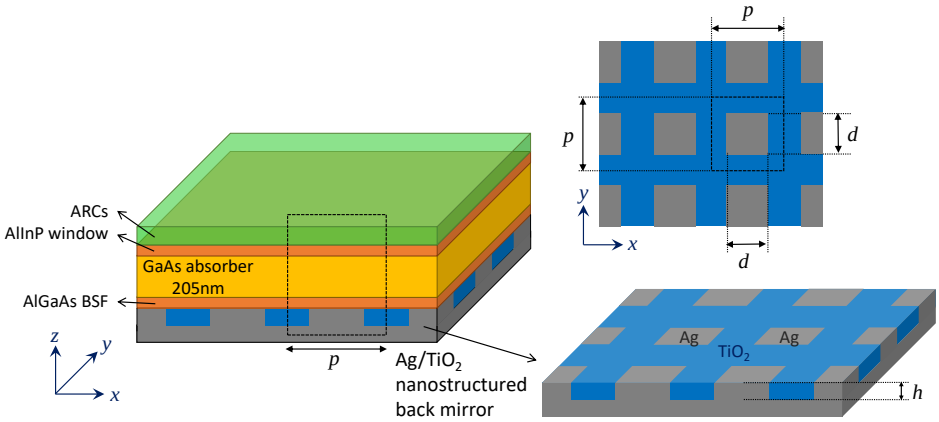

Figure 4.2 – *Left: a simplified picture of the ultrathin GaAs solar cells with a nanostructured back mirror. The front contact grid and back contact are not shown here. The major part of the rear side of the solar cell consists of TiO_2/Ag nanostructured back mirror. Right: details (top and perspective views) of the nanostructured TiO_2/Ag back mirror, with grating period p, height h and Ag nanostructure width d.*

calculate the absorption in each layer with 20×20 Fourier orders, and the calculation is done for each wavelength.

The complex refractive indices used for optical simulations of ultrathin GaAs solar cells are plotted in Figure 4.3. The refractive indices are taken from Ref. [106] for Ta_2O_5, from Ref. [107] for MgF_2 and $Al_{0.42}Ga_{0.58}As$, and from Ref. [108] for $Al_{0.51}In_{0.49}P$. For moderately doped GaAs, we take the complex refractive index of high-purity GaAs [36, 107] and extend its imaginary part (extinction coefficient) near and below the bandgap with an exponential Urbach tail of energy width 10 meV for n-GaAs and 20 meV for p-GaAs. Larger band tail is attributed for p-GaAs to reproduce the sub-bandgap absorption. The cubic spline interpolation is used to preserve the sign of the imaginary part of the optical indices. Amorphous silicon nitride SiN_x is also used as single-layer ARC and is deposited by room-temperature sputtering in C2N, and its refractive index was measured by ellipsometry. TiO_2 prepared from sol-gel with our process has typical refractive index of 1.9 at 500 nm, and is kept constant and non absorptive over the whole spectral range of interest. The optical index of Ag is taken from the measurement published recently in Ref. [109] to account for realistic absorption loss in Ag (Figure 4.3(c,d)).

After calculating the absorption spectra over the spectral range of interest (bandgap of GaAs: 872 nm), the theoretical short-circuit current density J_{th} is computed as:

$$J_{th} = q \int_0^\infty A(\lambda)\phi_{sun}(\lambda)\mathrm{d}\lambda, \tag{4.6}$$

where q denotes the elementary charge ($q \approx 1.602 \times 10^{-19}$ C). $A(\lambda)$ is the absorption in the main absorber of the solar cell, and $\phi_{sun}(\lambda)$ represents the standard AM1.5G solar spectrum (number of photons per unit time, per unit area and per unit wavelength). Assuming that the absorption of one photon creates one electron-hole pair and every generated minority carriers in the absorber are collected, J_{th} represents the short-circuit current density delivered by the solar cell. J_{th} is thus used as a figure of merit in the optical simulation to characterize the performance of light trapping.

The thickness of ARC is firstly optimized by maximizing J_{th} for GaAs solar cells with a flat Ag back mirror. For SiN_x single-layer ARC, it is found the optimal thickness of about 70 nm. For double-layer anti-reflection coating (DLARC), it is found the optimal thicknesses of MgF_2/Ta_2O_5 around 78/48 nm. For ultrathin GaAs solar cells with a nanostructured TiO_2/Ag back mirror, we use the same DLARC and determine the optimal geometry as: grating height

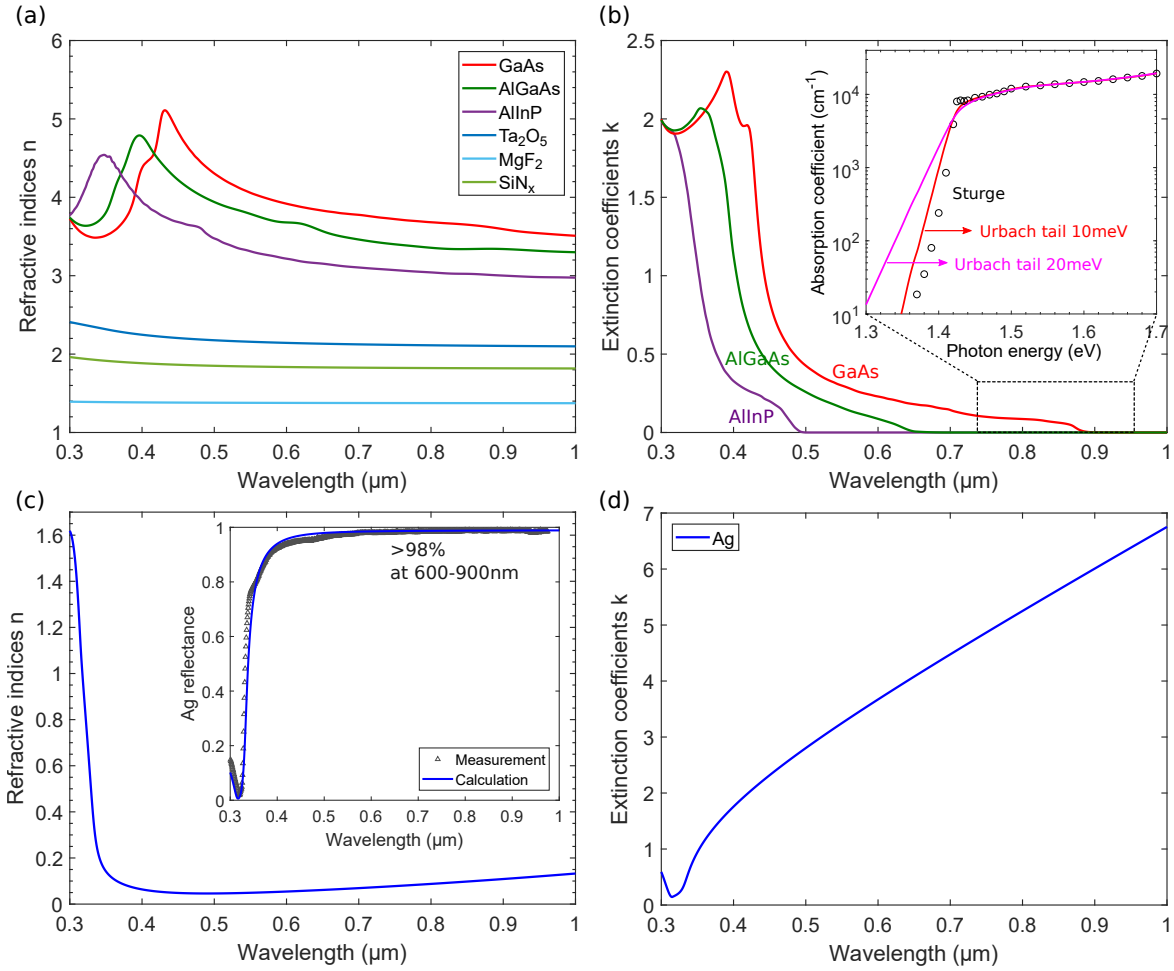

Figure 4.3 – *Complex refractive indices n+iκ of materials. (a,b) Real and imaginary part of the optical indices of semiconductors and dielectric materials. The inset of (b) shows the absorption coefficient of high-purity GaAs from Sturge [36] and extension with an Urbach tail below the bandgap. (c,d) Real and imaginary part of the optical index of silver [109]. The inset of (c) shows the reflectance measurement on flat Ag deposited by electron beam assisted evaporation (C2N) and the calculation using the optical index of Ag at normal incidence.*

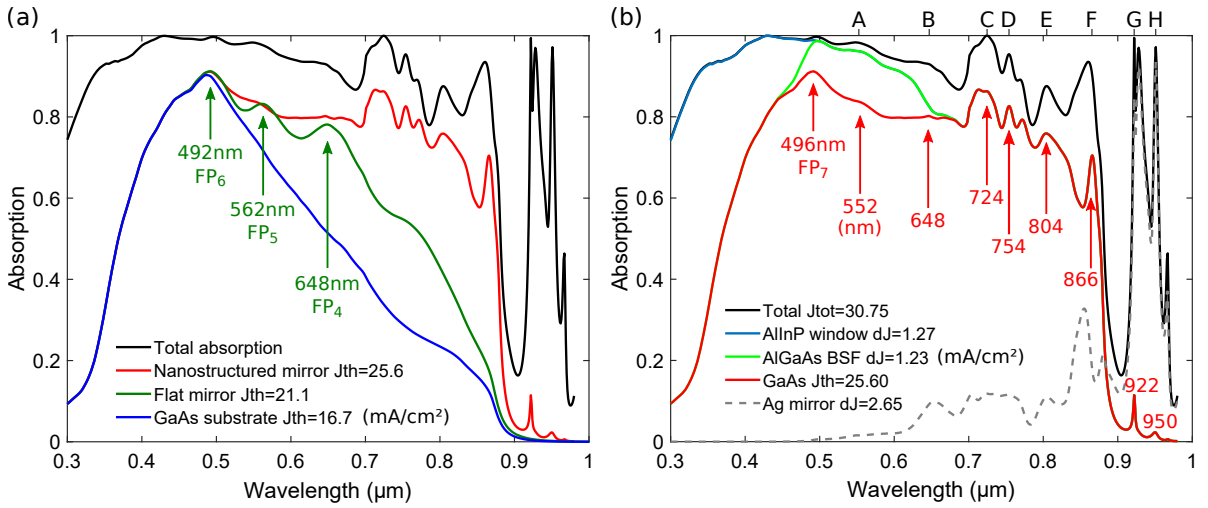

Figure 4.4 – *(a) Comparison of calculated absorption in the 205 nm-thick GaAs absorber with and without light trapping structures: (blue) solar cell on an inactive GaAs substrate, (green) on a flat Ag mirror, (red) on an optimized nanostructured TiO_2/Ag back mirror (period $p = 700$ nm, grating height $h = 120$ nm and Ag width $d = 420$ nm (60% of the period)). (b) Absorption spectra in each layers of the solar cells with the optimized geometry of the back mirror. Several resonant wavelengths are indicated and are labeled by capital letters A to H.*

$h = 120$ nm, period $p = 700$ nm, and Ag square nanostructure width $d = 420$ nm (60% of the period). The corresponding absorption spectra are plotted in Figure 4.4(a) and is compared to the absorption without back mirror (inactive GaAs substrate) and with a flat Ag mirror. Considering only the photogenerated carriers in the GaAs absorber, a flat mirror increases J_{th} from 16.7 to 21.1 mA/cm^2, and further to 25.6 mA/cm^2 using the nanostructured mirror. Figure 4.4(b) shows the detailed absorption spectra in the GaAs absorber and in other layers of the solar cell with the nanostructured mirror. We observe several absorption peaks, labeled by A to F, which are discussed as follows.

4.3.2 Analysis of resonance mechanisms

To gain more insights in the mechanisms of optical resonances and to visualize the absorption variation with some geometrical parameters of the device, we calculate the specular reflectance R of the solar cell with a nanostructured TiO_2/Ag back mirror by varying the GaAs absorber thickness (Figure 4.5(a)) and the grating period (Figure 4.5(b)). We present $1 - R$ as a function of the illumination wavelength and GaAs thickness from 50 to 300 nm for Figure 4.5(a), and $1 - R$ as a function of the illumination wavelength and grating period from 400 to 900 nm for Figure 4.5(b). In the case of varying GaAs thickness, the grating geometry (optimized for 205 nm-thick GaAs) is unchanged. In the case of varying period, the grating height h and the Ag-to-period ratio (60%) are kept constant.

In the short wavelength range ($\lambda = 400$–600 nm), $1 - R$ is relatively constant with the variation of the grating period (Figure 4.5(b)), and the absorption spectrum is similar to the one of a flat mirror (Figure 4.4(a)). The absorption maxima can be described by the vertical Fabry-Perot (FP) resonances. Considering a layer cavity of thickness t (refractive index n_2) and the semi-infinite medium of refractive index n_1 (resp. n_3) at front side (resp. back side) of the solar cell (see Figure 4.6). Conditions of FP resonances are given by:

$$2\,k_2 t + \varphi_{21} + \varphi_{23} = 2\pi q, \tag{4.7}$$

where $k_2 = \frac{2\pi n_2}{\lambda_0}$ is the vertical component (projection in z-direction) of wavevector in the layer. λ_0 is the wavelength and the integer q defines the FP order. φ_{21} and φ_{23} are the phase changes

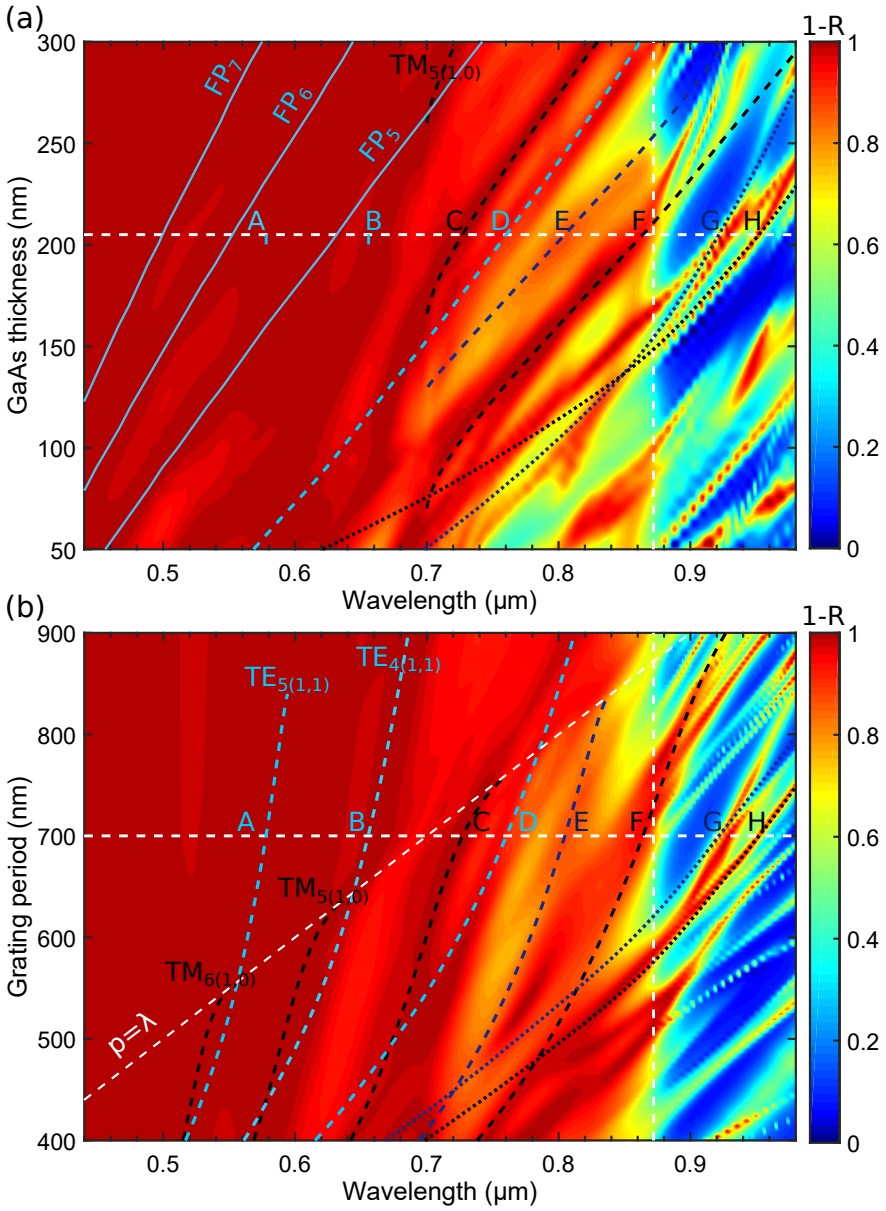

Figure 4.5 – *Dispersion diagrams showing the absorption evolution with the GaAs thickness and the grating period. (a) 1-R spectra as a function of the GaAs thickness. The horizontal white dashed line indicates 205 nm-thick GaAs studied experimentally and the vertical white dashed line marks the bandgap of GaAs. Solid lines represent the calculated resonant wavelengths of Fabry-Perot modes. The corresponding resonant wavelengths are labeled by A to H. (b) 1-R spectra as a function of the grating period for GaAs absorber thickness of 205 nm. The horizontal white dashed line indicates the grating period of 700 nm, giving rise to the optimum broadband absorption. Colored dashed lines are calculated dispersion curves of guided-mode resonances: (A) $TE_{5,(1,1)}$, (B) $TE_{4,(1,1)}$, (C) $TM_{4,(1,0)}$, (D) $TE_{3,(1,1)}$, (E) $TE_{3,(1,0)}$, (F) $TM_{3,(1,0)}$, (G) $TE_{1,(2,0)}$ and (H) $TM_{1,(2,0)}$.*

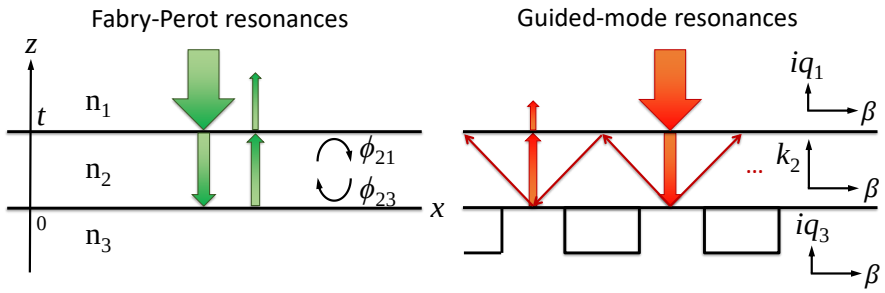

Figure 4.6 – *Schematics for vertical Fabry-Perot resonances (left) and guided-mode mode resonances supported by the back-side grating (right).*

acquired upon reflection at both ends of the layer cavity. They can be calculated from the complex Fresnel coefficient of reflection of TE or TM waves (see Equation 2.15 and 2.16), and they depend on the incident angle. At normal incidence, the phase change is nearly zero for reflection of waves encountering a low-index medium, and is nearly π when encountering a high-index medium. The phase changes due to metallic reflectors are more complicated and are typically found between $-\pi/2$ and $-\pi$. For a multi-layer cavity of total thickness t, the phase shift accumulated due to propagation of light is added over each layer i of thickness h_i. Equivalently, we use an average index defined as:

$$n_{\text{average}} = \frac{1}{t}\sum_i h_i n_i. \tag{4.8}$$

For the solar cell with a flat mirror, we consider the whole cavity including DLARC, and the phase change φ_{21} (resp. φ_{23}) is evaluated between the average complex refractive index of the solar cell and $n_1 = 1$ (resp. n_3 complex refractive index of Ag). We find the resonant wavelengths: 505 nm (FP_6), 567 nm (FP_5) and 663 nm (FP_4), close to the absorption peaks shown in Figure 4.4(a). The label FP_q denotes the FP resonance of order q so that order 0 corresponds to the fundamental mode (one field maximum in the layer). For the solar cell with a nanostructured TiO_2/Ag mirror, we use the same method but consider the whole cavity including DLARC and TiO_2. In this case, we find the resonant wavelengths: 500 nm (FP_7), 553 nm (FP_6) and 632 nm (FP_5). The calculated FP resonant wavelengths as a function of the GaAs thickness are plotted in Figure 4.5(a) (solid lines). The low contrast of these resonance peaks is due to the high absorption and efficient DLARC in this wavelength range.

In the long-wavelength range ($\lambda > 600$ nm), the $1-R$ peaks exhibit remarkable dependence on the grating period and shift to longer wavelengths at larger periods. They are attributed to guided-mode resonances and it is more difficult to calculate the resonant wavelengths using the vertical FP model because the evaluation of phase changes is not straightforward. Thus, we need to examine more in detail the optical modes in this situation. For a 2-dimensional grating of period p, it scatters light into diffracted waves of order (m_1, m_2) defined by their in-plane wavevectors:

$$\vec{k}_{\parallel\,(m_1,m_2)} = \vec{k}_{\parallel\,(0,0)} + m_1\frac{2\pi}{p}\vec{e}_x + m_2\frac{2\pi}{p}\vec{e}_y \tag{4.9}$$

where $\vec{k}_{\parallel\,(0,0)}$ is the in-plane wavevector of incident waves and (m_1,m_2) are integers. $\vec{e}_x$ and $\vec{e}_y$ are unit vectors in x- and y-direction. The additional in-plane momentum induced by the grating allows coupling through either transverse-electric (TE) or transverse-magnetic (TM) guided waves propagating in the solar cells. To identify the main resonance mechanisms and explain the dispersion observed with varying GaAs thickness and grating period, we calculate explicitly the guided modes supported in a planar waveguide.

Considering the configuration illustrated in Figure 4.6, we focus on a thin slab of high index layer (thickness t and refractive index n_2) and look for the solutions of Maxwell equations. In

particular, we search for the modes of planar waveguide propagating in the x-direction and being invariant in the y-direction. In this case, the Maxwell equations are decoupled into two sets of solutions: TE modes of (E_y,H_z,H_x) and TM modes of (H_y,E_z,E_x). The in-plane wavevector is conserved in all the three media since the tangential components of fields are continuous across the interfaces. Thereafter, it is denoted by β, called propagating constant. The z-component of wavevector in the waveguide is denoted by k_2, and those in the super- and substrate are denoted by iq_1 and iq_3, respectively. They can be written as a function of the propagating constant β:

$$\begin{aligned} q_1 &= \sqrt{\beta^2 - \left(\frac{2\pi n_1}{\lambda_0}\right)^2} \\ k_2 &= \sqrt{\left(\frac{2\pi n_2}{\lambda_0}\right)^2 - \beta^2} \\ q_3 &= \sqrt{\beta^2 - \left(\frac{2\pi n_3}{\lambda_0}\right)^2} \end{aligned} \tag{4.10}$$

In the following treatment, we make an approximation and consider the z-component of wavevector to be the real part of the square root in Eq. 4.10. First, we look for TE modes. The general expression of electric field is written in the three regions:

$$E_y(x,z) = \exp\left(i(\beta x)\right) \times \begin{cases} A\exp\left(-q_1(z-t)\right) & \text{for } z > t \\ B\cos(k_2 z) + C\sin(k_2 z) & \text{for } 0 < z < t \\ D\exp\left(q_3 z\right) & \text{for } z < 0 \end{cases} \tag{4.11}$$

Using the continuity of E_y at the plane $z = 0$ and $z = t$ and the continuity of H_x at the plane $z = 0$, where

$$H_x = \frac{i}{\omega\mu_0}\frac{\partial E_y}{\partial z}, \tag{4.12}$$

the constants (A, B, C, D) are reduced to a single proportionality constant (taken to be unity afterward).

$$E_y(x,z) = \exp\left(i(\beta x)\right) \times \begin{cases} \left[\cos(k_2 t) + \frac{q_3}{k_2}\sin(k_2 t)\right]\exp\left(-q_1(z-t)\right) & \text{for } z > t \\ \cos(k_2 z) + \frac{q_3}{k_2}\sin(k_2 z) & \text{for } 0 < z < t \\ \exp\left(q_3 z\right) & \text{for } z < 0 \end{cases} \tag{4.13}$$

The boundary condition for H_x at the plane $z = t$ leads to the following equation (TE mode):

$$\tan(k_2 t) = \frac{q_1 + q_3}{k_2\left(1 - \frac{q_1 q_3}{k_2^2}\right)}. \tag{4.14}$$

Replacing the expressions of Eq. 4.10 in the TE mode Eq. 4.14, we obtain a transcendent equation in β, which can be solved numerically. At a fixed wavelength and a given thickness of the waveguide slab, one or several discrete solutions of β can be found, corresponding to various guided modes propagating in the slab. In our case of ultrathin solar cells with nanostructured back mirror, the possible propagating vectors are related to the periodicity of the grating via Equation 4.9. The dispersion relation between resonant wavelengths and the GaAs thickness (Figure 4.5(a)) and the grating period (Figure 4.5(b)) can be calculated, allowing to distinguish between various guided-mode resonances.

The electric field intensity cross-sections in one period of the device are calculated using RCWA for several resonant wavelengths with TE polarization and are displayed in Figure 4.7

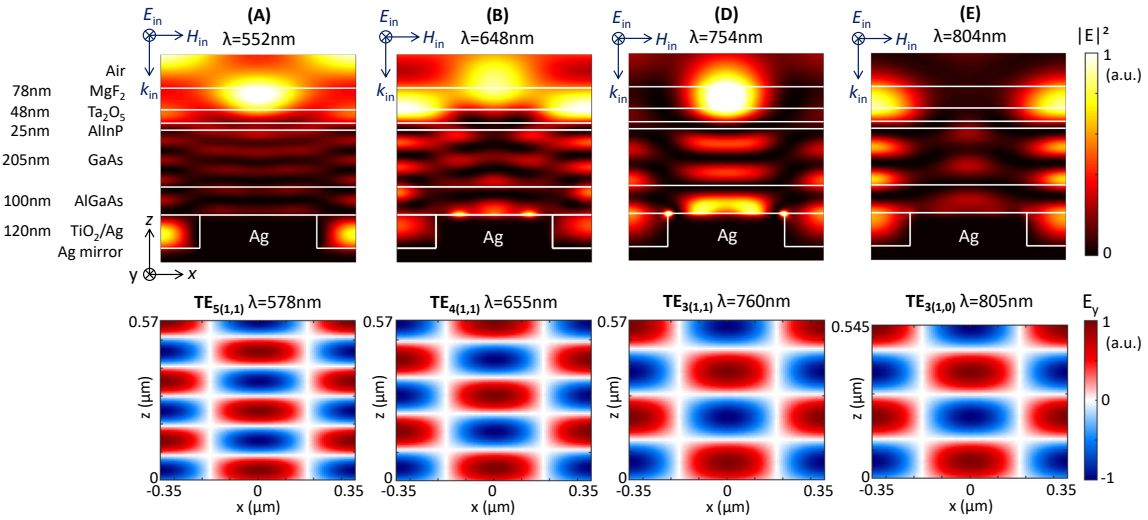

Figure 4.7 – *Electric field cross-section distribution (TE polarization) at several resonant wavelengths for the 205 nm-thick GaAs solar cell with the optimized grating structure. (Top) electric field intensity $|E|^2$ calculated using numerical RCWA. (Bottom) electric field amplitude E_y of TE guided modes calculated with an analytical model.*

(top). The cross-section (x-z incident plane) follows the symmetry of the grating passing through the center of the Ag nanostructure. These maps are compared to the electric field patterns calculated with the analytical expression of a planar waveguide (Figure 4.7 (bottom)). In the analytical calculation, we take $n_1 = 1$, n_2 the average complex index of the solar cell (including DLARC and TiO_2) and n_3 the complex refractive index of Ag. The use of complex indices allows proper description of reflection from Ag mirror, but we only consider guided modes and restrict to the real part of wavevectors (Eq. 4.10). Note that β complex describes leaky waves. The total thickness t is slightly adjusted to match the resonant wavelengths obtained from exact RCWA calculations.

As shown in the calculated field maps, the oscillation of electric field intensity in the vertical direction is similar to FP resonances. We associate the orders q of guided modes similarly to those of FP modes so that the number of field intensity maxima is $q+1$ in the cavity ($q = 0$ corresponds to the fundamental mode). The periodic variation of the electric field amplitude in the horizontal direction is typical for guided modes propagating in the thin layer. We observe one periodic variation per grating period, so the mode involves the ± 1 diffraction order. The (1,0) guided modes propagate in the x-direction (e.g. resonance E), while the (1,1) guided mode propagates in the diagonal direction of x- and y-axis (e.g. resonance A, B and D).

In the following discussions, we turn to TM guided modes: solutions (H_y, E_z, E_x) of Maxwell equations. The field descriptions used in Eq. 4.11 are applied for magnetic field H_y, while the examination of boundary conditions consists of the continuity of H_y and E_x at the plane $z = 0$ and $z = t$, where

$$E_x = \frac{1}{i\omega\varepsilon_0\varepsilon_r}\frac{\partial H_y}{\partial z}. \tag{4.15}$$

We note that the dielectric constants ε_r depend on the region considered: $\varepsilon_1 = 1$ in air, $\varepsilon_2 = n_2^2$ in the waveguide and $\varepsilon_3 = n_3^2$ in the substrate. The magnetic field is written as follows:

$$H_y(x,z) = \exp\left(i(\beta x)\right) \times \begin{cases} \left[\cos(k_2 t) + \dfrac{\varepsilon_2}{\varepsilon_3}\dfrac{q_3}{k_2}\sin(k_2 t)\right]\exp\left(-q_1(z-t)\right) & \text{for } z > t \\ \cos(k_2 z) + \dfrac{\varepsilon_2}{\varepsilon_3}\dfrac{q_3}{k_2}\sin(k_2 z) & \text{for } 0 < z < t \\ \exp\left(q_3 z\right) & \text{for } z < 0 \end{cases} \tag{4.16}$$

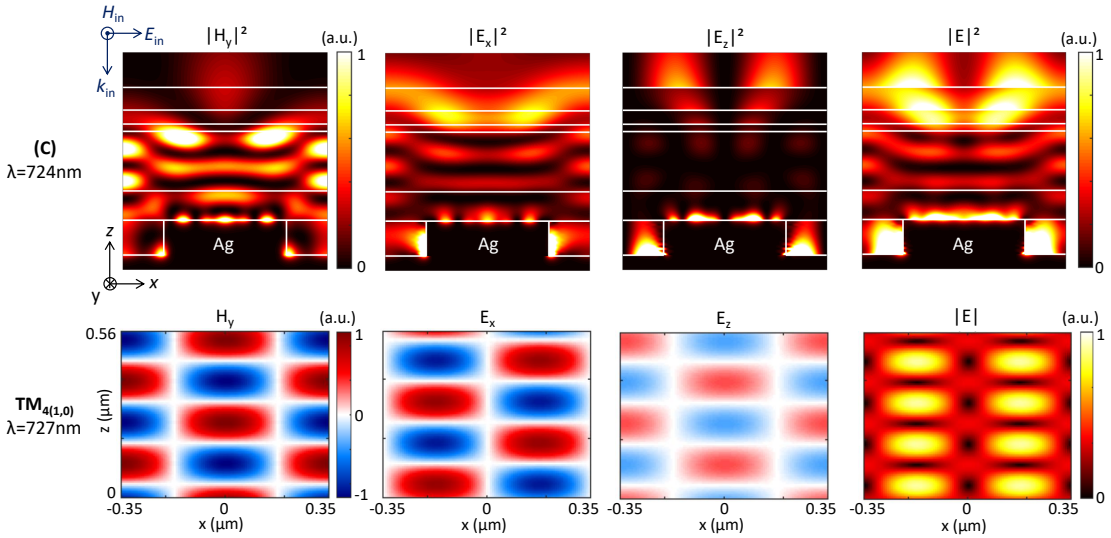

Figure 4.8 – *Electromagnetic field cross-section distribution (TM polarization) for the resonance (C) at 724 nm. (Top) electromagnetic field intensities calculated using numerical RCWA. (Bottom) corresponding electromagnetic field amplitudes (H_y,E_x,E_z) and $|E|$ of a $TM_{4,(1,0)}$ guided-mode calculated with a simplified analytical model.*

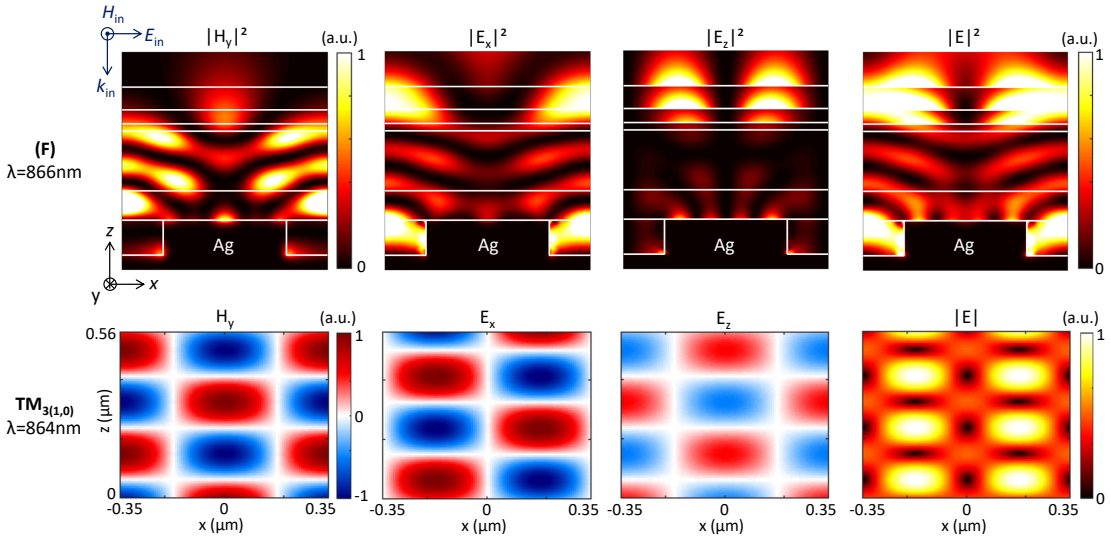

Figure 4.9 – *Electromagnetic field cross-section distribution (TM polarization) for the resonance (F) at 866 nm. (Top) electromagnetic field intensities calculated using numerical RCWA. (Bottom) corresponding electromagnetic field amplitudes (H_y,E_x,E_z) and $|E|$ of a $TM_{3,(1,0)}$ guided-mode calculated with a simplified analytical model.*

Finally, the continuity of E_x at the plane $z = 0$ leads to the following equation (TM mode):

$$\tan(k_2 t) = \frac{\frac{q_1}{\varepsilon_1} + \frac{q_3}{\varepsilon_3}}{\frac{k_2}{\varepsilon_2}\left(1 - \frac{\varepsilon_2^2}{\varepsilon_1 \varepsilon_3}\frac{q_1 q_3}{k_2^2}\right)}. \tag{4.17}$$

The equations relating wavevectors to the propagation constant (Eq. 4.10) are still valid for TM modes (Eq. 4.17). The resolution of the obtained transcendent equation results in another set of solutions of β. In Figure 4.8 and Figure 4.9, we show the electromagnetic field distributions (H_y,E_x,E_z) with TM polarization calculated by RCWA (top) and the analytical model (bottom) for resonance (A) and (D), respectively. These resonances are identified as TM modes because they correspond to in-plane coupling to a transverse magnetic waveguide mode (H_y only). The

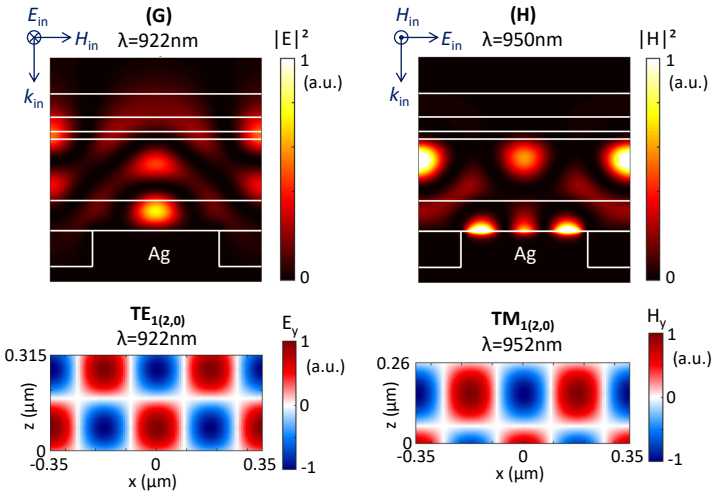

Figure 4.10 – *(Top) electromagnetic field intensities calculated using numerical RCWA for the resonance (G) and (H). (Bottom) corresponding electromagnetic field amplitudes E_y of a $TE_{1,(2,0)}$ guided-mode and H_y of a $TM_{1,(2,0)}$ guided-mode.*

combination of E_x and E_z makes the electric field intensity map to have more complicated features than the map of TE modes.

Resonance (G) and (H), despite below the bandgap of GaAs, show a strong absorption enhancement. They are attributed to higher order guided modes: $TE_{1(2,0)}$ for resonance (E) and $TM_{1(2,0)}$ for resonance (F). As shown in Figure 4.10, fields are confined in the core of high-index semiconductor layers. Therefore, we calculate the corresponding guided modes by taking n_2 the refractive index of GaAs and fit the thickness t near the total thickness of III-V layers. For the second order diffraction, we observe two periodic variations of field amplitude (four maxima of field intensity) in the propagation direction. They are also characterized by a strong dispersion with the grating period (Figure 4.5(b)).

4.3.3 Angular dependence of absorption

The dispersion of resonance modes can also be observed by varying the angle of incidence. For the 205 nm-thick GaAs solar cell with optimized grating structure, Figure 4.11 presents the maps of total absorption spectra (a,b) and absorption in GaAs (c,d) as functions of the incident angle, for both TE (a,c) and TM (b,d) polarizations. In the short wavelength range (400–600 nm), the absorption features are similar to vertical Fabry-Perot resonances and little variation with the incident angle is observed due to thin GaAs layer and its high refractive index. In the long wavelength range (600–1000 nm), strong angular dispersion is related to guided-mode resonances. For each guided mode, we calculate the angular dispersion based on the method presented in the previous section. We replace the propagation constant by:

$$\beta = \sqrt{\left(\frac{2\pi n_1}{\lambda_0}\sin\theta + m_1\frac{2\pi}{p}\right)^2 + \left(m_2\frac{2\pi}{p}\right)^2}. \tag{4.18}$$

The calculated resonant wavelengths as a function of incident angle are shown in Figure 4.11 for both TE and TM modes. We can see that the guided mode splits from normal incidence to two branches characterized by the diffraction orders (m_1,m_2) and ($-m_1$,m_2). Overall, the integrated absorption maintains a high short-circuit current ($J_{th} > 23.5$ mA/cm^2) up to 60° through overlaps of multiple resonances (Figure 4.11(e)).

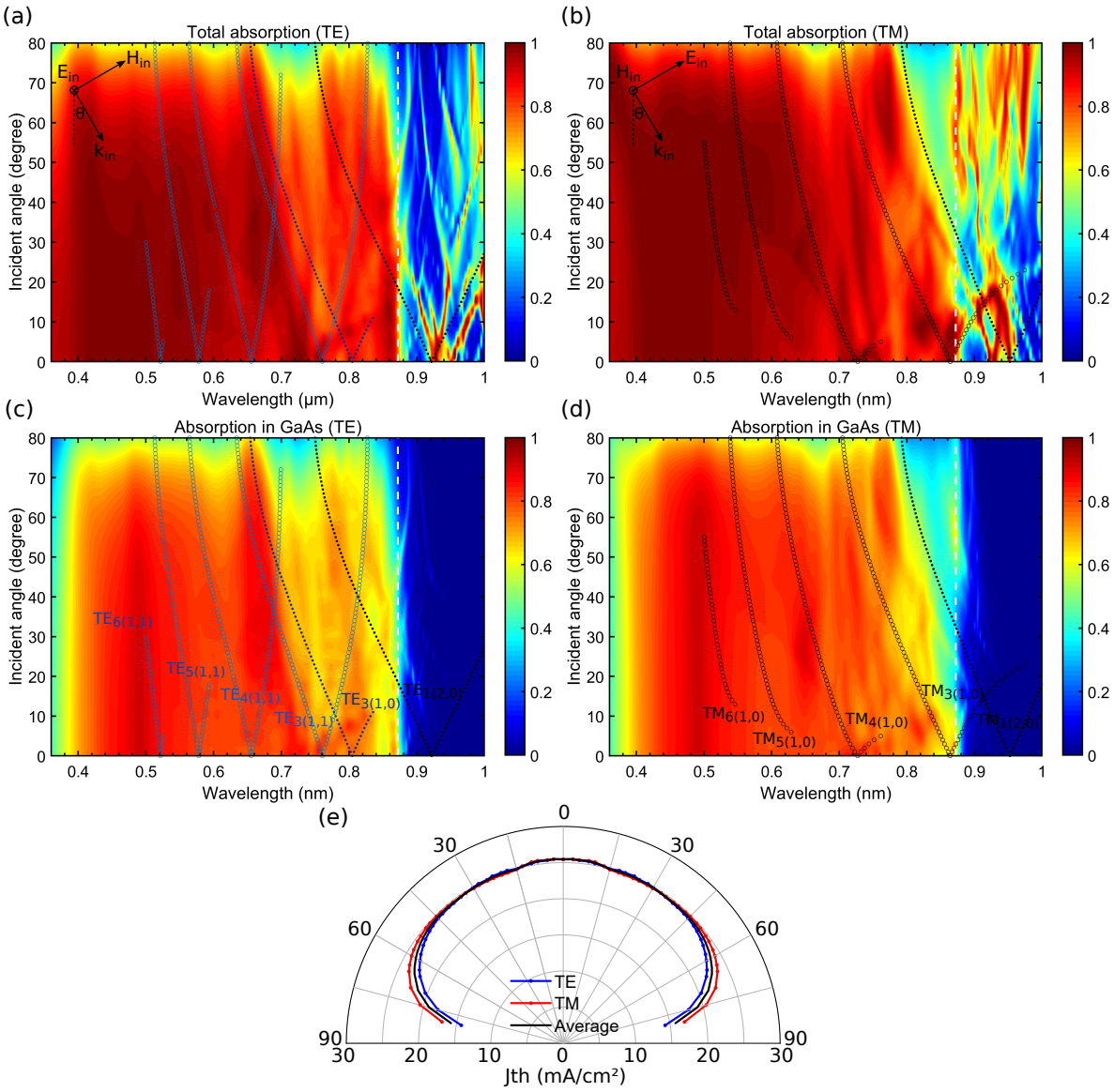

Figure 4.11 – *Two-dimensional plot of the absorption as a function of the incident angle. The angular dependence of the absorption is calculated for (a,c) TE incident polarization and for (b,d) TM incident polarization. (a,b) show the total absorption and (c,d) show the absorption in GaAs. (e) Polar plot of calculated J_{th} resulting from the incident angle dependence of the absorption in 205 nm-thick GaAs.*

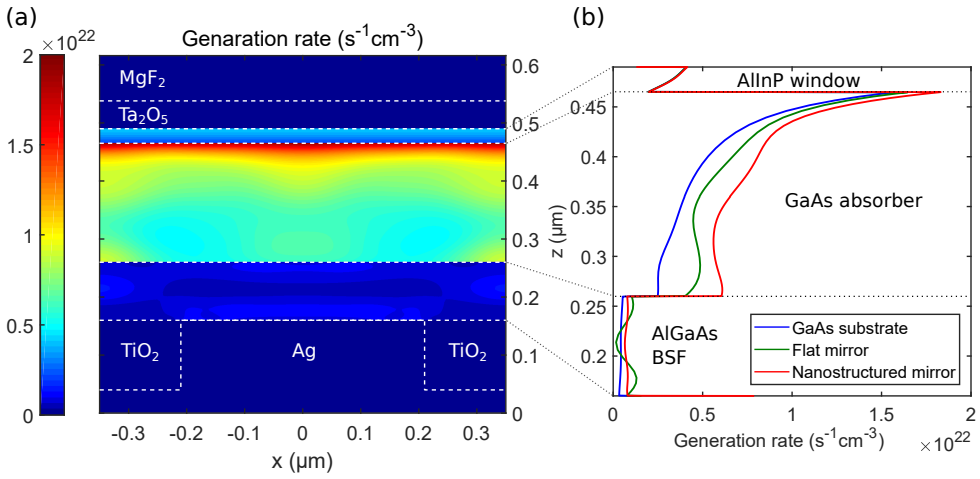

Figure 4.12 – *Generation of carriers by integrating the absorbed electromagnetic power density over all photon energies, assuming that each absorbed photon creates one eletron-hole pair. (a) Generation map in the x-z plane by averaging over the y-direction. (b) Generation profile in the z-direction by averaging over the x- and y-direction. Red curve is for the solar cell with nanostructured back mirror, green curve with a flat Ag mirror and blue curve on a GaAs substrate.*

4.3.4 Photogeneration rate

To visualize the spatial distribution or density of the photogeneration rate, we should firstly calculate the density of absorbed photons $g_\lambda(x, y, z)$ at a given wavelength (per unit time and per unit volume). The density of absorbed photons is related to the electromagnetic power absorbed in an elementary volume of the material. We write the time-averaged Poynting vector $\mathbf{S}$ using complex amplitudes of harmonic fields [110]:

$$\mathbf{S} = \frac{1}{2}\mathrm{Re}\left(\mathbf{E} \times \mathbf{H}^*\right) \tag{4.19}$$

where * stands for the complex conjugate and Re for the real part. Since the Poynting vector is the power flow density vector [J $\mathrm{s}^{-1}\mathrm{m}^{-2}$], the electromagnetic power density absorbed [J $\mathrm{s}^{-1}\mathrm{m}^{-3}$] is given by the divergence of $\mathbf{S}$:

$$\nabla \cdot \mathbf{S} = \frac{1}{2}\omega\varepsilon_0 \mathrm{Im}(\varepsilon_r)\left|\mathbf{E}\right|^2, \tag{4.20}$$

where ω is the frequency of a monochromatic impinging wave, $\mathrm{Im}(\varepsilon_r)$ is the imaginary part of the complex relative permittivity and $|\mathbf{E}|$ is the magnitude of the electric field. The electromagnetic power absorbed in the volume is also the number of absorbed photons multiplying the photon energy $\hbar\omega$, hence

$$g_\lambda(x, y, z) = \frac{\varepsilon_0 \mathrm{Im}(\varepsilon_r)\left|\mathbf{E}\right|^2}{2\hbar}. \tag{4.21}$$

The total carrier generation rate in a volume of semiconductor layers $g(x, y, z)$ [$\mathrm{s}^{-1}\mathrm{m}^{-3}$] can then be calculated from the photon absorption rate $g_\lambda(x, y, z)$ weighted by the AM1.5G solar spectrum, assuming that each photon absorbed generates one electron-hole pair.

A cross-section map of the photogeneration rate $g(x, z)$ is shown in Figure 4.12(a). The values are averaged along the y-direction for the TE incident polarization. The density of photogenerated carriers in the absorber is inhomogeneous due to the two-dimensional pattern of the back mirror. Figure 4.12(b) plots the generation rate $g(z)$ averaged in both x- and y-direction to show only the variation in the depth (polarization-independent because of the symmetry of the structure). We can observe that the z-profile of the carrier generation rate is not homogeneous even in a 205 nm thin GaAs absorber with a back reflector, due to the strong absorption coefficient

difference between high- and low-energy photon. The real-time distribution of photogenerated carriers depends also on the diffusion length of the material, thus may be homogenized in the volume of the semiconductor. These distributions of photogenerated carriers can be used as an input for transport equations to further model the electrical characteristics of the solar cell.

4.4 Modeling for solar cell structures

4.4.1 1D device simulation

We use SCAPS to perform simulation of the electrical characteristics of ultrathin GaAs solar cells. SCAPS is a one dimensional (1D) solar cell simulation program developed by Burgelman and coworkers at the department Electronics and Information Systems of the University of Gent, Belgium. The program is freely available to the photovoltaic research community[1]. A description of the program and the algorithms it uses are found in the literature [111, 112].

The optical response of the ultrathin solar cells with light trapping structures is calculated separately from RCWA method (section 4.3). The carrier generation rate under 1 sun AM1.5G illumination is obtained previously at the end of optical computation (Figure 4.12), which is injected to SCAPS as an input condition for the electrical models. The material parameters used in SCAPS simulation are listed in Table 4.2. Some are collected from the reference [113] for binary III-V compounds and from the reference [114] for III-V ternary alloys. Material parameters for AlInP are less available and are only found occasionally in some published papers [108, 115, 116]. The doping dependence of mobility data for GaAs and AlGaAs are deduced from reference [117].

Table 4.2 – *Material parameters used in device simulation.*

	GaAs	$Al_{0.4}Ga_{0.6}As$	$Al_{0.51}In_{0.49}P$
Bandgap [eV]	1.424	1.92	2.6
Electron affinity [eV]	4.07	3.63	4.12
Dielectric constant	12.9	11.76	11.36
CB effective DOS [cm^{-3}]	4.2×10^{17}	8.0×10^{17}	2.8×10^{18}
VB effective DOS [cm^{-3}]	9.5×10^{18}	1.2×10^{19}	5.5×10^{18}
Electron thermal velocity [cm/s]	4.4×10^{7}	3.5×10^{7}	1×10^{7}
Hole thermal velocity [cm/s]	1.8×10^{7}	1.6×10^{7}	1×10^{7}
Electron mobility [$cm^2/(Vs)$]	2700	300	100
Hole mobility [$cm^2/(Vs)$]	170	60	10
Radiative recombination coefficient [cm^3/s]	7.2×10^{-10}	1.8×10^{-10}	1×10^{-10}
Auger electron capture coefficient [cm^6/s]	10^{-30}	10^{-30}	10^{-30}
Auger hole capture coefficient [cm^6/s]	10^{-30}	10^{-30}	10^{-30}

The program solves the electrostatic Poisson's equation and drift-diffusion equations for electron and hole in one dimension, and obtain the band diagram and current-voltage (J-V) characteristics of the solar cell. Here, the *flat bands* condition is assumed, i.e. the metal work function is aligned with the Fermi level of the majority carrier at the metal-semiconductor interface, so that ideal ohmic contacts are established. In practice, highly-doped semiconductor contact layers are grown to facilitate a good ohmic contact formation with metal electrode because high doping reduces the potential barrier width so that carrier can tunnel through field emission. In the ideal case, no defect is introduced at interfaces and in the bulk of semiconductor layers. The band diagram at short-circuit and at open-circuit condition is given in Figure 4.13. The calculated photovoltaic parameters are grouped in Table 4.3 and J-V characteristics are plotted

[1]SCAPS 1D solar cell simulation program: http://scaps.elis.ugent.be/

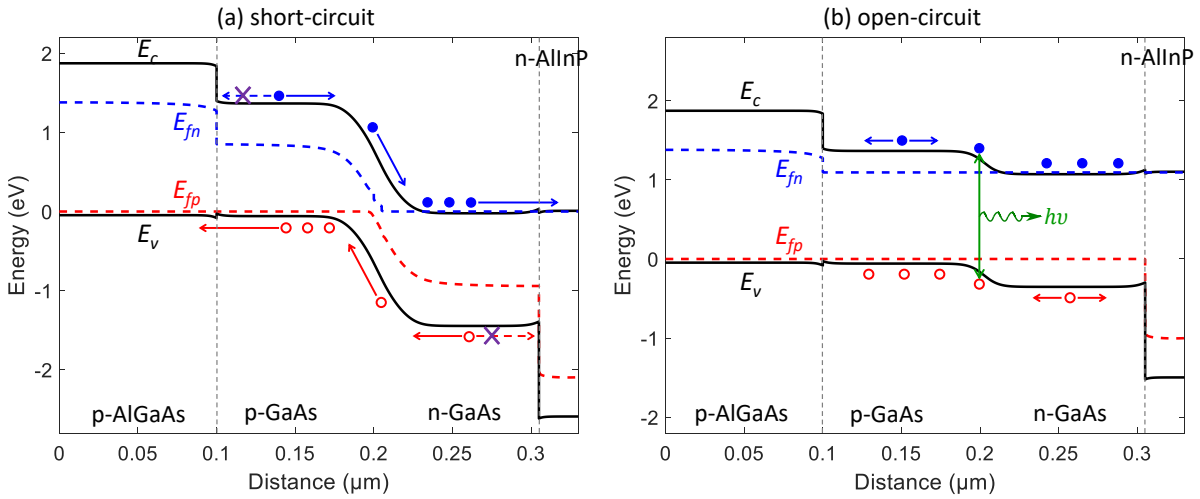

Figure 4.13 – *Calculated band diagram for ultrathin GaAs solar cell at (a) short-circuit and (b) open-circuit condition under 1 sun illumination (light comes in from the right hand side). Conduction band edge (E_c) and valence band edge (E_v) are shown together with the quasi-Fermi level for electron (blue dashed line E_{fn}) and for hole (red dashed line E_{fp}). The GaAs absorber is embedded in high bandgap materials: n-AlInP window layer and p-AlGaAs back surface field to prevent recombination of photogenerated carriers near the contact.*

in Figure 4.14 for the ultrathin solar cell with the optimized nanostructured back mirror (red curve) and reference structures (green curve: flat mirror, blue curve: GaAs substrate).

At short-circuit, the photogenerated carriers need to be collected efficiently to maximize the current delivered by the solar cell . Generally, the loss comes from the recombination of minority carriers near the surface in contact with a metal electrode. Unpassivated GaAs surface also suffers from high density of surface states which reduce greatly the non-radiative lifetime. This is prevented by growing a higher bandgap material, so-called window layer on top and back surface field (BSF) at rear side, as-shown in Figure 4.13(a). Photogenerated minority carriers in the main absorber are reflected back from the surface so that the collection efficiency is increased. Ideally, these high-bandgap materials should be transparent to avoid parasitic absorption losses. On the other hand, window and BSF should be sufficiently doped so that proper band alignment allows for the transport of majority carriers.

At open-circuit, no current flows through the exterior circuit, while a voltage is built up in the solar cell between the two contacts. This is the open-circuit voltage, given by the separation of the two quasi-Fermi levels. Since no current flows, each electron-hole pair generated from absorption of one photon is recombined in the solar cells. In high-quality materials with low non-radiative recombination losses, only radiative recombination occurs. Subsequently, photons are emitted and eventually re-absorbed in the main absorber to generate again one electron-hole pair. This is the photon recycling effect, leading to a higher population of minority carriers so a larger separation of quasi-Fermi levels. Meanwhile, regular electrical device simulations do not capture the photon recycling effect. Optical model and electrical solver should be coupled in an iterative way to correctly describe the J-V behavior near V_{oc}, as illustrate in references [116, 118]. We may calculate, at open-circuit, the spatial distribution of the spontaneous emission rate and add up an additional population of minority carriers to the initial input of the generation rate. Electrical simulation solves again the J-V characteristics then the photon emission is re-evaluated to add up another population of minority carriers and so on. Walker et al. have demonstrated numerically and experimentally that photon recycling can indeed improve V_{oc} of several tens of meV in thin-film GaAs solar cells with a highly reflective silver mirror [116].

Without photon recycling, the numerical simulations show V_{oc} values of about 1.083 V to

Table 4.3 – *Calculated photovoltaic parameters for ultrathin solar cells with and without light trapping structures under 1 sun illumination. DLARC is applied for the three structures. Optical responses are calculated from the RCWA method and electrical characteristics are simulated from SCAPS (no photon recycling).*

	J_{sc} mA/cm^2	V_{oc} V	FF	efficiency %
GaAs substrate	18.18	1.083	0.889	17.5
Flat mirror	23.09	1.089	0.889	22.4
Nanostructured mirror	27.35	1.094	0.889	26.6

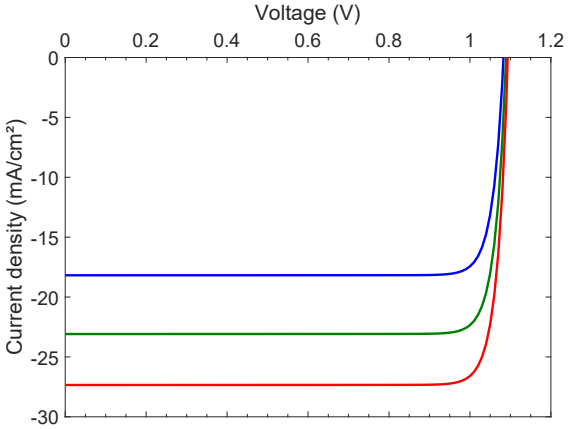

Figure 4.14 – *Calculated J-V characteristics of ultrathin solar cells with and without light trapping structures under 1 sun illumination. Blue curve is for the solar cell on a GaAs substrate, green curve with a flat Ag mirror and red curve with the optimized nanostructured back mirror. DLARC is applied for the three structures. Bulk non-radiative recombination and surface recombination are not considered in the electrical solver. Photon recycling effect is not included.*

1.094 V. Slight increase for flat mirror and nanostructured mirror cell is attributed to the increase of J_{sc}. Since we assume only radiative and Auger recombination in the simulation and Auger recombination is usually a minor effect for GaAs solar cell at 1 sun, 1.094 V appears as a reference V_{oc} optimum without photon recycling. This value is very close to the radiative limit calculated for 205 nm-thick GaAs solar cell on a GaAs substrate (see Chapter 3, Figure 3.13). High J_{sc} is resulted from the collection of photogenerated carriers in the window and BSF layers. The calculated photovoltaic parameters provide us a target for the potential performance of ultrathin GaAs solar cells.

4.4.2 Analysis of resistive losses

One aspect that cannot be captured by 1D simulation is the resistive losses due to limited contact area of the solar cell. In particular, the front surface of the solar cell is opened to allow for light to pass through and be absorbed in active regions. A minimum ratio of about 2% front contact area to the total surface is generally needed. Front contact is usually designed in the form of finger grids. The contact resistance should be controlled by careful fabrication considering the surface treatment and the choice of metals or alloys. The optimization of the spacing distance of front contact grids permits a reasonable current spreading to limit intrinsic resistive losses in the semiconductor layers. Here, we calculate these parameters with a simple model in order to decide which contact grid spacing should be used.

Figure 4.15 depicts a simple structure used to calculate the resistive losses in the solar cell. We consider a thin-film semiconductor layer of thickness t (for example moderately-doped GaAs)

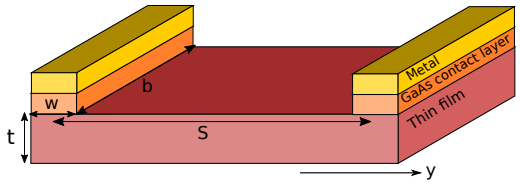

Figure 4.15 – *Sketch of a thin-film semiconductor layer and the top contact grid with finger width w and spacing distance S in the y-direction.*

and the contact grids contact (typically highly-doped GaAs and metallic layers). The finger grid is considered to be long in x-direction (here length b), periodically placed with a spacing S in y-direction. The finger width w is supposed to be small compared to S.

The thin-film layer of thickness t collects a current density J from the junction, and is supposed to conduct the current I horizontally to the grid contact. We consider the current in the semiconducting layer is uniform in x- and in vertical z-direction, so that the current is written as $I(y)$. By symmetry, I should be zero at the middle of two fingers. Supposing I increases linearly from the middle $y = 0$ to the contact $y = S/2$, we have

$$I(y) = Jby. \tag{4.22}$$

The ohmic loss due to lateral conduction in the semiconducting film is expressed with the resistivity ρ (Ωcm) of the semiconductor:

$$P_{loss} = 2\int_0^{S/2} I(y)^2 dR = 2\int_0^{S/2} (Jby)^2 \frac{\rho}{tb} dy = \frac{J^2 R_\square b S^3}{12}. \tag{4.23}$$

The sheet resistance $R_\square$ is generally used for thin-film: $R_\square = \rho/t$. At the maximum power point, the solar cell generates the power in the area considered here:

$$P_{gen} = J_{mp} V_{mp} bS. \tag{4.24}$$

The relative loss due to resistive effect in the thin semiconducting layer is thus:

$$\frac{P_{loss}}{P_{gen}} = \frac{R_\square J_{mp} S^2}{12 V_{mp}}. \tag{4.25}$$

In practice, a minimum finger width of about 5 μm is used, too small finger may cause fabrication difficulty (photolithography, lift-off and wet etching). Keeping $w = 5$ μm, reducing the finger spacing S mitigates the resistive loss, but increases the front contact shading loss because a higher ratio of the surface is covered by metal. There is an optimal spacing, which depends on the sheet resistance of the thin-film layer and on the operation conditions. The resistivity of a semiconductor can be calculated from its doping concentration N and majority carrier mobility μ.

$$\rho = \frac{1}{q\mu N} \tag{4.26}$$

We summarize the resistivity and resulting sheet resistance values in ultrathin GaAs solar cells in Table 4.4.

The relative loss due to lateral transport is calculated using Equation 4.25. We take for example $J_{mp} = 30$ mA/cm^2 (increases linearly with the concentration C) and $V_{mp} = 0.9$ V (increases logarithmically with the concentration C). The resistive loss can be drawn as a function of the finger spacing S in the layer associated with a sheet resistance. The relative loss increases as a quadratic function of S. On the other hand, the shading loss is proportional to the ratio of covered and uncovered surface. The total loss is the sum of resistive loss and shading loss, which

Table 4.4 – *Resistivity data of the semiconducting materials in ultrathin GaAs solar cells (C2853 layer stacks).*

material	thickness nm	doping cm^{-3}	mobility $cm^2/(Vs)$	resistivity Ω cm	sheet resistance $\Omega/\square$
n-AlInP window	25	2×10^{18}	100	0.031	12500
n-GaAs emitter	100	1×10^{18}	2700	0.0023	230
p-GaAs base	100	1×10^{18}	170	0.037	3670
p-AlGaAs BSF	100	2×10^{18}	60	0.052	5200

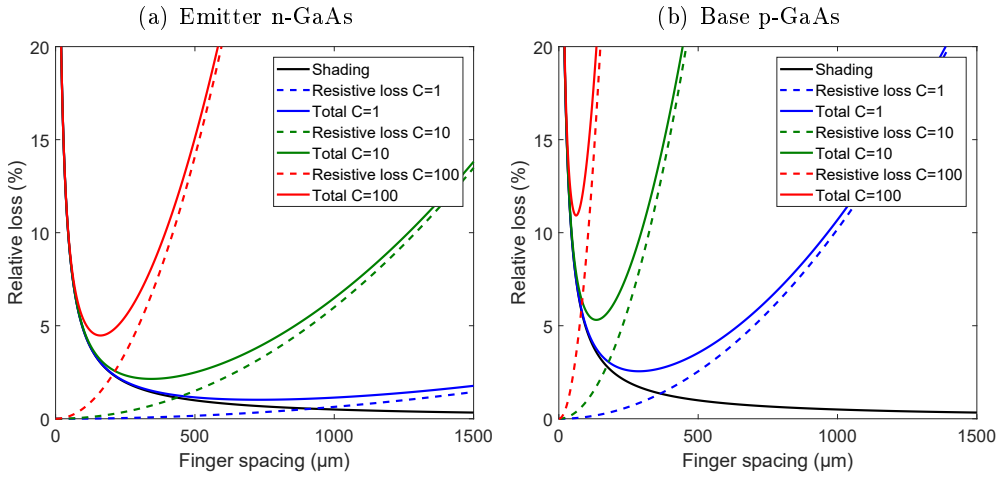

Figure 4.16 – *Plots of shading loss, resistive loss and the total loss under different illumination concentrations (C=sun). The optimal finger spacing is obtained at the point of minimum total loss. (a) Case for n-GaAs emitter with $R_\square = 230\,\Omega/\square$. (b) Case for p-GaAs base with $R_\square = 3670\,\Omega/\square$.*

presents an optimum finger spacing S. We can see that 600 to 800 μm is sufficient for n-GaAs emitter at 1 sun illumination, resulting in only 1% loss. Smaller contact grid spacing is required for concentrating sunlight. We note that p-GaAs has substantially lower mobility than n-GaAs, thus much higher sheet resistance if the thickness is the same. For full-area back contact, this may not be an issue. However, we still fabricated localized back contacts to reduce parasitic absorption in the back contact (see fabrication section), so reduced distance between localized back contact is needed.

4.5 Fabrication

4.5.1 Photolithography and wet etching

Photolithography is widely used in the semiconductor manufacturing to define patterns on planar wafers. The process sequences contain cleaning of the semiconductor surface, coating with a light-sensitive thin-film called *photoresist*, exposure of the photoresist using a mask defining the patterns, and development of the photoresist so that the photoresist replicates the desired patterns. Depending on applications, patterns are transferred on the top surface of the semiconductor through metal or dielectric deposition and lift-off, or through wet chemical solution and gas-phase etching (dry etching). Standard UV (mercury vapor lamp) photolithography with contact-mode mask aligner is used in C2N laboratory. Plasma dry etching creates poor electronic surface quality for III-V semiconductors, so is prohibited for high-efficient solar cells. Wet chemical etching is thus the first choice to pattern solar cell structures like contact area and

mesa.

AZ5214 photoresist from MicroChemicals[2]was used in all the fabrication process. It is an organic resin based on the *phenol-formaldehyde* (novolacs) matrix, containing photo active compounds belonging to the group of *diazonaphtho-quinone-sulphonates* (DNQ). The photoresist is mainly non-polar, a polar surface of semiconductor may results in poor adhesion of the photoresist, leading to peering and bad pattern quality of the photoresist. Oxidized semiconductor surface containing top-most -OH bounds or adsorption of H_2O molecules are sources for a polar surface. Therefore, deoxidation (dilute HCl or NH_4OH is usually used on GaAs for this purpose) and dehydrate the surface (for example baking on a hotplate) are useful before photoresist coating to have reproducible results. Spin-coating was used to have an uniform film at the center of the samples. Typical spin speed for AZ5214 is 3000 to 4000 rpm, acceleration 2000 rpm/s and spin time of 30 s, resulting in a thin-film thickness of about 1.4 μm. AZ5214 is prebaked at 128°C for 1 min to evaporate the residual solvent and to make the photoresist slightly denser and partly cross-linked.

Depending on the objective, positive or negative photolithography can be used for the reversible AZ5214 photoresist. In the first case (positive), the region undergoes UV exposure (about 15 s) dissolves faster in the developer. In fact, the presence of DNQ in photoresists reduces the alkaline solubility by more than one order of magnitude than pure novolacs. During exposure, the DNQ transforms into a carboxylic acid, accompanied by the release of nitrogen and absorption of water. Thus, the solubility increases by several orders of magnitude. Higher exposure dose leads to deeper bleach of the photoresist and thus creates the undercut for the remaining photoresist patterns. In the latter case (negative), AZ5214 photoresist undergoes a first exposure with a mask (5 s), then postbaked on a hotplate at 128°C for 1 min. Subsequently, the sample undergoes a second flood exposure without mask (30 s). The region masked in the first exposure becomes much more soluble in the developer. This is because the reversible resist contains a crosslinker which is activated during exposure and subsequent thermal baking step. Higher doses of the first exposure increase the degree of cross-linking, which improves the thermal and chemical stability. For wet etching purpose, a hardbake of the photoresists at 128°C for 1 to 2 min may improve the resin adhesion to avoid peering in chemical solutions.

Wet chemical etching

In most cases, the wet etching employs chemical solutions with the mixture of an oxidizer agent and a chemical etchant (acids or bases) diluted in deionized water. The most commonly used oxidizer is the hydrogen peroxide (H_2O_2), which oxidizes the surface atoms of semiconductors. The oxidized compounds are then dissolved chemically in the solution depending on the choice of etchant. The etching rates depend on the oxidation speed or the dissolution reaction (thus scale with the concentrations of the solution), and are inversely proportional to the exponential of the thermal energy kT (reaction rate limited). If the solution is so viscous that the transport of etching reagent is slower than chemical reaction, the overall etching rate is diffusion limited. On the other hand, etching rate might depend on the crystallographic orientation of the semiconductor. In this case, the wet etching is called anisotrope, in contrast with an isotropic wet etching. For example, the surface activities of (111)Ga and (111)As are very different due to inverse polarity. The chemical etching of the (111)Ga face tends to show crystallographic defects and etches more slowly.

Chemical solutions used in all experiments are commercial products with standard concentrations expressed in weight ratio with water. For example, hydrogen peroxide (H_2O_2 30%), hydrochloric acid (HCl 37%), sulfuric acid (H_2SO_4 95%), nitric acid (HNO_3 52.5%), phosphoric acid (H_3PO_4 85%), hydrofluoric acid (HF 40%) and ammonium hydroxide (NH_4OH 28%). Citric

[2]MicroChemicals: https://www.microchemicals.com/

Table 4.5 – *Overview for the wet chemical etching of III-V semiconductors. Colors correspond reactions of the material in the respective solution: (green) etch, (red) selective stop and (yellow) composition dependent.*

	GaAs	AlGaAs	InGaAs	InP	InGaP[3]	AlInP[4]
H_2SO_4:H_2O_2:H_2O	etch	etch	etch	stop		
H_3PO_4:H_2O_2:H_2O	etch	etch	etch	stop	stop	
(citric acid):H_2O_2	c.d.	c.d.	c.d.	stop		
HCl:H_2O	stop	c.d.[5]	stop	etch	c.d.[6]	etch
HCl:H_3PO_4	stop		stop	etch	etch	etch
HF:H_2O	stop	c.d.[7]				
NH_4OH:H_2O_2:H_2O	etch	c.d.				

acid solution is prepared by dissolving monohydrous $C_6H_8O_7$:H_2O in water for 1 g per mL. The mixtures of all chemical solutions and water are indicated in *volume ratio* of the above mentioned commercial products, in agreement with most of the literature data.

Table 4.5 gives some solution systems for six selected III-V compounds and alloys. As- and P-based III-V semiconductors act quite differently. For example, HCl solution without adding oxidizer can etch P-based semiconductors but not As-based ones. The presence of Al generally increases the reaction rates. We use mainly two solutions which are rather stable and reproducible. One is **H_3PO_4:H_2O_2:H_2O (3:1:40)** which etches GaAs at the speed of **100 nm/min**. The H_3PO_4:H_2O_2:H_2O system could have strong anisotropic behavior on GaAs depending on the mixture ratio [119]. The other one is **(citric acid):H_2O (5:1)** which etches GaAs at the speed of **300 nm/min**. This solution is useful to etch GaAs against AlGaAs. The selectivity is higher than 100 for GaAs over $Al_{0.3}Ga_{0.7}As$ and increases at higher Al concentrations. The etching rates also depend on the mixture ratio between (citric acid) and H_2O_2 [120].

4.5.2 Detailed description of the fabrication

In this part, the detailed fabrication processes are described for the transferred solar cells with a nanostructured TiO_2/Ag mirror. Non-transferred solar cells (as-grown on GaAs substrate) and transferred solar cells with a flat Ag mirror are fabricated in a similar way with simplified steps. Figure 4.17 shows the schematics of solar cell fabrication sequences. We keep the III-V layers flat in the solar fabrication to avoid electronic degradation. Ag is our first choice for light trapping because it has a high optical reflectivity compared to conventional Ni/Ge/Au contacts, but Ag has a rectifying behavior with GaAs [121]. We thus combined the TiO_2/Ag back mirror with localized ohmic contact to efficiently collect photo-generated charge carriers [82].

Localized back contacts.

Localized back contacts consist of 5×5 μm^2 squares regularly spaced with a period of 50 μm in both in-plane x- and y-direction (coverage: 1% of the total surface). They were defined by photolithography and lift-off of Ti/Au (20/200 nm) deposited by electron-beam assisted evaporation after deoxidation of the p+GaAs contact layer in a dilute HCl solution (HCl:H_2O 3:7). Uncovered area of p+GaAs is etched using a mixture of citric acid (monohydrate) at 1 g/L and

[3] If no specification, InGaP is lattice-matched with GaAs ($Ga_{0.51}In_{0.49}P$).
[4] If no specification, AlInP is lattice-matched with GaAs ($Al_{0.52}In_{0.48}P$).
[5] Concentrated HCl (i.e. 37%) etches AlGaAs for Al>60%. Boiling HCl may etch AlGaAs as well for Al>42%. The solution tends to become yellow and saturates quickly.
[6] Concentrated HCl (i.e. 37%) etches InGaP, while dilute HCl may not at all react with InGaP.
[7] HF:H_2O etches AlGaAs for Al>70%.

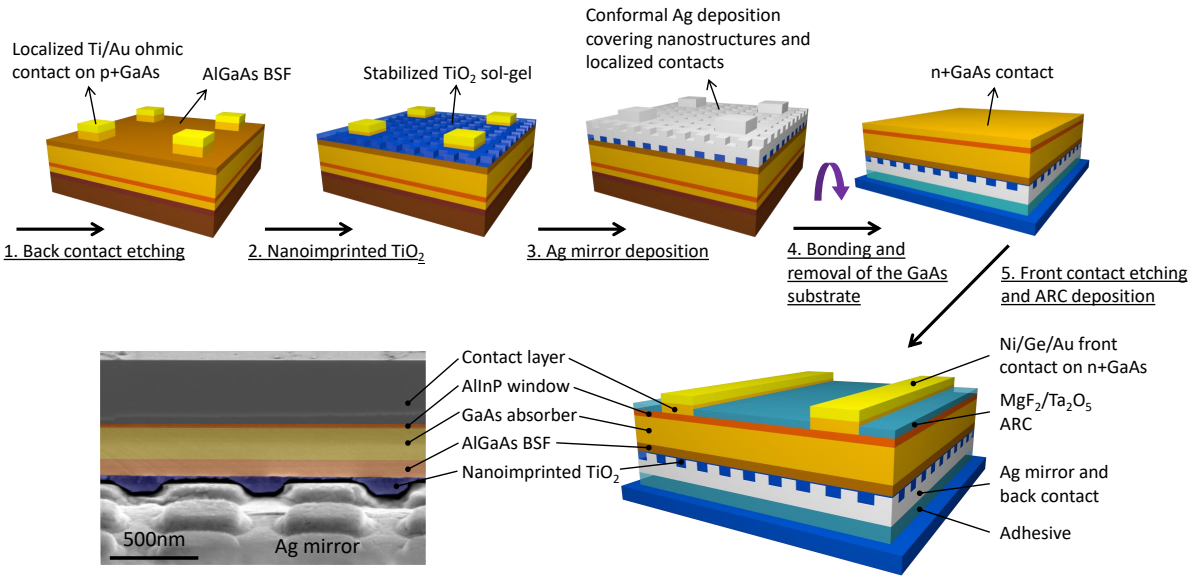

Figure 4.17 – *Sketches of the main fabrication steps of ultrathin GaAs solar cells with a nanostructured back mirror. A SEM cross-section image after removing the GaAs substrate is given, showing the TiO_2/Ag nanostructured mirror.*

hydrogen peroxide (30%) with a 5:1 volume ratio. Etching is naturally stopped at the AlGaAs surface (BSF).

Nanoimprinted dielectric layer.

For the fabrication of the nanostructured mirror, we used *Nanoimprint Lithography* (NIL) and in particular *Degassing Assisted Patterning* (DAP), a technique originally developed for the patterning of topographic and biochemical features for cell culture studies at the 100 μm scale and re-adapted for the embossing of commercial polymeric resist and sol-gel derived films. The technique makes use of a polydimethylsiloxane (PDMS) based stamp replicated from a Si master fabricated by electron beam lithography and reactive ion etching. Specifically, we used a bi-layer composed by a thin (5 μm) hard-PDMS layer and a thick (2-3 mm) conventional PDMS [122]. Compared to conventional PDMS, hard-PDMS has a reduced chain length which translates in a lower viscosity of its pre-polymer and a higher Young's modulus once thermally cured. In this way, the replication of high resolution Si masters is more accurate and local deformations occurring during the embossing are reduced. The thick PDMS layer serves as a flexible carrier so that the molding of the stamp on the substrate is assured even without applying a pressure.

Unlike conventional Soft-Nanoimprint performed with PDMS or other polymers, DAP does not require the use of an embossing machine and is still suitable for the patterning over large surface areas at low cost. The method is based on the fact that due to its high porosity, PDMS has a high gas solubility that obeys Henry's law, so that the equilibrium concentration of gas dissolved in PDMS is proportional to the partial pressure of the gas around the PDMS. Once degassed and brought back to atmospheric pressure, a PDMS piece behaves like a sponge by absorbing air to reach a new equilibrium. For a 3 mm-thick PDMS slab, the time constant of this phenomenon is about 5 min, which is enough to use the degassed PDMS as a pumping element, in this case to evacuate the air trapped between the stamp and the resist or the solvents still present in the sol-gel derived film.

We use DAP process applied to conventional sol-gel derived film. The hard-PDMS/PDMS stamp is first degassed in a dessicator for 5-10 min. The hard-PDMS/PDMS stamp is then molded (in air) onto a spin-coated substrate with a sol-gel hybrid film, eventual macroscopic air

bubbles surrounding defects or induced by imperfect molding are removed within few seconds through the diffusion of air in the degassed stamp. When using sol-gel hybrid film, the degassed stamp also quickly removes the solvents. Before the demolding of the stamp, the sol-gel is stabilized at a mild temperature (100°C) for few minutes on a hot plate. One of the main problems of using sol-gel based resist is the low fidelity of the replicated features due to partial filling of the nanocavities and to the deformation of the patterns induced by the volume shrinkage of the sol-gel material after stabilization and condensation. Stabilization of the sol-gel film before demolding, implies the removal of volatile solvents by soft annealing (100°C-190°C) and it results in volume shrinkage of the original nanostructures. A further shrinkage occurs after complete condensation of the inorganic network at higher temperatures (450°C-500°C).

In our case, dense TiO_2 thin films were prepared by spin coating solutions composed of $TiCl_4$:H_2O:EtOH with respective molar ratio of 1:10:50. F127 Pluronic surfactant was added (0.001) in order to improve the wettability of the substrate. The sol-gel formulation and the embossing conditions [123] were carefully chosen to control the rheology of the spin-coated sol-gel to permit the embossing without polymeric and organic molecules thus limiting the volumetric material shrinkage caused by solvent removal to less than 47%.

Figure 4.18(a) gives a picture of the sample after the NIL step, showing diffraction effects on visible light. Figure 4.18(b) gives a SEM image of the periodic nanostructures and a cross-section image of a cleaved sample showing the nanoimprinted TiO_2 shape. An additional treatment of heating the sample on a hotplate (∼120°C) under saturated H_2O vapor environment seems to improve the adhesion of TiO_2 on semiconductors (here AlGaAs) and gain stability for subsequent sample manipulation.

Nanostructured TiO_2/Ag mirror.

Subsequently, the top surface of the sample (coated with TiO_2 nanostructures) was protected with a photoresist mask, opening only the area of the localized ohmic contacts (see Figure 4.18(c)). The nanoimprinted TiO_2 above the contacts was etched by dipping shortly (∼10 s) the sample in dilute HF (HF:H_2O 1:20), and then the photoresist mask was removed in acetone. Ag (200 nm) was then deposited by electron-beam assisted evaporation using a rotating stage with a 10° tilt to the surface normal to ensure conformal deposition of Ag on both ohmic contacts and TiO_2 nanostructures. A TiO_2/Ag nanostructured back mirror was thus obtained and acted at the same time as the back electrode.

Bonding and substrate removal.

The Ag mirror-side of the sample was bonded to a glass host substrate using ormostamp, an UV-reticulated flexible hybrid inorganic/organic polymer. A glass substrate was chosen because it allows UV light to pass through. The surface of the glass substrate should be cleaned to ensure a good adhesion with the ormostamp. Dipping the glass substrate in a hot pirahna solution for several minutes can achieve this purpose. Applying ormoprime (adhesion promoter) can also improve the adhesion of ormostamp on glass. After preparing the glass substrate, ormostamp was spin-coated on the Ag mirror-side of the sample with a spin speed of about 3000 rpm (thickness $\approx$ 10 μm), then immediately applied on the freshly prepared glass substrate. The sample was bonded to the glass after reticulation of ormostamp under UV light for 20 minutes.

For the removal of GaAs substrates, the edge of the bonded sample needed to be protected, for example, with wax. The GaAs substrate was then etched in wet chemical solutions. Several solutions are possible depending on the requirement for etching rate, uniformity and selectivity between GaAs/AlGaAs. Pirahna-like solution H_2SO_4:H_2O_2:H_2O (2:1:1) was firstly used in continuous swirling to achieve uniform and fast chemical polish (10 to 20 μm per min depending on the solution temperature) but it is not selective with AlGaAs. After about 20 min when the

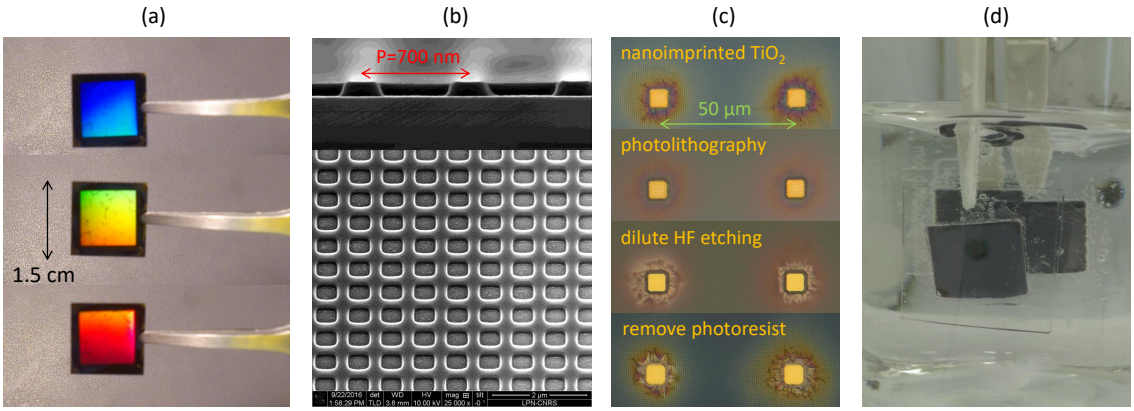

Figure 4.18 – *Some pictures at several intermediate steps of the fabricated samples. (a) Light diffraction effect due to incident angle change is visible after nanoimprint of the TiO_2 dielectric layer. (b) Cross-section and top view of the nanoimprinted TiO_2, forming 2-dimensional diffraction grating of period 700 nm. (c) Optical microscope images of TiO_2 nanostructures on the sample and the removal of TiO_2 above the localized ohmic contacts. (d) Picture of a wet etching bath for substrate removal when the etch stop layer (AlGaAs) was revealed (center region with shinny purple color).*

remaining GaAs substrate was thinner than about 100 μm, the etching solution was changed to the so-called base pirahna solution of NH_4OH:H_2O_2:H_2O (1:4:15), which etches GaAs at about 1 to 2 μm/min and is selective over AlGaAs, but the selectivity is not high enough so that 300 nm $Al_{0.85}Ga_{0.15}As$ may still be etched within approximately 10 min. A picture of the etched GaAs substrate is show in Figure 4.18(d). The center zone with a reflective shinny purple appearance corresponds to the AlGaAs etch stop. Subsequently, the solution was changed again to high-selectivity (citric acid):H_2O_2 (5:1). Finally, the remaining AlGaAs etch stop was removed in HF:H_2O (1:10). After this step, the III-V layer stack order was reversed (transferred).

Front contacts and anti-reflection coating

The front contacts with grid spacing of 600 or 800 μm were fabricated using the similar steps as localized back contacts. They consist of multilayers of Ni/Au/Ge/Au/Ni/Au (4/10/60/110/10/100 nm) on n+GaAs. We avoid post thermal annealing to prevent degradation of the Ag mirror as well as the ultrathin GaAs absorber. The final solar cells of 1×1, 2×2 and 3×3 mm^2 were delimited with photolithography mask and mesa etching in dilute HCl (removing AlInP) and in H_3PO_4:H_2O_2:H_2O (3:1:40) (removing GaAs). The front contact grids and labeling used for the solar cells are shown in Figure 4.19(a). After measuring the solar cell performances, MgF_2/Ta_2O_5 (78/48 nm) double-layer anti-reflection coating (DLARC) was deposited using electron-beam assisted evaporation at the Fraunhofer ISE. Figure 4.19(b-e) show the pictures of the sample with a flat Ag mirror (C2853a-18) and with a nanostructured TiO_2/Ag mirror (C2853a-19) before and after DLARC deposition.

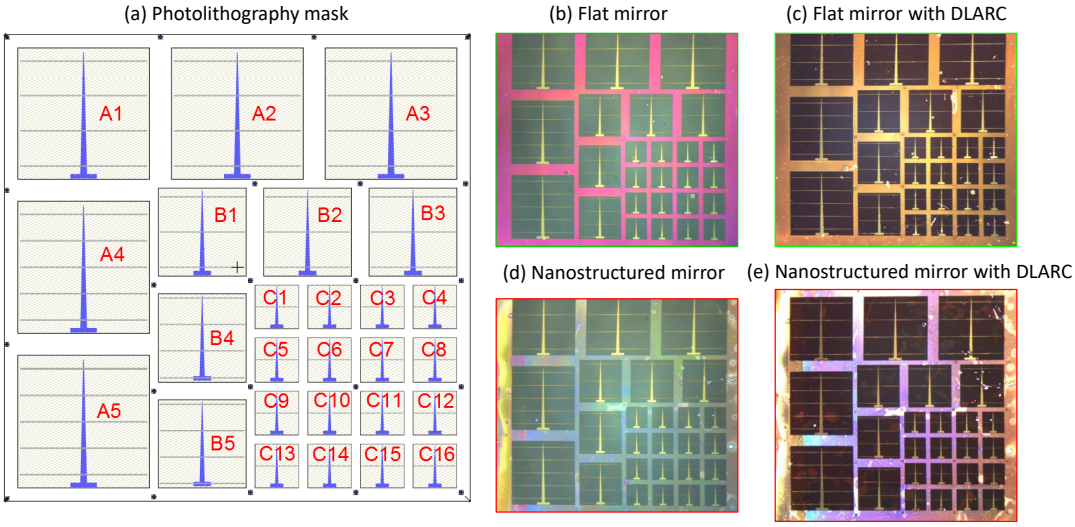

Figure 4.19 – *Overview of the final solar cell samples. (a) The mask pattern used for front contact grids and solar cell labeling. (b-c) C2853a-18 sample with a flat Ag back mirror before and after DLARC deposition. (d-e) C2853a-19 sample with a nanostructured TiO_2/Ag back mirror before and after DLARC deposition. The solar cells look darker from reduced reflection after DLARC deposition (MaF_2/Ta_2O_5 78/48 nm).*

4.6 Characterization and loss analysis

4.6.1 Spectral response

The spectral response of the solar cells is analyzed through *external quantum efficiency* (EQE), which is defined by the ratio of the number of carriers collected by the solar cell to the number of photons of a given wavelength or energy incident on the solar cell. If all photons of a certain wavelength are absorbed and the resulting minority carriers are collected, then the EQE at the given wavelength is unity. The quantum efficiency for photon energy below the bandgap is thus zero. The short-circuit current density (J_{sc}) at 1 sun is naturally given by the integral over all photon energies of EQE of the solar cell weighted by the solar spectrum $\phi_{sun}(\lambda)$ (number of incident photons per unit of time, per unit area and per unit wavelength). The standard AM1.5G solar spectrum (1000 W/m^2) is systematically used when referring to 1 sun.

$$J_{sc} = q \int_0^\infty EQE(\lambda)\phi_{sun}(\lambda)\mathrm{d}\lambda, \tag{4.27}$$

where q denotes the elementary charge. Below 300 nm, the solar spectrum contains very few photons and GaAs absorbs light up to approximately 900 nm, so the integral extends essentially between 300 and 900 nm. There are in fact two aspects included in a EQE measurement: one is the optical absorption and the other is the effective collection of generated minority carriers, which depends, for example, on the diffusion lengths and surface recombination. Internal quantum efficiency (IQE) is sometimes used to evaluate the electronic part of the EQE, which is defined by the ratio of the number of carriers collected by the solar cell to the number of photons of a given wavelength absorbed by the solar cell. If there is no transmission and negligible diffusion of light, the absorption A is equal to 1-Reflection $(1 - R)$. The IQE is then related to EQE through: IQE = EQE$/(1 - R)$. Apart from IQE, the optical response of the solar cell can be well understood by calculating the absorption in each layers of the solar cell. We have used the theoretical short-circuit current densities J_{th} as a figure of merit in the optical simulation section. It is calculated from the integral over all photon energies of the product of the absorption in GaAs $A(\lambda)$ with the AM1.5G spectrum. We distinguish J_{th} from J_{sc} because J_{th} is derived

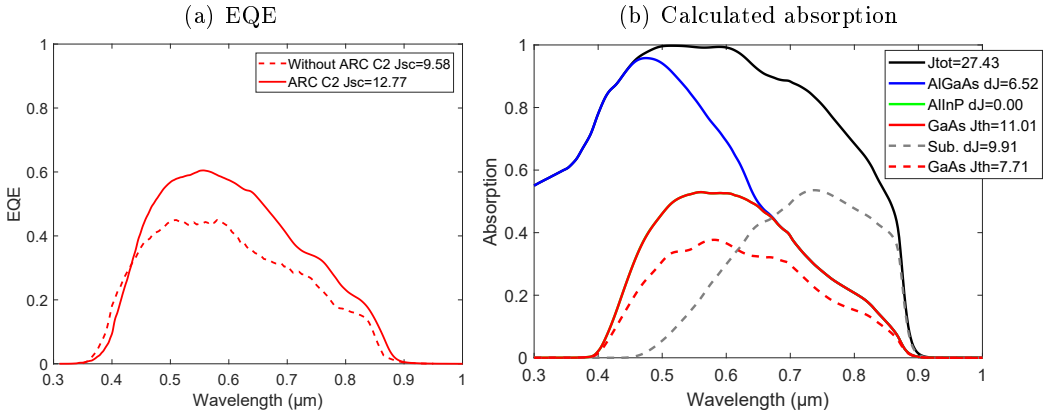

Figure 4.20 – *EQE and calculated absorption of the solar cell on a GaAs substrate. (a) EQE of the solar cell without (dashed line) and with (solid line) ARC deposition of 70 nm-thick SiN_x. (b) Absorption in each layer of the solar cell with ARC, except for the red dashed line, showing the absorption in GaAs without ARC for comparison. The blue line shows the absorption in the AlGaAs window above the one for GaAs absorber. The black line is the total absorption and the gray dashed line represents the absorption in the GaAs substrate. Equivalent currents at 1 sun (J_{sc} for EQE, J_{th} for absorption in the GaAs absorber and dJ for parasitic absorption in other layers) are given in the unit of mA/cm^2.*

from optical simulation, while J_{sc} is an experimental measurement.

At laboratory, two possible EQE measurement modes are available. One uses xenon light sources coupled with a Horiba Triax monochromator. The other uses a halogen lamp modulated with a Michelson interferometer (typical modulation frequency 10 kHz) and the measured signal is analyzed by Fourier transform to yield information in the frequency domain (FTPS, for Fourier-Transform Photocurrent Spectroscopy). In both cases, light is focused to a spot of several hundreds of μm on the solar cell at nearly normal incidence using a microscope objective. The solar cell is electrically contacted using four-point probes connected to a Keithley Source Meter, which measures the (photo)current delivered by the solar cell under illumination of light, and usually under zero bias voltage. A calibrated silicon photodiode with known spectral sensitivities is used to deduce unknown spectral response of solar cells after measuring both solar cell and the reference diode. FTPS measurement can provide better spectral resolution but its sensitivity in the short-wavelength range (0.3 to 0.5 μm) is poorer, so we combined the EQE from the two measurements. The EQE of the solar cell on a GaAs substrate (C2853a-01) before and after 70 nm-thick SiN_x anti-reflection coating (ARC) is presented in Figure 4.20(a) and the corresponding calculated absorption in the solar cell layers is given in 4.20(b). J_{sc} (resp. J_{th}) is systematically calculated for EQE measurement (resp. calculated absorption in the GaAs absorber) weighted by the AM1.5G 1 sun spectrum. Additional current dJ due to parasitic absorption in other layers (window, back-surface field etc) is also given.

The optimal thickness of ARC was previously calculated by minimizing the broadband reflection on the solar cell front surface, indeed, we can see that ARC leads to increased absorption in the absorber, thus increases J_{sc} from 9.6 to 12.8 mA/cm^2, in agreement with the calculated absorption. For non-transferred cells, the window layer is a 100 nm-thick AlGaAs, resulting in a significant part of parasitic absorption loss. In long wavelength range (about 0.6 to 0.9 μm), photons mainly pass through the absorber and are absorbed in the GaAs substrate, thus contribute to no photocurrent.

For transferred solar cells on a back mirror, we can assume that there is no transmission of light in the usual spectral range, thus reflectance (or reflectivity) measurements can be used to evaluate the total absorption in the solar cell. Specular reflectivity (R) is performed using a Sentech reflectometer operated with an objective (20X, NA=0.4) and a grating spectrometer

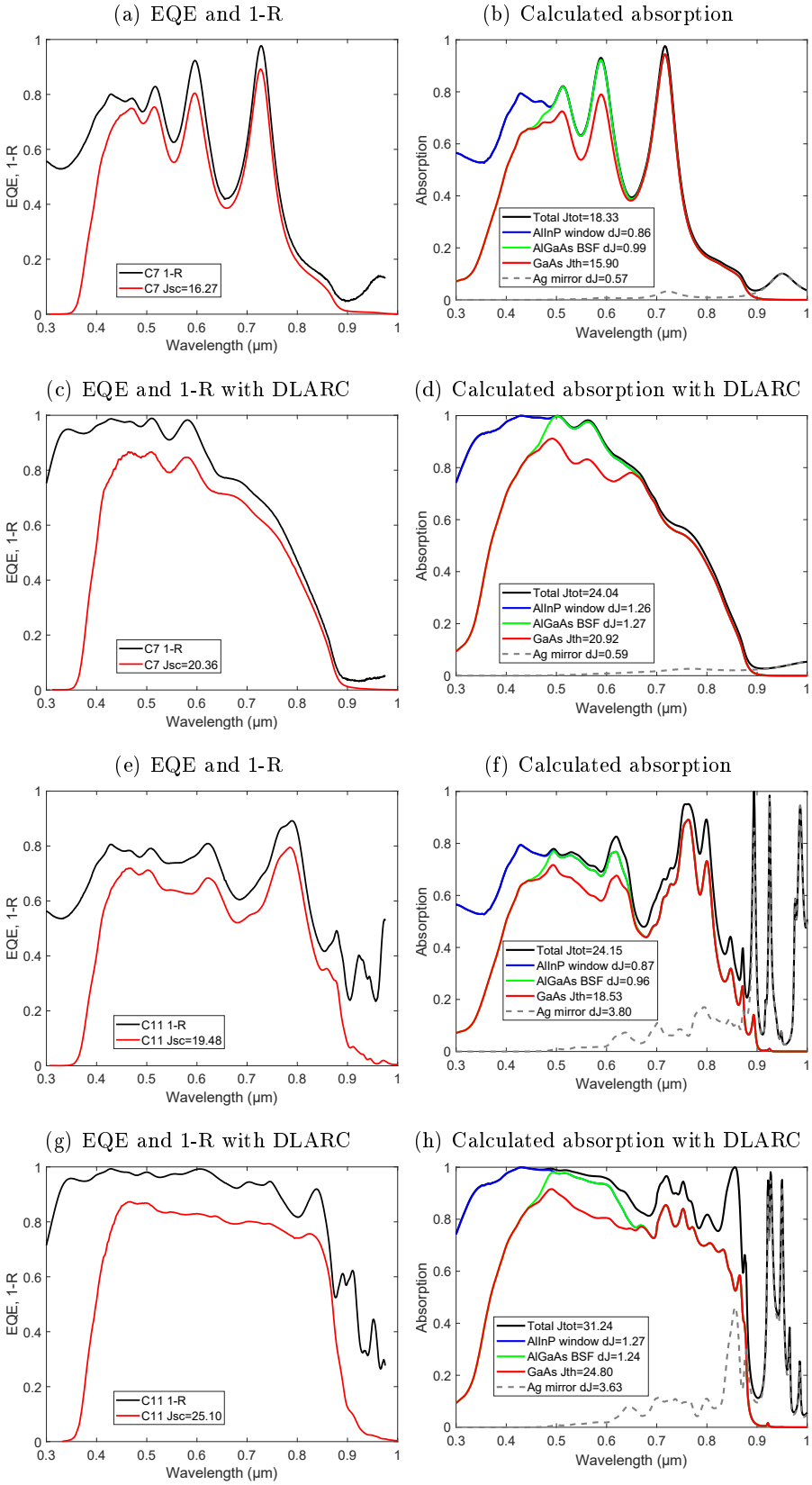

Figure 4.21 – *EQE, 1-Reflectivity (1-R) and calculated absorption of solar cells on a flat mirror (a-d) and nanostructured mirror (e-h). Left column is for EQE and 1-R measurement, and right column is for corresponding calculated absorption. (a,b,e,f) is for solar cells without ARC and (c,d,g,h) for solar cells after deposition of double-layer MgF_2/Ta_2O_5 (78/48 nm). Equivalent currents at 1 sun (J_{sc} for EQE, J_{th} for absorption in the GaAs absorber and dJ for parasitic absorption in other layers) are given in the unit of mA/cm^2.*

in the UV-visible range. The controlled reference is an oxidized silicon wafer of known oxide thickness. If the solar cell surface presents significant roughness, the diffused light may contribute to significant reflection loss that cannot be captured by the instrument. This is not the case for our GaAs solar cells where the surface is kept flat. With a periodic nanostructured back mirror, higher diffraction orders other than the zero order (specular reflection) is vanished for wavelengths longer than the grating period ($\lambda > p = 700$ nm). Therefore, the reflection loss may be slightly underestimated in the short-wavelength range. In this case, measurement with an integrated sphere is needed. For clarity, we summarize and label the three solar cells structures presented here as:

sample	name	light trapping structure	ARC(s)
(A)	C2853a-01	none (as-grown on GaAs substrate)	SiN_x
(B)	C2853a-18	flat Ag mirror	MgF_2/Ta_2O_5
(C)	C2853a-19	nanostructured Ag mirror	MgF_2/Ta_2O_5

Figure 4.21 gives the $1-R$ and EQE measurements for ultrathin solar cells with a flat Ag mirror (sample C2853a-18) and with a nanostructured TiO_2/Ag mirror (sample C2853a-19), before and after the deposition of double-layer anti-reflection coating (DLARC) of MgF_2/Ta_2O_5 (78/48 nm). Corresponding calculation of absorption in the solar cell layers are also shown. We can see a coherent match between measured spectral response with the calculated absorption spectra. After DLARC deposition, the maximal absorption at the resonant wavelength is decreased, instead, a broadband multi-resonant absorption is achieved. We predict, for the nanostructured back mirror, a high J_{sc} of 25.6 mA/cm^2 for a grating height of 120 nm. For the fabricated TiO_2 nanostructures, the height is about 100 nm, lowering the diffraction efficiencies of light. Figure 4.21(g,h) gives the calculation corresponding to the real shape of the TiO_2/Ag mirror with grating height of $h = 100$ nm and Ag diameter of $d = 420$ nm (60% of the grating period of $p = 700$ nm). The integrated absorption gives rise to slightly lower J_{sc} of 24.8 mA/cm^2. From EQE (without front contact shading), we measured the highest integrated J_{sc} of 25.1 mA/cm^2 (Figure 4.21(f)). Globally, the resonance features agree with the EQE and $1-R$ measurement, except for rounded overlapping peaks in real solar cells. This is because the diffraction efficiency depends strongly on the geometry of the TiO_2/Ag nanostructured mirror and a sharp square shape is assumed in the RCWA calculation.

In Figure 4.22, we compare the experimental EQE (Figure 4.22(a)) and the calculated absorption in GaAs (Figure 4.22(b)) for the three types of solar cell structures with DLARC. The increased absorption at each step of the fabricated structures is evidenced. Overall, the photocurrent enhancement originates from the multi-resonant response, leading to strong absorption improvement in the low-absorption region above and even below the bandgap of GaAs ($\sim$872 nm). In Figure 4.22(c), we show the optical path enhancement factor F calculated either from the EQE of the solar cell with a back mirror divided by that of the solar cell as-grown on a GaAs substrate (solid lines), or from the formula below:

$$EQE(\lambda) \simeq (1-R)\,(1-\exp(-F\alpha(\lambda)t))\,, \tag{4.28}$$

where R is the reflectivity of the solar cells and d the absorber thickness (here $d = 205$ nm). The factor F as a function of the wavelength is shown as dashed lines in Figure 4.22(c). Due to uncertainties of the real absorption coefficients of the GaAs solar cells below the bandgap, this calculation is only approximate. Still, we can notice an optical path enhancement of F close to 2 for the solar cells with a flat mirror, while F is well above 2 (maxima 4.8 and 6.4) close to the bandgap of GaAs.

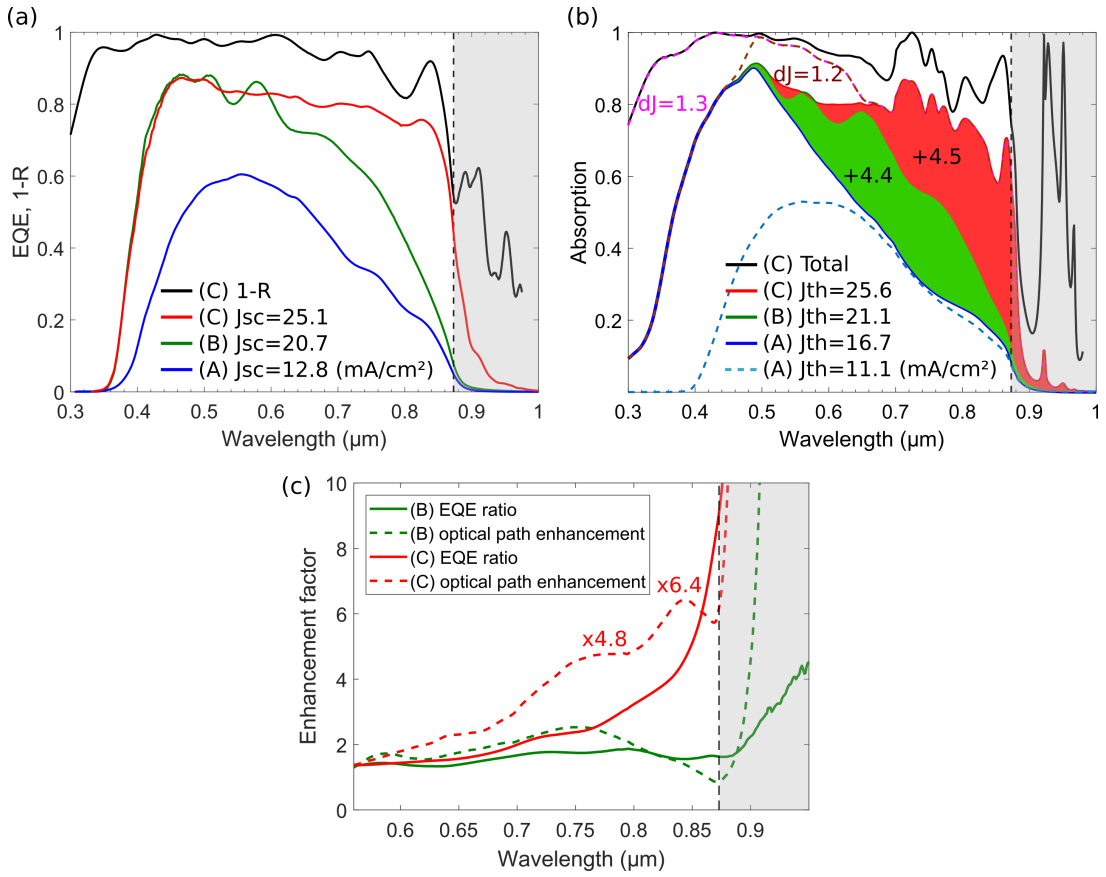

Figure 4.22 – *Comparison of the optical characteristics of ultrathin solar cells. (a) EQE measurement for 3 different types of solar cell structures: (A) on GaAs substrate, (B) flat Ag back mirror and (C) nanostructured Ag back mirror. 1-R of the solar cell with nanostructured mirror is also plotted (black curve). (b) Calculation of optical absorption in 205 nm-thick GaAs with various structures. The detailed absorption in III-V layers is also shown for the case with the nanostructured back mirror. (c) Optical enhancement factor in the long-wavelength range.*

4.6.2 Current-voltage characteristics

The current-voltage (IV) characteristics of the devices were measured in C2N laboratory using Oriel LCS-100 solar simulator and a Keithley 2400 Series Source Meter (maximum source power 22 W) with four-point contact. The solar simulator is equipped with a AM1.5G filter and the power is calibrated to 1000 W/m^2 using a known Si reference cell at 25°C. For the source meter, the resolution of measured voltage is 1 μV and measured current is 10 pA. The best cell is also measured at the Fraunhofer ISE calibration laboratory under standard test conditions (AM1.5G 1000 W/m^2, 25°C), as shown in Figure 4.23. We achieve a record efficiency of 19.9% using only 205 nm-thick GaAs absorber, with JV parameters: J_{sc} = 24.64 mA/cm^2, V_{oc} = 1.022 V and FF = 0.792.The solar cell area is 4.02 mm^2, which includes front contact grids (∼5.5% shading of the total surface) in the calculation of the current density and conversion efficiency. $1-R$ (specular reflectance) curve is also shown in Figure 4.23(b). The resonant absorption features match between $1-R$ and EQE measurements, and the integral over all photon energies of the EQE with AM1.5G solar spectrum gives rise to an equivalent short-circuit current density J_{sc} =24.39 mA/cm^2, close to the direct measurement under solar illumination.

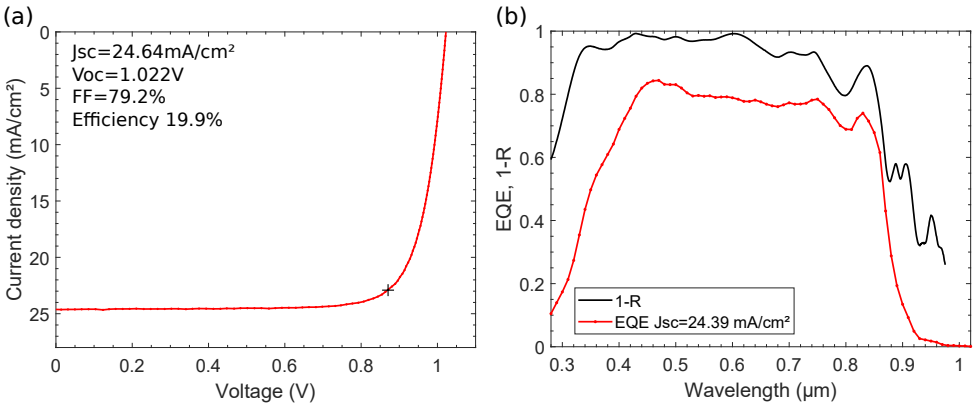

Figure 4.23 – *Photovoltaic performance of the ultrathin GaAs solar cell measured at the Fraunhofer ISE calibration laboratory. (a) IV characteristics of the 19.9%-efficient solar cell (cell area 4.02 mm^2) under standard conditions (AM1.5G 1000 W/m^2, 25° C). (b) EQE of the 19.9%-efficient solar cell (red curve). The specular reflectance (1-R: black curve) is superimposed, showing multi-resonant features in agreement with the EQE enhancement.*

In Figure 4.24, we give the current voltage characteristics (JV) measured in-house, with the surface area of 3 × 3 mm^2 for A cells, 2 × 2 mm^2 for B cells and 1 × 1 mm^2 for C cells in the calculation of current densities J_{sc} and efficiencies. For each samples, the JV curve corresponding to the highest conversion efficiency is shown. The increase in photocurrent by light trapping structures is evidenced, and the J_{sc} measured under solar simulator is consistent with the J_{sc} obtained by integrating EQE with the AM1.5G spectrum.

In Figure 4.25, we collect the photovoltaic parameters (J_{sc}, V_{oc}, fill factor and 1 sun conversion efficiencies) for the three samples before and after ARC deposition. For simplicity, we call (A) the sample on GaAs substrate, (B) flat mirror sample and (C) nanostructured mirror sample. Each sample contains several cells of different sizes (3 × 3 mm^2, 2 × 2 mm^2 and 1 × 1 mm^2). The steadily increased J_{sc} contributes to significant increases of the final conversion efficiencies. Note that the J_{sc} presented here is directly measured under solar simulator and normalized by the total area of the solar cells (including front contact grid of shading about 5% to 6%), thus may be slightly lower than J_{sc} deduced from EQE without shading. For sample (A), significant V_{oc} and FF decreases are observed after ARC deposition. It is suspected that the bombardment of high-energetic molecules during sputtering process of deposition degrades the electronic properties of the solar cells through edge and/or surface damages. For sample (B) and (C), DLARC deposition was conducted at the Fraunhofer ISE using electron-beam assisted

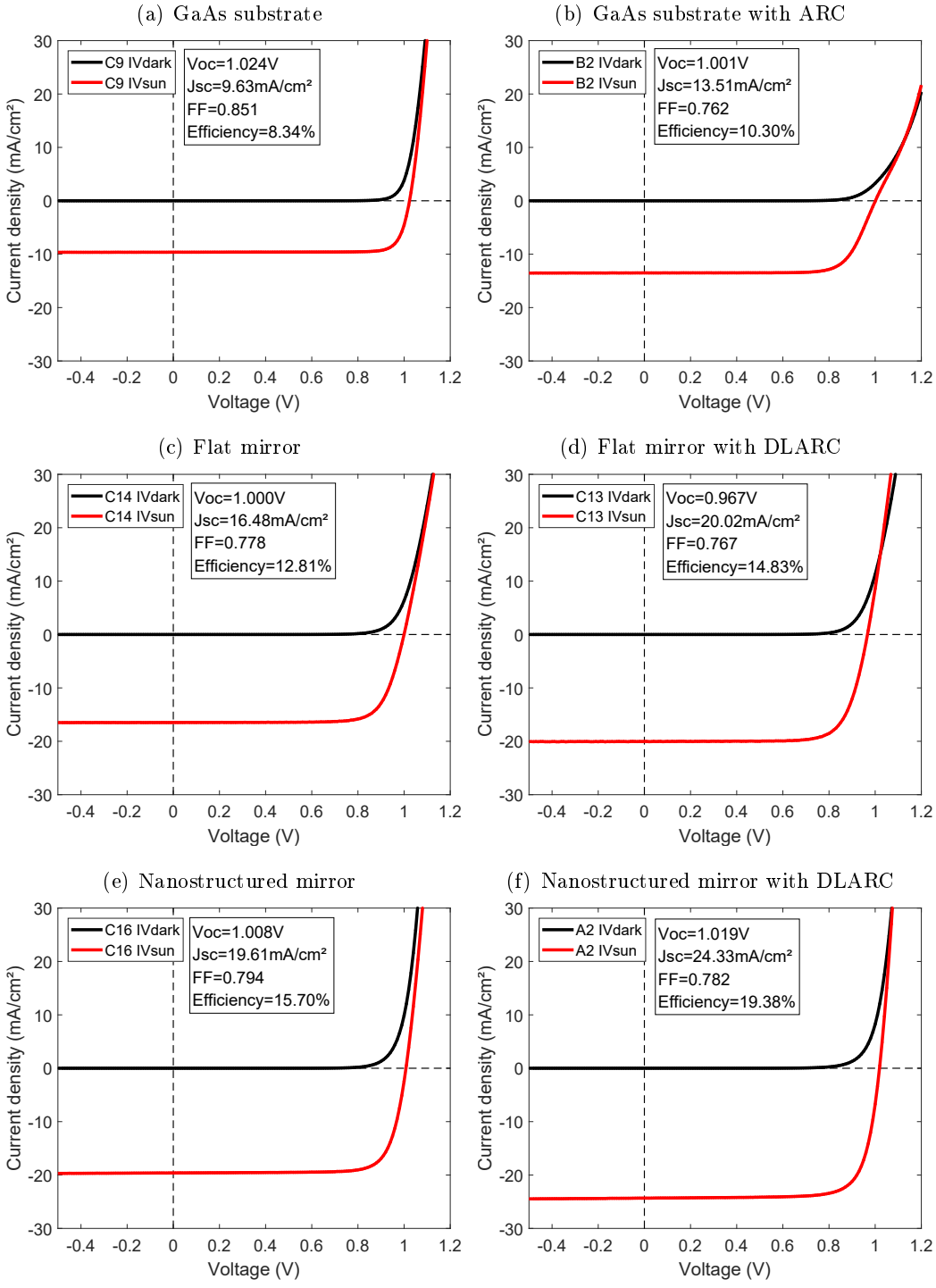

Figure 4.24 – *Current-voltage (JV) characteristics of the ultrathin GaAs solar cells with and without light trapping structures: (a,b) on GaAs substrate, (c,d) flat Ag back mirror, (e,f) nanostructured TiO_2/Ag back mirror. Left column is for solar cells without ARC and right column for the same sample after ARC deposition. The plots correspond to the most-efficient cell of each sample. Black curves are dark JV and red curves are JV measured under 1 sun illumination. Efficiencies and photovoltaic parameters are given in the insets.*

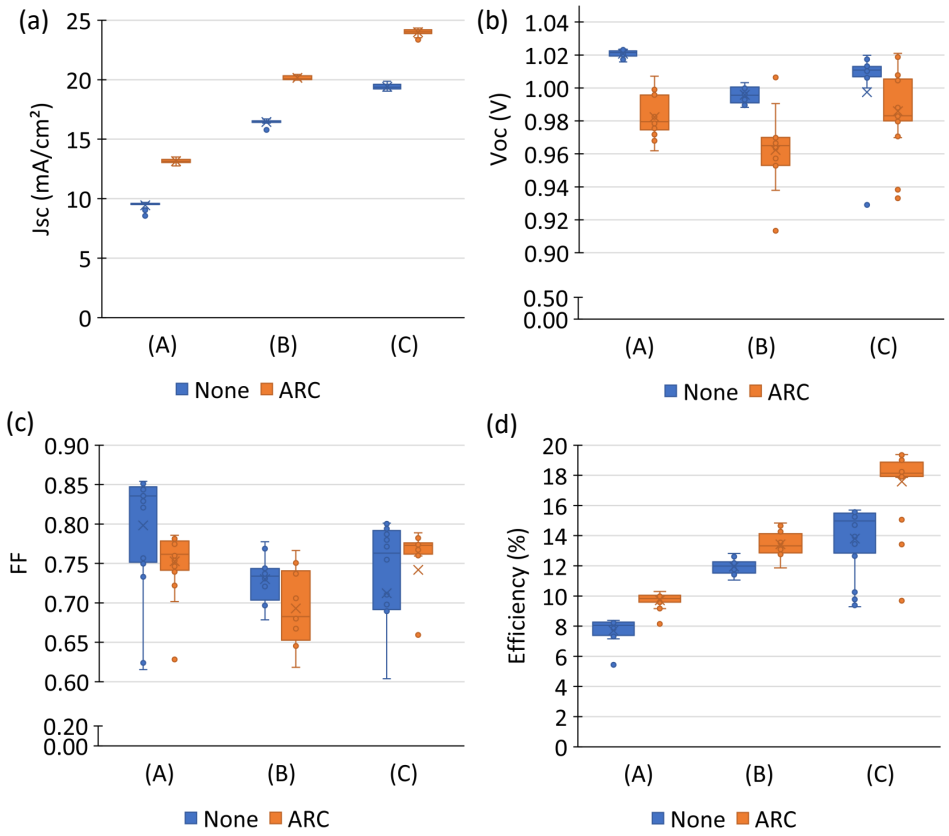

Figure 4.25 – *Statistics of the solar cell performances: (a) J_{sc}, (b) V_{oc}, (c) fill factor (FF) and (d) 1 sun efficiency. Three types of solar cell structures were studied: (A) on GaAs substrate, (B) flat Ag back mirror and (C) nanostructured TiO_2/Ag back mirror, before (blue) and after (orange) anti-reflection coating (ARC) deposition. For each data set, the box-and-whisker plot shows the average value (x), the median (segment), the box representing the first (25%) and the third (75%) quartile. The error bar gives the maximum and the minimum value excluding outliers (data points outside 1.5 times the upper and lower quartile).*

deposition. No significant decreases in FF is observed. Statistically, V_{oc} decreases slightly but the maxima remain unchanged and are even higher after DLARC deposition. Between different samples, lower V_{oc} and FF for sample (B) is probably due to an oxygen plasma cleaning step on n+GaAs contact layer, leading to increased series resistance which lower significantly the FF (see further JV fit and suns-V_{oc} measurement for series resistances).

To gain more insights, dark JV curves are fitted by the 2-diode model using the Matlab program developed by Suckow and coworkers at Aachen University[8]. The general form of the 2-diode model is written as:

$$J = J_{01}\left[\exp\left(\frac{q(V - R_s J)}{k_B T}\right) - 1\right] + J_{02}\left[\exp\left(\frac{q(V - R_s J)}{n_2 k_B T}\right) - 1\right] + \frac{V - R_s J}{R_p} - J_{ph} \quad (4.29)$$

where k_B is the Boltzmann constant and T the temperature. J_{01} and J_{02} are the saturation current densities, R_s and R_p are the specific series and parallel resistance, respectively, and J_{ph} denotes the photocurrent ($J_{ph} = 0$ for dark JV). Standard Shockley-Read-Hall recombination theory predicts the diode ideality of $n_2 = 2$ for the dominant recombination assisted by defect located in the middle of the bandgap. In real solar cell devices, diode ideality between 1 to 2 is possible, and sometimes, $n_2 > 2$ is observed which cannot be explained by conventional theory. High saturation current densities and a diode ideality greater than two is investigated by Breitenstein and coworkers. They attribute this commonly observed non-ideal diode characteristics to the presence of extended defects crossing the p-n junction (e.g. edge or grain boundary) through which a high current is flowing [124, 125]. These defects act similarly to an ohmic shunt observed at the reversed bias voltage. The locations of these defects can be identified using Lock-in Thermography (LIT) technique, which is based on thermal infrared imaging of a device subjected to periodically pulsed heat introduction [126].

In order to compare the saturation current densities between different samples, we fix the ideality factor $n_2 = 2$ in the two-diode model of Equation 4.29. The fitted results for representative JV curves are shown in Figure 4.26. The fitted diode ideality factor if we allow n_2 to be varied is also indicated in the figure, corresponding to the slope of the JV curve in log scale. We observed that the fitted ideality factor is smaller than two for non-transferred (A) sample, but increases to higher than two for transferred samples of (B) and (C) and the current is dominated by the diode of ideality 2 at low bias voltage up to the maximum power point. These differences may be due to degradation introduced in the process steps. The fact that the solar cell structure is reversed (the window layer of 25 nm-thick AlInP is etched for the mesa) could also lead to edge damage crossing the p-n junction that further influence the electronic performances of the solar cells.

The statistics of the fitted parameters are collected in Figure 4.27. The trends are in agreement with the observed photovoltaic parameters in Figure 4.25. Lowered V_{oc} after ARC deposition for sample (A) is revealed from the increased saturation current density J_{01}. For sample (B) and (C), only the diode 2 contribute to significant current up to 1 V and J_{02} is the most relevant parameter correlated with V_{oc} and FF. Series resistances remain unchanged before and after ARC deposition, but differences exist between samples. High R_s for sample (A) is partly due to uncertainty of fit and may be due to high sheet resistance of top p-type layers because hole mobility is significantly lower than electron mobility. The fact that high FF up to 0.85 is still observed suggests that R_s has a small influence here in the regime of weak current density (here $\sim$10 mA/cm^2). Parallel resistance decreased for sample (B) and (C), probably due to DLARC deposition after mesa etching, creating additional shunt path through the edge. R_p remains globally above 10^7 $\Omega\,\mathrm{cm}^2$ and is not an important efficiency-limiting factor here.

[8] 2-diode fit: https://nanohub.org/resources/14300

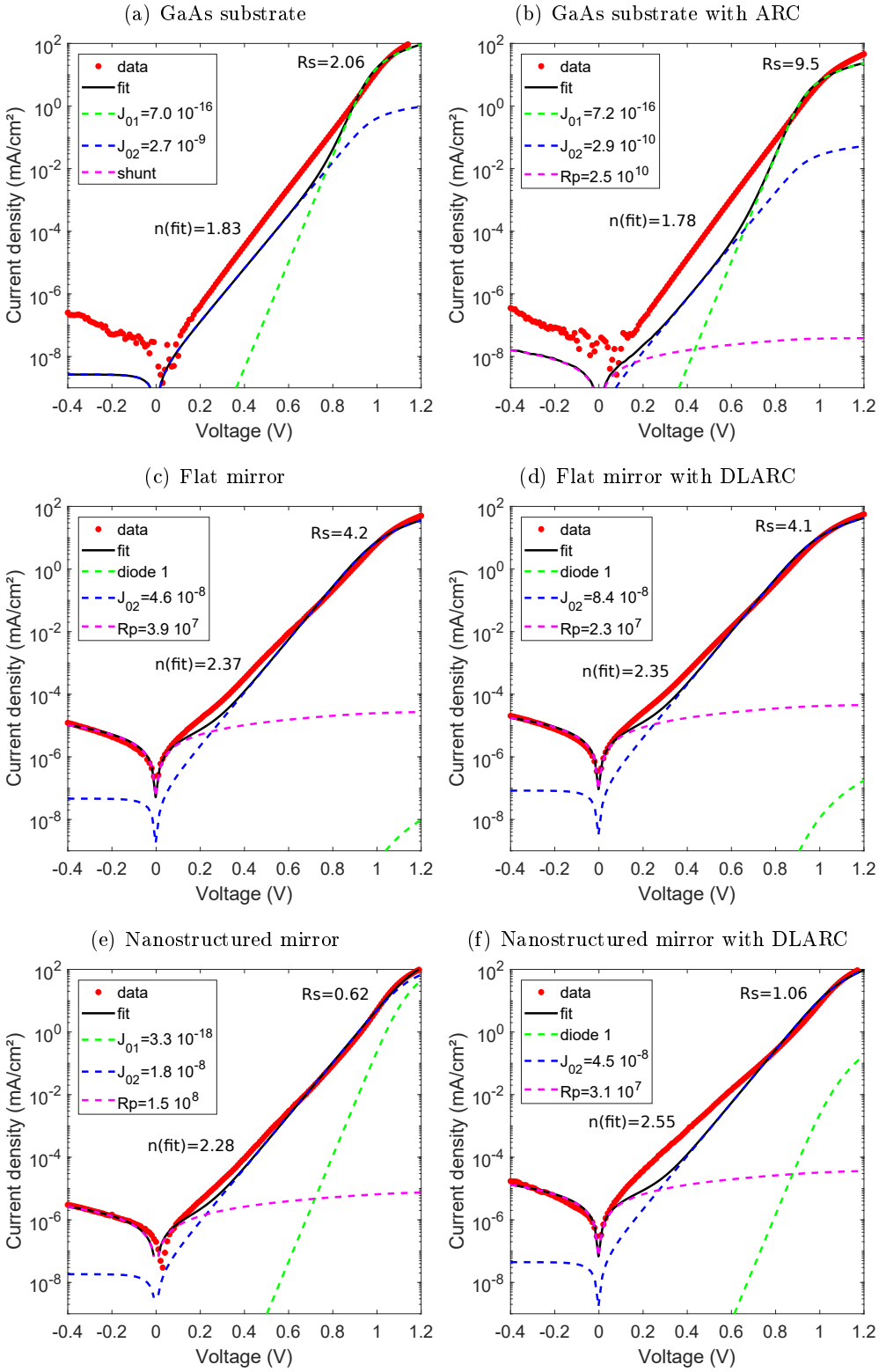

Figure 4.26 – *Dark JV characteristics and the fits using a two-diode model with the diode ideality of 1 and 2. Red dots show IV measurements, and black curves are the fits. Green, blue and pink dashed lines represents the current component from the two diodes and from the parallel resistance (shunt), respectively. The saturation current densities J_{01} and J_{02} are given in the unit of mA/cm^2, and the specific series and parallel resistances are in unit of $\Omega\,cm^2$. The fitted diode ideality n(fit) is also indicated.*

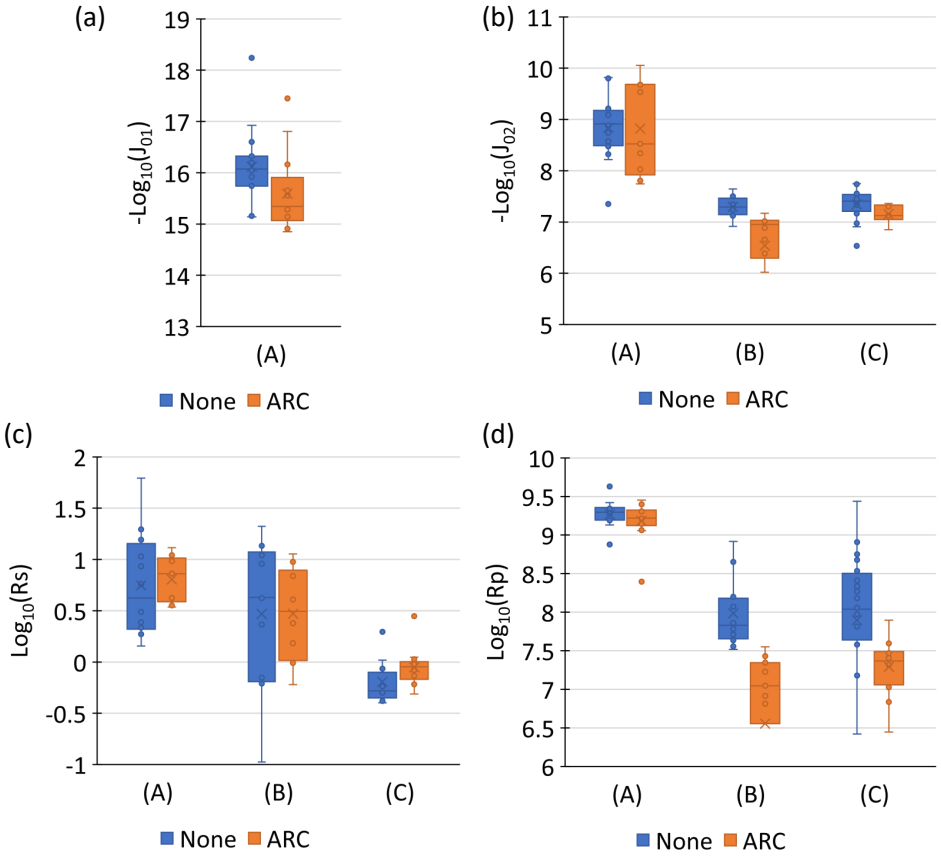

Figure 4.27 – *Box-and-whisker plot of the fitted parameters of dark JV curves using the two-diode model with diode idealities fixed to 1 and 2. (a) J_{01}, (b) J_{02}, (c) series resistance R_s and (d) parallel resistance R_p. The diode of ideality 1 is only relevant for (A) sample (on GaAs substrate). The unit for saturation current density is mA/cm^2 and for specific resistance is $\Omega\,\mathrm{cm}^2$.*

4.6.3 Suns-Voc measurement

Measuring the photovoltaic parameters with varying incident light intensities is another way to characterize the quality of solar cells. In fact, the photocurrent J_{ph} should be linear with the intensity of light, while the open-circuit voltage V_{oc} increases logarithmically. The voltage gain is the origin of increased efficiency of a solar cell under concentrated sun light. Considering a solar cell described by a diode of ideality n, the current-voltage characteristics is written:

$$J = J_0 \left[\exp\left(\frac{qV}{nk_BT}\right) - 1 \right] - J_{ph}. \tag{4.30}$$

We can then write down, at open-circuit condition when the external current J vanishes, the open-circuit voltage:

$$V_{oc} = \frac{nk_BT}{q} \log\left(\frac{J_{ph}}{J_0} + 1\right) \approx \frac{nk_BT}{q} \log\left(\frac{J_{ph}}{J_0}\right) \tag{4.31}$$

Measuring V_{oc} at various illumination intensities constitutes the so-called suns-V_{oc} measurement. Since the measurement of V_{oc} is realized at zero current flowing through the device, series resistance would not enter in the value of measured V_{oc}, suns-V_{oc} measurement can be performed in an intermediate step of solar cell fabrication with rough contacting of the solar cells to inspect the *health* of the absorber. A variant of suns-V_{oc} measurement is power-dependent photoluminescence measurement. If the absolute value of photoluminescence emission is calibrated, the separation of quasi-Fermi levels can be obtained through the generalized Planck's law [127]. Otherwise, relative intensity of photoluminescence provides insight into the radiative efficiency of the absorbing layer as a function of laser intensity. A detailed analysis method of power-dependent photoluminescence measurement is described by Walker et al. to extract non-radiative lifetime of GaAs double heterostructures [128]. In general, defect recombination ($n = 2$) dominates at low injection regime and a fast (∼ns) non-radiative lifetime governs the dynamics of photo-generated carriers. At higher injection levels, the trap saturation effect increases considerably the non-radiative lifetime and the carrier dynamics approach the one of pure radiative recombination regime ($n = 1$).

In Figure 4.28, we give a similar suns-V_{oc} measurement on sample (B) and sample (C) before DLARC deposition. A halogen lamp is used as light source and is focused to a spot larger than 2 mm covering 1×1 and 2×2 mm^2 cells (see inset in 4.28(a)). The intensity of light is controlled by a neutral density wheel through the inspection of photocurrent delivered by the solar cell at short-circuit. This relies on the linearity of photocurrent with the light intensity and on the J_{sc} measured precisely at 1 sun light. We note simply an equivalent number of suns for each measurement of a given light intensity. The V_{oc} and FF dependence is shown in Figure 4.28(a) and (b), respectively. The slope in V_{oc} curve allows to determine the diode ideality factor through Equation 4.31. We observe that the $n \approx 2.2$ dependence at low injection regime below 1 sun corresponds to the diode ideality from the fit of dark JV curve. Above 1 sun, the slope decreases to $n \approx 1.6$, which is still far from radiative regime. FF increases from low to intermediate intensity of light. For sample (B), FF encounters a drop before 1 sun, while the one for sample (C) continues to increase above 1 sun. We have shown previously that sample (B) presents more serious resistive effects (series resistances from the fit of dark JV are indicated on Figure 4.28(b)).

In Figure 4.28(c), we construct a *pseudo-JV* curve (blue) in comparison with the JV curve measured directly under 1 sun light (green curve). Each blue circle corresponds to a (V_{oc},J_{ph}) measurement at different incident light intensity (suns). These data points are plotted together with a vertical shift of the J_{sc} value measured at 1 sun. Since the suns-V_{oc} measurement is unaffected by the voltage drop due to series resistance, the pseudo-JV curve indicates a diode characteristic free from R_s. Figure 4.28(d) shows a zoom-in view of JV and pseudo-JV curve

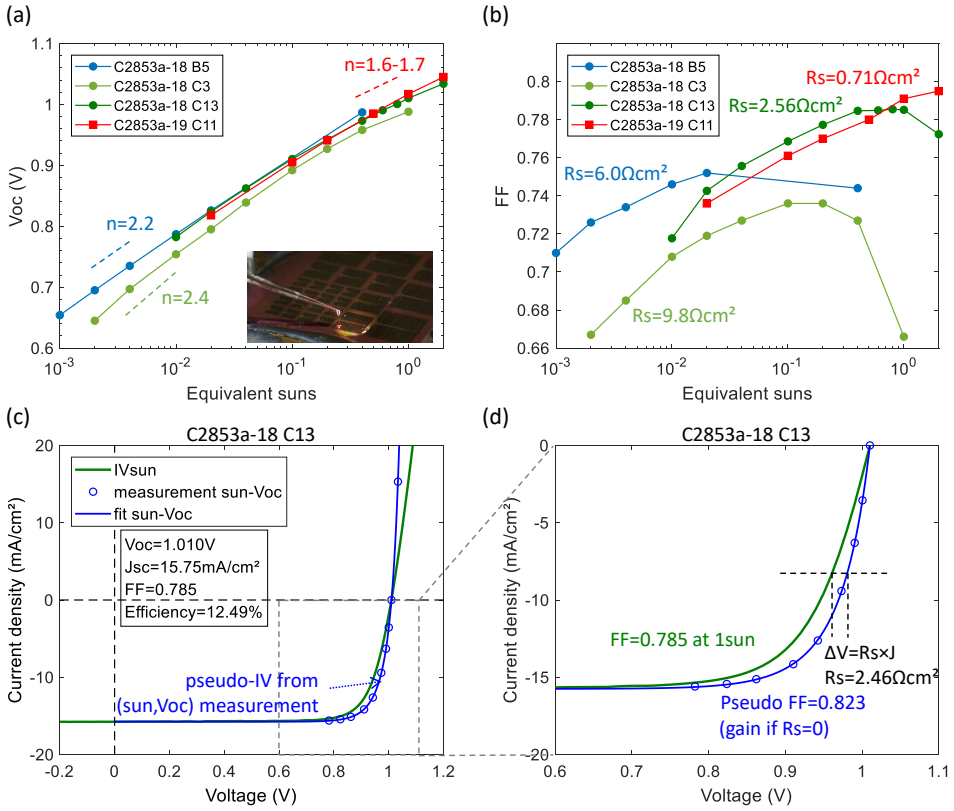

Figure 4.28 – *Characterization of solar cells (flat back mirror cells before DLARC deposition) with varying intensities of light expressed equivalently as number of suns. (a) V_{oc} evolution with suns. From the slope we extract the diode ideality factors. (b) Fill factor (FF) evolution with suns. The series resistance R_s (fit of dark JV curve with 2-diode model) is indicated. (c) Comparison of IVsun measurement and pseudo IV deduced from suns-V_{oc} measurement. (d) Zoom-in of the suns-V_{oc} measurement near the maximum power point. The series resistance (R_s) is obtained and a pseudo FF is deduced, showing the potential FF if R_s is zero.*

near the maximum power point. Comparing the two curve at a given current, the voltage drop is related to the series resistance of the device, thus R_s can be precisely fitted. For the solar cell under study (sample (B) C2853a-18 cell C13), we extract $R_s = 2.46\,\Omega\,\mathrm{cm}^2$, very close to $R_s = 2.56\Omega\mathrm{cm}^2$ obtained from the fit of dark JV curve using a 2-diode model (fitting n_2 for more precision). The pseudo-JV curve also allows to evaluate a pseudo-FF of 0.823, in comparison with real FF of 0.785, the 3.8% difference in FF is attributed to the resistive loss.

4.6.4 Loss analysis

In this section, we analyze the performance of the ultrathin solar cell with a nanostructured mirror (sample C2853a-19) and discuss the possibility to achieve even higher efficiency. Figure 4.29(d) summarizes the detailed loss analysis for J_{sc}, FF and V_{oc}: our experimental results are shown in bold and top values correspond to the calculated radiative limits (see Chapter 3.3). The J_{sc} limit of 31.9 mA/cm^2 is calculated for 205 nm-thick GaAs using the lambertian light trapping model [59, 60] (see Equation 3.81). We measured $J_{sc} = 24.6$ mA/cm^2 and the highest EQE without front contact shading results in $J_{sc} = 25.1$ mA/cm^2, close to the numerical calculation of 25.6 mA/cm^2 for the optimized TiO_2/Ag back mirror. Small discrepancy is due to the actual shape of fabricated structures. Parasitic optical losses contain absorption in the window layer ($dJ = 1.3$ mA/cm^2), in the BSF ($dJ = 1.2$ mA/cm^2), in the Ag mirror ($dJ = 2.7$ mA/cm^2) and due to reflection ($dJ = 1.1$ mA/cm^2). Parasitic absorption in the metallic reflector can be avoided through a combination of high-index-contrast gratings and all-dielectric or hybrid dielectric/metallic mirrors can be used as alternatives [129, 130]. The stack of semiconductor heterostructures needs further optimization to reduce the thickness of the AlInP and AlGaAs layers and improve collection of photogenerated carriers in these layers. The shape of the nanostructured back mirror could be also optimized to improve light trapping. For instance, replacing squares by an echelette blazed grating may enhance the diffraction efficiency and reduce the reflection loss by the 0th order diffraction. Overall, assuming half of the optical losses are recovered leads to a high short-circuit current J_{sc} over 28 mA/cm^2.

To analyze the electronic characteristics of the solar cells, 1 sun JV curves are fitted using a standard two-diode model with fixed diode idealities of 1 and 2 [80, 131]. An example of fit is given in Figure 4.29(a), showing the absolute values of $J(V)-J_{sc}$ in logarithmic scale and different components of the two-diode model. The fitted parameters are: $J_{01} = 2.8 \times 10^{-17}$ mA/cm^2, $J_{02} = 4.3\times10^{-8}$ mA/cm^2, $R_p = 2.4\times10^3\ \Omega\mathrm{cm}^2$ and $R_s = 0.8\ \Omega\mathrm{cm}^2$. This procedure is repeated for every solar cell of different surface areas of 1×1, 2×2 and 3×3 mm^2. The V_{oc} decreases with the cell size and is correlated with an increased dark current density J_{02}. The size-dependence of the recombination current is observed and analyzed in GaAs [132] and can be recovered through edge passivation using S-based chemicals [133]. In Figure 4.29(b), we plot the J_{02} values as a function of the perimeter-to-surface ratio (P/A). The linear trend allows to decompose J_{02} into a surface area component $J_{02,A}$ and a perimeter component $J_{02,P}$ [134]:

$$J_{02} = J_{02,A} + J_{02,P}\frac{P}{A} \tag{4.32}$$

For a large-area solar cells, edge recombination is suppressed. J_{02} reaches $J_{02,A} = 8.7 \times 10^{-9}$ mA/cm^2 and results in an increase of V_{oc} up to 1.045 V and FF up to 0.826. The corresponding JV characteristics are plotted in Figure 4.29(c). Further improvements of the FF are expected with improved parallel and series resistances: $FF = 0.84$ for $R_p = 10^6\ \Omega\,\mathrm{cm}^2$ and $FF = 0.857$ for $R_s = 0$ (values are collected in Figure 4.29(d)). The increase of the shunt conductance under illumination may be due to native oxides across the p-n junction at the edge or degradation from process steps after the mesa edges are revealed by chemical etching. The series resistance can be further optimized with GeAu alloys and a smaller spacing of contact grids. To achieve even higher FF, the dark current density J_{02} should be lowered down to about 10^{-9} mA/cm^2 [75].

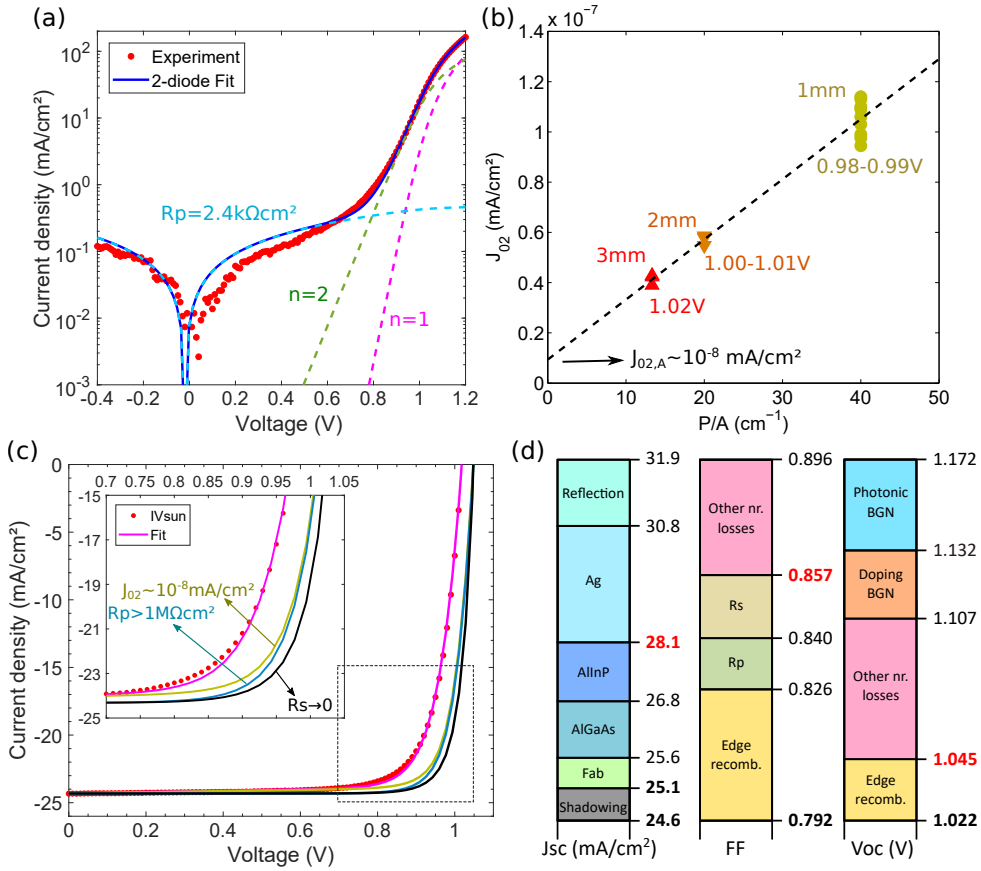

Figure 4.29 – *Current-voltage characteristics and loss analysis. (a) Typical J-V curve under 1 sun illumination shifted with J_{sc} in log scale (red dot: $J(V)-J_{sc}$) and fit with a two-diode model (blue curve). Different components of the model are shown in dashed lines. (b) Correlation of the J_{02} saturation current density with the perimeter-to-surface ratio P/A. (c) J-V characteristics of the record solar cell and the fit. Efficiency can be increased by successive improvements of fitted parameters (see the main text): saturation current density J_{02} (yellow green curve), shunt resistance (blue curve) and series resistance (black curve). Inset shows a zoom around the maximum power point. (d) Detailed loss analysis for J_{sc}, FF and V_{oc} (bold: measurement. red: realistic target). Top values represent the radiative limit for 205 nm-thick GaAs absorber.*

Regarding V_{oc}, we calculate the radiative limit using the detailed balance principle applied for 205 nm-thick GaAs solar cells in Chapter 3.3. The calculated limit efficiency (25°C, illumination AM1.5G spectrum) is $\eta = 24.6\%$ for the cell with a flat mirror ($J_{sc} = 23.4$ mA/cm^2, $V_{oc} = 1.172$ V, $FF = 0.896$) and $\eta = 32.3\%$ for the cell with lambertian light trapping ($J_{sc} = 31.9$ mA/cm^2, $V_{oc} = 1.132$ V, $FF = 0.893$). These values are collected in Figure 4.29(d). We note that the V_{oc} radiative limit is reduced by 40 meV for lambertian light trapping as compared to a flat mirror because of enhanced radiative emission (photonic bandgap narrowing, BGN). The choice of high doping is favorable for lateral conductivity and a high built-in potential in ultrathin absorber, but p-type GaAs is known for the bandgap narrowing (doping BGN) effect which lowers the bandgap of about 26 meV at $p = 10^{18}$ cm^{-3} [135]. There is still a discrepancy between theoretical limits and our analysis of experimental FF and V_{oc}, which may be attributed to other unknown non-radiative losses. To achieve high V_{oc}, reducing non-radiative loss and maintaining efficient photon recycling are of upmost important. Based on the above discussion, an efficiency of 25% ($J_{sc} = 28$ mA/cm^2, $V_{oc} = 1.05$ V, $FF = 0.85$) appears as a realistic target for 205 nm-thick GaAs solar cells with an optimized design.

4.7 Summary

We have designed and modeled ultrathin (205 nm) GaAs solar cells with a periodic 2-dimensional nanostructured back mirror. Rigorous coupled-wave analysis (RCWA) method is used to calculate the optical absorption in ultrathin GaAs absorber and to optimize the geometry of the nanostructured back mirror. We study the resonant mechanisms and show that Fabry-Perot and guided-mode resonances result in multiple overlapping absorption peaks, leading to a high J_{sc} up to **25.6 mA/cm^2** for absorption in ultrathin GaAs layers. Map of photogeneration rate is presented and is used for input in 1D electrical transport simulation (SCAPS). Electrical characteristics of the solar cell and band alignment are discussed.

We then fabricated and characterized ultrathin GaAs solar cells. Multi-resonant light trapping is achieved with a nanostructured TiO_2/Ag back mirror fabricated using soft nanoimprint lithography. An efficiency of **19.9%** under 1 sun illumination is obtained ($J_{sc} = 24.64$ mA/cm^2, $V_{oc} = 1.022\ V$, $FF = 0.792$). To our knowledge, this is the best performance for ultrathin GaAs solar cells to date. High J_{sc} is attributed to a broadband multi-resonant absorption illustrated by comparing EQE measurement with optical simulation, leading to near 50% photocurrent enhancement compared to the single-pass absorption and even surpassing the limit of double-pass absorption, as shown in the figure below (see Figure 4.1 for caption). Analysis of JV curves with 2-diode model allow us to extract important parameters (e.g. dark current densities and parasitic resistances). We identify the efficiency loss due to edge recombination and discuss the possible pathway toward 25% efficiency using only 200 nm-thick GaAs absorber.

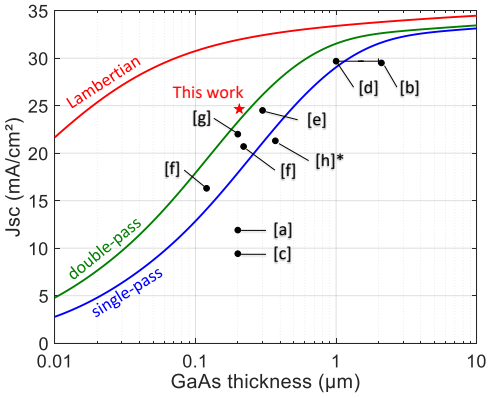

Chapter

5 Doping measurement by cathodoluminescence

Chapter content

Doping is a fundamental property of semiconductors and the control of doping is essential for photovoltaic cells and electrical injection devices (light emitting diode, nanowire lasers, etc.). However, characterization of doping at the nanoscale is a challenging task. Determination of doping levels in thin-films is traditionally performed using electrical methods such as Hall effect measurement and capacitance-voltage (C-V) profiling, but these methods are not easy to apply to nanowires. Therefore, we developed an alternative quantitative doping characterization method based on the analysis of luminescence spectra. In this chapter, the validity of this method is verified by comparing Hall effect measurements and CL measurements on GaAs thin-films.

In Section 5.1, we review briefly some techniques of doping characterization used in the community of semiconductor nanowires. Section 5.2 presents Hall effect measurements on a series of p-type and n-type GaAs thin-films. They were grown by MBE in our laboratory and used as doping calibration for the MBE growth. Section 5.3 presents CL measurements of these GaAs thin-film samples. In Section 5.4, we present a luminescence model and discuss in detail the features related to doping: non-parabolicity of the conduction band, band filling effect and bandgap narrowing at high doping levels.

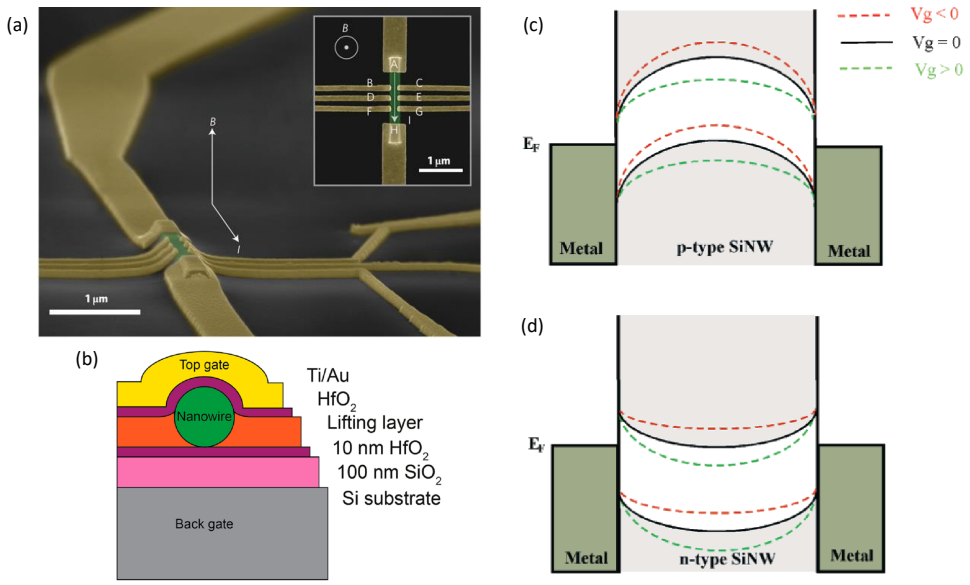

Figure 5.1 – *NW doping characterization by electrical methods. (a) Tilted and top-view (inset) SEM images of the nanowire Hall effect measurement set-up. Current is driven through contacts A and H. Terminals BC, DE and FG are used to locally probe the transport properties by means of the Hall effect (extracted from Ref. [136]). (b) Schematic of the cross-section through the NW device for field effect measurement (Ref. [137]). (c-d) Energy band diagrams for (c) p-type and (d) n-type SiNW devices. The diagrams show schematically the effect of gate voltage on the electrostatic potential for both types of NWs. (Ref. [138])*

5.1 Techniques overview

Doping measurements by electrical methods

A standard doping measurement on thin semiconductor layers is the Hall effect measurement. The principle of Hall effect is given in Section 5.2. In short, it requires four contacts and the layer thickness is known in advance. The charge carrier type (electrons or holes), carrier concentration and mobility are determined from the measurement of the Hall voltage, which results from the externally applied magnetic field to an electrical current. In a NW configuration, the upmost challenging task is to contact a horizontally lying NW on both longitudinal direction and the sidewall facets. An experimental realization was, however, achieved as shown in Figure 5.1(a). The Hall effect measurement on single NWs was reported for core-shell InP NWs, and spatial variations of carrier concentration were analyzed by placing multiple contacts along the wire and by comparing Hall effect measurement with CL spectra [136].

Conductivity and field effect measurements are alternative ways to determine the doping concentration. The conductivity ρ of a semiconductor can be written as the product of the elementary charge $q \approx 1.602 \times 10^{-19}$ C, the carrier mobility μ and the doping concentration n:

$$\sigma = q\mu n \tag{5.1}$$

In general, the conductivity increases with increasing doping levels, but the only measurement of conductivity is not sufficient for doping characterization because the carrier mobility is unknown. Conductivity measurement alone cannot tell the polarity of the majority carrier, neither. Field effect measurement can be added to provide further information.

Silicon nanowire-based field effect transistor (FET) has been fabricated in the early 2000s [139], and in this configuration, transport properties such as carrier mobility and concentration can be characterized [138]. The contact scheme is simpler as compared to Hall experiments: source

and drain are contacted at the two ends of the NW, and the gate is typically taken through a dielectric layer and a conductive substrate. Top-gate configuration is sometimes used (see Figure 5.1(b) for illustration). The conductivity of NWs is obtained by sweeping the current-voltage through the source and drain, and is repeated with applied gate voltage V_g.

Figure 5.1(c-d) show the energy band diagrams for (c) p-type Si NW and (d) n-type Si NW, contacted at the two ends by metal electrodes. As for conventional semiconductor-metal interface, the semiconductor bands bend down (resp. bend up) for p-type (resp. n-type) material to bring the Fermi level aligned with that of the metal. When $V_g > 0$, the bands are lowered, which depletes the holes in p-type semiconductor thus suppressing the conductivity, while it leads to an accumulation of electrons in n-type semiconductor and enhances the conductivity. Conversely, $V_g < 0$ results in the opposite effect on both semiconductor types. Quantitatively, the transconductance is related to the carrier mobility μ through:

$$\frac{dI}{dV_g} = \frac{C\mu}{L^2}V, \tag{5.2}$$

where I is the source-drain current, V and V_d are the source-drain and gate voltages respectively, C is the gate capacitance, and L is the length of active region (gate length).

The capacitance is a critical parameter to obtain the field mobility, but additional hypothesis is needed to have a simple expression. For a metallic back-gate and modeling the NW as a metallic cylinder of radius a, the general form of the capacitance for NW surrounded by a dielectric material of permittivity $\varepsilon = \varepsilon_r\varepsilon_0$ is [140]:

$$C = \frac{2\pi\varepsilon L}{\ln\left[\left(a+h+\sqrt{(a+h)^2-a^2}\right)/a\right]}, \tag{5.3}$$

where h is the distance between the gate and the bottom edge of the NW. In many cases, the dielectric does not surround the NW, but is rather a film of thin oxide, which leads to a reduction in capacitance. Exact value of the capacitance can be obtained by means of finite element methods including the cross section geometry of the NW and embedded or non-embedded NW-FET [141]. Another issue comes from the fact that the NW is a semiconductor. The metallic assumption is hold quite well for highly-doped NW, but in case of nonmetallic NW, the field penetrates the NW and the charge distribution is far from uniform. The geometry of the gate oxide, the semiconductivity and even the finite length of the NW affect both the total amount and the spatial distribution of the induced charges. Khanal and Wu performed 3D simulations resolving the Poisson's equation and provided correction factors to quantify carrier transport in NW-FET [142]. Moreover, the correct measurement is based on a good ohmic contact. The contact resistance should be significantly lower than that of the gate channel. However, ohmic contact may be problematic in certain materials (e.g. n-GaAs and p-InP). Highly-doped semiconductor can facilitate low-resistance ohmic contact since this creates a thin Schottky barrier through which carriers may tunnel, otherwise Schottky behavior will complicate the interpretation of the measurement.

Comparison between Hall effect and field effect measurements was also reported for InAs [143] and InP [137] NWs. Hall effect measurement is believed to be more precise since it does not rely heavily on the input parameters, and is more adapted to a complex geometry like core-shell NW and allows spatially resolved measurements by placing multiple Hall contacts. The cross-section of electrically active area should be known precisely to obtain the correct doping concentration, thus limiting the use for very thin NWs. On the other hand, only the volume of the device that can be depleted of carriers is available for field effect measurements. Charging effect of the surface states can be observed like the case of 2D electron gas at the surface of undoped InAs NWs [143].

Doping measurements by optical methods

Contactless methods are desirable to provide rapid feedback of NW growth without additional processing steps. Many techniques are proposed to investigate the NW doping by optical means such as Raman spectroscopy, terahertz spectroscopy, PL and CL. Raman scattering usually provides insight on the crystalline quality (broadening of Raman peaks) and lattice strain (shift of the characteristic phonon energy). Moreover, the coupling of longitudinal optical phonon (LO) with plasmon in polar semiconductors gives rise to characteristic Raman scattering modes that have been used to evaluate the doping concentration in n-type GaN NWs [144, 145]. Raman spectroscopy was also used to evidence local vibrational modes of Si atoms in GaAs lattice to investigate whether Si dopants occupy As sites (p-type doping) [146] or Ga sites (n-type doping) [147].

Terahertz spectroscopy was also used to probe the doping concentration of NW ensembles [148]. Terahertz radiation excites the collective oscillation of free charge carriers and the complex conductivity spectra can be extracted to estimate the free carrier density. Optical pump terahertz probe spectroscopy was further developed to reveal the dynamics of photogenerated carriers and extract important parameters such as carrier lifetime and surface recombination velocity in semiconductor NWs [149, 150]. However, the experimental setup is quite complicated, and the analysis is not straightforward and depends on several assumptions such as the the area density of NW ensemble and their orientation.

Luminescence-based techniques like PL and CL are another family of characterization tools. PL or CL spectra can be modeled by the generalized Planck's law [46]. The important parameters are the absorption near bandgap and the electron and hole quasi-Fermi levels. The spectrum usually broadens with increasing doping concentration due to enhanced carrier scattering and overlap of impurities wavefunctions. The full-width at half maximum (FWHM) of the emission spectra can be used to monitor the doping level at low concentration. At high doping concentration, the increased carrier-carrier interaction and disordered potential fluctuations of ionized dopants cause the bandgap shrinkage or narrowing. As a consequence, the emission spectrum continuously redshifts with increasing doping concentration. Empirical bandgap narrowing values for many III-V semiconductors are tabulated in Ref. [135].

For n-type III-V semiconductors (GaAs, InP etc.), this bandgap narrowing is in competition with the electron occupation in the conduction band. For example, the emission spectrum broadens and blueshifts (Burstein-Moss shift) for GaAs with electron concentration above the degenerative threshold of about 4×10^{17} cm^{-3}. Blueshift of luminescence spectrum has already been observed in GaAs [151] and InP [136, 152] NWs. We have demonstrated quantitative results by careful analysis of the emission spectra. CL mapping and full fit of the CL spectra were applied to precisely determine the electron concentration in single GaAs NWs [153]. CL also offers superior spatial resolution compared to PL, suitable for studying doping homogeneity in NWs. For example, local Mg dopant activity in core-shell GaN nanorods was studied by CL mapping to reveal doping mechanism in a complex nanostructure system [154].

Other techniques

An example of review paper for NW doping characterizations can be found in Ref. [155]. Standard time of flight-secondary ion mass spectrometry (ToF-SIMS) method cannot be directly applied to nanostructures because of their small size. ToF-SIMS has been used to evaluate Te and Be dopant concentration in GaAs/GaP NW ensembles embedded in a Cyclotene mask [156]. However, the encapsulation material may introduce artefacts, so a careful calibration using top-down etched NWs from thin films with a known doping profile is required [157]. Several other techniques are also explored to measure the doping in nanostructures, like atom probe tomography (APT). However, these atomic techniques determine the concentration of impurities, which

may not be equal to the carrier concentration if impurities are not electrically active or if compensation occurs. Off-axis electron holography employs electron interference to measure the electrical potential in a thin specimen, and it was recently used to demonstrate doping inhomogeneity in core-shell GaAs NW [158]. It is a powerful technique, but the specimen preparation is complicated and there is a high risk of degradation of the sample.

5.2 Hall effect measurements of thin-film GaAs

5.2.1 Principle of Hall effect

Figure 5.2 illustrates the principle of Hall effect in a semiconductor layer. When a current I is flowing in the semiconductor layer in presence of a magnetic field $\vec{B}$, the charge carriers of the semiconductor experience a force in the direction perpendicular to both the magnetic field and the current. At equilibrium, a voltage appears at the semiconductor edge and the resulting electric field $\vec{E}$ compensates the magnetic force through the Lorentz force written as:

$$\vec{F} = q(\vec{E} + \vec{v_d} \times \vec{B}), \tag{5.4}$$

where $\vec{v_d}$ is the drift velocity of the charge carriers. In a semiconductor slab of thickness d, width w and uniform doping, the electric current density is related to the carrier concentration n by: $\vec{j} = qn\vec{v_d}$, which is then written in projection of the current flowing direction as:

$$\frac{I}{wd} = qnv_d. \tag{5.5}$$

In steady state, the Hall voltage V_H is connected to the electric force $F_e = qV_H/w$ and the magnetic force is expressed as $F_m = qv_dB$. The resulting forces are compensated, so the Hall voltage can be written as a function of the carrier drift velocity and magnetic field. Using Equation 5.5, the Hall voltage is further expressed as a function of the electric current I and the carrier concentration n:

$$V_H = v_dBw = \frac{IB}{qnd}. \tag{5.6}$$

We should note that the sign of the Hall voltage is important for the polarity of the charge carriers. In n-type semiconductors, as well as metals, the electric current is carried by moving electrons. In p-type semiconductors, it is easier to think of the current as positive holes moving rather than negative electrons.

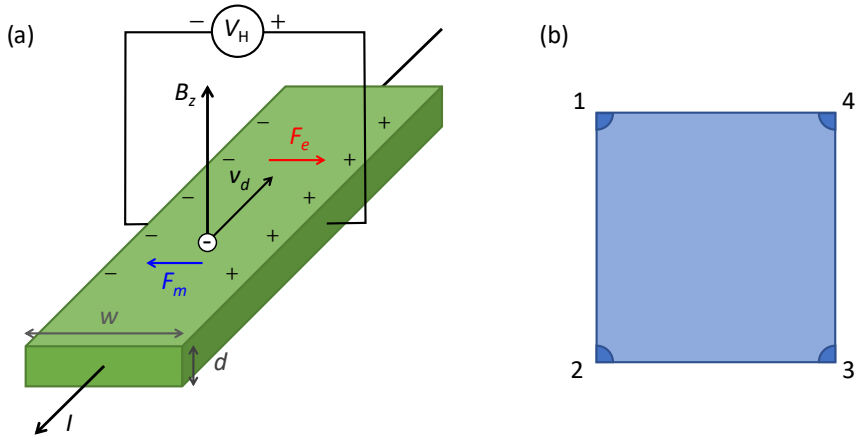

Figure 5.2 – *(a) Schematic illustration of the Hall effect in a semiconductor layer. (b) Contact electrodes used in the van der Pauw method for measuring thin-film doping concentration by Hall effect.*

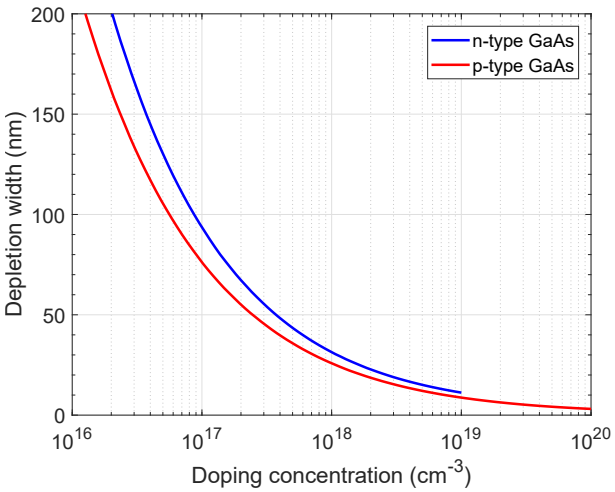

Figure 5.3 – *Calculation of the surface depletion width as a function of doping concentrations for bulk n-type (blue) and p-type (red) planar GaAs.*

In practice, the doping concentration of thin semiconductor layers is measured using the van der Pauw method [159]. This method allows measuring specific resistivity and Hall effect of flat samples of arbitrary shape, provided that the contacts are sufficiently small and located at the circumference of the sample. Figure 5.2(b) shows a general configuration of four contacts placed at the corners of a square piece of semiconductor, denoting 1, 2, 3 and 4 in the anti-clockwise direction. The semiconductor thin-film is usually grown on a semi-insulating substrate so that only the active layer of thickness d is characterized. Resistivity measurement is first performed. A current is caused to flow along one edge (for example I_{12}) and the voltage across the opposite edge (here V_{34}) is measured. A resistance can be found using Ohm's law: $R_{12,34} = V_{34}/I_{12}$. Van der Pauw showed that the sheet resistance R_s of samples can be determined from two of these resistances: one along a vertical edge (e.g. $R_{12,34}$), another along a horizontal edge (e.g. $R_{23,41}$), using the formula:

$$e^{-\pi R_{12,34}/R_s} + e^{-\pi R_{23,41}/R_s} = 1. \tag{5.7}$$

The sheet resistance can then be solved numerically, and it is related to the material resistivity by $R_s = \rho/d$, where d is the layer thickness.

For the Hall effect measurement, a magnetic field B is applied perpendicularly to the layer surface. For example, the electric current I is injected from contact 2 to 4 and the voltage across the contact 1 and 3 is measured and noted as V_{13}. This is repeated by reversing the magnetic field direction, and by alternating the 4 contacts (V_{24}, V_{31} and V_{42}), keeping the same value of the injected current and the magnitude of the magnetic field. The Hall voltage V_H is then obtained from the average of the above measured values. Using Equation 5.6, knowing the magnetic field B, current I and thickness d, the doping concentration n can be calculated. The carrier mobility is further calculated using the formula:

$$\rho = \frac{1}{q\mu_n n + q\mu_h p}, \tag{5.8}$$

where μ_n (resp. μ_h) is the electron (resp. hole) mobility, and n (resp. p) is the electron (resp. hole) concentration. Usually in a semiconductor, majority carriers dominate the conductivity and minority carriers have little influence on the transport properties, thus can be neglected.

5.2.2 Surface depletion

One issue raised in the Hall effect measurement is that only electrically active area contributes to effective free carrier transport. Therefore, the depletion zone should be excluded in the

calculation of free carrier concentration. In fact, the layer thickness d described previously should be replaced by $d - w$ where w represents the depletion zone thickness. Carrier depletion may occur at the non-passivated free surface due to unwanted surface states, or at the interface in contact with the semi-insulating substrate. For GaAs, the surface depletion is particularly problematic due to the formation of gallium oxide and arsenic segregation, creating trap levels near the mid-gap. The free surface of a semiconductor is characterized by a surface potential. For GaAs, the surface potential is found in the literature, with the value of $-0.75\ V$ for n-type GaAs and $-0.55\ V$ for p-type GaAs [160] measured with respect to the valence band maximum. The negative sign is chosen because the electrical potential is reversed compared to the electronic energy in conventional band diagram. The theoretical expression of the surface depletion width is given by [161]:

$$w_s = \sqrt{\frac{2\varepsilon_r\varepsilon_0\left(\phi_s - \phi_{ch} - k_BT/q\right)}{qN}}, \tag{5.9}$$

where $\varepsilon_r \approx 12.9$ is the dielectric constant for GaAs and $\varepsilon_0 \approx 8.854 \times 10^{-12}$ F/m the vacuum permittivity, N the free carrier concentration (electron for n-type and hole for p-type), k_B the Boltzmann's constant and T the temperature in Kelvin. ϕ_{ch} is the channel potential depending on the doping level, and is given by the Fermi level in the unperturbed quasi-neutral region. The term kT/q is due to the thermally activated majority carrier distribution tail [22]. Figure 5.3 gives the calculated surface depletion width in GaAs as a function of both n-type and p-type doping. For instance, the surface depletion width is $w_s \approx 32$ nm for n-type GaAs at the doping concentration of 1×10^{18} cm^{-3}.

5.2.3 Results

Tables 5.1 and 5.2 list the thin film GaAs samples grown by MBE using Be for p-type doping and Si for n-type doping. Carrier mobility and doping concentration were obtained by Hall effect measurements, taking into account the surface depletion width. These samples are used for doping calibration in our MBE machines, and also to validate the doping measurement by luminescence method (see Section 5.3 and 5.4).

Table 5.1 – *MBE-grown p-type GaAs:Be thin-film samples. Be effusion cell temperature and layer thickness are shown. Hole mobility and doping concentration are obtained from Hall effect measurements.*

sample	T(Be) °C	thickness nm	mobility cm^2/Vs	doping cm^{-3}
G3X005	675	500	117	6.7×10^{17}
G3X004	740	500	65	6×10^{18}
G3X003	788	500	31	6×10^{19}
76633	675	500	153	9.4×10^{17}
76631	700	380	122	2.9×10^{18}
76627	735	430	74	1.0×10^{19}

During the MBE growth, mainly two factors determine the doping concentrations in epilayers: the supply flux of the impurity source and the crystal growth rate. The supply of impurity atoms is mainly determined by the heating temperature T of the crucible. The incident flux of a chemical species ϕ [atoms/s/cm^2] can be related to its vapor pressure P through [162]:

$$\phi = \frac{P}{\sqrt{2\pi m k_B T}} \simeq k_1 P, \tag{5.10}$$

where m is the mass of the chemical species and k_1 is a constant. The vapor pressure is given

Table 5.2 – *MBE-grown n-type GaAs:Si thin-film samples. Si effusion cell temperature and layer thickness are shown. Electron mobility and doping concentration are obtained from Hall effect measurement.*

sample	T(Si) °C	thickness nm	mobility cm^2/Vs	doping cm^{-3}
G3X002	1031	500	1031	5.3×10^{17}
G3X001	1099	320	1039	1.7×10^{18}
E8U002	1160	852	1314	5.8×10^{18}
C2T12	1171.6	100	545	1.2×10^{19}
C2T13	1137.6	100	625	1.9×10^{19}
76625	1000	465	4066	4.0×10^{17}
76626	1075	473	1980	1.8×10^{18}
76623	1150	446	1165	7.6×10^{18}

by the Clapeyron relation:

$$P = k_2 \exp\left(-\frac{\Delta H_{\text{sub}}}{k_B T}\right), \tag{5.11}$$

where ΔH_{sub} the enthalpy of sublimation and k_2 is a constant.

As the total amount of impurity atoms is conserved, the concentration of impurities in the epilayer should be inversely proportional to the growth rate v [cm/s]. It is generally assumed that dopant atoms have an unity sticking coefficient, i.e. every incident atoms incorporated in the semiconductor. In this case, the concentration of impurity atoms in the epilayer is given by: ϕ/v.

If we can assume all impurity atoms are electrically active and neglect the dopant compensation, i.e. each impurity atom results in one carrier of the same type, the doping concentration N is equal to the concentration of impurity atoms in the semiconductor. As a result, the Clausius-Clapeyron-type dependence of the doping concentration N with the crucible temperature T is expected:

$$N = \frac{\phi}{v} \simeq \frac{k_3}{v} \exp\left(-\frac{\Delta H_{\text{sub}}}{k_B T}\right), \tag{5.12}$$

where $k_3 = k_1 k_2$ is a constant.

For all the GaAs samples characterized here, the growth rate is set to 0.2 nm/s, but small fluctuation may still exist between samples. As shown in Figure 5.4, the doping concentrations in log scale are plotted as a function of the reverse of the temperatures in Kelvin. Temperatures in °C are indicated at the top of the graph. Doping concentrations plotted in the graph are corrected with the actual growth rate such that every samples are comparable. Two series of samples for both Be-doped and Si-doped samples are shown, they correspond to epitaxial growth from two different MBE machines in the laboratory.

Electron and hole mobility, μ_n and μ_p, are two of the important parameters for characterizing the transport of charged carriers. The (majority) carrier mobility from Hall effect measurements is plotted as a function of the carrier concentration (Figure 5.5(a) for p-type and (b) for n-type GaAs). In general, the mobility reduces with increasing carrier concentration due to scattering of the moving charge carriers. These include alloy scattering, ionized impurity scattering, carrier-carrier scattering and various phonon scattering processes. The mobility is also reduced for compensated doping where a large amount of defects act as scattering centers. In contrast, very high eletron mobility can be obtained from spatially separated carriers with the ionized impurity. It is so-called modulation doping, achieved for example in a very thin undoped GaAs layer embedded within highly n-doped AlGaAs barriers. The black curves in Figure 5.5 are empirical model from Sotoodeh, Khalid, and Rezazadeh at 300 K. This model gives the mobility values as a function of the carrier concentration N and the temperature T by the formula [117]:

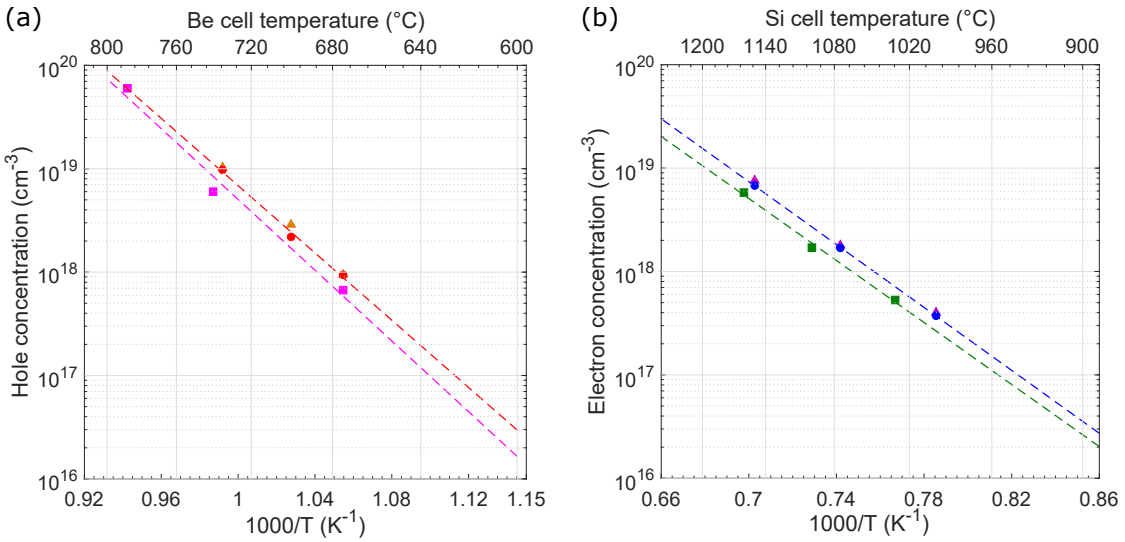

Figure 5.4 – *Clausius–Clapeyron-type plot of free carrier concentration as a function of the effusion cell temperature. (a) hole concentration measured by Hall effect as a function of the Be cell temperature. (b) electron concentration measured by Hall effect as a function of the Si cell temperature. Two sets of data points in each sub-figure present different series of GaAs samples grown from two different MBE machines. Doping concentrations are corrected to constant growth rate and fitted with an Arrhenius equation (dashed lines).*

$$\mu(N,T) = \mu_{\min} + \frac{\mu_{\max} \times (300\mathrm{K}/T)^{\theta_1} - \mu_{\min}}{1 + \left(\frac{N}{N_{\mathrm{ref}} \times (T/300\mathrm{K})^{\theta_2}}\right)^{\lambda}}. \tag{5.13}$$

The fitted parameters for III-V compounds and some alloys are provided in Ref. [117].

Physical descriptions of Equation 5.13 are considered as follows. At very low doping concentration, the mobility saturates at $\mu_{\max}(T)$, the lattice-limited mobility, which itself reduces with increasing temperature ($\theta_1 > 0$). At very high doping concentration, the mobility saturates at $\mu_{\min}$, which is temperature independent. $N_{\mathrm{ref}}(T)$ is the doping concentration at which the mobility reduces to almost half of the maximum value at low doping. At higher temperatures, lattice scattering mainly dominates, therefore, the contribution of ionized impurity scattering is expected to start at a higher doping concentration ($\theta_2 > 0$). The parameters were fitted with available GaAs mobility data, applicable in the range of temperature from 100 K to 400 K. Our mobility data are globally bellow the empirical model, especially for the epilayers grown from the first MBE machine, probably due to unknown defect scattering centers. For high-concentration Si-doped GaAs layers, Si dopant compensation may occur which reduces considerably the carrier mobility.

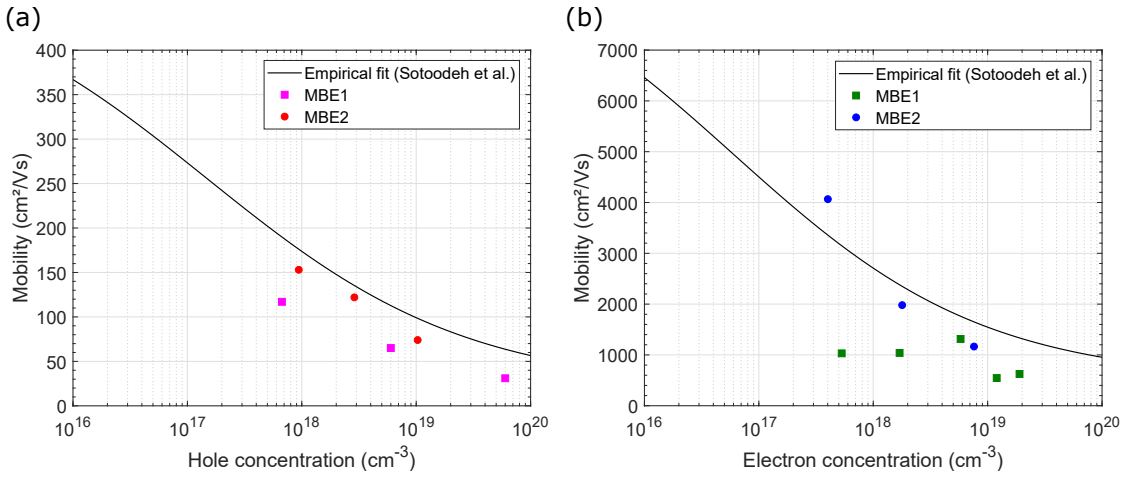

Figure 5.5 – *Relations between mobility and carrier concentration obtained from Hall effect measurement. (a) hole mobility and concentration. (b) electron mobility and concentration. GaAs epitaxial layers from two different MBE machines are distinguished by square and circle markers. Black lines are an empirical model from Sotoodeh et al. [117]*

5.3 CL measurements of thin-film GaAs

In this section, CL measurements on p-type and n-type GaAs thin-film layers are presented. Their thickness and results from Hall effect measurements (mobility and doping concentration) are given in Tables 5.1 and 5.2. The goal of this study is to verify the quantitative doping assessment by the analysis of luminescence spectra. The acceleration voltage used in CL measurements is 6 kV so that the electron-beam can pass through the surface depletion zone and excite bulk GaAs. The probe current is typically between 0.7 to 1 nA. For bulk GaAs with impinging current varying from about 0.3 to 3 nA, CL spectra do not shift in wavelength, neither do they change in shape. It is thus legitimate to assume that the generated carriers were in thermal equilibrium in these conditions of excitation.

5.3.1 Be-doped p-type GaAs

Figure 5.6 shows CL spectra of p-type GaAs thin-film samples, measured at both room temperature (RT) and low temperature (LT, 20 K). The spectra are normalized to their maximum intensity to facilitate their comparison. Peak energy (the energy position corresponding to the maximum CL intensity) and full width at half maximum (FWHM) values are indicated in the inset. At room temperature, CL spectra broaden at higher doping levels, and the spectra peak positions move gradually to lower energy due to bandgap narrowing effect (BGN) effect. BGN arises from many-body interactions at high doping levels. The determination of BGN values can thus be used to assess the doping levels (see details in Section 5.4.2). Tabulated BGN values for several III-V compounds are available in Ref. [135].

At low temperature, the spectra are plotted in both linear and log scale. For the slightly p-doped layer (green curve in Figure 5.6), the low temperature CL spectrum shows two separate peaks (1.510 eV may be due to exciton bound to acceptor, and 1.495 eV to transition of free electron to Be acceptor). For higher doping levels, the acceptor band merges with the valence band thus only one single emission peak is observed. Moreover, the emission spectra broaden and redshift with increasing doping levels, similar to the evolution of room temperature CL spectra. Regularly spaced peaks with separation of about 37 meV at lower energy tail can be attributed to the longitudinal optical (LO) phonon replica of the main emission peak.

Figure 5.7 shows the PL and CL spectra peak position energy as a function of the hole

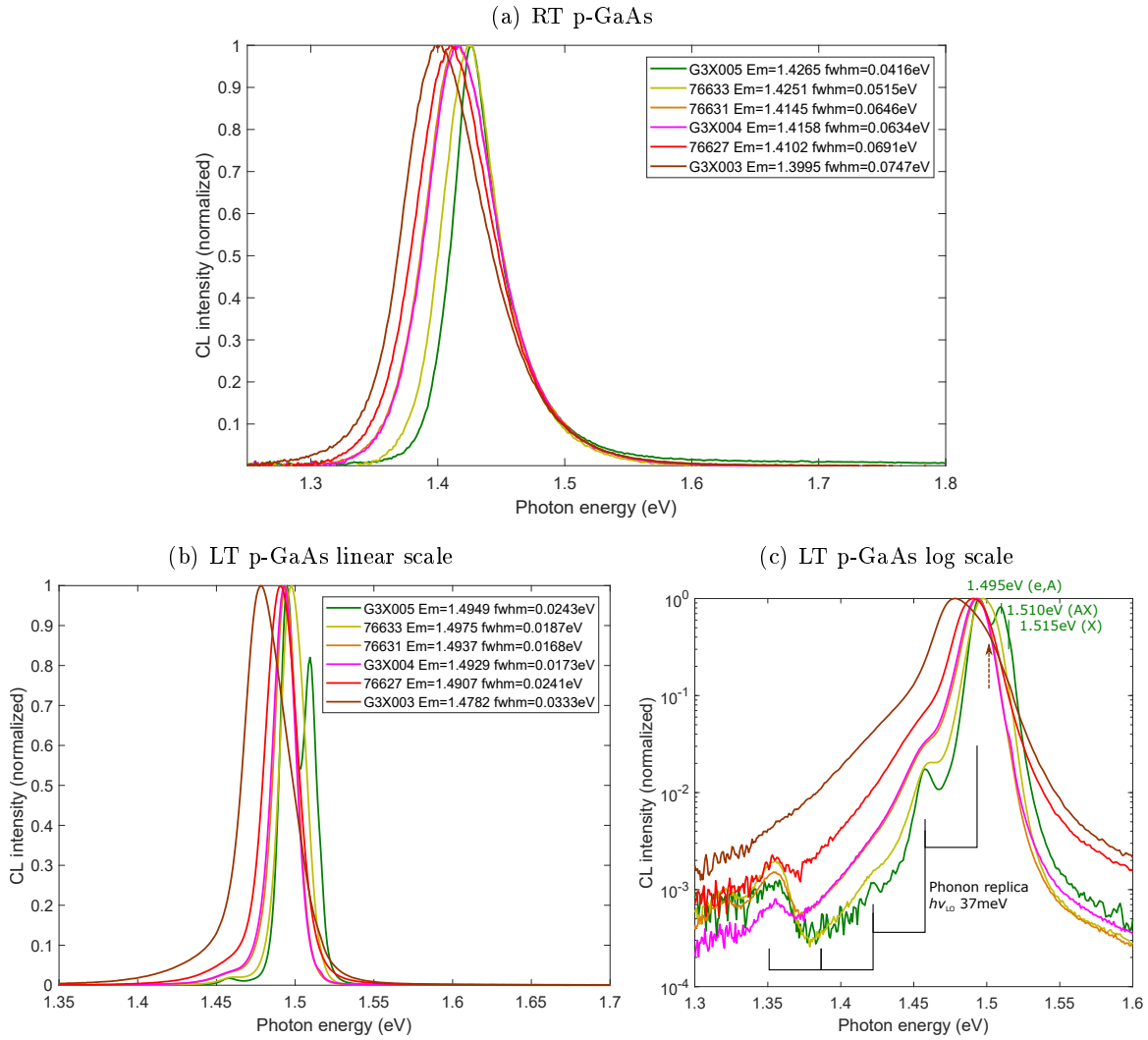

Figure 5.6 – *Comparison of normalized CL spectra for p-type GaAs thin films. (a) CL spectra measured at room temperature. (b,c) CL spectra measured at low temperature (20 K), shown in linear scale (b) and logarithmic scale (c).*

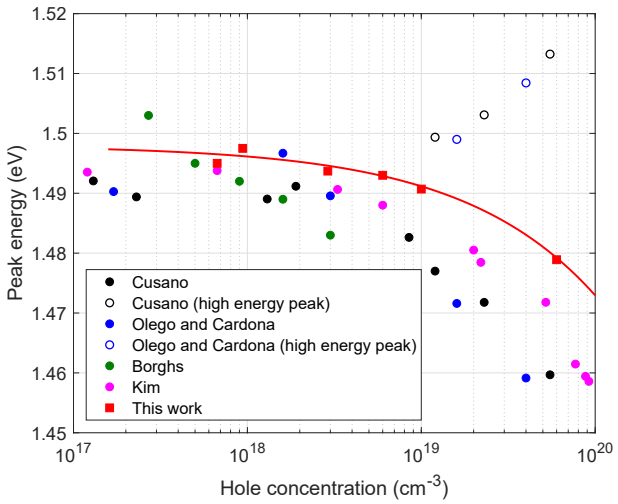

Figure 5.7 – *Peak position energy as a function of the hole concentration. Our CL spectra are compared to literature data from Cusano for 20 K CL of GaAs single crystal slices [163], Olego and Cardona for 4 K PL of Zn-doped GaAs single crystal [164], Borghs et al. for 30 K PL of MBE-grown Be-doped GaAs [165] and Kim et al. for 12 K PL of MOCVD-grown C-doped GaAs [166]*

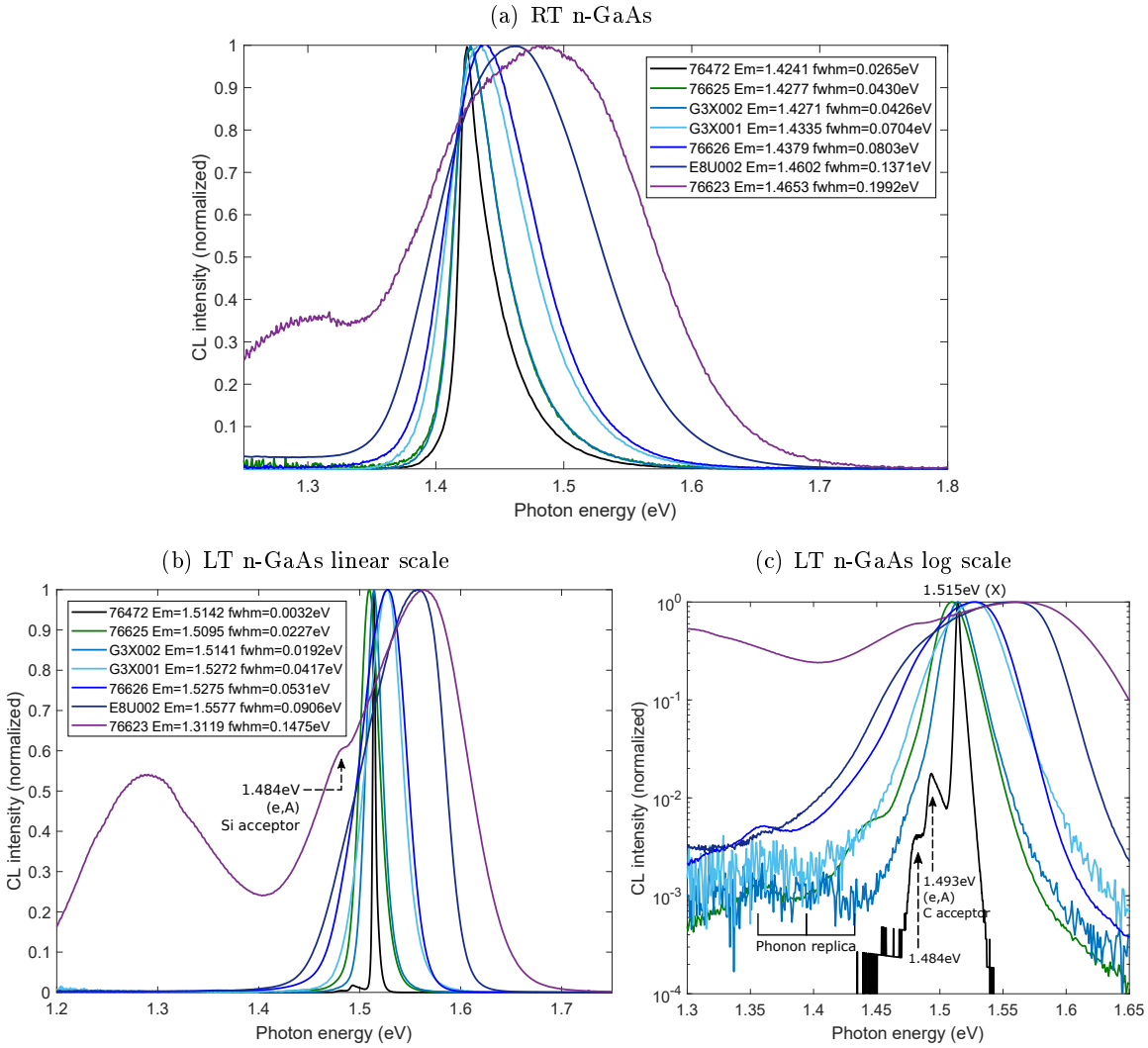

Figure 5.8 – *Comparison of normalized CL spectra for n-type GaAs thin films. (a) CL spectra measured at room temperature. (b,c) CL spectra measured at low temperature (20 K), shown in linear scale (b) and logarithmic scale (c).*

concentration at low temperature, for several p-doped GaAs samples. To retrieve the peak energy, our CL results (around 20 K) were fitted by two or three Gaussians depending on the asymmetrical shape, and compared with available literature data. Open circle markers present the high energy peak observed in the PL or CL spectra for high p-doping level above 10^{19} cm^{-3}. These features are often observed in degenerate p-type GaAs, and are explained by the excitonic enhancement of absorption near the Fermi level. It is referred to the so-called Mahan exciton, according to the theoretical work of Mahan for the prediction of an absorption singularity at the Fermi edge [167]. We observe a similar high energy shoulder in the highest doped p-GaAs sample (Figure 5.6(c) brown curve and arrow), which may be indicative for the degenerate hole Fermi level below the valence band maximum.

5.3.2 Si-doped n-type GaAs

Figure 5.8 shows CL spectra of n-type GaAs thin-film samples, measured at both room temperature and low temperature (20 K). The spectra are normalized to their maximum intensity to facilitate their comparison. A CL spectrum measured on an undoped GaAs thin-film (with residual n-type conductivity) is also included for reference. At room temperature, undoped GaAs

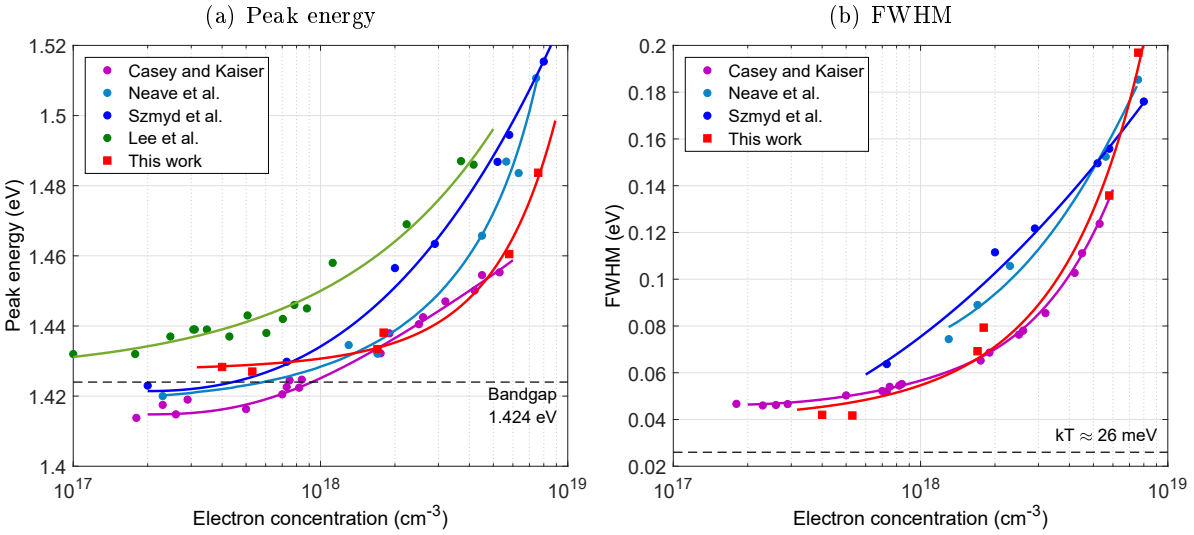

Figure 5.9 – *Peak energy (a) and FWHM (b) of luminescence spectra as a function of electron concentration at room temperature. Our CL measurements are compared with experimental data available in the literature: Casey and Kaiser for CL measurements on melt-grown Te-doped GaAs [175], Neave et al. for PL Si-doped GaAs grown by MBE [176], Szmyd et al. for PL Se-doped GaAs grown by MOCVD [177] and Lee et al. for PL Si-doped GaAs grown by MBE [178].*

has its peak position energy at 1.424 eV, corresponding to the bandgap of GaAs. With increasing n-doping levels, CL spectra broaden and the peak positions shift gradually to higher energy. The blueshift of the absorption edge and hence the emission peak is ascribed to the *Burstein-Moss shift*. The first experimental evidence of this effect is due to Burstein with the observation of anomalous absorption limit in n-doped InSb [168], which was explained by the conduction band filling due to very small effective mass of the conduction band electrons [169].

We note that the BGN effect is also present in n-type GaAs since the low-energy tail of the CL spectra move to lower energy with increasing doping levels. For n-type doping, blueshift and broadening are particularly sensitive to the electron concentration. Although the peak energy definition is straightforward, its determination for a broad spectrum may appear ambiguous depending on how the whole spectrum is fitted. Here, two or three gaussians are used to fit the CL spectra in order to extract the peak position. On the other hand, the determination of the FWHM is obtained by linear interpolation and is fairly precise with little variation.

At low temperature, (Figure 5.8(b) and (c)), undoped GaAs layer (black curve) shows a relatively sharp peak (FWHM≈3 meV) centered at 1.514 to 1.515 eV due to free exciton recombination or unresolved lines of exciton bound to Si donor. A small peak at 1.493 eV due to residuals of C acceptors is visible in log scale, and the even smaller shoulder at 1.484 eV is probably due to residual of Si acceptor. For slightly n-doped samples, the CL peak are mainly attributed to the shallow donor band (about 6 meV below the conduction band minimum). With increasing electron concentrations, the CL spectra broaden and shift to higher energy.

For the most n-doped layer (purple curve in Figure 5.8(b) and (b)), a shoulder at 1.484 eV may indicate the presence of Si acceptor, thus possible doping compensation in heavily Si-doped layer. Moreover, a wide Gaussian-like signal located around 1.2 to 1.4 eV was observed. This broad band emission was studied in compensated Si-doped GaAs, and was attributed to $Si_{Ga} - V_{Ga}$ and/or $Si_{As} - V_{As}$ donor-acceptor pair complexes [170, 171]. Theses features were observed in Si-doped GaAs layers under surface thermal annealing [172] and in LPE-grown GaAs:Si samples [173, 174].

Since the energy position of the maximum peak (peak energy) and the full width at half

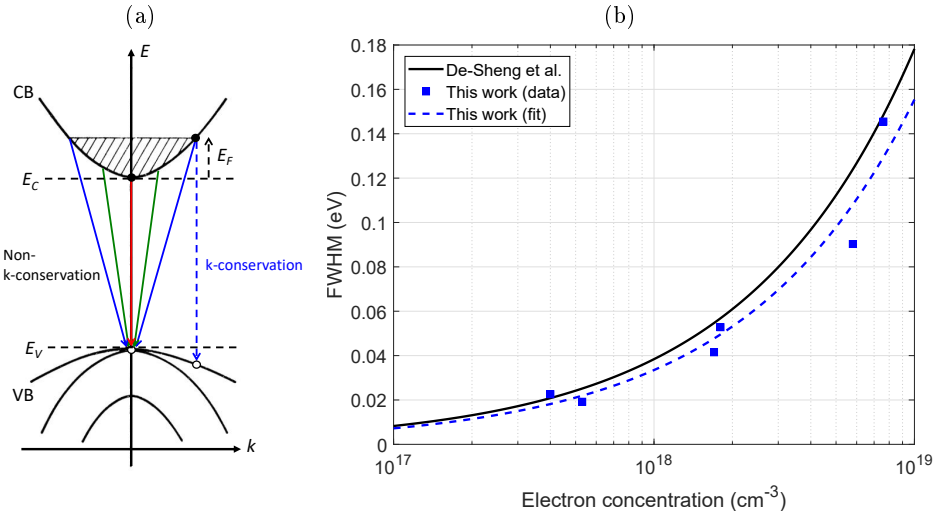

Figure 5.10 – *(a) Schematic energy band diagram for radiative transitions in degenerate n-type semiconductors. Either k-conserving transition or non k-conserving transition have been proposed. (b) FWHM as a function of the electron concentration at low temperature. Black curve is from De-Sheng et al. [179], blue markers and blue dashed line are CL measurements and fit with a $n^{2/3}$ power law.*

maximum (FWHM) are two main characteristics of luminescence spectra, we compare our results with the literature data of PL or CL measurements at room temperature (Figure 5.9). Globally, the blueshift and broadening follow a clear trend with increasing electron concentrations. At the limit of low doping level, the peak energy should tend to 1.424 eV (bandgap of undoped GaAs) and the FWHM should tend to 26 meV (broadening due to thermal energy). At a given electron concentration, there are slight differences of peak energy and FWHM between different measurements, probably due to different qualities of epitaxial layers. Therefore, peak energy and FWHM should not be considered separately and we will further analyze the CL measurements by fitting the whole spectra (see details in Section 5.4.3).

On the other hand, low temperature measurement may be more precise because the thermal broadening is largely suppressed. We can establish a first quantitative estimation of electron concentrations by examining the FWHM, which is a fairly sensitive and unique quantity at different n-doping levels. Figure 5.10(a) proposes a radiative recombination process in degenerate n-type semiconductors. For electron concentrations above the degenerate threshold (about $4\times10^{17}\,\mathrm{cm}^{-3}$ for GaAs), the Fermi level E_F is situated above the conduction band minimum. Assuming that the injected holes are thermalized to the band edge before they recombine radiatively with free electrons, the momentum k-conservation rule should be relaxed to explain the blueshift of the emission spectrum. Non-k-conservation is generally admitted for highly doped systems because the random distribution of ionized impurity atoms destroys the invariance of symmetry transformations. Some researchers, however, question the relaxation of k-conservation in degenerate semiconductors [180].

De-Sheng et al. studied MBE-grown n-type Te-doped GaAs films by PL at 1.8 K, and deduced that the FWHM is closely related to the Fermi level, thus to an empirical 2/3 power law of the electron concentration [179]. In fact, at near 0 K, free electrons fill all the states below the Fermi level. In k-space, a 3D electron gas occupies a so-called Fermi sphere of radius $k_F = (3\pi n)^{1/3}$, where n is the electron density. Assuming a parabolic conduction band, the Fermi level is expressed as a quadratic function of k_F, and thus a power 2/3 of the electron density n. Indeed, we can conveniently fit the experimental FWHM values with a 2/3 power function of n:

$$\mathrm{FWHM\,(eV)} = 3.348\times10^{-14}\times n^{2/3}, \tag{5.14}$$

where n is the electron density expressed in cm^{-3}. Our result is very close to that of De-Sheng et al. (comparison in Figure 5.10(b)). This empirical relation between the low temperature FWHM (eV) and the electron concentration n (cm^{-3}) then constitutes an easy way to determine the electron concentrations in the range of about 4×10^{17} to 1×10^{19} cm^{-3}.

5.3.3 Comparison

Figure 5.11 shows a scattering plot of the peak energy versus the FWHM of CL spectra measured at room temperature. The point data of a sample come from a hyperspectral CL measurement where each point is defined by the parameters extracted from the spectrum of a single pixel of the CL map. We can see the FWHM continuously enlarges with increasing doing levels. It can also be visualized that p-type doping causes the redshift of the peak energy, while n-type doping causes the opposite blueshift of the peak energy. A more precise lineshape analysis is further investigated to relate luminescence spectra with quantitative doping concentrations (Section 5.4).

(a) Peak and FWHM scattering plot

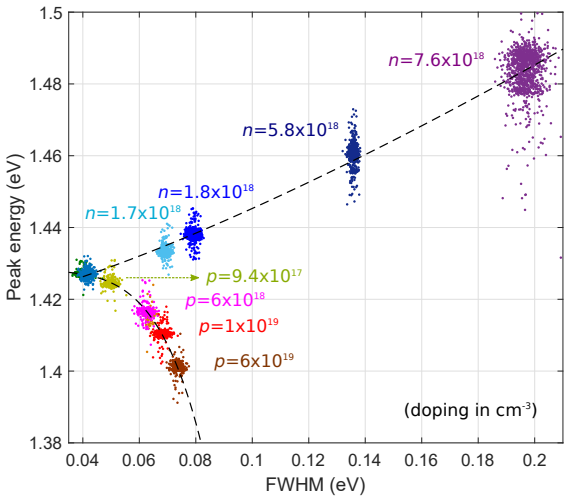

Figure 5.11 – *Scattering plot of peak energy versus FWHM from CL hyperspectral measurement for different doping layers. CL spectra broaden for increasing doping concentration, and the peak position shifts to higher energy for n-doping and to lower energy for p-doping. Dashed lines are shown as a guide to the eye.*

5.4 Modeling CL spectra for quantitative doping assessment

Free carrier concentration in a semiconductor is related to the corresponding Fermi level. CL spectra are presented in Section 5.3, and they can be used to determine the Fermi energy using the generalized Planck's law, following the description given in Chapter 3.2.4. Subsequently, free carrier concentrations can be deduced. The connection between the Fermi level and the carrier concentration is the effective density of states in the conduction band or valence band, which are determined from the approximation of the forms of E-k dependence near the major band maxima and minima through the band edge effective mass. Therefore, it is essential to give a coherent framework and values used for GaAs (Section 5.4.1). Although the hole Fermi level in p-type GaAs is not easily to be observed from luminescence experiment, the hole concentration is simply related to CL spectra through empirical bandgap narrowing values (Section 5.4.2). Section 5.4.3 presents n-type doping assessment using the electron Fermi level.

5.4.1 Band non-parabolicity

Parabolic band is usually taken as a starting point, but the real band structure may deviate from the ideal parabolic one and thus needs to be taken into account. For example, non-parabolicity of the Γ_6 minimum of the lowest conduction band affects the calculated electron concentration at high doping levels. For p-type ZB GaAs, the valence bands are degenerate at the Γ point, constituting heavy-hole and light-hole bands with very different characteristics. The split-off valence band is situated 0.34 eV below the valence band maximum. The thermal hole occupation in the split-off band is negligible in usual temperature range. Table 5.3 gives the parameters used for the determination of carrier concentrations.

Table 5.3 – *Material parameters used in the calculation of free carrier concentrations in GaAs [35].*

ZB GaAs	near 0 K	room temperature
Bandgap [eV]	1.519	1.424
Electron mass m_{co} $[m_0]$	0.067	0.063
CB non-parabolicity coefficient α	-0.824	-0.83
CB effective density of states N_c [cm^{-3}]	–	4.2×10^{17}
Heavy hole mass m_{hh} $[m_0]$	0.51	0.50
Light hole mass m_{lh} $[m_0]$	0.082	0.076
Light hole VB non-parabolicity β	-3.80	-3.57
Combined hole mass m_v $[m_0]$	0.53	0.524
VB effective density of states N_v [cm^{-3}]	–	9.5×10^{18}

Effective density of states for the conduction band

Following Blakemore's notations [35], supplementary indices are used to distinguish between different effective masses. The non-parabolicity of the conduction band is described using Kane's approach of 4-band $k \cdot p$ perturbation [181]. When $|k|$ is allowed to become a little larger, non-parabolicity is approximated through a k^4 term:

$$E \simeq E_c + \frac{\hbar^2 k^2}{2m_{co}} + \frac{\alpha}{E_g}\left(\frac{\hbar^2 k^2}{2m_{co}}\right)^2, \tag{5.15}$$

where the dimensionless non-parabolicity coefficient α turns out to be negative. The low temperature value $\alpha = -0.824$ and room temperature value $\alpha = -0.83$ are shown in Table 5.3. The $k \cdot p$ model is based on a perturbation approximation, thus is only reliable close to an extremum. The non-parabolicity correction coefficient may still not be adequate for more than 0.1 eV above the Γ_6 minimum.

If the lowest GaAs conduction band were a simple parabolic one with the band-edge mass m_{co}, the Fermi energy E_f could be related to the equilibrium conduction electron concentration n by:

$$n_0 = N_{co} \times \mathcal{F}_{1/2}\left(\frac{E_f - E_c}{k_B T}\right), \tag{5.16}$$

where

$$N_{co} = 2\left(\frac{2\pi m_{co} k_B T}{h^2}\right)^{\frac{3}{2}} \tag{5.17}$$

is usually called effective density of conduction band states (without non-parabolicity correction), and

$$\mathcal{F}_j(x) = \frac{1}{\Gamma(j+1)} \int_0^\infty \frac{t^j}{\exp(t-x)+1} dt \tag{5.18}$$

is the Fermi integral of order j. However, the non-parabolicity of the GaAs conduction band makes n_0 larger than that calculated by Equation 5.16 at a given temperature and Fermi level. Including the E-k behavior described in Equation 5.15, the conduction electron concentration becomes:

$$n_0 = N_{co}\left[\mathcal{F}_{1/2}(\eta) - \frac{15\alpha k_B T}{4E_g}\mathcal{F}_{3/2}(\eta)\right]. \tag{5.19}$$

where $\eta = (E_f - E_c)/k_B T$ represents a reduced variable at non-zero temperature. The latter term is actually additive since the non-parabolicity factor α is negative. It would be preferred to use usual relation between electron concentration n_0 and Fermi energy E_f in a form: $n_0 = N_c \times \mathcal{F}_{1/2}(\eta)$. In this case:

$$N_c = N_{co}\left(1 - \frac{15\alpha k_B T}{4E_g}\right)\frac{\mathcal{F}_{3/2}(\eta)}{\mathcal{F}_{1/2}(\eta)}. \tag{5.20}$$

We should note that the effective density of conduction states N_c depends on T and also on the relation of E_f to E_c. For non-degenerate electron concentration, all the Fermi-Dirac integrals reduce to an exponential asymptotic form. The multiplying factor account for 1.056 at room temperature ($N_c \approx 1.056 N_{co} \approx 4.21 \times 10^{17}\,\mathrm{cm}^{-3}$). Figure 5.12 gives the variation of the effective density of conduction states with electron concentration for GaAs at 300 K. The increase of the effective density of states is equivalent to the description of an augmentation in the effective electron mass at high concentration [182].

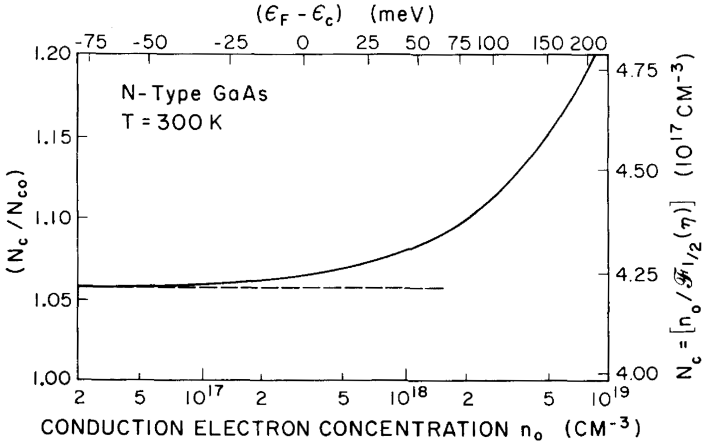

Figure 5.12 – *Variation of the effective density of conduction states with electron concentration n_0 for GaAs at 300 K (Figure extracted from Ref. [35]).*

For degenerate n-type semiconductor at very low temperature, the use of an effective density of states is not adequate and the Fermi-Dirac integral tends to infinity. This situation can be resolved using an asymptotic approximation: $\mathcal{F}_j(\eta) \to \eta^{j+1}/\Gamma(j+2)$ for $\eta \gg 1$. Inserting in Equation 5.19, a finite electron population at a near-zero temperature results in a Fermi energy E_f such that:

$$n_0 \simeq (8\pi/3)\left[2m_0(E_f - E_c)/h^2\right]^{3/2}\left[1 - (3\alpha/2E_g)(E_f - E_c)\right] \tag{5.21}$$

For n-type GaAs at near zero temperature, with $m_{co} = 0.067 m_0$, $E_g = 1.519\mathrm{eV}$ and $\alpha = -0.824$, this formula is evaluated numerically:

$$n_0 \approx 7.9 \times 10^{19} \times (E_f - E_c)^{3/2}\left[1 + 0.82 \times (E_f - E_c)\right], \tag{5.22}$$

where $(E_f - E_c)$ is expressed in eV and n_0 in cm^{-3}. We note the similitude of this formula with the empirical relation between the electron concentration and the low temperature FWHM (Equation 5.14).

Effective density of states for the valence band

The valence band of GaAs is degenerate at the Γ point and constitutes the heavy-hole band with an effective mass m_{hh} and the light-hole band with an effective mass m_{lh}. The total free hole density is the sum of the two contributions. The heavy-hole band can be assumed parabolic for the calculation of hole density, but not the light-hole band. A dimensionless non-parabolicity parameter β is thus introduced for the light-hole band, similar to the conduction band. Again, we want to write the total hole density in the form of $p_0 = N_v \times \mathcal{F}_{1/2}(\xi)$, where $\xi = (E_v - E_{fv})/k_B T$ is a dimensionless parameter of the hole Fermi energy E_{fv} relative to the valence bands edge E_v. In this case, the effective density of states for the valence band is given by:

$$N_v = 2\left(\frac{2\pi k_B T}{h^2}\right)^{\frac{3}{2}} \times \left[m_{hh}^{3/2} + m_{lh}^{3/2}\left(1 - \frac{15\beta k_B T}{4E_g}\right)\frac{\mathcal{F}_{3/2}(\xi)}{\mathcal{F}_{1/2}(\xi)}\right]. \tag{5.23}$$

The light-hole mass m_{ll} decreases as the temperature rises, but the non-parabolicity factor multiplying $m_{ll}^{3/2}$ increases with temperature. These two effects cancel out in a large temperature range above 200 K. It is simply assumed a light-hole mass of $m'_{lh} = 0.088\, m_0$ at room temperature and a spherical averaged heavy-hole mass of $m_{hh} = 0.50\, m_0$, then light holes constitute about 7% of the total hole population shared between these two bands [35]. The combination makes the effective density of states $N_v = 9.5 \times 10^{18}\ \mathrm{cm}^{-3}$ at room temperature. Degenerate hole density does occur in GaAs, but it is less common compared to n-type materials.

5.4.2 Bandgap narrowing effect

The bandgap narrowing (BGN) is referred to a bandgap diminution when a semiconductor is heavily doped. There are several confusions in the literature concerning this topic, so we need to clarify the definition of the bandgap itself. We call bandgap, denoted E_g, the energy separation between the conduction band minimum and the valence band maximum. This definition is clear for pure semiconductors, but may becomes ambiguous for doped semiconductors because of the formation of band tails. More generally, we call bandgap the energy gap between the two hypothetic parabolic band edges, which is consistent with the absorption model used in Equation 3.69. The states below the band edges are referred to band tails. The BGN for a doped semiconductor ΔE_g is then the difference of the bandgap compared to the bandgap of the pure semiconductor. For degenerate doping density, the Fermi level E_f may lie inside the parabolic band. For example in n-type semiconductors when E_f is above the conduction band minimum, $E_g + E_f$ is sometimes called optical gap because relevant optical properties depend on it.

Background

To explain the origin of BGN in doped semiconductors, quantum mechanical descriptions are required and many-body interactions at high density are no more negligible. Moreover, the random distribution of impurities in a many-body system makes the treatment extremely complicated. Here we give only some essential results. A dimensionless parameter for the doping concentration, r_s, is usually used, which is the average distance between impurity atoms divided by the effective Bohr radius $a_{D,A}$ (see Equation 3.42):

$$r_s = \frac{1}{a_{D,A}}\left(\frac{3}{4\pi N}\right)^{1/3} \tag{5.24}$$

Assuming that the semiconductor doping is not compensated: N is the impurity concentration which is equal to the free carrier concentration if every dopant is electrically active. At high

doping concentrations such that $r_s < 1$, many-body interactions begin to have significant effect. Wolff used many-body perturbation methods to show that to lowest order in r_s the electron-electron interaction could be modeled by using a screened Coulomb interaction for the impurities together with a rigid band shift due to exchange and correlation energy E_{xc} of the electron gas and a small renormalization of the effective mass m_e^* [183]. The Wolff effective one-electron Hamiltonian writes [184]:

$$H = \frac{\mathbf{p}^2}{2m_e^*} + E_{xc} + V(\mathbf{r}) \tag{5.25}$$

The electrons have mutually repulsive Coulomb interactions. The Fermion nature of the particles tend to keep electrons with similar spin away from each other (Pauli exclusion). This spatial exclusion reduces the amount of repulsive energy that the electrons would have from a uniform distribution of particles. The reduction of repulsive energy is equivalent to an attractive energy, which is called the exchange energy [185]. Jain and Roulston gave a general expression for the shift in the majority band edge due to exchange interactions [186]:

$$\Delta E_{g,x} = -\frac{fe^2\left(3\pi^2 N\right)^{1/3}}{\pi\varepsilon_0\varepsilon_r}, \tag{5.26}$$

where f is a dimensionless correction factor depending on the material and the doping type. Another contribution to the ground state energy for the homogeneous electron gas is the correlation energy. Numeral calculations show that this quantity is much smaller than the exchange energy for most densities, thus can be neglected in semiconductors [185]. The exchange and correlation together are usually referred to many-body effects. The electron-donor interactions may also contribute to the total BGN, though it is expected to count for only a few percentage of the total BGN. Jain et al. gave a practical expression of BGN that may be useful for device simulation [135].

$$\Delta E_g = A \times N^{1/3} + B \times N^{1/4} + C \times N^{1/2}. \tag{5.27}$$

The first term with 1/3 power of the doping concentration N is the main contribution from the carrier-carrier exchange interactions. The second term with $N^{1/4}$ is related to the correlation energy and the third term with $N^{1/2}$ is from the carrier-impurity interactions.

For direct gap III-V semiconductor like GaAs, the BGN effect was studied at the beginning from optical absorption measurements [54]. Casey and Stern calculated absorption and spontaneous emission rates for various GaAs doping levels based on the density of states and optical matrix element, and derived experimentally an expression of the BGN for p-type GaAs ($p = 1 \times 10^{18}$ to 2×10^{19} cm^{-3}) by fitting the absorption edge near bandgap at 300 K [187].

$$E_g\ (300\,\mathrm{K}) = 1.424 - 1.6{\cdot}\,10^{-8} \times p^{1/3} \tag{5.28}$$

where E_g is expressed in eV and p is the hole concentration in cm^{-3}. Casey's absorption model includes Kane's gaussian band tail and the occupancy of the valence and the conduction bands, which is close to our approach using the generalized Planck's law.

In the 1980s, PL experiments were extensively used and lineshape analysis with doping concentration was investigated. Olego and Cardona gave a systematic method to extract bandgap through the intersection of a linear fit of the low energy tail of PL spectrum with the baseline [164]. Borghs et al. investigated low-temperature (30 K) PL characteristics for GaAs at high doping levels and used the method described by Olego and Cardona to obtain the GaAs bandgap [165]. They obtained somewhat a different value of the multiplying factor before the $p^{1/3}$ term of BGN than that of Casey and Stern. The BGN values from Borghs et al. are collected in the paper of Jain et al. [135]

$$E_g\ (30\,\mathrm{K}) = 1.515 - 2.6{\cdot}\,10^{-8} \times p^{1/3} \tag{5.29}$$

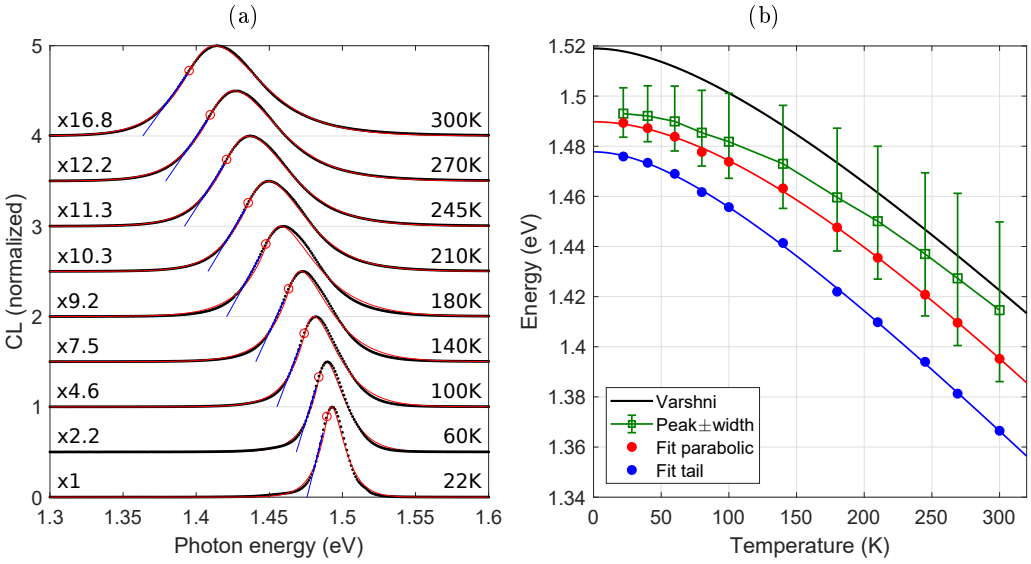

Figure 5.13 – *CL spectra of the p-GaAs sample (G3X004) with hole concentration of* $p = 6 \times 10^{18}\,\mathrm{cm}^{-3}$. *(a) Temperature dependence of the CL spectra and the fit by two methods to extract the bandgap. The open circles show the bandgap (parabolic band edges) from the fit using generalized Planck's law (red curves) and the blue lines are linear fits to the low energy side of the CL spectra. (b) Temperature evolution of the CL peak position and half width (green markers with bars), bandgap from the parabolic band edges (red circles) and low energy tail (blue circles). The red and blue lines are fits of the bandgap using the Varshni equation. The black line is the pure GaAs bandgap calculated using the Varshni equation.*

We emphasize that the BGN from Borghs et al. was obtained at low temperature and by fitting only the low energy tail of the PL spectra, which may lead to an overestimation of the BGN because band tails were ignored.

Analysis of CL spectra

To illustrate the two different methods of analysis, we show in Figure 5.13(a) the CL spectra measured at various temperatures of the GaAs:Be layer (sample G3X004) with hole concentration of 6×10^{18} cm^{-3}. CL spectra are normalized to the maximum intensity and shifted vertically for clarity, with normalization factors indicated for each curve in the figure. Black dots are as-measured data and red curves are the fits using the generalized Planck's law as described in Chapter 3.2.4. We choose the parabolic absorption model modified by an Urbach tail to fit the whole spectra (Equation 3.69). Here, the parameters (E_{fc}, E_{fv}, T, d) are varying but they hardly change the bandgap E_g. We can visualize in Figure 5.13(a) that red circles mark the bandgap obtained from the fits of the whole spectra, and blue straight lines show linear fits at the low energy side.

In Figure 5.13(b), we compare the bandgaps obtained by the two different methods. Red dots are bandgaps E_g(parabolic) from the fits of the whole spectra with parabolic absorption model, blue dots are bandgaps E_g(tail) from the linear fits at the low energy tail. The well-known bandgap of pure GaAs (black curve) is determined from the Varshni equation:

$$E_g(T) = E_g(0\,\mathrm{K}) - \frac{\alpha T^2}{T + \beta} \quad [\mathrm{eV}] \tag{5.30}$$

with the parameters $E_g(0\,\mathrm{K}) = 1.519\,\mathrm{eV}$, $\alpha = 5.405 \cdot 10^{-4}$ and $\beta = 204$ [35]. Green markers with bars are as-measured peak positions and half widths at both high and low energy side of the CL spectra. We can see that the difference between the peak positions of a wide luminescence

spectrum and the bandgap of pure GaAs is temperature dependent, which cannot be easily associated with a meaningful physical quantity. On the contrary, the difference between the fitted bandgap and the bandgap of pure GaAs is nearly independent of the temperature (almost vertical translation of the black line in Figure 5.13(b)), which can be associated to BGN values.

The bandgap extracted from the linear fit at the low energy side of the spectra (blue dots) can be fitted with the Varshni equation: $E_g(\text{tail}) = 1.478 - 5.631 \cdot 10^{-4} \times T^2/(T + 155)$ (blue line). On the other hand, the bandgap from the fit using a parabolic absorption model (red dots) can be fitted with the Varshni equation: $E_g(\text{parabolic}) = 1.490 - 6.490 \cdot 10^{-4} \times T^2/(T + 318)$ (red line). Subsequently, BGN values are very different from different methods of treatment: BGN 41 meV for the former, 29 meV for the latter (take high-purity bandgap to be 1.519 eV at 0 K). The method of Olego and Cardona (linear fit at low energy tail) seems to overestimate the BGN (underestimates the bandgap) since the contribution of a band tail is neglected.

In the followings, the same procedure with the parabolic absorption model is applied to fit the whole CL spectra of the six GaAs:Be samples. Luminescence spectra are calculated following Chapter 3.2.4. In the fitting procedure, the parameters (E_{fc}, E_{fv}, d) are varying within defined ranges: E_{fc}(eV) in $[-0.4; 0]$ with respect to the conduction band minimum, E_{fv}(eV) in $[-0.1; 0.2]$ with respect to the valence band maximum, and $d(\mu\text{m})$ in $[0; 0.5]$ (maximum 0.5 μm is the thickness of the layer). Only the shape of luminescence spectra is fitted, so the positions of Fermi levels have no influence if they are far from the band edges. The temperature T is either varying or fixed at 300 K for room temperature CL spectra. In any case, the bandgap is rather independent from the influence of other parameters. Table 5.4 gives the resulting fitted bandgap and Urbach tail energy (with variation due to uncertainty of carrier temperatures).

Table 5.4 – *Peak energy, FWHM and optimal fit parameters (bandgap E_g and Urbach tail γ) for CL spectra measured on planar p-type GaAs at room temperature. Doping levels from Hall effect measurements are indicated.*

sample	doping cm^{-3}	peak eV	FWHM eV	E_g eV	γ eV
G3X005	6.7×10^{17}	1.427	0.040	1.412±0.003	0.008±0.001
76633	9.4×10^{17}	1.425	0.050	1.408±0.002	0.011±0.001
76631	2.9×10^{18}	1.416	0.064	1.396±0.001	0.016±0.001
G3X004	6×10^{18}	1.417	0.062	1.398±0.001	0.015±0.001
76627	1.0×10^{19}	1.410	0.068	1.390±0.001	0.017±0.001
G3X003	6×10^{19}	1.401	0.074	1.378±0.001	0.018±0.001

Figure 5.14(a) displays the room temperature CL spectra of the GaAs:Be samples with different doping levels, together with the bandgaps indicated by open circles superimposed on the corresponding CL spectra. They are fitted with a constant temperature $T = 300$ K. For low-doped samples, CL spectra differ from the fits using the parabolic absorption model due to excitonic enhancement of absorption near the bandgap, and the uncertainty on bandgap is slightly larger (about 3 meV) compared to the bandgap of highly-doped samples. The temperature evolution of the bandgaps is displayed in Figure 5.14(b). Several data points at low temperature for the two lowest doped samples are disregarded because the acceptor band tend to separate from the band edge luminescence. Compared with the bandgap of pure GaAs (black line), we can see that the BGN for all samples is rather independent of the temperature, which allows to extract reliable and consistent bandgap.

Finally, we plot the BGN values as a function of hole concentration in Figure 5.15, together with empirical BGN values from the literature. We show bandgaps deduced either from the whole fit of CL spectra (blue) or fit of only the low energy tail (red). The errorbars associated with the bandgaps from whole fit of CL spectra are due to observed peak energy shifts and uncertainties

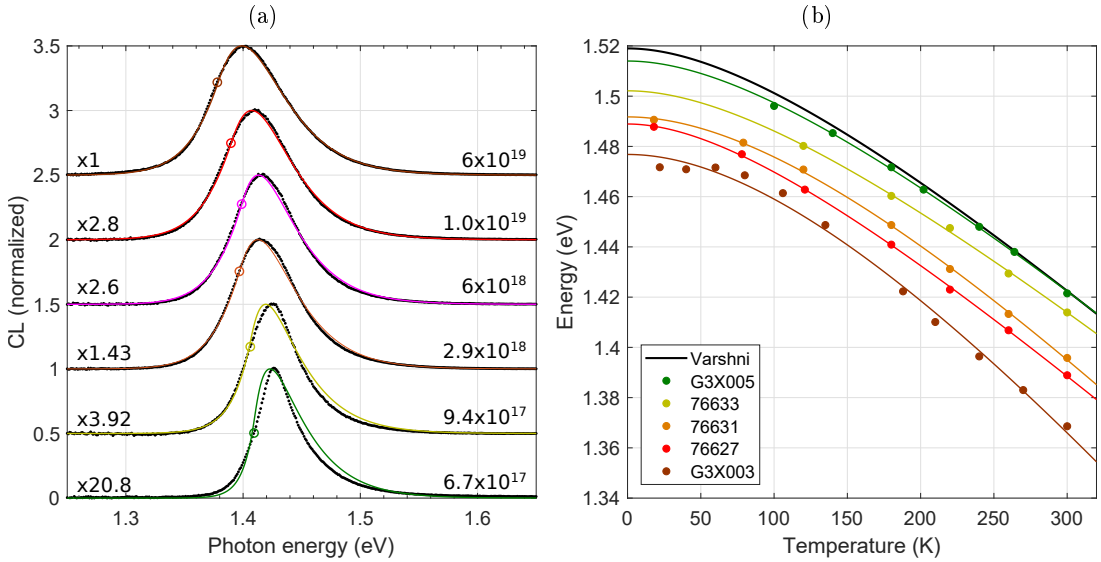

Figure 5.14 – *Comparison of CL spectra for planar p-type GaAs and fits. (a) Room temperature CL spectra of different p-type doping concentrations indicated in the figure (cm^{-3}). The normalization factors are also indicated. The open circles mark the bandgaps from the fit. (b) Temperature evolution of the bandgap, data points correspond to a CL spectrum and the solid lines are fits using Varshni equations.*

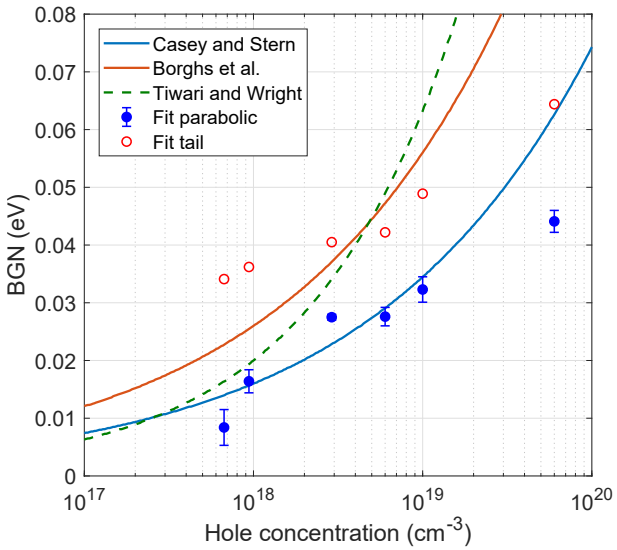

Figure 5.15 – *BGN as a function of hole concentration for p-type GaAs. Blue circles are bandgaps obtained based on a parabolic absorption model with Urbach tails in the generalized Planck's law and blue line is the empirical determination from Casey and Stern [187] (Equation 5.28). Red open circles are bandgaps obtained from the linear fit to the low energy tail of the low temperature CL spectra, and red line is the empirical results from Borghs et al. [165] (Equation 5.29). The green dashed line is another experimental BGN values from Tiwari and Wright using electrical transport measurement [188].*

of temperature dependence. Part of the diverging BGN values in the literature seems to come from different methods to extract the bandgap. Our results are quite close to that of Casey et al. in the validity range of about $p = 1 \times 10^{18}$ to 2×10^{19} cm^{-3}.

The last comment concerns the BGN from the device point of view. The product np of the electron and hole concentrations is equal to the square of the intrinsic carrier density n_i^2 at relatively low doping levels. At least for p-type GaAs, this relation was shown to break down at high concentrations. An apparent or effective BGN ΔE_g^a is introduced to better describe the transport properties from minority carriers [189]:

$$np = n_i^2 \times \exp\left(\frac{\Delta E_g^a}{k_B T}\right) \tag{5.31}$$

The green dashed curve in Figure 5.15 is an effective BGN in p-type GaAs determined by measuring the transport properties on heterostructure bipolar transistors [188]. These values may be very different from the values determined by optical methods, so care should be taken when referring to BGN.

In summary, we have carried out careful analysis of CL spectra measured on a series of p-type GaAs:Be epitaxial layers. The bandgap is obtained by fitting the whole spectrum with a parabolic absorption model. The bandgap narrowing (BGN) is the difference between the bandgap of pure GaAs and that of doped GaAs, and is determined through analysis of either room temperature or low temperature CL spectra. We verify that the relation between BGN and hole concentration p (cm^{-3}) of p-type GaAs: BGN (eV) $= 1.6 \cdot 10^{-8} \times p^{1/3}$ is valid for the doping range of approximately 1×10^{18} to 2×10^{19} cm^{-3}. This can be used to determine p-type GaAs doping concentration by analysis of luminescence spectra.

5.4.3 Band filling effect

For n-type III-V semiconductors, the luminescence spectra are very different from that of p-type counterpart due to predominant Burstein-Moss shift. In the literature, quantitative doping assessment of n-type GaAs from luminescence analysis has been done to some extends. De-Sheng et al. analyzed the PL of Te-doped GaAs taking into account the electron occupation but no band tail was considered [179]. Lee et al. fitted room temperature PL spectra of Si-doped GaAs including the conduction band filling and the gaussian band tail [178]. However, re-absorption of luminescent photons before emission may distort the spectral shape and should not be neglected, otherwise, the re-absorption tends to reduce the observed electron Fermi level.

Following Chapter 3.2.4, we fit the CL spectra of n-type GaAs using the generalized Planck's law (Equation 3.65) and include all the features mentioned above. Because we only observe simple exponential decays in the lower-energy part of CL spectra, an Urbach tail with an adjustable energy parameter γ is chosen (Equation 3.69). For the sake of simplicity, the bandgap and Urbach tail are firstly fitted using the parabolic absorption model, following the same procedure as for fitting CL spectra of p-type GaAs (Section 5.4.2). The bandgap is obtained regardless of other parameters, and it serves as the reference for Fermi levels.

The electron Fermi level E_{fc} is then considered in detail. We define E_{fc} with respect to the conduction band minimum (see also the band diagram notations in Figure 5.10(a)). The conduction band filling at high electron concentration is the reason for the blueshift and broadening of luminescence spectra. The rise of electron Fermi level above the conduction band edge causes the absorption edge to shift to higher energy (Equation 3.70). For low doping concentrations ($n \lesssim 1 \times 10^{18}$ cm^{-3}), we use the absorption coefficient of semi-insulating GaAs (Sturge) [36] as input in Equation 3.69 to capture the excitonic enhancement of absorption near bandgap. For high doping concentrations ($n \gtrsim 2 \times 10^{18}$ cm^{-3}), Coulomb interaction is screened by high carrier concentrations, so the absorption edge raised less rapidly and a parabolic model provides an

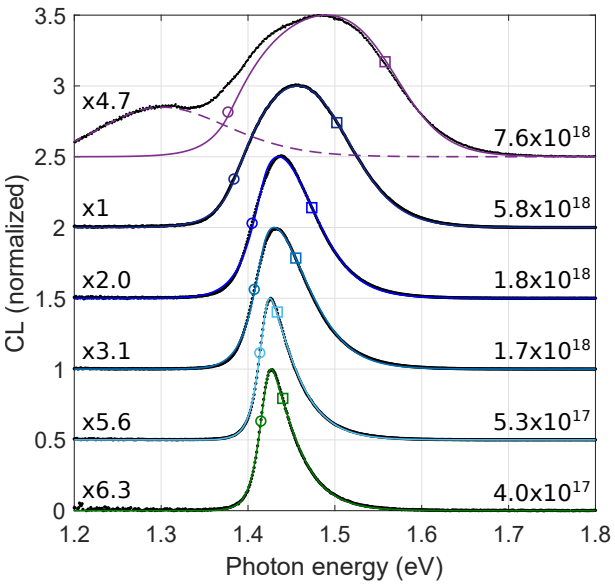

Figure 5.16 – *Comparison of room temperature CL spectra (black dots) for planar n-type GaAs and fits (colored lines). Different n-type doping concentrations measured by Hall effect (cm^{-3}) and intensity normalization factors of CL spectra are indicated in the figure. The open circles mark the bandgap positions from the fit and the square markers indicate the electron Fermi level superimposed on the CL spectra. For the highest doped sample, luminescence from deep levels was subtracted using a gaussian fit (dashed line).*

accurate fit of the whole spectra. In the intermediate doping concentrations, either high-purity GaAs absorption or parabolic absorption can be used. We fix the carrier temperature to be $T = 300\ K$ in the calculation of luminescence spectra.

Table 5.5 – *Peak energy, FWHM and optimal fit parameters (bandgap E_g, electron Fermi level E_{fc}, Urbach tail γ, and characteristic length d) for CL spectra measured on planar n-type GaAs at room temperature. Doping levels from Hall effect measurements are indicated.*

sample	doping cm^{-3}	peak eV	FWHM eV	E_g eV	E_{fc} eV	γ eV	d μm
76625	4.0×10^{17}	1.428	0.042	1.414±0.004	0.003±0.023	0.006±0.002	3.7
G3X002	5.3×10^{17}	1.427	0.042	1.413±0.003	0.003±0.018	0.006±0.001	2.8
G3X001	1.7×10^{18}	1.433	0.069	1.407±0.001	0.028±0.019	0.013±0.001	1
76626	1.8×10^{18}	1.438	0.079	1.404±0.002	0.053±0.016	0.016±0.001	1.6
E8U002	5.8×10^{18}	1.461	0.136	1.384±0.003	0.116±0.003	0.022±0.002	0
76623	7.6×10^{18}	1.484	0.197	1.377±0.007	0.177±0.007	0.025±0.004	0

Table 5.5 gathers the optimal parameters resulting from the fit of CL spectra measured at room temperature on GaAs planar layers, and Figure 5.16 displays the room temperature CL spectra of the GaAs:Si samples with different doping levels, together with the fits (colored lines). For the four samples of lower doping levels ($n < 2 \times 10^{18}$ cm^{-3}), fits using high-purity GaAs absorption coefficient are displayed. For the two samples of higher doping levels ($n > 5 \times 10^{18}$ cm^{-3}), fits using parabolic absorption model are displayed. The fitted bandgaps E_g (open circles) and position of electron Fermi levels $E_g + E_{fc}$ (open square markers) are superimposed on the corresponding CL spectra. For the mostly doped sample, luminescence from deep levels is deconvoluted with a Gaussian term and is excluded from the fit.

The parameter d used in Equation 3.64 is considered here as a fitted parameter without upper bound, and the resulting optimal values are shown in Table 5.5. We recall that d can be

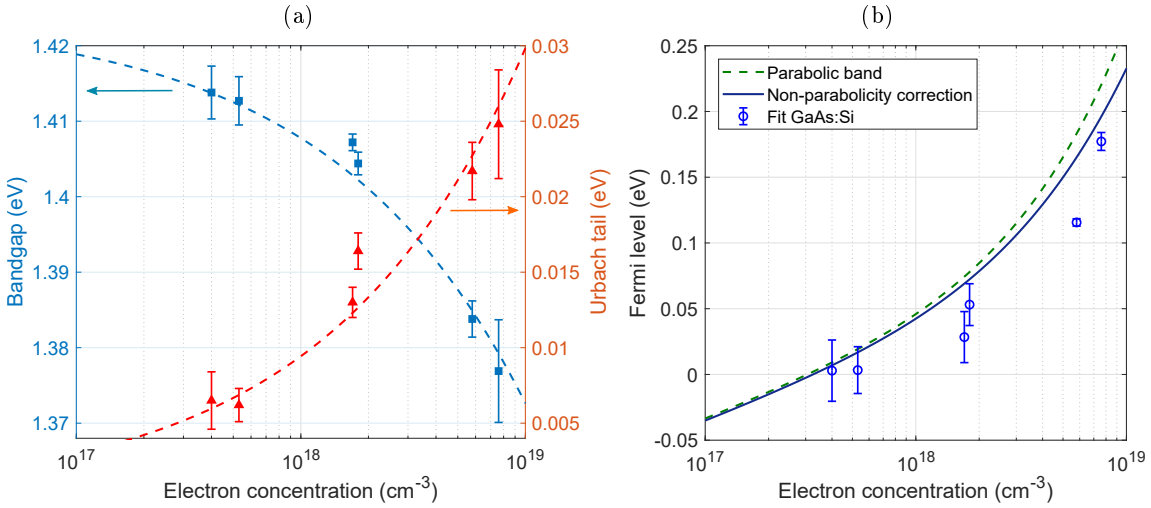

Figure 5.17 – *(a) Bandgap (squares, left axis) and Urbach tail energy (triangles, right axis) from the fit of CL spectra using the parabolic absorption model and empirical fit (dashed lines) with a power function of the electron concentration n. (b) Electron Fermi level obtained from the fit of CL spectra (circles) and theoretical curves calculated by assuming parabolic conduction band (dashed line) and non-parabolicity correction (solid line).*

described as a characteristic length scale over which carriers are generated, travel, and recombine radiatively. A large value of d indicates a long diffusion length for the minority carriers so the luminescence is produced deep in depth and the effect of re-absorption is strong. d close to zero means that the diffusion length is short and most of the CL signal comes from near the surface. An effective higher value of d may be attributed to the uncertainty of the absorption model used, or to the presence of optical resonances which favor the light out-coupling.

We also fit the CL spectra with the parameter d being set within a fixed upper bound (the thickness of the layer), and we obtain somewhat different results on the electron Fermi level E_{fc} because E_{fc}, temperature T and d all contribute to some extends to the high-energy part of luminescence spectra. The fitted parameters shown in Table 5.5 are averaged over different methods of fits concerning the uncertainties on the absorption model (parabolic or not) and on the value of d (free parameter or upper bounded by the thickness). The bandgap E_g and Urbach tail γ, which determine the spectral position and the lineshape at low energy tail, are rather insensitive to the variation of other parameters like T and d. Their uncertainties are relatively small and are mainly due to experimental variations of the CL peak position and FWHM. Electron Fermi level E_{fc} and d (characteristic length for diffusion and re-absorption) are somewhat dependent to each other, leading to higher variation ranges of fitted E_{fc}.

In Figure 5.17(a), the bandgap and the energy width of Urbach tail are plotted as a function of the electron concentration n, showing the trend of bandgap narrowing (BGN) and wider absorption tail with increasing doping concentration. The bandgap E_g (eV) can be fitted conveniently with the power function of n expressed in cm^{-3} (blue dashed line):

$$E_g\ (\mathrm{eV}) = 1.424 - 1.624 \cdot 10^{-11} \times n^{1/2}. \tag{5.32}$$

The energy width γ (eV) of Urbach tail can be fitted with the power function (red dashed line):

$$\gamma\ (\mathrm{eV}) = 9.434 \cdot 10^{-12} \times n^{1/2}. \tag{5.33}$$

In the literature, BGN values of n-type GaAs are very controversy. For example, the BGN values of n-type GaAs collected by Jain et al. [135] are extremely large (BGN up to 0.1 eV at $n = 10^{18}$ and over 0.3 eV at $n = 10^{19}$). Our results seem to be close to the calculated values of

Bennett [190]. The bandgap may vary from sample to sample depending on the growth quality and the level of dopant compensation, which may be difficult to use as a reliable quantity to assess doping concentrations. Instead, we can focus on the electron Fermi level.

In Figure 5.17(b), the electron Fermi level E_{fc} values from the fit of CL spectra (open circles) are plotted as a function of the electron concentration. The error bars show the variation of E_{fc} due to uncertainty of the absorption model and the values of d, as discussed previously. The dashed line represents the theoretical relation between electron concentration and Fermi energy in GaAs using the known parameters listed in Table 5.3 and the solid line represents the relation corrected for the non-parabolicity of the conduction band using Equation 5.19 (see details in Section 5.4.1). The non-parabolicity of the conduction band results in a lower electron Fermi level at a given electron concentration, and should be taken into account to assess doping levels. The electron Fermi levels extracted from the analysis of CL spectra are in fair agreement with the expected relation (solid line). At low doping level, it is more difficult to extract precise electron Fermi level from luminescence spectra. Still, we show that this method of analysis can provide a reasonable measure to determine the electron concentration between approximately 5×10^{17} to 1×10^{19} cm^{-3}.

5.5 Summary

In order to investigate the properties of III-V semiconductor nanowires (NWs) and to explore their potential as photovoltaic absorber, we need a characterization method able to resolve nanoscale variations. In particular, doping is a key parameter in the design and fabrication of solar cells, but the characterization of doping at the nanoscale remains challenging. We develop an alternative doping measurement by cathodoluminescence (CL). In this chapter, we validate this method by comparing Hall and CL measurements on a series of p-type and n-type GaAs thin-films of different doping levels.

In Section 5.2, we present the doping measurements of thin-film GaAs by Hall effect. In Section 5.3, we shows the CL results of the same samples measured at both room temperature and low temperature, and discusses several features observed from the CL spectra. For general III-V semiconductors, p-type doping exhibits redshift emission due to dominant bandgap narrowing (BGN), while n-type doping shows characteristic blueshift emission from the conduction band filling. In Section 5.4, we further analyze the CL spectra with the generalized Planck's law and fit the whole spectra to extract important parameters, like bandgap (p-type) and electron Fermi level (n-type). The BGN of p-type GaAs is verified: BGN (eV) $= 1.6 \cdot 10^{-8} \times p^{1/3}$, valid for the doping p in the range of approximately 1×10^{18} to 2×10^{19} cm^{-3}. For n-type GaAs, electron Fermi levels are determined from the analysis of CL spectra, and the electron concentration is related to the Fermi level through known band parameters and non-parabolicity correction. This method is effective for n-type GaAs of doping concentration in the range of approximately 4×10^{17} to 1×10^{19} cm^{-3}. CL constitutes an advanced and versatile quantitative doping assessment method which can be extended to other semiconductors and nanostructures.

Chapter

6 Characterization of III-V nanowires

Chapter content

In this chapter, we present cathodoluminescence (CL) measurements on GaAs nanowires. The study of CL has multiple purposes: visualize possible crystal defects and inhomogeneities in single nanowires (CL hyperspectral mapping), characterize the effectiveness of surface passivation (comparison of CL intensity and lifetime measurements by time-resolved CL), and assess the doping levels (analysis of CL spectra), etc. CL probes the optical properties of semiconductors at the nanoscale. Therefore, it is a very useful tool to study nanowires for photovoltaic applications and for other opto-electronic devices.

In Section 6.1, we give an overview of III-V semiconductor nanowires and describe nanowire growth by molecular beam epitaxy (MBE) carried out at C2N. We discuss some particularities of nanowires growth as compared to thin-films: shadowing effect in nanowire arrays, growth rate in axial or radial directions of nanowires, dopant flux, etc. The unique nanowire structure and growth method sometimes lead to the formation of the particular hexagonal wurtzite crystal structure of GaAs. In Section 6.2, we present CL measurements on undoped GaAs nanowires containing zinc-blende and wurtzite segments. In material science, wurtzite GaAs is not well-known and exhibits very different optical characteristics than zinc-blende GaAs. Hence, we study in detail the optical properties of wurtzite GaAs by means of polarization-resolved CL. In

Section 6.3, we show CL measurements on Be-doped GaAs nanowires and analyze the bandgap narrowing to assess p-type doping levels. In Section 6.4, Si-doped GaAs nanowires are studied and n-type doping levels are determined through analysis of CL spectra. Si dopant compensation and doped wurtzite GaAs are also discussed.

6.1 Nanowire growth

Nanowires (NWs) or nanowhiskers are free-standing nanostructures with diameters of a few tens of nanometers and lengths up to several micrometers. They can be fabricated for a wide range of semiconductors like group IV elements (Si and Ge) and III-V compounds (nitrides, phosphides and arsenides). Material fabricated in such a small size may substantially change the physical properties compared to its bulk form, due to wave optics and electronic confinement. Exploring the fundamental properties and pursuing for novel applications have motivated intense research works and development of nanotechnologies.

Figure 6.1 shows the bandgaps and lattice constants of some usual semiconductors. Epitaxial growth of high-quality materials usually requires a crystalline substrate with similar lattice parameters to avoid threading dislocations. Taking GaAs as an example, within 1% of lattice-mismatch shown as red area in Figure 6.1, there is a limited choice of materials that can be easily grown. One of the most appealing advantages of NWs is the ability to relax significant misfit strain. Figure 6.2 shows the critical thickness of a misfitting layer grown on top of a nanowhisker as a function of the whisker radius. The variations with various values of the misfit were derived from the theoretical work of Glas [191]. We can see that it is possible to grow a large misfit material without formation of dislocation using very thin NWs. This opens a great opportunity, for instance, to integrate III-V semiconductors on the silicon technology. A monolithic GaAs NW solar cell on Si bottom cell has already been demonstrated with the observation of voltage addition of the bottom and top cell and an efficiency of 11.4% [192].

6.1.1 Historical overview

It has been a long time that nanofabrication was developed and constitutes the building block of modern semiconductor industry. There are two distinct methods to fabricate a vertically aligned NW array, namely top-down and bottom-up approaches. The top-down method consists in etching a bulk layer with desire patterns defined by lithography techniques. It is already a mature technology widely used in the semiconductor manufacturing, but this approach losses the advantage of misfit relaxation previously described. The bottom-up approach, which consists in growing a NW array on a substrate, has attracted a great attention for future applications like the integration of large-scale direct bandgap III-V semiconductors on Si platform.

The main approach to grow NWs is based on vapor-liquid-solid (VLS) mechanism, which employs liquid phase catalysts for crystallization. In 1964, Wagner and Ellis reported the mechanism responsible for forming Si wiskers from liquid Au droplets [194]. VLS-grown III-V compound semiconductor NWs were investigated and novel optoelectronic devices were demonstrated in the early 2000s [195, 196]. Since then, VLS has become a common tool to synthesize almost all semiconductor NWs through rather simple procedures. The growth of GaAs NWs has been conducted using Au catalysts [197]. The metal catalysts, however, may act as unintended impurities inside the NWs and form deep levels that degrade the electrical and optical properties. The self-catalyzed method has recently been investigated to grow NWs regardless of foreign impurities from metal catalysts [198, 199]. In self-catalyst method, the droplets are formed by one of the element constituting the III-V compound itself (e.g. liquid Ga for GaAs NWs). A comparison of Au-catalyzed and Au-free self-catalyzed growth of GaAs NWs was investigated and the self-assisted method seems to produce GaAs NWs with better optical quality, concluded

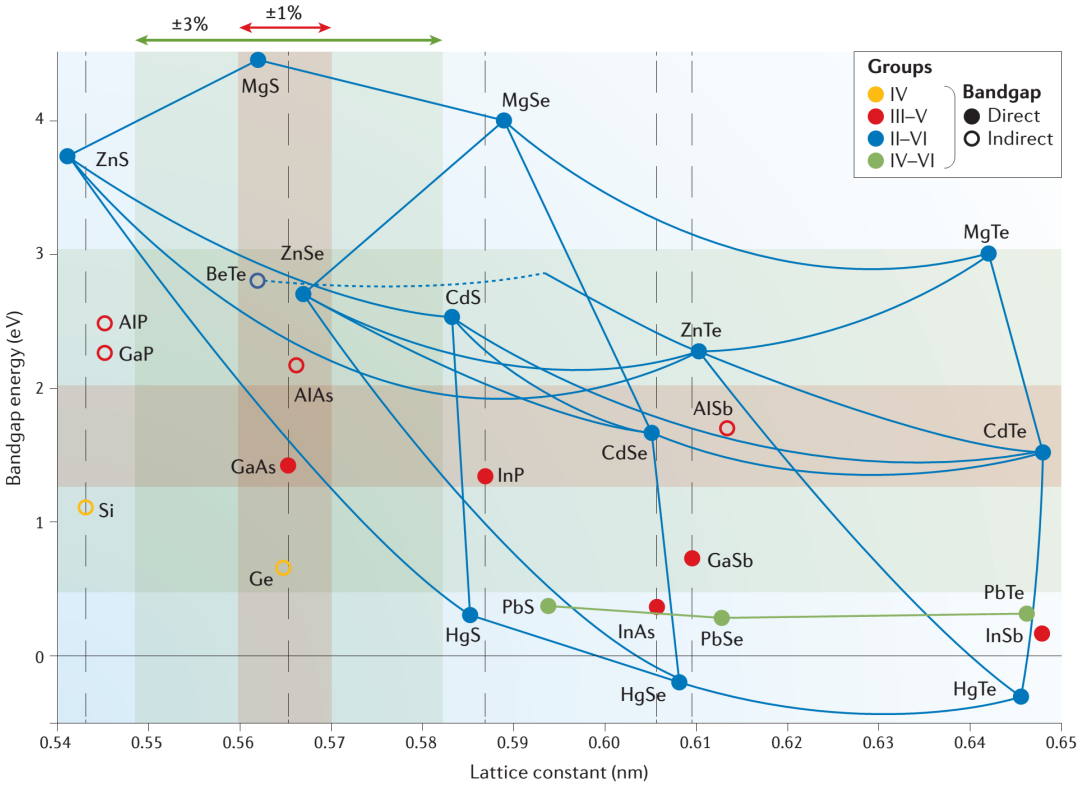

Figure 6.1 – *Bandgaps and lattice constants of several semiconductors and their alloys. Filled and unfilled circles represent, respectively, direct and indirect bandgap materials. Solid and dashed connecting lines represent, respectively, direct and indirect alloys. The five dashed vertical lines indicate commonly available substrates for epitaxial growth: Si, GaAs, InP, InAs and GaSb. The ranges of 1% and 3% lattice mismatch with GaAs are indicated by the red and green shaded areas. (Figure extracted from Ref. [193])*

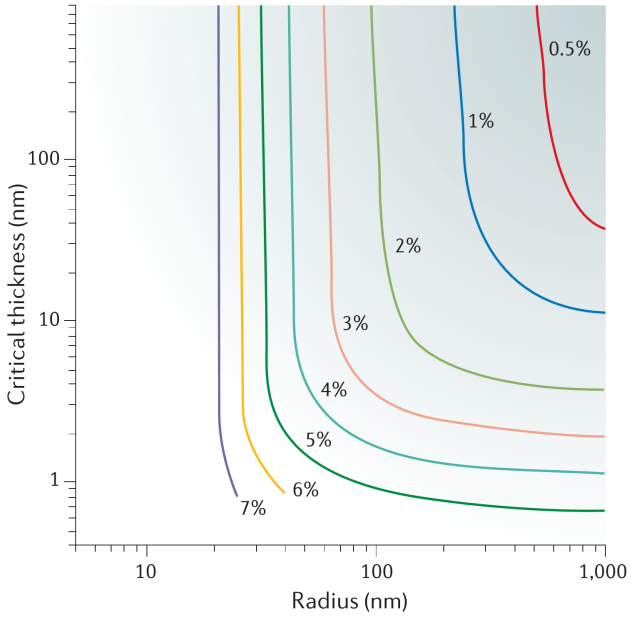

Figure 6.2 – *The critical thickness of a misfitting layer grown on top of a nanowhisker as a function of the whisker radius, for various values of the misfit given in percentage. (Figure extracted from Ref. [193] and is originated from Ref. [191])*

from the observation of a longer PL lifetime [200].

Another approach to grow NWs is catalyst-free selective-area growth. Selective-area metal-organic vapor-phase epitaxy (SA-MOVPE) is the most common technique. A mask is usually used with this method, constituting an amorphous film, such as SiO_2 and SiN_x deposited on a crystalline substrate. Opening patterns of the mask are fabricated by lithography techniques, which enables the growth of nanostructures with well-defined dimensions and positioning. However, serious problems remain in controlling the growth directions of III-V NWs and their alignment on Si. In fact, III-V zincblende crystal structure constitutes polar surfaces of (111)A (surface termination with group-III atoms) and (111)B (surface termination with group-V atoms). GaAs is preferentially grown along the <111>B direction, which enables to fabricate vertically free-standing NWs on (111)B GaAs substrate. The growth of polar III-V NWs on non-polar Si substrate appears much more delicate, and successful control of vertical GaAs NWs on Si was achieved through a careful treatment of appropriate termination of the surface [201]. The preferential direction of crystallization also depends on the growth conditions. At high temperature and low V/III ratio, GaAs is grown in the <111>B direction, forming hexagonal nanopilars surrounded by vertical {1-10} sidewalls [202]. Lowering the temperature and increasing the V/III ratio, the axial growth can be inhibited and a faster growth rate along the {1-10} facets is obtained, which enables to fabricate core-shell junctions or heterostructures in the radial direction.

6.1.2 Substrate preparation and MBE growth

We focus on III-V NWs grown on Si substrates using the self-catalyzed VLS method in a MBE reactor. The p-type (111)-oriented Si wafers were used for the starting substrates. About 30 nm thick SiO_2 films were deposited by plasma-enhanced chemical vapor deposition (PECVD). The opening patterns of the SiO_2 mask were fabricated by electron-beam lithography, which consists in a hexagonal array of holes with 500 nm array pitch and holes diameters ~50 nm (Figure 6.3(a)). The holes were obtained from a short reactive-ion etching (RIE) with SF_6/CHF_3-based gases, followed by wet chemical etching to remove the last nm of SiO_2 in dilute $HF:H_2O$ (1:100) just before loading the substrate into the MBE chamber for degassing in ultra-high vacuum. The use of gentle wet chemical etching to remove the SiO_2 in contact with the Si substrate is essential to avoid surface degradation of the underneath crystalline Si substrate, and the isotropic nature of wet etching slightly increases the hole diameters.

MBE growth was carried out in a Compact 32 system from Riber, using standard effusion cells for gallium, as well as for beryllium (p-type dopant) and for silicon (n-type dopant). Arsenic was supplied by a solid-source cell equipped with individual valve and shutter, producing either As_4 or As_2 molecules. The NW growth begins with a pre-deposition of Ga to form liquid droplets locally in the opening holes of the SiO_2 mask (Figure 6.3(b)). Ga flux was provided by heating the effusion cell, and was calibrated from reflection high-energy electron diffraction (RHEED) oscillations as to produce an equivalent GaAs planar growth rate on (001) substrates. Controlling the Ga and As flux can also be done by monitoring the beam equivalent pressure (BEP) measured by an ion gauge. Self-catalyzed GaAs NWs were grown underneath the Ga-catalyst at a temperature of about 600°C, as shown schematically in Figure 6.3(c). Typical NW diameters grown in this first step is approximately 80-100 nm. Depending on the applications, doped NWs can be grown by adding one of the dopant sources. In the axial junction configuration, the structure can be obtained by simply switching the dopant species during axial VLS-growth. In the core-shell structure, the Ga droplet was crystallized by closing the Ga shutter and exposing the sample to only As_4 flux. The shell growth was then conducted in the vapor-solid (VS) mode with continuous rotations of the substrate holder to form radial junction or surface passivation layer (Figure 6.3(d)).

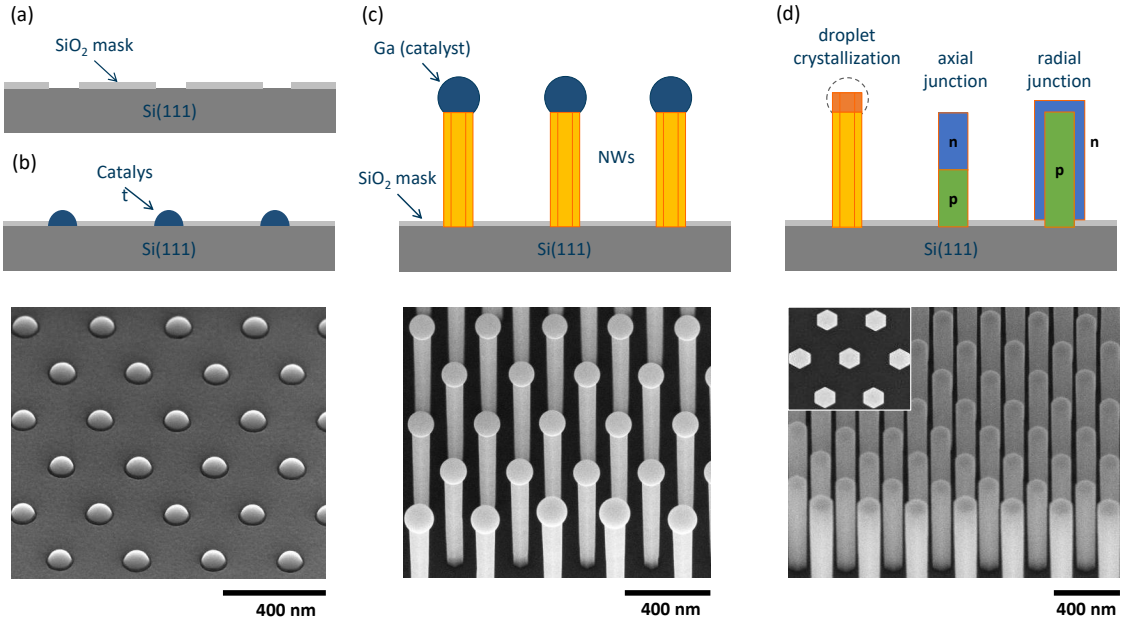

Figure 6.3 – *Substrate preparation and NW growth sequences. (a) Fabrication of SiO_2 mask on Si substrate with localized holes. (b) The opening of the mask is exposed in Ga molecular beam flux and forms localized liquid droplets. (c) NWs are promoted through the Ga liquid droplet which acts as a catalyst of nucleation. (d) Ga droplets can be crystallized then shell growth can be started subsequently. The p-n doping of the NW can be conducted during the VLS growth (axial junction) or grown in the core-shell configuration (radial junction). Selected SEM images corresponding to each step are shown under the schematics.*

6.1.3 Vapor-liquid-solid growth model

Here, we give a succinct description of the self-catalyzed VLS growth of GaAs NWs. In usual MBE thin-film growth, As-overpressure is desired to avoid surface degradation because As is the more volatile species. On the contrary, VLS-growth is conducted in Ga-rich condition to sustain a constant volume of the liquid Ga droplet. Glas et al. modeled the self-catalyzed GaAs NW growth by an As-only approach that is able to explain some experimental observations like variation of NW growth rate with As flux, temperature and NW radius [203]. A schematic for the NW grown vertically to a substrate is given in Figure 6.4(a), with the NW diameter $2R$ and a truncated sphere of radius R_d representing the liquid droplet sitting on top of the NW. The contact angle of the droplet is defined as the angle β shown on the figure. Because of the low solubilities of group V elements (other than Sb) in group III liquids, the droplet is mainly made of group III atoms, in which a small concentration of group V atoms ($\sim$1%) is dissolved.

Classical nucleation theory can be employed for the NW growth. The crystal growth cannot occur spontaneously in thermodynamic equilibrium. A supersaturation is provided from the supply of gas sources and fed into the liquid droplet. We note $\Delta\mu$ the difference of chemical potential per III-V pair between the liquid and solid phase, and the volume occupied by a III-V pair in ZB GaAs is noted ω. The formation of a spherical nucleus of radius r will decrease the free energy of the system by an amount of $(4\pi/3)r^3\Delta\mu/\omega$. On the other hand, the newly formed nucleus creates an additional surface area through which the free energy is increased by $4\pi r^2\gamma$, where γ is the effective surface energy of the nucleus. The total change in free energy is (Figure 6.4(b)):

$$\Delta G = -\frac{4\pi}{3}r^3\frac{\Delta\mu}{\omega} + 4\pi r^2\gamma. \tag{6.1}$$

The free energy change presents a maximum value of ΔG^* at the critical radius $r^* = (2\omega\gamma)/\Delta\mu$.

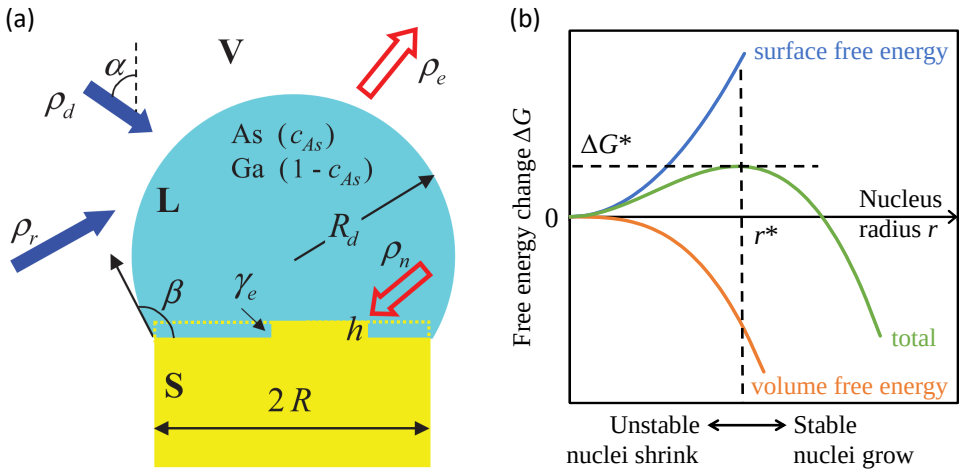

Figure 6.4 – *(a) schematic illustration for the VLS method in NW growth (extracted from Ref. [203], see text for symbol definitions). (b) Diagram of Gibbs free energy versus the nucleus radius. The blue curve represents the increase of the free energy due to newly created surface, and the orange curve represents the decrease of the free energy by forming solid crystal. The total change in free energy of the system is plotted with green curve. r^* is the critical radius of the nucleus and ΔG^* is the nucleation barrier.*

For $r < r^*$, the nucleus can lower the free energy by reducing its size (unstable). For $r > r^*$ the nucleus can be grown (stable). The maximum of free energy change at the critical radius is called the nucleation barrier. If the supersaturation increases, the critical radius and the nucleation barrier decrease. This increases the rate of formation of stable nuclei.

When looking back into the structure of VLS-grown NWs, it is suggested that, once a nucleus of critical size forms at the liquid-solid interface, it rapidly spreads out laterally over the whole interface unless the NW is very wide. Since the lateral growth does not create any new interfaces, the nucleation barrier is zero. This fast completion of monolayers is known as the step flow growth. Glas et al. proposed a theoretical model for the nucleation at the triple phase line in Au-assisted growth of GaAs NWs, and explained the occurrence of wurtzite phase due to substantial surface energies of different crystal phases entered in play [204]. For the self-catalyzed growth, the formation of the ZB structure suggests that nucleation occurs not (or not only) at the triple phase line but anywhere else on the top facet of the NW [205]. The complete thermodynamic model of the NW growth remains a delicate subject due to large amounts of unknown material parameters like surface energies and due to various growth parameters (temperature, flux etc.).

In the picture of an ensemble of NWs, the growth of an individual NW may also be affected by its environment. This complication makes the modeling of NW growth extremely difficult. In general, Ga atoms have a high diffusion length and thus the mass transport of Ga at a certain temperature may be important for the NW morphology and is responsible for the growth selectivity of on the mask. On the other hand, the diffusion of As can be ignored, while the evaporation must be taken into account. Direct beam of As_4 is not sufficient to explain experimental observation of NW elongation rate, and re-evaporation of As from the substrate and from neighbor NWs can act as an efficient secondary arsenic source [207].

For a dense NW array, the shadowing from neighboring NWs may influence the local growth conditions. Statistical computations can help to understand the shadowing effect, as illustrated for a periodic hexagonal array of NWs [206]. In this model (Figure 6.5(a,b,c)), Ga atoms are traced statistically and the final hit density is shown either on the mask or on the NW sidewalls. The shadowing of the NW sidewalls depends on the NW height and diameter compared to the array period, and also on the orientation of the incident beam to the substrate normal. For a long NW, sidewall shadowing is due to the nearest neighbors, and even to the second, and the third nearest neighbors etc. This effect may have significant impact on the shell growth.

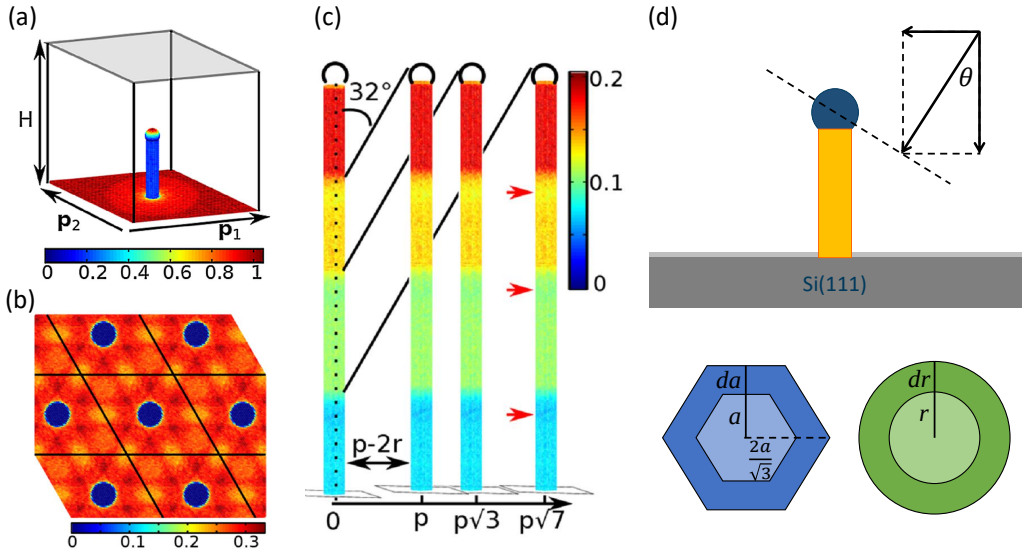

Figure 6.5 – *(a,b,c) Simulation of the impinging Ga flux. All color bars are normalized so that unity is the reference 2D-growth hit density (extracted from Ref. [206]). (a) Schematics of the rhombic unit cell used for the numerical computations. Here the short NW only shadows the surrounding surface of the mask but not its neighbor NWs. (b) Example of hit pattern resulting from the complex shadowing of the mask by several NWs. The unit cell is replicated to better show the hexagonal symmetry. (c) Illustration of the shadowing of the NW sidewalls by several neighbor NWs located at different distances. The Ga incident beam is inclined at 32° from the substrate normal. Red arrows mark the deeper shadows caused by the droplets with contact angle 135°. (d) Schematics of an isolated NW and a incident beam inclined with an angle θ to the substrate normal. Bottom: hexagonal cross-section of a core-shell NW and a simplified picture of concentric circles.*

We describe in the last part some different features of growing NW shells compared to usual growth of planar thin-films. As shown in Figure 6.5(d), an incident beam is inclined with an angle θ to the substrate normal. Only direct beam is considered here, re-emission and shadowing effect cannot be evaluated without rescue for numerical simulation. Since the substrate is in continuous rotation, the incident beam can be seen to rotate with respect to the NW axis. Although NW has a hexagonal cross section, we consider its equivalent circle (equal surface area) of diameter r for simplicity. During a short time dt, the shell is grown with thickness dr. We note ϕ [atoms/(s.cm^2)] the atomic flux and $\phi\cos(\theta)$ corresponds to the flux normal to the substrate. We call ω the volume of a III-V pair. The 2-dimensional thin-film growth rate V_{2D} [cm/s] is related to the incident flux:

$$V_{2D} = \omega\phi\cos(\theta). \tag{6.2}$$

For shell growth, the situation is a little different: only the projection of the direct beam normal to the NW sidewalls is effective, and the amount of atomic flux intercepted by the NW sidewalls is proportional to the NW diameter. For an isolated NW, the shell growth rate V_{shell} [cm/s] can be written:

$$V_{shell} = \frac{dr}{dt} = \omega\frac{2r\phi\sin(\theta)}{2\pi r} = \frac{\tan(\theta)}{\pi}V_{2D}. \tag{6.3}$$

We can see that V_{2D} and V_{shell} differ by a factor $\tan(\theta)$, corresponding to the inclined direct beam. V_{shell} is further reduced by a factor π due to the higher surface-to-volume ratio. To evaluate the crystal growth rate, the direct beam entered in play should correspond to the limited species, i.e. Ga flux in As-overpressure condition. In this case, θ(Ga) is 32° in our MBE machine and V_{shell} is reduced by a factor 0.2 to V_{2D}, which coincides to the simulation of hit density on the top NW sidewalls (Figure 6.5(c)).

This consideration should also be applied for the impurity dopant flux in order to evaluate a theoretical doping concentration in NWs. In our MBE machine, θ(Si) is 35° and θ(Be) is 16°. In absence of re-emission and shadowing, Si impurity concentration should be similar in the shell region or in the equivalent 2D layer, while Be impurity concentration may scale differently in shell as in equivalent 2D layer due to a distinct orientation angle (see Be-doping in Section 6.3 and Si-doping in Section 6.4).

6.2 Undoped GaAs nanowires and wurtzite phase

In this section, we focus on undoped GaAs NWs. By accident, we found a clear hexagonal wurtzite phase in GaAs NWs. Wurtzite GaAs is not a well-known material and exhibits very different optical properties than zinc-blende GaAs. For example, the fundamental optical transition in wurtzite GaAs is polarized perpendicularly to the NW axis. Wurtzite GaAs may have a different bandgap than zinc-blende GaAs and forms a heterostructure of unknown conduction band and valence band offsets with zinc-blende GaAs. It is thus interesting to investigate wurtzite GaAs and to understand its fundamental properties. Firstly, we compare the solid-state physics of wurtzite and zinc-blende crystal structures in order to have a clear overview of optical properties of wurtzite GaAs studied in the literature. Subsequently, we present our polarization-resolved CL measurements and compare our results to the up-to-date understanding of wurtzite GaAs.

6.2.1 Wurtzite GaAs properties

Atomic structures

Many III-V compounds form a cubic zincblende (ZB) crystal structure in bulk or thin films (GaP, GaAs, InP, InAs, etc.). They may adopt a hexagonal wurtzite (WZ) structure when grown in the

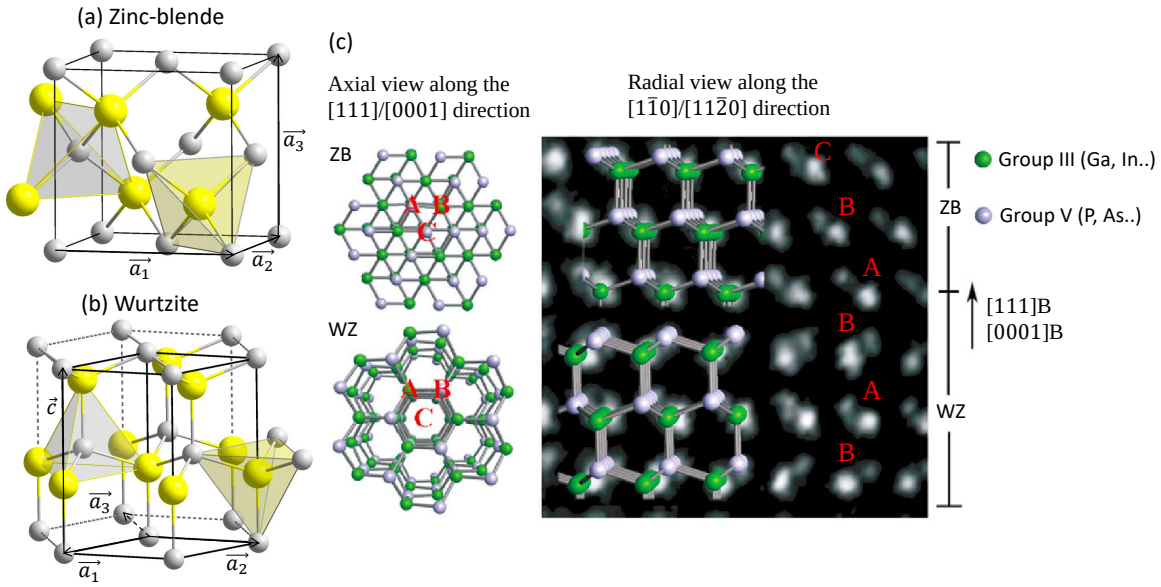

Figure 6.6 – *Atomic lattice structure of (a) cubic zincblende (ZB) and (b) hexagonal Wurtzite (WZ) crystals. The conventional unit cell is emphasized with black contour lines and a set of translation vectors are indicated. (c) The ZB and WZ crystal structures in III-V NWs, view along the axial [111]/[0001] growth directions and radial [1-10]/[11-20] crystal directions. The background of the radial view is a high-resolution high-angle annular dark field (HAADF) scanning TEM image of InAs NW (adapted from Ref. [210]).*

NW form. Generally, ZB/WZ polytypism coexists in single NWs. Due to the different symmetry of the lattice structure, WZ and ZB crystals may exhibit dramatic differences in their optical and transport properties. For example, GaP is an indirect-gap semiconductor, the band structure was predicted to become direct-gap in the WZ form and was investigated experimentally [208, 209]. This transformation into direct bandgap is also expected for crystalline Si and Ge, which has attracted considerable attention owning to their potential photonic application. Many efforts have been devoted to study fundamental material properties in the WZ form, which are still not well understood.

Figure 6.6(a,b) shows the atomic structure of ZB and WZ crystals. III-V ZB crystal structure is built based on the face-centered cubic (FCC) system: one type of the III-V atoms (Ga for example) occupies the FCC lattice points, then the other type of atoms (As) occupies one half of the tetrahedral sites. It can also be thought as a FCC lattice of As atoms inserted into the FCC lattice of Ga atoms, with a shift by 1/4 of the cubic diagonal. In this arrangement, each atom has 4 nearest atoms of opposite type (tetrahedral coordination). Figure 6.6(a) indicates three independent translation vectors $(\vec{a_1}, \vec{a_2}, \vec{a_3})$, forming an unit cell of the lattice structure (not primitive). For GaAs, the lattice constant is referred to the size of this unit cube. Its value is $a = 5.65325\ \mathring{A}$ at 300 K deduced from X-ray diffraction experiments [35].

On the other hand, III-V WZ structure belongs to the hexagonal crystal family. The atomic arrangement can be constructed as follows: group III atoms occupy the hexagonal close-packed (HCP) lattice points, then group V atoms fill one half of the tetrahedral sites (see Figure 6.6(b)). The group V atoms can also be seen to form a HCP lattice, and view together, each atom is surrounded by four atoms of the other type. The only difference with ZB structure is the placement of the third nearest neighbors. The conventional unit cell is defined as a vertically oriented prism, with the base vectors $(\vec{a_1}, \vec{a_2})$ of equal length a and forming 120° angle. Owing to a 3-fold symmetry, a third vector $\vec{a_3}$ contained in the same horizontal plane is often included for convenience. The height of the unit cell is defined by the vector $\vec{c}$. In the ideal HCP structure, the following relation holds: $c = 2\sqrt{2/3}\,a$. Four Miller indices (i, j, k, l) are used to designate

crystal planes or directions in connection with the set of translation vectors $(\vec{a_1}, \vec{a_2}, \vec{a_3}, \vec{c})$. Seen from a macroscopic scale, we can note that the partly ionic III-V bounds built up an electric dipole along the c-axis, and cancel out in the directions perpendicular to the c-axis. This is why wurtzite crystals (e.g. GaN) possess piezoelectric property. For WZ GaAs, uniaxial stress is indeed a critical factor that can modify greatly the material property, as demonstrated in theoretical calculations [211] and in experiments [212].

Now looking along the ZB [111] and WZ [0001] directions, which is the general NW growth axis, both ZB and WZ can be constructed using hexagonal close-packing atomic planes (see Figure 6.6(c)). ZB has a stacking sequence of ABCABC... where A, B, and C denote three monolayers of different positions seen from the top, while WZ has a stacking sequence of ABAB... where every two monolayers are at the same position. The lattice parameters of WZ GaAs obtained by powder diffraction at ambient pressure and 300 K are $a = 3.989\,\mathring{A}$ and $c = 6.564\,\mathring{A}$, corresponding to a c/a ratio of 1.6455 (slightly larger than the close-packing limit $2\sqrt{2/3} = 1.6330$) [213]. These values are slightly different from the corresponding ZB part: $a_{(110)} = 3.9975\,\mathring{A}$ and $c_{(111)} = 6.5278\,\mathring{A}$. As a consequence, strain may be induced in GaAs ZB/WZ heterostructures. Indeed, from Raman spectroscopy, the ZB phonon modes are shifted to lower wave numbers for NWs with high percentage of WZ phase. This indicates that in regions where WZ dominates, ZB sections are under tensile strain, and WZ segments are compressively strained in regions with mainly ZB phase [214].

Growth

The control of WZ phase in GaAs NWs has been studied and it appears to be a difficult task. It mainly occurs in Au-catalyst VLS growth of GaAs NWs, depending on the growth conditions such as the temperature and V/III ratio [215]. It is more likely to be observed in NWs of small diameters. The smaller surface energy in WZ phase compared to ZB phase may explain this trend [216]. The VLS growth and polytypism of III-V NWs was modeled based on thermodynamic considerations [204, 217]. One of the important parameters is the contact angle of the liquid droplet, which results from the equilibrium at the triple phase point, where the nucleation is triggered. In-situ TEM imaging in a MOCVD reactor was used to visualize the real-time NW growth and confirmed the existence of a critical contact angle of the droplet [218]. ZB GaAs is formed at large contact angle (low V/III ratios), while WZ is preferential at smaller contact angle (high V/III ratios). Therefore, the control of ZB and WZ phase can be achieved by simply tuning the V/III ratio at a given temperature. For self-catalyzed MBE growth, the critical droplet contact angle was found to be 121° according to the in-situ TEM imaging system in the framework of NANOMAX French research project. It was also visualized that the formation mechanisms of the two crystal phases differ singularly: WZ monolayers grow by slow and continuous step flow on a flat top facet; ZB monolayers appear incrementally and concomitantly with a truncation of the nanowire top facet. With both theoretical and technological efforts, the growth control of pure ZB and WZ crystal phase is becoming possible.

Electronic band structure

Owing to the specific periodic arrangement of atoms, the band structures of WZ semiconductors present remarkable differences with the ZB counterparts. Theoretical calculation of the band structure is performed by different approximation and computation techniques. Figure 6.7 shows an example of simulation for GaAs ZB and WZ band structures from Ref. [219] using quasiparticle computations within the local density approximation, including spin-orbit interaction. The horizontal red dash lines indicate the branch-point energy level, which is the reference level corresponding to the energy at which the band states change their character from predominately acceptor-like states to mostly donor-like states. This is an important reference especially in the

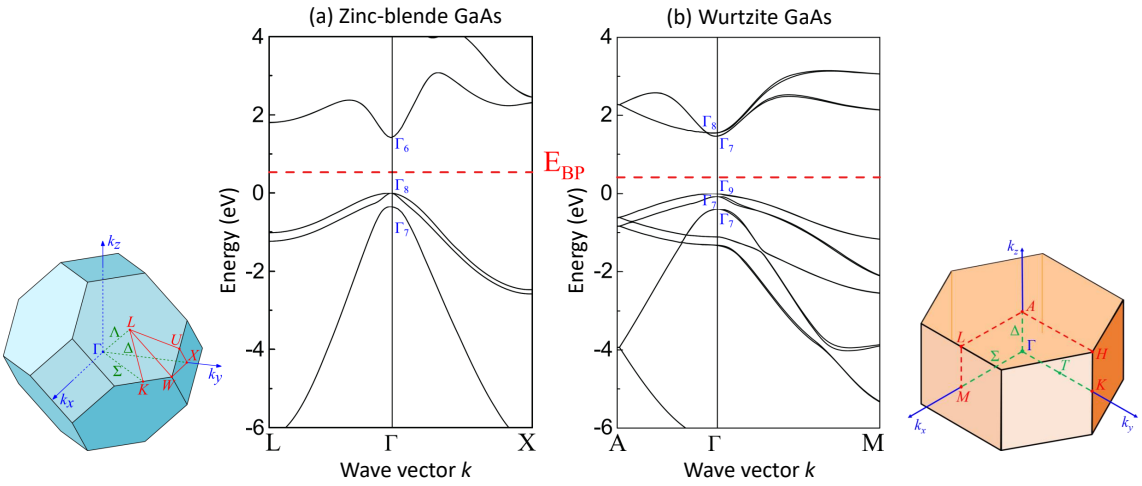

Figure 6.7 – *Calculated band diagram of (a) zincblende GaAs and (b) wurtzite GaAs near the* Γ *point (extracted from Ref. [219]). The branch-point energy is indicated by a horizontal red dashed line. The first Brillouin zone for the two lattices is shown, indicating important high-symmetry points.*

prediction of band offset between ZB and WZ heterostructures. The first Brillouin zone of cubic ZB structure and of hexagonal WZ structure are also shown in Figure 6.7 to have a clear image of high-symmetry points and directions in the reciprocal space.

Figure 6.8 presents a simplified picture of the ZB and WZ GaAs band structure near the zone center of reciprocal space (Γ point) that is important for optical properties. Without complicated computation, we can still recognize some important features in the band structure using basic group theory on symmetry operations. The textbook of Klingshirn explains very well the implication of group theory in semiconductor optics [15]. With the Schoenflies notations, the ZB structure belongs to the T_d group (symmetry of a tetrahedron including improper rotation operations) and the WZ structure belongs to the C_{6v} group (6-fold rotation axis with the addition of 6 mirror planes parallel to the rotation axis). The ZB GaAs was well studied in the past, and it is known that the highest valence band consist of degenerated heavy-hole and light-hole bands. The split-off valence band arises from the spin coupling with the atomic p-state of the hole wavefunction.

For WZ structure, the length of the unit cell along the c-axis is doubled compared to the one of ZB along the equivalent [111] direction. Hence, the reciprocal L point in ZB is zone-folded to the Γ point in WZ, giving rise to a supplementary conduction band close to the ZB-like conduction band. Therefore, indirect gap ZB materials with an L valley conduction-band minimum would be expected to have a direct gap in the WZ phase unless the energy of state was significantly shifted by the crystal potential [220]. At top of the valence band, the p-orbital splits from the hexagonal crystal field and from the spin-orbit coupling. The irreducible representations of each band are also indicated on the band diagrams. Figure 6.8(c) depicts the dipole transitions perpendicular (red) or parallel (blue) to the c-axis in WZ structure. Since the dipole operator transforms in C_{6v} like Γ_1 for $\vec{E} \parallel \hat{c}$ and like Γ_5 for $\vec{E} \perp \hat{c}$ [15], the transition between the initial valence band state and the final conduction band state is interpreted by the multiplication table of the group C_{6v}. One of the remarkable features is that the dipole interaction for the $\Gamma_{9V} - \Gamma_{7C}$ and $\Gamma_{9V} - \Gamma_{8C}$ transition is forbidden in the direction parallel to the c-axis. This selection rule predicts the absorption (thus emission) of photon is polarized perpendicular to the NW c-axis.

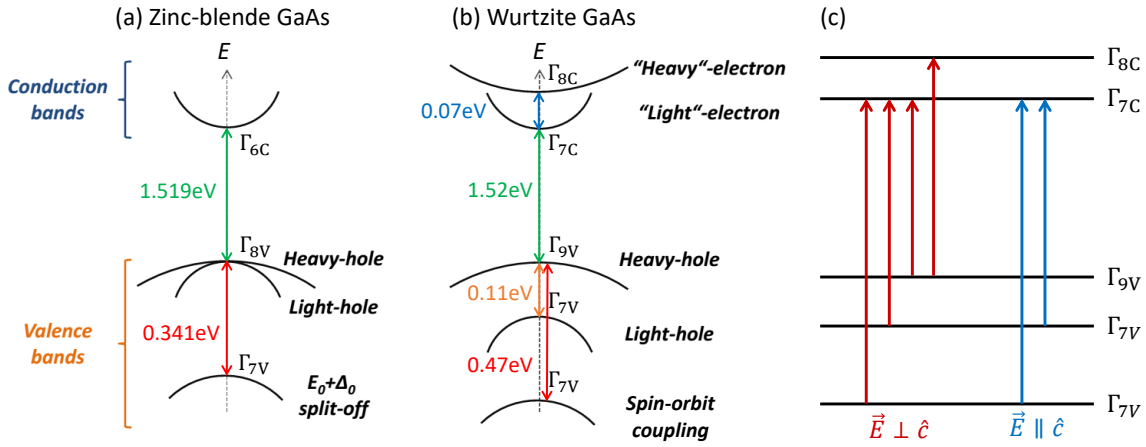

Figure 6.8 – *Simplified band diagram near the zone center for (a) ZB GaAs and (b) WZ GaAs (Figure adapted from Ref. [221]). The symmetries of the irreducible representations Γ_i are given. Band parameters of ZB GaAs are well known, while those of WZ GaAs are less certain. A selection of plausible values is indicated (see Table 6.1 for details). (c) Permitted dipole transitions in the WZ semiconductors.*

Bandgap of WZ-GaAs

Although the group theory helps to predict whether transitions are permitted or not, it cannot tell the magnitude of the matrix elements, neither does the energy level separation nor the band ordering. Theoretical work on WZ GaAs hardly predicts the precise bandgap, and even a contradictory conduction band ordering of the Γ_{7C} and the Γ_{8C} exists [219, 220]. The reported experimental bandgap values are also diverging from different publications. Photoluminescence (PL) and Raman spectroscopy are the most commonly used technique to probe the electronic transition levels in a novel material system. PL measures the light spectrum due to the radiative band-to-band recombination. Photogenerated carriers are generally thermalized to the band edge, thus the spectral position of PL should give an indication of the transition levels. However, the exact bandgap may be hindered by the residual of impurities or native defects, which introduces unknown donor or acceptor-like energy levels in the bandgap. Defect luminescence may govern especially at low temperature.

For ZB GaAs, low-temperature PL of sharp free exciton line at 1.515 eV is well known and is an indication for high-purity crystal. For WZ GaAs NWs, exciton line at 1.544 eV has been reported from 4 K PL measurement on an ensemble of WZ-rich GaAs NWs [222, 223]. PL emission of up to 50 meV above the ZB GaAs bandgap has also been observed in WZ GaAs NWs depending on growth parameters [224]. However, quantum confinement in both small radius and axial ZB/WZ heterostructures or stacking fault can not be totally excluded [225]. Other research groups reported exciton ground state recombination of WZ GaAs NWs of 1.522 to 1.524 eV from 10 K PL measurement, only slightly higher than ZB free exciton [226]. By careful control of the crystal purity, WZ GaAs NWs of few stacking faults and of larger diameter (about 110 nm) have been grown by Au-catalyst method and show low-temperature free exciton line at 1.515 to 1.516 eV, with relatively small FWHM of 4 to 6 meV [225, 227]. Ahtapodov et al. shown that the same NW exhibits low-temperature exciton line at 1.516 eV and PL peak energy of 20 meV above that of ZB counterpart at room temperature [225]. Lu et al. also measured up to 4 ns of PL decay time at 4.5 K for WZ GaAs NWs passivated with an AlGaAs shell [227].

On the other hand, Raman spectroscopy probes the phonon modes from the inelastic scattering of light. Resonant Raman spectroscopy is a variant in which the energy of the excitation light is varied. When the energy of the incident light approaches an interband transition of a semiconductor, real electronic states may mediate the thereby enhanced scattering process [221].

Table 6.1 – *Band parameters of ZB and WZ GaAs near 0 K. All effective masses are given in units of the free-electron mass m_0. ZB GaAs parameters are collected according to Blakemore [35]. WZ calculation is extracted from Ref. [229]. The calculated bandgap of WZ GaAs may be underestimated and is actually 0.032 eV larger than that of ZB GaAs calculated using the same method. The masses are evaluated along the directions ΓA ($m_\parallel$), and ΓM ($m_\perp$) in the hexagonal Brillouin zone. Data of WZ experiments are collected from various works in the literature.*

GaAs	ZB	WZ calculation			WZ experiment
Bandgap E_g [eV]	1.519	1.453 (ZB+0.032)			
Free exciton [eV]	1.515	–			1.515-1.524 [221, 226, 230]
Spin-orbit coupling Δ_{so} [eV]	0.341	0.348			0.47 [221]
Crystal-field splitting Δ_{cf} [eV]	0	0.129			0.11 [231]
Valence band offset [eV]	–	0.117			0.115 [232]
Conduction band offset [eV]	–	0.149			0.115 [232]
Electron effective mass m_e^*	0.067		Γ_{8C}	Γ_{7C}	$\mu_\parallel = 0.057$ [231] $\mu_\perp = 0.052$ [231]
		$m_\parallel$	0.17	0.08	
		$m_\perp$	0.09	0.11	
Heavy hole effective mass m_{hh}^*	0.51		Γ_{9V}		0.45 [232]
		$m_\parallel$	0.96		
		$m_\perp$	0.16		
Light hole effective mass m_{lh}^*	0.082		Γ_{7V}		
		$m_\parallel$	0.12		
		$m_\perp$	0.12		
Split-off valence band m_{so}^*	0.154		Γ_{7V}		
		$m_\parallel$	0.11		
		$m_\perp$	0.09		

The similar technique used in PL is the PL excitation (PLE). Absorption and radiative emission is enhanced when the energy of the laser excitation matches the interband transitions. As a consequence, information on the electronic band structure can be obtained by finding the conditions leading to resonant enhancement. Table 6.1 lists some important parameters of ZB and WZ GaAs. The effective masses are spherical equivalent values, which can interpret fairly well many observable properties. WZ GaAs calculations are extracted from the work of Bechstedt and Belabbes [229]. We should note that the density-functional theory usually underestimates the fundamental gap, and the calculated WZ bandgap is actually 32 meV higher than the calculated ZB bandgap using the same method.

ZB/WZ heterostructure

Beside the unknown WZ GaAs bandgap, ZB/WZ heterostructure is believed to form a type II band alignment where electrons are confined in the ZB part and holes in the WZ region [233]. PL spectra of NWs containing a mix of ZB and WZ phases usually exhibit complex and redshift peaks compared to the bandgap of both pure ZB and WZ phase [234]. The large redshift is explained from the spatially indirect recombination of electrons and holes. This mechanism was evidenced using CL mapping in polytypic GaAs NWs, where low-energy CL peaks are found to localize only in certain regions of the wire [235, 236]. These early studies attempted to assess the band offset between the ZB/WZ heterostructures by fitting PL results with the calculated confined energy levels. The difficulties arise from the unknown WZ bandgap and complicated crystal phase mixing in NWs. In a more recent work from Vainorius et al., the authors precisely controlled the crystal phase and thickness of a single quantum-dot inside the GaAs NWs [232]. Either ZB insertion in WZ NW or WZ insertion in ZB NW was fabricated for TEM and PL

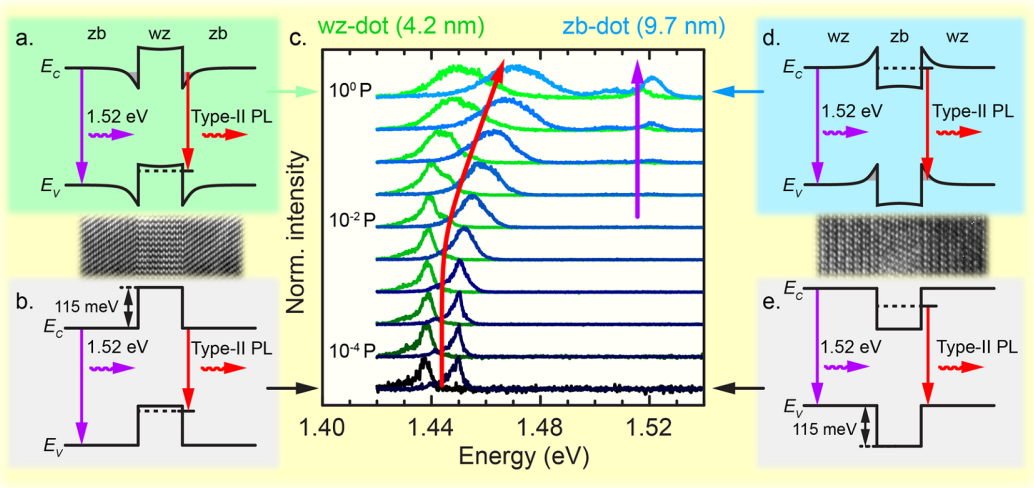

Figure 6.9 – *Band diagram of a WZ GaAs nanodot (a,b) embedded in a ZB GaAs NW, and of ZB GaAs nanodot (d,e) embedded in a WZ GaAs NW, along with representative high-resolution TEM images. (a,d) and (b,e) depict the band diagram at high and low excitation power respectively. (c) PL spectra of both type of dots as a function of excitation power density. The green traces correspond to a WZ-dot and the blue traces to a ZB-dot. (Figure extracted from Ref. [232])*

characterization. Figure 6.9 shows the schematics of band alignment and the PL results for both confinement structures. PL spectra shift to higher energy with increasing excitation power due to state filling in the quantum confined structure. Emission from the host material of NW is visible under high power excitation. The ground state of the transition energy was extracted from the PL spectra with lowest excitation power, for a series of samples with various thicknesses of the quantum-dot. The authors then extracted, though approximately, the band offsets and hole effective mass in WZ GaAs.

De Luca et al. performed another PL experiment with applied magnetic field parallel or perpendicular to the NWs. The quantitative analysis of the diamagnetic shift of the PL emission as a function of the applied magnetic field allows the determination of the exciton reduced mass, for the exciton motion in planes perpendicular ($\mu_\perp = 0.052\, m_0$) and parallel ($\mu_\parallel = 0.057\, m_0$) to the c-axis of the WZ lattice [231]. This study pointed out that the measured exciton reduced mass should accompany a ZB-like small electron effective mass, thus the lowest conduction band should possess ZB-like Γ_7 symmetry. It seems to resolve the long-time debating issue: whether the WZ GaAs lower conduction band is the Γ_7 or Γ_8 symmetry. If it were the contrary, electron mobility in WZ GaAs would be largely reduced and electron filling in highly n-doped WZ GaAs would not be expected (see 6.4 for more details).

6.2.2 CL measurements

For all CL measurements presented in this chapter, NWs were dispersed on a Si substrate in order to scan along the wire and to check eventual inhomogeneities. Single NWs were excited by electron beam with 4-6 kV acceleration voltages and impinging currents in the range of about 0.2 to 0.7 nA (see Chapter 3.4 for the detailed experimental setup). Figure 6.10(a) shows a schematic of the typical configuration of an electron-beam exciting a horizontally lying NW (here the NW has a core-shell structure). Figure 6.10(b) gives an example of a NW on a Si substrate and the illustration of light polarized parallel or perpendicular to the NW growth axis of ZB-(111) or WZ c-axis.

In general, unpassivated GaAs NWs have very low luminescence efficiency due to inherent surface states that act as efficient non-radiative recombination centers and leads to Fermi level

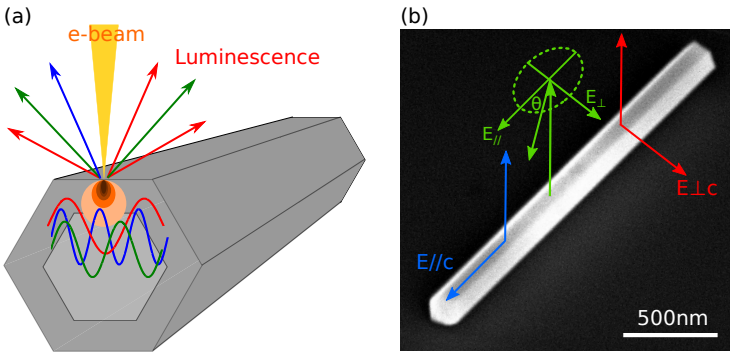

Figure 6.10 – *(a) Illustration of the electron beam interaction with a core-shell NW and luminescence emission. (b) Example of a tilted SEM image of a NW transferred on a Si substrate and orientation showing the polarization of light. Illustration for emission of light polarized parallel (blue) or perpendicular (red) to the NW (111)/c-axis. Generally, we decompose the electric field into a parallel $E_{\parallel}$ and a perpendicular $E_{\perp}$ components.*

pinning even under electron-beam or laser excitation. With decreasing NW diameter, the surface effect becomes more and more pronounced and a critical diameter of about 130 nm was found, below which the PL intensity dropped considerably [237]. We have observed the same trend so that only passivated NWs showing significant CL signal will be presented here. For passivation, AlGaAs shell was chosen since it is nearly lattice-matched with GaAs regardless of the Al ratio.

Meanwhile, at fix growing conditions, we systematically observed in our NWs an unintentional WZ segment appeared at the top of the wire. Figure 6.11 shows (a) an SEM image of a GaAs NW array as-grows on a Si substrate, (b) an STEM image of a dispersed NW and (c) TEM study of the atomic structure of a NW from this sample. The NWs consist of nearly 1 μm long pure ZB at the NW base, a transition region containing a mix of ZB/WZ phases or stacking faults at the middle-top, and a 300 nm long pure WZ segment at the top. At the very end of the wire, stacking faults appear and turn to be ZB dominated again. The crystal phase switching can be explained by the contact angle of the catalyst droplet [204, 218]. The WZ phase appears when the contact angle decreases, corresponding to the beginning of the crystallization step when the Ga flux was stopped. When the contact angle shrinks below a critical value, the crystal phase turns to ZB again. This ZB/WZ/ZB structure was also found in other wires of the same sample, as well as other samples using identical growth parameters.

CL mapping

Figure 6.12 presents the results from CL measurement at 10 K, with 6 kV acceleration voltage and impinging current about 260 pA, and Figure 6.13 gives the corresponding CL measurement at room temperature (similar NW of the same sample). CL measurements are systematically displayed with the corresponding SEM image for morphology inspection, CL integrated intensity with a color bar showing the recorded signal from our CCD camera (counts per second, intensity integrated over the whole wavelength range in nm). CL spectra extracted along the NW growth axis and normalized by the maximum intensity are displayed in a vertical sequence. The CL peak position energy and FWHM are automatically computed for the NW region. From the CL maps, the top region of the NW with a distinct CL characteristic can be recognized, corresponding to a pure WZ segment as show from previous TEM images.

At low temperature, carrier diffusion is reduced, thus we expect that the CL spectra recorded when the electron beam excites ZB or WZ region correspond mainly to the emission from the same region. CL characteristics are fairly constant in the respective ZB or WZ part, indicating a high-purity crystal phase in the two regions. Except for the transition region at middle-top of the wire, CL broadening to low-energy side can be seen. As well as at the very ends of the wire,

(a) SEM

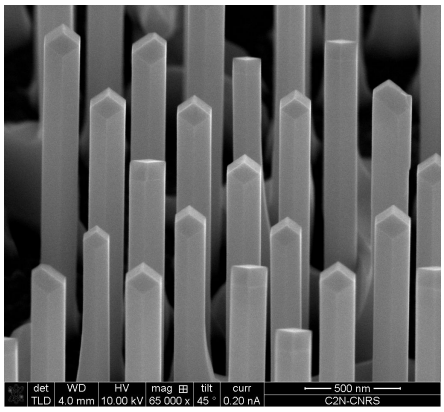

(b) STEM

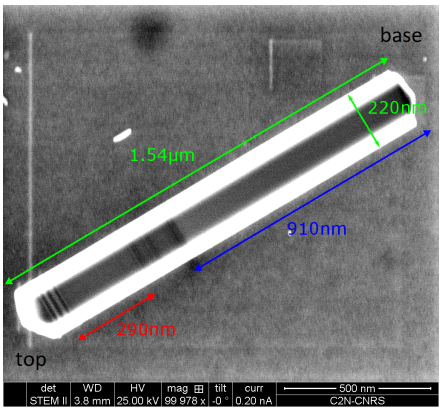

(c) TEM

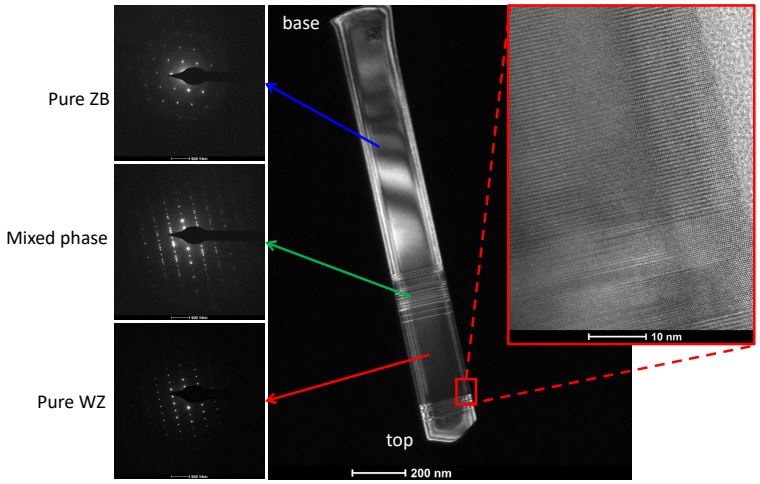

Figure 6.11 – *Electron micrographs of undoped GaAs NWs with an AlGaAs shell (sample 76715). (a) Tilted SEM image of as-grown GaAs NWs on Si(111) substrate. (b) STEM image of a typical GaAs NW containing two clear regions of about* 910 nm *and* 290 nm *in length. (c) Dark field TEM micrograph and electron diffraction patterns showing a ZB structure at the base of the wire and a short WZ segment at the top of the wire. Inset shows a HAADF high-resolution TEM image of the top of the WZ section, where the crystal structure turns to ZB at the very top of the wire.*

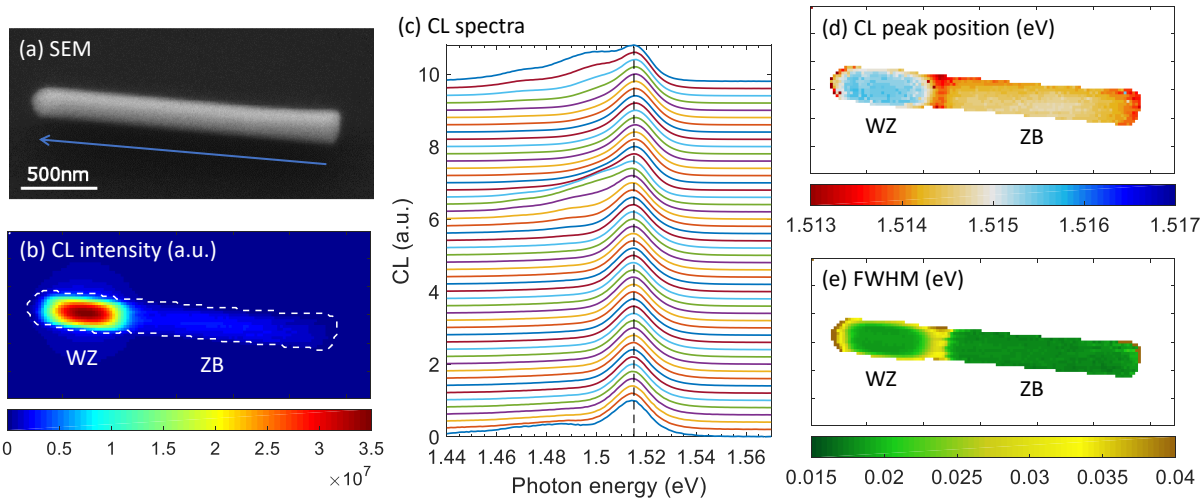

Figure 6.12 – *CL maps of an undoped GaAs NW with an AlGaAs shell (sample 76715) measured at low temperature (10 K). (a) SEM image with an arrow showing the growth direction. (b) Integrated CL intensity map. (c) CL spectra extracted from the bottom to the top of the NW. The vertical dashed line indicates the* 1.515 eV *position. (d) Map of the CL peak position energy. (e) Map of the CL FWHM.*

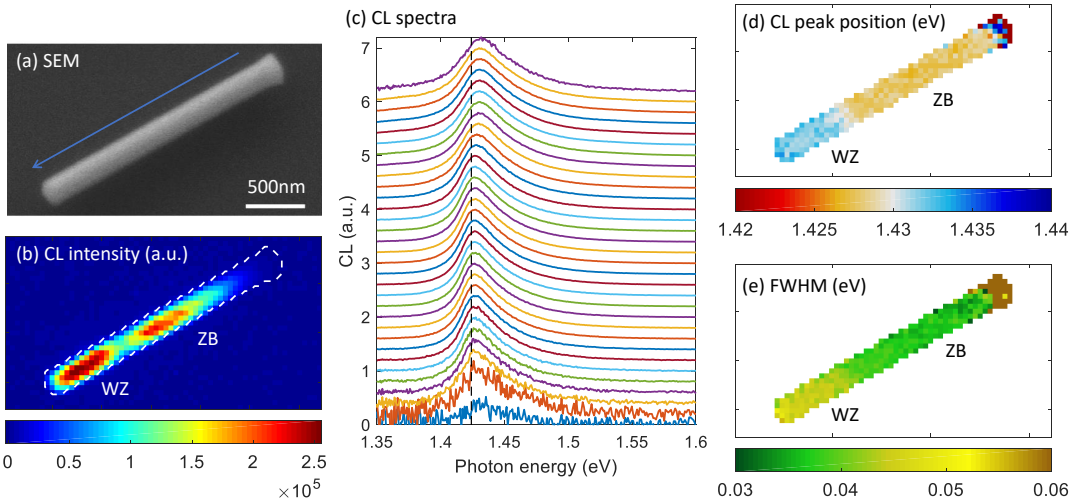

Figure 6.13 – *CL maps of an undoped GaAs NW with an AlGaAs shell (sample 76715) measured at room temperature. (a) SEM image with an arrow showing the growth direction. (b) Integrated CL intensity map. (c) CL spectra extracted from the bottom to the top of the NW. The vertical dashed line indicates the* 1.424 eV *position. (d) Map of the CL peak position energy. (e) Map of the CL FWHM.*

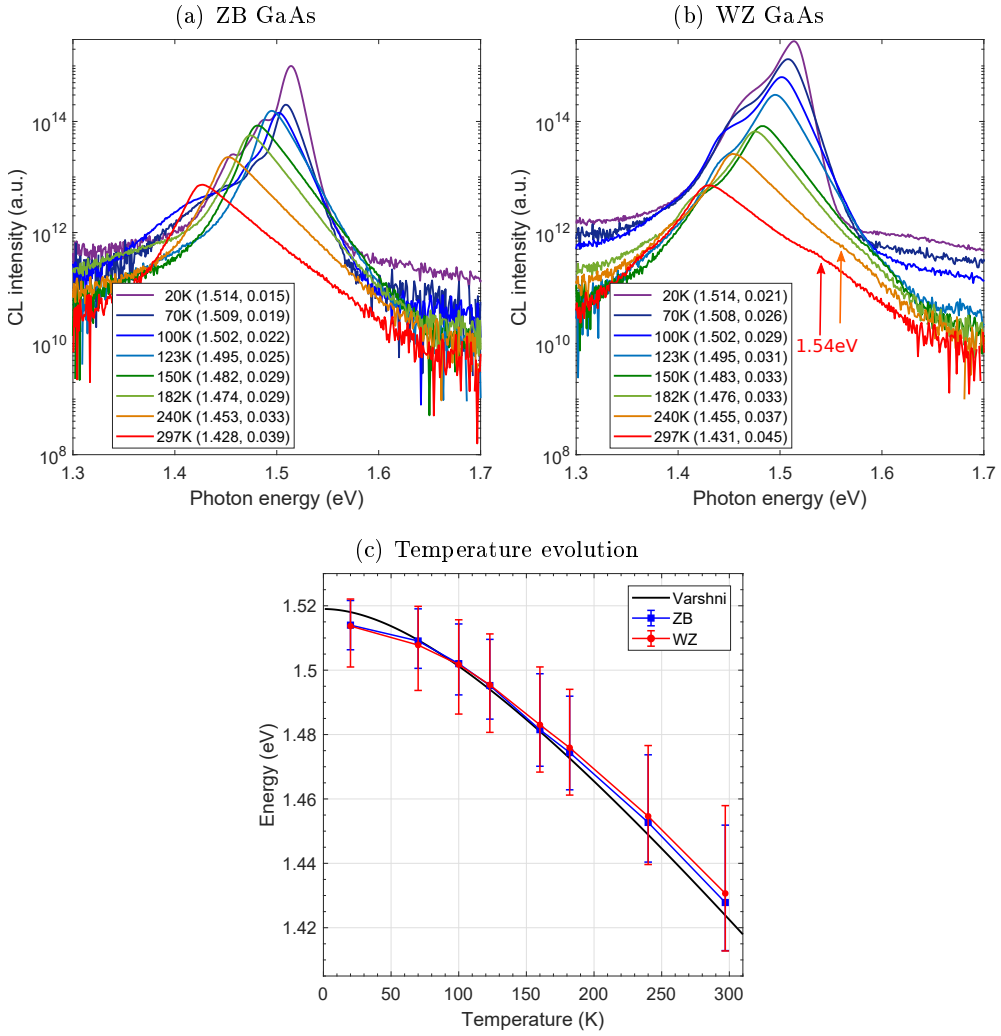

Figure 6.14 – *Temperature evolution of the CL spectra from (a) the ZB part and from (b) the WZ part of an undoped GaAs NW with an AlGaAs shell (sample 76715). (c) CL peak position energy vs temperature. The vertical bars indicate the half-width positions at both high- and low-energy side of the CL spectra. Black solid line is the GaAs bandgap calculated using the Varshni equation.*

defect luminescence was usually observed. From pure ZB GaAs, CL peak centered at 1.515 eV corresponds to the energy of free exciton recombination. The relatively broad peak of about 15 meV FHWM may due to unresolved bound exciton and shallow donor levels. From pure WZ GaAs, CL peak centered at about 1.516 eV is close to the free exciton level reported in the literature [225, 227, 238]. Again the FWHM is large, about 21 meV, unintentional impurity of native defects associated with WZ crystal may be present. At room temperature, similar trends are observed. WZ GaAs shows a slightly blueshifted and wider CL spectrum compared to ZB GaAs.

Figure 6.14 shows the CL spectra extracted from the ZB region and from the WZ region, measured at different temperatures and under identical excitation condition. The WZ region emit stronger luminescence at low temperature, but quenches rapidly with elevated temperature. Despite possible carrier diffusion at higher temperature, WZ always shows a wider CL spectrum. Moreover, a shoulder at 1.54 eV (about 110 meV above the main CL peak) at room temperature is present in WZ GaAs (and not ZB GaAs), may corresponds to the transition from the conduction band to the light-hole band, with the split of heavy-hole and light-hole to be ∼110 meV [231]. Figure 6.14(c) plots the peak position energy as a function of the temperature for CL spectra

extracted from ZB (blue) and WZ (red) part. The vertical bars indicate the half width of the CL spectra at both high and low energy side across the peak maximum. The black line shows the well-known bandgap of pure GaAs described by the Varshni equation (see Equation 5.30). Our measurement supports that the bandgap of WZ GaAs is only slightly higher than that of ZB GaAs.

6.2.3 CL polarimetry

To further verify the optical characteristics of WZ GaAs, a linear polarizer was used to measure the polarization state of the light emitted from the NW containing a clear ZB and WZ segment. The degree of polarization is defined as follows:

$$P = \frac{I_{\parallel} - I_{\perp}}{I_{\parallel} + I_{\perp}}, \tag{6.4}$$

where $I_{\parallel}$ (resp. $I_{\perp}$) is the component of light intensity polarized parallel (resp. perpendicular) to the NW growth direction. For unpolarized light, the parallel and perpendicular components of light are equivalent, hence the degree of polarization should be close to zero. For light polarized parallel (resp. perpendicular) to the NW axis, the degree of polarization is positive (resp. negative), with the absolute value approaching to 1 when the polarization is purely parallel or perpendicular. When a linear polarizer is used to select light only in a linear direction, forming an angle θ with respect to the NW growth direction. The resulting intensity I can be expressed as:

$$I = I_{\parallel}\cos^2(\theta) + I_{\perp}\sin^2(\theta). \tag{6.5}$$

Figure 6.15 presents the CL measurement using the same excitation conditions as described previously at 10 K, and in addition using a linear polarizer with various polarizer angles. Nearly horizontal or vertical NWs (seen from the SEM image) were selected for CL hyperspectral acquisition to facilitate the choose of the polarizer angle. In fact, the image of NW at the entrance slit of the spectrometer is the mirror of the image seen from SEM image, with respect to the mirror plane at the 45° diagonal of the SEM (see orientation at Figure 3.14(a)). The integrated CL intensities measured at 0°, 45° and 90° polarizer angles are shown, with the 0° angle corresponding the polarizer aligned with the NW axis. The CL intensities extracted from the ZB and WZ regions with various polarizer angles covering a quarter of the full angle are plotted in Figure 6.15(b-c), and are fitted using Equation 6.5. The light emitted from the WZ segment presents a remarkable dichroism behavior with up to 73% degree of polarization perpendicular to the NW c-axis. This can also be seen from the comparison of CL intensity maps: ZB emission is little sensitive to the polarizer angle but the WZ emission is strongly quenched when the polarizer angle is chosen parallel to the NW.

In Figure 6.15(d), we plot the CL intensities extracted along the NW, for measurement without polarizer (black), with polarizer parallel to the NW (blue) and perpendicular to the NW (red). The sum of the intensities at 0° and 90° corrected with the transmission efficiency of the polarizer (green) is superimposed with the measurement without polarizer. If the orientation of the NW with respect to the linear polarizer is known in advance (in CL this task is ease by inspecting the SEM image), two measurements at 0° and 90° should be sufficient to determine the degree of polarization. Figure 6.15(e) shows the degree of polarization along the NW calculated by point-by-point treatment of the hyperspectral CL maps at different angle. Slightly positive value (parallel polarization) is observed along the ZB region, which may originate from the dielectric mismatch between the NW with the environment (air). This phenomenon depends strongly on the diameter of the wire, and has an opposite effect to the WZ emission. We still measured a high degree of polarization perpendicular to the NW, as a result of the selection rule in the hexagonal WZ lattice. Up to 70% perpendicular polarization was also observed with PL by Ahtapodov et al. [225].

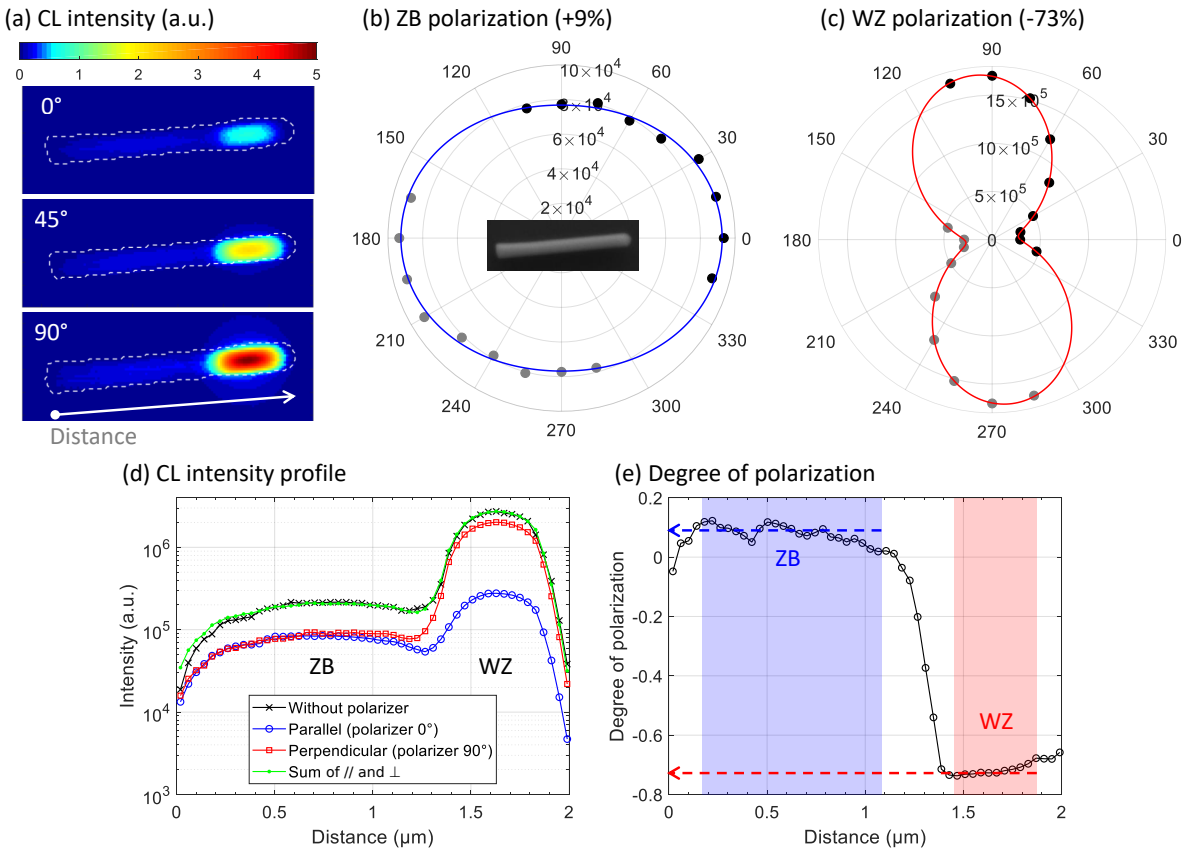

Figure 6.15 – *Polarization of the CL emission from an undoped GaAs NW with an AlGaAs shell (sample 76715). (a) Integrated CL intensity maps of the NW measured with 3 different polarizer angles: 0° (parallel to the NW axis), 45° and 90° (perpendicular to the NW axis). (b-c) Polar plot of CL intensities from the ZB and WZ parts measured under different polarizer angles (dots) and fit with a degree of polarization of 9% (ZB) and -73% (WZ). (d) Intensity profile extracted along the NW for parallel (blue), perpendicular (red) and no polarizer (black). (e) Degree of polarization along the NW, showing 2 distinct polarization states for ZB and WZ regions.*

In summary, we have used high-resolution CL polarimetry which allows to extract a continuous variations of polarizations along single NWs. The degree of polarization is fairly constant in the respective ZB (+9%) or WZ (-73%) region, suggesting that the carrier diffusion should be limited at 10 K. As a result, the CL spectra recorded when the electron-beam excited the WZ region (peak 1.516 eV and FWHM 21 meV) can be unambiguously attributed to the exciton level in WZ GaAs. At room temperature, the bandgap of WZ-GaAs seems to be slightly higher than the bandgap of ZB-GaAs, with a difference of less than 10 meV (see Figrue 6.14).

6.3 Be-doped GaAs nanowires

6.3.1 Background

Beryllium is a commonly used p-type dopant for GaAs in MBE systems. It is characterized by a relatively high, thermally activated diffusion coefficient in GaAs: $D = D_0 \exp(-E_0/kT)$, where $D_0 = 0.66\ \mathrm{cm^2 s^{-1}}$ and $E_0 = 2.43\,\mathrm{eV}$ in the temperature range of 700 to 900°C [239]. For example, the characteristics diffusion length $\sqrt{D\tau}$ for $\tau = 1$ h is 960 nm at 800°C and 250 nm at 700°C. If we extrapolate this relation down to 600°C, the usual temperature range for VLS NWs growth, the diffusion length decreases to about 50 nm for 1 h. This may still has impacts on controlling the NW doping position and concentration.

One of the issues raised in the Be-doped VLS-grown GaAs NWs is whether the Be dopants incorporate into the NWs through the Ga liquid droplet or via the parasitic growth of a shell surrounding the core. Casadei et al. investigated relatively long Be-doped GaAs NWs by 4-point electrical contact measurements on single NWs to obtain the conductivity for NWs grown under different conditions, and concluded that Be atoms incorporate preferentially via the NW side facets, while the incorporation path through the Ga droplet is negligible [240]. The diffusion of Be atoms from the shell into the less doped core was approximately evaluated. However, the observed low-doped cores compared to shells under identical Be flux may simply due to the very fast growth rate of cores in the VLS mode, thus the doping concentration is diluted. More recently, off-axis electron holography revealed a new incorporation mechanism in Ga-assisted GaAs NWs grown by MBE. A lamella of NW was cut using focused-ion beam (FIB) techniques and then the electrical potential was imaged by electron interference. A remarkable three-fold symmetry of electrical potential in the hexagonal cross-section of NW was observed, and the Be dopants were thought to be incorporated through the three (112)A truncated facets [158]. Due to diffusion of Be atoms, the triangular shape should be smeared out along with the growth time and the three-fold symmetry feature is indeed clearer for a lamella cut near the top of the wire (shorter time for diffusion) than that cut at the bottom (longer time for diffusion). By comparison of the two lamellae and solving the diffusion equation in 2-dimensional NW cross-section, a diffusion coefficient of $0.038\,\mathrm{nm^2 s^{-1}}$ was evaluated at 600°C (corresponds to $\sqrt{D\tau} = 12\,\mathrm{nm}$ for a duration of $\tau = 1\,\mathrm{h}$).

On the other hand, Be atoms were also found to be incorporated into self-catalyst GaAs NWs predominately through the Ga droplet, and the distribution of Be in GaAs NWs was rather homogeneous using the 3D reconstruction of atom probe tomography (APT) [241]. Observations of contradictory behaviors exist because various growth conditions (temperature, flux etc.) combined with a nanoscale liquid phase constitute a very complicated system and make the doping mechanism very different from the thin-film growth. Introducing Be atoms during the growth forms Be-Ga alloy droplets that can also suppress the WZ nucleation and facilitate the droplet consumption [242]. The accumulation of high concentration of Be atoms in the droplets may also cause unwanted morphological changes and kinking of NWs [241, 243].

6.3.2 Experiments

In the following, we show CL measurements on Be-doped GaAs NWs. Table 6.2 lists important growth parameters and geometries of the samples. SEM images of as-grown NWs on Si substrates are given in Figure 6.16. A picture of GaAs NWs with direct Be doping during the VLS growth is shown in Figure 6.16(a). However, it is very difficult to measure clear CL spectra for this sample even at low temperature, probably due to small diameter (∼100 nm), resulting in the pinning of the two Fermi levels at the surface. For core-doping samples (Figure 6.16(b,c), the dopants were introduced during VLS-growth of NWs), the droplets were consumed after the VLS-growth, then a thin AlGaAs shell was grown to passivate the NW surface, leading to a strong enhancement of luminescence yield. Shell-doping samples (Figure 6.16(d,e,f)) consist in undoped core and VS-growth of the Be-doped shell with thickness ranging from 60 nm to 110 nm. The relatively large volumes allow the NWs to be measured by optical means without passivation.

In Table 6.2, the atomic flux of Be corresponds to the number of incident Be atoms per cm^2 surface per second. It is converted from the Be cell temperature using the reference planar GaAs samples, assuming Be dopant has an unity sticking coefficient on GaAs and is not compensated (see details in Chapter 5.2). For core-doping, the growth rates are determined from the elongation of the NWs, excluded the top WZ segments due to growth during the catalyst droplet crystallization. For shell-doping, the total volumes of doped shells are calculated by subtracting the final NW diameter with the average diameter typical of NW cores only. Theoretical doping concentration are then calculated using the Be flux and the effective growth rate determined for each sample. For shell doping, the surface normal is orientated differently, so an additional angular correction factor is needed. In fact, the Be flux forms an angle of about 16° with respect to the substrate normal in our MBE machine. The growth rates are deduced by examining the geometrical features of NWs after growth, with errors corresponding to the standard deviation for several NWs.

Table 6.2 – *MBE-grown GaAs:Be NW samples. Both core-doping and shell-doping were investigated. Beryllium effusion cell temperature, NW length, diameter and shell thickness are shown. The parameters for NW geometry were obtained by taking the average and the standard deviation of several randomly selected NWs from SEM images. Shell thickness was deduced from the difference between the final diameter and initial diameter without shell. The flux of Be atoms was converted from the Be cell temperature as calibrated on GaAs thin-film samples. Growth rates indicate the elongation of NWs per unit of time in the case of core-doping and the shell thickness growth in case of shell-doping. Theoretical doping concentrations were deduced from the Be flux and the growth rate, corrected with the incident angle for shell growth.*

sample	T(Be) °C	length μm	diameter nm	shell thickness nm
76847 (core-1)	730	2.54±0.02	196±10	
76741 (core-2)	780	1.88±0.08	202±10	
76720 (shell-1)	680	2.00±0.12	260±10	64±10
76718 (shell-2)	730	1.03±0.04	310±20	86±10
76723 (shell-3)	780	1.99±0.10	370±50	110±20

sample	flux(Be) atoms/(s.cm^2)	growth rate Å/s	th. doping conc. cm^{-3}
76847 (core-1)	1.5×10^{11}	15±0.2	$(9.9 \pm 0.2)\ 10^{17}$
76741 (core-2)	8.8×10^{11}	10±0.4	$(8.8 \pm 0.4)\ 10^{18}$
76720 (shell-1)	2.1×10^{10}	0.19±0.02	$(1.0 \pm 0.2)\ 10^{18}$
76718 (shell-2)	1.5×10^{11}	0.25±0.03	$(5.4 \pm 0.8)\ 10^{18}$
76723 (shell-3)	8.8×10^{11}	0.32±0.06	$(2.5 \pm 0.6)\ 10^{19}$

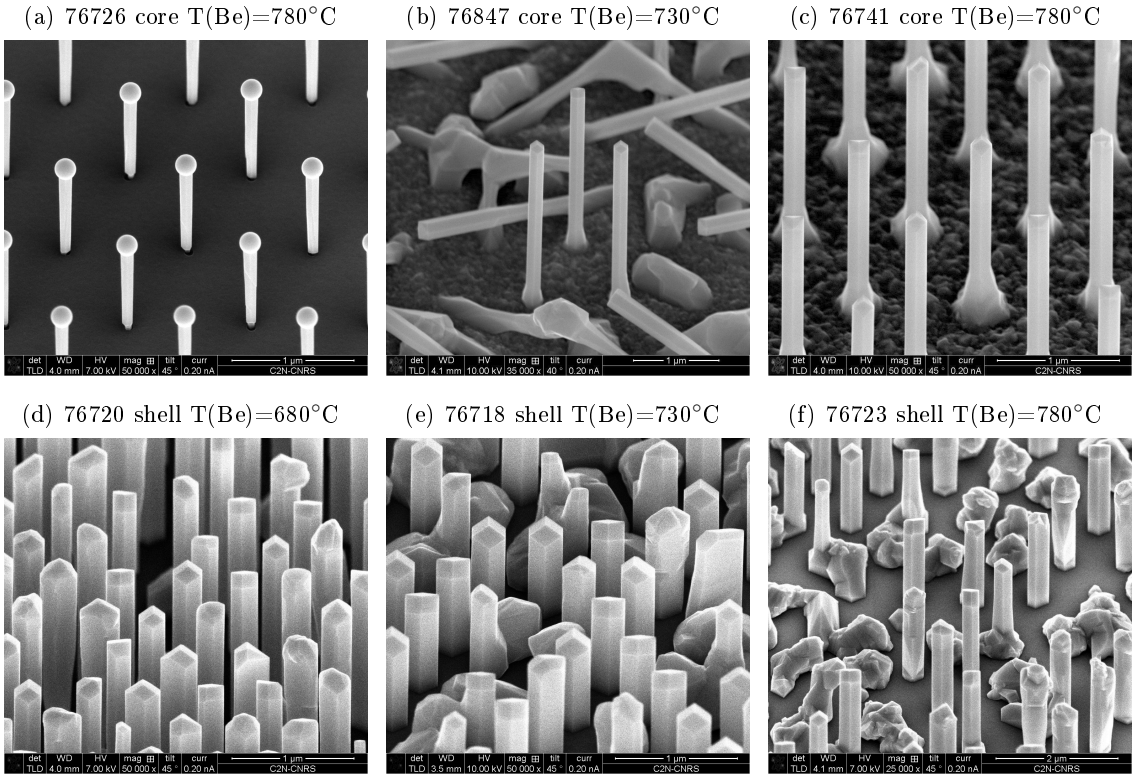

Figure 6.16 – *Tilted SEM images of GaAs:Be NWs on Si(111) substrate. (a,b,c) NWs with direct Be-doping during VLS-growth. For (b,c), the Ga catalyst droplets were crystallized and a thin AlGaAs shell (∼10 nm) was grown to passivate the NW surface. (d,e,f) NW structures containing undoped GaAs NW core, crystallization of the Ga droplets, then growth of Be-doped shell without additional surface passivation layers.*

CL mapping

Figure 6.17 shows the CL measurement at low temperature (∼20 K) of three NWs samples (two passivated core-doped NWs with different concentrations, and one of the shell-doped samples). CL features are fairly homogeneous in the radial direction, thus we only display CL spectra extracted along the wire. For core-doped NWs, two distinct regions can be visualized, like the case of undoped GaAs NWs, pure ZB in the bottom and probably a WZ segment at the top of the wire formed during the crystallization of Ga liquid droplets. The region between the two phases usually constitutes a high density of twin planes and a mixed ZB/WZ crystals, which reflects a broad and redshift CL characteristics. In the ZB regions, the CL peaks can be understood as free-to-bound recombination involving the localized Be acceptor levels in GaAs and eventually band-to-band recombination with acceptor band merged with the valence bands. In the WZ regions, the CL peaks are very similar to that of ZB regions. We have seen that the WZ-GaAs bandgap, or at least the free exciton level, should be close and only slightly higher to that of ZB-GaAs, but characteristic impurity levels in WZ-GaAs remain unknown due to very few studies of doped WZ-GaAs.

In Figure 6.19, CL spectra are compared and plotted in log scale with their relative intensities for core-doped samples (a,b), and shell doped samples (c,d) at both LT and RT under identical excitation current. For each NW, one spectrum is extracted from the middle (m) homogeneous part (ZB) and the other extracted from the top (t) region containing the WZ crystal phase. The intensities for the core-doped samples are very strong, showing the effective passivation effect of an AlGaAs shell. The intensities for the shell-doped samples increase with the doping levels, in particular, the lowest doped NWs have very low intensity due to thinner shells and thicker surface depletion width. Redshift and broadening of CL spectra are consistent with the behaviors of increasing p-type doping with increasing Be flux supply. For WZ spectra, the CL characteristics are close to the ZB counter parts, except that the FWHM from the WZ part is slightly larger than from the ZB part, probably due to unintentional defects or different scattering processes. As we observe similar bandgap of WZ-GaAs compared to ZB-GaAs and similar CL spectra of Be-doped GaAs, we can conclude that Be acceptor level in WZ-GaAs should be similar to that of ZB-GaAs.

(a) 76847 core T(Be)=730°C (with AlGaAs shell passivation)

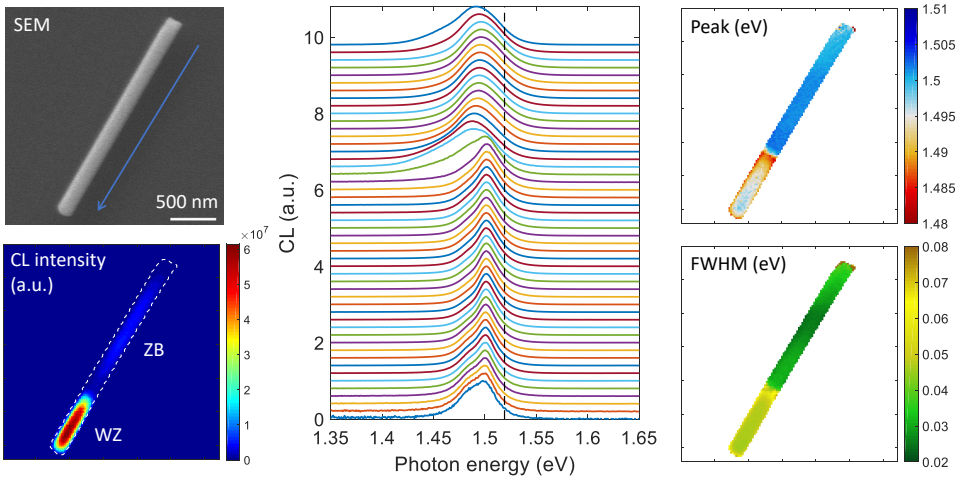

(b) 76741 core T(Be)=780°C (with AlGaAs shell passivation)

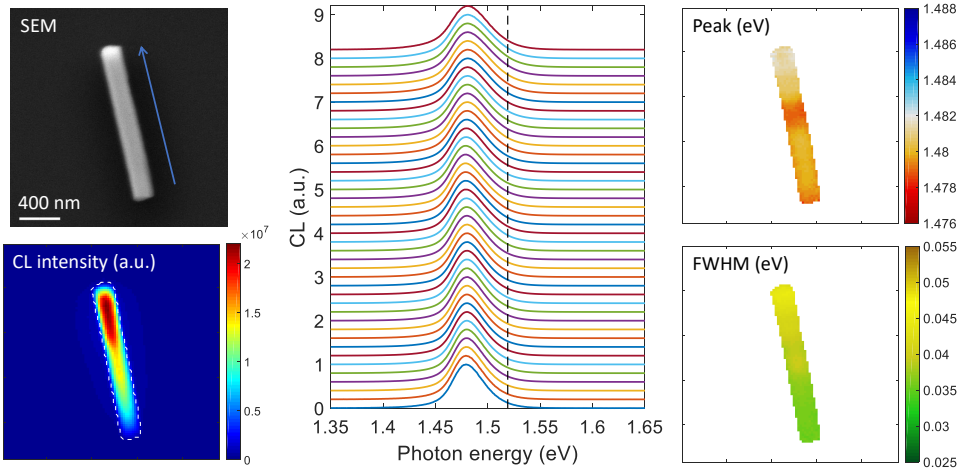

(c) 76723 shell T(Be)=780°C (without passivation)

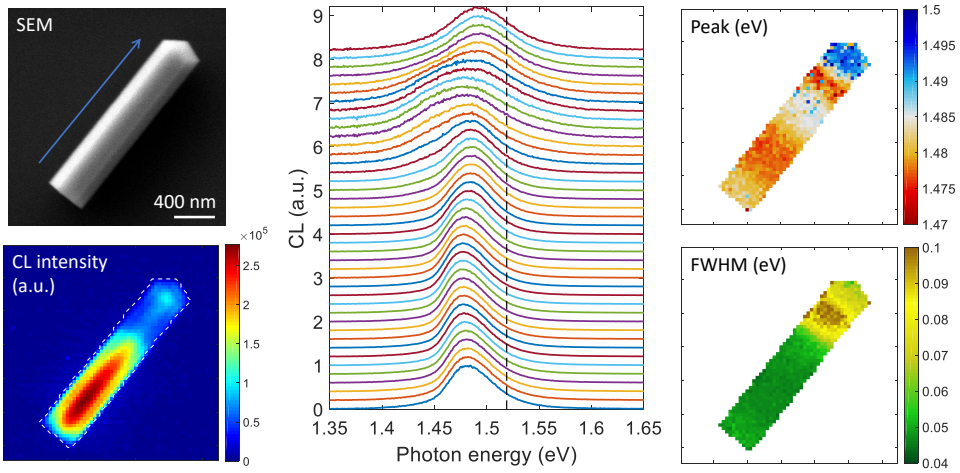

Figure 6.17 – *Low temperature (∼20 K) CL maps of three Be-doped GaAs NWs. For each CL measurement, SEM image of the NW and CL maps (cartography of integrated CL intensity, CL peak position and FWHM) are shown. CL spectra extracted from the bottom to the top of NWs (arrows shown in SEM images indicate the growth direction) are displayed vertically from the bottom to top of the graph, and the vertical dashed lines indicate the pure GaAs bandgap of 1.519 eV at 0 K.*

(a) 76847 core T(Be)=730°C (with AlGaAs shell passivation)

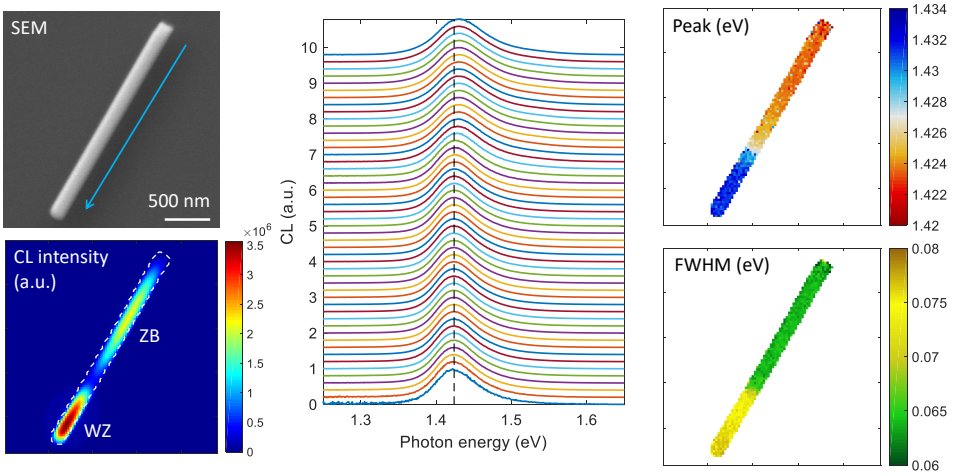

(b) 76741 core T(Be)=780°C (with AlGaAs shell passivation)

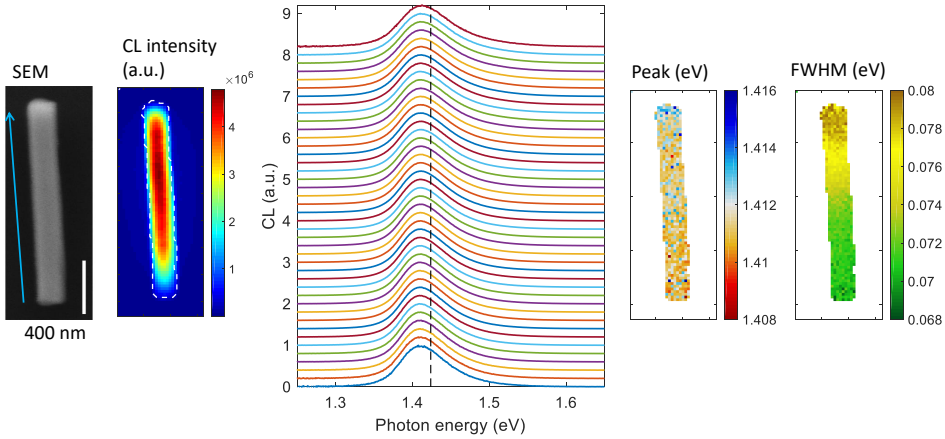

(c) 76723 shell T(Be)=780°C (without passivation)

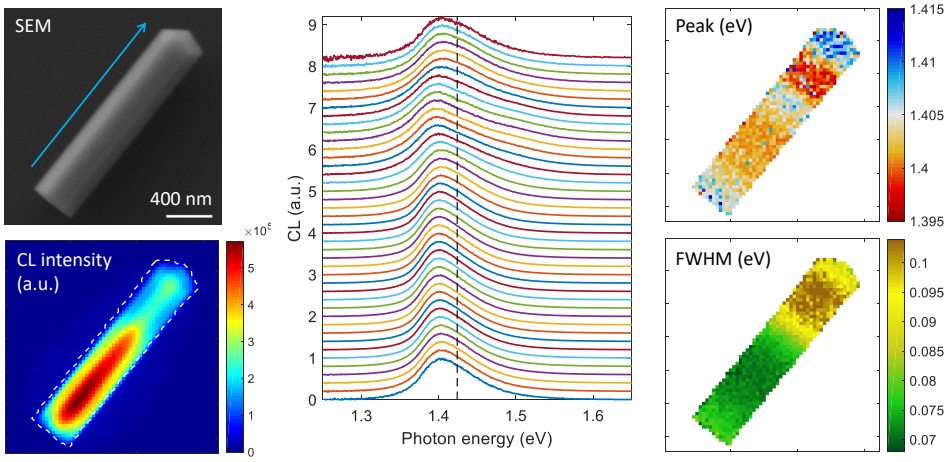

Figure 6.18 – *Room temperature CL maps of three Be-doped GaAs NWs. For each CL measurement, SEM image of the NW and CL maps (cartography of integrated CL intensity, CL peak position and FWHM) are shown. CL spectra extracted from the bottom to the top of NWs (arrows shown in SEM images indicate the growth direction) are displayed vertically from the bottom to top of the graph, and the vertical dashed lines indicate the pure GaAs bandgap of 1.424 eV at room temperature.*

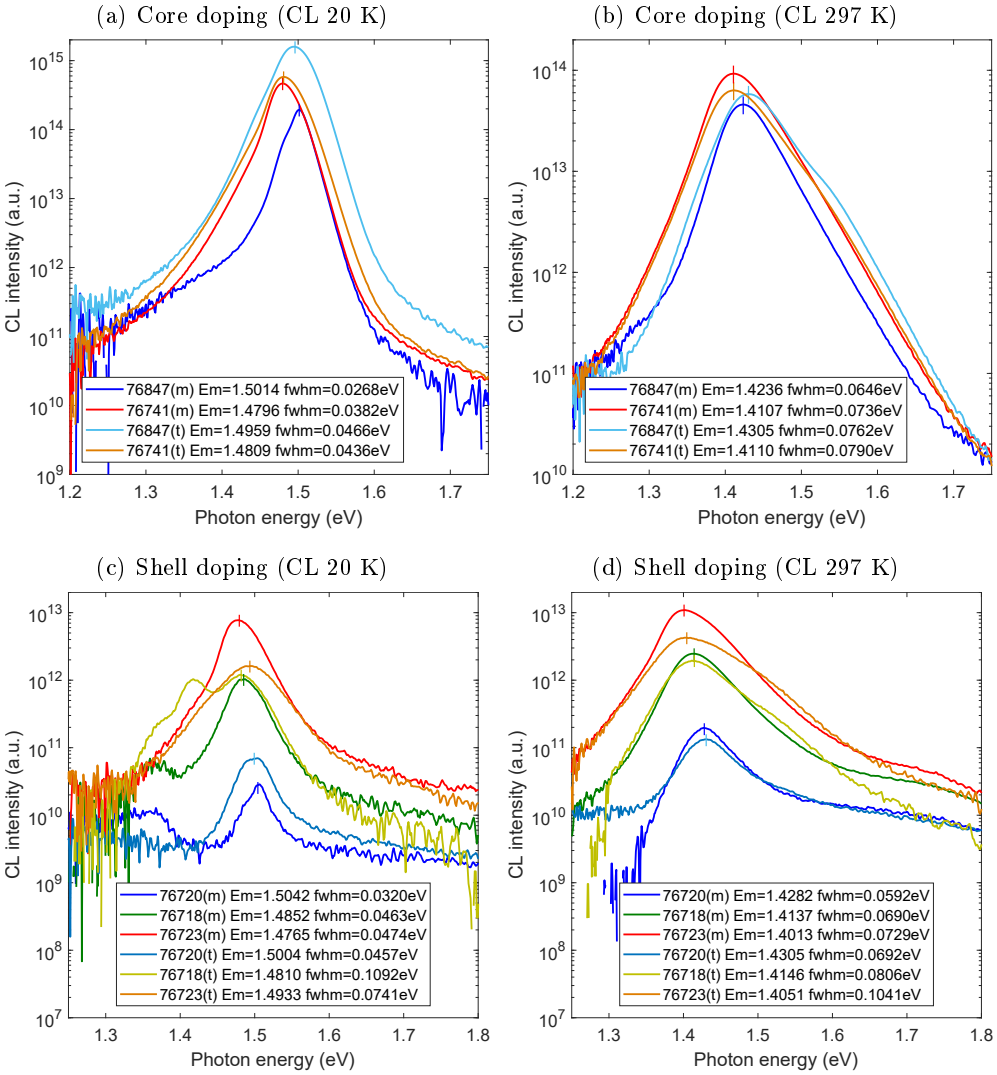

Figure 6.19 – *CL spectra of Be-doped GaAs NWs for (a,b) core-doping structure (with AlGaAs passivation) and (c,d) shell-doping structure (un-passivated). (a,c) show CL spectra measured at low temperature (20 K) and (b,d) at room temperature (297 K). CL spectra are extracted from the middle (m) homogeneous part of the wire (ZB), and from the top (t) region (WZ). The spectra are displayed in relative intensity under identical excitation condition so that a comparison of radiative efficiency between samples is possible. Vertical bars mark the CL peak positions.*

CL polarimetry

Like undoped GaAs NWs, we performed polarization measurement of the CL emission to verify the characteristics connected with the WZ phase. Figure 6.20 shows the results for a slightly core-doped NW with surface passivation measured at 10 K. CL intensity maps show clearly two distinct segments with different behaviors under various polarizer angles. The middle-bottom (ZB) part of the wire has a slightly parallel polarization due to dielectric mismatch between the NW and the environment since this NW has a small diameter of about 220 nm and is as long as 2.8 μm. The top (WZ) region presents a remarkable degree of polarization (-70%) perpendicular to the NW axis, similar to undoped NWs. The observed high degree of polarization supports the fact that the radiative recombination is of band-to-band nature. The WZ-GaAs should be sufficiently doped so that the holes are found in the extended states of the Γ_9 heavy-hole valence band and their symmetric nature is preserved. Localization destroys the strong polarization anisotropy as shown in InGaN/GaN multiple quantum wells [244].

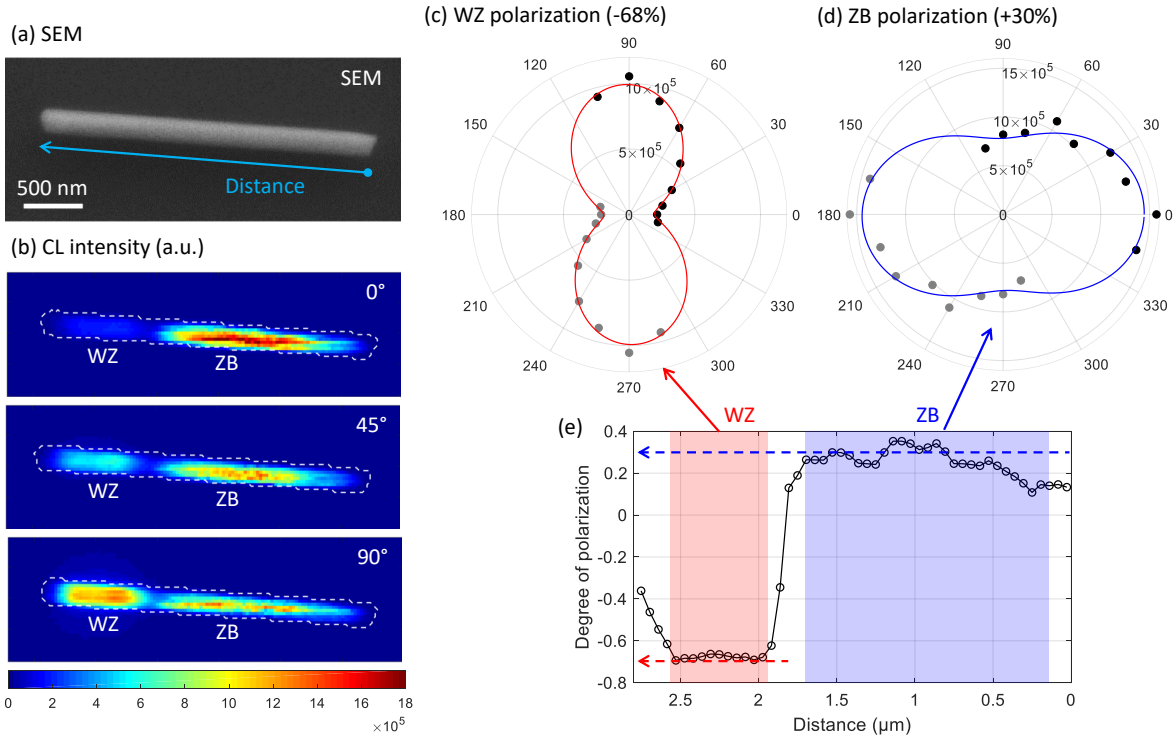

Figure 6.20 – *Polarization of the CL emission for Be-doped GaAs NW (sample 76847). (a) SEM image of the NW. (b) Integrated CL intensity maps of the NW acquired with three polarizer angles:* 0° *(parallel to the NW axis),* 45° *and* 90° *(perpendicular to the NW axis). (c,d) Polar plot of CL intensities extracted from the ZB and WZ part measured with different polarizer angles. (e) Degree of polarization along the NW, showing 2 distinct polarization behaviors of the ZB and WZ regions.*

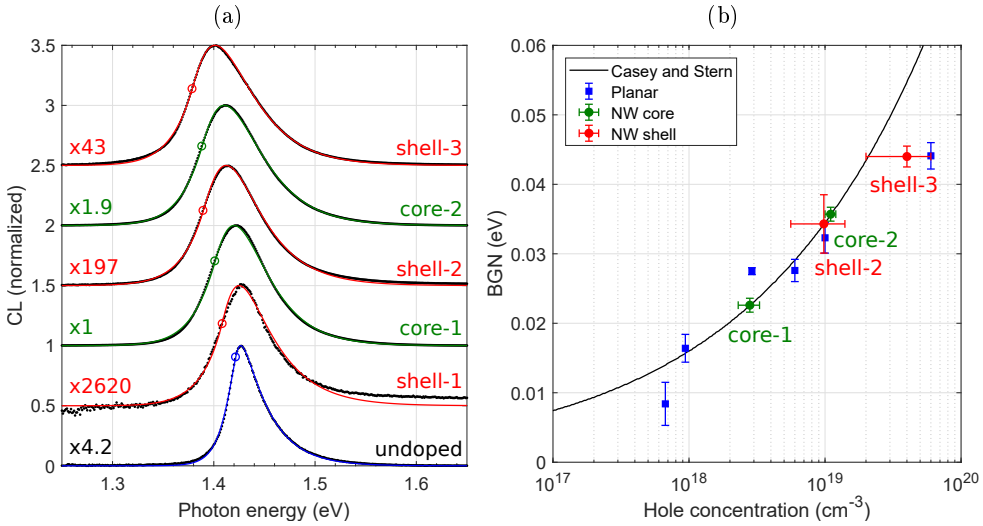

Figure 6.21 – *Comparison of CL spectra for p-type GaAs:Be NWs and fits. (a) Room temperature CL spectra of different Be-doped GaAs NWs extracted from the middle (ZB) homogeneous part. The intensity normalization factors are indicated. Green curves for core-doped NWs and red curves for shell-doped NWs, and an undoped GaAs NW is also included for comparison (blue). The open circles mark the bandgaps from the fit. (b) BGN as a function of hole concentration for p-type GaAs (planar thin-films and NWs). NWs doping concentrations are evaluated through the BGN measurements. Dark curve: Casey and Stern [187] (Equation 5.28).*

6.3.3 Analysis of doping levels

Table 6.3 lists the Be-doped GaAs NWs studied here and the characteristics (peak position and FWHM) of CL spectra extracted from the homogeneous part of ZB-GaAs in the middle of NWs. We fit the whole CL spectra following the same method as described in Section 5.4.2 with the parabolic absorption model (Figure 6.21(a)). The bandgap E_g and energy width of the Urbach tail γ are given. The fitted parameters are averaged over different fits and the errors come from uncertainties of the absorption model and other parameters, as well as typical dispersion of CL peak position and FWHM. Experimental doping concentrations are deduced from the bandgap narrowing (BGN) values using Equation 5.28 (Figure 6.21(b)).

Table 6.3 – *GaAs:Be NW samples and doping concentration assessments. Peak position and FWHM are typical for CL spectra extracted from the homogeneous middle part (ZB) of the NWs. The bandgap E_g and Urbach tail γ are determined from the fit of CL spectra with a parabolic absorption model. Experimental doping concentrations are obtained from the fitted BGN values and Equation 5.28.*

sample	peak eV	fwhm eV	E_g eV	γ eV	exp. doping conc. cm^{-3}
76847 (core-1)	1.423	0.065	1.401±0.001	0.016±0.001	$(2.8 \pm 0.5)\ 10^{18}$
76741 (core-2)	1.411	0.073	1.388±0.001	0.017±0.001	$(1.1 \pm 0.1)\ 10^{19}$
76720 (shell-1)	1.429	0.060	1.415±0.014	0.013±0.004	$< 1 \cdot 10^{18}$
76718 (shell-2)	1.413	0.070	1.390±0.004	0.018±0.004	$(9.8 \pm 4.2)\ 10^{18}$
76723 (shell-3)	1.401	0.073	1.380±0.002	0.016±0.002	$(4.0 \pm 2.0)\ 10^{19}$

For the sample 76720, BGN value is relatively small, so the doping concentration should be lower than 1×10^{18} cm^{-3}. The thinner shell of this sample and the fact that it is only slightly doped also lead to a deeper surface depletion width. For doping concentration higher than 2×10^{19} cm^{-3}, the assessment is approximate due to no reliable BGN values available in such high degenerate regime. We still have a fair agreement between the theoretical and experimental

doping concentrations.

For core-doped samples, experimental doping concentrations are slightly higher than the theoretical ones. This can be related to a larger cross-section of the liquid droplets than that of the NWs, so a larger amount of Be atoms are captured (by the liquid droplets) during the VLS-growth of NWs and contribute to the overall doping of the core. Suspicious Be incorporation through the truncated facets may concentrate the dopants locally in the NW core [158], leading to a larger BGN observed from CL. For shell-doped samples, small discrepancy exists between the theoretical and experimental doping concentrations. Theoretical estimation of doping concentration in the shell configuration is more difficult due to uncertainty of the growth rate and unknown orientation of the impinging dopant flux.

6.4 Si-doped GaAs nanowires

6.4.1 Background

Silicon is a widely used dopant in epitaxial growth of GaAs. It has a unity sticking coefficient, a low diffusion length, and does not exhibit a segregation problem, making it possible to obtain abrupt changes in the doping profile. However, silicon is amphoteric as group IV elements, it acts as donors if it incorporates in Ga sites (Si_{Ga}), or as acceptors if it incorporates in As site (Si_{As}). It is normally utilized as n-type dopant for GaAs thin-films grown with (001) surface orientation and typical free electron concentrations up to $7\times10^{18}cm^{-3}$ can be achieved in MBE systems [176]. At higher Si concentrations, the lattice strain becomes the driving force for increasing proportions of Si to occupy As sites [245]. The screened Coulomb interaction was proposed to explain the formation of neutral $Si_{Ga}-Si_{As}$ pairs or $Si_{Ga}-V_{Ga}$ complexes during the growth [246]. These defects are responsible for reducing the doping efficiency through electrical deactivation of the Si_{Ga} donors. The growth parameters that are important for Si incorporation are the effective V-III flux ratio and the substrate temperature. Too low V-III ratio increases the proportion of As-vacancy at the growing surface, thus the formation of Si_{As} acceptors is more probable. A high substrate temperature also causes an increased rate of As desorption from the surface, resulting in increased As surface concentration.

The incorporation behaviors also depend on the surface orientation of the crystal. It was demonstrated, under the same run of the MBE growth, that the epitaxial layer grown on planar (110) surface of GaAs presented lower electron concentration and lower mobility than that on (100) surface, and (110) samples even became p-type at growth temperatures higher than 560°C [247]. (110) surface morphology was also degraded at high temperature or under low V-III ratio [248]. (111)B surface presents steadily n-type conductivity, while (111)A and more generally (n11) polar A surfaces lead to mostly p-type doping [249]. Moreover, Si-doped GaAs grown by LPE is mainly compensated [250]. The incorporation mechanism differs largely from MBE growth due to the presence of a liquid phase. For self-catalyzed VLS growth of GaAs NWs on (111) surface, Si doping becomes a very complex system due to the presence of a nanoscale liquid droplet and concurrent growth of parasitic shells. P-type doping has been observed in MBE-grown self-assisted GaAs NWs and the doping mechanism was attributed to incorporation from the side facets [146, 251]. This conclusion was based on the local vibrational mode (LVM) of resonant Raman spectra at low temperature. In fact, Si occupying a lattice site in GaAs is lighter than the atoms of the host lattice, giving rise to spatially localized vibrational modes with frequencies higher than the ones of the pure GaAs modes. These LVMs can be detected by Raman spectroscopy or infrared absorption techniques. Si_{Ga} donors having four As neighbors give rise to a sharp LVM in the Raman spectrum at 384 cm^{-1}. The compensating Si_{As} acceptors is found at 399 cm^{-1} and $Si_{As}-Si_{As}$ at 393 cm^{-1} in case of dominant n-type doping in the GaAs sample [252].

On the other hand, shell-doping on NW facets of {110} family was investigated using micro-Raman scattering and conductivity measurement on NW ensemble, and n-type doping with possible compensation depending on the growth conditions was achieved [147]. Here, we studied the n-type doping characteristics by cathodoluminescence. Undoped GaAs cores with Si-doped shells were grown in view of further fabrication of radial junction solar cells. The NW core-shell structure for which only the shell is doped allows unambiguously investigation of the electron concentrations from the Si impurities incorporated during the shell growth.

6.4.2 Experiments

Table 6.4 lists the samples studied here with their growth parameters, and Figure 6.22 gives some SEM images of selected Si-doped GaAs samples as grown on Si substrates. Globally,

three series of Si-doped samples can be distinguished: grown at high temperature (HT) with varying Si flux (76710, 76697, 76709), various growth temperature from medium temperature (MT) to low temperature (LT) at fixed Si flux (76728, 76729, 76749, 76766), and LT growth with other conditions such as the use of As_2 molecules (76449 and 76846). For HT growth (580°C), the NW morphology is relatively smooth and very few parasitic growth is present on the SiO_2 mask. This is resulted from the Ga diffusion at high temperature. However, high temperatures favor As desorption on the surface. Lowering progressively the growth temperature degrades the NW morphology and increases parasitic growth, whereas the luminescence intensities increase steadily with lower growth temperature. Finally, we focus on LT growth to explore various growth conditions like difference between As_4 (sample 76844) and As_2 (sample 76846) molecules, crystallization methods and WZ crystal phase.

Table 6.4 – *MBE-grown GaAs:Si NW samples. Shell doping was investigated (introduce dopants in VS-growth of the shell after formation of an undoped core). The growth substrate temperature, silicon effusion cell temperature, NW length, diameter and shell thickness are shown. The parameters for NW geometry were obtained by taking the average and the standard deviation of several randomly selected NWs from SEM images. Shell thickness was deduced as the difference between the final diameter and initial diameter without shell. Most of the samples were grown with As_4 molecules (except for the sample 76449 and 76846 which were grown with As_2 molecules).*

sample	T(growth) °C	T(Si) °C	length μm	diameter nm	shell thickness nm
76449 (As_2)	465	1150	4.11±0.50	302±35	55±16
76710	585	1000	1.61±0.13	311±39	91±17
76697	585	1100	2.10±0.19	318±48	94±21
76709	585	1200	2.17±0.10	262±21	70±9
76728	540	1100	2.33±0.12	303±71	88±31
76729	485	1100	1.42±0.13	261±19	70±9
76749	475	1100	2.15±0.06	313±24	92±11
76766	430	1100	2.12±0.04	309±18	90±8
76844	450	1090	2.06±0.10	321±15	96±7
76846 (As_2)	450	1090	1.86±0.17	291±20	83±9

Influence of growth temperature

For the three samples grown at high temperature, despite a regular morphology, the CL maps present significant inhomogeneities (see further Figure 6.24(a)). Due to low CL intensities, a high excitation current of several tens of nA was used in order to compare the relative intensities of these samples. The spectra extracted from the center homogeneous part of the three NWs are compared, as shown in Figure 6.23. The intensities increase with higher Si flux, but the peaks redshift and do not follow the behavior expected for n-type doping. According to the MBE experiment of Si-doped GaAs layers grown on (110) substrate from Tok et al. [248], p-type doping can be obtained at this high growth temperature. Moreover, the luminescence bump in the spectral range of about 0.34 eV higher than the main emission peak may be attributed to the recombination of electrons with holes at the split-off valence band. The observation of the split-off valence band is also indicative of the presence of high density of holes, typically in highly doped p-type semiconductors or in high injection regimes.

In Figure 6.24, CL maps and spectra extracted from the bottom to the top of the NWs are given for three samples with decreasing growth temperature and with fixed Si flux. The measurements were performed at 20 K with an acceleration voltage of 6 kV and a probe current of 0.7 nA. Figure 6.25 gives the corresponding CL maps and spectra of the same NWs measured at

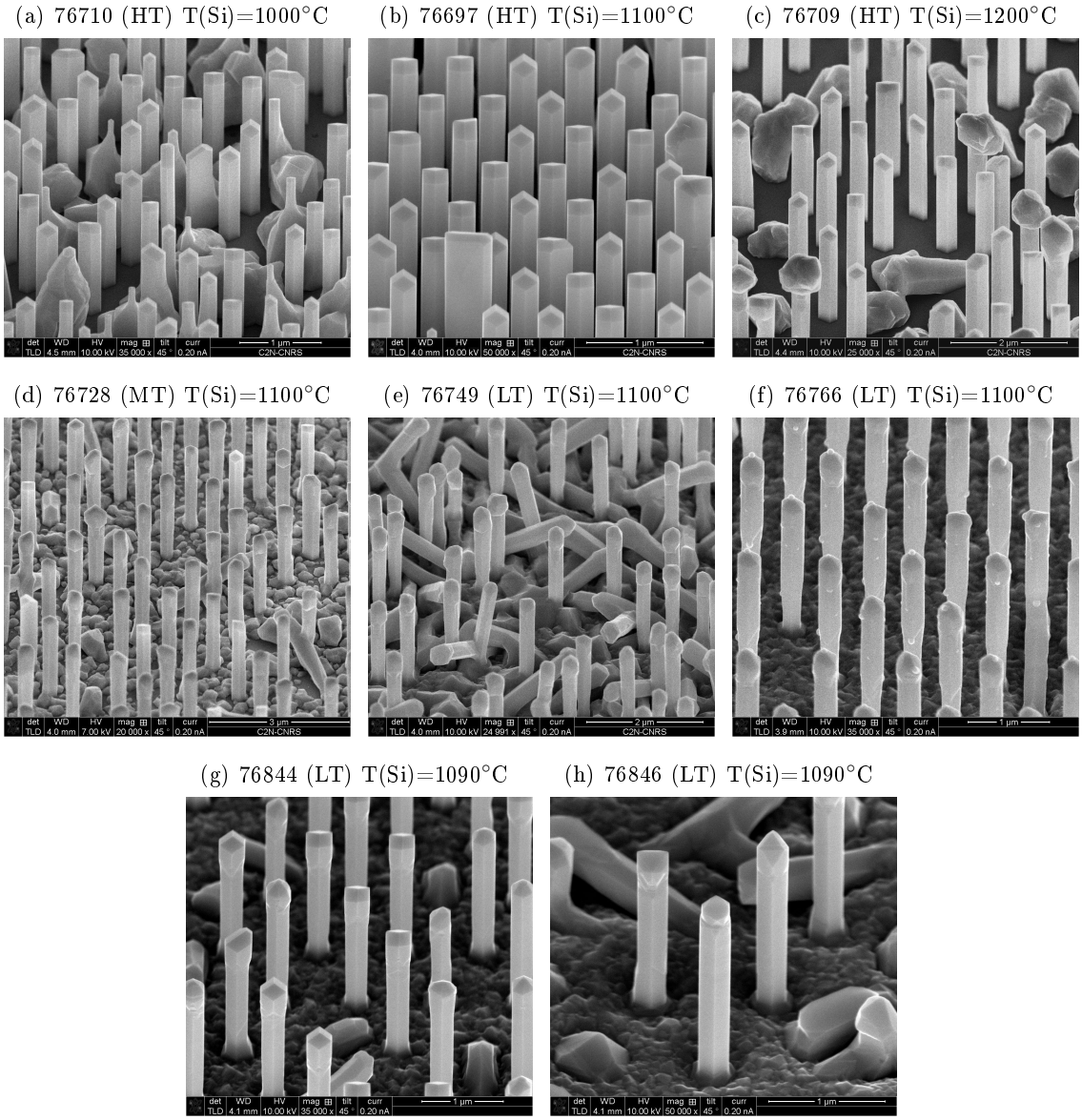

Figure 6.22 – *Tilted SEM images of GaAs:Si NWs on Si(111) substrates. (a,b,c) NWs grown at high temperature (HT) with increasing Si flux. (d,e,f) Decreasing growth temperature from high to medium (MT) and low temperature (LT) at a constant Si flux. (g,h) Low temperature (LT) growth of GaAs:Si shell after different crystallization method to impede the formation of a WZ segment. As_4 molecules were used for the sample 76844 and As_4 molecules for the sample 76846.*

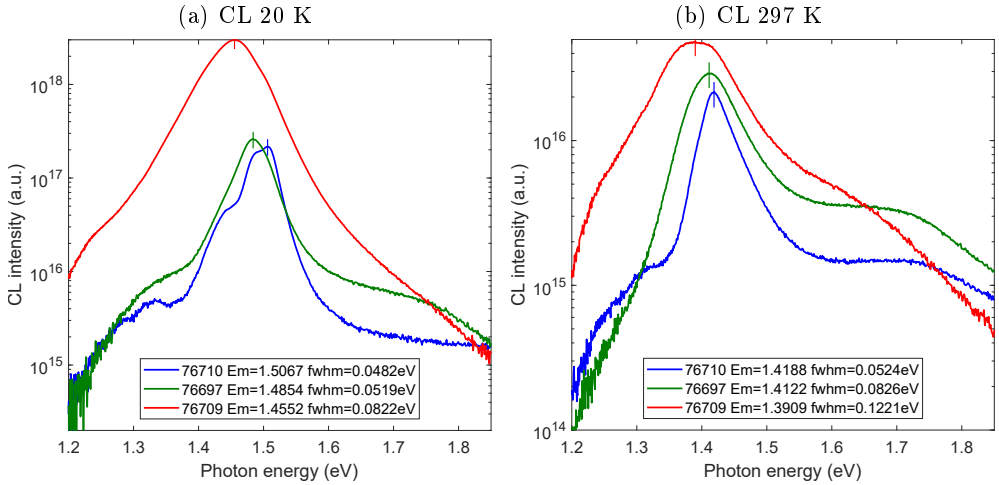

Figure 6.23 – *(a) Low temperature and (b) room temperature CL spectra of GaAs:Si NWs grown at high temperature with various Si flux. Vertical bars indicate the CL peak positions, which shift toward lower photon energy with increasing Si flux. CL spectra are displayed with their relative intensities acquired under the same excitation power density, showing that the intensities increase with the Si flux.*

room temperature with the same excitation conditions. Higher CL intensities with decreasing growth temperature indicate a better crystal quality and lower defect densities. For the growth temperature below 540°C, the CL emission from middle-bottom part of the NWs is fairly homogeneous and the peak energy (around 1.510 eV) slightly lower than the GaAs bandgap at low temperature can be attributed to the donor band. The small FMWH (∼20 meV) of the donor band emission is also indicative for an electron concentration below approximately $8 \times 10^{17}\,\mathrm{cm}^{-3}$ (see Figure 5.10(b) and Equation 5.14). At the middle-top region, a segment with distinct CL characteristics appears due to the WZ crystal phase grown during the crystallization of the droplet and subsequently Si-doped WZ-GaAs shell was obtained at this region. The very top region corresponds to the shell overgrowth. The irregular surface morphology makes this region defect-rich, and correlates to the broad and low-energy lying CL spectra.

The presence of pure WZ crystal structure was verified by TEM observation, as-shown in Figure 6.26(a). The appearance of a pure WZ segment in the middle-top of the wire is reproducible, as already observed in undoped and Be-doped GaAs NWs with similar VLS growth process of the NW cores. CL maps measured at low temperature on a similar NW from the same sample are shown in Figure 6.26(b) for comparison. The remarkable shift of CL peaks to lower energy compared to the donor band of ZB-GaAs is correlated to the WZ crystal phase. The emission characteristic of Si-doped WZ-GaAs is further investigated with CL polarimetry and temperature-dependent measurements.

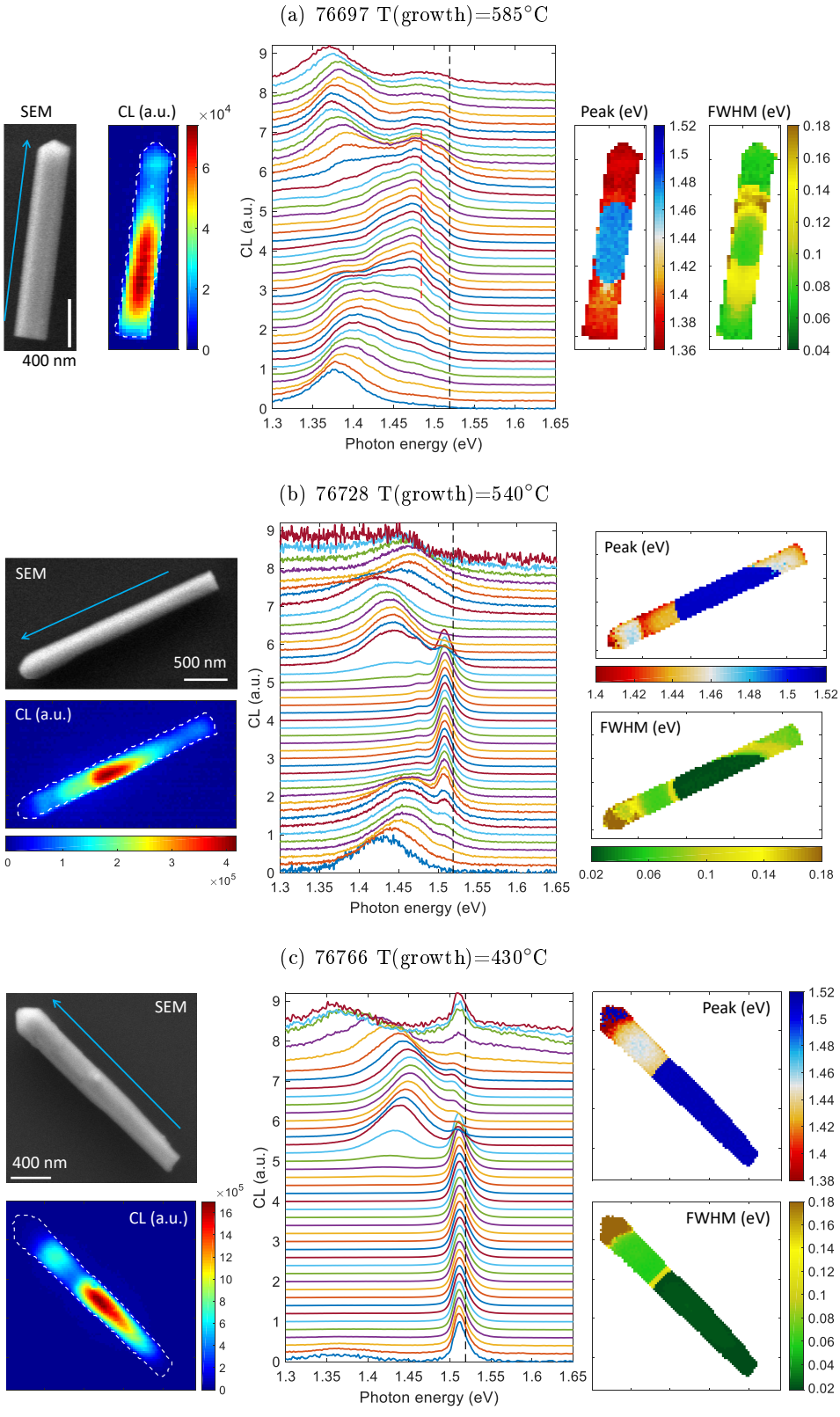

Figure 6.24 – *Low temperature (∼20 K) CL maps of three Si-doped GaAs NWs. For each CL measurement, SEM image of the NW and CL maps (cartography of integrated CL intensity, CL peak position and FWHM) are shown. CL spectra extracted from the bottom to the top of NWs (arrows shown in SEM images indicate the growth direction) are displayed vertically from the bottom to top of the graph, and the vertical dashed lines indicate the pure GaAs bandgap of 1.519 eV at 0 K.*

(a) 76697 T(growth)=585°C

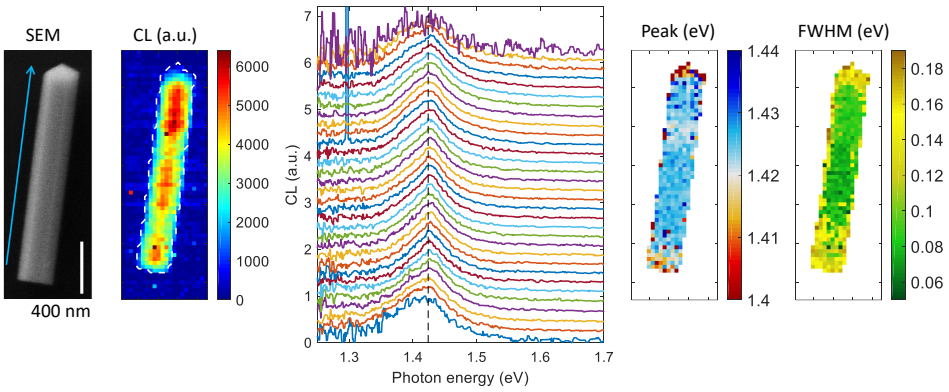

(b) 76728 T(growth)=540°C

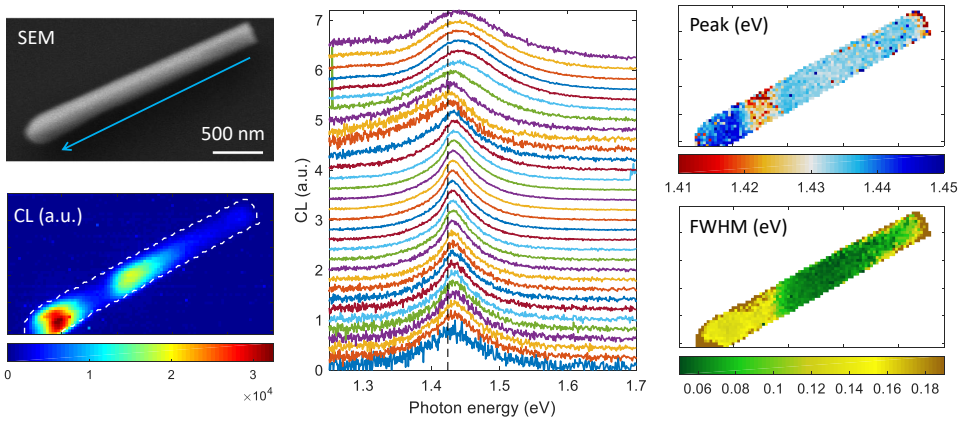

(c) 76766 T(growth)=430°C

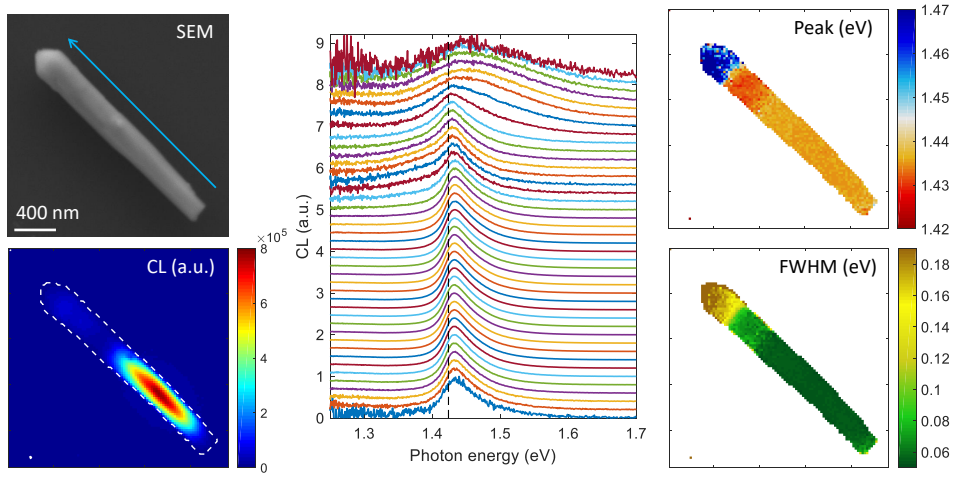

Figure 6.25 – *Room temperature CL maps of three Si-doped GaAs NWs. For each CL measurement, SEM image of the NW and CL maps (cartography of integrated CL intensity, CL peak position and FWHM) are shown. CL spectra extracted from the bottom to the top of NWs (arrows shown in SEM images indicate the growth direction) are displayed vertically from the bottom to top of the graph, and the vertical dashed lines indicate the pure GaAs bandgap of 1.424 eV at room temperature.*

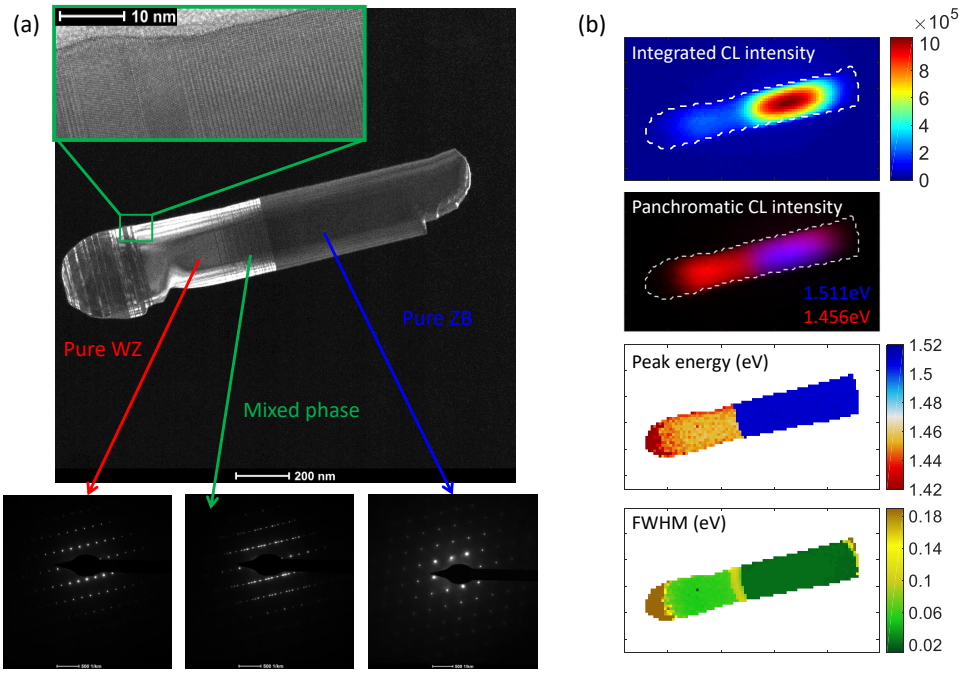

Figure 6.26 – *(a) Dark-field TEM micrograph of a Si-doped GaAs NW (sample 76729) and selective area electron diffraction patterns showing a pure ZB structure at the base of the wire and a WZ segment at the top of the wire. Inset shows a HAADF high-resolution TEM image of the top of the WZ segment, where the crystal structure turns to ZB-dominant at the very top of the wire. (b) CL maps (cartography of integrated CL intensity, two-color CL intensity, peak position energy and FWHM) of a similar NW from the same sample measured at LT (∼15 K).*

CL polarimetry

Like undoped and Be-doped GaAs NWs containing a WZ segment, the polarization degree of CL emission is shown in Figure 6.27 for a longer Si-doped GaAs NW. The very top of the NW presents significant defects and lowers considerably the CL intensity, thus is disregarded here. The average CL spectra present two peaks, one at 1.52 eV from the donor band of ZB-GaAs with FWHM about 15 to 18 meV, corresponding to the electron concentration of about 3×10^{17} to 4×10^{17} cm^{-3} (Equation 5.14). The other broad peak centered at 1.47 eV is spatially located at the WZ region. The spatial localization of the two peaks is clear in the two-color CL maps with superimposed colors of integrated intensities from two different spectral ranges (Figure 6.27(b)). Moreover, the spectrally separated CL emission allows easy deconvolution, as shown in Figure 6.27(c), the average CL spectrum is decomposed using four gaussians fit. This procedure is applied for every spectra of the hyperspectral map, and the intensity profiles along the NW of the 1.52 eV (blue) and the 1.47 eV (red) peaks are plotted in Figure 6.27(d). We can see that the signal of the 1.52 eV decreases exponentially when the electron beam excitation moves from ZB into WZ region. We find an exponential decay of characteristic length of 54 nm, corresponding to a diffusion length in the WZ region at low temperature. The diffusion would be driven by injected holes if the WZ region is also n-type doped. In the ZB region, the low-energy signal around 1.47 eV (red) decreases exponentially from the ZB/WZ interface region with a characteristic length of 172 nm. The direct emission from the small trace of defect states in ZB-GaAs cannot be totally excluded, so we still observe low-energy signal when the electron beam excite the ZB part far from the WZ region. Thus, the estimated hole diffusion length (172 nm) in ZB GaAs should be taken as rough approximation.

As the effect of diffusion is limited at low temperature, the spectra extracted from the center of ZB and WZ regions should be representative for the characteristics of respective crystal

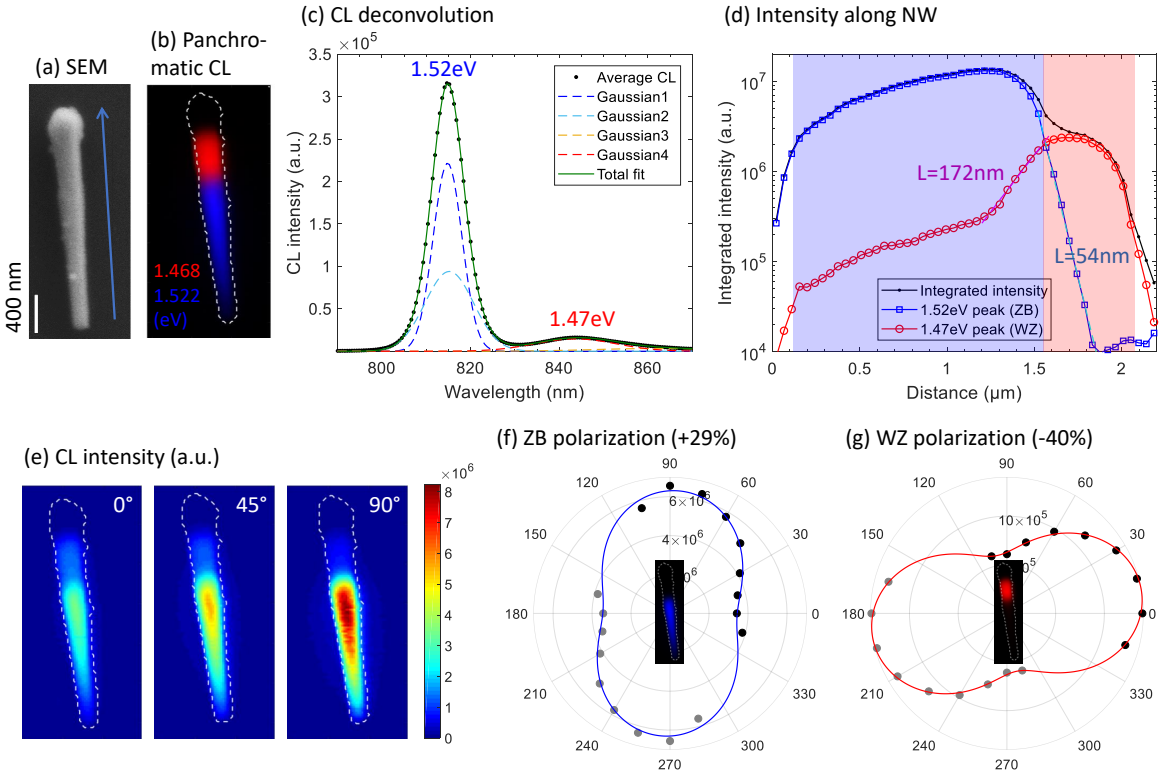

Figure 6.27 – *Polarization-resolved CL emission at 10 K for Si-doped GaAs NW (sample 76766). (a) SEM image of the NW. (b) Two-color CL intensity map. Blue: 1.522 eV from the emission of ZB GaAs with moderate electron concentration. Red: broad CL spectrum centered at 1.468 eV is attributed to the emission of Si-doped WZ GaAs. (c) Spectral deconvolution of the 1.52 eV and 1.47 eV CL peaks using a fit of four gaussians. (d) CL intensities of the 1.52 eV peal (blue) and of the 1.47 eV peak (red) along the NW, showing two distinct dominant ZB and WZ regions, as well as the exponential-like decay away from the ZB/WZ interface. (e) CL intensity maps of the NW acquired with three polarizer angles: 0° (perpendicular to the NW axis), 45° and 90° (parallel to the NW axis). (f,g) Polar plot of CL intensities extracted from the ZB and WZ part measured with different polarizer angles.*

phases. Their dependence on the polarizer angle corrected with the system response is shown in Figure 6.27(f) for ZB and (g) for WZ. CL intensity maps can also be visualized in Figure 6.27(e) for three polarizer angles. 29% degree of polarization parallel to the NW axis is observed from ZB emission and −40% of polarization perpendicular to the NW axis is from WZ emission. The parallel polarization is still attributed to the dielectric mismatch of the NW antenna, while the degree of polarization perpendicular to the NW axis is lowered for Si-doped WZ-GaAs than previously observed for undoped and Be-doped WZ-GaAs. This difference can help to understand the origin of the WZ-GaAs emission from relatively deep levels (about 50 meV below the bandgap), which is probably due to donor-acceptor (DA) pair recombination. The localization nature of DA pair induced by Si impurities destroys the translational invariance, so it relaxes the selection rule of dipole transitions and results in a smaller polarization anistropy of luminescence.

Temperature-dependent CL

Figure 6.28 (low temperature) presents the CL measurement on a NW of another sample grown under similar conditions, containing a clear WZ segment and the very top of the NW probably turns back to ZB structure. The top most region is characterized by very broad CL spectra with the peak maximum shifted to even 1.57 eV at 15 K. The strong Burstein-Moss shift indicates a high electron density in this region. Indeed, the crystallization of the NW droplets usually terminates with (n11)B facets (n=1,2,3...) and the Si incorporation through these surfaces tends to produce Si_{Ga} donors. In the middle-base region of the NW, donor band luminescence of ZB-GaAs is observed, with FWHM varying between 15 to 21 meV, corresponds to electron densities of about 3×10^{17} to 5×10^{17} (see Equation 5.14). No degenerate electron density is observed in this region compared to top of the wire, probably due to (110) surface chemistry or shadowing from the neighboring NWs. In the middle-top region, similarly broad and redshifted CL peaks are present as in the previous NWs, which is attributed to DA pairs related to Si impurities in WZ-GaAs. The peak positions are also very sensitive to the location of the excitation beam, which is characteristic for DA recombination because the energy of the emission depends on the average distance of the DA pairs and on the excess carrier densities. Very few studies of Si-doped WZ-GaAs are found in the literature, such as Ihn et al., where undoped, Be- and Si-doped GaAs NWs are studied and PL emission from Si-doped WZ-GaAs is found to be very broad and defect-related [223].

Figure 6.29 gives the corresponding CL maps and spectra extracted along the same NW measured at room temperature. The CL characteristics between the three regions discussed previously become less noticeable due to increased carrier diffusion at room temperature and thermally quenched defect luminescence. Near bandgap luminescence is dominant at room temperature. We can still observe a significant decrease of CL intensity and broadening of CL spectra in the WZ and the top-most region of the NW.

Figure 6.30 presents the temperature variations of the CL characteristics (peak energies and half widths) of the NW previously studied containing the base of ZB (green), a segment of WZ (red) and degenerate n-type ZB top (blue). From the base, the CL spectra closely follow the bandgap of pure GaAs, consistent with the donor band emission at very low temperature, and with slightly blueshift emission at room temperature from the thermal ionization of donors. The degenerate electron gas presented at the top most overgrown region of the NW steadily shows blueshift and broad peaks covering across the bandgap. The temperature evolution of the DA pair recombination presents a S-shape variation with the temperature. For temperature lower than about 100 K, carriers are trapped in the lower energy defect levels of donors and acceptors. The DA pairs ionize at higher temperature, so the DA recombination is thermally quenched and band-to-band recombination dominates. At room temperature, these deep levels in WZ-GaAs also contribute to broader CL spectra at the low-energy tail compared with ZB-GaAs.

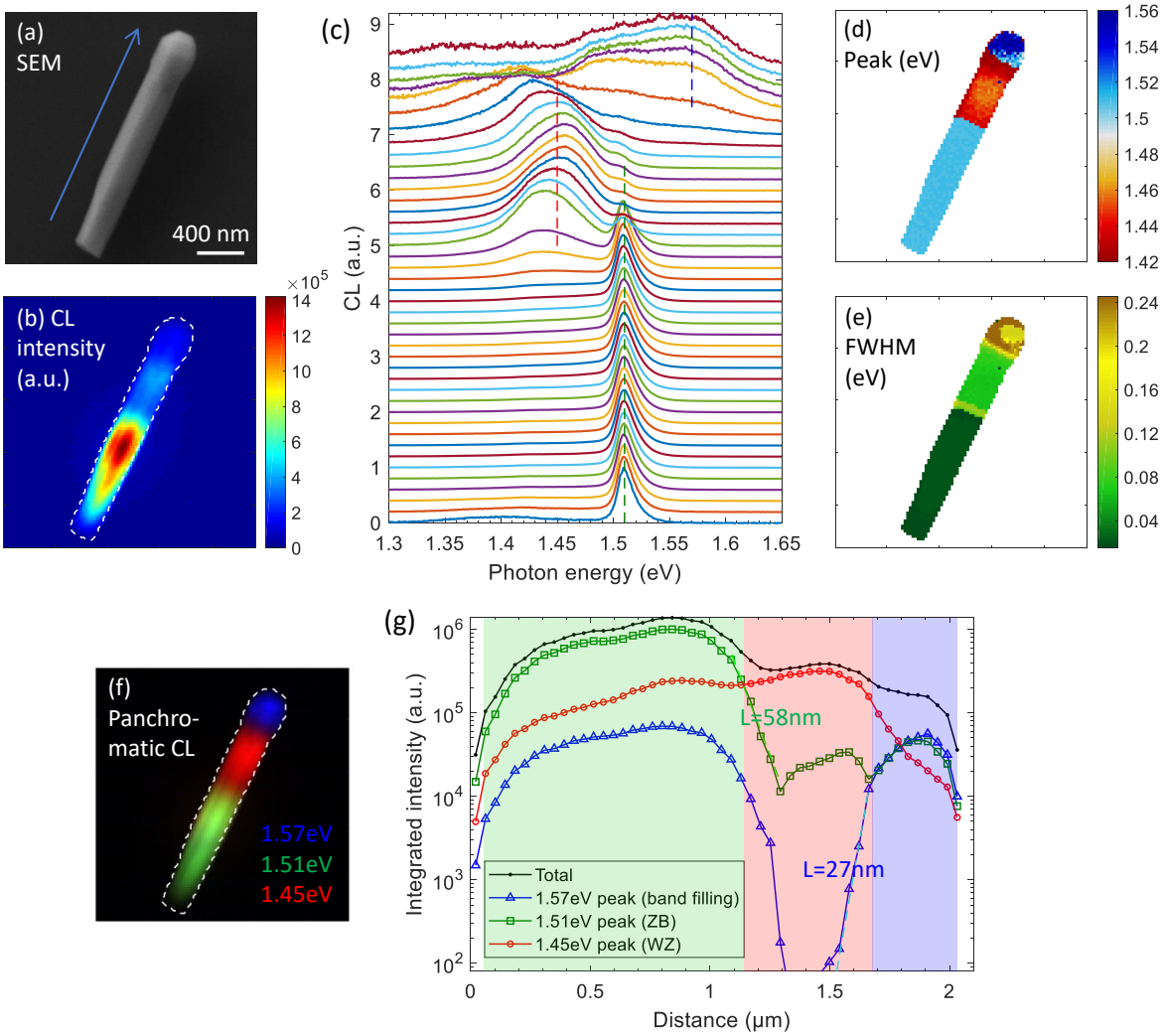

Figure 6.28 – *Low temperature (∼15 K) CL measurement of a Si-doped GaAs NW (sample 76749) containing a ZB base and a WZ top middle segment, showing distinct CL emission characteristics. At the very top of the wire, the crystal phase probably turns back to ZB. CL spectra acquired when the electron beam excited the very top end of the wire show a wide and blueshifted peak, which is attributed to a high electron concentration. This strong blueshift is not present in the bottom of the NW, probably due to shadowing effect and/or the (110) surface orientation that lower the doping efficiency. Si-doped WZ GaAs shows a broad CL spectra but redshifts to about 1.45 eV. (g) presents the variation along the NW axis of three intensity profiles obtained from the spectral deconvolution (green: 1.51 eV, red: 1.45 eV, blue: 1.57 eV).*

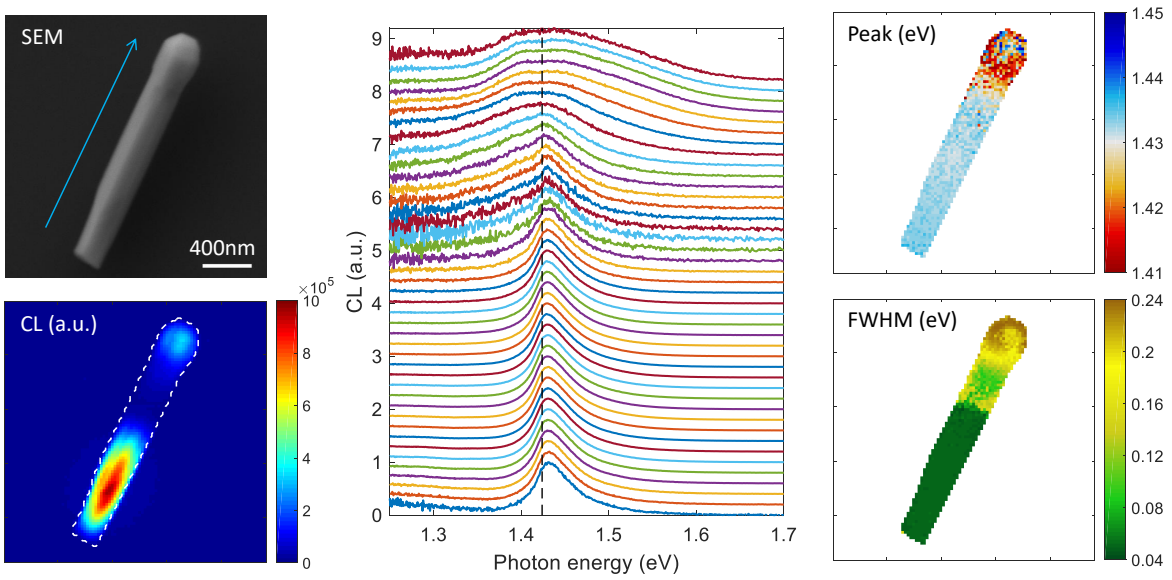

Figure 6.29 – *Room temperature CL measurement of the Si-doped GaAs NW (sample 76749) containing a ZB base and a WZ top segment. Near bandgap luminescence is dominant at room temperature due to thermal ionization of shallow defects. CL maps show similar trends compared to those measured at low temperature: decreased luminescence intensity in the WZ segment and broadened CL spectra toward the top region.*

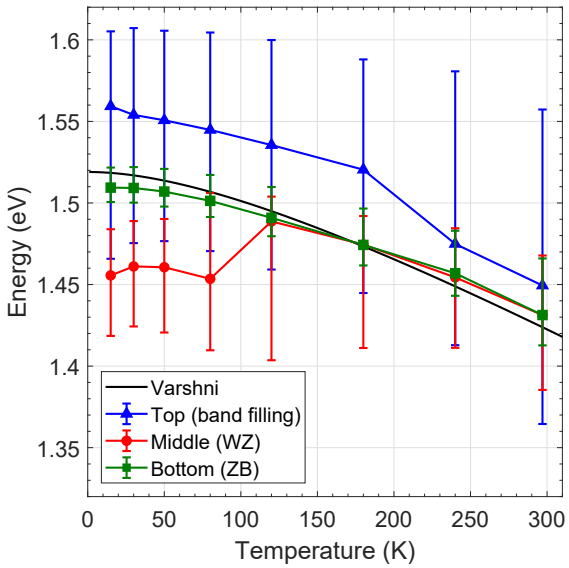

Figure 6.30 – *Temperature evolution of CL characteristics (peak position energy and half widths) of the NW containing a ZB base and a WZ top segment (sample 76749). The very top end of the wire shows a wide and blueshifted CL peak for the whole temperature range, consistent with a presence of high electron concentration. Defect luminescence from Si-doped WZ GaAs is rapidly quenched at temperature higher than about 100 K.*

6.4.3 Analysis of doping levels

Table 6.5 lists several Si-doped GaAs NWs grown at relative low temperatures (<500°C) to avoid severe compensation of Si impurities. Atomic flux of Si was converted from the Si cell temperature using the reference planar GaAs:Si samples (Chapter 5.2). Like the case of Be dopant, we assume that Si atoms have an unity sticking coefficient, and that every Si impurities are electrically active and are not compensated. We study only shell doping, so the surface normal to the NW (110) facets is orientated differently than that of usual planar growth. In fact, the Si flux forms an angle of approximately 35° with respect to the normal of planar layers in our MBE machine. The growth rates are deduced by examining the geometry of NWs after growth, with errors corresponding to the standard deviation for several NWs. The total volumes of doped shells are calculated by subtracting the final NW diameter with the average diameter typical of NW cores only. Theoretical doping concentrations are then calculated using the Si flux and the effective growth rate determined for each samples. We expect to incorporate Si impurities in GaAs with Si atom concentration [Si] ranging from 3×10^{18} to 2×10^{19} per cm^3.

Table 6.5 – *GaAs:Si NW samples and theoretical doping concentrations. The flux of Si atoms were deduced from the Hall measurement of planar calibration samples, assuming Si atoms have an unity sticking coefficient. Growth rates indicate the speed of the shell thickness growth. Theoretical doping concentrations were deduced from the Si flux and the shell growth rate, corrected with the incident angle of the Si flux.*

sample	flux(Si) atoms/(s.cm^2)	growth rate $\mathring{A}$/s	th. doping conc. cm^{-3}
76844	4.6×10^{10}	0.28±0.02	$(3.6 \pm 0.3) \times 10^{18}$
76846	4.6×10^{10}	0.24±0.03	$(4.2 \pm 0.6) \times 10^{18}$
76749	5.5×10^{10}	0.20±0.03	$(6.1 \pm 1.1) \times 10^{18}$
76766	5.5×10^{10}	0.20±0.02	$(6.1 \pm 0.7) \times 10^{18}$
76729	5.5×10^{10}	0.20±0.03	$(6.1 \pm 1.1) \times 10^{18}$
76449	1.3×10^{11}	0.15±0.04	$(2.0 \pm 0.8) \times 10^{19}$

Table 6.6 gives the averaged CL characteristics (peak position energy and FWHM) measured at low temperature (LT) and at room temperature (RT). Errors represent the typical variation observed in the NW and in several measured NWs of the same sample. Only the homogeneous bottom-middle (ZB) part of the NWs is of interest here, since WZ and the top most regions contain significant defects and are hard to analyze. Experimental doping concentration or free electron concentration is obtained either from LT measurement (Equation 5.14) or RT measurement (electron Fermi level). Following Section 5.4.3, fits of RT CL spectra using generalized Planck's law are displayed in Figure 6.31(a). The fitted bandgap is marked by open circles and the electron Fermi level is marked by open squares. For low electron concentration below the degenerate limit, it is difficult to obtain reliable Fermi level from luminescence lineshape analysis because the feature of conduction band filling is not clearly visible. In this case, CL spectra can be fitted regardless of the electron Fermi level below the bandgap (all samples except for 76449).

Note that the sample 76449 was grown on an unpatterned Si(111) substrate, leading to a larger dispersion of NW length and diameter. This is also reflected by a larger wire-to-wire dispersion of CL characteristics, although we have selected only the center homogeneous part of NWs to analyze the CL spectra. Whereas, this sample was grown with higher Si flux using As_2 molecules. Analysis of doping levels for several NWs from this sample was published in Ref. [153]. In Figure 6.31(b), the CL spectrum and the fit for a NW of sample 76449 are shown in log scale. A signal in the range of 1.2 to 1.3 eV is present for nearly every GaAs NWs with Si-doped shells. This broad spectrum is very similar to the luminescence spectrum observed for compensated Si-doped GaAs, and leads to an enlarged Urbach tail at low energy side compared

Table 6.6 – *GaAs:Si NWs samples and experimental doping concentration. Low temperature (LT) CL spectra are used for a first doping estimation through Equation 5.14. Room temperature (RT) CL spectra give a second quantitative doping assessment through the electron Fermi levels. For low concentrations, electron Fermi levels are not easy to obtain from the luminescence lineshape, thus only estimations from low temperature FWHM are given.*

	LT		
sample	peak eV	fwhm meV	doping conc. cm^{-3}
76844	1.504	20±1	$(4.6 \pm 0.4)\ 10^{17}$
76846	1.504	21±1	$(5.0 \pm 0.4)\ 10^{17}$
76749	1.508	21±2	$(5.0 \pm 0.8)\ 10^{17}$
76766	1.511	24±2	$(6.1 \pm 0.8)\ 10^{17}$
76729	1.509	24±2	$(6.1 \pm 0.8)\ 10^{17}$
76449	1.518	32±12	$(9.3 \pm 5.8)\ 10^{17}$

	RT					
sample	peak eV	fwhm meV	E_g eV	E_{fc} eV	γ eV	doping conc. cm^{-3}
76844	1.429	45±2	1.418±0.007	-	0.010±0.002	
76846	1.430	48±1	1.416±0.004	-	0.008±0.002	
76749	1.430	51±2	1.415±0.002	-	0.010±0.001	
76766	1.433	52±3	1.419±0.003	-	0.010±0.001	
76729	1.431	56±2	1.417±0.003	-	0.014±0.001	
76449	1.434	61±5	1.419	0.013	0.015	$4.8\ 10^{17}$

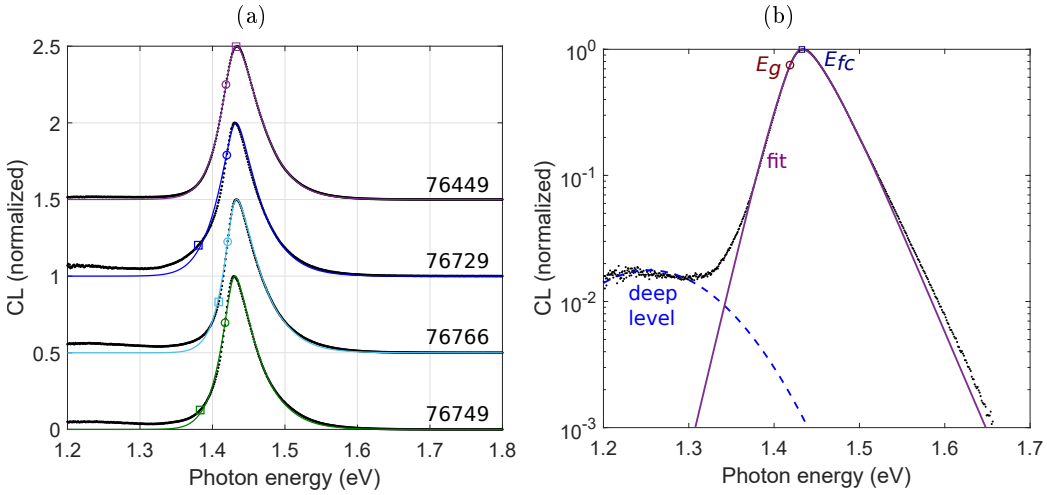

Figure 6.31 – *Comparison of CL spectra for n-type GaAs:Si NWs and fits. (a) Room temperature CL spectra of different Si-doped GaAs NWs extracted from the middle (ZB) homogeneous part. The intensity normalization factors are indicated. The open circle markers indicate the bandgaps and the open square markers show the electron Fermi levels. (b) CL spectrum (black dots) from the sample 76449 at room temperature and the fit (purple line). Small luminescence signal at low energy is attributed to deep levels (blue dashed line).*

to uncompensated GaAa at similar electron concentration [175]. The larger tails may also be related to surface states which cause the surface depletion. We notice that a discrepancy of one order of magnitude exists between expected doping levels (Table 6.5) and the values deduced from the measurements (Table 6.6). Surface depletion and/or Si dopant compensation may be responsible for the observed lower doping concentrations determined by CL. We suspect also a growth issue which hinders the incorporation of Si dopants. Finally, n close to 10^{18} cm^{-3} may be achieved which is acceptable for NW radial-junction solar cells (see Chapter 7).

6.5 Summary

This chapter begins with a succinct description of III-V semiconductor NWs grown in the molecular beam epitaxy (MBE) system. We employ the so-called self-catalyzed vapor-liquid-solid method to grow GaAs NWs on patterned Si(111) substrate. The peculiar crystal growth method results in several unexpected results: the coexistence of cubic zinc-blende (ZB) and hexagonal wurtzite (WZ) crystal structures in single NWs and the amphoteric behavior of Si dopants in GaAs. Cathodoluminescence (CL) is used to characterize GaAs NWs in terms of crystal phases, homogeneity and defects, surface passivation and doping levels, etc.

Section 6.2 is dedicated to the understanding of the WZ GaAs properties and to the CL measurements of undoped GaAs NWs containing ZB/WZ segments. WZ GaAs almost exists only in NW forms, so its properties are little known, and even the bandgap and the band structure are debated in the literature. We use CL mapping measured at various temperatures to clearly distinguish light emitted from ZB and WZ regions. We further evidence the optical transition of WZ GaAs using CL polarimetry. Light emitted from WZ GaAs is polarized perpendicular to the NW growth axis (i.e. c-axis of WZ lattice), as expected from the selection rule of dipole transitions in hexagonal lattice structure. We have measured up to 73% degree of polarization perpendicular to the WZ c-axis. CL spectra of WZ GaAs shows an exciton peak at 1.515-1.516 eV (FWHM 21 meV), and room temperature CL spectra of WZ GaAs shows a blueshifted peak compared to that of ZB GaAs (with a difference of less than 10 meV). We confirm that the bandgap of WZ GaAs should be close and slightly higher than that of ZB GaAs. CL and its variants (high-resolution mapping, temperature-dependent measurement and polarimetry etc.) constitute an advanced and versatile tool to investigate low-dimensional materials for opto-electronic applications.

In Section 6.3, CL measurements on Be-doped GaAs NWs are presented. We show CL maps as well as polarization measurements of Be-doped GaAs NWs containing WZ segments, which allows to attribute unambiguously the observed CL spectra to Be-doped WZ GaAs. Both ZB and WZ GaAs present similar CL spectra and bandgap narrowing (BGN) at high doping concentrations. The BGN values of ZB GaAs is used to quantitatively determine the p-type doping concentrations in single GaAs NWs, which is in agreement with expected doping levels as calibrated. Section 6.4 presents CL measurements on Si-doped GaAs NWs. Si dopant in GaAs seems to be more complicated due to its amphoteric characteristics, and the presence of a WZ phase in GaAs NWs causes unexpected CL features. Si-doped WZ GaAs shows a broad Gaussian-like CL shape centered at about 1.45 to 1.47 eV at low temperature, which is thermally quenched at room temperature. In ZB GaAs, donor band luminescence is identified at low temperature and the FWHM is used to assess the n-type doping concentration to be in the range of 4×10^{17} to 1×10^{18} cm^{-3}. To summarize, we have determined both p-type and n-type doping levels in GaAs NWs and have visualized inhomogeneities with nanometer resolution using CL mapping and spectral analysis. Contactless doping measurement by CL can also be extended to other material systems and is well suited for studying semiconductor nanostructures.

Chapter

7 GaAs Nanowire-Based Solar Cells

Chapter content

The unique shape of nanowires (NWs) has attracted a great attention for use in optoelectronic devices owning to their unprecedented optical properties such as waveguides [253] and optical antennas [254, 255]. The ability to concentrate light in a small volume and to collect diffuse sunlight thanks to a high angle tolerance make NWs attractive for photovoltaic solar cells. The direct growth of III-V NWs on lattice-mismatched substrates also provides a way to avoid the use of costly GaAs or InP substrates, and to integrate directly III-V on Si for tandem solar cells. Figure 7.1 shows a schematic of solar cell structures made of vertical NWs array, with charge carrier separation obtained in either (a) axial or (b) radial p-n (or p-i-n) junction. The axial junction approach is more suitable for tandem solar cells by engineering one or several heterojunctions with various bandgap materials. The constraint on lattice-mismatch of different semiconductors can be relaxed through small footprint of NW bases. The radial junction configuration (core-shell) emerges from the novel concept of decoupling the direction of charge carrier collection and the absorption of light. NWs can be made long enough to absorb sunlight while the photogenerated carriers are collected within a short distance. In this thesis, we focus on GaAs core-shell junction NW array solar cells.

In Section 7.1, we review the state-of-the-art of III-V NW solar cells and discuss the challenges of making efficient solar cell devices. For GaAs NW solar cells, we theoretically study the design of solar cell structures in terms of optical absorption and electrical core-shell junction. In Section 7.2, we use optical simulations based on the RCWA to calculate the absorption in a periodic GaAs NW array and to optimize the geometry (array period and NW diameter). The influences of NW length, diameter and array period on the absorption spectra are investigated.

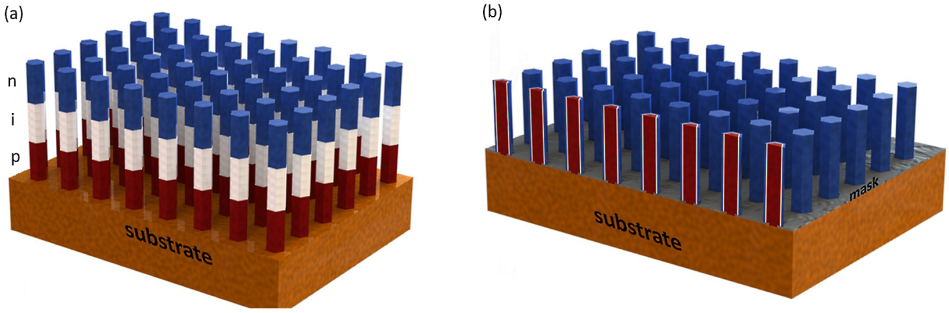

Figure 7.1 – *Schematic of NW array solar cells. Electronics structures (e.g. p-n junction or heterostructure) can be implemented (a) along the NW axis or (b) in the radial direction (Figure adapted from Ref. [256]).*

In Section 7.3, we calculate the built-in potential in core-shell junction at a given NW geometry in order to target the doping levels required in GaAs NW solar cells. In Section 7.4, we present the experimental works of fabrication and characterization of GaAs NW solar cell devices and we discuss the perspectives for efficiency improvement.

7.1 State-of-the-art

7.1.1 Single-nanowire solar cells

The use of III-V NWs as solar cell active regions has been investigated during the last ten years. Early-stage experimental demonstrations were based on the measurement of single-nanowire photovoltaic properties by contacting the two ends of the NW. Colombo et al. fabricated GaAs single-nanowire solar cells with radial p-i-n structure [257]. The growth was conducted in a MBE machine using the self-catalyzed method on a GaAs substrate and employing Si for both p-type doping during high-temperature (630°C) vapor-liquid-sold (VLS) growth and for n-type doping during low-temperature (465°C) vapor-solid (VS) growth. NWs were dispersed on an oxidized Si substrate and the contact on p-type core was achieved using citric acid solution for selective wet etching (Figure 7.2(a,b)). 4.5% efficiency was obtained under 1 sun illumination using the total projected area of the NW. Krogstrup et al. fabricated free-standing GaAs single-nanowire solar cells with a core-shell p-i-n structure using the similar MBE growth on a Si substrate with Be doping for GaAs NW core and ITO n-type top contact [258] (Figure 7.2(c)). They obtained photovoltaic performances of $V_{oc} = 0.43$ V, $FF = 0.52$ and an unreasonably high J_{sc} value owning to a small projected area used in the calculation.

Holm et al. fabricated horizontally lying GaAsP single-nanowire solar cell with radial p-i-n structure [259]. GaAsP NWs were grown by MBE on a Si substrate using the Ga-assisted method with Be and Si doping. H_3PO_4-based solution was used to selectively etch the n-type shell and to expose p-type core for contacting. They obtained the best efficiency of 10.2% under 1 sun illumination ($J_{sc} = 14.7$ mA/cm^2, $V_{oc} = 0.9$ V, $FF = 0.77$, ideality factor 2.0) with n+InGaP passivation, compared to 6.8% ($J_{sc} = 13.2$ mA/cm^2, $V_{oc} = 0.76$ V, $FF = 0.68$, ideality factor 2.2) without surface passivation.

However, one should be careful of the reported efficiency values of single-nanowire solar cells. The efficiency limit of nanowire-based solar cells is a highly debating subject, and the use of the physical projection area of a single NW is misleading and results in an overestimation of the short-circuit current. NWs possess optical antenna effects, leading to a higher apparent area called optical cross-section (see Figure 7.2(d) for illustration). The use of nanostructures can reduce the mismatch between absorption and emission angle. Therefore, the underlying physics of nanowire-based solar cells is still bounded by the Shockley-Queisser detailed balance limit

with a built-in optical concentration [58].

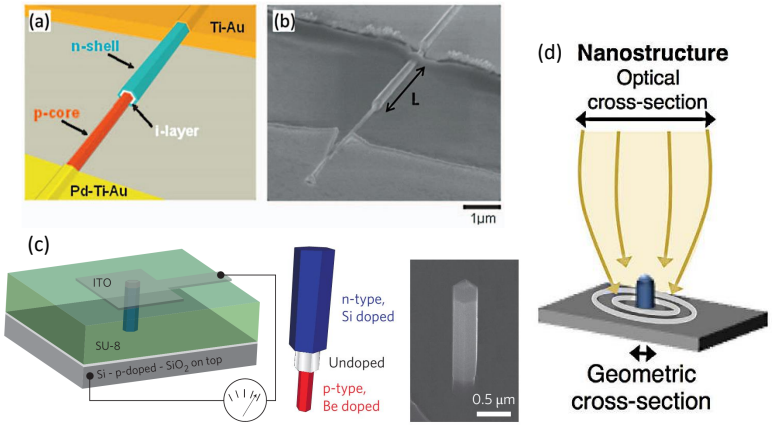

Figure 7.2 – *(a,b) Sketch of the radial p-i-n junction structure and SEM image of a typical device (extracted from reference [257]). (c) Schematic of the vertical radial p-i-n device connected to p-type Si wafer and ITO top contact. SEM image of a single GaAs NW is shown (extracted from reference [258]). (d) Schematic of the optical concentration using a nanostructure (extracted from reference [58]).*

7.1.2 Nanowire-array solar cells

For large-area photovoltaic applications, nanowire-based solar cells need to be scaled up, leading to nanowire-array solar cells. This requires a more stringent growth control of the position of each NW and of the uniformity of material quality and doping. The realization of devices also demands technical efforts such as planarization of the NW array for mechanical stability and deposition of transparent conductive oxide (TCO) to connect each NW.

LaPierre and coworkers at McMaster University are one of the earliest research groups to explore III-V NW arrays for solar cells, and demonstrated in 2009 the first GaAs p-i-n core-shell NW array solar cell with efficiency of 0.83% under 1 sun illumination [260]. They focused on the self-catalyzed MBE-growth of III-V NWs on Si substrates using the VLS method, with Be for p-type doping and tellurium (Te) for n-type doping. Te produced significant change of the NW surface morphology due to its surfactant effect and seems to severely impact the operating characteristics of photovoltaic devices. The surface passivation and TCO top contact were also studied and appeared to be critical issues for GaAs NW array solar cells. Employing sulfur passivation seemed to improve the efficiencies of p-n core-shell GaAs NWs, but the long-term stability remained problematic [261].

More recently, the same group reported GaAs NW array solar cells with efficiency of 3.3% under 1 sun illumination (J_{sc} = 18.2 mA/cm^2, V_{oc} = 0.39 V, FF = 0.465) [262]. A SiO_x mask (∼30 nm thick) was deposited by plasma-enhanced chemical vapor deposition (PECVD) on a p-Si substrate. The NW array was defined by writing hexagonal patterns of holes using electron beam lithography (EBL) and opening SiO_x holes by reactive-ion etching (RIE) with CF_4 chemicals and then in 10:1 H_2O:(10:1 buffered HF) solution. The NW structure and band diagram is shown in Figure 7.3(a). MBE growth was initiated with highly-doped GaP:Be stems which promoted the NW vertical yield on the Si substrate and served as back surface field (BSF) of GaAs solar cells. NW growth consisted in p-GaAs:Be core, then switched to shell growth of i-GaAs, n-GaAs:Te emitter, n+GaAs:Te contact layer and i-AlInP passivation. After growth, the NW arrays were planarized by spin-coating of benzocyclobutene (BCB) polymer; RIE with CF_4/O_2 chemicals was used to expose NW heads before the deposition of a continuous TCO contact. Note that the AlInP on top of the NWs was etched in dilute HCl to expose underlying n+GaAs contact. The front contact consisted of a 25 nm In/250 nm ITO bilayer deposited by RF sputtering, followed by

Ni/Ge/Au (25/50/325 nm) contact pads. After the contact deposition, an annealing was carried out at 250°C for 4 min under N_2 flow. The measured $J_{sc} = 18.2\,\mathrm{mA/cm^2}$ is relatively high, and the reduced EQE in the short-wavelength region was attributed to extended crystal defects in the NWs top facets occurring during the growth upon Ga droplet consumption, resulting in severe recombination losses at the top facet emitter. Low V_{oc} was attributed to lower doping levels than expected during the NW growth. The built-in potential across the radial junction was measured by off-axis electron holography [263] and less than 0.4 V was obtained [262]. The Be p-type doping concentration was confirmed to be equal to the nominal value of about $5 \times 10^{18}\,\mathrm{cm^{-3}}$ using secondary ion mass spectroscopy (SIMS) [157]. The severe V_{oc} loss was due to carrier depletion caused by lower Te n-type doping concentration in n-GaAs shell (one order of magnitude lower than the nominal value) [264].

Mariani et al. at University of California Los Angeles developed EBL patterned GaAs radial junction solar cells grown by catalyst-free selective-area MOCVD on GaAs substrates. In 2011, the group reported a GaAs nanopillar solar cell with power conversion efficiency of 2.54% under 1 sun illumination ($J_{sc} = 17.6\,\mathrm{mA/cm^2}$, $V_{oc} = 0.39\,\mathrm{V}$, $FF = 0.37$) [265]. The structure consisted in p-type GaAs core (diethyl-zinc doping) and n-type GaAs shell (disilane doping). Ex-situ passivation was performed using aqueous $(NH_4)_2S$ ammonium sulfide treatment then capped with BCB planarization. The same group then published the improved GaAs nanopillar solar cells employing in situ surface passivation with an efficiency of 6.63% ($J_{sc} = 24.3\,\mathrm{mA/cm^2}$, $V_{oc} = 0.44\,\mathrm{V}$, $FF = 0.62$) [266]. The substrate was changed to n+doped GaAs, and the structure consisted in n-type GaAs core (tetra-ethyl-tin) and p-type GaAs shell (dimethyl-zinc). In this device, the n-GaAs:Sn diameter is about 180 nm, the p-GaAs:Zn shell thickness about 40 nm and the InGaP passivating shell is 5 nm-thick, resulting in a total diameter of 270 nm (pitch 600 nm, orthogonal array) and nanopillar height of 1.3 μm. The effectiveness of the high-bandgap InGaP passivation was evidenced by the EQE enhancement and the higher V_{oc} obtained. Front contact Ti(4 nm)/ITO(350 nm) was found to be an ohmic anode on p-GaAs after rapid thermal annealing performed at 300°C for 1 min in an Argon-purged atmosphere. Later, the efficiency was slightly improved to 7.43% ($J_{sc} = 18.9\,\mathrm{mA/cm^2}$, $V_{oc} = 0.57\,\mathrm{V}$, $FF = 0.69$) [267]. The NW structure and J-V characteristics at 1 sun are shown in Figure 7.3(b). There was little modification compared to the previous structure, except for an intrinsic layer about 10 nm-thick between the n-p regions, leading to a nanopillar of total diameter of about 290 nm. The n-core doping target was $1 \times 10^{17}\,\mathrm{cm^{-3}}$, and the p-shell doping target was increased from $1 \times 10^{18}\,\mathrm{cm^{-3}}$ to $3 \times 10^{18}\,\mathrm{cm^{-3}}$. The BCB planarization was etched back to expose about 350 nm tips, making subsequent ITO deposition dome-shaped, forming local optical lens that focus light into active NW regions.

Yao et al. at University of Southern California reported an axial n-i-p GaAs NW solar cells with efficiency of 7.58% ($J_{sc} = 21.08\,\mathrm{mA/cm^2}$, $V_{oc} = 0.565\,\mathrm{V}$, $FF = 0.6365$) [268]. Device simulations were performed and showed that axial junctions are more tolerant to doping variation than radial junctions. V_{oc} and J_{sc} of radial junction solar cell decreases dramatically if the base doping is below $10^{17}\,\mathrm{cm^{-3}}$. The choice of an axial junction made the junction design easier than radial junction, and enables easier integration for multijunction solar cells. GaAs NWs were fabricated by selective-area MOCVD growth on n+GaAs (111)B substrate, with a SiN_x mask patterned by EBL over 1 $\mathrm{mm^2}$ surface area. The NW array was planarized by BCB and capped with ITO to contact the p-GaAs emitter. No passivation step was carried out specifically. The NW array had the following geometry parameters: orthogonal array with period 600 nm, 320 nm NW diameter and 2.5 μm height. Different samples with varying NW diameter and p-GaAs emitter thickness were investigated. Small diameters below 100 nm degraded the solar cell performances because of the unpassivated lateral surface. For thin wire we can expect them to be nearly depleted while minority carriers are captured by surface states and subsequently annihilated through recombination. Deeper junctions (thicker p-GaAs emitter) also showed degraded performance because highly doped emitter has small minority carrier lifetime, and

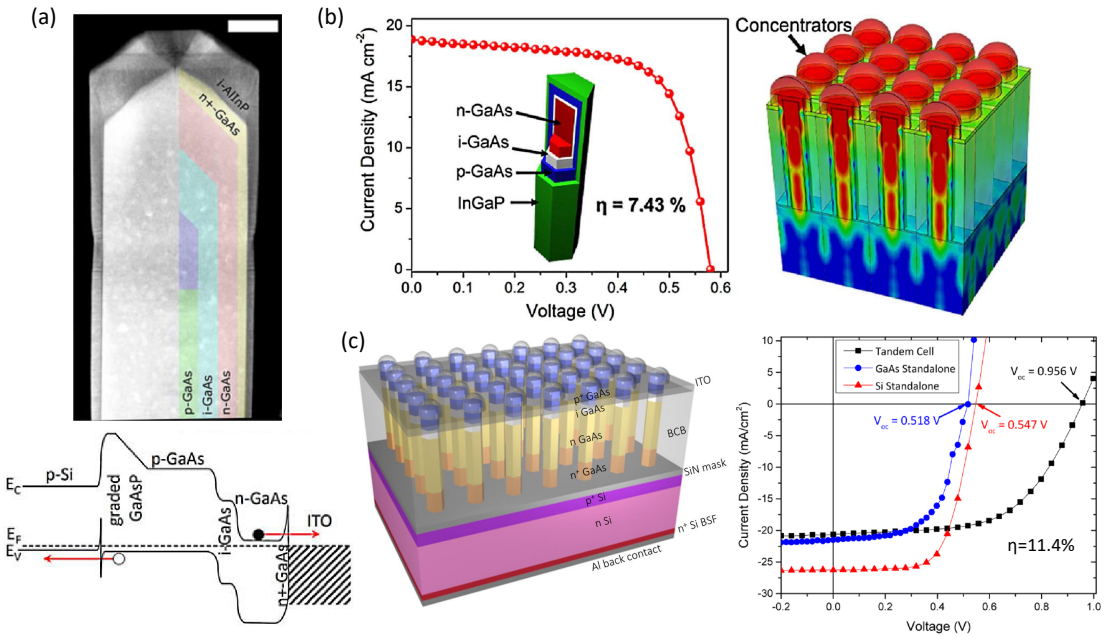

Figure 7.3 – *(a) HAADF image of a FIB cross-sectioned NW with color overlay indicating approximate device structure including p-GaAs core (green), GaAs growth during Ga-droplet consumption (purple), i-GaAs (light blue), n-GaAs (red), n+GaAs (yellow) and i-AlInP (dark gray). TEM scale bar is 100 nm. Bottom: energy band diagram along the NW axis, indicating the different layers of the solar cell (extracted from reference [262]). (b) Current-voltage characteristics of the GaAs p-i-n nanopillar array solar cells under AM1.5G illumination and illustration of the core-shell structure. Right: optical power flux within the periodic structure, with ITO dome acting as a subwavelength nanolens to concentrate the optical power in the active nanopillar region (extracted from reference [267]). (c) Schematic of GaAs NW-on-Si tandem solar cell and current-voltage characteristics of the device. The arrows indicate the open-circuit voltages for each cell, showing an addition of V_{oc} of the tandem cell from separate stand-alone GaAs NW and Si bottom cells (extracted from reference [192]).*

most of the photo-generated carriers are located near the top surface. This effect was also studied by cathodoluminescence mapping, which revealed lowered CL intensity at the highly-doped top region. The best solar cells featured NWs with a 320 nm diameter and a 100 nm junction depth. This work was further extended for GaAs NWs on silicon tandem solar cells with the observation of voltage addition of the GaAs NW top cell and the Si bottom cell for an open circuit voltage of 0.956 V and an efficiency of 11.4% [192] (see Figure 7.3(c)). Simulations showed that the current-matching condition plays an important role in the overall efficiency. Despite of technical challenges, this first realization of nanowire-on-silicon tandem solar cell opens great opportunities for III-V NWs integrated in industrially matured Si technologies.

To date, researchers at Lund University hold the record for GaAs NW solar cells with 15.3% efficiency (J_{sc} = 21.3 mA/cm^2, V_{oc} = 0.906 V, FF = 0.792) [88]. GaAs NWs were grown by MOCVD on patterned p-type GaAs (111)B substrate using nanoimprint lithography and Au-catalyzed VLS method. The structure consisted in an axial p-i-n junction including a thin AlGaAs passivation shell (25-40 nm thick). The geometries of the NW array were: pitch 400 or 500 nm, NW diameter 165 nm and height 2.8-3.1 μm. Electron-beam induced current (EBIC) linescan along the NW showed an extended diffusion length, revealing the efficient collection of charge carriers resulted from the effective passivation of GaAs NWs.

InP is also a material of interest for photovoltaic applications. InP NWs and related alloys (e.g. GaInP and AlInP) are extensively studied. For example, Fukui group at Hokkaido University fabricated InP NW array using catalyst-free selective-area MOVPE growth [269], and demonstrated core-shell InP NW solar cells with efficiency of 6.35% using an lattice-mismatched AlInP window layer [270]. On the other hand, best axial junction NW solar cells shown higher efficiencies. Cui et al. fabricated axial p-n junction InP NW array solar cells using nanoimprint lithography and An-catalyzed MOVPE growth, and demonstrated an efficiency enhancement up to 11.1% after surface cleaning by piranha etching [271]. Wallentin et al. fabricated 13.8%-efficient axial p-i-n junction InP NW array solar cells (J_{sc} = 24.6 mA/cm^2, V_{oc} = 0.779 V, FF = 72.4%) [272]. The NW diameter and the length of the top n-segment were found to be critical for cell performance. A high J_{sc} was achieved by using resonant light trapping in 180 nm-diameter NWs that only covered 12% of the surface. 17.8%-efficienct InP NW solar cells was also demonstrated using top-down etching of InP epilayers [273].

To summarize, we can see that there is still room of efficiency improvement for single-junction NW solar cells toward the theoretical Shockley-Queisser limit. We also notice that the photovoltaic performance of core-shell junction solar cells is still lower than that of axial junction solar cells. The control of doping levels seems to be one of the critical issues in core-shell junction NW solar cells. The challenges toward efficient NW solar cells include the homogeneity of NW arrays, junction designs, surface passivation, front contacts, etc. In the following, we will study the optical absorption of NW arrays (Section 7.2) and electrical designs of core-shell junction (Section 7.3).

7.2 Optical absorption of nanowires

In this section, we discuss the optical properties of NW arrays, and perform RCWA simulations to optimize the geometry of vertical GaAs NW arrays on a Ag mirror as well as a Si substrate for light harvesting. We compare the shape of the NW cross-section (square or circle) and the arrangement array patterns (square or hexagonal). The influence of the array period, the NW diameter and the NW length on the absorption spectra are illustrated.

7.2.1 Absorption of nanowire arrays

We calculate the optical absorption of periodic NW arrays using Reticolo software which implements a RCWA solver as described in Chapter 2.1.4. In Reticolo calculations, the patterns of periodic nanostructures are defined in Cartesian coordinates, thus a square NW shape is easier to be defined. However, the cross-section of a NW grown along (111) direction exhibits a hexagonal shape. Reticolo can be adapted to define an arbitrary shape by overlapping several squares or rectangles (parameter *Ntre* is the number of the overlapping objects). A hexagonal cross-section may be calculated, but the dependence on the polarization direction increases the time of calculations, hence we drop the hexagonal cross-section. Instead, a circular NW cross-section is chosen and the cylindrical symmetry nature make it easier for subsequent transport modeling, especially for core-shell junction. The array arrangement may also have some differences: NWs can be placed at the orthogonal grid points or arranged as hexagonal packing, as illustrated in Figure 7.4.

For each NW shape associated with an array arrangement, we give the geometrical parameters used in the calculations. They are: diameter (d_x, d_y) of NWs and array period (p_x, p_y) which is the size of an unit cell. We define the NW density or the filling ratio (FR) as the volume fraction occupied by NWs. The diameter is clear for circular NW, but may become ambiguous for other shapes. The period is also misleading in a hexagonal array. We adapt the notations here for general diameter d and array period p, except for explicit mentions.

- Orthogonal array of squares: $p = p_x = p_y$; $d = d_x = d_y$; FR $= \frac{d^2}{p^2}$.
- Orthogonal array of circles: $p = p_x = p_y$; $d = d_x = d_y$; FR $= \frac{\pi d^2}{4p^2}$.
- Hexagonal array of circles: $p = p_x = p_y/\sqrt{3}$; $d = d_x = d_y$; FR $= \frac{\pi d^2}{2\sqrt{3}p^2}$.

The space between NWs is filled with a polymer which is assumed to be non absorptive and has a constant refractive index of 1.5 over the spectral range of interest for GaAs absorption. A flat silver back mirror is used in the calculations here to maximize absorption of light in GaAs NWs. Here, we calculate only the zero-order reflectivity (R) at normal incidence to save the computation time (Fourier order $M_x = M_y = 20$, $Ntre = 20$ to define the circle). We then calculate the total short-circuit current density J_{tot} by integrating $1 - R$ with the AM1.5G solar spectrum. J_{tot} maps as a function of the array period p and the NW diameter d (fixed NW length of 1 μm) are displayed in Figure 7.4. Note that J_{tot} calculated here is to visualize of optimal geometry. J_{tot} is slightly higher than expected photocurrent because it includes absorption in Ag and higher order reflection for the wavelength of light smaller than the period of NW arrays.

NW shapes and array geometries

Comparing the three configurations mentioned above for NW shapes and array arrangements, we draw white dashed lines for constant FR on the J_{tot} photocurrent maps in Figure 7.4. The trend of photocurrent is very similar between different NW shapes and array geometries. The optimal geometrical parameters lies, for the three cases, at 25% to 30% FR (triangle markers), with $d = 350$ nm and $p = 580$ nm for orthogonal array of circular NWs and $d = 360$ nm and $p = 640$ nm for hexagonal array of circular NWs. In these cases, we obtain the total short-circuit current of about 29.5 mA/cm^2. The photocurrent maps also show that a large range of parameters leads to globally high absorption with J_{tot} above 29 mA/cm^2: for circular NWs, $d = 300$–360 nm and $p = 540$–640 nm. Foldyna et al. have studied optical absorption in c-Si NW array and also concluded that the NW density has the major impact on the short-circuit current, while the NW organization is less important [274].

We note that another local maximum of total photocurrent exists around $d = 160$ nm and $p = 400$ nm (FR about 15%) for circular NWs. This enhancement is attributed to HE_{11} leaky/guided

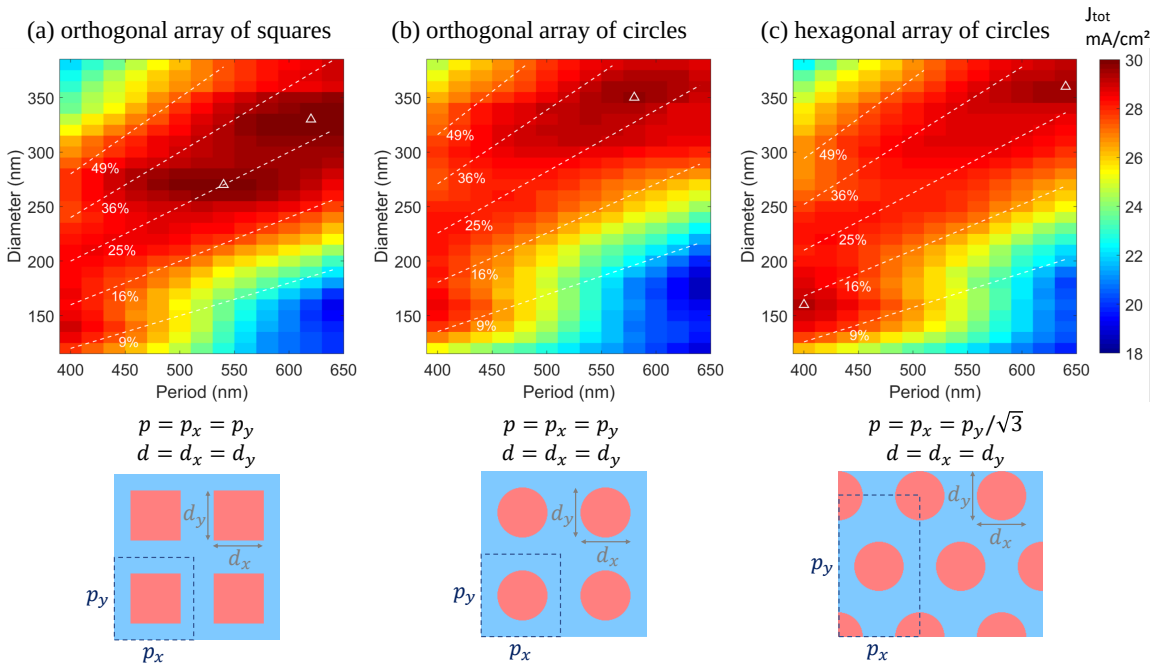

Figure 7.4 – *RCWA simulation of J_{tot} in GaAs NW arrays on a Ag back mirror. The NW length (height) is fixed at 1μm and the array pitch (period) and NW diameter are varying. Total short-circuit current J_{tot} (mA/cm^2) is used as a figure of merit of the broadband absorption over the AM1.5G solar spectrum, and is shown with a color scale in 2-dimensional maps as a function of the array period and the NW diameter. Different array arrangements and shapes of NW cross section are possible and are illustrated below the J_{tot} maps. The optical calculations correspond to three simple cases: (a) orthogonal array of square NWs, (b) orthogonal array of circular NWs and (c) hexagonal array of circular NWs (average TE/TM polarizations). White dashed lines with percentages on the J_{tot} maps mark the surface filling ratio (FR) of NWs.*

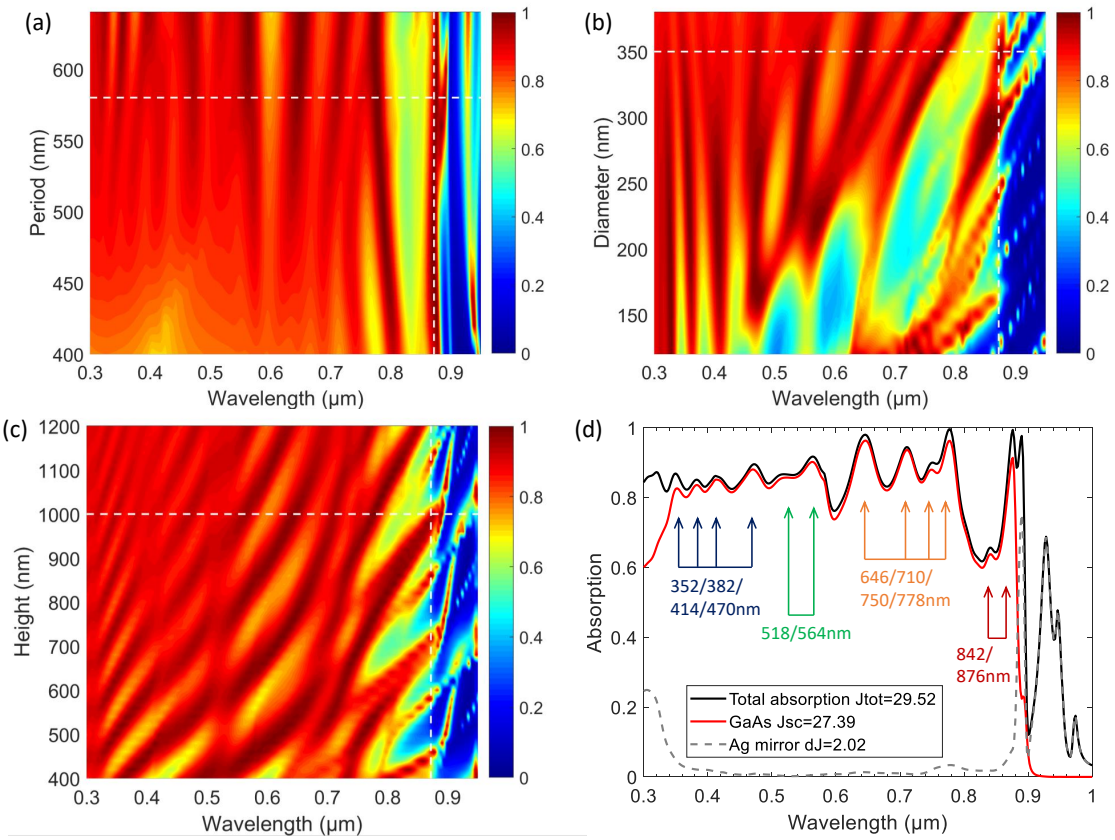

Figure 7.5 – *Calculated absorption in cylindrical GaAs NW arranged in square arrays on a flat Ag mirror filled with a non-absorbing dielectric material of refractive index of 1.5. (a) 1-R spectra as a function of the array period for GaAs NWs length of 1 μm and diameter of 350 nm. The horizontal white dashed line indicates the array period of 580 nm, and gives rise to the optimum broadband absorption. (b) 1-R spectra as a function of the cylindrical GaAs NW diameter at a fixed array period of 580 nm and length of 1 μm. The horizontal white dashed line indicates the diameter of 350 nm. (c) 1-R spectra as a function of the GaAs NW length at a fixed array period of 580 nm and diameter of 350 nm. The horizontal white dashed line indicates the NW length of 1 μm. (d) Absorption spectra in GaAs NW array of 1 μm-length with the optimized geometry (array period $p = 580$ nm and NW diameter $d = 350$ nm).*

mode in individual NWs [275]. This also corresponds to the choose of GaAs NW diameter of 165 nm for the 15.3%-efficient axial junction NW solar cells [88]. Managing radial junction in 160 nm thin NW diameter becomes more challenging, hence we explore the HE_{12} leaky/guided mode in larger NW diameter of about 350 nm.

In the following, we focus on a square array of circular cross-section NWs. The optimum geometry of 1 μm-long NWs is $d = 350$ nm and $p = 580$ nm. The corresponding absorption spectra in GaAs and in the Ag mirror are given in Figure 7.5(d). Multiple resonances overlap and give rise to $J_{th} = 27.4\,\mathrm{mA/cm^2}$ for absorption in GaAs. The electric field intensity cross-sections are given in Figure 7.6 for several selected resonant wavelengths. In order to visualize the influences of the geometry on the absorption spectrum, we start from the optimal structure and we vary the array period (Figure 7.5(a)), the NW diameter (Figure 7.5(b)), and the NW height (Figure 7.5(c)). 1−Reflectivity $(1 - R)$ is plotted as a function of wavelengths and the varying parameters, with the white dashed lines indicating the optimum structure and NW height of 1 μm.

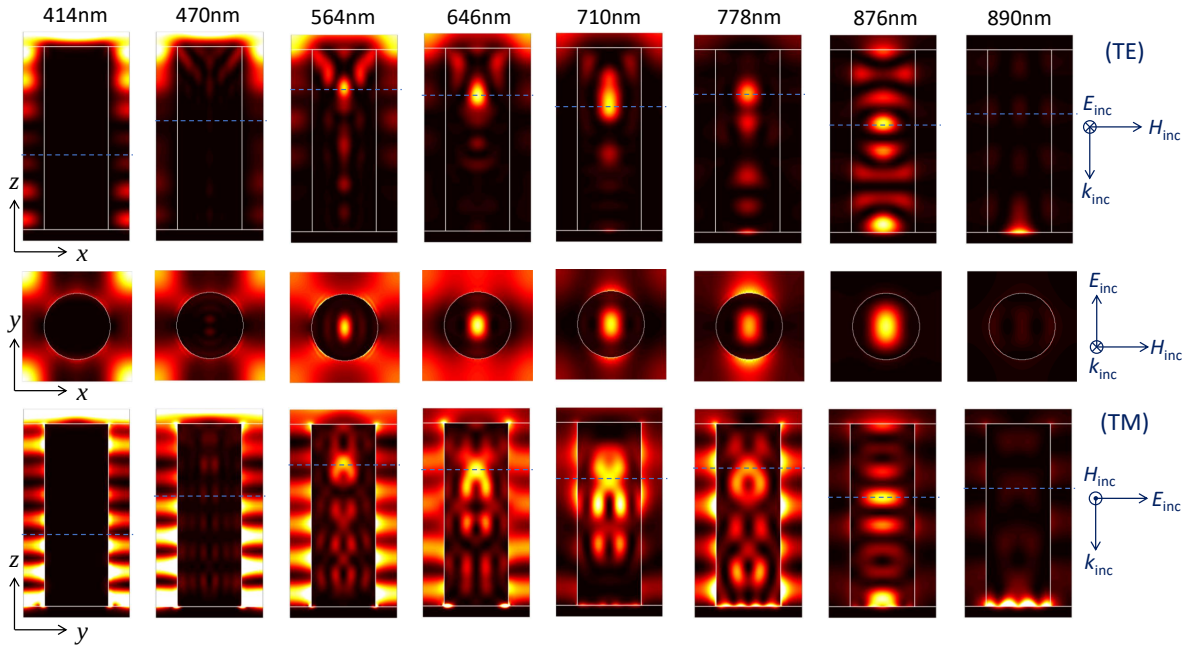

Figure 7.6 – *Electric field intensity distributions at several resonant wavelengths for the GaAs NWs of height 1 µm arranged in a square array with optimized period of 580 nm and NW diameter of 350 nm. Either TE or TM incident electromagnetic fields are used to calculate the electric field patterns in NWs. Corresponding NW cross-section views of electric field distribution are also shown (at the position indicated by the blue dashed lines).*

Influence of array period

Sturmberg et al. proposed a semi-analytical approach to study the influence of the NW array parameters on the broadband absorption [276]. They investigated the period variation at a given volume fraction for NW arrays on an absorptive substrate. Increasing the period and thus the diameter increases the number of resonance modes, but leads to higher transmission into the substrate through non-zero order diffractions. Hence, there is a compromise on the array period to support multiple resonances while keeping only a single transmission channel at long wavelengths. Fountaine at al. studied resonant absorption in periodic array of silicon NWs that combined a leaky waveguide theory and that of photonic crystals supporting Bloch modes [277]. As array period decreases for a given NW diameter, the NW array progresses from sparse to dense and the dominant resonant mechanism turns from the leaky mode resonances in individual NWs to the photonic Bloch modes governing the coupled NW arrays. This can be understood by taking analogy with the electronic band structure in solid-state physics: when inter-wire spacing is large, the isolated photonic modes of a NW are only slightly perturbed by the NW "lattice".

In our case, we place a back mirror so that non-zero order diffraction can only occur through reflection back in air. From the period dependence of total absorption (Figure 7.5(a)), we observe relatively small variation of absorption peaks in the vicinity of the optimal period of 580 nm. This suggests minor influence of optical coupling between NWs for the optimized structure, and resonances in individual NWs are more significant.

Influence of NW diameter

The resonance features in single NWs are confirmed by plotting the absorption spectra as varying the NW diameter (Figure 7.5(b)) and keeping all other parameters constant. Especially in the long wavelength range ($\lambda > 550$ nm), we observe that the resonant wavelengths increase with

the NW diameter. This is typical for leaky/guided modes in individual NWs. The electric field intensity in NW cross-sections (Figure 7.6) also show very similar field patterns compared to fiber waveguides.

Anttu and Xu optimized the geometry of InP NW arrays and found the existence of optimal NW diameters which depend specifically on the bandgap of the material [278]. For InP, these diameters are 170 nm and 410 nm. Surprisingly, we find 160 nm and 350 nm for GaAs NWs, with slightly higher bandgap (thus shorter cut-off wavelength) than InP. The redshift of the absorption peaks due to leaky/guided mode resonances with the increase of NW diameters is calculated in GaAs NW arrays [279, 280], which provides a rational choice of NW diameter by placing the resonant peak energy with the full-width at half maximum just above the bandgap of the material. Having in mind the strong diameter-dependent resonant absorption, improvement of broadband absorption is proposed by tapered NW shape (decreasing NW diameter from bottom to top) [279] or by introducing several different NW diameters to maximize the overlap of absorption peaks associated with each diameters [280].

Influence of NW height

Figure 7.5(c) shows the evolution of absorption spectra with the NW height (length) and keeping all other parameters identical: $p = 580$ nm and diameter $d = 350$ nm. The influence of NW lengths is generally related to the absorption coefficient of the material itself. For low absorptive material like c-Si, the absorption of the NW arrays increase with the length of NWs logarithmically [274]. Typically, c-Si NW length up to 10 μm and beyond is needed to absorb efficiently the solar spectrum, while 1–2 μm is sufficient for direct bandgap semiconductors like GaAs. Here we choose for GaAs NW a length of 1 μm with a reflective back mirror. The spectral shift with the NW length indicates some influence of vertical Fabry-Perot resonances. As shown in the field intensity distribution cut in a vertical plane of a NW (Figure 7.6), vertical oscillation patterns exist. In the short wavelength range (λ =300–600 nm), Fabry-Perot resonance appears in the air/polymer/Ag mirror cavity, and the absorption in GaAs is very efficient because of high absorption coefficient in this spectral range. At longer wavelengths, the field distributions show both vertical oscillations and lateral patterns. This can be understood as light couples to the guided modes of NWs which propagates back and forth in the NW, resulting in the Fabry-Perot resonances.

In summary, we find a high value of short-circuit current J_{sc} up to 27.4 mA/cm^2 for absorption in GaAs NWs of height 1 μm, diameter 350 nm and square array period 580 nm. This results in less than 300 nm-thick equivalent thin-film layer used for the absorber material. It is thus possible to achieve broadband absorption with reduced volume of active GaAs. The geometry of NW arrays (diameter and period) can be tuned depending on the NW length chosen. Anti-reflection coatings can be further added to reduce the reflection loss and to maximize optical absorption in GaAs.

GaAs NWs on a Si substrate

One of the advantages of III-V NWs is their ability to be integrated directly on Si to make tandem devices. In Figure 7.7, we show the absorption calculation for GaAs NW arrays on a Si bottom cell. The NW height is always fixed to 1 μm, and the square array period p and NW circular diameter d are varying. Figure 7.7(a) shows the map of the photocurrent generated from the absorption in GaAs NWs, Figure 7.7(b) from the absorption in the Si bottom cell and Figure 7.7(c) is their difference. It is obvious that dense NW arrays generate large currents from top GaAs NWs, and sparse NW arrays favor light transmission into the Si bottom cell. The condition for current matching (white band in Figure 7.7(c)) is shown to be very sensitive to the variation of the NW array geometries. The precise control of NW arrays is critical to achieve

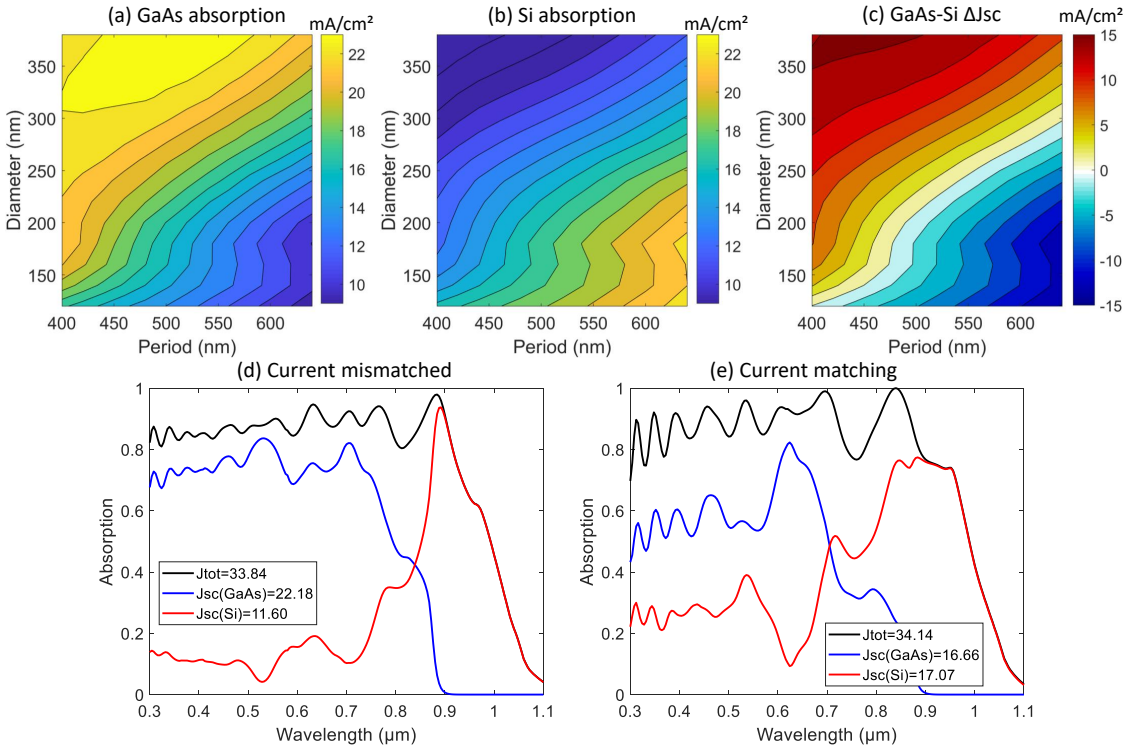

Figure 7.7 – *Calculated absorption in cylindrical GaAs NWs arranged in a square array on Si substrate filled with a non-absorbing dielectric material of refractive index of 1.5. (a) Short-circuit current J_{sc} in GaAs, (b) in Si and (c) difference of 1 sun short-circuit current density (ΔJ_{sc}). (d) Absorption spectra for the NW array of period 580 nm and diameter of 350 nm, leading to higher absorption in GaAs. (e) Absorption spectra in the case of an array period of 620 nm and diameter of 280 nm, lowering the absorption on GaAs to achieve current matching with Si.*

current matching and play an important role on the efficiency of tandem cells [192].

In Figure 7.7(d), we give the absorption spectrum in GaAs (blue) and in Si (red) for the NW array: $p = 580$ nm and $d = 350$ nm, which leads to over 10 mA/cm^2 higher current generated in GaAs than in Si. With a slightly larger array period $p = 620$ nm and a smaller NW diameter $d = 280$ nm, we arrive near the current matching condition (Figure 7.7(e)). However, lowering the current generated in GaAs is accompanied by non-absorption of high-energy photons, which are subsequently absorbed in the Si bottom cell. In this way, the photon energies are wasted in the thermalization process of the Si bottom cell. A reasonable design should decrease considerably the array period and GaAs NW diameter to absorb efficiently high-energy photon, otherwise, higher bandgap material like GaInP or GaAsP can be used to make tandem solar cells with Si.

7.2.2 Photogeneration in cylindrical symmetry

In this last part, we calculate the rate of photogenearated carriers in GaAs NWs at normal incidence. Since cylindrical NWs are invariant upon rotation, electronic simulation can be performed in a reduced 2-dimensional manner (in vertical z and radial r direction) hence can largely reduce the computation time and memory. By symmetry of the device, the optical simulation can also be performed for only one polarization orientation, for example, TE incident light. Because sunlight is unpolarized, the resulting distribution of generated carriers is identical to the calculation using TE polarization and then averaging over the rotation angles.

The rate of photogenerated carriers is already presented in Chapter 4 for ultrathin GaAs solar cells. The step consists in expressing the electromagnetic power absorbed by the material which is given by the divergence of the Poynting vector (Equation 4.20) then calculating the density of absorbed photons (Equation 4.21). After summing the absorbed photons over the AM1.5G solar spectrum, we obtain the photogeneration rate $g(x, y, z)$ in 3-dimension. We calculate it for the square array of cylinder GaAs NWs ($d = 350$ nm and $p = 580$ nm) with TE incident polarization. Figure 7.8(a) displays a cross-section map of the generation rate $g(x, 0, z)$, and Figure 7.8(b) for the other plane of visualization $g(0, y, z)$. The later can also be regarded as TM incident polarization for the plane of incidence $y = 0$. The generation profile $g(z)$ averaged over x- and y-direction is shown in Figure 7.8(c).

For NW with circular cross-section, we write the different elementary volumes in cylinder coordinates: $g(x, y, z)\, dx\, dy\, dz = g(r, \theta, z)\, rdr\, d\theta\, dz$. We can then average the generation rate through angle θ and obtain

$$\overline{g}(r, z)\, rdr\, dz = \frac{1}{2\pi} \int_0^{2\pi} g(r, \theta, z)\, rdr\, d\theta\, dz. \tag{7.1}$$

Figure 7.8(d) displays the angle averaged generation map $\overline{g}(r, z)$ [s^{-1}cm^{-3}]. This constitutes an input for electrical simulation solving electrostatic and transport equations in cylinder coordinates.

We can notice that most of the photogenerated carriers are concentrated in the center of the NWs due to the guided-mode nature of optical resonances. Globally, the photogenerated carriers decrease from top to the base of the NWs, therefore, defects present at top of the NWs may degrade severely the photovoltaic performance. We can further add a high-bandgap material surrounding the GaAs NWs to avoid non-radiative recombination of photogenerated carriers near the top surface.

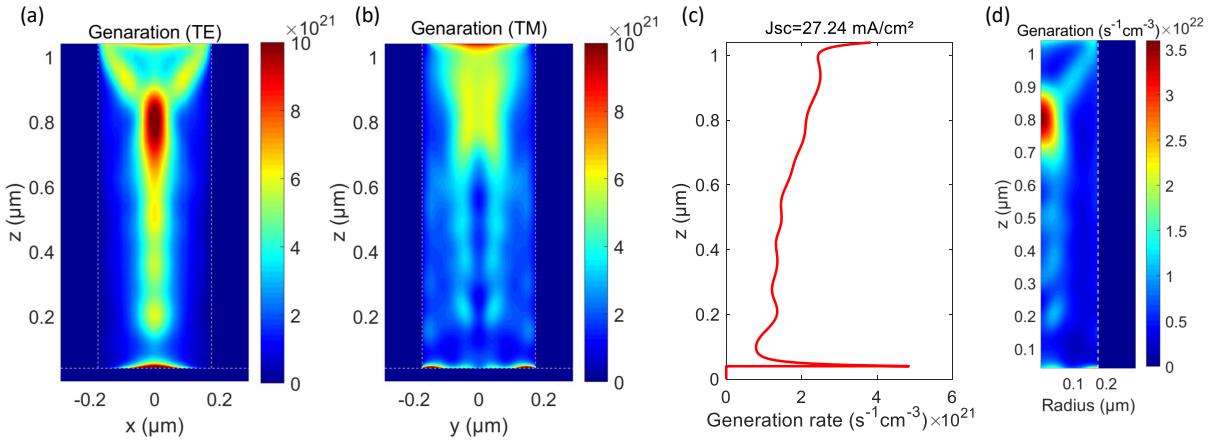

Figure 7.8 – *Generation of carriers by integrating the absorbed electromagnetic power over all photon energies, assuming that each absorbed photon creates one eletron-hole pair. (a) and (b) Generation map cut at the symmetry plane with TE and TM incident electromagnetic field, respectively. (c) Generation profile in the z-direction by summing over the x- and y-direction. (d) Generation map in the z- and radial r-direction by summing over the angular distribution.*

7.3 Electrical model in cylindrical symmetry

Due to the small dimension of NWs, electronic and transport properties inside single NWs may be very different from that of conventional planar solar cells. In particular, we focus on core-shell junction. To take advantage of the charge carrier separation in the radial direction, we should consider carefully the solar cell design in terms of core-shell thicknesses and doping levels. Here, we study the energy band profile analytically to have a comprehension overview on the underlying physics behind material parameters and device performances.

Electrostatic potential of planar surfaces and p-n junctions is treated classically with an abrupt junction and formation of a space-charge region which is totally depleted of free carriers. In a radial configuration, the physical mechanism is the same. We denote (r, θ, z) the position coordinates in a NW. With the symmetry of a long cylindrical NW, it can be assumed that the electric field $\mathbf{E} = E(r)\mathbf{e}_r$ and the electric potential $\psi(r)$ depend only on the radial position r. Poisson's equation is reduced to an ordinary differential equation in r.

$$\frac{1}{r}\frac{d}{dr}\left(r\frac{d\psi}{dr}\right) = -\frac{1}{r}\frac{d}{dr}\left(rE(r)\right) = -\frac{\rho}{\varepsilon}, \tag{7.2}$$

where ρ is the local net charge density, ε is the permittivity of the NW material. For n-type semiconductor, we adopt the complete ionization assumption (i.e. $N_D = N_D^+$) and full depletion approximation (i.e. $n \ll N_D^+$) such that $\rho = qN_D$ is constant in the depletion region and $\rho = 0$ in the quasi-neutral region. The general solution of the Poisson's equation for $E(r)$ and $\psi(r)$ is given by

$$\begin{aligned} E(r) &= \frac{\rho}{2\varepsilon}r - \frac{C_1}{r} \\ \psi(r) &= -\frac{\rho}{4\varepsilon}r^2 + C_1\ln(r) + C_2 \end{aligned} \tag{7.3}$$

where C_1 and C_2 are constants. Note that theses constants are different depending on which region is considered: space charged region or quasi-neutral region, so they should be calculated case by case with proper boundary conditions. Compared to planar configuration where the electric field is linear with the distance and the electrical potential is quadratic, cylinder symmetry results in another term in $1/r$ in $E(r)$ and $\ln(r)$ in $\psi(r)$. Therefore, a different field and potential distribution in thin NWs than in thin-films could be expected. In the following, we first calculate

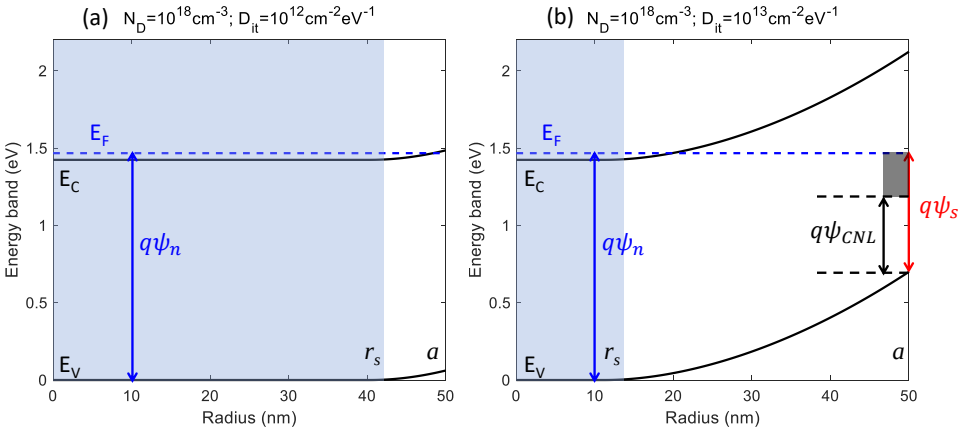

Figure 7.9 – *Calculated band diagram for n-type GaAs NW of diameter 100 nm (radius 50 nm) and doping concentration* $N_D = 10^{18}\,\mathrm{cm}^{-3}$. *The density of surface or interface states* D_{it} *is (a)* $D_{it} = 10^{12}\,\mathrm{cm}^{-2}eV^{-1}$ *and (b)* $D_{it} = 10^{13}\,\mathrm{cm}^{-2}eV^{-1}$. *The blue background represents the quasi-neutral region. High density of surface states enlarges the depletion zone and creates a surface barrier.*

the surface deletion in n-type NW to investigate the influence of surface states on the electrical properties of NWs. We then calculate the built-in potential in the p-core/n-shell homojunction in order to target the doping levels required in NW solar cells.

7.3.1 NW surface depletion

We begin by considering n-type GaAs NWs with diameter of 100 nm (radius $a = 50$ nm) and we study the surface depletion effect as a function of doping level and density of surface states. Surface depletion may degrade the performance of solar cells and may be responsible for the low electron concentration observed in NWs (Chapter 6.4). The surface of GaAs is known to have detrimental surface states near the mid-gap, which is characterized by a parameter D_{it} called density of surface (or interface) states. We found typically $D_{it} \simeq 10^{13}\,\mathrm{cm}^{-2}\mathrm{eV}^{-1}$ for free GaAs surface with native oxide [281]. We have shown in Figure 5.3 the variation of planar surface depletion width as a function of doping levels for unpassivated GaAs surfacse characterized by a fixed surface potential. In general, the depletion width is reduced at higher doping levels. Here, we solve the problem in cylinder symmetry and model the effect of density of surface states.

Considering that a shell near the surface is completely depleted of free carriers ($\rho = +qN_D$) and the inner core is neutral ($\rho = 0$), the interface is marked by the radius position r_s in the total radius a of NW. The solution of Poisson's equation for the electrical potential is

$$\psi(r) = \begin{cases} \psi_n & \text{for } 0 < r < r_s \\ \psi_n + \dfrac{qN_D r_s^2}{2\varepsilon}\left[-\dfrac{r^2}{2r_s^2} + \ln\left(\dfrac{r}{r_s}\right) + \dfrac{1}{2}\right] & \text{for } r_s < r < a \end{cases} \tag{7.4}$$

where ψ_n is the potential at the unperturbed (quasi-neutral) region. We note the continuity of potential at $r = r_s$. Since the potential is defined relatively with a reference, we choose here the measure of valence band with respect to the Fermi level at equilibrium. ψ_n depends on the electron Fermi level E_{fc} and thus on the free carrier concentration, and is calculated in general with the Fermi integral (see also Section 5.4.1 for details): $q\psi_n = E_g + (E_{fc} - E_c) = E_g + kT\mathcal{F}_{1/2}^{-1}(N_D/N_c)$ where N_c is the effective density of states in the conduction band. This can be done by numerical interpolation with tabulation values of the Fermi integral.

The calculated potential is plotted as an energy band diagram in Figure 7.9 for $N_D = 10^{18}\,\mathrm{cm}^{-3}$ with different densities of surface states. To determine the thickness of depleted shell, we need to examine the potential at the surface $\psi_s = \psi(r = a)$, which is calculated independently

by the density of surface states and the conservation of charge. The charge neutrality level (CNL) of GaAs is taken as $\psi_{\mathrm{CNL}} = 0.53\,\mathrm{V}$ [22]. At the surface, we consider that surface states (acceptor-like) are negatively charged from CNL up to the Fermi level (see gray zone in Figure 7.9(b) for illustration), and assume that the density of surface states D_{it} is uniform in this energy range. The surface charge Q_{it} is then given by

$$Q_{it} = -q^2 D_{it}(\psi_s - \psi_{\mathrm{CNL}}). \tag{7.5}$$

Charge conservation states that the sum of all bulk and surface charges in the system is zero

$$\pi(a^2 - r_s^2)\, qN_D + 2\pi a\, Q_{it} = 0. \tag{7.6}$$

Substituting Equation 7.5 into Equation 7.6, we obtain an expression of surface potential ψ_s as a function of the density of surface states D_{it}. On the other hand, ψ_s should be equal to the potential given by Equation 7.4 at the surface boundary $r = a$.

$$\psi_s = \frac{(a^2 - r_s^2)N_D}{2aqD_{it}} + \psi_{\mathrm{CNL}} = \frac{qN_D r_s^2}{2\varepsilon}\left[-\frac{a^2}{2r_s^2} + \ln\left(\frac{a}{r_s}\right) + \frac{1}{2}\right] + \psi_n \tag{7.7}$$

This yield a transcendent equation in r_s, which can be solved numerically (for example using *fsolve* function in Matlab). However, this equation cannot be solved for all a values. For a defined set of N_D and D_{it} values, there exists a certain critical GaAs NW radius a_{crit} for which the NW is fully depleted. More detailed calculations concerning the case of total depletion are found in Ref. [282].

With $D_{it} = 10^{13}\,\mathrm{cm^{-2}eV^{-1}}$, we find $a_{crit} = 44\,\mathrm{nm}$ for $N_D = 10^{18}\,\mathrm{cm^{-3}}$ and $a_{crit} = 74\,\mathrm{nm}$ for $N_D = 4 \times 10^{17}\,\mathrm{cm^{-3}}$. Note that the width of the depleted shell $a - r_s$ depends not only on the doping concentration and the density of surface states, but also on the NW radius a. For a given set of N_D and D_{it} values, this depletion width of large NWs is similar to that of thin-films. For decreasing NW radius, the depletion width increases and tends to the critical radius a_{crit}. This shows that more severe surface depletion effects are present in thin NWs due to high surface-to volume ratio compared to thin-films. For this reason, the surface passivation is even more critical for efficient NW devices. For the NW diameters considered in this work (diameter$>$ 200 nm), the depletion width can be safely approximated by the planar model shown in Figure 5.3 if the doping concentration N_D is higher than $4 \times 10^{17}\,\mathrm{cm^{-3}}$, while total depletion may occur in lower doped or thinner NWs.

7.3.2 Core-shell p-n junction

In the following, we would like to examine a core-shell p-n junction and calculate the built-in potential, which is an upper bound of the open-circuit voltage of the solar cell. We consider a GaAs NW with a p-type core (doping level N_A $\mathrm{cm^{-3}}$, diameter $2a_p$ =120 nm) and a n-type shell (doping level N_D $\mathrm{cm^{-3}}$, thickness $a_n = a - a_p$ =80 nm). The dimensions are chosen as an example for a total NW diameter of 280 nm and can be varied easily in the model. There are two possible depletion cases for the core (fully or partially depleted core) and two possible depletion cases for the shell (fully or partially depleted shell). We need to separate each case.

The most common case in analogy with planar p-n junction is partially depleted core and partially depleted shell. We denote r_p as the radius separating the quasi-neutral p-core ($\rho = 0$) and the depleted p-core ($\rho = -qN_A$), and r_n as the radius separating the depleted n-shell ($\rho = +qN_D$) and the quasi-neutral n-shell ($\rho = 0$). The effect of surface depletion can also be included using the model of the previous section, with r_s the radius separating the unperturbed n-shell to the depleted surface shell. In the following, we consider only the NW of radius r_s that is electrically active.

By carefully analyzing the boundary conditions of each region (continuity of electric field and electrical potential), we arrive at the complete expression for the electric field as a function of the radius [283]:

$$E(r) = \begin{cases} 0 & \text{for} \quad 0 < r < r_p \\ -\dfrac{qN_A}{2\varepsilon r}\left(r^2 - r_p^2\right) & \text{for} \quad r_p < r < a_p \\ -\dfrac{qN_D}{2\varepsilon r}\left(r_n^2 - r^2\right) & \text{for} \quad a_p < r < r_n \\ 0 & \text{for} \quad r_n < r < r_s \end{cases} \tag{7.8}$$

and for the potential as a function of the radius

$$\psi(r) = \begin{cases} \psi_p & \text{for} \quad 0 < r < r_p \\ \psi_p - \dfrac{qN_A r_p^2}{2\varepsilon}\left[-\dfrac{r^2}{2r_p^2} + \ln\left(\dfrac{r}{r_p}\right) + \dfrac{1}{2}\right] & \text{for} \quad r_p < r < a_p \\ \psi_n + \dfrac{qN_D r_n^2}{2\varepsilon}\left[-\dfrac{r^2}{2r_n^2} + \ln\left(\dfrac{r}{r_n}\right) + \dfrac{1}{2}\right] & \text{for} \quad a_p < r < r_n \\ \psi_n & \text{for} \quad r_n < r < r_s \end{cases} \tag{7.9}$$

where ψ_p and ψ_n denote the potential at the quasi-neutral region of p-core and n-shell, respectively. They are calculated using the Fermi integral.

We can see that in the set of potentials (Equation 7.9), there are still two unknown variables (r_p,r_n). We need two other equations to solve the problem. The first one is given by the conservation of total charges in the system.

$$N_A\left(a_p^2 - r_p^2\right) = N_D\left(r_n^2 - a_p^2\right). \tag{7.10}$$

The second equation is obtained from the continuity of potential at the p-n junction boundary $r = a_p$:

$$\begin{aligned} V_{\text{bi}} &\equiv \psi_n - \psi_p \\ &= \frac{q}{4\varepsilon}\left[N_D r_n^2\left(2\ln\left(\frac{r_n}{a_p}\right) - 1\right) + a_p^2(N_A + N_D) + N_A r_p^2\left(2\ln\left(\frac{r_p}{a_p}\right) - 1\right)\right]. \end{aligned} \tag{7.11}$$

Here we write the built-in potential V_{bi} across the p-n junction and its value is calculated independently from the free carrier concentrations in the quasi-neutral regions. Substituting Equation 7.10 into Equation 7.11, we face a transcendent equation which can be solved numerically. Once (r_p,r_n) is solved, the potential and electric profile in NW is completely determined. As mentioned in the previous section for solving the surface depletion width, solutions of (r_p,r_n) cannot be found for any pair of doping concentrations (N_A,N_D). Real solution of (r_p,r_n) is only found for the case (1) of the following possible situations:

- (1) partially depleted core and partially depleted shell: $0 < r_p < a_p$ and $a_p < r_n < r_s$
- (2) totally depleted core and partially depleted shell: $r_p = 0$ and $a_p < r_n < r_s$
- (3) partially depleted core and totally depleted shell: $0 < r_p < a_p$ and $r_n > r_s$
- (4) totally depleted core and totally depleted shell: $r_p = 0$ and $r_n > r_s$

In cases (2), (3) and (4), different conditions happen and the above equations should be modified. The relation for charge conservation is easily adapted, but the use of potential ψ_p and ψ_n in quasi-neutral regions is no longer valid. Case (2) is relatively similar to case (1) with $r_p = 0$, while case (3) and (4) are more complicated and involve the boundary conditions connected to

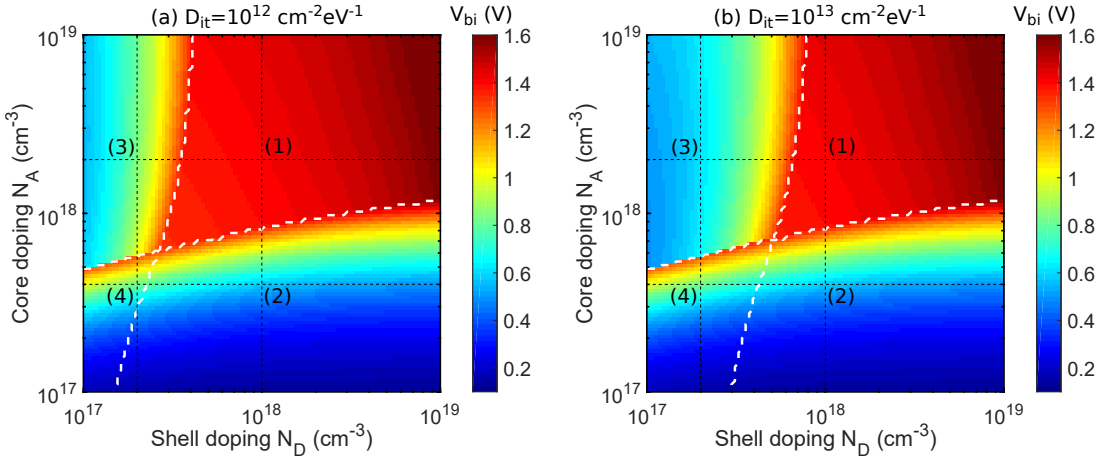

Figure 7.10 – *Calculated built-in potential (V_{bi}) maps as a function of doping concentrations in p-core (radius 60 nm) and n-shell (thickness 80 nm). Two cases of different densities of surface states are shown: (a) good surface passivation with $D_{it} = 10^{12}$ cm^{-2}eV^{-1} and (b) unpassivated surface with $D_{it} = 10^{13}$ cm^{-2}eV^{-1}. White dashed lines mark the boundaries for totally depleted core and totally depleted shell at low doping concentrations. Black dashed lines indicate particular doping levels studied in Figure 7.11.*

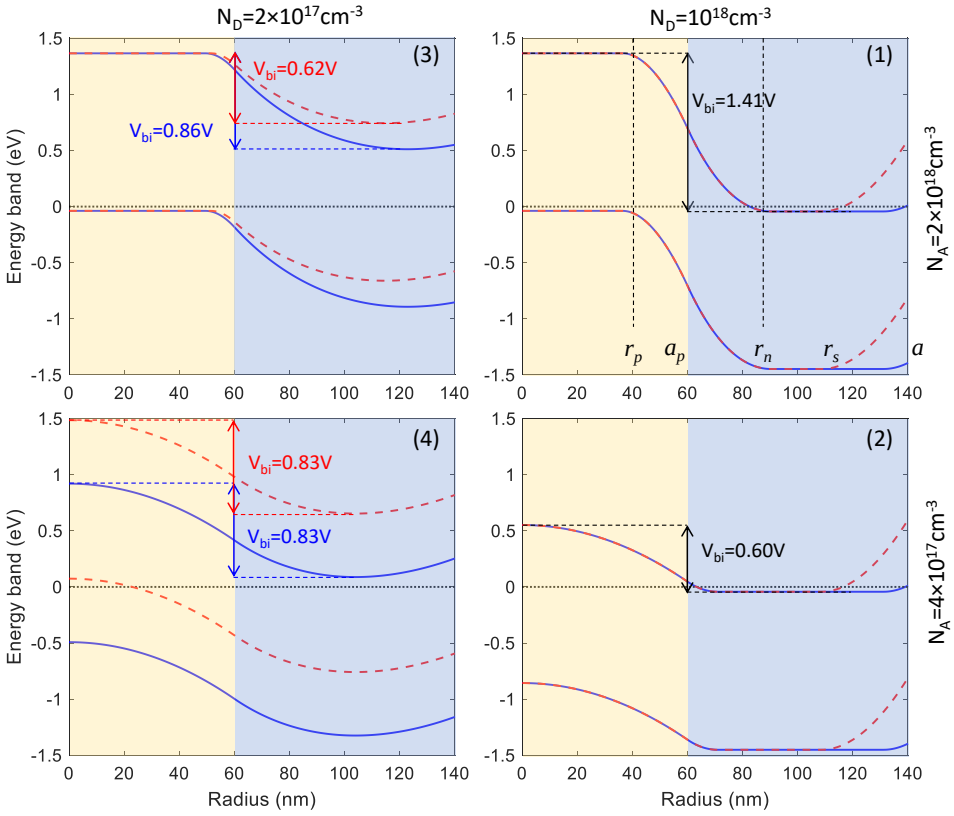

Figure 7.11 – *Examples of calculated energy band diagrams for NWs with p-core (radius 60 nm, yellow region) and n-shell (thickness 80 nm, blue region). The p-core doping is $N_A = 4 \times 10^{17}$ cm^{-3} or $N_A = 2 \times 10^{18}$ cm^{-3} and the n-shell doping is $N_D = 2 \times 10^{17}$ cm^{-3} or $N_D = 1 \times 10^{18}$ cm^{-3}. These four cases correspond to different depletion possibilities: (1) partially depleted core and shell, (2) totally depleted core and partially depleted shell, (3) partially depleted core and totally depleted shell, (4) totally depleted core and shell. The equilibrium Fermi level is placed at the zero energy level. Blue lines are CB and VB with density of surface states $D_{it} = 10^{12}$ cm^{-2}eV^{-1}, and red dashed lines are for $D_{it} = 10^{13}$ $cm^{-2}eV^{-1}$.*

the surface potential. Details of analytical formulations in these cases can be found in Ref. [283]. We present here only the calculated results and discuss the profound implications of doping on the potential performance of solar cells.

Figure 7.10 presents the calculated built-in potential V_{bi} as a function of p-core and n-shell doping concentrations for a fixed NW geometry (core radius 60 nm and shell thickness 80 nm) and two densities of surface states: (a) $D_{it} = 10^{12}$ cm^{-2}eV^{-1} and (b) $D_{it} = 10^{13}$ cm^{-2}eV^{-1}. The white dashed lines separate the regions for the four depletion situations (1) to (4). Selected energy band diagrams corresponding to each case are shown in Figure 7.11. From the maps of built-in potential, we can recognize immediately that the region of high V_{bi} is located at high doping levels. We have included explicitly the bandgap narrowing (Equation 5.28) in the calculation but its magnitude is small compared to the total built-in voltage. Once the core or shell begins to be totally depleted due to low doping concentrations, V_{bi} decreases dramatically, which lowers the achievable V_{oc} of NW solar cells.

The density of surface states D_{it} affects mainly the n-doped shell. If N_D is high enough, D_{it} changes merely V_{bi} but creates a potential barrier for electron transport. The formation of a contact Schottky barrier will also reduce the V_{oc} of NW solar cells and increases unwanted contact resistance. If N_D is too low such that the shell is already depleted, high value of D_{it} will further decrease V_{bi}. As can be seen from the comparison of V_{bi} map in Figure 7.10, V_{bi} drops at moderate N_D values if the surface is not passivated.

Another feature from the core-shell band diagram concerns the case (4) in Figure 7.11 when both core and shell are depleted at low doping concentrations. We observed that the shape of the potential profile in r is independent from the density of surface states. This is coherent with the full depletion approximation so that the macroscopic bulk charge density ρ is identical regardless of the surface states. However, the potential shifts vertically to match the boundary condition imposed by the surface. For high density of surface states, electrons are trapped at the surface and a conducting hole channel in the inner core is formed. This shows the possibility of tunning the conductivity of thin NW core by manipulation of the electronic surface states.

In summary, we have used a comprehensive electrical model and found the doping range of core-shell GaAs NWs in which the high V_{bi} is realized: we target p-core doping concentration of about 2×10^{18} cm^{-3} and n-shell doping concentration of about 1×10^{18} cm^{-3}. Total depletion in low-doped core-shell NWs is the main cause of V_{oc} drop, as shown by LaPierre using COMSOL solver to model NW solar cell devices [284]. These critical doping levels acquired to avoid total depletion depends also on the NW diameter and shell thickness which are investigated by Chia and LaPierre [283]. In the literature, coupled optical (Lumerical) and electrical (COMSOL) simulations for core-shell junction GaAs NW solar cells are used and confirm high core and shell doping are essential to achieve high performance [285]. More recently, Lumurical and Sentaurus coupled simulations are used to optimize GaAs NW solar cells by introducing AlGaAs/GaAs heterojunctions [286]. The electrical model presented here can be further extended to core-shell heterojunctions, which may release the constraint on the high doping levels in core-shell homojunctions.

7.4 Device fabrication and characterization

In this section, we present our experimental works. GaAs NWs were grown on patterned p-type Si(111) substrate by the colleagues at the material department of C2N laboratory. I began to explore the device fabrication methods and made a first device which is not optimal in terms of growth structures. I will present the fabrication steps and the device characteristics. At the end of my thesis, the epitaxial growth and device fabrication continued to make progress in the group's work. I will show the last device performance and discuss future perspectives.

7.4.1 Fabrication

One of the most critical fabrication step is the choice of the transparent conductive oxide (TCO) used at the top surface to connect NWs together. TCO is in general not needed for III-V homojunction solar cells because a high lateral conductance is ensured by the continuous semiconductor top layers. TCO may profoundly modify carrier extraction/injection mechanisms once they come into contact with p-type and n-type semiconductors. A successful contact depends on many factors such as the GaAs doping type and doping concentration, surface chemical treatment, TCO deposition method and thermal treatment and so on. For example, AZO (or ZnO:Al for Al doped zinc oxide) and ITO (indium tin oxide) were deposited by sputtering to contact n-doped GaAs NW shell [265], but the results are not very satisfactory. Ti/ITO was used to contact p-doped GaAs NW shell and showed Schottky behavior as-sputtered but turned to ohmic after low-temperature (300°C) thermal annealing for 1 min in an Argon-purged atmosphere [266]. In/ITO was fabricated by RF sputtering to contact n-type GaAs NW shell and was found ohmic after annealing for 4 min at 300°C under N_2 flow [262]. The underlying mechanism of GaAs/TCO contact is not clear and there is no convincing solution by present. The chemical treatment on GaAs NWs surface (e.g. S or Se chalcogen passivation) is also used to manipulate the surface states and can even switch the p-n conductivity [287].

We attempted the use of ZnO:Al fabricated by atomic layer deposition (ALD) at the *Institut de recherche et développement sur l'énergie photovoltaïque* (IRDEP), which is mainly used for top TCO in CIGS solar cells and is believed to have low-damage on III-V semiconductor surface compared to sputtering techniques using physical deposition of high-energetic atoms. The NW array structure is shown in Figure 7.12(a), which consists of a p-Si substrate patterned with an hexagonal array of opening holes (period 500 nm) over 1 cm^2 area on the SiO_x mask, epitaxial growth of i-GaAs NW core and n-GaAs NW shell (this growth was performed prior to the study of p-doping calibration presented in Chapter 6.3). Eventually, a shell of high bandgap alloy (e.g. AlGaAs) can be grown, but not for this sample. Figure 7.12(b) and (c) show SEM images before and after the deposition of 100 nm ZnO:Al by ALD. Prior deposition, GaAs NWs were dipped in diluted HCl solution to removed native oxides. From the SEM image, we can observe that ZnO:Al is deposited conformally and connects all NWs.

After ZnO:Al deposition, the space between NWs is filled by a polymer to protect NWs against mechanical damages during processes. In the literature, BCB is widely used, but requires relatively high temperature baking. We choose ormostamp which is a UV-sensitive hybrid polymer and is already used for gentle bonding of ultrathin GaAs solar cells. With typical spin-coating speed of 3000 rpm, ormostamp forms a 10 μm-thick layer. To get a thinner film, we dilute ormostamp in ethanol with weight ratio of 1:3 ormostamp:ethanol, enabling to control the layer thickness to 1 to 2 μm. The dilute ormostamp is dropped on NW arrays and spin-coated with speed 3000 rpm, acceleration 2000 rpm/s for 30 s. The sample is then prebaked on a hotplate at 80°C for 2 min, allowing to lower the surface tension of ormostamp thus enabling a better surface wetting and filling the space between NWs. Subsequently, ormostamp is reticulated under exposure of UV light. If the polymer covers totally the top of NWs, reactive-ion etching (RIE) with a mixture of O_2/CHF_3 is used to etch back the ormostamp layer. Figure 7.13(a) shows the sample after spin-coating of ormostamp and a SEM image of planarized NWs array with opening of the top contact.

After planarization of the NW array, the sample can be manipulated with gentle process without mechanical damage. We fabricate a Ti/Au 20/200 nm front contact electrode using photolithography and lift-off. Figure 7.13(b) shows an optical microscope image of gold electrodes and a SEM image showing the contact with ZnO:Al on top of the NWs. Finally, the solar cell area is defined by photolithography and mesa etch. Polymer is etched by RIE and exposed ZnO:Al is etched in 1:100 $HCl:H_2O$. Figure 7.13(b) show the active zone of solar cell with Au electrodes and the solar cell edge by etching the ZnO:Al front contact. The back contact electrode is a

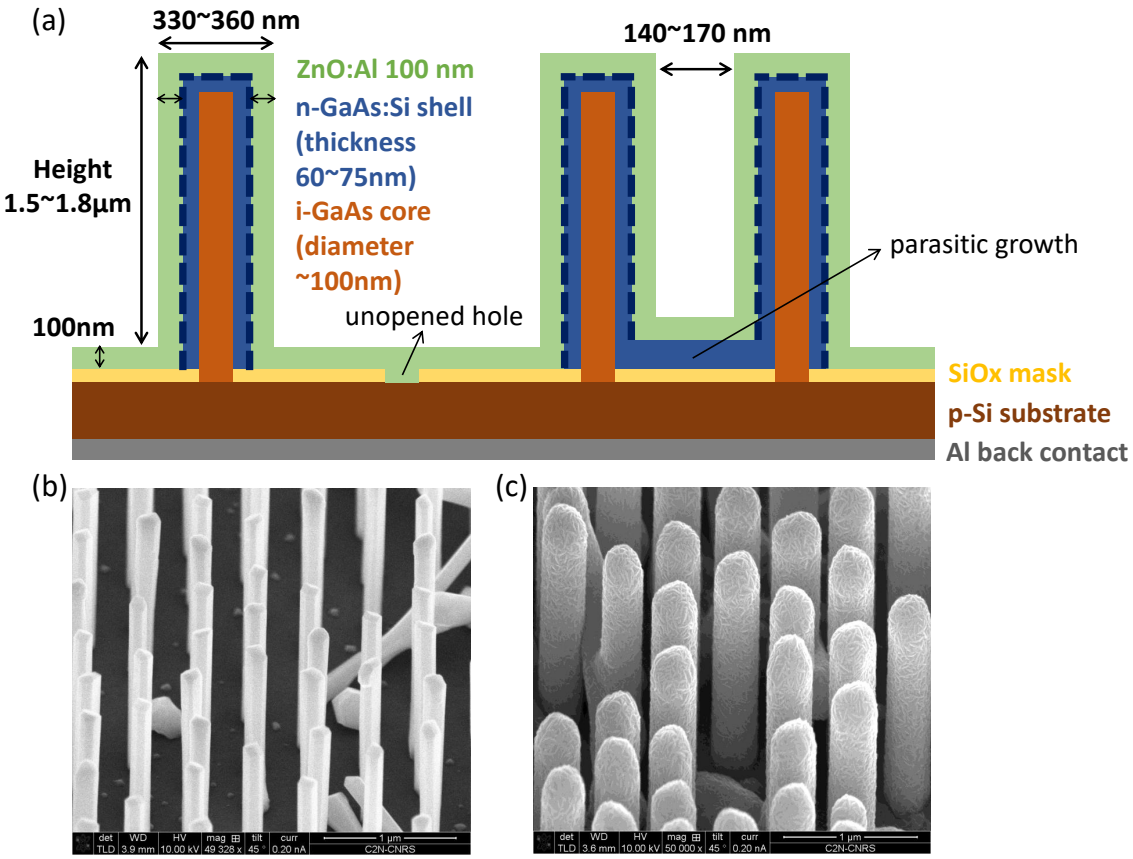

Figure 7.12 – *(a) Schematics of the GaAs NW solar cell structures, containing p-Si substrate/i-GaAs NW core/n-GaAs:Si NW shell/ZnO:Al top contact. NW array is hexagonal packing with period of 500 nm and NW sizes are indicated in the figure. NW array may have unopened hole on the SiO_x mask and parasitic growth of GaAs:Si crystals. (b) SEM image of as-grown GaAs NWs before ZnO:Al deposition. (c) SEM image of the sample after ZnO:Al deposition.*

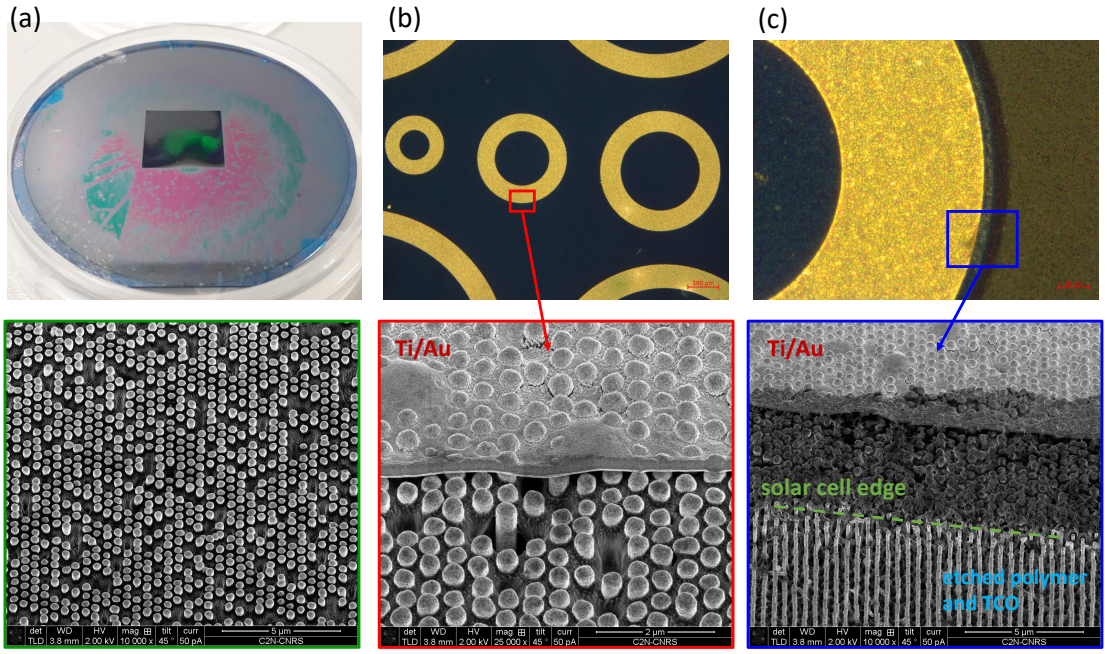

Figure 7.13 – *Pictures and microscope images of the solar cell device fabrication. (a) view of the sample after planarization of NW array by spin-coating of ormostamp. Green light shows the zone of diffraction from the ordered NW array. SEM image reveals the top of NWs is free of polymer after the RIE process. (b) Images after fabrication of Au top electrodes. The SEM image shows the physical contact of metal electrodes on ZnO:Al. (c) Images after mesa etching to define solar cell units.*

simply 200 nm Al deposited on the back side of p-Si substrate.

7.4.2 Results and perspectives

The current-voltage characteristics (dark and 1 sun) of the sample is shown in Figure 7.14(a), and subsequently improved device characteristic is shown in Figure 7.14(b). The J_{sc} conversion efficiencies are deduced using the illumination area of the solar cell (indicated in the figure caption), thus excludes the shading from the top contact electrode. We can see a noticeable improvement of conversion efficiency from 0.003% to 2.093% under 1 sun illumination. The EQE of the improved device is given in Figure 7.15.

We should note that several technical improvements and material understanding led to this progress. The reduction of shunt conductance may be due to improved growth control (lower parasitic growth on the mask, higher yield, etc.) and due to the fact that TCO is deposited after planarization for the improved device. The GaAs core-shell junction quality is largely improved by Be-doping of the NW core and low-temperature growth of the Si-doped GaAs, which was conducted initially at high temperature, leading to severe Si dopant compensation and lowered CL intensities (see Chapter 6.4). Moreover, an AlGaAs shell was grown on the improved device (sample 76838) to passivate the NW surface. All of these improvements contribute to a higher V_{oc} and higher J_{sc} through efficient collection of photogenerated carriers.

As we focus on the characteristics of the sample 76838, we obtained a quite good J_{sc} value of 12.67 mA/cm^2 under 1 sun illumination, in agreement with the EQE of the solar cell. Lower V_{oc} in core-shell NW devices may be attributed to lower doping efficiency in the shells of GaAs NWs [262, 264]. To maintain a high V_{oc} in core-shell NW solar cells, high doping levels above $\sim 10^{18}$ cm^{-3} are desired as we can see from Figure 7.10 for the built-in potential map as a function of core and shell doping levels (Section 7.3). However, we have measured the n-type doping concentration of only 4–6$\times 10^{17}$ cm^{-3} from CL characterization (Chapter 6.4), which is

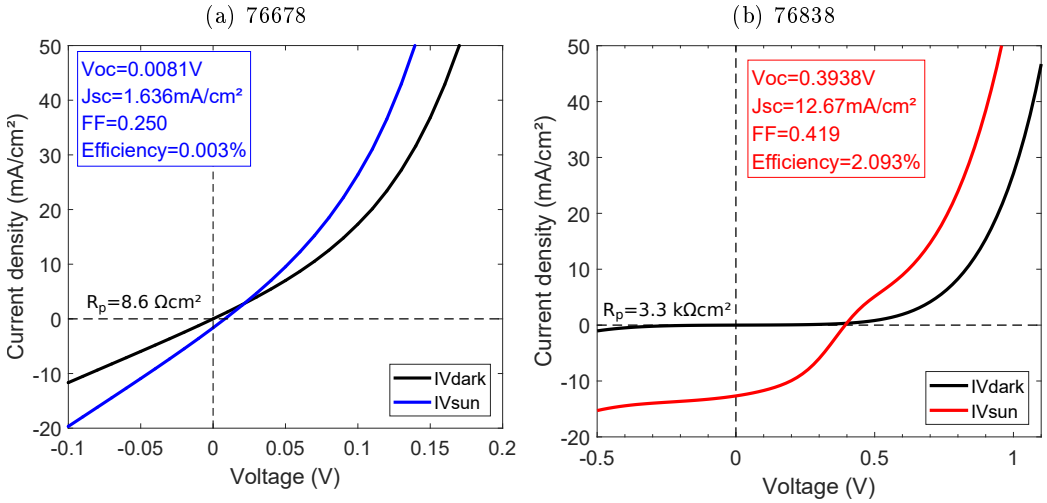

Figure 7.14 – *Current-voltage characteristics of GaAs NW array solar cells. (a) The first fabricated device (sample 76678) has low conversion efficiency of 0.003% (solar cell size 0.785 mm^2, illumination area 0.576 mm^2). (b) Improved fabricated device (sample 76838) with conversion efficient of 2.093% (solar cell size 0.785 mm^2, illumination area 0.576 mm^2). Illumination area excludes the front contact electrode and is used to calculate the current density and define the efficiency.*

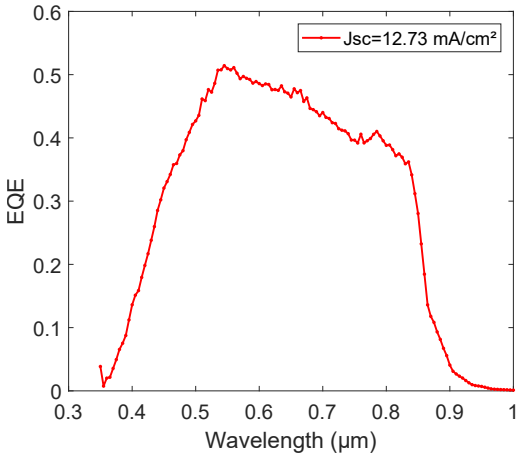

Figure 7.15 – *EQE of the 2.093%-efficient device. The integrated EQE with the AM1.5G solar spectrum gives rise to a J_{sc} value of about 12.73 mA^2, in agreement with direct measurements under solar simulator.*

not enough to prevent the total depletion of the NW shells. Moreover, the crossover of dark and sun JV curves (here ∼0.4 V for the sample 76838) also indicates the contact-to-contact built-in potential [288]. The Schottky barrier between the NW shells and ITO may be present which degrades the electrical properties of the solar cells. Improving the doping level and reducing the Si dopant compensation in the NW shells, efficient surface passivation, and fabrication of good ohmic contacts are needed for future device improvement. A core-shell p-GaAs/n-GaInP heterojunction is also studied which may overcome the constraint of high doping levels.

7.5 Summary

In this chapter, we study theoretically the solar cell structures using GaAs nanowires as active photovoltaic absorber and present the very beginning of the experimental work. A detailed review of III-V nanowire solar cells in the literature is given in the beginning of the chapter. Either single nanowires or nanowire arrays have been fabricated for photovoltaic applications. In terms of junction configuration, either axial junctions or radial (core-shell) junctions have been used. We focus on p-core/n-shell GaAs nanowire arrays, which offer a promising way to decouple direction of absorption of light and collection of charge carriers.

In Section 7.2, we calculate the optical absorption of GaAs nanowire array using RCWA method and optimize the geometry of nanowire diameter and array period. We find, for cylinder nanowires of 1 μm in length and square array arrangement, the nanowire diameter of 350 nm with array period of 580 nm yield the highest J_{sc} of $\mathbf{27.4\ mA/cm^2}$ for absorption in GaAs nanowires. This can be further improved by adding a dielectric anti-reflection coating. In this case, the nanowire filling ratio is 0.286, results in less than 300 nm-thick equivalent thin-film layer used for the absorber material. We also discuss the influence of different geometry parameters on the optical resonances. The photogeneration rate is integrated over the symmetry of rotational angles and can be used for future coupled optoelectronic simulations. In Section 7.3, the electrical characteristics of core-shell junctions are calculated in an analytical way by solving the Poisson equation in cylindrical coordinates. For a fixed geometry of p-core diameter of 120 nm and n-shell thickness of 80 nm, we identify both the p-doping and n-doping ranges above approximately 1×10^{18} cm^{-3} to avoid total depletion of the nanowire and hence, to maintain a high built-in potential for solar cell applications.

We then fabricated solar cell devices with GaAs nanowire arrays. Continuous progresses have been carried out by the colleagues of C2N and efficiency of **2.09%** under 1 sun illumination was achieved ($J_{sc} = 12.67$ mA/cm^2, $V_{oc} = 0.394$ V, $FF = 0.419$). To take advantage of the nanowire core-shell structure, high doping levels are desired. The required shell doping level is also related to the quality of surface passivation, which will have an impact on the V_{oc} of the solar cells and on the formation of a good ohmic contact.

Chapter

8 Conclusion and perspectives

Within this thesis work, we have studied the design, fabrication and characterization of ultrathin and nanowire-based GaAs solar cells. As introduced in Chapter 1, reducing the volume of the photovoltaic absorber allows to relieve the limitation on scarce materials and opens new routes toward III-V high-efficiency and low-cost photovoltaic cells. Our study has been motivated by the ability of nanophotonic structures to achieve high optical absorption either in ultrathin semiconductor layers or in semiconductor nanowires. III-V semiconductor nanowires (NWs) are particularly interesting for photovoltaic applications owning to their light-trapping properties and the possibility of direct growth on inexpensive Si substrates.

On the other hand, the electrical aspects of ultrathin and NW-based solar cells are also addressed. As the volume of active material is diminished, the surface-to-volume ratio increases and may be detrimental to the electrical characteristics of the solar cells. Effective surface passivation is needed and turns out to be critical in NW-based solar cells. In order to understand the properties of semiconductor nanostructures, we also need a nanocale-resolution characterization tool. We used cathodoluminescence (CL) to study the properties of single NWs. In the following, we summarize our theoretical approaches and the main results of this thesis.

Theoretical background

In Chapter 2, we have presented several theoretical aspects, including electromagnetic wave optics and physics of semiconductors. Wave optics is essential to understand light-trapping in ultrathin and NW-based solar cells containing sub-wavelength features. The short-circuit current density (J_{sc}) relies on the optical absorption in the absorber region of a solar cell. The open-circuit voltage (V_{oc}) and fill factor (FF) of a solar cell are essentially electrical parameters. V_{oc} is strongly related to the quality of the semiconductors, surface passivation, junction design, etc. We gave essential parameters of semiconductors: carrier concentrations, transports, photogeneration and recombination rates, the p-n junction and metal-semiconductor junction. We introduced carrier lifetime and diffusion length of minority carriers, which are important indicators characterizing the photovoltaic materials.

In Chapter 3, we have described the luminescence theories. Luminescence characterization is widely used in photovoltaic research. The spectrum of emitted light is closely related to the absorption of the material. Hence, we calculated the general absorption coefficient of a direct-gap semiconductor as a function of the oscillator strength and the semiconductor joint density of states. Influences of excitons, shallow donors and acceptors were discussed. These descriptions provide a solid basis to understand low-temperature CL spectra. Subsequently, we derived the generalized Planck's law, which provides a powerful tool to analyze photovoltaic absorber and for many other purposes. For example, the absolute intensity of luminescence is related to the V_{oc} of a solar cell through the separation of quasi-Fermi levels. Therefore, an ideal solar cell should also be designed as a good light emitter. Luminescence measurements thus constitute a guideline toward high-efficiency solar cells. We also adapt the generalized Plank's law to assess both n-

type and p-type doping concentrations. It provides a robust and versatile doping measurement method with a broad applicability.

Ultrathin GaAs solar cells

In Chapter 4, we have designed an ultrathin (205 nm) GaAs solar cell with a 2D nanostructured TiO_2/Ag back mirror. A theoretical short-circuit current density of $J_{th} = 25.6$ mA/cm^2 is predicted with the optimized mirror structure: grating period $p = 700$ nm, Ag nanostructure width $d = 420$ nm, and grating height $h = 120$ nm. We have studied the mechanisms of optical resonances by varying the parameters of the grating structure, the thickness of the absorber and the angle of incidence. Broadband multi-resonant absorption in ultrathin GaAs layers was achieved through the overlap of vertical Fabry-Perot resonances and guided-mode resonances induced by the nanostructured back mirror.

Subsequently, we carried out the fabrication of ultrathin GaAs solar cells with TiO_2/Ag nanostructured back reflector using the III-V epitaxial layers grown at the Fraunhofer ISE. We employed soft nanoimprint lithography, a key step to produce large-area periodic TiO_2 nanopatterns, in order to integrate nanophotonic structures in the ultrathin GaAs solar cells. We performed the solar cells characterization: current-voltage (JV), EQE, specular reflectance and data analysis. The Fraunhofer ISE calibration lab subsequently confirmed the record efficiency of 19.9% under 1 sun illumination for the best solar cell ($J_{sc} = 24.64$ mA/cm^2, $V_{oc} = 1.022$ V, $FF = 0.792$).

The optical performances of the solar cells were characterized by the EQE, which is in good agreement with the calculated absorption spectra in GaAs. The highest experimental J_{sc} from EQE measurements is 25.1 mA/cm^2, very close to the theoretical prediction of 25.6 mA/cm^2. We have analyzed the electrical performances of the solar cells by fitting the JV curves with a two-diode model and identified the edge recombination as an important efficiency-limiting factor. We have discussed routes for future optimizations of the solar cell structure (decreasing the thickness of the AlGaAs BSF layer, for instance) and careful fabrication for a large-area device (1 cm^2). The front contact shading can be further decreased from actual 5-6% down to 2%. The diffraction efficiency of the nanostructured back mirror may be further improved by implementing a blazed grating to reduce the zero-order reflection. 25%-efficiency using only 200 nm-thick ultrathin GaAs solar cells appears as a realistic target.

Doping measurement by cathodoluminescence

In the second part of this thesis work, we focused on GaAs NWs as a potential photovoltaic absorber. III-V semiconductor nanowires used in this study were grown in collaboration with the material group at C2N. In Chapter 5, we developed an alternative doping characterization method based on the analysis of luminescence spectra. This work was motivated by the difficulty of measuring material doping down to the nanometer scale, while doping is a fundamental material parameter to design efficient solar cells. We present CL measurements on thin-film GaAs samples with various doping levels (measured by Hall effect). For p-type GaAs doping concentration below approximately $7-8\times10^{17}$ cm^{-3}, we observed two separated CL peaks at low temperature due to recombinations involving shallow acceptors. At higher p-type doping, the acceptor band merges with the valence band thus only a single CL peak was observed. CL spectra continuously broaden and redshift with increasing doping concentrations due to the bandgap narrowing effect (BGN). We fitted the CL spectra using the generalized Planck's law with a parabolic absorption model convoluted with an Urbach tail to extract the bandgap E_g at a given doping concentration p [cm^{-3}]. The difference between E_g and the bandgap of undoped GaAs (1.424 eV at room

temperature) defines the BGN value. We verified that the relation

$$\mathrm{BGN\ (eV)} = 1.6 \cdot 10^{-8} \times p^{1/3},$$

can be used to determine the p-type doping of GaAs in the doping range of about 1×10^{18} to 2×10^{19} cm^{-3}.

For n-type GaAs, we observed single-peak CL spectra due to near-bandgap recombination. The CL spectra steadily broaden and blueshift with increasing doping concentrations. The broadening at the low-energy side of the CL spectra is due to increased BGN and band tail at high doping levels, while the broadening at the high-energy side of the CL spectra is explained by the conduction band filling. We fitted the whole CL spectra measured at room temperature taking into account the position of the electron Fermi level above the conduction band minimum, which provides a direct and precise measure of electron concentrations in the doping range of about 5×10^{17} to 1×10^{19} cm^{-3}. At lower doping levels n [cm^{-3}], the empirical FWHM values of low temperature CL spectra can be used:

$$\mathrm{FWHM\ (eV)} = 3.348 \times 10^{-14} \times n^{2/3}$$

We have demonstrated a novel and rigorous method for contactless doping characterization at the nanoscale using cathodoluminescence, and is of particular interest for III-V nanowires and other semiconductor nanostructures.

Characterization of GaAs nanowires by cathodoluminescence

In Chapter 6, we presented CL measurements on GaAs NWs. This study aims to characterize material qualities, homogeneity and doping levels. We summarize the main results in two parts. First, we observed an unusual hexagonal wurtzite (WZ) crystal phase existing in numerous NWs measured by CL. The coexistence of cubic zinc-blende (ZB) and WZ structures in a single nanowire offers a new way of engineering bandgap and band alignment. However, the properties of WZ GaAs are less known. We used high-resolution CL mapping measured on single GaAs NWs combined with polarization analysis to distinguish light emitted from WZ GaAs, which is polarized perpendicularly to the NW growth axis (measured perpendicular degree of polarization up to 72%). Low-temperature CL mapping measured on an undoped WZ/ZB GaAs NW showed that WZ GaAs exhibits a peak centered at around 1.515-1.516 eV (FWHM 21 meV), while ZB GaAs presents the exciton peak at around 1.514-1.515 eV (FWHM 15 meV). At room temperature, CL spectrum from WZ GaAs is slightly blueshifted and broadened compared to that from ZB GaAs. We conclude that the bandgap of WZ GaAs should be slightly higher than the bandgap of ZB GaAs, with a difference of less than 10 meV.

Second, a series of Be-doped and Si-doped GaAs NWs of unknown doping concentrations were measured by CL. We present CL maps and temperature evolution of CL spectra to investigate the material property and doping homogeneity. Surprisingly, WZ segments are also present in many doped NWs measured by CL. Polarization-resolved CL mapping was used to clearly identify the luminescence emitted due to WZ phase by examining the degree of polarization perpendicular to the NW c-axis. For Be-doped GaAs NWs, analysis of BGN values allows to determine quantitatively the p-type doping concentrations in ZB GaAs, which are in good agreement with the target doping levels. WZ GaAs shows similar BGN and broadening with increasing Be doping concentrations. For Si-doped GaAs NWs, analysis of low temperature FMHM and electron Fermi levels allow to estimate the n-type doping concentrations in ZB GaAs to be about 4×10^{17} to 1×10^{18} cm^{-3}. These values are substantially lower than expected, probably due to surface depletion, Si dopant compensation, or unknown growth issue which

hinders the incorporation of Si. On the other hand, Si-doped WZ GaAs exhibits a broad defect-related CL spectrum at low temperature, which has a lower perpendicular degree of polarization (29%). This may be due to localized Si donor-acceptor pair recombination in WZ GaAs.

Nanowire-based GaAs solar cells

In Chapter 7, we designed and fabricated GaAs core-shell junction NW array solar cells. My work was focused on the optical and electrical simulations to investigate the potential light trapping and to identify the doping levels required in the core-shell junction. First, high optical absorption of GaAs NW arrays was obtained and we predicted a short-circuit current density J_{sc} up to 27.4 mA/cm^2 for absorption in GaAs NW arrays (NW height 1μm, diameter 350 nm, arranged in a square array of period 580 nm with a Ag back reflector). We studied the absorption spectra by varying the period of the arrays, the diameter and the height of NWs, and we attributed the main electromagnetic modes to the Fabry-Perot resonances and leaky/guided modes of individual NWs. In this configuration, the GaAs material consumption is equivalent to a thin-film of thickness less than 300 nm. Second, the band diagram in a core-shell homojunction was calculated using analytical solutions of Poisson equation in cylinder coordinates. Built-in potential was then expressed as a function of the NW geometry, doping levels and the density of surface states. We target high doping concentrations above 1×10^{18} cm^{-3} to maintain a high built-in potential and to take advantage of efficient charge carrier collection in the radial direction of NWs. I have fabricated first nanowire-based GaAs solar cells. This work is ongoing in the group and led recently to GaAs core-shell NW solar cells with 2.09% efficiency under 1 sun illumination ($J_{sc} = 12.67$ mA/cm^2, $V_{oc} = 0.394$ V, $FF = 0.419$).

To further improve the conversion efficiency of the NW solar cells, the shell doping, surface passivation, and ohmic contact between GaAs/ITO seem to be the major issues. To release the requirement of high doping in the NW shells, p-GaAs core/n-GaInP shell NW array solar cells were also studied experimentally. We can further perform the optical simulations on this structure to finely tune the optimal geometry and thickness of core-shell NW arrays. The analytical model of cylindrical core-shell junction can also be extended to the case of a heterojunction GaAs/AlGaAs or GaAs/GaInP, provided correct band offsets.

Perspectives

Nanoscience and nanotechnologies bring new tools to overcome bottlenecks in conventional photovoltaic devices. For example, we have demonstrated the use of nanostructured back mirror in ultrathin GaAs solar cells and obtained a substantially high J_{sc}. In principle, the back mirror should also boost the V_{oc} of the solar cells through the photon recycling effect compared to the reference cell without back mirror. Photoluminescence or electroluminescence measurements calibrated to absolute flux may provide indications of the external radiative efficiency of the solar cells. Coupled opto-electrical simulations can be further developed to model the whole device and help to find out the most important design factors. The same perspectives should also apply for NW solar cells, which still have room for improvements toward the radiative limit of conversion efficiency.

The work on ultrathin GaAs solar cells can be applied to other photovoltaic materials (thin-film CIGS, CdTe, perovskite, etc.). For instance, similar architectures made of ultrathin CIGS solar cells with a nanostructured back mirror are currently developed in our group, in the framework of the ARCIGS-M H2020 European project (PhD of Louis Gouillart, started in January 2017). Nanophotonic structures can also be used to design advanced anti-reflection coatings, spectral or angular selective filters, luminescence coupling on multijunction solar cells, etc. The

ongoing collaboration with the Fraunhofer ISE will now target to extend the results of ultrathin GaAs solar cells to novel architectures made of ultrathin III-V/Si tandem solar cells (PhD of Phung-Linh Nguyen starting in October 2018 in collaboration with IPVF and EDF). My thesis work can also be extended to next-generation high-efficiency photovoltaic cells. Even thinner III-V solar cells (thickness down to 50 nm) are under investigation for application to hot-carrier solar cells in the framework of an international collaboration between the C2N, the IPVF-UMR and the University of Tokyo (PhD of Maxime Giteau, started in October 2017, LIA NEXT PV). Employing nanophotonic structures is also very useful in intermediate-band solar cells and photon up-conversion systems where efficient light-trapping is essential due to the low absorption strength of the dedicated optical transitions.

NW-based III-V solar cells are also the subject of several ongoing projects of our group at C2N (ANR NANOCELL and HETONAN) and at IPVF. The results presented in this manuscript constitute the basis for the development of single-junction GaAs solar cells, and more importantly of tandem III-V/Si solar cells fabricated by the direct growth of III-V nanowires on Si (PhD of Romaric de Lépinau, started in April 2017). Such architecture provides a promising way to integrate III-V on Si solar cells at low cost, with potential efficiencies above 30 %, but it still raises many technological challenges.

On the other hand, CL technique was used to reveal valuable information of GaAs properties at the nanoscale and should find many applications in other materials for photovoltaics like other III-V semiconductors, CIGS, CdTe,... (PhD of Thomas Bidaud, started in October 2017). CL polarimetry can probe unique features of low dimensional materials. CL can also be used in the pulsed mode (time-resolved CL) to measure the carrier lifetime and thus help to optimize the material quality and to characterize the effectiveness of surface passivation for photovoltaic materials. Diffusion lengths can also be measured with CL technique if the sample presents a localized and spectrally distinguishable feature or using a partial mask (e.g. thin Al film) which allows electron beam to pass through while blocking the luminescence produced below the mask. Combining CL mapping with electron beam induced current (EBIC) at the same time is also possible and provides complementary information because the EBIC signal is usually strong at the depletion zone, where the CL signal is usually weak due to the internal field that separates the electron-hole pairs. CL experiments may be further adapted to switch between electron-beam excitation or laser excitation, enabling in-situ Raman scattering measurements. For example, Raman spectroscopy can be used to distinguish the polarity of Si dopants in GaAs. More generally, the CL technique and its variants open up numerous possibilities of applications to investigate material properties for photovoltaic cells, LED, Laser, single photon emitters, etc.

Annexe

A Résumé en français

Introduction

L'énergie solaire est l'une des ressources les plus abondantes de la nature, ce qui peut résoudre les demandes croissantes d'électricité et contribuer à un système électrique basé sur les énergies renouvelables. Les cellules solaires convertissent la lumière du soleil en électricité grâce à l'effet photovoltaïque, qui combine optique et physique du solide. Le développement récent de dispositifs opto-électroniques tire parti du confinement de la lumière dans les nanostructures. Le piégeage optique dans un volume réduit de la cellule solaire permet de maintenir un forte génération de photocourant, et la concentration de la lumière fournit potentiellement une tension en circuit ouvert plus élevée grâce à l'effet de recyclage des photons. D'autre part, réduire le volume de l'absorbeur de cellules solaires sera bénéfique pour réduire le coût des matériaux, conduisant ainsi à une production moins coûteuses, et trouvera des applications dans les cellules solaires à haut rendement.

Dans ce travail de thèse, je me focalise sur les cellules solaires en GaAs et je travaille avec les semi-conducteurs III-V pour explorer les dispositifs photovoltaïques à haut rendement dans un volume réduit d'absorbeur actif. Deux approches sont étudiées séparément. La première utilise 200 nm de couche ultra-mince de GaAs (dix fois plus fine que les cellules conventionnelles en couche mince de GaAs). Cette étude s'appuie sur la simulation et des résultats expérimentaux, elle est décrite dans le Chapitre 4. L'autre utilise les nanofils de GaAs comme l'absorbeur de la cellule solaire. Mesurer les propriétés d'un nanofils unique est l'un des principaux verrous de cet axe de recherche. J'ai développé une méthode sans contact pour déterminer le niveau de dopage (Chapitre 5) afin de pouvoir l'appliquer aux nanofils. Le Chapitre 6 présente les caractérisations des nanofils de GaAs par la cathodoluminescence. Dans le Chapitre 7, j'étudie les cellules solaires à nanofils de GaAs par la simulation optique pour optimiser l'absorption du réseau de fils et par une modèle électrostatique pour voir l'effet du dopage sur la performance de la cellule. Je présente les premiers résultats expérimentaux dans la fin du Chapitre 7.

Ce manuscrit est organisé comme suit : le chapitre 1 résume le principe de fonctionnement d'une cellule solaire en général, et le développement des différentes filières de technologies photovoltaïques. Le Chapitre 2 décrit plus en détail les notions physiques importantes pour la compréhension de la cellule solaire, en terme d'optique électromagnétique et de physique des semi-conducteurs. Le Chapitre 3 traite la théorie de le luminescence et la loi de Planck généralisée, qui apparaissent dans beaucoup d'aspects de cette thèse. Par exemple, la limite de Shockley-Queisser d'une cellule solaire est bien connectée au principe du bilan détaillé de l'absorption et l'émission. L'analyse du spectre de luminescence permet également de déterminer quantitativement le niveau de dopage d'un semi-conducteur III-V, ce qui pourrait être appliqué à d'autre domaines, par exemple différents matériaux et nanostructures. Les résultats essentiels de ce manuscrit (Chapitre 4 au Chapitre 7) sont résumés dans la suite.

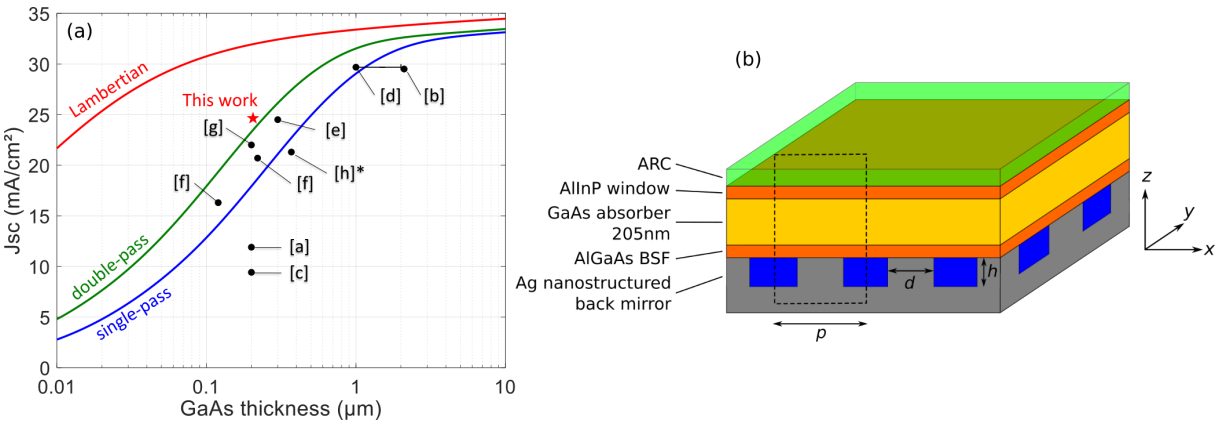

Figure A.1 – *(a) J_{sc} maximum en fonction de l'épaisseur de couche d'absorbeur en GaAs selon trois modèles différents incluant un anti-reflet parfait : (bleu) absorption simple passage, (vert) absorption double passage (miroir plan en face arrière), et (rouge) piégeage optique par diffusion lambertienne avec un miroir parfait en face arrière. Les points noirs marquent les résultats expérimentaux de la littérature : [a] Nakayama et al. [84], [b] Bauhuis et al. [74], [c] Liu et al. [85], [d] Kayes et al. (épaisseur 1-2 μm) [75], [e] Yang et al. [86], [f] Vandamme et al. [82], [g] Lee et al. [87] et [h] Aberg et al. (épaisseur équivalente d'une couche planaire pour le réseau de nanofils) [88]. Nous avons atteint un $J_{sc} = 24.64\ mA/cm^2$ avec 205 nm d'épaisseur d'absorbeur de GaAs. (b) Schéma simplifié de la structure de cellules solaires ultra-minces en GaAs avec un miroir arrière nanostructuré. Les contacts grilles en face avant et les contacts localisés en face arrière ne sont pas montrés ici (voir la Figure 4.17 détaillée). La plupart de la surface arrière consiste en un miroir nanostructuré TiO_2/Ag avec une période de réseau p, une hauteur h et une largeur d de nanostructures d'Ag.*

Cellules solaires ultra-minces en GaAs

La figure A.1(a) montre le courant de court-circuit J_{sc} de la cellule solaire en fonction de l'épaisseur de GaAs utilisée, avec ou sans structure de piégeage optique. Réduire l'épaisseur de couche est notre but pour les cellules photovoltaïques à haut rendement et bas coût. L'absorption faible dans les cellules ultra-minces doit être compensée par une structure de piégeage optique pour maintenir la génération de photocourant. Nous avons conçu et modélisé des cellules solaires ultra-fines (205 nm) avec un miroir arrière nanostructuré périodique et bidimensionnel (Figure A.1(b)). La structure détaillée de la cellule se trouve dans le Tableau 4.1, et les étapes de la fabrication sont décrites dans la Section 4.5.

On utilise la méthode RCWA (*Rigorous coupled-wave analysis*) pour calculer l'absorption optique dans un absorbeur ultra-mince de GaAs et pour optimiser la géométrie du miroir arrière nanostructuré. La Figure A.2 montre l'absorption calculée en fonction de la période du réseau, de l'épaisseur d'absorbeur de GaAs et de la longueur d'onde. On étudie les mécanismes de résonances et on montre que les résonances de Fabry-Pérot et de modes guidés aboutissent à de multiples pics d'absorption, conduisant à une valeur élevée de photocourant J_{sc} jusqu'à 25.6 mA/cm^2 pour l'absorption dans la couche de GaAs ultra-mince. Avec la carte d'absorption en fonction de la période, on voit bien l'évolution des modes guidés qui subissent un décalage vers les grandes longueurs d'onde lorsque la période augmente.

Ensuite, on a fabriqué et caractérisé les cellules ultra-minces en GaAs. Les efficacités obtenues et les caractéristiques courant-tension (JV) sont montrés dans la Figure A.3(a) en comparant les trois échantillons avec ou sans structure de piégeage optique. Le piégeage de la lumière par un mécanisme multi-résonant est démontré avec un miroir arrière en TiO_2/Ag fabriqué en utilisant la lithographie de nanoimpression, et la réponse spectrale montre bien l'effet bénéfique d'absorption améliorée dans les grandes longueurs d'onde (Figure A.3(b)). Ceci conduit à une efficacité de 19.9% sous éclairement d'un soleil, mesure certifiée ensuite au Fraunhofer ISE ($J_{sc} = 24.64$ mA/cm^2, $V_{oc} = 1.022\,V$, $FF = 0.792$). À notre connaissance, c'est la meilleure performance

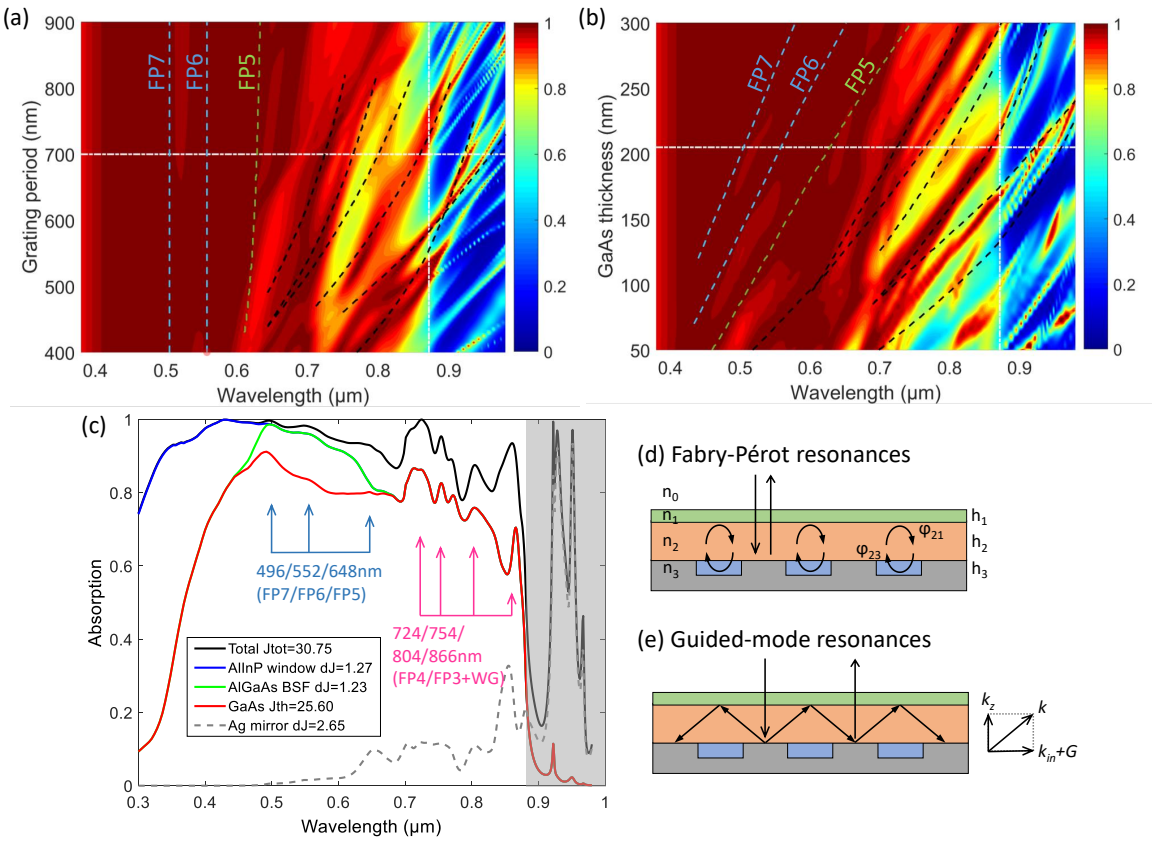

FIGURE A.2 – *Absorption calculée dans la cellule ultra-mince en GaAs avec un miroir nanostructuré en TiO_2/Ag. (a) Spectres de 1-Reflectivité (1-R) en fonction de la période p du réseau pour une épaisseur de GaAs de 205 nm. Le trait blanc horizontal indique la période du réseau $p = 700$ nm qui donne lieu à la meilleure absorption sur une large bande spectrale. (b) Spectres de 1-R en fonction de l'épaisseur de GaAs. Le trait blanc horizontal indique l'épaisseur 205 nm de GaAs étudiée expérimentalement. (c) Spectres d'absorption dans chacune des couches de la cellule solaire avec la géométrie optimale du miroir arrière (réseau de période $p = 700$ nm, hauteur $h = 120$ nm et largeur de nanostructure d'Ag $d = 420$ nm (60% de la période)) (d) Représentation schématique des résonances de Fabry-Pérot. (e) Représentation schématique des résonances de modes guidés.*

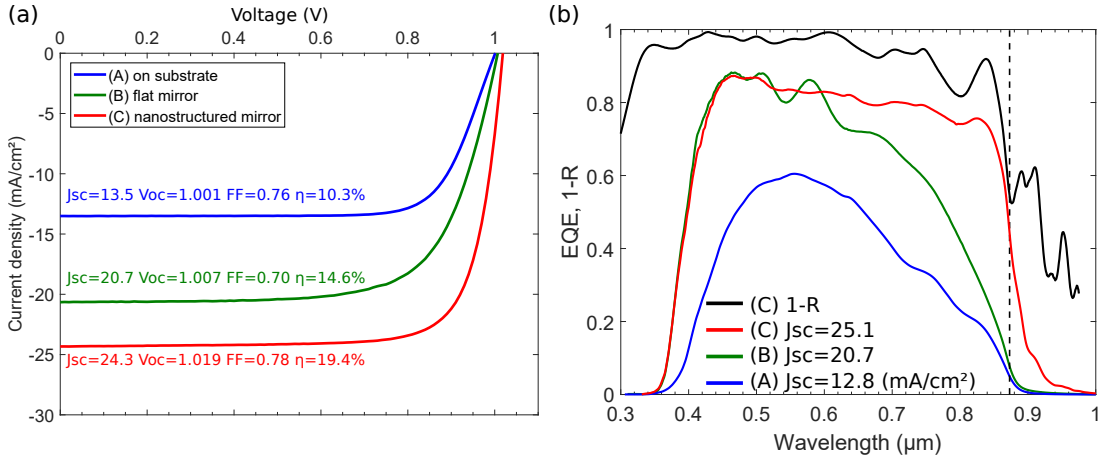

FIGURE A.3 – *(a) Comparaison des caractéristiques courant-tension des cellules solaires ultra-minces sous illumination à un soleil : (A) cellule non-transférée sur le substrat de croissance en GaAs, (B) cellule avec un miroir plan en argent et (C) avec un miroir nanostructuré. (b) Comparaison de la réponse spectrale (EQE) des cellules solaires ultra-minces. Le spectre 1-R de la cellule avec un miroir nanostructuré est également montré (courbe noire). Le trait vertical marque le gap de GaAs.*

pour les cellules solaires ultra-minces en GaAs à ce jour. L'analyse des courbes JV avec un modèle à deux diodes permet d'extraire des paramètres importants (les courants d'obscurité et les résistances parasites, notamment). On identifie la perte due à la recombinaison en bord de la cellule et nous proposons des voies d'amélioration possibles vers une efficacité de 25% en utilisant un absorbeur de GaAs de seulement 200 nm d'épaisseur.

Caractérisation des nanofils III-V par cathodoluminescence

Afin d'étudier les propriétés des nanofils de semi-conducteurs III-V et d'explorer leur potentiel en tant qu'absorbeur photovoltaïque, nous avons besoin d'une méthode de caractérisation capable de résoudre les variations à l'échelle nanométrique. En particulier, contrôler le dopage n et p est indispensable à la réalisation de la cellule solaire à nanofils, mais les méthodes pour mesurer le dopage dans des nanofils sont techniquement difficiles (effet Hall en contactant individuellement des nanofils par lithographie électronique). Nous proposons la cathodoluminescence (CL) pour mesurer les nanofils crûs sur substrat Si en collaboration avec le département Matériau. La méthode a été démontrée sur des couches de GaAs planaire de référence dopées n et p, puis appliquée à la caractérisation de nanofils. Les nanofils ont été crûs en épitaxie par jets moléculaires (MBE) et par la méthode dite de vapeur-liquide-solide (VLS) en utilisant le Ga liquide comme catalyseur. Dans certaines conditions, cette méthode particulière de croissance de cristaux conduit à la coexistence de structures cristallines cubiques de zinc-blende (ZB) et de wurtzite hexagonale (WZ) dans les nanofils uniques.

La Figure A.4 montre les mesures de CL d'un nanofil de GaAs non dopé contenant des segments ZB et WZ. Le GaAs WZ n'existe presque que dans les formes de nanofils, donc ses propriétés sont peu connues, et même le gap et la structure de bande sont controversés dans la littérature. Nous utilisons la cartographie de CL mesurée à diverses températures et en polarimétrie pour confirmer que la bande interdite du GaAs WZ doit être proche et légèrement supérieure à celle du GaAs ZB. On étudie également la transition optique dans le GaAs WZ en analysant le degré de polarisation des spectres CL. La lumière émise par le GaAs WZ montre clairement la direction de polarisation perpendiculaire à l'axe de croissance (c'est-à-dire l'axe c du réseau WZ), ce qui est attendu par les règles de sélection sur les transitions dipolaires dans le réseau cristallin hexagonal compact.

La Figure A.5 présente un exemple de mesure de CL sur un nanofil de GaAs dont la coquille est dopé Si (a priori dopage de type n). On peut voir essentiellement trois zones qui présentent des caractéristiques CL très différentes. La mesure de CL a plusieurs objectifs : déterminer la qualité cristalline des nanofils (homogénéité des spectres CL), les niveaux de dopage (décalage et élargissement spectral), et l'effet de la passivation (l'intensité d'émission et la mesure du temps de vie des porteurs). Pour le GaAs dopé n, on observe l'élargissement et le décalage du spectre CL vers le bleu en augmentant la concentration d'élections (*Burstein-Moss shift*). Ce décalage et l'élargissement du spectre d'émission sont la conséquence de l'occupation des électrons au-dessus de la bande de conduction. Ici, on attribue au bas du nanofil un dopage n léger, tandis que la tête du nanofil est fortement dopé n. Le segment en milieu-haut du nanofil émet des spectres CL décalés vers le rouge à cause de niveaux de défaut Si dans le GaAs WZ. J'ai développé un modèle physique basé sur la loi de Planck généralisé pour fitter le spectre d'émission et déterminer précisément les niveaux de Fermi et donc la concentration d'électrons (Figure A.6).

Dans les semi-conducteurs III-V de type p, l'effet du remplissage de bande est moins présent parce que la densité effective de la bande de valence est beaucoup plus grande (de l'ordre de 10^{19} cm^{-3}) que celle de la bande de conduction. On identifie le gap comme un paramètre important que l'on peut relier à la concentration de trous, et qui peut être extrait précisément en fittant tout le spectre de CL. Cette méthode est reproductible pour analyser les spectres de CL mesurés à différentes températures (20 K à 300 K). Le gap effectif diminue en augmentant

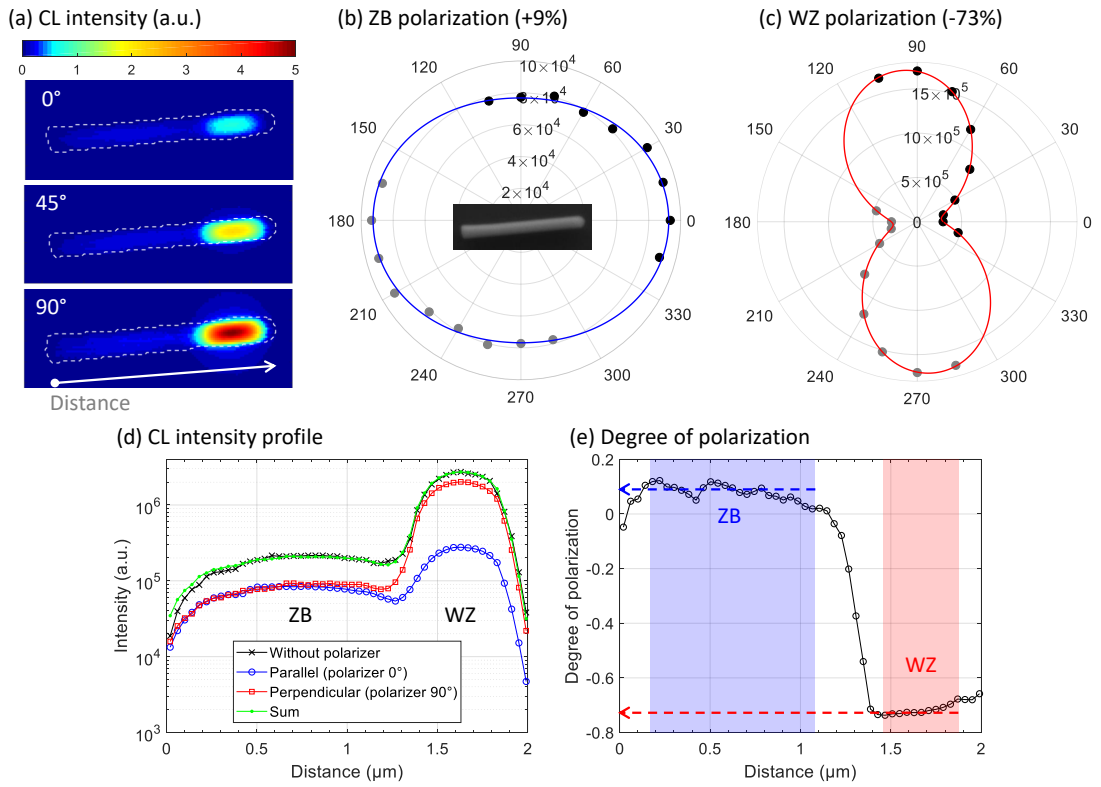

Figure A.4 – *Émission CL résolue en polarisation mesurée à 10 K. (a) Cartographies d'intensités intégrées d'un nanofils de GaAs (non-dopé) mesurées avec trois différents angles du polariseur :* 0° *(champ électrique parallèle à l'axe du nanofil),* 45°*, et* 90° *(perpendiculaire à l'axe du nanofil). (b-c) Tracé en angle polaire des intensités de CL à partir des parties ZB et WZ mesurées sous différents angles de polarisation. (d) Profils d'intensités extraits le long du nanofil mesuré sans polariseur (noir) et avec polariseur parallèle (bleu) et perpendiculaire (rouge) à l'axe du nanofil. (e) Degré de polarisation (voir la définition, Équation 6.4) le long du nanofil, montrant deux régions distinctes en polarisation : les segments ZB et WZ.*

la concentration de trous p, et la différence du gap entre un semi-conducteur dopé p et le même semi-conducteur intrinsèque (appelé *bandgap narrowing*, BGN) est proportionnel à la puissance $1/3$ de la concentration de trous p. Ceci permet de calibrer le dopage p pour la croissance de nanofils de GaAs dans le laboratoire (dopage par béryllium dans le système MBE).

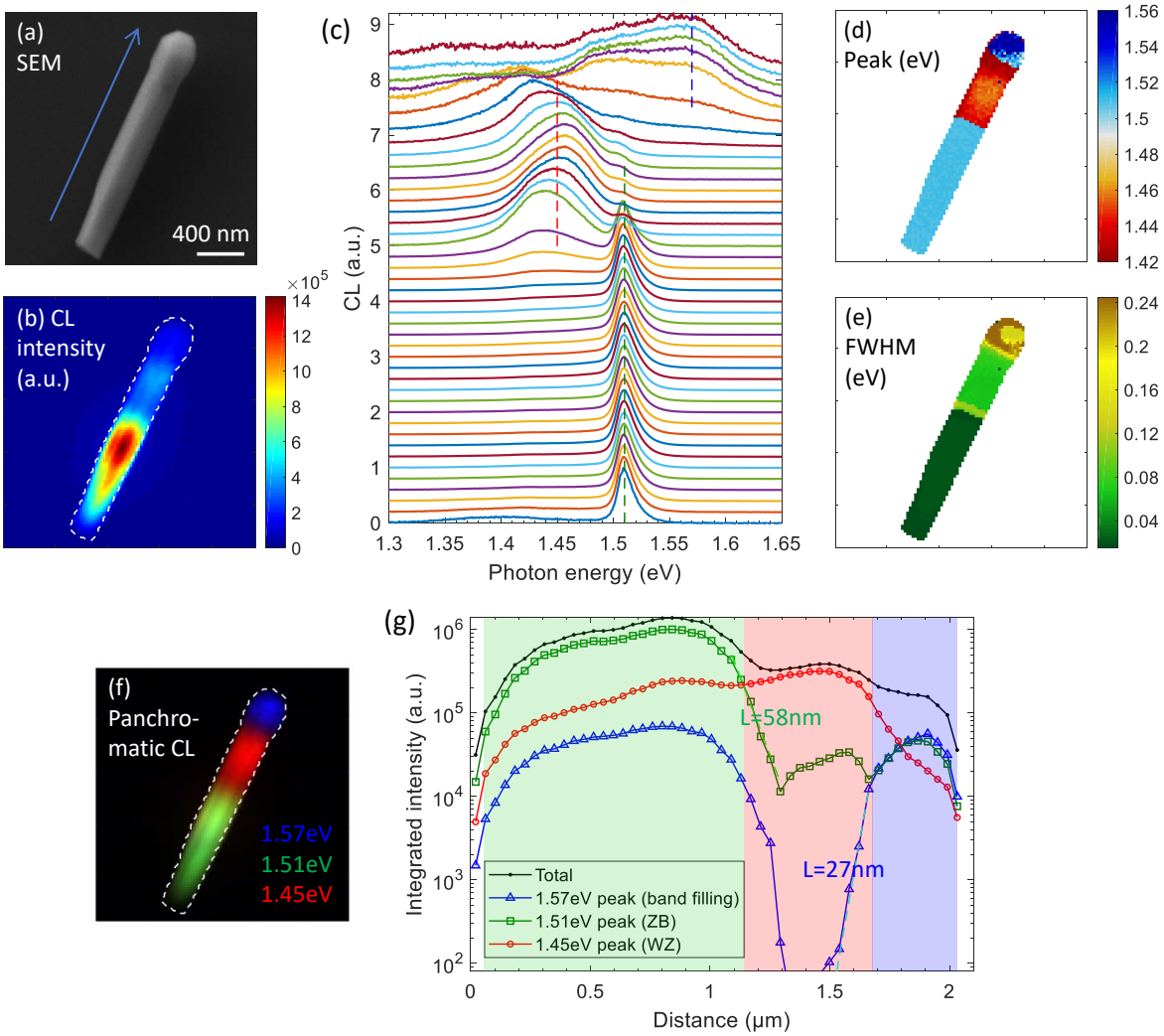

Figure A.5 – *Mesure de CL à basse température (∼15 K) d'un nanofil de GaAs dopé Si qui contient un segment ZB en bas et en haut, et qui a un segment WZ en milieu-haut du fil. (a) Image MEB du nanofil. (b) Cartographie d'intensités de CL intégrées sur tout le spectre. (c) Spectres de CL extraits le long du fil (flèche : de bas en haut) (d) Cartographie de l'énergie du pic d'émission des spectres de CL. (e) Cartographie de la largeur à mi-hauteur (FWHM) des pics d'émission de CL. (f) Carte de CL présentée par la superposition de trois couleurs qui correspondent à trois régions spectrales d'émission. (g) Variation le long du fil pour les trois profils d'intensités obtenus par déconvolution des trois régions spectrales (vert : 1.51 eV, rouge : 1.45 eV, bleu : 1.57 eV). Le nanofil présente trois régions distinctes mises en évidence par les différentes cartes de CL. La tête du fil a une caractéristique de CL élargie et décalée vers le bleu, correspondant à la concentration d'électrons élevée. Le GaAs WZ dopé Si présente des caractéristiques de CL élargie et décalée vers le rouge (∼1.45 eV).*

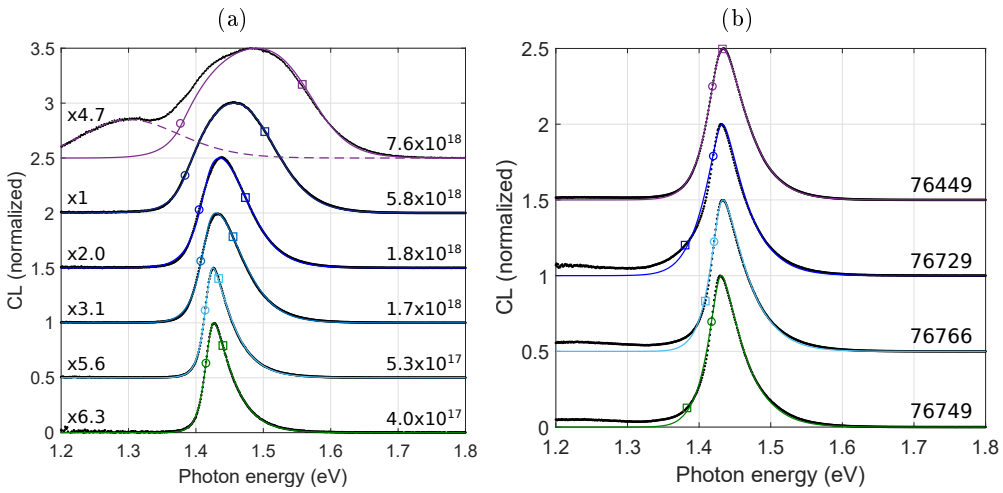

Figure A.6 – *(a) Comparaison des spectres de CL mesurés à température ambiante (points noirs) et leurs fits (lignes de couleur) pour les différentes couches minces de GaAs dopé n. Les différents niveaux de dopage (cm^{-3}) sont indiqués sur la figure et les intensités sont normalisées par le maximum (facteurs de normalisation indiqués). Pour l'échantillon le plus dopé, la luminescence venant des niveaux de défauts est fittée par une gaussienne (trait pointillé). (b) Comparaison des spectres CL mesurés à température ambiante (points noirs) et leurs fits (lignes de couleur) pour les différents échantillons de nanofils en GaAs dopé Si. Les marqueurs circulaires indiquent les positions du gap et les marqueurs carrés indiquent les niveaux de Fermi obtenus à l'issu du fit.*

Cellules solaires à base de nanofils en GaAs

Dans le Chapitre 7, on étudie la structure de cellule solaire à nanofils et on montre les premiers résultats expérimentaux. Dans la littérature, les dispositifs à nanofil unique ou à réseaux de nanofils ont été démontrés. La structure consiste soit en une jonction axiale, soit en une jonction radiale (cœur-coquille). On se focalise sur des réseaux de nanofils de GaAs de type p-cœur/n-coquille, et on étudie théoriquement les performances d'un tel dispositif en terme d'optique et d'électronique.

On calcule l'absorption optique du réseau de nanofils par la méthode RCWA pour optimiser les paramètres du réseau et le diamètre des nanofils. On trouve, pour une géométrie cylindrique de nanofils à hauteur fixée à 1 μm et pour le réseau rangé en carré, que le diamètre optimal de nanofils est 350 nm et la période du réseau est 580 nm. Ceci donne lieu au meilleur photocourant $J_{sc} = 27.4$ mA/cm^2 avec un miroir plan d'argent en face arrière (Figure A.7(a,b)), qui pourrait être encore amélioré par l'ajoute des couches anti-reflets. Dans ce cas, le volume de GaAs utilisé est équivalent à une couche planaire de moins de 300 nm d'épaisseur. Les effets des paramètres géométriques sur les résonances optiques sont étudiés. Du côté de la performance électrique, on calcule la différence de potentiels V_{bi} dans la jonction p-n en cœur-coquille, qui est donc un paramètre clé qui limite la tension de circuit-ouvert V_{oc} de la cellule solaire. V_{bi} est obtenu par la résolution de l'équation de Poisson en cordonnées cylindriques, et est exprimé en fonction des niveaux de dopage en cœur et en coquille, ainsi que la densité de défauts en surface. On conclut qu'un fort dopage est souhaité dans les nanofils cœur-coquille pour éviter la déplétion totale du fil, ce qui réduit le V_{bi} et dégrade la performance électrique de la cellule à nanofils.

Finalement, nous avons fabriqué un dispositif de cellule solaire à nanofils, qui a montré un rendement de 1.2% sous éclairement d'un soleil avec un V_{oc} de 0.6 V. Malgré les difficultés techniques, notamment le contrôle de la croissance (qualité cristalline, dopage, uniformité, etc.) et le contact en face avant sur le réseau de nanofils, ce résultat est très encourageant pour continuer à explorer le potentiel de la cellule à nanofils.

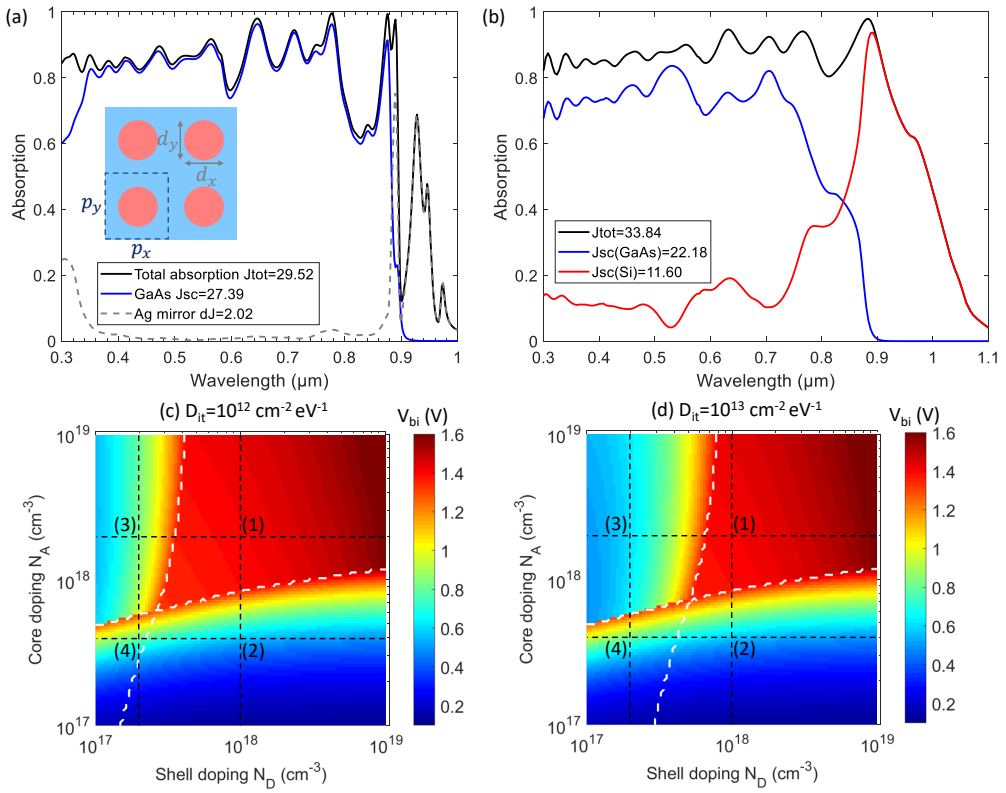

Figure A.7 – *(a,b) Spectres d'absorption calculés pour un réseau de nanofils en GaAs (période du réseau $p = 580$ nm et nanofils de hauteur 1 μm et de diamètre $d = 350$ nm). L'espace entre les nanofils est supposé rempli avec un diélectrique non-absorbant d'indice optique constant égal à 1.5 : (a) pour le cas d'un substrat en miroir d'argent et (b) pour le cas d'un substrat Si. (c,d) La différence de potentiel de la jonction p-n en cœur-coquille (V_{bi}) calculée en fonction des niveaux de dopage p en cœur (diamètre 60 nm) et n en coquille (épaisseur 80 nm) : (c) cas d'une densité de défauts en surface $D_{it} = 10^{12}\, cm^{-2}eV^{-1}$ et (d) cas $D_{it} = 10^{13}\, cm^{-2}eV^{-1}$. Les traits blancs marquent les frontières pour la déplétion totale du coeur et de la coquille en faible dopage.*

Conclusion

En conclusion générale, cette thèse aborde divers aspects des cellules solaires structurées à l'échelle nanométrique : le piégeage optique, l'émission de la luminescence et l'analyse des caractéristiques électriques des cellules en GaAs, à base de films ultra-minces et de nanofils. L'ensemble s'est présenté comme le fruit de la rencontre du photovoltaïque avec l'optique électromagnétique, la thermodynamique et la science de matériaux. En effet, la réduction du volume de la cellule solaire pourrait ouvrir la voie à des dispositifs photovoltaïques à la fois plus efficaces et moins coûteux. La caractérisation avancée par la cathodoluminescence fournit également une méthode de caractérisation très performante pour les matériaux du photovoltaïque et au-delà.

Appendix

B List of publications

Journal articles

1. N. Vandamme, **H.-L. Chen**, A. Gaucher, B. Behaghel, A. Lemaître, A. Cattoni, C. Dupuis, N. Bardou, J.-F. Guillemoles, S. Collin, Ultrathin GaAs Solar Cells With a Silver Back Mirror, IEEE Journal of Photovoltaics. 5 (2015) 565–570.

2. **H.-L. Chen**, C. Himwas, A. Scaccabarozzi, P. Rale, F. Oehler, A. Lemaître, L. Lombez, J.-F. Guillemoles, M. Tchernycheva, J.-C. Harmand, A. Cattoni, S. Collin, Determination of n-Type Doping Level in Single GaAs Nanowires by Cathodoluminescence, Nano Letters. 17 (2017) 6667–6675.

3. **H.-L. Chen**, A. Cattoni, R. De Lépinau, A. Walker, O. Hoehn, D. Lackner, G. Siefer, N. Vandamme, J. Goffard, B. Behaghel, C. Dupuis, N. Bardou, F. Dimroth, S. Collin, A 19.9%-efficient ultrathin 205nm-thick GaAs Solar Cell with a Silver Nanostructured Back Mirror, in preparation.

4. C. Himwas, S. Collin, **H.-L. Chen**, G. Patriarche, F. Oehler, L. Travers, F. H. Julien, J.-C. Harmand, M. Tchernycheva, Correlated optical and structural analyses of individual GaAsP/GaP core-shell nanowires, in preparation.

5. H.-L. Chen et al., Cathodoluminescence for Quantitative GaAs Doping Assessment (1): reference thin films and modeling, in preparation.

6. H.-L. Chen et al., Cathodoluminescence for Quantitative GaAs Doping Assessment (2): nanowire mapping, in preparation.

7. H.-L. Chen et al., Optical Properties of Wurtzite in GaAs Nanowires Probed by Cathodoluminescence Polarimetry, in preparation.

Book chapters

1. V. Piazza, L. Mancini, **H.-L. Chen**, S. Collin, M. Tchernycheva, Chapter Four - Nanoscale Analyses Applied to Nanowire Devices, in: S. Mokkapati, C. Jagadish (Eds.), Semiconductors and Semimetals, Elsevier, 2018: pp. 231–319.

Conference proceedings

1. **H.-L. Chen**, A. Cattoni, N. Vandamme, J. Goffard, A. Lemaître, A. Delamarre, B. Behaghel, K. Watanabe, M. Sugiyama, J.-F. Guillemoles, S. Collin, 200nm-Thick GaAs solar cells with a nanostructured silver mirror, in: 2016 IEEE 43rd Photovoltaic Specialists Conference (PVSC), 2016: pp. 3506–3509.

2. P. Rale, B. Behaghel, **H.-L. Chen**, A. Delamarre, N. Vandamme, S. Collin, R. Tamaki, Y. Shoji, Y. Okada, L. Lombez, J.-F. Guillemoles, All optical IBSC characterization method, in: 2017 IEEE 44th Photovoltaic Specialist Conference (PVSC), 2017: pp. 1-4.

3. **H.-L. Chen**, A. Scaccabarozzi, R. De Lépinau, C. Himwas, P. Rale, F. Oehler, A. Lemaître, M. Tchernycheva, J.-C. Harmand, A. Cattoni, S. Collin, Cathodoluminescence Characterization of Semiconductor Doping at the Nanoscale, in: 2018 World Conference on Photovoltaic Energy Conversion (WCPEC-7), 2018: in print.

Bibliography

References for Chapter 1: Introduction

[1] M. A. Green and S. P. Bremner. "Energy Conversion Approaches and Materials for High-Efficiency Photovoltaics". In: *Nature Materials* 16.1 (2017), pp. 23–34. DOI: 10.1038/nmat4676 *Cited on pages 6, 10.*

[2] P. Würfel. *Physics of Solar Cells: From Basic Principles to Advanced Concepts*. 2 edition. WILEY-VCH, 2009 *Cited on pages 7, 25, 37, 47, 51–53.*

[3] K. Yoshikawa, H. Kawasaki, W. Yoshida, T. Irie, K. Konishi, K. Nakano, T. Uto, D. Adachi, M. Kanematsu, H. Uzu, and K. Yamamoto. "Silicon Heterojunction Solar Cell with Interdigitated Back Contacts for a Photoconversion Efficiency over 26%". In: *Nature Energy* 2.5 (2017), p. 17032. DOI: 10.1038/nenergy.2017.32 *Cited on page 9.*

[4] M. A. Green, Y. Hishikawa, W. Warta, E. D. Dunlop, D. H. Levi, J. Hohl-Ebinger, and A. W. Ho-Baillie. "Solar Cell Efficiency Tables (Version 50)". In: *Progress in Photovoltaics: Research and Applications* 25.7 (2017), pp. 668–676. DOI: 10.1002/pip.2909 *Cited on pages 9, 11.*

[5] P. Jackson, R. Wuerz, D. Hariskos, E. Lotter, W. Witte, and M. Powalla. "Effects of Heavy Alkali Elements in Cu(In,Ga)Se2 Solar Cells with Efficiencies up to 22.6%". In: *physica status solidi (RRL) – Rapid Research Letters* 10.8 (2016), pp. 583–586. DOI: 10.1002/pssr.201600199 *Cited on page 11.*

[6] T. Kato, A. Handa, T. Yagioka, T. Matsuura, K. Yamamoto, S. Higashi, J. L. Wu, K. F. Tai, H. Hiroi, T. Yoshiyama, T. Sakai, and H. Sugimoto. "Enhanced Efficiency of Cd-Free Cu(In,Ga)(Se,S)2 Minimodule Via (Zn,Mg)O Second Buffer Layer and Alkali Metal Post-Treatment". In: *IEEE Journal of Photovoltaics* 7.6 (2017), pp. 1773–1780. DOI: 10.1109/JPHOTOV.2017.2745710 *Cited on page 11.*

[7] M. A. Green, K. Emery, Y. Hishikawa, W. Warta, and E. D. Dunlop. "Solar Cell Efficiency Tables (Version 40)". In: *Progress in Photovoltaics: Research and Applications* 20.5 (2012), pp. 606–614. DOI: 10.1002/pip.2267 *Cited on pages 11, 72.*

[8] J. F. Geisz, M. A. Steiner, I. García, S. R. Kurtz, and D. J. Friedman. "Enhanced External Radiative Efficiency for 20.8% Efficient Single-Junction GaInP Solar Cells". In: *Applied Physics Letters* 103.4 (2013), p. 041118. DOI: 10.1063/1.4816837 *Cited on pages 11, 73.*

[9] M. A. Green, Y. Hishikawa, E. D. Dunlop, D. H. Levi, J. Hohl-Ebinger, and A. W. Y. Ho-Baillie. "Solar Cell Efficiency Tables (Version 51)". In: *Progress in Photovoltaics: Research and Applications* 26.1 (2017), pp. 3–12. DOI: 10.1002/pip.2978 *Cited on page 11.*

[10] S. Essig, C. Allebé, T. Remo, J. F. Geisz, M. A. Steiner, K. Horowitz, L. Barraud, J. S. Ward, M. Schnabel, A. Descoeudres, D. L. Young, M. Woodhouse, M. Despeisse, C. Ballif, and A. Tamboli. "Raising the One-Sun Conversion Efficiency of III–V/Si Solar Cells to 32.8% for Two Junctions and 35.9% for Three Junctions". In: *Nature Energy* 2.9 (2017), p. 17144. DOI: 10.1038/nenergy.2017.144 *Cited on page 11.*

[11] R. Cariou, J. Benick, F. Feldmann, O. Höhn, H. Hauser, P. Beutel, N. Razek, M. Wimplinger, B. Bläsi, D. Lackner, M. Hermle, G. Siefer, S. W. Glunz, A. W. Bett, and F. Dimroth. "III–V-on-Silicon Solar Cells Reaching 33% Photoconversion Efficiency in Two-Terminal Configuration". In: *Nature Energy* 3.4 (2018), pp. 326–333. DOI: 10.1038/s41560-018-0125-0 *Cited on page 11.*

[12] W. S. Yang, J. H. Noh, N. J. Jeon, Y. C. Kim, S. Ryu, J. Seo, and S. I. Seok. "High-Performance Photovoltaic Perovskite Layers Fabricated through Intramolecular Exchange". In: *Science* 348.6240 (2015), pp. 1234–1237. DOI: 10.1126/science.aaa9272 *Cited on page 12.*

[13] K. A. Bush, A. F. Palmstrom, Z. J. Yu, M. Boccard, R. Cheacharoen, J. P. Mailoa, D. P. McMeekin, R. L. Z. Hoye, C. D. Bailie, T. Leijtens, I. M. Peters, M. C. Minichetti, N. Rolston, R. Prasanna, S. Sofia, D. Harwood, W. Ma, F. Moghadam, H. J. Snaith, T. Buonassisi, Z. C. Holman, S. F. Bent, and M. D. McGehee. "23.6%-Efficient Monolithic Perovskite/Silicon Tandem Solar Cells with Improved Stability". In: *Nature Energy* 2.4 (2017), p. 17009. DOI: 10.1038/nenergy.2017.9 *Cited on page 12.*

[14] M. A. Green. *Third Generation Photovoltaics*. Vol. 12. Springer series in photonics. Springer Berlin Heidelberg, 2006 *Cited on page 13.*

References for Chapter 2: Physics of Solar Cells

[2] P. Würfel. *Physics of Solar Cells: From Basic Principles to Advanced Concepts*. 2 edition. WILEY-VCH, 2009 *Cited on pages 7, 25, 37, 47, 51–53.*

[15] C. F. Klingshirn. *Semiconductor Optics*. 4th ed. Graduate Texts in Physics. Berlin Heidelberg: Springer-Verlag, 2012 *Cited on pages 16, 17, 19, 34, 42, 44, 46, 155.*

[16] L. Li. "Formulation and Comparison of Two Recursive Matrix Algorithms for Modeling Layered Diffraction Gratings". In: *JOSA A* 13.5 (1996), pp. 1024–1035. DOI: 10.1364/JOSAA.13.001024 *Cited on page 21.*

[17] M. G. Moharam, E. B. Grann, D. A. Pommet, and T. K. Gaylord. "Formulation for Stable and Efficient Implementation of the Rigorous Coupled-Wave Analysis of Binary Gratings". In: *Journal of the Optical Society of America A* 12.5 (1995), p. 1068. DOI: 10.1364/JOSAA.12.001068 *Cited on page 22.*

[18] P. Lalanne and G. M. Morris. "Highly Improved Convergence of the Coupled-Wave Method for TM Polarization". In: *Journal of the Optical Society of America A* 13.4 (1996), pp. 779–784. DOI: 10.1364/JOSAA.13.000779 *Cited on page 22.*

[19] L. Li. "New Formulation of the Fourier Modal Method for Crossed Surface-Relief Gratings". In: *JOSA A* 14.10 (1997), pp. 2758–2767. DOI: 10.1364/JOSAA.14.002758 *Cited on page 22.*

[20] P. Lalanne and M. P. Jurek. "Computation of the Near-Field Pattern with the Coupled-Wave Method for Transverse Magnetic Polarization". In: *Journal of Modern Optics* 45.7 (1998), pp. 1357–1374. DOI: 10.1080/09500349808230634 *Cited on page 23.*

[21] O. Isabella, K. Jäger, A. Smets, R. van Swaaij, and M. Zeman. *Solar Energy: The Physics and Engineering of Photovoltaic Conversion, Technologies and Systems*. UIT Cambridge Ltd., 2016 *Cited on pages 23, 30.*

[22] S. M. Sze and K. K. Ng. *Physics of Semiconductor Devices*. 3 edition. Hoboken, N.J: Wiley-Interscience, 2006 *Cited on pages 23, 30, 31, 123, 206.*

[23] U. Würfel, A. Cuevas, and P. Würfel. "Charge Carrier Separation in Solar Cells". In: *IEEE Journal of Photovoltaics* 5.1 (2015), pp. 461–469. DOI: 10.1109/JPHOTOV.2014.2363550 *Cited on page 25.*

[24] C. J. Hwang. "Quantum Efficiency and Radiative Lifetime of the Band-to-Band Recombination in Heavily Doped n-Type GaAs". In: *Physical Review B* 6.4 (1972), pp. 1355–1359. DOI: 10.1103/PhysRevB.6.1355 *Cited on page 27.*

[25] R. J. Nelson and R. G. Sobers. "Minority-Carrier Lifetimes and Internal Quantum Efficiency of Surface-Free GaAs". In: *J. Appl. Phys.; (United States)* 49:12 (1978). DOI: 10.1063/1.324530 *Cited on page 27.*

[26] A. Richter, M. Hermle, and S. W. Glunz. "Reassessment of the Limiting Efficiency for Crystalline Silicon Solar Cells". In: *IEEE Journal of Photovoltaics* 3.4 (2013), pp. 1184–1191. DOI: 10.1109/JPHOTOV.2013.2270351 *Cited on page 27.*

[27] P. Kowalczewski, L. Redorici, A. Bozzola, and L. C. Andreani. "Silicon Solar Cells Reaching the Efficiency Limits: From Simple to Complex Modelling". In: *Journal of Optics* 18.5 (2016), p. 054001. DOI: 10.1088/2040-8978/18/5/054001 *Cited on page 27.*

[28] W. Shockley and W. T. Read. "Statistics of the Recombinations of Holes and Electrons". In: *Physical Review* 87.5 (1952), pp. 835–842. DOI: 10.1103/PhysRev.87.835 *Cited on page 27.*

[29] J. G. Fossum and D. S. Lee. "A Physical Model for the Dependence of Carrier Lifetime on Doping Density in Nondegenerate Silicon". In: *Solid-State Electronics* 25.8 (1982), pp. 741–747. DOI: 10.1016/0038-1101(82)90203-9 *Cited on page 28.*

[30] J. G. Fossum, R. P. Mertens, D. S. Lee, and J. F. Nijs. "Carrier Recombination and Lifetime in Highly Doped Silicon". In: *Solid-State Electronics* 26.6 (1983), pp. 569–576. DOI: 10.1016/0038-1101(83)90173-9 *Cited on page 28.*

[31] H. C. Casey, B. I. Miller, and E. Pinkas. "Variation of Minority-Carrier Diffusion Length with Carrier Concentration in GaAs Liquid-Phase Epitaxial Layers". In: *Journal of Applied Physics* 44.3 (1973), pp. 1281–1287. DOI: 10.1063/1.1662340 *Cited on page 29.*

[32] U. Rau, D. Abou-Ras, and T. Kirchartz, eds. *Advanced Characterization Techniques for Thin Film Solar Cells*. 1 edition. Weinheim, Germany: Wiley-VCH, 2011 *Cited on page 30.*

References for Chapter 3: Luminescence for Photovoltaic Materials

[2] P. Würfel. *Physics of Solar Cells: From Basic Principles to Advanced Concepts*. 2 edition. WILEY-VCH, 2009 *Cited on pages 7, 25, 37, 47, 51–53.*

[15] C. F. Klingshirn. *Semiconductor Optics*. 4th ed. Graduate Texts in Physics. Berlin Heidelberg: Springer-Verlag, 2012 *Cited on pages 16, 17, 19, 34, 42, 44, 46, 155.*

[33] P. Yu and M. Cardona. *Fundamentals of Semiconductors: Physics and Materials Properties*. 4th ed. Graduate Texts in Physics. Berlin Heidelberg: Springer-Verlag, 2010 *Cited on pages 34, 38–41, 51.*

[34] M. Grundmann. *The Physics of Semiconductors: An Introduction Including Nanophysics and Applications*. 2nd ed. Graduate Texts in Physics. Berlin Heidelberg: Springer-Verlag, 2010 *Cited on pages 34, 41.*

[35] J. S. Blakemore. "Semiconducting and Other Major Properties of Gallium Arsenide". In: *Journal of Applied Physics* 53.10 (1982), R123–R181. DOI: 10.1063/1.331665 *Cited on pages 35, 36, 132–134, 136, 153, 157.*

[36] M. D. Sturge. "Optical Absorption of Gallium Arsenide between 0.6 and 2.75 eV". In: *Physical Review* 127.3 (1962), pp. 768–773. DOI: 10.1103/PhysRev.127.768 *Cited on pages 42, 54, 59, 79, 80, 139.*

[37] M. A. Gilleo, P. T. Bailey, and D. E. Hill. "Uniaxial-Strain Effects on n = 1 Free-Exciton and Free-Carrier Lines in GaAs". In: *Journal of Luminescence* 1-2 (1970), pp. 562–571. DOI: 10.1016/0022-2313(70)90068-2 *Cited on page 43.*

[38] D. D. Sell. "Resolved Free-Exciton Transitions in the Optical-Absorption Spectrum of GaAs". In: *Physical Review B* 6.10 (1972), pp. 3750–3753. DOI: 10.1103/PhysRevB.6.3750 *Cited on page 43.*

[39] R. J. Elliott. "Intensity of Optical Absorption by Excitons". In: *Physical Review* 108.6 (1957), pp. 1384–1389. DOI: 10.1103/PhysRev.108.1384 *Cited on page 43.*

[40] D. C. Herbert. "An Extension of Haynes' Rule for Bound Excitons". In: *Journal of Physics C: Solid State Physics* 17.34 (1984), p. L901. DOI: 10.1088/0022-3719/17/34/001 *Cited on page 45.*

[41] F. Urbach. "The Long-Wavelength Edge of Photographic Sensitivity and of the Electronic Absorption of Solids". In: *Physical Review* 92.5 (1953), pp. 1324–1324. DOI: 10.1103/PhysRev.92.1324 *Cited on pages 45, 54.*

[42] J. I. Pankove. "Absorption Edge of Impure Gallium Arsenide". In: *Physical Review* 140.6A (1965), A2059–A2065. DOI: 10.1103/PhysRev.140.A2059 *Cited on page 46.*

[43] J. Serre and A. Ghazali. "From Band Tailing to Impurity-Band Formation and Discussion of Localization in Doped Semiconductors: A Multiple-Scattering Approach". In: *Physical Review B* 28.8 (1983), pp. 4704–4715. DOI: 10.1103/PhysRevB.28.4704 *Cited on page 46.*

[44] N. Mott. "The Mobility Edge since 1967". In: *Journal of Physics C: Solid State Physics* 20.21 (1987), p. 3075. DOI: 10.1088/0022-3719/20/21/008 *Cited on page 46.*

[45] N. F. Mott. "Metal-Insulator Transition". In: *Reviews of Modern Physics* 40.4 (1968), pp. 677–683. DOI: 10.1103/RevModPhys.40.677 *Cited on page 47.*

[46] P. Würfel. "The Chemical Potential of Radiation". In: *Journal of Physics C: Solid State Physics* 15.18 (1982), p. 3967. DOI: 10.1088/0022-3719/15/18/012 *Cited on pages 47, 49, 120.*

[47] W. van Roosbroeck and W. Shockley. "Photon-Radiative Recombination of Electrons and Holes in Germanium". In: *Physical Review* 94.6 (1954), pp. 1558–1560. DOI: 10.1103/PhysRev.94.1558 *Cited on pages 49, 52.*

[48] G. Lasher and F. Stern. "Spontaneous and Stimulated Recombination Radiation in Semiconductors". In: *Physical Review* 133.2A (1964), A553–A563. DOI: 10.1103/PhysRev.133.A553 *Cited on page 49.*

[49] Y. Okada, N. J. Ekins-Daukes, T. Kita, R. Tamaki, M. Yoshida, A. Pusch, O. Hess, C. C. Phillips, D. J. Farrell, K. Yoshida, N. Ahsan, Y. Shoji, T. Sogabe, and J.-F. Guillemoles. "Intermediate Band Solar Cells: Recent Progress and Future Directions". In: *Applied Physics Reviews* 2.2 (2015), p. 021302. DOI: 10.1063/1.4916561 *Cited on page 51.*

[50] B. Feuerbacher and P. Wurfel. "Verification of a Generalised Planck Law by Investigation of the Emission from GaAs Luminescent Diodes". In: *Journal of Physics: Condensed Matter* 2.16 (1990), p. 3803. DOI: 10.1088/0953-8984/2/16/010 *Cited on page 53.*

[51] K. Schick, E. Daub, S. Finkbeiner, and P. Würfel. "Verification of a Generalized Planck Law for Luminescence Radiation from Silicon Solar Cells". In: *Applied Physics A* 54.2 (1992), pp. 109–114. DOI: 10.1007/BF00323895 *Cited on page 53.*

[52] E. O. Kane. "Thomas-Fermi Approach to Impure Semiconductor Band Structure". In: *Physical Review* 131.1 (1963), pp. 79–88. DOI: 10.1103/PhysRev.131.79 *Cited on page 54.*

[53] J. K. Katahara and H. W. Hillhouse. "Quasi-Fermi Level Splitting and Sub-Bandgap Absorptivity from Semiconductor Photoluminescence". In: *Journal of Applied Physics* 116.17 (2014), p. 173504. DOI: 10.1063/1.4898346 *Cited on pages 54, 56.*

[54] H. C. Casey, D. D. Sell, and K. W. Wecht. "Concentration Dependence of the Absorption Coefficient for N- and P-type GaAs between 1.3 and 1.6 eV". In: *Journal of Applied Physics* 46.1 (1975), pp. 250–257. DOI: 10.1063/1.321330 *Cited on pages 54, 135.*

[55] W. Shockley and H. J. Queisser. "Detailed Balance Limit of Efficiency of P-n Junction Solar Cells". In: *Journal of Applied Physics* 32.3 (1961), pp. 510–519. DOI: 10.1063/1.1736034 *Cited on page 56.*

[56] A. Martı´, J. L. Balenzategui, and R. F. Reyna. "Photon Recycling and Shockley's Diode Equation". In: *Journal of Applied Physics* 82.8 (1997), pp. 4067–4075. DOI: 10.1063/1.365717 *Cited on pages 57, 61.*

[57] S. Sandhu, Z. Yu, and S. Fan. "Detailed Balance Analysis of Nanophotonic Solar Cells". In: *Optics Express* 21.1 (2013), pp. 1209–1217. DOI: 10.1364/OE.21.001209 *Cited on page 58.*

[58] Y. Xu, T. Gong, and J. N. Munday. "The Generalized Shockley-Queisser Limit for Nanostructured Solar Cells". In: *Scientific Reports* 5 (2015), p. 13536. DOI: 10.1038/srep13536 *Cited on pages 58, 193.*

[59] E. Yablonovitch and G. Cody. "Intensity Enhancement in Textured Optical Sheets for Solar Cells". In: *IEEE Transactions on Electron Devices* 29.2 (1982), pp. 300–305. DOI: 10.1109/T-ED.1982.20700 *Cited on pages 60, 113.*

[60] M. A. Green. "Lambertian Light Trapping in Textured Solar Cells and Light-Emitting Diodes: Analytical Solutions". In: *Progress in Photovoltaics: Research and Applications* 10.4 (2002), pp. 235–241. DOI: 10.1002/pip.404 *Cited on pages 60, 113.*

[61] R. T. Ross. "Some Thermodynamics of Photochemical Systems". In: *The Journal of Chemical Physics* 46.12 (1967), pp. 4590–4593. DOI: 10.1063/1.1840606 *Cited on pages 60, 73.*

[62] I. Schnitzer, E. Yablonovitch, C. Caneau, and T. J. Gmitter. "Ultrahigh Spontaneous Emission Quantum Efficiency, 99.7% Internally and 72% Externally, from AlGaAs/GaAs/AlGaAs Double Heterostructures". In: *Applied Physics Letters* 62.2 (1993), pp. 131–133. DOI: 10.1063/1.109348 *Cited on page 61.*

[63] M. A. Green. "Radiative Efficiency of State-of-the-Art Photovoltaic Cells". In: *Progress in Photovoltaics: Research and Applications* 20.4 (2012), pp. 472–476. DOI: 10.1002/pip.1147 *Cited on page 61.*

[64] U. Rau, U. W. Paetzold, and T. Kirchartz. "Thermodynamics of Light Management in Photovoltaic Devices". In: *Physical Review B* 90.3 (2014), p. 035211. DOI: 10.1103/PhysRevB.90.035211 *Cited on page 61.*

[65] G. Smestad and H. Ries. "Luminescence and Current-Voltage Characteristics of Solar Cells and Optoelectronic Devices". In: *Solar Energy Materials and Solar Cells* 25.1 (1992), pp. 51–71. DOI: 10.1016/0927-0248(92)90016-I *Cited on page 61.*

[66] O. D. Miller, E. Yablonovitch, and S. R. Kurtz. "Strong Internal and External Luminescence as Solar Cells Approach the Shockley-Queisser Limit". In: *IEEE Journal of Photovoltaics* 2.3 (2012), pp. 303–311. DOI: 10.1109/JPHOTOV.2012.2198434 *Cited on pages 61, 73.*

[67] V. Ganapati, M. A. Steiner, and E. Yablonovitch. "The Voltage Boost Enabled by Luminescence Extraction in Solar Cells". In: *IEEE Journal of Photovoltaics* 6.4 (2016), pp. 801–809. DOI: 10.1109/JPHOTOV.2016.2547580 *Cited on page 61.*

[68] M. Merano, S. Collin, P. Renucci, M. Gatri, S. Sonderegger, A. Crottini, J. D. Ganière, and B. Deveaud. "High Brightness Picosecond Electron Gun". In: *Review of Scientific Instruments* 76.8 (2005), p. 085108. DOI: 10.1063/1.2008975 *Cited on page 62.*

[69] M. Merano, S. Sonderegger, A. Crottini, S. Collin, P. Renucci, E. Pelucchi, A. Malko, M. H. Baier, E. Kapon, B. Deveaud, and J.-D. Ganière. "Probing Carrier Dynamics in Nanostructures by Picosecond Cathodoluminescence". In: *Nature* 438.7067 (2005), pp. 479–482. DOI: 10.1038/nature04298 *Cited on page 62.*

[70] D. Drouin, A. R. Couture, D. Joly, X. Tastet, V. Aimez, and R. Gauvin. "CASINO V2.42—A Fast and Easy-to-use Modeling Tool for Scanning Electron Microscopy and Microanalysis Users". In: *Scanning* 29.3 (2007), pp. 92–101. DOI: 10.1002/sca.20000 *Cited on page 66.*

References for Chapter 4: Ultrathin GaAs Solar Cells

[7] M. A. Green, K. Emery, Y. Hishikawa, W. Warta, and E. D. Dunlop. "Solar Cell Efficiency Tables (Version 40)". In: *Progress in Photovoltaics: Research and Applications* 20.5 (2012), pp. 606–614. DOI: 10.1002/pip.2267 *Cited on pages 11, 72.*

[8] J. F. Geisz, M. A. Steiner, I. García, S. R. Kurtz, and D. J. Friedman. "Enhanced External Radiative Efficiency for 20.8% Efficient Single-Junction GaInP Solar Cells". In: *Applied Physics Letters* 103.4 (2013), p. 041118. DOI: 10.1063/1.4816837 *Cited on pages 11, 73.*

[36] M. D. Sturge. "Optical Absorption of Gallium Arsenide between 0.6 and 2.75 eV". In: *Physical Review* 127.3 (1962), pp. 768–773. DOI: 10.1103/PhysRev.127.768 *Cited on pages 42, 54, 59, 79, 80, 139.*

[59] E. Yablonovitch and G. Cody. "Intensity Enhancement in Textured Optical Sheets for Solar Cells". In: *IEEE Transactions on Electron Devices* 29.2 (1982), pp. 300–305. DOI: 10.1109/T-ED.1982.20700 *Cited on pages 60, 113.*

[60] M. A. Green. "Lambertian Light Trapping in Textured Solar Cells and Light-Emitting Diodes: Analytical Solutions". In: *Progress in Photovoltaics: Research and Applications* 10.4 (2002), pp. 235–241. DOI: 10.1002/pip.404 *Cited on pages 60, 113.*

[61] R. T. Ross. "Some Thermodynamics of Photochemical Systems". In: *The Journal of Chemical Physics* 46.12 (1967), pp. 4590–4593. DOI: 10.1063/1.1840606 *Cited on pages 60, 73.*

[66] O. D. Miller, E. Yablonovitch, and S. R. Kurtz. "Strong Internal and External Luminescence as Solar Cells Approach the Shockley-Queisser Limit". In: *IEEE Journal of Photovoltaics* 2.3 (2012), pp. 303–311. DOI: 10.1109/JPHOTOV.2012.2198434 *Cited on pages 61, 73.*

[71] L. C. Hirst, M. K. Yakes, J. H. Warner, M. F. Bennett, K. J. Schmieder, R. J. Walters, and P. P. Jenkins. "Intrinsic Radiation Tolerance of Ultra-Thin GaAs Solar Cells". In: *Applied Physics Letters* 109.3 (2016), p. 033908. DOI: 10.1063/1.4959784 *Cited on page 71.*

[72] G. J. Bauhuis, J. J. Schermer, P. Mulder, M. M. a. J. Voncken, and P. K. Larsen. "Thin Film GaAs Solar Cells with Increased Quantum Efficiency Due to Light Reflection". In: *Solar energy materials and solar cells* 83.1 (2004), pp. 81–90 *Cited on page 72.*

[73] G. J. Bauhuis, P. Mulder, J. J. Schermer, E. J. Haverkamp, J. van Deelen, and P. K. Larsen. "High Efficiency Thin Film GaAs Solar Cells with Improved Radiation Hardness". In: *20th European Photovoltaic Solar Energy Conference, 6 – 10 June 2005, Barcelona, Spain* (2005), pp. 468–471 *Cited on page 72.*

[74] G. J. Bauhuis, P. Mulder, E. J. Haverkamp, J. C. C. M. Huijben, and J. J. Schermer. "26.1% Thin-Film GaAs Solar Cell Using Epitaxial Lift-Off". In: *Solar Energy Materials and Solar Cells* 93.9 (2009), pp. 1488–1491. DOI: 10.1016/j.solmat.2009.03.027 *Cited on pages 72, 75, 222.*

[75] B. M. Kayes, H. Nie, R. Twist, S. G. Spruytte, F. Reinhardt, I. C. Kizilyalli, and G. S. Higashi. "27.6% Conversion Efficiency, a New Record for Single-Junction Solar Cells under 1 Sun Illumination". In: *2011 37th IEEE Photovoltaic Specialists Conference*. 2011, pp. 000004–000008. DOI: 10.1109/PVSC.2011.6185831 *Cited on pages 72, 75, 113, 222.*

[76] E. Yablonovitch, O. Miller, and S. Kurtz. "The Opto-Electronic Physics That Broke the Efficiency Limit in Solar Cells". In: *2012 38th IEEE Photovoltaic Specialists Conference (PVSC)*. 2011, pp. 001556–001559. DOI: 10.1109/PVSC.2012.6317891 *Cited on page 73.*

[77] A. Braun, E. a. Katz, D. Feuermann, B. M. Kayes, and J. M. Gordon. "Photovoltaic Performance Enhancement by External Recycling of Photon Emission". In: *Energy & Environmental Science* 6 (2013), p. 1499. DOI: 10.1039/c3ee40377g *Cited on page 73.*

[78] M. A. Steiner, J. F. Geisz, I. García, D. J. Friedman, A. Duda, and S. R. Kurtz. "Optical Enhancement of the Open-Circuit Voltage in High Quality GaAs Solar Cells". In: *Journal of Applied Physics* 113.12 (2013), p. 123109. DOI: 10.1063/1.4798267 *Cited on page 73.*

[79] G. Bauhuis, P. Mulder, Y.-Y. Hu, and J. Schermer. "Deep Junction III–V Solar Cells with Enhanced Performance". In: *physica status solidi (a)* 213.8 (2016), pp. 2216–2222. DOI: 10.1002/pssa.201532903 *Cited on page 73.*

[80] C. t Sah, R. N. Noyce, and W. Shockley. "Carrier Generation and Recombination in P-N Junctions and P-N Junction Characteristics". In: *Proceedings of the IRE* 45.9 (1957), pp. 1228–1243. DOI: 10.1109/JRPROC.1957.278528 *Cited on pages 73, 113.*

[81] S.-T. Hwang, S. Kim, H. Cheun, H. Lee, B. Lee, T. Hwang, S. Lee, W. Yoon, H.-M. Lee, and B. Park. "Bandgap Grading and Al0.3Ga0.7As Heterojunction Emitter for Highly Efficient GaAs-Based Solar Cells". In: *Solar Energy Materials and Solar Cells* 155 (2016), pp. 264–272. DOI: 10.1016/j.solmat.2016.06.009 *Cited on page 74.*

[82] N. Vandamme, H. L. Chen, A. Gaucher, B. Behaghel, A. Lemaître, A. Cattoni, C. Dupuis, N. Bardou, J. F. Guillemoles, and S. Collin. "Ultrathin GaAs Solar Cells With a Silver Back Mirror". In: *IEEE Journal of Photovoltaics* 5.2 (2015), pp. 565–570. DOI: 10.1109/JPHOTOV.2014.2371236 *Cited on pages 74, 75, 96, 222.*

[83] E. Yablonovitch. "Statistical Ray Optics". In: *JOSA* 72.7 (1982), pp. 899–907. DOI: 10.1364/JOSA.72.000899 *Cited on page 74.*

[84] K. Nakayama, K. Tanabe, and H. A. Atwater. "Plasmonic Nanoparticle Enhanced Light Absorption in GaAs Solar Cells". In: *Applied Physics Letters* 93.12 (2008), p. 121904. DOI: 10.1063/1.2988288 *Cited on pages 75, 222.*

[85] W. Liu, X. Wang, Y. Li, Z. Geng, F. Yang, and J. Li. "Surface Plasmon Enhanced GaAs Thin Film Solar Cells". In: *Solar Energy Materials and Solar Cells* 95.2 (2011), pp. 693–698. DOI: 10.1016/j.solmat.2010.10.004 *Cited on pages 75, 222.*

[86] W. Yang, J. Becker, S. Liu, Y.-S. Kuo, J.-J. Li, B. Landini, K. Campman, and Y.-H. Zhang. "Ultra-Thin GaAs Single-Junction Solar Cells Integrated with a Reflective Back Scattering Layer". In: *Journal of Applied Physics* 115.20 (2014), p. 203105. DOI: 10.1063/1.4878156 *Cited on pages 74, 75, 222.*

[87] S.-M. Lee, A. Kwong, D. Jung, J. Faucher, R. Biswas, L. Shen, D. Kang, M. L. Lee, and J. Yoon. "High Performance Ultrathin GaAs Solar Cells Enabled with Heterogeneously Integrated Dielectric Periodic Nanostructures". In: *ACS Nano* 9.10 (2015), pp. 10356–10365. DOI: 10.1021/acsnano.5b05585 *Cited on pages 75, 76, 222.*

[88] I. Åberg, G. Vescovi, D. Asoli, U. Naseem, J. P. Gilboy, C. Sundvall, A. Dahlgren, K. E. Svensson, N. Anttu, M. T. Björk, and L. Samuelson. "A GaAs Nanowire Array Solar Cell With 15.3% Efficiency at 1 Sun". In: *IEEE Journal of Photovoltaics* 6.1 (2016), pp. 185–190. DOI: 10.1109/JPHOTOV.2015.2484967 *Cited on pages 75, 196, 199, 222.*

[89] S. Liu, W. Yang, J. Becker, Y. S. Kuo, and Y. H. Zhang. "Non-Lambertian Reflective Back Scattering and Its Impact on Device Performance of Ultrathin GaAs Single-Junction Solar Cells". In: *IEEE Journal of Photovoltaics* 5.3 (2015), pp. 832–839. DOI: 10.1109/JPHOTOV.2015.2400332 *Cited on page 74.*

[90] H. A. Atwater and A. Polman. "Plasmonics for Improved Photovoltaic Devices". In: *Nature Materials* 9.3 (2010), pp. 205–213. DOI: 10.1038/nmat2629 *Cited on page 75.*

[91] V. E. Ferry, M. A. Verschuuren, H. B. T. Li, R. E. I. Schropp, H. A. Atwater, and A. Polman. "Improved Red-Response in Thin Film a-Si:H Solar Cells with Soft-Imprinted Plasmonic Back Reflectors". In: *Applied Physics Letters* 95.18 (2009), p. 183503. DOI: 10.1063/1.3256187 *Cited on page 75.*

[92] M. van Lare, F. Lenzmann, M. A. Verschuuren, and A. Polman. "Mode Coupling by Plasmonic Surface Scatterers in Thin-Film Silicon Solar Cells". In: *Applied Physics Letters* 101.22 (2012), p. 221110. DOI: 10.1063/1.4767997 *Cited on page 75.*

[93] I. Massiot, C. Colin, N. Péré-Laperne, P. R. i Cabarrocas, C. Sauvan, P. Lalanne, J.-L. Pelouard, and S. Collin. "Nanopatterned Front Contact for Broadband Absorption in Ultra-Thin Amorphous Silicon Solar Cells". In: *Applied Physics Letters* 101.16 (2012), p. 163901. DOI: 10.1063/1.4758468 *Cited on page 75.*

[94] Z. Yu, A. Raman, and S. Fan. "Nanophotonic Light-Trapping Theory for Solar Cells". In: *Applied Physics A* 105.2 (2011), pp. 329–339. DOI: 10.1007/s00339-011-6617-4 *Cited on page 76.*

[95] S. Collin, J. Goffard, A. Cattoni, C. Colin, C. Sauvan, P. Lalanne, and J.-F. Guillemoles. "Multi-Resonant Light Trapping: New Paradigm, New Limits". In: *2015 IEEE 42nd Photovoltaic Specialist Conference (PVSC)*. New Orleans, LA: IEEE, 2015, pp. 1–3. DOI: 10.1109/PVSC.2015.7356159 *Cited on page 76.*

[96] M. L. Brongersma, Y. Cui, and S. Fan. "Light Management for Photovoltaics Using High-Index Nanostructures". In: *Nature Materials* 13.5 (2014), pp. 451–460. DOI: 10.1038/nmat3921 *Cited on page 76.*

[97] P. Yu, C.-H. Chang, C.-H. Chiu, C.-S. Yang, J.-C. Yu, H.-C. Kuo, S.-H. Hsu, and Y.-C. Chang. "Efficiency Enhancement of GaAs Photovoltaics Employing Antireflective Indium Tin Oxide Nanocolumns". In: *Advanced Materials* 21.16 (2009), pp. 1618–1621. DOI: 10.1002/adma.200802563 *Cited on page 76.*

[98] H.-C. Chen, C.-C. Lin, H.-V. Han, K.-J. Chen, Y.-L. Tsai, Y.-A. Chang, M.-H. Shih, H.-C. Kuo, and P. Yu. "Enhancement of Power Conversion Efficiency in GaAs Solar Cells with Dual-Layer Quantum Dots Using Flexible PDMS Film". In: *Solar Energy Materials and Solar Cells* 104 (2012), pp. 92–96. DOI: 10.1016/j.solmat.2012.05.003 *Cited on page 76.*

[99] J. Grandidier, D. M. Callahan, J. N. Munday, and H. A. Atwater. "Gallium Arsenide Solar Cell Absorption Enhancement Using Whispering Gallery Modes of Dielectric Nanospheres". In: *IEEE Journal of Photovoltaics* 2.2 (2012), pp. 123–128. DOI: 10.1109/JPHOTOV.2011.2180512 *Cited on page 76.*

[100] J. W. Leem, J. Su Yu, D.-H. Jun, J. Heo, and W.-K. Park. "Efficiency Improvement of III–V GaAs Solar Cells Using Biomimetic TiO2 Subwavelength Structures with Wide-Angle and Broadband Antireflection Properties". In: *Solar Energy Materials and Solar Cells* 127 (2014), pp. 43–49. DOI: 10.1016/j.solmat.2014.03.041 *Cited on page 76.*

[101] D. Liang, Y. Kang, Y. Huo, Y. Chen, Y. Cui, and J. S. Harris. "High-Efficiency Nanostructured Window GaAs Solar Cells". In: *Nano Letters* 13.10 (2013), pp. 4850–4856. DOI: 10.1021/nl402680g *Cited on page 76.*

[102] C. van Lare, G. Yin, A. Polman, and M. Schmid. "Light Coupling and Trapping in Ultrathin Cu(In,Ga)Se2 Solar Cells Using Dielectric Scattering Patterns". In: *ACS Nano* 9.10 (2015), pp. 9603–9613. DOI: 10.1021/acsnano.5b04091 *Cited on page 76.*

[103] U. W. Paetzold, E. Moulin, D. Michaelis, W. Böttler, C. Wächter, V. Hagemann, M. Meier, R. Carius, and U. Rau. "Plasmonic Reflection Grating Back Contacts for Microcrystalline Silicon Solar Cells". In: *Applied Physics Letters* 99.18 (2011), p. 181105. DOI: 10.1063/1.3657513 *Cited on page 76.*

[104] U. W. Paetzold, S. Lehnen, K. Bittkau, U. Rau, and R. Carius. "Nanoscale Observation of Waveguide Modes Enhancing the Efficiency of Solar Cells". In: *Nano Letters* 14.11 (2014), pp. 6599–6605. DOI: 10.1021/nl503249n *Cited on page 76.*

[105] B. Gai, Y. Sun, H. Lim, H. Chen, J. Faucher, M. L. Lee, and J. Yoon. "Multilayer-Grown Ultrathin Nanostructured GaAs Solar Cells as a Cost-Competitive Materials Platform for III-V Photovoltaics". In: *ACS nano* 11.1 (2017), pp. 992–999. DOI: 10.1021/acsnano.6b07605 *Cited on page 76.*

[106] L. Gao, F. Lemarchand, and M. Lequime. "Exploitation of Multiple Incidences Spectrometric Measurements for Thin Film Reverse Engineering". In: *Optics Express* 20.14 (2012), pp. 15734–15751 *Cited on page 79.*

[107] E. D. Palik. *Handbook of Optical Constants of Solids*. 1 edition. San Diego: Academic Press, 1997 *Cited on page 79.*

[108] M. Schubert, J. A. Woollam, G. Leibiger, B. Rheinländer, I. Pietzonka, T. Saß, and V. Gottschalch. "Isotropic Dielectric Functions of Highly Disordered AlxGa1-xInP Lattice Matched to GaAs". In: *Journal of Applied Physics* 86 (1999) *Cited on pages 79, 90.*

[109] Y. Jiang, S. Pillai, and M. A. Green. "Realistic Silver Optical Constants for Plasmonics". In: *Scientific Reports* 6 (2016), p. 30605. DOI: 10.1038/srep30605 *Cited on pages 79, 80.*

[110] A. D. Yaghjian. "Internal Energy, Q-Energy, Poynting's Theorem, and the Stress Dyadic in Dispersive Material". In: *IEEE Transactions on Antennas and Propagation* 55.6 (2007), pp. 1495–1505. DOI: 10.1109/TAP.2007.897350 *Cited on page 89.*

[111] M. Burgelman, P. Nollet, and S. Degrave. "Modelling Polycrystalline Semiconductor Solar Cells". In: *Thin Solid Films* 361-362 (2000), pp. 527–532. DOI: 10.1016/S0040-6090(99)00825-1 *Cited on page 90.*

[112] M. Burgelman, K. Decock, S. Khelifi, and A. Abass. "Advanced Electrical Simulation of Thin Film Solar Cells". In: *Thin Solid Films* 535 (2013), pp. 296–301. DOI: 10.1016/j.tsf.2012.10.032 *Cited on page 90.*

[113] M. Levinshtein, S. Rumyantsev, and M. Shur. *Handbook Series on Semiconductor Parameters: Si, Ge, C (Diamond), GaAs, GaP, GaSb, InAs, InP, InSb*. World Scientific, 1997 *Cited on page 90.*

[114] M. Levinshtein, S. Rumyantsev, and M. Shur. *Handbook Series on Semiconductor Parameters: Ternary and Quaternary III-V Compounds*. World Scientific, 1999 *Cited on page 90.*

[115] A. S. Gudovskikh, N. A. Kaluzhniy, V. M. Lantratov, S. A. Mintairov, M. Z. Shvarts, and V. M. Andreev. "Numerical Modelling of GaInP Solar Cells with AlInP and AlGaAs Windows". In: *Thin Solid Films*. Proceedings on Advanced Materials and Concepts for Photovoltaics EMRS 2007 Conference, Strasbourg, France 516.20 (2008), pp. 6739–6743. DOI: 10.1016/j.tsf.2007.12.016 *Cited on page 90.*

[116] A. W. Walker, O. Höhn, D. N. Micha, B. Bläsi, A. W. Bett, and F. Dimroth. "Impact of Photon Recycling on GaAs Solar Cell Designs". In: *IEEE Journal of Photovoltaics* 5.6 (2015), pp. 1636–1645. DOI: 10.1109/JPHOTOV.2015.2479463 *Cited on pages 90, 91.*

[117] M. Sotoodeh, A. H. Khalid, and A. A. Rezazadeh. "Empirical Low-Field Mobility Model for III-V Compounds Applicable in Device Simulation Codes". In: *Journal of Applied Physics* 87.6 (2000), pp. 2890–2900. DOI: 10.1063/1.372274 *Cited on pages 90, 124–126.*

[118] M. P. Lumb, M. A. Steiner, J. F. Geisz, and R. J. Walters. "Incorporating Photon Recycling into the Analytical Drift-Diffusion Model of High Efficiency Solar Cells". In: *Journal of Applied Physics* 116.19 (2014), p. 194504. DOI: 10.1063/1.4902320 *Cited on page 91.*

[119] Y. Mori and N. Watanabe. "A New Etching Solution System H3PO4-H2O2-H2O for GaAs and Its Kinetics". In: *Journal of The Electrochemical Society* 125.9 (1978), pp. 1510–1514. DOI: 10.1149/1.2131705 *Cited on page 96.*

[120] G. C. DeSalvo, W. F. Tseng, and J. Comas. "Etch Rates and Selectivities of Citric Acid/Hydrogen Peroxide on GaAs , Al0.3Ga0.7As , In0.2Ga0.8As , In0.53Ga0.47As , In0.52Al0.48As , and InP". In: *Journal of The Electrochemical Society* 139.3 (1992), pp. 831–835. DOI: 10.1149/1.2069311 *Cited on page 96.*

[121] T. Kampen, A. Schüller, D. R. T. Zahn, B. Biel, J. Ortega, R. Pérez, and F. Flores. "Schottky Contacts on Passivated GaAs(100) Surfaces: Barrier Height and Reactivity". In: *Applied Surface Science*. The Ninth International Conference on the Formation of Semiconductor Interfaces, 234.1 (2004), pp. 341–348. DOI: 10.1016/j.apsusc.2004.05.257 *Cited on page 96.*

[122] A. Cattoni, E. Cambril, D. Decanini, G. Faini, and A. M. Haghiri-Gosnet. "Soft UV-NIL at 20 Nm Scale Using Flexible Bi-Layer Stamp Casted on HSQ Master Mold". In: *Microelectronic Engineering*. The 35th International Conference on Micro- and Nano-Engineering (MNE) 87.5–8 (2010), pp. 1015–1018. DOI: 10.1016/j.mee.2009.11.106 *Cited on page 97.*

[123] T. Bottein, O. Dalstein, M. Putero, A. Cattoni, M. Faustini, M. Abbarchi, and D. Grosso. "Environment-Controlled Sol-Gel Soft-NIL Processing for Optimized Titania, Alumina, Silica and Yttria-Zirconia Imprinting at Sub-Micron Dimensions". In: *Nanoscale* 10.3 (2018), pp. 1420–1431. DOI: 10.1039/c7nr07491c *Cited on page 98.*

[124] O. Breitenstein, P. P. Altermatt, K. Ramspeck, and A. Schenk. "The Origin of Ideality Factors N>2 of Shunts and Surfaces in the Dark I-V Curves of Si Solar Cells". In: *2006 European Photovoltaic Solar Energy Conference*. 2006 *Cited on page 108.*

[125] O. Breitenstein, J. Bauer, P. P. Altermatt, and K. Ramspeck. "Influence of Defects on Solar Cell Characteristics". In: *Solid State Phenomena* 156-158 (2010), pp. 1–10. DOI: 10.4028/www.scientific.net/SSP.156-158.1 *Cited on page 108.*

[126] O. Breitenstein, J. Bauer, A. Lotnyk, and J. .-.-M. Wagner. "Defect Induced Non-Ideal Dark Characteristics of Solar Cells". In: *Superlattices and Microstructures*. Proceedings of the 9th International Workshop on Beam Injection Assessment of Microstructures in Semiconductors (BIAMS 2008)Toledo (Spain), 29 June–3 July 2008 45.4–5 (2009), pp. 182–189. DOI: 10.1016/j.spmi.2008.10.025 *Cited on page 108.*

[127] A. Delamarre, L. Lombez, and J.-F. Guillemoles. "Characterization of Solar Cells Using Electroluminescence and Photoluminescence Hyperspectral Images". In: *Journal of Photonics for Energy* 2.1 (2012), pp. 027004–1. DOI: 10.1117/1.JPE.2.027004 *Cited on page 111.*

[128] A. W. Walker, S. Heckelmann, C. Karcher, O. Höhn, C. Went, M. Niemeyer, A. W. Bett, and D. Lackner. "Nonradiative Lifetime Extraction Using Power-Dependent Relative Photoluminescence of III-V Semiconductor Double-Heterostructures". In: *Journal of Applied Physics* 119.15 (2016), p. 155702. DOI: 10.1063/1.4945772 *Cited on page 111.*

[129] S. M. Fu, Y.-C. Lai, C. W. Tseng, S. L. Yan, Y. K. Zhong, C.-H. Shen, J.-M. Shieh, Y.-R. Li, H.-C. Cheng, G.-c. Chi, P. Yu, and A. Lin. "Approaching Conversion Limit with All-Dielectric Solar Cell Reflectors". In: *Optics Express* 23.3 (2015), A106–A117. DOI: 10.1364/OE.23.00A106 *Cited on page 113.*

[130] C. Barugkin, F. J. Beck, and K. R. Catchpole. "Diffuse Reflectors for Improving Light Management in Solar Cells: A Review and Outlook". In: *Journal of Optics* 19.1 (2017), p. 014001. DOI: 10.1088/2040-8978/19/1/014001 *Cited on page 113.*

[131] M. Wolf, G. T. Noel, and R. J. Stirn. "Investigation of the Double Exponential in the Current-Voltage Characteristics of Silicon Solar Cells". In: *IEEE Transactions on Electron Devices* 24.4 (1977), pp. 419–428. DOI: 10.1109/T-ED.1977.18750 *Cited on page 113.*

[132] M. Ochoa, C. Algora, P. Espinet-González, and I. García. "3-D Modeling of Perimeter Recombination in GaAs Diodes and Its Influence on Concentrator Solar Cells". In: *Solar Energy Materials and Solar Cells* 120 (2014), pp. 48–58. DOI: 10.1016/j.solmat.2013.08.009 *Cited on page 113.*

[133] M. T. Sheldon, C. N. Eisler, and H. A. Atwater. "GaAs Passivation with Trioctylphosphine Sulfide for Enhanced Solar Cell Efficiency and Durability". In: *Advanced Energy Materials* 2.3 (2012), pp. 339–344. DOI: 10.1002/aenm.201100666 *Cited on page 113.*

[134] P. Espinet-González, I. Rey-Stolle, M. Ochoa, C. Algora, I. García, and E. Barrigón. "Analysis of Perimeter Recombination in the Subcells of GaInP/GaAs/Ge Triple-Junction Solar Cells". In: *Progress in Photovoltaics: Research and Applications* 23.7 (2015), pp. 874–882. DOI: 10.1002/pip.2501 *Cited on page 113.*

[135] S. C. Jain, J. M. McGregor, and D. J. Roulston. "Band-gap Narrowing in Novel III-V Semiconductors". In: *Journal of Applied Physics* 68.7 (1990), pp. 3747–3749. DOI: 10.1063/1.346291 *Cited on pages 114, 120, 126, 135, 141.*

References for Chapter 5: Doping measurement by cathodoluminescence

[22] S. M. Sze and K. K. Ng. *Physics of Semiconductor Devices*. 3 edition. Hoboken, N.J: Wiley-Interscience, 2006 *Cited on pages 23, 30, 31, 123, 206.*

[35] J. S. Blakemore. "Semiconducting and Other Major Properties of Gallium Arsenide". In: *Journal of Applied Physics* 53.10 (1982), R123–R181. DOI: 10.1063/1.331665 *Cited on pages 35, 36, 132–134, 136, 153, 157.*

[36] M. D. Sturge. "Optical Absorption of Gallium Arsenide between 0.6 and 2.75 eV". In: *Physical Review* 127.3 (1962), pp. 768–773. DOI: 10.1103/PhysRev.127.768 *Cited on pages 42, 54, 59, 79, 80, 139.*

[46] P. Würfel. "The Chemical Potential of Radiation". In: *Journal of Physics C: Solid State Physics* 15.18 (1982), p. 3967. DOI: 10.1088/0022-3719/15/18/012 *Cited on pages 47, 49, 120.*

[54] H. C. Casey, D. D. Sell, and K. W. Wecht. "Concentration Dependence of the Absorption Coefficient for N- and P-type GaAs between 1.3 and 1.6 eV". In: *Journal of Applied Physics* 46.1 (1975), pp. 250–257. DOI: 10.1063/1.321330 *Cited on pages 54, 135.*

[117] M. Sotoodeh, A. H. Khalid, and A. A. Rezazadeh. "Empirical Low-Field Mobility Model for III-V Compounds Applicable in Device Simulation Codes". In: *Journal of Applied Physics* 87.6 (2000), pp. 2890–2900. DOI: 10.1063/1.372274 *Cited on pages 90, 124–126.*

[135] S. C. Jain, J. M. McGregor, and D. J. Roulston. "Band-gap Narrowing in Novel III-V Semiconductors". In: *Journal of Applied Physics* 68.7 (1990), pp. 3747–3749. DOI: 10.1063/1.346291 *Cited on pages 114, 120, 126, 135, 141.*

[136] K. Storm, F. Halvardsson, M. Heurlin, D. Lindgren, A. Gustafsson, P. M. Wu, B. Monemar, and L. Samuelson. "Spatially Resolved Hall Effect Measurement in a Single Semiconductor Nanowire". In: *Nature Nanotechnology* 7.11 (2012), pp. 718–722. DOI: 10.1038/nnano.2012.190 *Cited on pages 118, 120.*

[137] O. Hultin, G. Otnes, M. T. Borgström, M. Björk, L. Samuelson, and K. Storm. "Comparing Hall Effect and Field Effect Measurements on the Same Single Nanowire". In: *Nano Letters* 16.1 (2015), pp. 205–211. DOI: 10.1021/acs.nanolett.5b03496 *Cited on pages 118, 119.*

[138] Y. Cui, X. Duan, J. Hu, and C. M. Lieber. "Doping and Electrical Transport in Silicon Nanowires". In: *The Journal of Physical Chemistry B* 104.22 (2000), pp. 5213–5216. DOI: 10.1021/jp0009305 *Cited on page 118.*

[139] Y. Cui, Z. Zhong, D. Wang, W. U. Wang, and C. M. Lieber. "High Performance Silicon Nanowire Field Effect Transistors". In: *Nano Letters* 3.2 (2003), pp. 149–152. DOI: 10.1021/nl0258751 *Cited on page 118.*

[140] S. A. Dayeh, D. P. R. Aplin, X. Zhou, P. K. L. Yu, E. T. Yu, and D. Wang. "High Electron Mobility InAs Nanowire Field-Effect Transistors". In: *Small* 3.2 (2006), pp. 326–332. DOI: 10.1002/smll.200600379 *Cited on page 119.*

[141] O. Wunnicke. "Gate Capacitance of Back-Gated Nanowire Field-Effect Transistors". In: *Applied Physics Letters* 89 (2006), p. 083102. DOI: 10.1063/1.2337853 *Cited on page 119.*

[142] D. R. Khanal and J. Wu. "Gate Coupling and Charge Distribution in Nanowire Field Effect Transistors". In: *Nano Letters* 7.9 (2007), pp. 2778–2783. DOI: 10.1021/nl0713301 *Cited on page 119.*

[143] C. Blömers, T. Grap, M. I. Lepsa, J. Moers, S. Trellenkamp, D. Grützmacher, H. Lüth, and T. Schäpers. "Hall Effect Measurements on InAs Nanowires". In: *Applied Physics Letters* 101.15 (2012), p. 152106. DOI: 10.1063/1.4759124 *Cited on page 119.*

[144] K. Jeganathan, R. K. Debnath, R. Meijers, T. Stoica, R. Calarco, D. Grützmacher, and H. Lüth. "Raman Scattering of Phonon-Plasmon Coupled Modes in Self-Assembled GaN Nanowires". In: *Journal of Applied Physics* 105.12 (2009), p. 123707. DOI: 10.1063/1.3148862 *Cited on page 120.*

[145] M. S. Mohajerani, S. Khachadorian, T. Schimpke, C. Nenstiel, J. Hartmann, J. Ledig, A. Avramescu, M. Strassburg, A. Hoffmann, and A. Waag. "Evaluation of Local Free Carrier Concentrations in Individual Heavily-Doped GaN:Si Micro-Rods by Micro-Raman Spectroscopy". In: *Applied Physics Letters* 108.9 (2016), p. 091112. DOI: 10.1063/1.4943079 *Cited on page 120.*

[146] B. Ketterer, E. Mikheev, E. Uccelli, and A. F. i Morral. "Compensation Mechanism in Silicon-Doped Gallium Arsenide Nanowires". In: *Applied Physics Letters* 97.22 (2010), p. 223103. DOI: 10.1063/1.3517254 *Cited on pages 120, 175.*

[147] E. Dimakis, M. Ramsteiner, A. Tahraoui, H. Riechert, and L. Geelhaar. "Shell-Doping of GaAs Nanowires with Si for n-Type Conductivity". In: *Nano Research* 5.11 (2012), pp. 796–804. DOI: 10.1007/s12274-012-0263-9 *Cited on pages 120, 175.*

[148] J. L. Boland, A. Casadei, G. Tütüncüoglu, F. Matteini, C. L. Davies, F. Jabeen, H. J. Joyce, L. M. Herz, A. Fontcuberta i Morral, and M. B. Johnston. "Increased Photoconductivity Lifetime in GaAs Nanowires by Controlled N-Type and p-Type Doping". In: *ACS Nano* 10.4 (2016), pp. 4219–4227. DOI: 10.1021/acsnano.5b07579 *Cited on page 120.*

[149] H. J. Joyce, J. Wong-Leung, C.-K. Yong, C. J. Docherty, S. Paiman, Q. Gao, H. H. Tan, C. Jagadish, J. Lloyd-Hughes, L. M. Herz, and M. B. Johnston. "Ultralow Surface Recombination Velocity in InP Nanowires Probed by Terahertz Spectroscopy". In: *Nano Letters* 12.10 (2012), pp. 5325–5330. DOI: 10.1021/nl3026828 *Cited on page 120.*

[150] H. J. Joyce, J. L. Boland, C. L. Davies, S. A. Baig, and M. B. Johnston. "A Review of the Electrical Properties of Semiconductor Nanowires: Insights Gained from Terahertz Conductivity Spectroscopy". In: *Semiconductor Science and Technology* 31.10 (2016), p. 103003. DOI: 10.1088/0268-1242/31/10/103003 *Cited on page 120.*

[151] S. Arab, M. Yao, C. Zhou, P. D. Dapkus, and S. B. Cronin. "Doping Concentration Dependence of the Photoluminescence Spectra of N-Type GaAs Nanowires". In: *Applied Physics Letters* 108.18 (2016), p. 182106. DOI: 10.1063/1.4947504 *Cited on page 120.*

[152] D. Lindgren, O. Hultin, M. Heurlin, K. Storm, M. T. Borgström, L. Samuelson, and Anders Gustafsson. "Study of Carrier Concentration in Single InP Nanowires by Luminescence and Hall Measurements". In: *Nanotechnology* 26.4 (2015), p. 045705. DOI: 10.1088/0957-4484/26/4/045705 *Cited on page 120.*

[153] H.-L. Chen, C. Himwas, A. Scaccabarozzi, P. Rale, F. Oehler, A. Lemaître, L. Lombez, J.-F. Guillemoles, M. Tchernycheva, J.-C. Harmand, A. Cattoni, and S. Collin. "Determination of N-Type Doping Level in Single GaAs Nanowires by Cathodoluminescence". In: *Nano Letters* 17.11 (2017), pp. 6667–6675. DOI: 10.1021/acs.nanolett.7b02620 *Cited on pages 120, 186.*

[154] V. Hortelano, O. Martínez, R. Cuscó, L. Artús, and J. Jiménez. "Cathodoluminescence Study of Mg Activation in Non-Polar and Semi-Polar Faces of Undoped/Mg-Doped GaN Core–Shell Nanorods". In: *Nanotechnology* 27.9 (2016), p. 095706. DOI: 10.1088/0957-4484/27/9/095706 *Cited on page 120.*

[155] J. Wallentin and M. T. Borgström. "Doping of Semiconductor Nanowires". In: *Journal of Materials Research* 26.17 (2011), pp. 2142–2156. DOI: 10.1557/jmr.2011.214 *Cited on page 120.*

[156] A. C. E. Chia, J. P. Boulanger, and R. R. LaPierre. "Unlocking Doping and Compositional Profiles of Nanowire Ensembles Using SIMS". In: *Nanotechnology* 24.4 (2013), p. 045701. DOI: 10.1088/0957-4484/24/4/045701 *Cited on page 120.*

[157] A. C. E. Chia, N. Dhindsa, J. P. Boulanger, B. A. Wood, S. S. Saini, and R. R. LaPierre. "Nanowire Dopant Measurement Using Secondary Ion Mass Spectrometry". In: *Journal of Applied Physics* 118.11 (2015), p. 114306. DOI: 10.1063/1.4931148 *Cited on pages 120, 194.*

[158] M. H. T. Dastjerdi, E. M. Fiordaliso, E. D. Leshchenko, A. Akhtari-Zavareh, T. Kasama, M. Aagesen, V. G. Dubrovskii, and R. R. LaPierre. "Three-Fold Symmetric Doping Mechanism in GaAs Nanowires". In: *Nano Letters* 17.10 (2017), pp. 5875–5882. DOI: 10.1021/acs.nanolett.7b00794 *Cited on pages 121, 165, 174.*

[159] L. J. van der Pauw. "A Method of Measuring Specific Resistivity and Hall Effect of Discs of Arbitrary Shape". In: *Philips Research Reports* 13 (1958), pp. 1–9 *Cited on page 122.*

[160] W. E. Spicer, I. Lindau, P. Skeath, C. Y. Su, and P. Chye. "Unified Mechanism for Schottky-Barrier Formation and III-V Oxide Interface States". In: *Physical Review Letters* 44.6 (1980), pp. 420–423. DOI: 10.1103/PhysRevLett.44.420 *Cited on page 123.*

[161] D. C. Look, C. E. Stutz, and K. R. Evans. "Surface and Interface Free-Carrier Depletion in GaAs Molecular Beam Epitaxial Layers: Demonstration of High Interface Charge". In: *Applied Physics Letters* 56.7 (1990), pp. 668–670. DOI: 10.1063/1.102731 *Cited on page 123.*

[162] A. Y. Cho and J. R. Arthur. "Molecular Beam Epitaxy". In: *Progress in Solid State Chemistry* 10 (1975), pp. 157–191. DOI: 10.1016/0079-6786(75)90005-9 *Cited on page 123.*

[163] D. A. Cusano. "Identification of Laser Transition in Electron-Beam-Pumped GaAs". In: *Applied Physics Letters* 7.6 (1965), pp. 151–152. DOI: 10.1063/1.1754351 *Cited on page 127.*

[164] D. Olego and M. Cardona. "Photoluminescence in Heavily Doped GaAs. I. Temperature and Hole-Concentration Dependence". In: *Physical Review B* 22.2 (1980), pp. 886–893. DOI: 10.1103/PhysRevB.22.886 *Cited on pages 127, 135.*

[165] G. Borghs, K. Bhattacharyya, K. Deneffe, P. Van Mieghem, and R. Mertens. "Bandgap Narrowing in Highly Doped N- and P-type GaAs Studied by Photoluminescence Spectroscopy". In: *Journal of Applied Physics* 66.9 (1989), pp. 4381–4386. DOI: 10.1063/1.343958 *Cited on pages 127, 135, 138.*

[166] S.-I. Kim, M.-S. Kim, S.-K. Min, and C. Lee. "Experimental and Theoretical Photoluminescence Study of Heavily Carbon Doped GaAs Grown by Low-pressure Metalorganic Chemical Vapor Deposition". In: *Journal of Applied Physics* 74.10 (1993), pp. 6128–6132. DOI: 10.1063/1.355177 *Cited on page 127.*

[167] G. D. Mahan. "Excitons in Degenerate Semiconductors". In: *Physical Review* 153.3 (1967), pp. 882–889. DOI: 10.1103/PhysRev.153.882 *Cited on page 128.*

[168] E. Burstein. "Anomalous Optical Absorption Limit in InSb". In: *Physical Review* 93.3 (1954), pp. 632–633. DOI: 10.1103/PhysRev.93.632 *Cited on page 129.*

[169] T. S. Moss. "The Interpretation of the Properties of Indium Antimonide". In: *Proceedings of the Physical Society. Section B* 67.10 (1954), p. 775. DOI: 10.1088/0370-1301/67/10/306 *Cited on page 129.*

[170] L. Pavesi, N. H. Ky, J. D. Ganière, F. K. Reinhart, N. Baba-Ali, I. Harrison, B. Tuck, and M. Henini. "Role of Point Defects in the Silicon Diffusion in GaAs and Al0.3Ga0.7As and in the Related Superlattice Disordering". In: *Journal of Applied Physics* 71.5 (1992), pp. 2225–2237. DOI: 10.1063/1.351120 *Cited on page 129.*

[171] N. H. Ky and F. K. Reinhart. "Amphoteric Native Defect Reactions in Si-Doped GaAs". In: *Journal of Applied Physics* 83.2 (1998), pp. 718–724. DOI: 10.1063/1.366743 *Cited on page 129.*

[172] S. Y. Chiang and G. L. Pearson. "Photoluminescence Studies of Vacancies and Vacancy-Impurity Complexes in Annealed GaAs". In: *Journal of Luminescence* 10.5 (1975), pp. 313–322. DOI: 10.1016/0022-2313(75)90054-X *Cited on page 129.*

[173] H. Kressel, J. U. Dunse, H. Nelson, and F. Z. Hawrylo. "Luminescence in Silicon-Doped GaAs Grown by Liquid-Phase Epitaxy". In: *Journal of Applied Physics* 39.4 (1968), pp. 2006–2011. DOI: 10.1063/1.1656480 *Cited on page 129.*

[174] H. Kressel and H. Nelson. "Electrical and Optical Properties of N-Type Si-Compensated GaAs Prepared by Liquid-Phase Epitaxy". In: *Journal of Applied Physics* 40.9 (1969), pp. 3720–3725. DOI: 10.1063/1.1658261 *Cited on page 129.*

[175] H. C. Casey and R. H. Kaiser. "Analysis of N-Type GaAs with Electron-Beam-Excited Radiative Recombination". In: *Journal of The Electrochemical Society* 114.2 (1967), pp. 149–153. DOI: 10.1149/1.2426527 *Cited on pages 129, 188.*

[176] J. H. Neave, P. J. Dobson, J. J. Harris, P. Dawson, and B. A. Joyce. "Silicon Doping of MBE-Grown GaAs Films". In: *Applied Physics A* 32.4 (1983), pp. 195–200. DOI: 10.1007/BF00820260 *Cited on pages 129, 175.*

[177] D. M. Szmyd, P. Porro, A. Majerfeld, and S. Lagomarsino. "Heavily Doped GaAs:Se. I. Photoluminescence Determination of the Electron Effective Mass". In: *Journal of Applied Physics* 68.5 (1990), pp. 2367–2375. DOI: 10.1063/1.346520 *Cited on page 129.*

[178] N.-Y. Lee, K.-J. Lee, C. Lee, J.-E. Kim, H. Y. Park, D.-H. Kwak, H.-C. Lee, and H. Lim. "Determination of Conduction Band Tail and Fermi Energy of Heavily Si-doped GaAs by Room-temperature Photoluminescence". In: *Journal of Applied Physics* 78.5 (1995), pp. 3367–3370. DOI: 10.1063/1.359963 *Cited on pages 129, 139.*

[179] J. De-Sheng, Y. Makita, K. Ploog, and H. J. Queisser. "Electrical Properties and Photoluminescence of Te-doped GaAs Grown by Molecular Beam Epitaxy". In: *Journal of Applied Physics* 53.2 (1982), pp. 999–1006. DOI: 10.1063/1.330581 *Cited on pages 130, 131, 139.*

[180] K. Mergenthaler, N. Anttu, N. Vainorius, M. Aghaeipour, S. Lehmann, M. T. Borgström, L. Samuelson, and M.-E. Pistol. "Anti-Stokes Photoluminescence Probing k-Conservation and Thermalization of Minority Carriers in Degenerately Doped Semiconductors". In: *Nature Communications* 8.1 (2017), p. 1634. DOI: 10.1038/s41467-017-01817-5 *Cited on page 130.*

[181] E. Kane. "Band Structure of Indium Antimonide". In: *Journal of Physics and Chemistry of Solids* 1 (1957), pp. 249–261. DOI: 10.1016/0022-3697(57)90013-6 *Cited on page 132.*

[182] A. Raymond, J. L. Robert, and C. Bernard. "The Electron Effective Mass in Heavily Doped GaAs". In: *Journal of Physics C: Solid State Physics* 12.12 (1979), p. 2289. DOI: 10.1088/0022-3719/12/12/014 *Cited on page 133.*

[183] P. A. Wolff. "Theory of the Band Structure of Very Degenerate Semiconductors". In: *Physical Review* 126.2 (1962), pp. 405–412. DOI: 10.1103/PhysRev.126.405 *Cited on page 135.*

[184] E. O. Kane. "Band Tails in Semiconductors". In: *Solid-State Electronics* 28.1 (1985), pp. 3–10. DOI: 10.1016/0038-1101(85)90203-5 *Cited on page 135.*

[185] G. D. Mahan. "Energy Gap in Si and Ge: Impurity Dependence". In: *Journal of Applied Physics* 51.5 (1980), pp. 2634–2646. DOI: 10.1063/1.327994 *Cited on page 135.*

[186] S. C. Jain and D. J. Roulston. "A simple expression for band gap narrowing (BGN) in heavily doped Si, Ge, GaAs and Ge_x Si_{1-x} strained layers". In: *Solid State Electronics* 34 (1991), pp. 453–465. DOI: 10.1016/0038-1101(91)90149-S *Cited on page 135.*

[187] H. C. Casey and F. Stern. "Concentration-dependent Absorption and Spontaneous Emission of Heavily Doped GaAs". In: *Journal of Applied Physics* 47.2 (1976), pp. 631–643. DOI: 10.1063/1.322626 *Cited on pages 135, 138, 173.*

[188] S. Tiwari and S. L. Wright. "Material Properties of P-type GaAs at Large Dopings". In: *Applied Physics Letters* 56.6 (1990), pp. 563–565. DOI: 10.1063/1.102745 *Cited on pages 138, 139.*

[189] M. E. Klausmeier-Brown, M. S. Lundstrom, M. R. Melloch, and S. P. Tobin. "Effects of Heavy Impurity Doping on Electron Injection in P+-n GaAs Diodes". In: *Applied Physics Letters* 52.26 (1988), pp. 2255–2257. DOI: 10.1063/1.99529 *Cited on page 139.*

[190] H. S. Bennett. "High Dopant and Carrier Concentration Effects in Gallium Arsenide: Band Structure and Effective Intrinsic Carrier Concentrations". In: *Journal of Applied Physics* 60.8 (1986), pp. 2866–2874. DOI: 10.1063/1.337071 *Cited on page 142.*

References for Chapter 6: Characterization of III-V nanowires

[15] C. F. Klingshirn. *Semiconductor Optics*. 4th ed. Graduate Texts in Physics. Berlin Heidelberg: Springer-Verlag, 2012 *Cited on pages 16, 17, 19, 34, 42, 44, 46, 155.*

[35] J. S. Blakemore. "Semiconducting and Other Major Properties of Gallium Arsenide". In: *Journal of Applied Physics* 53.10 (1982), R123–R181. DOI: 10.1063/1.331665 *Cited on pages 35, 36, 132–134, 136, 153, 157.*

[146] B. Ketterer, E. Mikheev, E. Uccelli, and A. F. i Morral. "Compensation Mechanism in Silicon-Doped Gallium Arsenide Nanowires". In: *Applied Physics Letters* 97.22 (2010), p. 223103. DOI: 10.1063/1.3517254 *Cited on pages 120, 175.*

[147] E. Dimakis, M. Ramsteiner, A. Tahraoui, H. Riechert, and L. Geelhaar. "Shell-Doping of GaAs Nanowires with Si for n-Type Conductivity". In: *Nano Research* 5.11 (2012), pp. 796–804. DOI: 10.1007/s12274-012-0263-9 *Cited on pages 120, 175.*

[153] H.-L. Chen, C. Himwas, A. Scaccabarozzi, P. Rale, F. Oehler, A. Lemaître, L. Lombez, J.-F. Guillemoles, M. Tchernycheva, J.-C. Harmand, A. Cattoni, and S. Collin. "Determination of N-Type Doping Level in Single GaAs Nanowires by Cathodoluminescence". In: *Nano Letters* 17.11 (2017), pp. 6667–6675. DOI: 10.1021/acs.nanolett.7b02620 *Cited on pages 120, 186.*

[158] M. H. T. Dastjerdi, E. M. Fiordaliso, E. D. Leshchenko, A. Akhtari-Zavareh, T. Kasama, M. Aagesen, V. G. Dubrovskii, and R. R. LaPierre. "Three-Fold Symmetric Doping Mechanism in GaAs Nanowires". In: *Nano Letters* 17.10 (2017), pp. 5875–5882. DOI: 10.1021/acs.nanolett.7b00794 *Cited on pages 121, 165, 174.*

[175] H. C. Casey and R. H. Kaiser. "Analysis of N-Type GaAs with Electron-Beam-Excited Radiative Recombination". In: *Journal of The Electrochemical Society* 114.2 (1967), pp. 149–153. DOI: 10.1149/1.2426527 *Cited on pages 129, 188.*

[176] J. H. Neave, P. J. Dobson, J. J. Harris, P. Dawson, and B. A. Joyce. "Silicon Doping of MBE-Grown GaAs Films". In: *Applied Physics A* 32.4 (1983), pp. 195–200. DOI: 10.1007/BF00820260 *Cited on pages 129, 175.*

[187] H. C. Casey and F. Stern. "Concentration-dependent Absorption and Spontaneous Emission of Heavily Doped GaAs". In: *Journal of Applied Physics* 47.2 (1976), pp. 631–643. DOI: 10.1063/1.322626 *Cited on pages 135, 138, 173.*

[191] F. Glas. "Critical Dimensions for the Plastic Relaxation of Strained Axial Heterostructures in Free-Standing Nanowires". In: *Physical Review B* 74 (2006), p. 121302. DOI: 10.1103/PhysRevB.74.121302 *Cited on pages 146, 147.*

[192] M. Yao, S. Cong, S. Arab, N. Huang, M. L. Povinelli, S. B. Cronin, P. D. Dapkus, and C. Zhou. "Tandem Solar Cells Using GaAs Nanowires on Si: Design, Fabrication, and Observation of Voltage Addition". In: *Nano Letters* 15.11 (2015), pp. 7217–7224. DOI: 10.1021/acs.nanolett.5b03890 *Cited on pages 146, 195, 196, 203.*

[193] C.-Z. Ning, L. Dou, and P. Yang. "Bandgap Engineering in Semiconductor Alloy Nanomaterials with Widely Tunable Compositions". In: *Nature Reviews Materials* 2.12 (2017), p. 17070. DOI: 10.1038/natrevmats.2017.70 *Cited on page 147.*

[194] R. S. Wagner and W. C. Ellis. "Vapor-liquid-solid Mechanism of Single Crystal Growth". In: *Applied Physics Letters* 4.5 (1964), pp. 89–90. DOI: 10.1063/1.1753975 *Cited on page 146.*

[195] Y. Xia, P. Yang, Y. Sun, Y. Wu, B. Mayers, B. Gates, Y. Yin, F. Kim, and H. Yan. "One-Dimensional Nanostructures: Synthesis, Characterization, and Applications". In: *Advanced Materials* 15.5 (2003), pp. 353–389. DOI: 10.1002/adma.200390087 *Cited on page 146.*

[196] W. Lu and C. M. Lieber. "Semiconductor Nanowires". In: *Journal of Physics D: Applied Physics* 39.21 (2006), R387. DOI: 10.1088/0022-3727/39/21/R01 *Cited on page 146.*

[197] K. A. Dick. "A Review of Nanowire Growth Promoted by Alloys and Non-Alloying Elements with Emphasis on Au-Assisted III-V Nanowires". In: *Progress in Crystal Growth and Characterization of Materials* 54.3-4 (2008), pp. 138–173. DOI: http://dx.doi.org/10.1016/j.pcrysgrow.2008.09.001 *Cited on page 146.*

[198] A. F. i Morral, C. Colombo, G. Abstreiter, J. Arbiol, and J. R. Morante. "Nucleation Mechanism of Gallium-Assisted Molecular Beam Epitaxy Growth of Gallium Arsenide Nanowires". In: *Applied Physics Letters* 92.6 (2008), p. 063112. DOI: 10.1063/1.2837191 *Cited on page 146.*

[199] F. Jabeen, V. Grillo, S. Rubini, and F. Martelli. "Self-Catalyzed Growth of GaAs Nanowires on Cleaved Si by Molecular Beam Epitaxy". In: *Nanotechnology* 19.27 (2008), p. 275711. DOI: 10.1088/0957-4484/19/27/275711 *Cited on page 146.*

[200] S. Breuer, C. Pfüller, T. Flissikowski, O. Brandt, H. T. Grahn, L. Geelhaar, and H. Riechert. "Suitability of Au- and Self-Assisted GaAs Nanowires for Optoelectronic Applications". In: *Nano Letters* 11.3 (2011), pp. 1276–1279. DOI: 10.1021/nl104316t *Cited on page 148.*

[201] K. Tomioka, Y. Kobayashi, J. Motohisa, S. Hara, and T. Fukui. "Selective-Area Growth of Vertically Aligned GaAs and GaAs/AlGaAs Core-Shell Nanowires on Si(111) Substrate". In: *Nanotechnology* 20.14 (2009), p. 145302. DOI: 10.1088/0957-4484/20/14/145302 *Cited on page 148.*

[202] K. Tomioka, K. Ikejiri, T. Tanaka, J. Motohisa, S. Hara, K. Hiruma, and T. Fukui. "Selective-Area Growth of III-V Nanowires and Their Applications". In: *Journal of Materials Research* 26.17 (2011), pp. 2127–2141. DOI: 10.1557/jmr.2011.103 *Cited on page 148.*

[203] F. Glas, M. R. Ramdani, G. Patriarche, and J.-C. Harmand. "Predictive Modeling of Self-Catalyzed III-V Nanowire Growth". In: *Physical Review B* 88.19 (2013), p. 195304. DOI: 10.1103/PhysRevB.88.195304 *Cited on pages 149, 150.*

[204] F. Glas, J.-C. Harmand, and G. Patriarche. "Why Does Wurtzite Form in Nanowires of III-V Zinc Blende Semiconductors?" In: *Physical Review Letters* 99.14 (2007), p. 146101. DOI: 10.1103/PhysRevLett.99.146101 *Cited on pages 150, 154, 159.*

[205] G. E. Cirlin, V. G. Dubrovskii, Y. B. Samsonenko, A. D. Bouravleuv, K. Durose, Y. Y. Proskuryakov, B. Mendes, L. Bowen, M. A. Kaliteevski, R. A. Abram, and D. Zeze. "Self-Catalyzed, Pure Zincblende GaAs Nanowires Grown on Si(111) by Molecular Beam Epitaxy". In: *Physical Review B* 82.3 (2010), p. 035302. DOI: 10.1103/PhysRevB.82.035302 *Cited on page 150.*

[206] F. Oehler, A. Cattoni, A. Scaccabarozzi, G. Patriarche, F. Glas, and J.-C. Harmand. "Measuring and Modeling the Growth Dynamics of Self-Catalyzed GaP Nanowire Arrays". In: *Nano Letters* 18.2 (2018), pp. 701–708. DOI: 10.1021/acs.nanolett.7b03695 *Cited on pages 150, 151.*

[207] M. R. Ramdani, J. C. Harmand, F. Glas, G. Patriarche, and L. Travers. "Arsenic Pathways in Self-Catalyzed Growth of GaAs Nanowires". In: *Crystal Growth & Design* 13.1 (2013), pp. 91–96. DOI: 10.1021/cg301167g *Cited on page 150.*

[208] S. Assali, I. Zardo, S. Plissard, D. Kriegner, M. A. Verheijen, G. Bauer, A. Meijerink, A. Belabbes, F. Bechstedt, J. E. M. Haverkort, and E. P. A. M. Bakkers. "Direct Band Gap Wurtzite Gallium Phosphide Nanowires". In: *Nano Letters* 13.4 (2013), pp. 1559–1563. DOI: 10.1021/nl304723c *Cited on page 153.*

[209] S. Assali, J. Greil, I. Zardo, A. Belabbes, M. W. A. de Moor, S. Koelling, P. M. Koenraad, F. Bechstedt, E. P. a. M. Bakkers, and J. E. M. Haverkort. "Optical Study of the Band Structure of Wurtzite GaP Nanowires". In: *Journal of Applied Physics* 120.4 (2016), p. 044304. DOI: 10.1063/1.4959147 *Cited on page 153.*

[210] P. Krogstrup, H. I. Jørgensen, E. Johnson, M. H. Madsen, C. B. Sørensen, A. F. i Morral, M. Aagesen, J. Nygård, and F. Glas. "Advances in the Theory of III–V Nanowire Growth Dynamics". In: *Journal of Physics D: Applied Physics* 46.31 (2013), p. 313001. DOI: 10.1088/0022-3727/46/31/313001 *Cited on page 153.*

[211] T. Cheiwchanchamnangij and W. R. L. Lambrecht. "Band Structure Parameters of Wurtzite and Zinc-Blende GaAs under Strain in the GW Approximation". In: *Physical Review B* 84.3 (2011), p. 035203. DOI: 10.1103/PhysRevB.84.035203 *Cited on page 154.*

[212] G. Signorello, E. Lörtscher, P. A. Khomyakov, S. Karg, D. L. Dheeraj, B. Gotsmann, H. Weman, and H. Riel. "Inducing a Direct-to-Pseudodirect Bandgap Transition in Wurtzite GaAs Nanowires with Uniaxial Stress". In: *Nature Communications* 5 (2014), ncomms4655. DOI: 10.1038/ncomms4655 *Cited on page 154.*

[213] M. I. McMahon and R. J. Nelmes. "Observation of a Wurtzite Form of Gallium Arsenide". In: *Physical Review Letters* 95.21 (2005), p. 215505. DOI: 10.1103/PhysRevLett.95.215505 *Cited on page 154.*

[214] I. Zardo, S. Conesa-Boj, F. Peiro, J. R. Morante, J. Arbiol, E. Uccelli, G. Abstreiter, and A. Fontcuberta i Morral. "Raman Spectroscopy of Wurtzite and Zinc-Blende GaAs Nanowires: Polarization Dependence, Selection Rules, and Strain Effects". In: *Physical Review B* 80.24 (2009), p. 245324. DOI: 10.1103/PhysRevB.80.245324 *Cited on page 154.*

[215] K. A. Dick, P. Caroff, J. Bolinsson, M. E. Messing, J. Johansson, K. Deppert, L. R. Wallenberg, and L. Samuelson. "Control of III-V Nanowire Crystal Structure by Growth Parameter Tuning". In: *Semiconductor Science and Technology* 25.2 (2010), p. 024009. DOI: 10.1088/0268-1242/25/2/024009 *Cited on page 154.*

[216] T. Akiyama, K. Sano, K. Nakamura, and T. Ito. "An Empirical Potential Approach to Wurtzite–Zinc-Blende Polytypism in Group III–V Semiconductor Nanowires". In: *Japanese Journal of Applied Physics* 45.3L (2006), p. L275. DOI: 10.1143/JJAP.45.L275 *Cited on page 154.*

[217] V. G. Dubrovskii and N. V. Sibirev. "Growth Thermodynamics of Nanowires and Its Application to Polytypism of Zinc Blende III-V Nanowires". In: *Physical Review B* 77.3 (2008), p. 035414. DOI: 10.1103/PhysRevB.77.035414 *Cited on page 154.*

[218] D. Jacobsson, F. Panciera, J. Tersoff, M. C. Reuter, S. Lehmann, S. Hofmann, K. A. Dick, and F. M. Ross. "Interface Dynamics and Crystal Phase Switching in GaAs Nanowires". In: *Nature* 531.7594 (2016), pp. 317–322. DOI: 10.1038/nature17148 *Cited on pages 154, 159.*

[219] A. Belabbes. "Electronic Bands of III-V Semiconductor Polytypes and Their Alignment". In: *Physical Review B* 86.7 (2012). DOI: 10.1103/PhysRevB.86.075208 *Cited on pages 154–156.*

[220] A. De and C. E. Pryor. "Predicted Band Structures of III-V Semiconductors in the Wurtzite Phase". In: *Physical Review B* 81.15 (2010), p. 155210. DOI: 10.1103/PhysRevB.81.155210 *Cited on pages 155, 156.*

[221] B. Ketterer, M. Heiss, E. Uccelli, J. Arbiol, and A. Fontcuberta i Morral. "Untangling the Electronic Band Structure of Wurtzite GaAs Nanowires by Resonant Raman Spectroscopy". In: *ACS Nano* 5.9 (2011), pp. 7585–7592. DOI: 10.1021/nn202585j *Cited on pages 156, 157.*

[222] T. B. Hoang, A. F. Moses, H. L. Zhou, D. L. Dheeraj, B. O. Fimland, and H. Weman. "Observation of Free Exciton Photoluminescence Emission from Single Wurtzite GaAs Nanowires". In: *Applied Physics Letters* 94.13 (2009), p. 133105. DOI: 10.1063/1.3104853 *Cited on page 156.*

[223] S.-G. Ihn, M.-Y. Ryu, and J.-I. Song. "Optical Properties of Undoped, Be-Doped, and Si-Doped Wurtzite-Rich GaAs Nanowires Grown on Si Substrates by Molecular Beam Epitaxy". In: *Solid State Communications* 150.15 (2010), pp. 729–733. DOI: 10.1016/j.ssc.2010.01.037 *Cited on pages 156, 183.*

[224] F. Martelli, G. Priante, and S. Rubini. "Photoluminescence of GaAs Nanowires at an Energy Larger than the Zincblende Band-Gap: Dependence on Growth Parameters". In: *Semiconductor Science and Technology* 30.5 (2015), p. 055020. DOI: 10.1088/0268-1242/30/5/055020 *Cited on page 156.*

[225] L. Ahtapodov, J. Todorovic, P. Olk, T. Mjåland, P. Slåttnes, D. L. Dheeraj, A. T. J. van Helvoort, B.-O. Fimland, and H. Weman. "A Story Told by a Single Nanowire: Optical Properties of Wurtzite GaAs". In: *Nano Letters* 12.12 (2012), pp. 6090–6095. DOI: 10.1021/nl3025714 *Cited on pages 156, 162, 163.*

[226] M. De Luca, G. Lavenuta, A. Polimeni, S. Rubini, V. Grillo, F. Mura, A. Miriametro, M. Capizzi, and F. Martelli. "Excitonic Recombination and Absorption in InGaAs/GaAs Heterostructure Nanowires". In: *Physical Review B* 87.23 (2013), p. 235304. DOI: 10.1103/PhysRevB.87.235304 *Cited on pages 156, 157.*

[227] Z. Lu, S. Shi, J. Lu, and P. Chen. "Photoluminescence of the Single Wurtzite GaAs Nanowire with Different Powers and Temperatures". In: *Journal of Luminescence*. 18th International Conference on Dynamical Processes in Excited States of Solids 152.Supplement C (2014), pp. 258–261. DOI: 10.1016/j.jlumin.2014.01.066 *Cited on pages 156, 162.*

[228] Y.-J. Lu, C.-Y. Wang, J. Kim, H.-Y. Chen, M.-Y. Lu, Y.-C. Chen, W.-H. Chang, L.-J. Chen, M. I. Stockman, C.-K. Shih, and S. Gwo. "All-Color Plasmonic Nanolasers with Ultralow Thresholds: Autotuning Mechanism for Single-Mode Lasing". In: *Nano Letters* 14.8 (2014), pp. 4381–4388. DOI: 10.1021/nl501273u *Cited on page 156.*

[229] F. Bechstedt and A. Belabbes. "Structure, Energetics, and Electronic States of III–V Compound Polytypes". In: *Journal of Physics: Condensed Matter* 25.27 (2013), p. 273201. DOI: 10.1088/0953-8984/25/27/273201 *Cited on page 157.*

[230] N. Vainorius, S. Lehmann, A. Gustafsson, L. Samuelson, K. A. Dick, and M.-E. Pistol. "Wurtzite GaAs Quantum Wires: One-Dimensional Subband Formation". In: *Nano Letters* 16.4 (2016), pp. 2774–2780. DOI: 10.1021/acs.nanolett.6b00482 *Cited on page 157.*

[231] M. De Luca, S. Rubini, M. Felici, A. Meaney, P. C. M. Christianen, F. Martelli, and A. Polimeni. "Addressing the Fundamental Electronic Properties of Wurtzite GaAs Nanowires by High-Field Magneto-Photoluminescence Spectroscopy". In: *Nano Letters* 17.11 (2017), pp. 6540–6547. DOI: 10.1021/acs.nanolett.7b02189 *Cited on pages 157, 158, 162.*

[232] N. Vainorius, S. Lehmann, D. Jacobsson, L. Samuelson, K. A. Dick, and M.-E. Pistol. "Confinement in Thickness-Controlled GaAs Polytype Nanodots". In: *Nano Letters* 15.4 (2015), pp. 2652–2656. DOI: 10.1021/acs.nanolett.5b00253 *Cited on pages 157, 158.*

[233] M. Murayama and T. Nakayama. "Chemical Trend of Band Offsets at Wurtzite/Zinc-Blende Heterocrystalline Semiconductor Interfaces". In: *Physical Review B* 49.7 (1994), pp. 4710–4724. DOI: 10.1103/PhysRevB.49.4710 *Cited on page 157.*

[234] M. Heiss, S. Conesa-Boj, J. Ren, H.-H. Tseng, A. Gali, A. Rudolph, E. Uccelli, F. Peiró, J. R. Morante, D. Schuh, E. Reiger, E. Kaxiras, J. Arbiol, and A. Fontcuberta i Morral. "Direct Correlation of Crystal Structure and Optical Properties in Wurtzite/Zinc-Blende GaAs Nanowire Heterostructures". In: *Physical Review B* 83.4 (2011), p. 045303. DOI: 10.1103/PhysRevB.83.045303 *Cited on page 157.*

[235] D. Spirkoska, J. Arbiol, A. Gustafsson, S. Conesa-Boj, F. Glas, I. Zardo, M. Heigoldt, M. H. Gass, A. L. Bleloch, S. Estrade, M. Kaniber, J. Rossler, F. Peiro, J. R. Morante, G. Abstreiter, L. Samuelson, and A. Fontcuberta i Morral. "Structural and Optical Properties of High Quality Zinc-Blende/Wurtzite GaAs Nanowire Heterostructures". In: *Physical Review B* 80.24 (2009), p. 245325. DOI: 10.1103/PhysRevB.80.245325 *Cited on page 157.*

[236] U. Jahn, J. Lähnemann, C. Pfüller, O. Brandt, S. Breuer, B. Jenichen, M. Ramsteiner, L. Geelhaar, and H. Riechert. "Luminescence of GaAs Nanowires Consisting of Wurtzite and Zinc-Blende Segments". In: *Physical Review B* 85.4 (2012), p. 045323. DOI: 10.1103/PhysRevB.85.045323 *Cited on page 157.*

[237] O. Demichel, M. Heiss, J. Bleuse, H. Mariette, and A. Fontcuberta i Morral. "Impact of Surfaces on the Optical Properties of GaAs Nanowires". In: *Applied Physics Letters* 97.20 (2010), p. 201907. DOI: 10.1063/1.3519980 *Cited on page 159.*

[238] B. Ketterer. "Determination of the Band Gap and the Split-off Band in Wurtzite GaAs Using Raman and Photoluminescence Excitation Spectroscopy". In: *Physical Review B* 83.12 (2011). DOI: 10.1103/PhysRevB.83.125307 *Cited on page 162.*

[239] K. Masu, M. Konagai, and K. Takahashi. "Diffusion of Beryllium into GaAs during Liquid Phase Epitaxial Growth of P-Ga0.2Al0.8As". In: *Journal of Applied Physics* 54.3 (1983), pp. 1574–1578. DOI: 10.1063/1.332139 *Cited on page 165.*

[240] A. Casadei, P. Krogstrup, M. Heiss, J. A. Röhr, C. Colombo, T. Ruelle, S. Upadhyay, C. B. Sørensen, J. Nygård, and A. Fontcuberta i Morral. "Doping Incorporation Paths in Catalyst-Free Be-Doped GaAs Nanowires". In: *Applied Physics Letters* 102.1 (2013), p. 013117. DOI: 10.1063/1.4772020 *Cited on page 165.*

[241] Y. Zhang, Z. Sun, A. M. Sanchez, M. Ramsteiner, M. Aagesen, J. Wu, D. Kim, P. Jurczak, S. Huo, L. J. Lauhon, and H. Liu. "Doping of Self-Catalyzed Nanowires under the Influence of Droplets". In: *Nano Letters* 18.1 (2018), pp. 81–87. DOI: 10.1021/acs.nanolett.7b03366 *Cited on page 165.*

[242] Y. Zhang, H. A. Fonseka, M. Aagesen, J. A. Gott, A. M. Sanchez, J. Wu, D. Kim, P. Jurczak, S. Huo, and H. Liu. "Growth of Pure Zinc-Blende GaAs(P) Core–Shell Nanowires with Highly Regular Morphology". In: *Nano Letters* 17.8 (2017), pp. 4946–4950. DOI: 10.1021/acs.nanolett.7b02063 *Cited on page 165.*

[243] M. Hilse, M. Ramsteiner, S. Breuer, L. Geelhaar, and H. Riechert. "Incorporation of the Dopants Si and Be into GaAs Nanowires". In: *Applied Physics Letters* 96.19 (2010), p. 193104. DOI: 10.1063/1.3428358 *Cited on page 165.*

[244] Y. J. Sun, O. Brandt, M. Ramsteiner, H. T. Grahn, and K. H. Ploog. "Polarization Anisotropy of the Photoluminescence of M-Plane (In,Ga)N/GaN Multiple Quantum Wells". In: *Applied Physics Letters* 82.22 (2003), pp. 3850–3852. DOI: 10.1063/1.1579563 *Cited on page 172.*

[245] Y. G. Chai, R. Chow, and C. E. C. Wood. "The Effect of Growth Conditions on Si Incorporation in Molecular Beam Epitaxial GaAs". In: *Applied Physics Letters* 39.10 (1981), pp. 800–803. DOI: 10.1063/1.92562 *Cited on page 175.*

[246] C. Domke. "Microscopic Identification of the Compensation Mechanisms in Si-Doped GaAs". In: *Physical Review B* 54.15 (1996), pp. 10288–10291. DOI: 10.1103/PhysRevB.54.10288 *Cited on page 175.*

[247] J. M. Ballingall and C. E. C. Wood. "Crystal Orientation Dependence of Silicon Autocompensation in Molecular Beam Epitaxial Gallium Arsenide". In: *Applied Physics Letters* 41.10 (1982), pp. 947–949. DOI: 10.1063/1.93345 *Cited on page 175.*

[248] E. S. Tok, J. H. Neave, M. J. Ashwin, B. A. Joyce, and T. S. Jones. "Growth of Si-Doped GaAs(110) Thin Films by Molecular Beam Epitaxy; Si Site Occupation and the Role of Arsenic". In: *Journal of Applied Physics* 83.8 (1998), pp. 4160–4167. DOI: 10.1063/1.367169 *Cited on pages 175, 176.*

[249] L. Pavesi and M. Henini. "Photoluminescence Investigation of Si-Doped GaAs Grown by Molecular Beam Epitaxy on Non-(100) Oriented Surfaces". In: *Microelectronics Journal.* Novel Index Semiconductor Surfaces: Growth, Characterization and Devices 28.8 (1997), pp. 717–726. DOI: 10.1016/S0026-2692(96)00109-7 *Cited on page 175.*

[250] D. T. J. Hurle. "A Comprehensive Thermodynamic Analysis of Native Point Defect and Dopant Solubilities in Gallium Arsenide". In: *Journal of Applied Physics* 85.10 (1999), pp. 6957–7022. DOI: 10.1063/1.370506 *Cited on page 175.*

[251] J. Dufouleur, C. Colombo, T. Garma, B. Ketterer, E. Uccelli, M. Nicotra, and A. Fontcuberta i Morral. "P-Doping Mechanisms in Catalyst-Free Gallium Arsenide Nanowires". In: *Nano Letters* 10.5 (2010), pp. 1734–1740. DOI: 10.1021/nl100157w *Cited on page 175.*

[252] R. C. Newman. "The Lattice Locations of Silicon Impurities in GaAs: Effects Due to Stoichiometry, the Fermi Energy, the Solubility Limit and DX Behaviour". In: *Semiconductor Science and Technology* 9.10 (1994), p. 1749. DOI: 10.1088/0268-1242/9/10/001 *Cited on page 175.*

References for Chapter 7: GaAs Nanowire-Based Solar Cells

[22] S. M. Sze and K. K. Ng. *Physics of Semiconductor Devices.* 3 edition. Hoboken, N.J: Wiley-Interscience, 2006 *Cited on pages 23, 30, 31, 123, 206.*

[58] Y. Xu, T. Gong, and J. N. Munday. "The Generalized Shockley-Queisser Limit for Nanostructured Solar Cells". In: *Scientific Reports* 5 (2015), p. 13536. DOI: 10.1038/srep13536 *Cited on pages 58, 193.*

[88] I. Åberg, G. Vescovi, D. Asoli, U. Naseem, J. P. Gilboy, C. Sundvall, A. Dahlgren, K. E. Svensson, N. Anttu, M. T. Björk, and L. Samuelson. "A GaAs Nanowire Array Solar Cell With 15.3% Efficiency at 1 Sun". In: *IEEE Journal of Photovoltaics* 6.1 (2016), pp. 185–190. DOI: 10.1109/JPHOTOV.2015.2484967 *Cited on pages 75, 196, 199, 222.*

[157] A. C. E. Chia, N. Dhindsa, J. P. Boulanger, B. A. Wood, S. S. Saini, and R. R. LaPierre. "Nanowire Dopant Measurement Using Secondary Ion Mass Spectrometry". In: *Journal of Applied Physics* 118.11 (2015), p. 114306. DOI: 10.1063/1.4931148 *Cited on pages 120, 194.*

[192] M. Yao, S. Cong, S. Arab, N. Huang, M. L. Povinelli, S. B. Cronin, P. D. Dapkus, and C. Zhou. "Tandem Solar Cells Using GaAs Nanowires on Si: Design, Fabrication, and Observation of Voltage Addition". In: *Nano Letters* 15.11 (2015), pp. 7217–7224. DOI: 10.1021/acs.nanolett.5b03890 *Cited on pages 146, 195, 196, 203.*

[253] R. Yan, D. Gargas, and P. Yang. "Nanowire Photonics". In: *Nature Photonics* 3.10 (2009), pp. 569–576. DOI: 10.1038/nphoton.2009.184 *Cited on page 191.*

[254] L. Cao, P. Fan, A. P. Vasudev, J. S. White, Z. Yu, W. Cai, J. A. Schuller, S. Fan, and M. L. Brongersma. "Semiconductor Nanowire Optical Antenna Solar Absorbers". In: *Nano Letters* 10.2 (2010), pp. 439–445. DOI: 10.1021/nl9036627 *Cited on page 191.*

[255] G. Grzela, R. Paniagua-Domínguez, T. Barten, Y. Fontana, J. A. Sánchez-Gil, and J. Gómez Rivas. "Nanowire Antenna Emission". In: *Nano Letters* 12.11 (2012), pp. 5481–5486. DOI: 10.1021/nl301907f *Cited on page 191.*

[256] V. Piazza, L. Mancini, H.-L. Chen, S. Collin, and M. Tchernycheva. "Chapter Four - Nanoscale Analyses Applied to Nanowire Devices". In: *Semiconductors and Semimetals*. Ed. by S. Mokkapati and C. Jagadish. Vol. 98. Nanowires for Energy Applications. Elsevier, 2018, pp. 231–319. DOI: 10.1016/bs.semsem.2018.03.001 *Cited on page 192.*

[257] C. Colombo, M. Heiβ, M. Grätzel, and A. F. i Morral. "Gallium Arsenide P-i-n Radial Structures for Photovoltaic Applications". In: *Applied Physics Letters* 94.17 (2009), p. 173108. DOI: 10.1063/1.3125435 *Cited on pages 192, 193.*

[258] P. Krogstrup, H. I. Jørgensen, M. Heiss, O. Demichel, J. V. Holm, M. Aagesen, J. Nygard, and A. Fontcuberta i Morral. "Single-Nanowire Solar Cells beyond the Shockley-Queisser Limit". In: *Nature Photonics* 7.4 (2013), pp. 306–310. DOI: 10.1038/nphoton.2013.32 *Cited on pages 192, 193.*

[259] J. V. Holm, H. I. Jørgensen, P. Krogstrup, J. Nygård, H. Liu, and M. Aagesen. "Surface-Passivated GaAsP Single-Nanowire Solar Cells Exceeding 10% Efficiency Grown on Silicon". In: *Nature Communications* 4 (2013), p. 1498. DOI: 10.1038/ncomms2510 *Cited on page 192.*

[260] J. A. Czaban, D. A. Thompson, and R. R. LaPierre. "GaAs Core-Shell Nanowires for Photovoltaic Applications". In: *Nano Letters* 9.1 (2009), pp. 148–154. DOI: 10.1021/nl802700u *Cited on page 193.*

[261] N. Tajik, Z. Peng, P. Kuyanov, and R. R. LaPierre. "Sulfur Passivation and Contact Methods for GaAs Nanowire Solar Cells". In: *Nanotechnology* 22.22 (2011), p. 225402. DOI: 10.1088/0957-4484/22/22/225402 *Cited on page 193.*

[262] J. P. Boulanger, A. C. E. Chia, B. Wood, S. Yazdi, T. Kasama, M. Aagesen, and R. R. LaPierre. "Characterization of a Ga-Assisted GaAs Nanowire Array Solar Cell on Si Substrate". In: *IEEE Journal of Photovoltaics* PP.99 (2016), pp. 1–7. DOI: 10.1109/JPHOTOV.2016.2537547 *Cited on pages 193–195, 210, 212.*

[263] S. Yazdi, A. Berg, M. T. Borgström, T. Kasama, M. Beleggia, L. Samuelson, and J. B. Wagner. "Doping GaP Core-Shell Nanowire Pn-Junctions: A Study by Off-Axis Electron Holography". In: *Small* 11.22 (2015), pp. 2687–2695. DOI: 10.1002/smll.201403361 *Cited on page 194.*

[264] N. I. Goktas, E. M. Fiordaliso, and R. R. LaPierre. "Doping Assessment in GaAs Nanowires". In: *Nanotechnology* 29.23 (2018), p. 234001. DOI: 10.1088/1361-6528/aab6f1 *Cited on pages 194, 212.*

[265] G. Mariani, P.-S. Wong, A. M. Katzenmeyer, F. Léonard, J. Shapiro, and D. L. Huffaker. "Patterned Radial GaAs Nanopillar Solar Cells". In: *Nano Letters* 11.6 (2011), pp. 2490–2494. DOI: 10.1021/nl200965j *Cited on pages 194, 210.*

[266] G. Mariani, A. C. Scofield, C.-H. Hung, and D. L. Huffaker. "GaAs Nanopillar-Array Solar Cells Employing in Situ Surface Passivation". In: *Nature Communications* 4 (2013), p. 1497. DOI: 10.1038/ncomms2509 *Cited on pages 194, 210.*

[267] G. Mariani, Z. Zhou, A. Scofield, and D. L. Huffaker. "Direct-Bandgap Epitaxial Core–Multishell Nanopillar Photovoltaics Featuring Subwavelength Optical Concentrators". In: *Nano Letters* 13.4 (2013), pp. 1632–1637. DOI: 10.1021/nl400083g *Cited on pages 194, 195.*

[268] M. Yao, N. Huang, S. Cong, C.-Y. Chi, M. A. Seyedi, Y.-T. Lin, Y. Cao, M. L. Povinelli, P. D. Dapkus, and C. Zhou. "GaAs Nanowire Array Solar Cells with Axial P-i-n Junctions". In: *Nano Letters* 14.6 (2014), pp. 3293–3303. DOI: 10.1021/nl500704r *Cited on page 194.*

[269] H. Goto, K. Nosaki, K. Tomioka, S. Hara, K. Hiruma, J. Motohisa, and T. Fukui. "Growth of Core–Shell InP Nanowires for Photovoltaic Application by Selective-Area Metal Organic Vapor Phase Epitaxy". In: *Applied Physics Express* 2.3 (2009), p. 035004. DOI: 10.1143/APEX.2.035004 *Cited on page 196.*

[270] M. Yoshimura, E. Nakai, K. Tomioka, and T. Fukui. "Indium Phosphide Core–Shell Nanowire Array Solar Cells with Lattice-Mismatched Window Layer". In: *Applied Physics Express* 6.5 (2013), p. 052301. DOI: 10.7567/APEX.6.052301 *Cited on page 196.*

[271] Y. Cui, J. Wang, S. R. Plissard, A. Cavalli, T. T. T. Vu, R. P. J. van Veldhoven, L. Gao, M. Trainor, M. A. Verheijen, J. E. M. Haverkort, and E. P. A. M. Bakkers. "Efficiency Enhancement of InP Nanowire Solar Cells by Surface Cleaning". In: *Nano Letters* 13.9 (2013), pp. 4113–4117. DOI: 10.1021/nl4016182 *Cited on page 196.*

[272] J. Wallentin, N. Anttu, D. Asoli, M. Huffman, I. Åberg, M. H. Magnusson, G. Siefer, P. Fuss-Kailuweit, F. Dimroth, B. Witzigmann, H. Q. Xu, L. Samuelson, K. Deppert, and M. T. Borgström. "InP Nanowire Array Solar Cells Achieving 13.8% Efficiency by Exceeding the Ray Optics Limit". In: *Science* 339.6123 (2013), pp. 1057–1060. DOI: 10.1126/science.1230969 *Cited on page 196.*

[273] D. van Dam, N. J. J. van Hoof, Y. Cui, P. J. van Veldhoven, E. P. A. M. Bakkers, J. Gómez Rivas, and J. E. M. Haverkort. "High-Efficiency Nanowire Solar Cells with Omnidirectionally Enhanced Absorption Due to Self-Aligned Indium–Tin–Oxide Mie Scatterers". In: *ACS Nano* 10.12 (2016), pp. 11414–11419. DOI: 10.1021/acsnano.6b06874 *Cited on page 196.*

[274] M. Foldyna, L. Yu, and P. Roca i Cabarrocas. "Theoretical Short-Circuit Current Density for Different Geometries and Organizations of Silicon Nanowires in Solar Cells". In: *Solar Energy Materials and Solar Cells* 117 (2013), pp. 645–651. DOI: 10.1016/j.solmat.2012.10.014 *Cited on pages 197, 201.*

[275] S. Mokkapati, D. Saxena, H. H. Tan, and C. Jagadish. "Optical Design of Nanowire Absorbers for Wavelength Selective Photodetectors". In: *Scientific Reports* 5 (2015), p. 15339. DOI: 10.1038/srep15339 *Cited on page 199.*

[276] B. C. P. Sturmberg, K. B. Dossou, L. C. Botten, A. A. Asatryan, C. G. Poulton, R. C. McPhedran, and C. M. de Sterke. "Optimizing Photovoltaic Charge Generation of Nanowire Arrays: A Simple Semi-Analytic Approach". In: *ACS Photonics* 1.8 (2014), pp. 683–689. DOI: 10.1021/ph500212y *Cited on page 200.*

[277] K. T. Fountaine, W. S. Whitney, and H. A. Atwater. "Resonant Absorption in Semiconductor Nanowires and Nanowire Arrays: Relating Leaky Waveguide Modes to Bloch Photonic Crystal Modes". In: *Journal of Applied Physics* 116.15 (2014), p. 153106. DOI: 10.1063/1.4898758 *Cited on page 200.*

[278] N. Anttu and H. Q. Xu. "Efficient Light Management in Vertical Nanowire Arrays for Photovoltaics". In: *Optics Express* 21.103 (2013), A558–A575. DOI: 10.1364/OE.21.00A558 *Cited on page 201.*

[279] K. T. Fountaine, C. G. Kendall, and H. A. Atwater. "Near-Unity Broadband Absorption Designs for Semiconducting Nanowire Arrays via Localized Radial Mode Excitation". In: *Optics Express* 22.103 (2014), A930–A940. DOI: 10.1364/OE.22.00A930 *Cited on page 201.*

[280] D. Wu, X. Tang, K. Wang, and X. Li. "Effective Coupled Optoelectrical Design Method for Fully Infiltrated Semiconductor Nanowires Based Hybrid Solar Cells". In: *Optics Express* 24.22 (2016), A1336–A1348. DOI: 10.1364/OE.24.0A1336 *Cited on page 201.*

[281] D. E. Aspnes. "Recombination at Semiconductor Surfaces and Interfaces". In: *Surface Science* 132.1 (1983), pp. 406–421. DOI: 10.1016/0039-6028(83)90550-2 *Cited on page 205.*

[282] A. C. E. Chia and R. R. LaPierre. "Analytical Model of Surface Depletion in GaAs Nanowires". In: *Journal of Applied Physics* 112.6 (2012), p. 063705. DOI: 10.1063/1.4752873 *Cited on page 206.*

[283] A. C. E. Chia and R. R. LaPierre. "Electrostatic Model of Radial Pn Junction Nanowires". In: *Journal of Applied Physics* 114.7 (2013), p. 074317. DOI: 10.1063/1.4818958 *Cited on pages 207, 209.*

[284] R. R. LaPierre. "Numerical Model of Current-Voltage Characteristics and Efficiency of GaAs Nanowire Solar Cells". In: *Journal of Applied Physics* 109.3 (2011), p. 034311. DOI: 10.1063/1.3544486 *Cited on page 209.*

[285] Z. Li, Y. C. Wenas, L. Fu, S. Mokkapati, H. H. Tan, and C. Jagadish. "Influence of Electrical Design on Core-Shell GaAs Nanowire Array Solar Cells". In: *IEEE Journal of Photovoltaics* 5.3 (2015), pp. 854–864. DOI: 10.1109/JPHOTOV.2015.2405753 *Cited on page 209.*

[286] Y. Wu, X. Yan, W. Wei, J. Zhang, X. Zhang, and X. Ren. "Optimization of GaAs Nanowire Pin Junction Array Solar Cells by Using AlGaAs/GaAs Heterojunctions". In: *Nanoscale Research Letters* 13 (2018), p. 126. DOI: 10.1186/s11671-018-2503-8 *Cited on page 209.*

[287] Z.-x. Yang, Y. Yin, J. Sun, L. Bian, N. Han, Z. Zhou, L. Shu, F. Wang, Y. Chen, A. Song, and J. C. Ho. "Chalcogen Passivation: An in-Situ Method to Manipulate the Morphology and Electrical Property of GaAs Nanowires". In: *Scientific Reports* 8.1 (2018), p. 6928. DOI: 10.1038/s41598-018-25209-x *Cited on page 210.*

[288] J. E. Moore, S. Dongaonkar, R. V. K. Chavali, M. A. Alam, and M. S. Lundstrom. "Correlation of Built-In Potential and I-V Crossover in Thin-Film Solar Cells". In: *IEEE Journal of Photovoltaics* 4.4 (2014), pp. 1138–1148. DOI: 10.1109/JPHOTOV.2014.2316364 *Cited on page 213.*

References for Chapter A: Résumé en français

[74] G. J. Bauhuis, P. Mulder, E. J. Haverkamp, J. C. C. M. Huijben, and J. J. Schermer. "26.1% Thin-Film GaAs Solar Cell Using Epitaxial Lift-Off". In: *Solar Energy Materials and Solar Cells* 93.9 (2009), pp. 1488–1491. DOI: 10.1016/j.solmat.2009.03.027 *Cited on pages 72, 75, 222.*

[75] B. M. Kayes, H. Nie, R. Twist, S. G. Spruytte, F. Reinhardt, I. C. Kizilyalli, and G. S. Higashi. "27.6% Conversion Efficiency, a New Record for Single-Junction Solar Cells under 1 Sun Illumination". In: *2011 37th IEEE Photovoltaic Specialists Conference*. 2011, pp. 000004–000008. DOI: 10.1109/PVSC.2011.6185831 *Cited on pages 72, 75, 113, 222.*

[82] N. Vandamme, H. L. Chen, A. Gaucher, B. Behaghel, A. Lemaître, A. Cattoni, C. Dupuis, N. Bardou, J. F. Guillemoles, and S. Collin. "Ultrathin GaAs Solar Cells With a Silver Back Mirror". In: *IEEE Journal of Photovoltaics* 5.2 (2015), pp. 565–570. DOI: 10.1109/JPHOTOV.2014.2371236 *Cited on pages 74, 75, 96, 222.*

[84] K. Nakayama, K. Tanabe, and H. A. Atwater. "Plasmonic Nanoparticle Enhanced Light Absorption in GaAs Solar Cells". In: *Applied Physics Letters* 93.12 (2008), p. 121904. DOI: 10.1063/1.2988288 *Cited on pages 75, 222.*

[85] W. Liu, X. Wang, Y. Li, Z. Geng, F. Yang, and J. Li. "Surface Plasmon Enhanced GaAs Thin Film Solar Cells". In: *Solar Energy Materials and Solar Cells* 95.2 (2011), pp. 693–698. DOI: 10.1016/j.solmat.2010.10.004 *Cited on pages 75, 222.*

[86] W. Yang, J. Becker, S. Liu, Y.-S. Kuo, J.-J. Li, B. Landini, K. Campman, and Y.-H. Zhang. "Ultra-Thin GaAs Single-Junction Solar Cells Integrated with a Reflective Back Scattering Layer". In: *Journal of Applied Physics* 115.20 (2014), p. 203105. DOI: 10.1063/1.4878156 *Cited on pages 74, 75, 222.*

[87] S.-M. Lee, A. Kwong, D. Jung, J. Faucher, R. Biswas, L. Shen, D. Kang, M. L. Lee, and J. Yoon. "High Performance Ultrathin GaAs Solar Cells Enabled with Heterogeneously Integrated Dielectric Periodic Nanostructures". In: *ACS Nano* 9.10 (2015), pp. 10356–10365. DOI: 10.1021/acsnano.5b05585 *Cited on pages 75, 76, 222.*

[88] I. Åberg, G. Vescovi, D. Asoli, U. Naseem, J. P. Gilboy, C. Sundvall, A. Dahlgren, K. E. Svensson, N. Anttu, M. T. Björk, and L. Samuelson. "A GaAs Nanowire Array Solar Cell With 15.3% Efficiency at 1 Sun". In: *IEEE Journal of Photovoltaics* 6.1 (2016), pp. 185–190. DOI: 10.1109/JPHOTOV.2015.2484967 *Cited on pages 75, 196, 199, 222.*

université PARIS-SACLAY
ÉCOLE DOCTORALE
Physique et ingénierie : électrons, photons, sciences du vivant (EOBE)

Titre : Cellules solaires en GaAs ultra-minces et à base de nanofils

Mots clés : photovoltaïque, GaAs, piégeage optique, nanofils, dopage, cathodoluminescence

Résumé : Confiner la lumière dans un volume réduit d'absorbeur photovoltaïque offre de nouvelles voies pour les cellules solaires à haute rendement. Ceci peut être réalisé en utilisant des nanostructures pour le piégeage optique ou des nanofils de semi-conducteurs. Dans une première partie, nous présentons la conception et la fabrication de cellules solaires ultra-minces (205 nm) en GaAs. Nous obtenons des résonances multiples grâce à un miroir arrière nanostructuré en TiO_2/Ag fabriqué par nanoimpression, résultant en un courant de court-circuit élevé de 24,6 mA/cm^2. Nous obtenons le record d'efficacité de 19,9%. Nous analysons les mécanismes des pertes et nous proposons une voie réaliste vers un rendement de 25% en utilisant un absorbeur de GaAs de 200 nm d'épaisseur seulement. Dans une deuxième partie, nous étudions les propriétés de nanofils en GaAs crûs sur substrats Si et nous explorons leur potentiel comme absorbeur photovoltaïque. Un dopage élevé est souhaité dans les cellules solaires à nanofils en jonction coeur-coquille, mais la caractérisation à l'échelle d'un nanofil unique reste difficile. Nous montrons que la cathodoluminescence (CL) peut être utilisée pour déterminer les niveaux de dopage de GaAs de type n et p avec une résolution nanométrique. Les semi-conducteurs III-V de type n présentent une émission décalée vers le bleu, à cause du remplissage de la bande de conduction, tandis que les semi-conducteurs de type p présentent une émission décalée vers le rouge due à la réduction du gap. La loi de Planck généralisée est utilisée pour fitter tout le spectre et ainsi évaluer quantitativement le niveau de dopage. Nous utilisons également la polarimétrie de CL pour déterminer sélectivement les propriétés de phases wurtzite/zinc-blende d'un nanofil unique. Nous montrons enfin des cellules solaires fonctionnelles à nanofils de GaAs. Ces travaux ouvrent des perspectives vers une nouvelle génération de cellules photovoltaïques.

Title: Ultrathin and nanowire-based GaAs solar cells

Keywords: photovoltaics, GaAs, light trapping, nanowires, doping, cathodoluminescence

Abstract: Confining sunlight in a reduced volume of photovoltaic absorber offers new directions for high-efficiency solar cells. This can be achieved using nanophotonic structures for light trapping, or semiconductor nanowires. First, we have designed and fabricated ultrathin (205 nm) GaAs solar cells. Multi-resonant light trapping is achieved with a nanostructured TiO_2/Ag back mirror fabricated using nanoimprint lithography, resulting in a high short-circuit current of 24.6 mA/cm^2. We obtain the record 1 sun efficiency of 19.9%. A detailed loss analysis is carried out and we provide a realistic pathway toward 25% efficiency using only 200 nm-thick GaAs absorber. Second, we investigate the properties of GaAs nanowires grown on Si substrates and we explore their potential as active absorber. High doping is desired in core-shell nanowire solar cells, but the characterization of single nanowires remains challenging. We show that cathodoluminescence (CL) mapping can be used to determine both n-type and p-type doping levels of GaAs with nanometer scale resolution. n-type III-V semiconductor shows characteristic blueshift emission due to the conduction band filling, while p-type semiconductor exhibits redshift emission due to the dominant bandgap narrowing. The generalized Planck's law is used to fit the whole spectra and allows for quantitative doping assessment. We also use CL polarimetry to determine selectively the properties of wurtzite and zincblende phases of single nanowires. Finally, we demonstrate successful GaAs nanowire solar cells. These works open new perspectives for next-generation photovoltaics.

Université Paris-Saclay
Espace Technologique / Immeuble Discovery
Route de l'Orme aux Merisiers RD 128 / 91190 Saint-Aubin, France